Army Science Conference Proceedings

17-19 June 1964
Volume II

Principal Authors I Through Z

OFFICE, CHIEF OF RESEARCH AND DEVELOPMENT
DEPARTMENT OF THE ARMY

AVAILABILITY NOTICE

Qualified requestors may obtain copies of this report from the Defense Documentation Center (DDC). Individual papers may be obtained by submitting appropriate AD numbers as listed in the Technical Abstract Bulletin.

Organizations or individuals not accredited to DDC may purchase unclassified separate papers or complete Volumes I or II from the Office of Technical Services, Department of Commerce, Washington, D. C., 20230.

HEADQUARTERS
DEPARTMENT OF THE ARMY
OFFICE OF THE ADJUTANT GENERAL
WASHINGTON, D.C. 20310

IN REPLY REFER TO
AGAM-P (M) (31 Dec 64) CRD/P

22 Janaury 1965

SUBJECT: 1964 Army Science Conference Proceedings

TO: SEE DISTRIBUTION

1. Inclosed for your information and use is Volume Two of the 1964 Army Science Conference Proceedings, which is comprised of the unclassified papers by principal authors I thru Z, which were presented at the conference.

2. Volumes One and Three of the Proceedings are being distributed separately.

BY ORDER OF THE SECRETARY OF THE ARMY:

J. C. LAMBERT
Major General, USA
The Adjutant General

1 Incl
Vol II, 1964 Army Science
Conference Proceedings

DISTRIBUTION:
As Indicated in Distribution
List in Volume

P R O C E E D I N G S

O F T H E

1964 ARMY SCIENCE CONFERENCE

UNITED STATES MILITARY ACADEMY, WEST POINT, N.Y.

17-19 JUNE 1964

V O L U M E II

(Principal Authors "I" thru "Z")

INTRODUCTION

1. The proceedings of the 1964 Army Science Conference is a compilation of all papers presented at the conference. Its purposes are to:

    a. Provide a historical record of the conference

    b. Provide source material for scientists engaged in research

    c. Enable conference participants to review papers in which they have a special interest

2. The report consists of three volumes as follows:

Volume I	Unclassified papers, principal authors, A thru H
Volume II	Unclassified papers, principal authors, I thru Z
Volume III	Classified papers, alphabetically by principal authors

3. Three Invited Papers, which were presented at the Opening General Session are grouped together at the beginning of Volume I. These papers are essentially different in nature inasmuch as they were oriented toward the general scientific and lay interests of a mixed audience, rather than reporting on a specific research effort within a given discipline.

4. All experiments involving live animals which are reported in the Proceedings were performed in accordance with the principles of laboratory animal care as promulgated by the National Society for Medical Research.

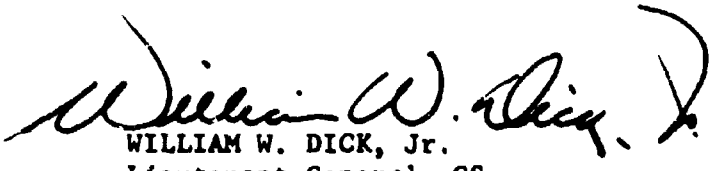

WILLIAM W. DICK, Jr.
Lieutenant General, GS
Chief of Research and Development

TABLE OF CONTENTS

PROCEEDINGS OF 1964 ARMY SCIENCE CONFERENCE

Invited Papers

AUTHOR	TITLE	VOL	PAGE
Barila, Lt. Col, T.G.	Medical Trends in Life Support Systems	1	1
Horton, B.M.	Control, Amplification and Fluids	1	9
Johnston, Brig Gen, J.W.	Army Participation in Project SYNCOM	1	23
Aaron, H.S. Ferguson, C.P., Jr.	Incapacitating Agents: Eight Stereoisomers of a Synthetic Tetrahydrocannabinol	3	1
Abbott, K.H.	Effects of Alloy Segregation on Spalling of Metallic Armor Materials	1	45
Agrios, J.P. Neudorfer, C.D. Stern, R.A.	TE_{01}^{o} Cross-Guide Transducer and Isolator	1	57
Ahearn, P.J. Quigley, F.C.	Dendritic Morphology of High-Strength Steel Castings	1	71
Ahlstrom, E.R.	SEE GERBER, E.A.	1	375
Allan, B.D. Croomes, E. Duncan, W. Murfree, J. Sandlin, B. Wharton, W.	Characterization of Nitrogen-Fluorine Containing Compounds as Propellants	3	13
Allen, H.C.	Crystallization in Solid Propellant Binders and Its Effect on Low-Temperature Missile Capability	3	27

AUTHOR	TITLE	VOL	PAGE
Alley, B.J.	Control of Propellant Composition by X-Ray Fluorescence Analysis	3	41
Anderson, V.H.	The Interpretation of Aerial Imagery of Sea Ice	3	55
Andreotti, R.	SEE KRONMAN, M.J.	2	121
Appleby, J.F. Ohmstede, W.D.	Numerical Solution of the Distribution of Wind and Turbulence in the Planetary Boundary Layer	1	85
Arendt, P.R. Papayoanou, A. Soicher, H.	Determination of the Ionospheric Electron Content Utilizing Satellite Signals	1	101
Autera, J.R.	SEE CASTORINA, T.C.	1	163
Babbitt, R.W.	SEE MALINOFSKY, W.W.	2	197
Ball, D.H. Williams, J.M. Long, L., Jr.	Potential Radiation - Protective Compounds. Synthesis of the Three Isomeric Three-Carbon Aminohydroxy Bunte Salts and Related Compounds	1	115
Balton, I.A.	SEE BOMKE, H.A.	3	99
Bauer, V.E.	SEE ROSENBLATT, D.H.	3	261
Bergdoll, M.S.	SEE SCHANTZ, E.J.	2	309
Berning, W.W.	High Altitude Ionization Associated with Nuclear Detonations	3	71
Black, Capt., J.N.	SEE CRAWLEY, G.J., 1st Lt.	1	207
Bluford, B.L., Jr.	Applications of Light-Emitting Diodes to Certain Infrared Communications and Surveillance Problems.	3	85
Blum, R.	SEE KRONMAN, M.J.	2	121

AUTHOR	TITLE	VOL	PAGE
Bomke, H.A. Balton, I.A. Grote, H.H. Harris, A.K.	Analysis of Magnetic Signals from the High-Altitude Nuclear Tests of Operation Dominic.	3	99
Brady, Lt. Col, J.V.	SEE SHARP, Capt., J.C.	2	375
Breslin, J.T.	SEE GAULE, G.K.	1	363
Brzonkala, K.J.	SEE KITTL, E.	2	105
Burke, C.L.	SEE ZEHLER, E.	2	507
Buser, R.G. Kainz, J. J. Sullivan, J.J.	The Use of Intense Pinch Discharges for Laser Illumination	1	121
Cabelli, V.J.	SEE HAYES, D.K.	1	457
Carlson, F.F.	A Paramagnetic Resonance Study of Nitrogen Atoms Trapped in X-Irradiated Alkali Azides	1	135
Cason, C.	Gas Velocity Probe for Moving Ionized Gases	1	149
Castorina, T.C. Autera, J.R.	Nitrogen-15 Tracer Studies of the Nitrolysis of Hexamethylenetetramine	1	163
Clawson, R.J.	Attenuation of ABM Radar Frequencies by High-Altitude Nuclear Fireballs	3	113
Colton, R.M. Dobbins, E.B.	Re-entry Vehicle for Radar Selectivity Evaluations	1	179
Cox, J.T. Hass, G. Ramsey, J.B.	Improved Dielectric Films for Optical and Space Applications	1	193
Crawley, 1st Lt., G.J. Black, Capt., J.N. Gray, Col., I. LeBlang, 1st Lt., W.	The Mechanism of Action of Staphylococcal Enterotoxin Poisoning	1	207
Creedon, J.E.	SEE SCHNEIDER, S.	2	331
Crim, W.M., Jr.	Closed Cycle Gas Turbine	1	221

AUTHOR	TITLE	VOL	PAGE
Croomes, E.	SEE ALLAN, B.D.	3	13
Davidson, T.E. Uy, J.C. Lee, A.P.	The Effect of Pressure on the Structure and Properties of Metals	1	237
Davis, G.T.	SEE ROSENBLATT, D.H.	3	261
Dawson, J.W. Niedenzu, K.	Hindered Rotation in Aminoboranes	1	251
Deluca, 1st Lt., D.C.	SEE ROSENBLATT, D.H.	3	261
Dienes, G.J.	SEE ROSENBLATT, D.B.	2	283
Dixon, S. Jr. Savage, R.O., Jr. Tauber, A.	High Power Microwave Device Applications for New Narrow Resonance Linewidth Planar Hexagonal Ferrites	1	261
Dobbins, E.B.	SEE COLTON, R.M.	1	179
Donnert, H.J. Sasse, R.A. Klein, N.	The Response of Selected Gamma Radiation Detectors to Radiation Delivered of Very High Dose Rates	3	127
Dressel, R.W.	Retrofugal Electron Flux from Massive Targets Irradiated with a Monoenergetic Primary Beam	1	275
Duncan, W.	SEE ALLAN, B.D.	3	13
Dunnery, D.A.	SEE SCHANTZ, E.J.	2	309
Edwards, R.L.	Functional Dependence of the Radar Cross Section of the Wake of a Re-entry Vehicle of C_DA	3	141
Egli, J.J.	Electronics Counter-Counter-Measures Design Techniques for Communications	3	155
Einberg, F.	Preparation of 5-Dinitromethyl-tetrazole from Salts of Dinitroacetonitrile	1	289

AUTHOR	TITLE	VOL	PAGE
Elder, A.S.	Modal Analysis of Transient Vibration Problems in Linearly Viscoelastic Solids	1	301
Ennulat, R.D. Sherman, R.J. Schaer, F.M.	Light Scattering by Materials in the Cholesteric Mesophase	3	169
Epstein, J.	SEE ROSENBLATT, D.H.	3	261
Ferguson, C.P., Jr.	SEE AARON, H.S.	3	1
Finkelstein, R.A.	SEE NORRIS, Capt., H.T.	2	247
Flathau, W.J. Strange, J.N.	Response of Gravity Type Dams to Nuclear Weapons Effects	3	183
Frankel, J.	The Recovery of the Ultrasonic Attenuation in Copper Single Crystals Following Small Plastic Deformation	1	317
Freitag, D.R. Powell, C.J.	Laboratory Investigation of the Mobility of Pneumatic Tires in Cohesionless Soil	1	333
Galos, G.E.	Accuracy and Information Rate Studies on Target Cross Sections Utilizing the Nike Hercules Radars	1	349
Garber, E.B.	SEE LEVINSON, H.S.	2	169
Gaule, G.K. Breslin, J.T. Ross, R.L. Logan, 2nd Lt.,R.S.	Superconductors in Advanced Electronics	1	363
Gerber, B.V.	SEE MYERS, K.A.	3	223
Gerber, E.A. Ahlstrom, E.R.	Ruby Laser with Vibrating Reflector	1	375
Gisser, H. Sadjian, S.	Evaporation of Organic Compounds from Metal Surfaces at High Vacuum	1	391
Gray, Col., I.	SEE CRAWLEY, 1st Lt., G.J.	1	207

AUTHOR	TITLE	VOL	PAGE
Gray, Col, I. Hildebrandt, Capt.,P.V.	The Effect of Hyperthermia on Protein Turnover in Infection	1	405
Green, E.	SEE SCHOENFELD, M.	2	345
Grote, H.H.	SEE BOMKE, H.A.	3	99
Hahn, F.E.	Molecular Mechanisms of Antimicrobial Action	1	413
Hardaway, Col, R.M.,III	Influence of Trauma and Hemolysis on Hemorrhagic Shock in Dogs	1	427
Harris, A.K.	SEE BOMKE, H.A.	3	99
Hass, G.	SEE COX, J.T.	1	193
Hart, Maj, W.J.,Jr. Otto, R.J. Sinclair, A.H.	Friction Hydro Pneumatic Suspension System	1	441
Hayes, D.K. Cabelli, V.J.	The Influence of Storage Aerosolization and Rehydration on the Permeability of Pasteurella Tularensis	1	457
Hearn, H.J., Jr.	SEE TRIBBLE, H.R., JR.	2	469
Hendron, 1st Lt., A.J.	SEE KENNEDY, T.E.	2	89
Henry, M.C.	Preparation and Uses of Some New Organolead Chemicals	1	469
Higgins, V.J.	X Band Semiconductor Switching and Limiting Using Waveguide Series Tees	1	477
Hildebrandt, Capt.P.V.	SEE GRAY, Col., I.	1	405
Holmes, L.	SEE KRONMAN, M.J.	2	121
Howard, C.D. Huskins, C.W.	A New Fuel for High Energy Rocket Propellants	3	199
Hsu, Y.C.	SEE SADOWSKY, M.A.	2	297

AUTHOR	TITLE	VOL	PAGE
Huber, W.A.	Monocycle Position Modulation	1	495
Hull, L.A.	SEE ROSENBLATT, D.H.	3	261
Huskins, C.W.	SEE HOWARD, C.D.	3	199
Hussain, M.A.	SEE SADOWSKY, M.A.	2	297
Ikrath, K. Schneider, W.	The Realization of Active Seismic Systems and Their Practical Applications	2	1
Jakubowski, E.H. Swieskowski, H.P.	Surge Waves in Automatic Weapons	2	15
Jones, G.R.	Surface Dependence of Magnetostatic Mode Line-Widths in Yttrium Iron Garnet	2	33
Kalmus, H.P.	A New Gravity Meter	2	41
Kains, J.J.	SEE BUSER, R.G.	1	121
Kant, A. Strauss, B.	The Maximum Dissociation Energies of Diatomic Molecules of Transition Elements	2	55
Kasemir, H.W.	The Relation Between Cloud Charges Precipitation and Lightning Discharges	2	67
Keithley, S.M.	Performance Evaluation of a Special Armor System	3	213
Kendall, D.P.	The Effect of Strain Rate on Yielding Characteristics of High Strength Alloy Steels	2	79
Kennedy, T.E. Hendron, Lt. A.J.,Jr.	The Dynamic Stress-Strain Relation for a Sand as Deduced by Studying its Shock Wave Propagation Characteristics in a Laboratory Device.	2	89
Kittl, E. Brzonkala, K.J. Shapiro, S.J.	Performance of the Germanium-Photovoltaic Cell Under Intensive Monochromatic Light	2	105

AUTHOR	TITLE	VOL	PAGE
Klein, N.	SEE DONNERT, H.J.	3	127
Kronman, M.J. Blum, R. Andreotti, R. Vitols, R. Holmes, L.	Molecular Structure and Protein Stability; The Acid Denaturation of Alpha Lactalbumin	2	121
Laible, R.C.	High Speed Penetration of Non-woven Fabric	2	137
LeBlang, Lt., W.	SEE CRAWLEY, 1st Lt., G.L.	1	207
Lee, A.P.	SEE DAVIDSON, T.E.	1	237
Lentz, S.S.	An Optical System for Measuring the Angular Motion of the Gun Tube and the Projectile in the Bore	2	153
Levinson, H.S. Garber, E.B.	Radiation Biodosimetry and Screening for Radio-protective Compounds	2	169
Logan, 2nd Lt., R.S.	SEE GAULE, G.K.	1	363
Long, L., Jr.	SEE BALL, D.H.	1	115
Lontz, R.J.	Fluorine Hyperfine Interaction in Electron Spin Resonance	2	185
Malinofsky, W.W. Babbitt, R.W. Sands, G.C.	A Novel Process for Ultra-Fine Crystallites, and their Theory and Application in Magnetic Ferrites	2	197
Martin, D.L., Jr.	Effect of Filler Concentration on the Viscoelastic Response of a Filled Polymer System	2	211
Mather, B.	The Strength of Portland Cement Concrete as Affected by Air, Water, and Cement Content	2	227

AUTHOR	TITLE	VOL	PAGE
Mertwoy, H.E.	SEE SOLLOTT, G.P.	2	441
Miller, J.I.	SEE WILLIAMSON, C.E.	2	493
Murfree, J.	SEE ALLAN, B.D.	3	13
Myers, K.A. Gerber, B.V.	Casualty Estimations for Chemical (GB) Munitions Delivery Systems	3	223
Nagle, S.C., Jr.	SEE TRIEBLE, H.R., Jr.	2	469
Nemarich, J.	Relaxation Processes in Ferromagnetic Insulators	2	233
Neudorfer, C.D.	SEE AGRIOS, J.P.	1	57
Niedenzu, K.	SEE DAWSON, J.W.	1	251
Norris, Capt., H.T. Finkelstein, R.A. Sprinz, Col., H.	A Morphologic Study of the Pathogenesis of Experimental Cholera in the Infant Rabbit	2	247
Ohmstede, W.D.	SEE APPLEBY, J.F.	1	85
Otto, R.J.	SEE HART, Maj., W.J., Jr.	1	441
Papayoanou, A.	SEE ARENDT, P.R.	1	101
Peterson, W.R., Jr.	SEE SOLLOTT, G.P.	2	441
Portnoy, S.	SEE SOLLOTT, G.P.	2	441
Powell, C.J.	SEE FREITAG, D.R.	1	333
Prickett, M.E.	An Investigation of Aerosols of Viruses Disseminated in Very Small Particles	3	235
Quigley, F.C.	SEE AHEARN, P.J.	1	71
Ramsey, J.B.	SEE COX, J.T.	1	193
Reago, D.A.	SEE SCHOENFELD, M.	2	345
Ringel, S.	Information Assimilation from Command Systems Displays	2	261

AUTHOR	TITLE	VOL	PAGE
Roessler, W.G.	SEE SCHANTZ, E.J.	2	309
Rogers, E.B.	An Electrostatic Fuse for Antiaircraft Mines and Other Antiaircraft Weapons	3	247
Romba, J.J.	A Design for Animal-Hearing Research	2	275
Rosenblatt, D.B. Dienes, G.J.	The Effect of Reactor Irradiation Upon Hydrogen Adsorption by an Alumina Catalyst	2	283
Rosenblatt, D.H. Bauer, V.E. Epstein, J. Davis, G.T. Hull, L.A. Weglein, R.C. DeLuca, Lt., D.C.	Destruction of Toxic Agents and Model Compounds with Chlorine Dioxide	3	261
Ross, R.L.	SEE GAULE, G.K.	1	363
Sadjian, S.	SEE GISSER, H.	1	391
Sadowsky, M.A. Hsu, Y.C. Hussain, M.A.	Boundary Layers in Couple-Stress Elasticity and Stiffening of Thin Layers in Shear	2	297
Sandlin, B.	SEE ALLAN, B.D.	3	13
Sands, G.C.	SEE MALINOFSKY, W.W.	2	197
Sass, S.	SEE WILLIAMSON, C.E.	2	493
Sasse, R.A.	SEE DONNERT, H.J.	3	127
Savage, R.O., Jr.	SEE DIXON, S., Jr.	1	261
Schaer, F.M.	SEE ENNULAT, R.D.	3	169
Schantz, E.J. Roessler, W.G. Wagman, J. Spero, L. Stefanye, D. Dunnery, D.A. Bergdoll, M.S.	The Purification and Characterization of Staphylococcal Enterotoxin B	2	309

AUTHOR	TITLE	VOL	PAGE
Schiel, E.J.	Direct Modulation of a HE-NE Gas Laser	2	321
Schneider, S. Creedon, J.E. Yeamans, N.L.	Hydrogen System Dependence on Discharge Parameters	2	331
Schneider, W.	SEE IKRATH, K.	2	1
Schoenfeld, M. Reago, D.A. Green, E.	Optimization of the Rotating Reflector Q-Switch	2	345
Shapiro, S.J.	SEE KITTL, E.	2	105
Sharenow, M.	New High-Altitude Fast Rising Balloons	2	361
Sharp, Capt., J.C. Brady, Lt.Col.,J.V.	The Effects of Massive Doses of Ionizing Radiation Upon Conditioned Avoidance Behavior of the Primate	2	375
Shear, R.E.	Predicted Blast Properties of Pentolite and Their Comparison with Experiment	2	391
Sherman, R.J.	SEE ENNULAT, R.D.	3	169
Silverstein, A.M.	Homograft Rejection in the Fetal Lamb	2	401
Sinclair, A.H.	SEE HART, Maj., W.J., Jr.	1	441
Sliney, J.L.	Biaxial Tensile Behavior of Anisotropic Titanium Sheet Materials	2	413
Snead, J.L.	SEE SOLLOTT, G.P.	2	441
Sodano, E.M.	Optical-Electronic Azimuth and Range Between Non-intervisible Distant Ground Stations	2	427
Soicher, H.	SEE ARENDT, P.R.	1	101

AUTHOR	TITLE	VOL	PAGE
Sollott, G.P. Snead, J.L. Portnoy, S. Peterson, W.R., Jr. Martwoy, H.E.	Phosphorus, Arsenic & Boron-Containing Ferrocene Derivatives	2	441
Soper, W.T.	SEE TRIBBLE, H.R., JR.	2	469
Spero, L.	SEE SCHANTZ, E.J.	2	309
Sprinz, Col., H.	SEE NORRIS, Capt., H.T.	2	247
Stefanye, D.	SEE SCHANTZ, E.J.	2	309
Stern, R.A.	SEE AGRIOS, J.P.	1	57
Steverding, B.	The Mechanism of Preferential Ablation	2	453
Strange, J.N.	SEE FLATHAU, W.J.	3	183
Strauss, B.	SEE KANT, A.	2	55
Sullivan, J.J.	SEE BUSER, R.G.	1	121
Swieskowski, H.P.	SEE JAKUBOWSKI, E.H.	2	15
Tauber, A.	SEE DIXON, S., JR.	1	261
Taylor, Lt., T.D.	On the Interaction of a Bow Shock of a Re-entry Body and Blast Wave	3	273
Thiele, O.W.	Ballistic Procedure for Unguided Rocket Studies of Nuclear Environments	3	289
Tribble, H.R.,Jr. Hearn, H.J., Jr. Nagle, S.C., Jr. Soper, W.T.	Growth of Selected Arboviruses in Serum-Free Suspension Cell Cultures	2	439
Uy, J. C.	SEE DAVIDSON, T.E.	1	237
Vitols, R.	SEE KRONMAN	2	121
Wagman, J.	SEE SCHANTZ, E.J.	2	309

AUTHOR	TITLE	VOL	PAGE
Walton, Maj.,B.C.	The Effect of Migrating Nematode Larve as a Provoking Factor in Viral Encephalitis in Mice	2	483
Weglein, R.C.	SEE ROSENBLATT, D.H.	3	261
Weickmann, H.K.	Mesometeorological Applications of Infrared Instrumentation	3	299
Wharton, W.	SEE ALLAN, B.D.	3	13
Williams J.M.	SEE BALL, D.H.	1	115
Williamson, C.E. Miller, J.I. Sass, S. Witten, B.	Design and Reaction Mechanism of Short-Lived Alkylating Agents	2	493
Witten, B.	SEE WILLIAMSON, C.E.	2	493
Yeamans, N.L.	SEE SCHNEIDER, S.	2	331
Zehler, E. Burke, C.L.	Measurements of True Dark Conductivities in Ferrocene Crystals	2	507

THE REALIZATION OF ACTIVE SEISMIC SYSTEMS AND THEIR PRACTICAL APPLICATIONS

KURT IKRATH and W. SCHNEIDER
U. S. ARMY ELECTRONICS RESEARCH AND DEVELOPMENT LABORATORIES
FORT MONMOUTH, NEW JERSEY

INTRODUCTION:

Steady-state seismic waves could be used for seismic communication if seismic transducers were available that would serve as efficient transmitters and receivers. An approach has been made to the development of efficient transducers with an elastic analogue to tuned radio transmitters. The latter use a quarter wave dipole antenna as a resonant matching transformer between the drive system and the radio propagation medium. Analogously, the seismic transducers described below have an artificial elastic transmission line section that acts as a resonant matching transformer between the low impedance of the electrodynamic speaker drive systems and the high mechanical impedances of seismic propagation media.

DISCUSSION:

Two transducers are shown in Figures 1 and 2. With respect to Figure 1, first and second resonant vibration modes are about 80 and 260 cps, which roughly correspond to the one-quarter and three-quarter wave resonances of the elastic transmission line. The exact operating frequency that corresponds to the ground reasonance mode depends upon the mechanical impedance of the ground medium. In this mode, the reactance part of the mechanical ground impedance is tuned by the output reactance of the elastic transmission line section. The detuning by different ground media, which is the load impedance for the transducer, is usually less than 3 cps; to compensate for frequency discrepancies that may arise when transmitter and receiver are placed on different ground media, some of the transducers have been equipped with a mechanical frequency trimmer, in the form of an adjustable large compliance in series with the mass of the drive coil.

The transmitter performance characteristics of one 80-cps transducer are shown in Figure 3. The transducer piston and vertical ground-surface displacement velocity of sand-gravel soil, and the electrical input impedance, are plotted versus frequency for constant drive power. The receiver performance characteristics of a

transducer are shown in Figure 4. Here, the open-circuit voltage output is plotted versus frequency for a constant shake-table displacement, and the practical voltage step-up ratio is given. The nominal 80 cps transducers can be operated continuously with 10 watts of drive power, and intermittently with up to 20 watts. The electrical input impedance depends upon the ground medium and is between 3 and 6 ohms. The drive system is electrodynamic, employing a permanent ceramic magnet. The static force versus deflection characteristic of the slotted steel tube which serves as the artificial elastic transmission line transformer section has a slope of 10^5 newtons/meter. The slots correspond to shunt capacitances and the mass of the slot sections correspond to serial inductances in the analogous electrical transmission line.

Though differing in size and weight, the nominal 12-cps transducer, shown in Figure 2, is similar to that of Figure 1. Here, a conventional locomotive coil spring is used as the elastic transmission-line section. The necessary high Q and low frequency of this transducer provide some difficulties for the drive circuit. Typical performance data for this transducer for sand-gravel soil are: 0.6 and 3.3 mm/sec vertical and horizontal ground-surface displacement velocities, respectively, at a distance of 1 meter, at 12.5 cps, and with 1 watt of drive power; input impedance 30.4 ohms (including 3.5 ohms d-c resistance) and 50- percent power bandwidth for constant ground-surface displacement, approximately $\pm$ 0.02 cps.

The precise efficiency of the transducers is difficult to determine. The difference of the electrical input impedance on and off the soil surface, which is in the order of 2 to 3 ohms, indicates that the efficiency is of the order of 30 percent or more. A practical measure of the efficiency of the transducers is expressed by the following experimental data: with 10 mw of transducer drive power, an 80-cps seismic signal produced in the soil of the Hexagon yard was received at a distance of 300 feet with a 2:1 signal-to-noise amplitude ratio with the use of a ParJB-4 lock-in amplifier-detector circuit to partly overcome the manmade seismic noise caused by traffic and machinery around and in the laboratory. Similarly, in the ice cover of Lake Waramough, Conn., which is approximately 40-cm thick, 80 mw of transducer drive power produced a flexural wave received at a distance of 300 feet with a transducer and an a-c millivoltmeter as 80 cps voltage with a 30-db signal-to-noise ratio.

The efficiency of the transmitter-transducer is ultimately dependent on the elastic range of the seismic medium. Specifically, local overstressing of the ground medium at the edges of the transducer piston reduces the radiation efficiency at high-drive-power levels. On sandy soil, for example, a small amount of signal strength is gained by increasing the drive-power level of the 80-cps transducers above 6 to 7 watts. These considerations, and the performance characteristics of ground-resonant transducers, largely determine the applications to which the transducers may be put in active seismic systems.

In active systems, seismic waves are launched along the surface and into the ground under the control of the system operator.

Dependent upon the particular applications (communication, geological exploration, and surveillance), the original characteristics of the waves are used either to transmit information or their variations during propagation are used to yield information about properties of the seismic medium and about natural or manmade boundary conditions of the medium. Active seismic systems may be classified by the form and function of signal paths between transmitter and receiver. The narrow bandwidth of the 80-cps transducers, for instance, limits signalling speeds to one or two bauds/sec. In all other cases, the conventional methods of signal-carrier modulation are possible within the given limits (including striking the transmitter-transducer).

On the surface of the weathered layer of the earth, the communication ranges are short. The amplitude of an 80-cps cw seismic signal received versus distance on a dirt road at the Earle Test Area, N. J., is shown in Figure 5. The wiggles of the curve come from interference between seismic-wave modes of different speeds. The system used for this measurement consists of two transducers only, a signal generator with audio amplifier, and an a-c voltmeter with preamplifier. The actual range limitations are the elastic range and the noise, which in this case comes from the wideband transistor preamplifier. When the transmitter drive power was doubled from 6 to 12 watts, there was an increase of only 25 percent in signal amplitude at 500 feet. With a more sophisticated system, using a phase-detection system with a ParJB-4 lock-in amplifier as a receiver, a communications range of up to 0.3 miles, which ran partly through a wooded area, was bridged with a 4:1 signal-to-noise amplitude ratio (Figure 6).

Since the power radiating from one transducer is limited by the elastic range of the seismic medium, there is a definite need for seismic-transmitter arrays and a means of controlling the direction of the radiated wave. Preliminary tests with a two-transducer array demonstrated that it was possible to make significant improvements in the communication range along and through the weathered layer of the earth. The propagation velocity of seismic signals in soil is extremely low, and the frequency dispersion is large.

Three different methods with corresponding circuits were used to measure the phase velocity and group velocity of seismic waves in sand-gravel soil and in floating sheets of lake ice. Measurements were made of the accumulated phase of received relative to transmitted 80-cps cw seismic signals versus distance with radio and cable feed forward systems in Figure 7a-b. The slope of the accumulated phase-versus-distance curve of Figure 8 yields the wave-length and phase velocity in the respective distance region. The phase-velocity transition from 410- to 170-m/sec occurs 22 m from the transmitter, at the same distance where the wiggle appears on the signal amplitude-versus-distance curve. Beyond 50 m distance, a high-speed propagation mode of 433 m/sec phase velocity is resumed. Practically the same values are measured with the standing-wave method in the respective distance region. The interference of a low-speed mode from one transducer with a high-speed mode of the other transducer results in the respective distance range in a double-periodic standing wave

(Figure 9). In the same way, the group velocities are measured by recording time phase of the envelope of a modulated seismic wave received at different distances from the transmitter or at different distances between receivers. We used recordings of 80-cps signals, 100 percent modulated with 0.16 cps, received at distances up to 100m. The mean group velocity on sand-gravel soil was determined to be approximately 120 m/sec at 80 cps.

By the same methods and measurement systems, the attenuation and phase velocity of 80- and 260-cps flexural waves were determined in the sheets of ice on Lake Waramoug, Conn. and Lake Hopatcong, N. J. The theoretical unique dependence of the phase and group velocity of flexural waves on the thickness of the floating ice sheets (1) was verified experimentally with a high degree of numerical accuracy. With the conventional values for the elastic properties of "standard ice" and water (1), the ice thickness on Lake Waramough was 32 cm, as derived by wavelength measurement. Eight days later, it was found to be 40 cm. The standing-wave method of measuring the flexural wavelengths at 80- and 260-cps was used at Lake Hopatcong. The experimental wavelengths ratio was found to agree within 3 percent with the theoretical ratio for the existing ice thickness of 50 cm.

The measurement of the propagation characteristics of seismic wave in sand-gravel soil, in almost entirely wooded terrain, and in lake ice supplied the necessary experience required for the applications and operation of specific active seismic systems for communications and surveillance. The systems found to be most versatile and useful are the seismic-electric feed forward and feedback systems. The open-loop system (Figure 7a), with an external signal generator, was used for phase-velocity measurements and for communication. The radio signal can be used for communications purposes and will carry one part of the information, and the seismic signal will act as the standard of coherence carrying the other part of the information required to decode the radio signal or vice versa, the radio signal can be used to supply the standard coherence for the detection of the seismic signal. Since seismic signals 30 to 40 db below the microseismic noise can be detected with this system, it is applicable to protected communications. Obviously, larger distances can be bridged by buried seismic relays analogous to radio relay, and by directed seismic wavebeams into ducting ground layers. In another application of the open-loop system, changes of propagation velocity of seismic surface waves, produced by the loading of the ground-surfaces by vehicles, are recorded as relative phase changes of the received signals. Theoretical calculations show that changes of the ground-surface boundary conditions manifest themselves as changes of attenuation and velocity of seismic waves.

Figure 10 shows a recording of the phase change of the received relative to the transmitted seismic cw signal caused by a car moving very slowly on a 70-m portion of the transmission path. In like manner, weather-produced changes of seismic-propagation characteristics of sand-gravel soil have been recorded over several weeks at the Earle Test Area. The introduction of a switching circuit which when activated by the received seismic wave, turns the seismic trans-

mitter-transducer off via radio, and upon interruption of the seismic wave reception turns the transmitter on again, leads to a seismic multivibrator system. The resultant seismic signal is a pulse-modulated single-frequency wave. Since the pulse duration depends in part on the distance and propagation characteristics of the seismic medium, it is possible to derive the group velocity from measurements of the pulse repetition rate at different distances. Natural or man-made changes of the seismic-propagation condition will bring about corresponding changes of the pulse rates. The close-loop system, (Figure 7b) without an external signal source, appears to be the most practical for surveillance. Two operating conditions are possible. With critical gain, a 50- to 150-m seismic electric-loop system acts as an extremely sensitive seismic detector. With overcritical gain, the system becomes a seismic oscillator, the frequency of which is within the limits set by the transducers dependent upon the propagation characteristics of the seismic-transmission path. Hence, quasi-static changes of the ground-surface boundary conditions (for instance by a vehicle) are therefore recorded as changes of the frequency produced by mixing of the seismic-oscillator signal with a reference signal of constant frequency. Figure 11 shows recordings of the beat-frequency signal produced by a vehicle slowly moving in the seismic-transmission path.

During these experiments, it was observed that the beat-frequency changed rather abruptly when the vehicle was about 60 m from the transmitter and 30 m from the receiver. However, the exact initial frequency of the seismic oscillator is not re-established upon removal of the vehicle from the seismic-propagation path. At present, it is possible to speculate only concerning the cause of this residual permanent change. Conceivably, it can be attributed to the permanent change of the surface-wave path produced by the tracks in the soft soil.

CONCLUSIONS:

The experimental seismic transducers, together with the ancillary devices and circuits described, proved valuable as measurement instruments in the investigation of elastic-wave propagation in sand-gravel soil and lake ice. Seismic communication at 80-cps carrier and 2-cps bandwidth, over a distance of up to 0.5 km in soil-covered, partially wooded terrain (Earle Test Area) was achieved with less than 14 watts of 80-cps transducer drive power, employing a PARJB-4 lock-in amplifier. It was found that a minimum of 10 mw of 80-cps transducer drive power is necessary for the detection of the radiated seismic signal at a distance of about 100 m on sand-gravel soil as in the courtyard of the Hexagon Building and vicinity. This figure is a measure of the efficiency of the transducers compared to other conventional seismic-wave exciters and receivers. The transducer's transmitter-conversion ratio, defined as vertical ground-surface displacement velocity at 0.305 m from the edge of the transducer piston, per square root of the drive power, is .64 mm $sec^{-1} Watt^{-\frac{1}{2}}$ and its peak electrical impedance is 6.2 ohms. The transducer's receiver-conversion ratio is 0.1 to 0.15 open-circuit volts/mm/sec ground-

surface displacement velocity. In practice, the transducer output voltage is stepped up from 6 to 16 times, with a transformer to match the transducer impedance to the input impedances of conventional transistor preamplifiers and a-c millivoltmeters. Several systems involving these transducers as seismic-wave transmitters and receivers have been designed and tested in the field. A continuous seismic-wave phase-distance graph was recorded with one of these systems. From this graph, the seismic-wave phase velocities of the various propagation modes were derived. A seismic standing-wave measurement system was designed and tested. The phase velocities of the seismic waves derived from the standing wave-versus-distance graph were found to be in agreement with those derived from the signal-versus-distance attenuation curve (1) which were predicted theoretically, and the velocity (mode) transition occurred at the same distance from the seismic transmitter.

Group-velocity measurements were made by measuring the phase of the envelope of a 100-percent modulated 80-cps seismic signal (modulated with 0.16 cps) as a function of distance between receivers. Pulse-signalling systems were tried, and it was found that the stratification of the ground produces ripples in the top of the pulses. Recordings of amplitude and phase of seismic signals were made on a continuous basis to investigate the effects of weather on the elastic-wave propagation characteristics of the weathered layer of the earth. Ground-surface loading experiments were conducted, and corresponding changes of the seismic-wave propagation conditions were recorded in various ways, with active seismic systems having open- and closed-feedback-loop circuits. The propagation characteristics of flexural waves in thin lake ice were investigated, using active seismic systems. The applied steady-state measurement methods and techniques yielded data that are in close agreement with theory, and with data derived by other investigators from conventional dynamite blast-excited wave recordings.

REFERENCE:

(1) ELASTIC WAVES in LAYERED MEDIA, Ewing, Jardetzky and Press, (McGraw-Hill 1957) pp 298 and 305.

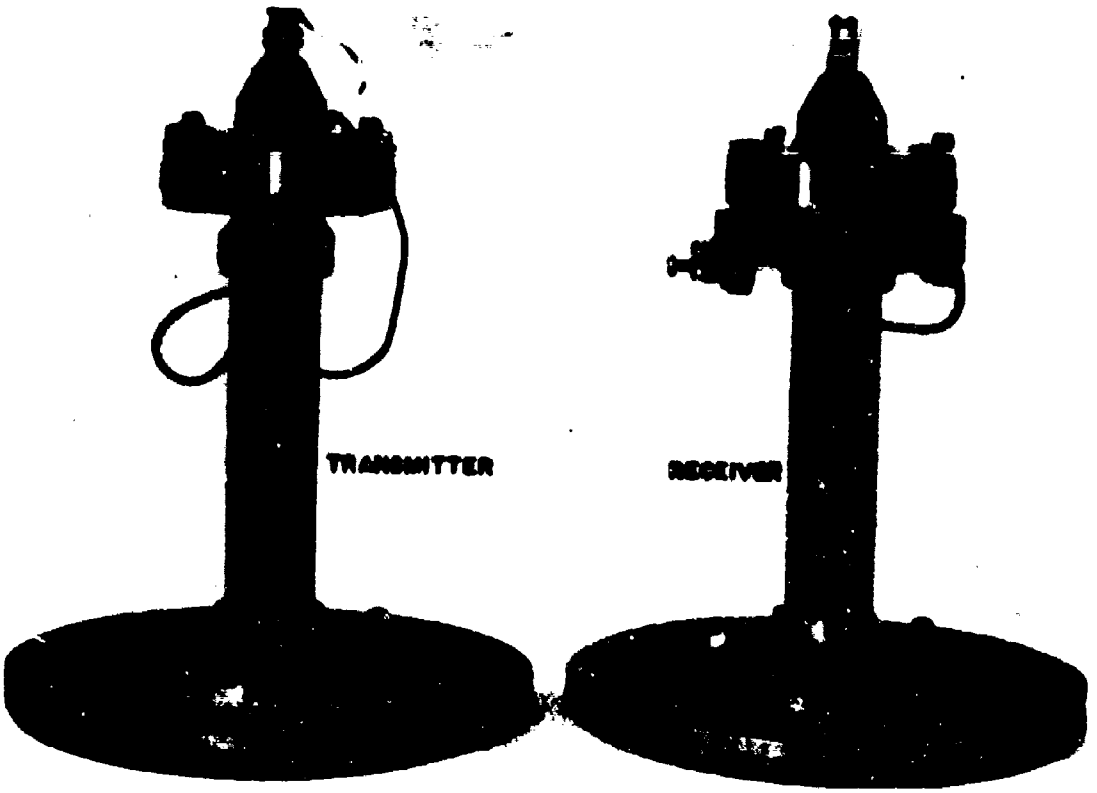

80 cps - SEISMIC TRANSDUCER WITH INDOX V MAGNET

FIG. 1

12 cps SEISMIC TRANSDUCER

FIG. 2

TD #2 RECEIVER PERFORMANCE CHARACTERISTIC.

OPEN CIRCUIT VOLTAGE OUTPUT OF TD #2 FOR CONSTANT SHAKE TABLE DISPLACEMENT OF ABOUT $\Delta = .05 \times 10^{-3}$ INCHES. (2.7 μm). VOLTAGE MEASURED WITH HP-403 A METER.

(NOTE: 12 VOLT OPEN CIRCUIT VOLTAGE STEPPED UP TO 21 VOLTS AT HP-403 A METER INPUT BY INSERTION OF VARIAC (ASSOC. TYPE 10A, SUPERELECTRIC CO. SET AT ABOUT 100:3 TO 100:4)

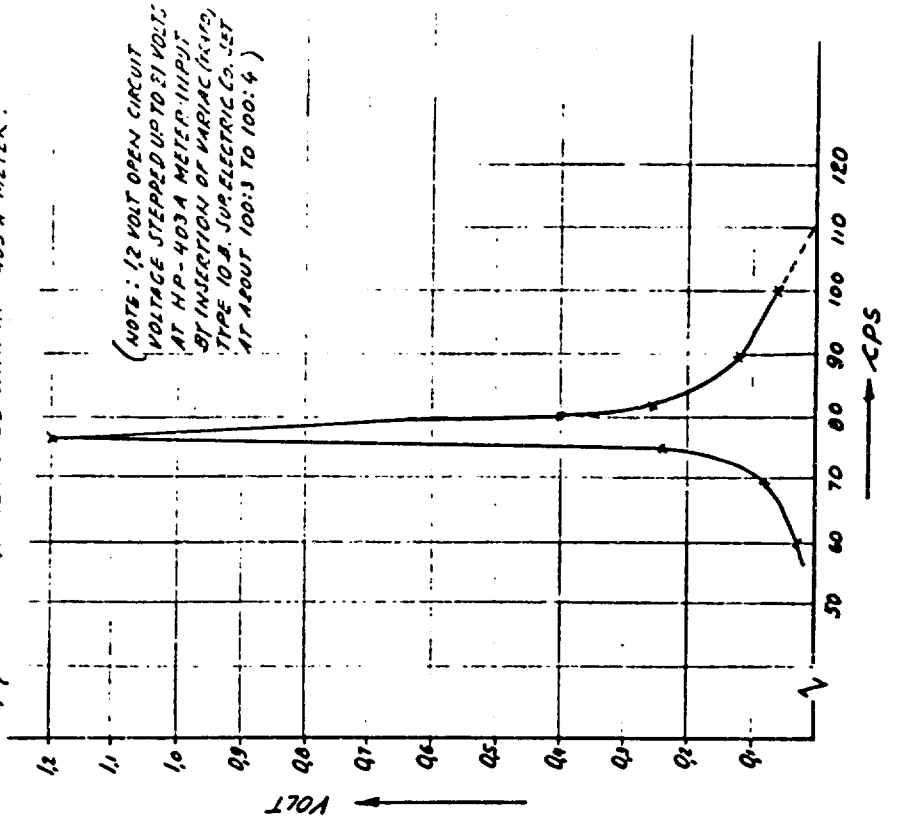

FIG. 4

TD #3 TRANSMITTER PERFORMANCE CHARACTERISTIC.

CALIBRATION OF SEISMIC TRANSDUCER TD #3 ON SAND GRADED SOIL (NEVADA TEST) WITH MB-M1 VIBRATION METER (MAY 3, 1963)
(TD #3 DRIVE POWER LEVELS: 0.39 to 0.96 WATT)

TD #3 - RMS/RMS VELOCITY AND VERTICAL GROUND SURFACE VELOCITY IN mm/sec AT ONE FOOT FROM TD #3 PER WATT DRIVE POWER, AND TD #3 ELECTRICAL INPUT IMPEDANCE Z_i IN OHMS VERSUS FREQUENCY IN CPS.

$\left(\frac{V_{Piston}}{\sqrt{P}}\right)$

$\left[\left(\frac{V_{Ground}}{\sqrt{P}}\right) \times 10\right]$ AT 1 FOOT FROM TD #3

Z_i

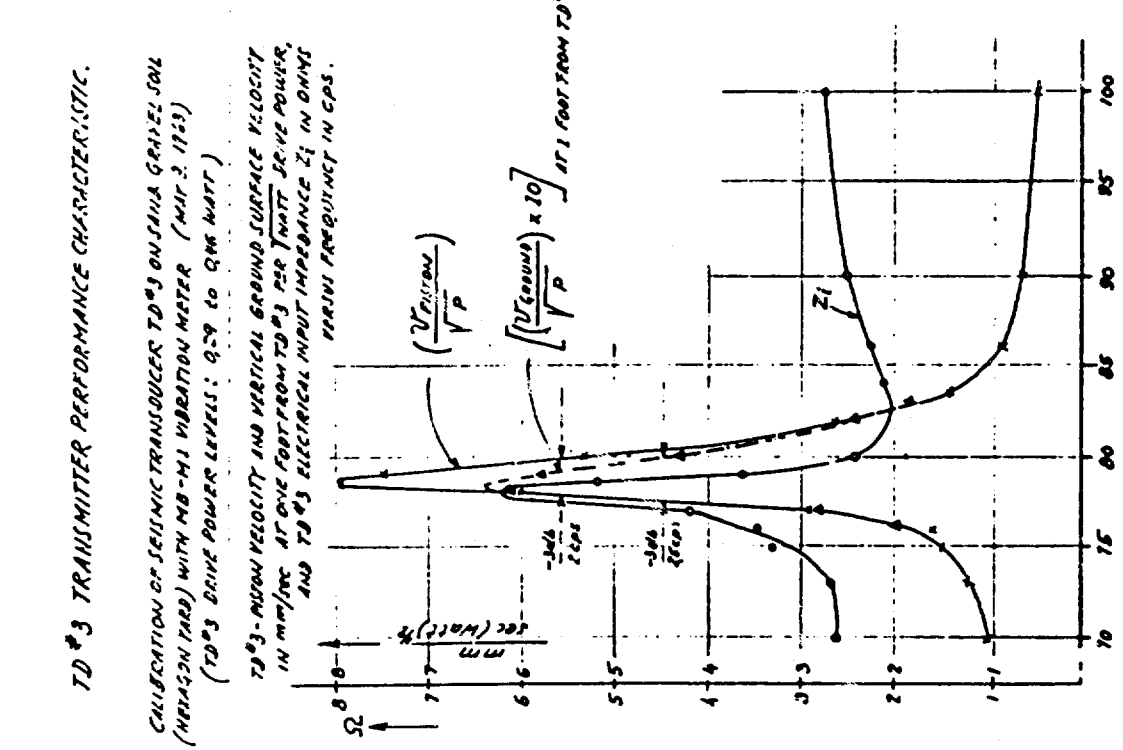

FIG. 3

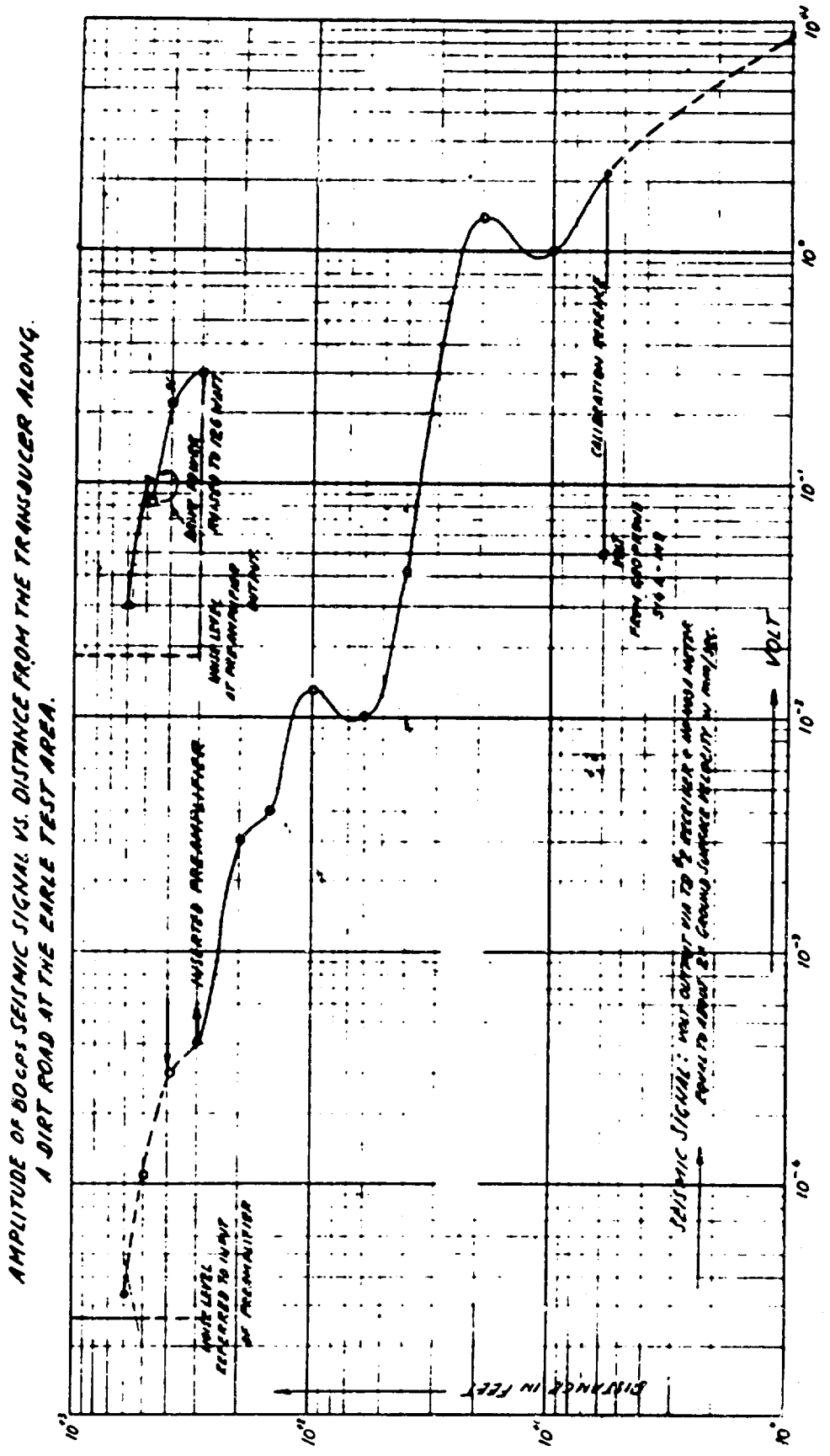
AMPLITUDE OF 60 CPS SEISMIC SIGNAL VS. DISTANCE FROM THE TRANSDUCER ALONG A DIRT ROAD AT THE EARLE TEST AREA.
DISTANCE IN FEET
VOLT
CALIBRATION PULSE
SEISMIC SIGNAL: WAS OUTPUT OF 10 PICKUPS CONNECTED IN SERIES AND FED TO A HUM BUCKING AMPLIFIER

FIG 5

TERRAIN AND EXPERIMENTAL SETUP AT EARLE TEST AREA

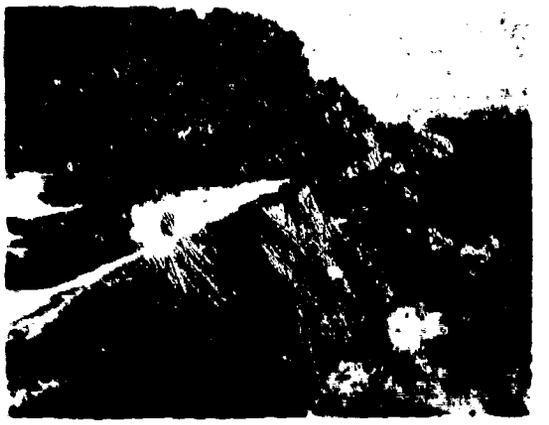

FIG. 6

SCHEMATIC OF SEISMIC ELECTRIC FEEDBACK OR FEED FORWARD SYSTEMS.

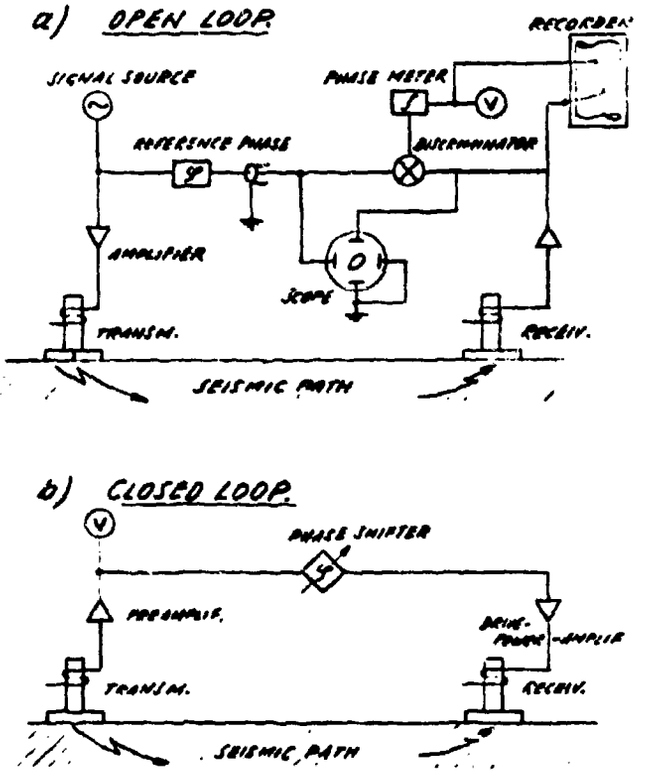

FIG. 7

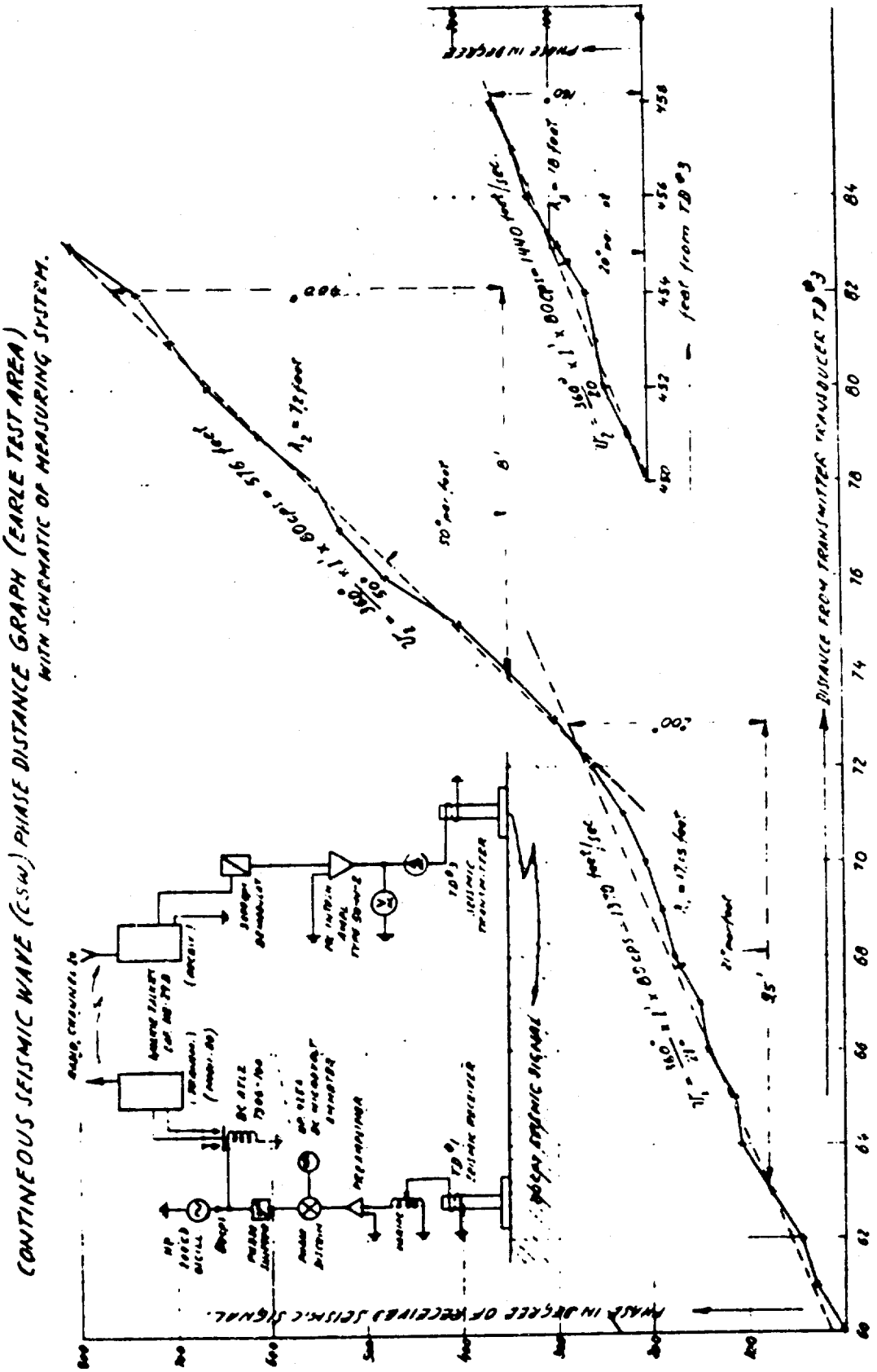
CONTINEOUS SEISMIC WAVE (CSW) PHASE DISTANCE GRAPH (EARLE TEST AREA)
WITH SCHEMATIC OF MEASURING SYSTEM.
PHASE IN DEGREE OF RECEIVED SEISMIC SIGNAL.
DISTANCE FROM TRANSMITTER TO RECEIVER
feet from TD #3
PHASE IN DEGREE

FIG 8

SEISMIC STANDING WAVE (EARLE TEST AREA) WITH SCHEMATIC OF MEASURING SYSTEM.

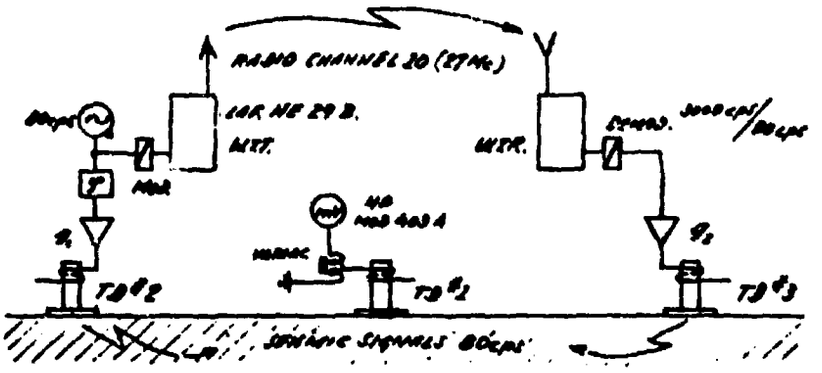

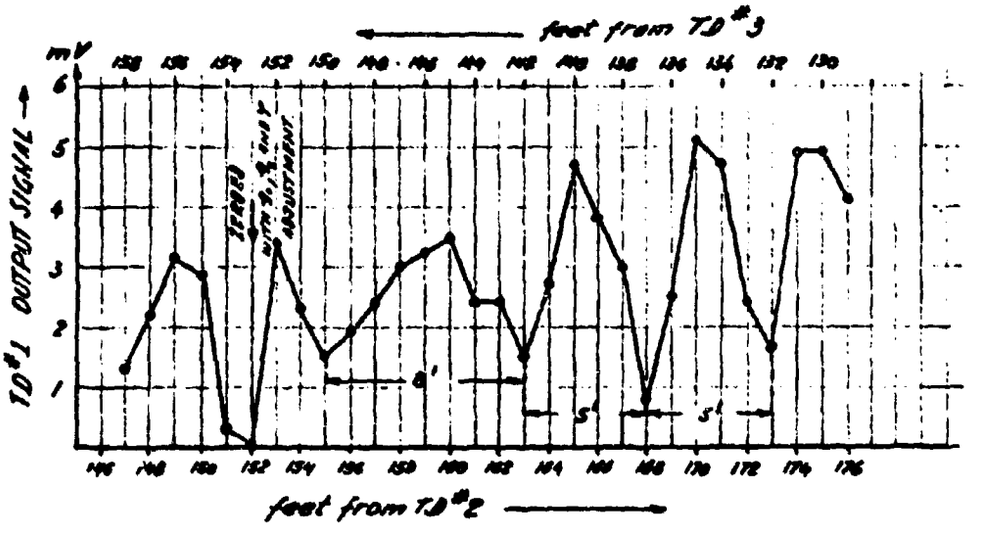

EVALUATION:

$\Delta R_1 \triangleq 8' = \frac{\lambda_1}{2}$ YIELDS $\lambda_1 \triangleq 16'$ AND $V_1 = 80\,cps \times 16' = 1280\ feet/sec.$

$\Delta R_2 \triangleq 5' = \frac{1}{\frac{1}{\lambda_2} + \frac{1}{\lambda_1}} = \frac{1}{\frac{1}{\lambda_2} + \frac{1}{16}}$ YIELDS $\lambda_2 = \frac{16 \times 5}{16 - 5} = 7{,}25'$ AND

$V_2 = 80\,cps \times 7{,}25' = 580\ feet/sec$

FIG. 9.

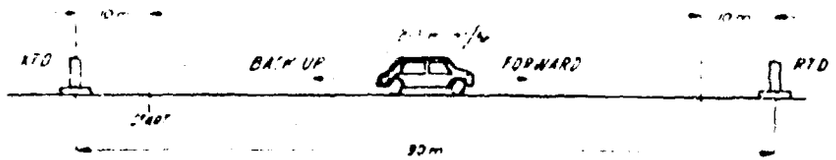

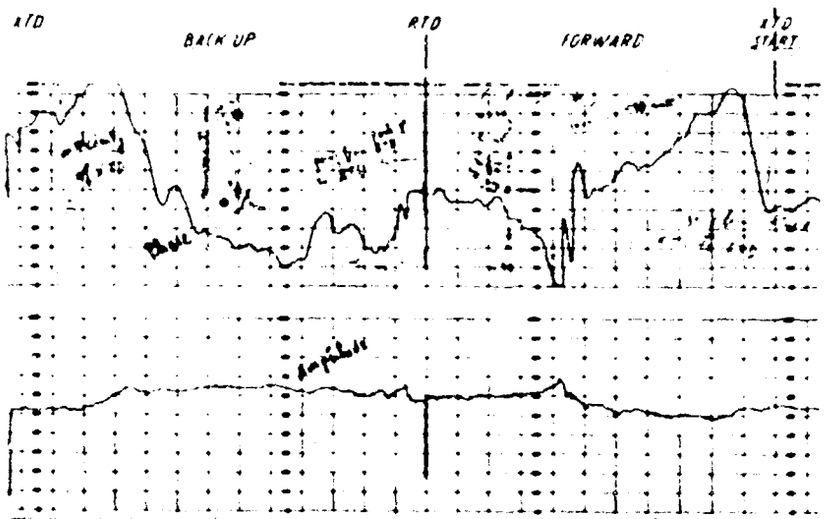

FIG 10a

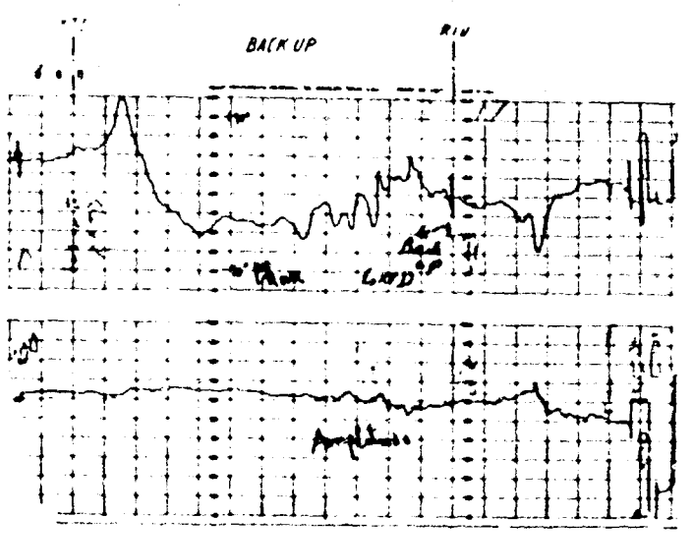

FIG 10b

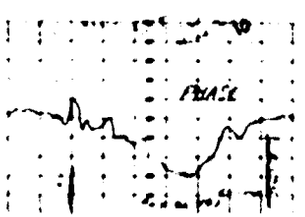

FIG 10c

RECORDINGS OF PHASE AND AMPLITUDE VARIATIONS OF 80cps CSW SIGNAL PRODUCED BY THE PRESENCE OF A CAR ON THE SURFACE WAVE TRANSMISSION PATH.

RECORDING OF FREQUENCY VARIATION OF SEISMIC FEEDBACK OSCILLATOR SYSTEM PRODUCED BY A CAR

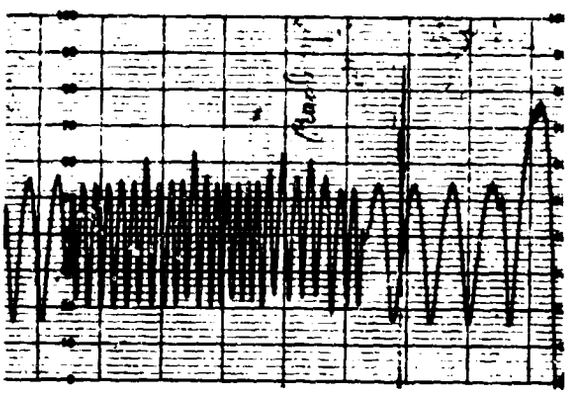

Fig 11 a

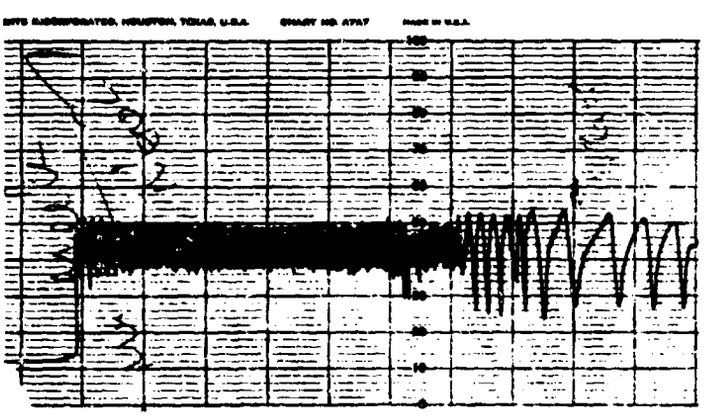

Fig. 11 b

SURGE WAVES IN AUTOMATIC WEAPONS

EDWIN H. JAKUBOWSKI - HENRY P. SWIESKOWSKI

U.S. ARMY WEAPONS COMMAND
SPRINGFIELD ARMORY
SPRINGFIELD, MASS.

OBJECTIVE:

To minimize the dynamic stresses and increase the service life of automatic weapon driving springs.

CONCLUSIONS:

1. The propagation velocity, c, associated with the Wave Equation is inversely proportional to the spring index, $\frac{D}{d}$, i.e., $c = 80{,}000 \frac{d}{D}$ in/sec.

2. A graphical solution of the Wave Equation shows that a compression time-to-surge time ratio, $T_s/T = 2$, causes the dynamic stresses to be equal to the static stresses. Since this ratio is a function of the spring dimensions, proper selection of d, D, and N can minimize the dynamic stresses.

3. A 10-cell finite difference representation of the Wave Equation provides adequate analog computer solutions.

4. The equations of motion of a distributed mass system and the finite difference equations are identical.

5. The analog computer can be used to solve realistic automatic weapon surge wave problems by extending the program to include preload, friction, buffer devices, locking forces and impulse due to exploding ammunition.

6. The analog computer may be utilized to evaluate the damping forces in single and multistrand wire springs, thereby providing design parameters to minimize the dynamic stresses.

NOTATIONS

d	Wire diameter
D	Mean Coil Diameter
$H_g = N \cdot d$	Nominal solid height of spring
x, x_i, x_n, u, u_n	Displacement, location
l	Length
L	Length of spring wire
P, F	Load or force on spring
K	Load-deflection rate, spring stiffness
k	Stiffness/unit length of spring
M	Mass of spring
m	Mass/unit length
γ	Specific weight of spring wire
W	Weight of spring
G	Modulus of torsion for spring steel
S	Stress
ΔS	Change of stress
t	Time
T	Travel time of disturbance over length of spring wire
T_S	Duration of compression stroke
V	Velocity
c	Propagation velocity
g	Gravitational constant
D/d	Spring index
N	Number of active coils

JAKUBOWSKI, SWIESKOWSKI

INTRODUCTION:

The driving spring is one of the primary components in an automatic weapon system. A well designed driving spring will insure proper weapon function over extended endurance life. Although manufacturing processes such as shot peening, cold-setting, and stress relieving have extended the life of springs, premature failures still occur.

It has been observed (Figure 1) that when an impact is imparted to a spring, the load is not distributed uniformly throughout the length of the spring and that some coils tend to oscillate. Furthermore, the stresses between adjacent coils are higher than those predicted by static considerations. When a repetitive load is applied, the clashing of coils, which cause the rate of the spring to change, can be observed. These observed changes indicate that a disturbance at the loaded end of the spring is propagated through the spring wire. Therefore, if a driving spring is to be properly designed, the propagation of the surge wave must be taken into consideration.

It has been found that springs fabricated from stranded wire are superior to those fabricated from single wire in both endurance and fatigue. As these springs are compressed, the pressure between adjacent strands is increased, thereby creating a damping device. Consequently, the amplitude of the surge wave is attenuated.

SPRING RELATIONSHIPS:

The basic formulae used for the design of helical round wire springs are:

Load-deflection rate: $$K = \frac{P}{X} = \frac{G}{8} \cdot \frac{d^4}{D^3} \cdot \frac{1}{N} \quad \cdots\cdots 1$$

Stress-deflection rate: $$\frac{S}{X} = \frac{G}{\pi} \cdot \frac{d}{D^2} \cdot \frac{1}{N} \quad \cdots\cdots\cdots 2$$

Load-Stress rate: $$\frac{P}{S} = \frac{\pi}{8} \cdot \frac{d^3}{D} \quad \cdots\cdots\cdots 3$$

Solid height: $$H_s = N \cdot d \quad \cdots\cdots\cdots 4$$

Stranded wire springs react essentially the same as single wire springs, i.e., the spring coils are subjected to a twisting moment upon compression. This twisting moment requires that the spring helix be of opposite direction to the stand helix (Figure 2). In this case the twisting moment tends to cause the individual strands to "wind up" and tighten the strands. This tightening increases the friction between strands and introduces a damping which is beneficial in dynamic applications.

JAKUBOWSKI, SWIESKOWSKI

The basic formulae for design of stranded wire springs are proportional to those used for single wire. The load-deflection rate of a stranded wire spring is determined by summing the rates of the individual single wires; whereas the stress-deflection rate is obtained by the given formula for an individual wire diameter. This indicates that the behavior of a stranded wire spring is similar to a number of single wire springs acting in parallel.

DYNAMIC FORMULAE:

The impact at the free end of a spring will cause any point on the spring to vibrate back and forth about its original position. The displacement of the moving end coil is not equally distributed among all the coils; consequently the stresses are not equal. Since a spring is nothing more than a piece of straight wire wound into a helix, it is expected that the motion of a point on a spring would be similar to the motion of a cross-sectional area of a rod. The general equation of motion,

$$\frac{\partial^2 u}{\partial t^2} = c^2 \frac{\partial^2 u}{\partial x^2} \quad \ldots\ldots\ldots 5$$

describes many physical systems and is known as the Wave Equation.

When a spring is compressed by a force parallel to its length, there exists a longitudinal compression and a lateral expansion. In the case of a short spring, the lateral and longitudinal motions of a point will be of the same order of magnitude. Therefore, this lateral motion cannot be neglected without serious risk of error. When the length to diameter ratio of a spring is large, the lateral motion is small relative to the longitudinal motion. Therefore, the inertial effect of the lateral motion may be neglected without introducing serious error.

If the distances to two points, A and B, on an uncompressed spring are x and $x+dx$ (Figure 3), any compressive force will cause point A to move a distance u and to occupy a new position A'. Point B will also move to a new position B' which is $\left[x + dx + u + \frac{\partial u}{\partial x} dx\right]$ from the reference line. The displacement due to the compressive force of points A and B is u and $u + \frac{\partial u}{\partial x} dx$, respectively. Therefore, the relative displacement is $\frac{\partial u}{\partial x} dx$ where $\frac{\partial u}{\partial x}$ is the unit elongation.

The force at any point may then be given by $F = k \frac{\partial u}{\partial x}$

The force/unit length is $\frac{\partial F}{\partial x} = k \frac{\partial^2 u}{\partial x^2}$

hence the difference in force across the element is $\partial F = k \frac{\partial^2 u}{\partial x^2} dx$

The inertial force of the element dx is $m \frac{\partial^2 u}{\partial t^2} dx$ and by d'Alembert's principle

$$\frac{\partial^2 u}{\partial t^2} = \frac{k}{m} \frac{\partial^2 u}{\partial x^2} \quad \cdots\cdots\cdots 6$$

The dimensions of k and m are $M\,t^{-2}$ and M respectively; therefore, $\sqrt{k/m}$ has the dimensions of velocity. Since "c" of Equation 5 is defined as the propagation velocity of a disturbance, $\sqrt{k/m}$ is then the propagation velocity of a surge wave in a spring. In terms of load-deflection rate and weight of the entire spring

$$c^2 = \frac{k}{m} = \frac{k L^2 g}{W} \quad \cdots\cdots\cdots\cdots 7$$

By letting the spring length $L = \pi N D$ and spring weight $W = \frac{\pi d^2 L \gamma}{4}$ and substituting Equation 1 into Equation 7, the propagation velocity is obtained in terms of spring index

$$c = \frac{d}{D} \sqrt{\frac{G g}{2 \gamma}}$$

Using the usual values for g, γ, and G results in the following approximate formula

$$c \approx 88{,}600 \frac{d}{D} \text{ in/sec.} \quad \cdots\cdots\cdots 8$$

Therefore, the propagation velocity of the surge wave is a function of spring index, $\frac{D}{d}$.

When the dynamic motion in a spring is considered, the time, T, for a disturbance to travel the entire length of the spring wire, L, is defined as the surge time

$$T = \frac{L}{c} = \sqrt{\frac{2\gamma}{G g}}\ \pi \frac{N D^2}{d} = \sqrt{\frac{2\gamma}{G g}}\ H_s \left(\frac{D}{d}\right)^2 \cdots 9$$

Here the surge time, T, is given as a function of the basic spring dimensions. The surge time increases with spring index and is much greater for smaller springs than for lengthy ones.

GRAPHICAL SOLUTION:

The utility of the derived relationship is demonstrated by considering two illustrated examples. In each case the spring is suddenly compressed from its free height to a displacement of two inches by a mass moving with a constant velocity of 400 in/sec. The springs considered are defined by the following parameters:

	Spring A	Spring B
K	30.5 lb/in	17.4 lb/in
d	.100 in	.089 in
D	.840 in	.840 in
N	8	8.93
H_S	4 in	4 in

therefore

c	10,550 in/sec	9,450 in/sec
T	2 msec.	2.5 msec.

The propagation of the surge wave is illustrated in Figure 4. The status of Spring A is studied for the times

t = 0, 2, 4, 5, 6, and 6.5 msec.

At t = 0

The first coil is given an impact and it starts to move at a velocity of 400 in/sec and all coils have loads and stresses equal to zero. Since it requires 2 msec. for the surge wave to travel the entire length of spring wire, successive coils start to move with a velocity of 400 in/sec at .25 msec. intervals.

At t = 2 msec.

All the coils are moving at 400 in/sec and the surge wave arrives at the anchored end of the spring. This surge wave is reflected at the boundary, and the sign of the propagated velocity is changed. When the surge wave arrives at each coil at .25 msec. intervals, the propagated velocity is equal and opposite to that of the coil; therefore, the resultant coil velocity is zero.

At t = 4 msec.

The surge wave is reflected a second time again causing a change in the sign of the velocity. Since all coils are motionless, the velocity is imparted to successive coils at .25 msec. intervals.

At t = 5 msec.

The first coil is abruptly halted. This action causes a second surge wave to be propagated. Since the relative velocity change is -400 in/sec, the second disturbance propagates a negative velocity.

At t = 6 msec.

The first surge wave is reflected a third time.

At t = 6.5 msec.

The first and the second surge waves arrive simultaneously at coil #7. Since both surge waves are negative and the coil is moving with a positive velocity, the resultant velocity of coil #7 is -400 in/sec. The other coils are influenced by the propagated surge waves at such times as the waves require to travel the distance between successive coils.

At other times

Since friction was not considered, the magnitude of the propagated surge waves will remain constant and the spring coils will continue to oscillate as dictated by the propagation velocity.

From Equation 3, the change in the stress is

$$\Delta S = \frac{8}{\pi} \frac{D}{d^3} \Delta P$$

This relationship shows that, for each 0.1 inch change in relative displacement of adjacent coils, the change in the stress is

$$\Delta S = 52,200 \ LB/IN^2$$

For a comparison, the values of corresponding static stresses are also found. Since the free end is displaced one-half its maximum stroke, the compression of each coil is one-half of the original displacement. For Spring A, each coil having a rate of 244 lbs/in will be displaced .25 inch; therefore, the static stress is

$$S = 130,500 \ LB/IN^2$$

Quantitative analyses of the coil displacements (Figure 4) show that a peak stress is

$$\Delta S = 208,800 \ LB/IN^2$$

Furthermore, the dynamic stress in the middle coils is 20 per cent higher and that of the end coils is 60 per cent higher than the corresponding stresses in the static case.

Considering Spring B (Figure 5), the time for the disturbance to travel the entire length of the spring is 2.5 msec. and the reflected surge wave will arrive at the first coil after 5 msec. Since this is also the same time at which the first coil is halted, the resultant propagated velocity is zero.

These dynamic coil displacements are identical to those obtained by static compression of Spring B. Therefore, the stresses are equal and the dynamic stresses are minimized.

If the compression time is defined as T_S, it can be seen (Spring B) that for a ratio

$$\frac{T_S}{T} = 2,$$

the dynamic stresses equal the static stresses. Therefore, in the design of driving springs, the T_S/T ratio may be optimized by the proper selection of d, D, and N.

ANALOG COMPUTER APPROACH:

The graphical solution provides a good rapid approach to the design of driving springs, but occasions exist when the illustrated method is ineffective. Failure is attributed to the fact that the ramp function is not typical of the displacement of the spring end in an operating automatic weapon. A triangular or a fully rectified sine wave function would be more representative. Even so, these functions do not include the recoiling mass at the free end and the force applied by an exploding round of ammunition. When the mass and the applied force are considered, neither the graphical nor analytic solutions of the Wave Equation can be readily obtained

without tedious time-consuming computation. Therefore, it is expedient to utilize an analog computer.

Because an analog computer is capable of solving ordinary differential equations, finite differences are utilized to transform the Wave Equation into a system of total differential equations. The Wave Equation, being a function of time and displacement, i.e. U(x,t), is transformed by obtaining solutions for the variable U at certain predetermined distances, x_1, by dividing the length into "n" cells (Figure 6).

Since $\left.\frac{\partial u}{\partial x}\right|_{n-\frac{1}{2}}$ designates the slope at any midpoint, then from Figure 6

$$\left.\frac{\partial u}{\partial x}\right|_{n-\frac{1}{2}} = \frac{u_n - u_{n-1}}{\Delta x}$$

When the slopes of consecutive midpoints are known, the second derivatives may be obtained as

$$\left.\frac{\partial^2 u}{\partial x^2}\right|_n = \frac{1}{\Delta x}\left\{\left.\frac{\partial u}{\partial x}\right|_{n+\frac{1}{2}} - \left.\frac{\partial u}{\partial x}\right|_{n-\frac{1}{2}}\right\}$$

$$= \frac{u_{n+1} - 2u_n + u_{n-1}}{\Delta x^2}$$

The Wave Equation may then be represented by (n-1) difference equations:

$$\frac{\partial^2 u_n}{\partial t^2} = \frac{c^2}{(\Delta x)^2}\left(u_{n-1} - 2u_n + u_{n+1}\right)$$

WHERE $n = 1, 2, 3 \cdots\cdots n-1$

For the Wave Equation representing a spring anchored on one end and free on the other the boundary conditions are

i: $u = 0$ AT $x = 0$

ii: $\frac{\partial u}{\partial x} = 0$ AT $x = L$

When the spring is divided into eight equal increments, the seven difference equations are

$$\ddot{u}_1 = \frac{64K}{L^2 N}\left(-2u_1 + u_2\right)$$

$$\ddot{u}_2 = \frac{64K}{L^2 N}\left(u_1 - 2u_2 + u_3\right)$$

$$\ddot{u}_7 = \frac{64K}{L^2 N}\left(u_6 - 2u_7 + u_8\right)$$

A spring having a stiffness K and mass M may be represented as the distributed mass system shown in Figure 7. If this spring is divided into n equal parts, the mass and stiffness of each element is

$$m_1 = \frac{m}{n} \quad \text{AND} \quad K_1 = nK$$

The equation of motion of any mass element other than the first may be written as

$$m_1 \ddot{X}_{n-i} - K_1(X_{n-i+1} - X_{n-i}) + K_1(X_{n-i} - X_{n-i-1}) = 0$$

The equation of motion for the first mass element is

$$m_1 \ddot{x}_1 - K_1(-2x_1 + x_2) = 0$$

If the spring is divided into eight equal parts, then the (n-1) equations of motion become

$$\left.\begin{aligned} \ddot{x}_1 &= \frac{64K}{n}(-x_1 - x_2) \\ \ddot{x}_2 &= \frac{64K}{n}(x_1 - 2x_2 + x_3) \\ &\cdots\cdots\cdots\cdots\cdots\cdots \\ \ddot{x}_7 &= \frac{64K}{n}(x_6 - 2x_7 + x_8) \end{aligned}\right\} \quad \cdots\cdots 11$$

Since M and K are mass and stiffness for the entire spring, the mass/unit length and stiffness/unit length are, respectively,

$$m = \frac{M}{L} \quad \text{AND} \quad k = KL$$

Hence,

$$\frac{K}{M} = \frac{k}{mL^2}$$

Comparison of the difference equations (Equation 10) with the equations for the distributed mass system shows that the equations are identical. Hence, it is concluded that the distributed mass system is a finite difference representation of the Wave Equation. This conclusion permits the analysis of a realistic weapon system where otherwise it might be difficult to impose precise boundary conditions on the Wave Equation. Problems involving preloaded springs, viscous and coulomb, buffer action, locking, and the application of repetitive gas forces can now be readily solved.

The Wave Equation has been solved by the separation of variables. Comparison of the normal mode frequencies shows that although the finite difference frequencies are somewhat lower than the true frequencies, a 10-cell representation of the Wave Equation on an analog computer will provide solutions within the desired accuracy limits. In terms of a spring, a 10-cell representation will produce solutions for consecutive tenths (10%) of wire length.

The analog computer solution for Spring A (Figure 8) compares favorably with that obtained by use of the graphical method (Figure 4).

When an analog computer is solving a system of differential equations, the internal voltages are analogous to the displacements, velocities, and accelerations and they are proportional to the individual dynamic forces exerted on all cell elements. The dynamic stresses between any two points may then be recorded (Figure 9) as a function of time.

The motion of the first coil may be readily changed from a ramp function to a repetitive triangular wave by simply introducing an electronically operated switch to change the velocity of the first coil at predetermined displacements. The surge wave propagation for this condition is shown in Figure 10.

Since the boundary conditions considered in the previous instances are not representative of practical weapon applications, a more realistic condition was considered, i.e., an impulsive force applied to a .245 pound bolt. The resulting propagation of the surge waves is shown in Figure 11.

In any real spring system, the surge waves are eventually damped out. Internal hysteresis and boundary reflection losses, along with friction between strands in multistrand wire springs, introduce the damping factors. Since these factors have never been evaluated, they are not considered in the designing of a spring. The analog computer program may be readily extended to consider viscous, coulomb and boundary reflection damping. A study may then be performed to define the damping parameters thereby providing the spring designer with accurate design data.

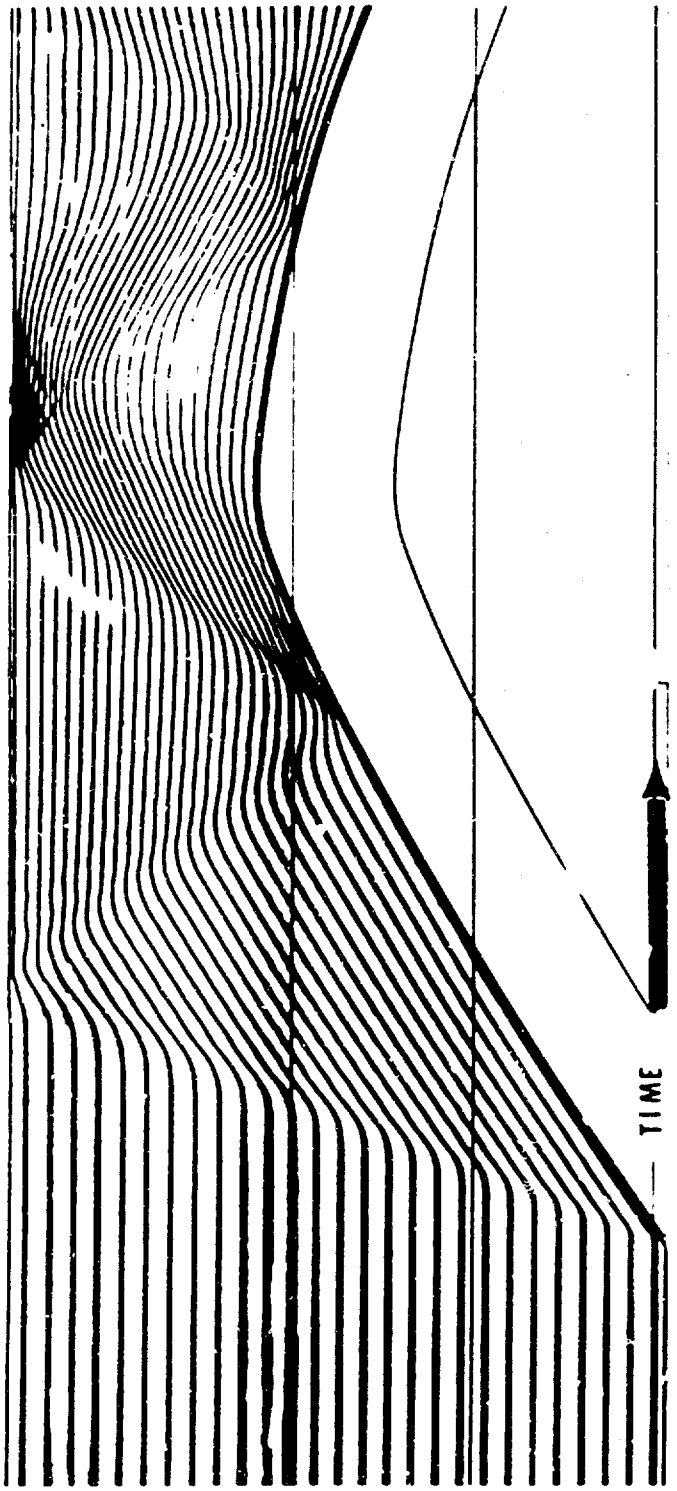

FIG. 1

TIME DISPLACEMENT CURVES OF SPRING COILS DUE TO IMPACT LOADING

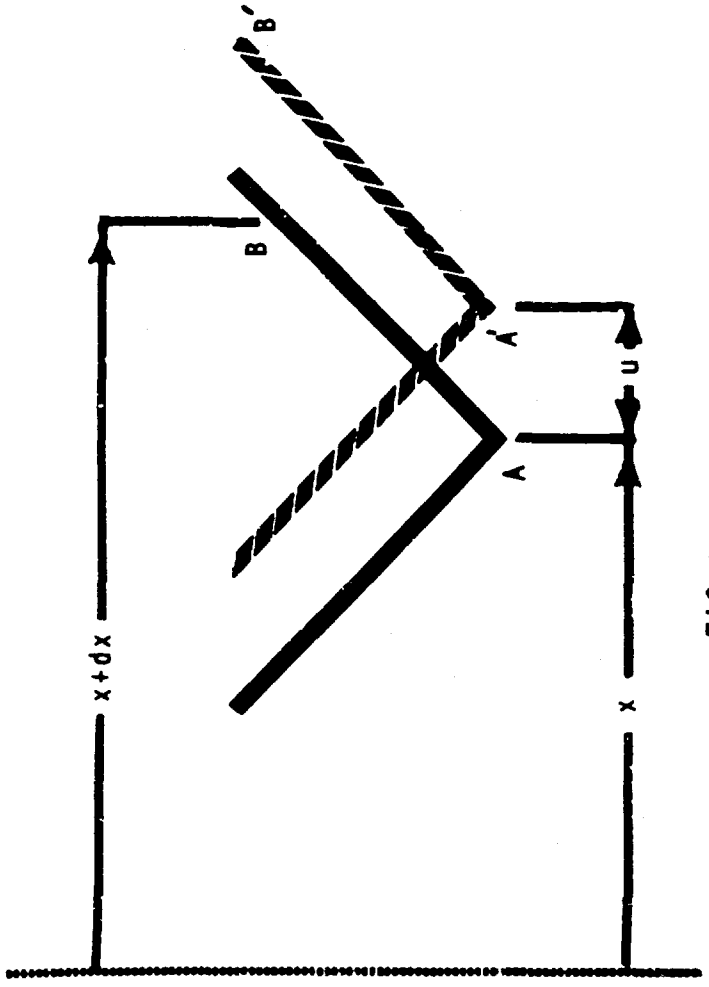

FIG.1
DISPLACEMENT OF TWO ADJACENT POINTS ON A SPRING

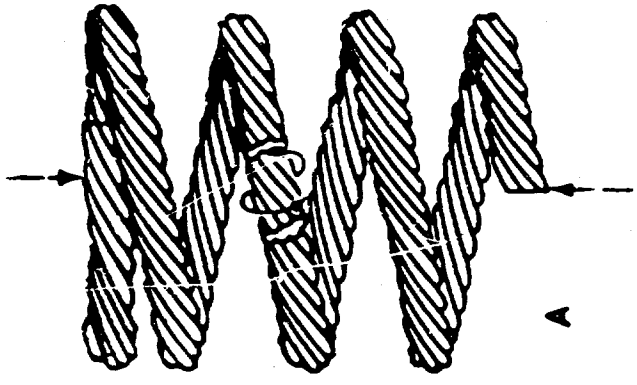

FIG. 2
STRANDED WIRE SPRING.

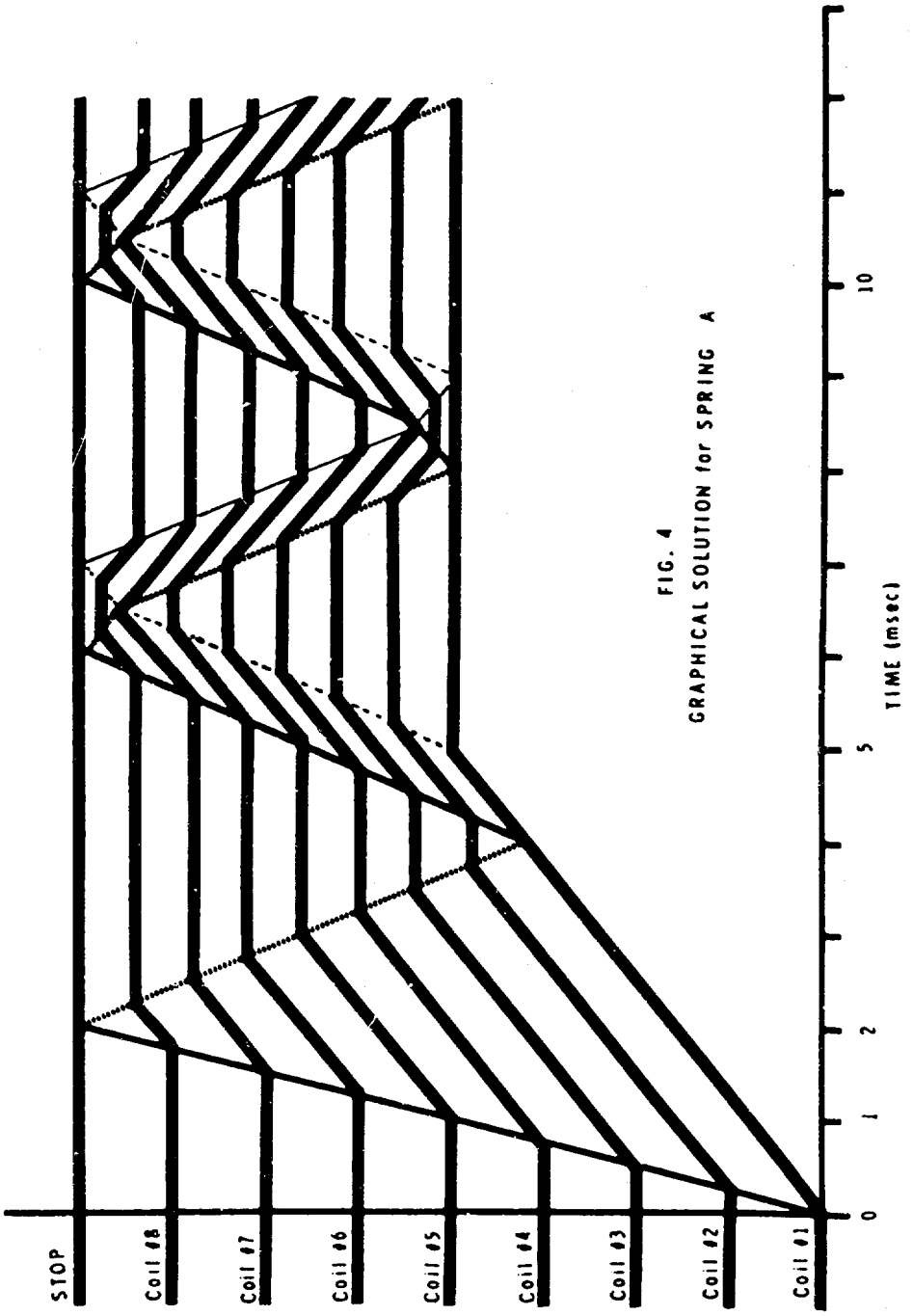

FIG. 4
GRAPHICAL SOLUTION for SPRING A

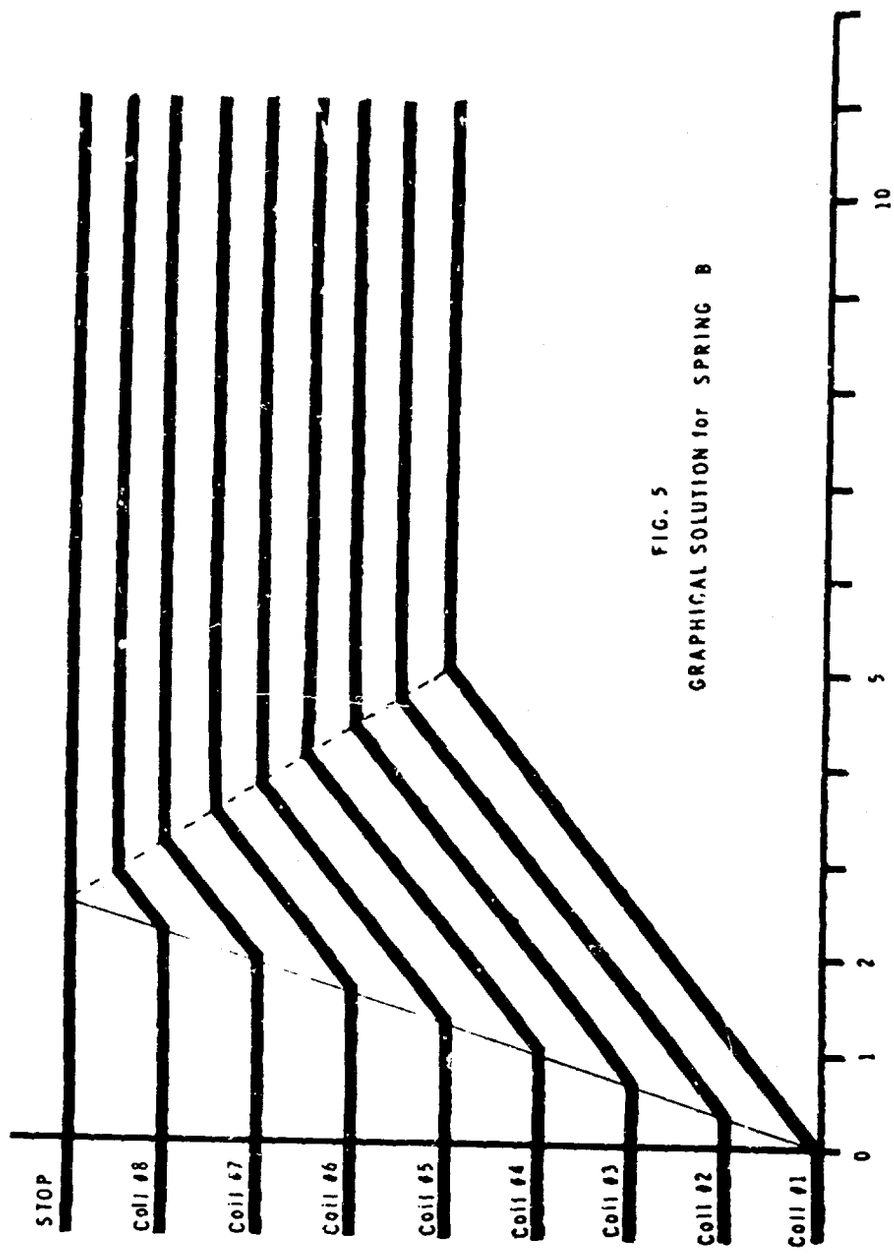

FIG. 5
GRAPHICAL SOLUTION for SPRING B

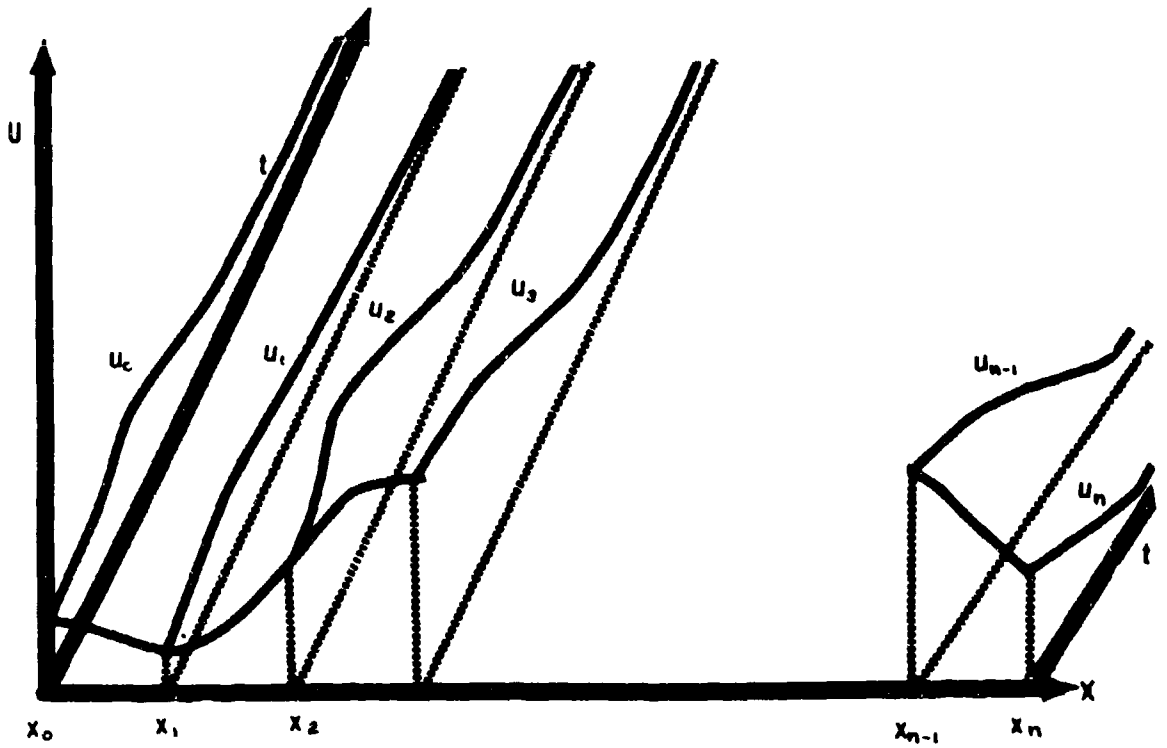

FIG. 6

WAVE EQUATION DESCRIBING U IN TERMS OF TWO INDEPENDENT VARIABLES, X and t, AT DISCRETE VALUES OF X.

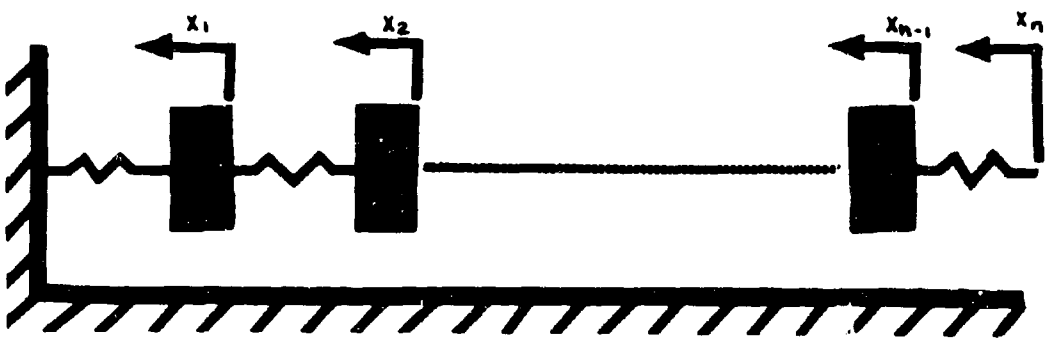

FIG. 7
DISTRIBUTED MASS SYSTEM

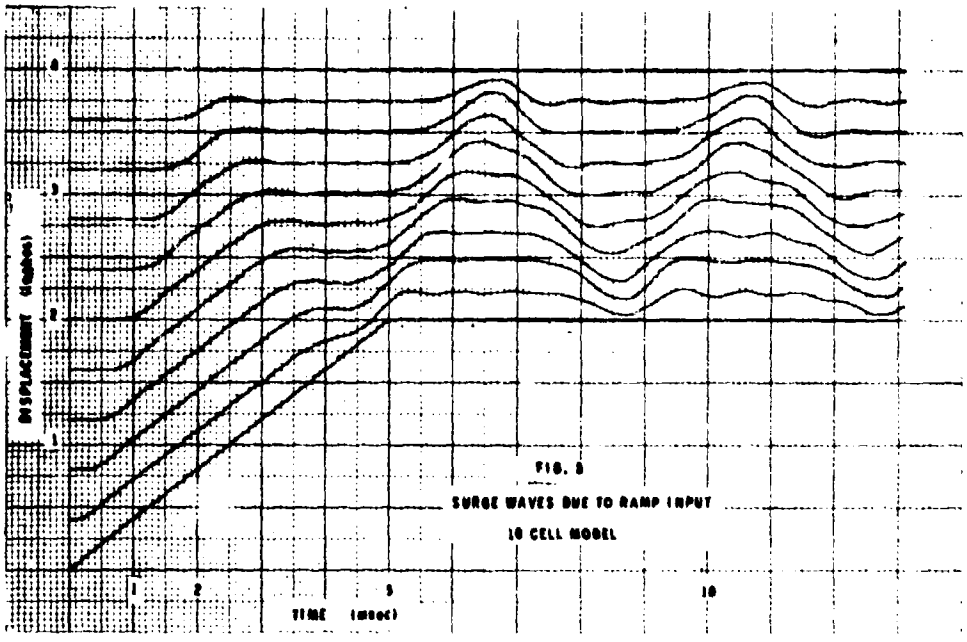

FIG. 8
SURGE WAVES DUE TO RAMP INPUT
10 CELL MODEL

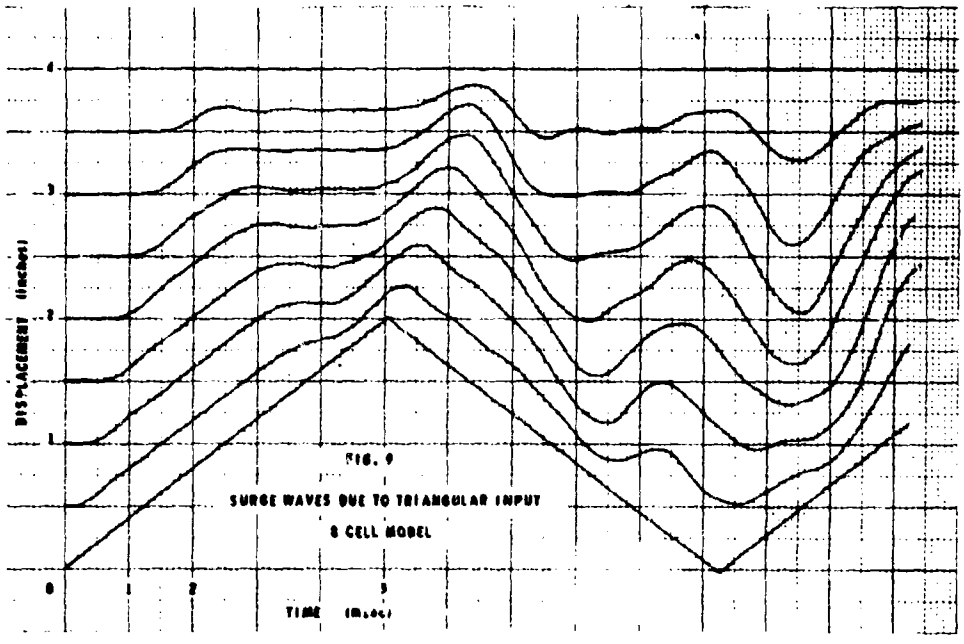

FIG. 9
SURGE WAVES DUE TO TRIANGULAR INPUT
8 CELL MODEL

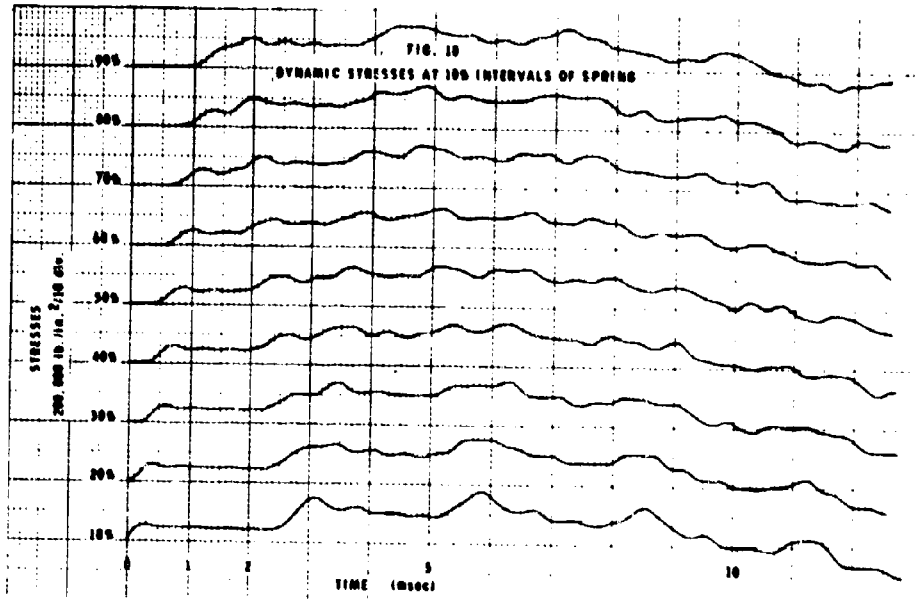

FIG. 10
DYNAMIC STRESSES AT 10% INTERVALS OF SPRING

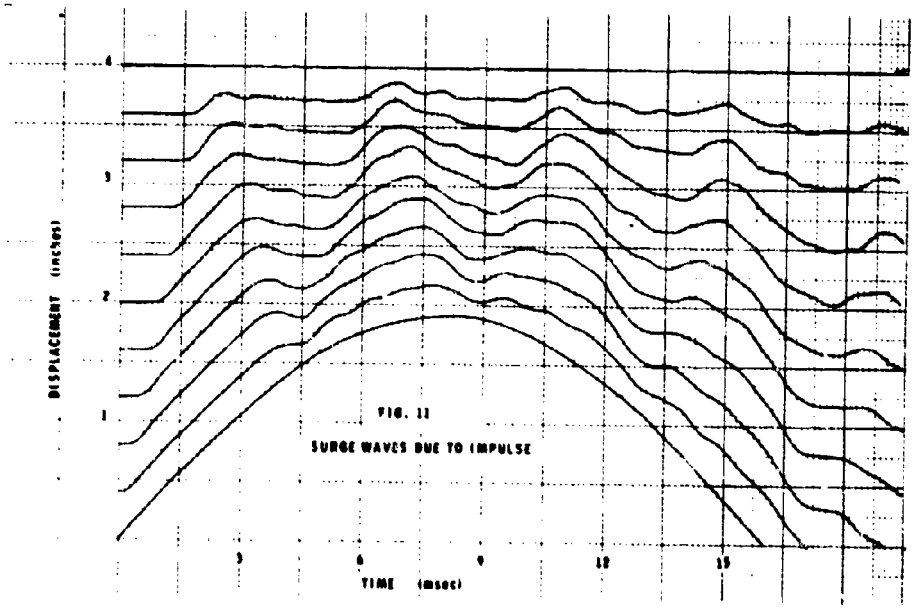

FIG. 11
SURGE WAVES DUE TO IMPULSE

SURFACE DEPENDENCE OF MAGNETOSTATIC MODE LINEWIDTHS IN YTTRIUM IRON GARNET

GEORGE R. JONES
HARRY DIAMOND LABORATORIES
WASHINGTON, D. C.

I. INTRODUCTION

Magnetic materials that are electrical insulators have many useful applications to electronic devices. The properties of one such ferrimagnetic substance, yttrium iron garnet (YIG), make it particularly interesting to microwave technology. Some of the unique properties of this material have made possible a wide variety of microwave devices that are useful to many differing military systems. A particularly important property is that well-prepared single-crystal specimens of YIG have exceptionally narrow ferromagnetic resonance linewidths at microwave frequencies. The Harry Diamond Laboratories has contributed to the development of applications of this material and to studies of the fundamental physical processes underlying its useful properties.

The particular study that is reported here represents one phase of a detailed study of factors that influence the ferromagnetic resonance linewidth. The degree and method of surface preparation have been found to influence greatly the observed resonance linewidth of spherical specimens of YIG. It was found that irregularities in the sample, either on the surface or distributed over the volume provided a means by which energy was coupled from the ferromagnetic resonance mode to a large number of degenerate short wavelength spinwave states, after which the magnetic excitation energy in these spinwaves was dissipated by other processes. It was not until recently that detailed measurements of the sample surface made possible a quantitative test of the degenerate spinwave theory as applied to surface irregularities (1). The behavior of the uniform precession mode of ferromagnetic resonance alone was considered.

The observed linewidths of the magnetostatic modes (2) did not appear to be related in an orderly manner to the magnetic properties or to the surface irregularities. The purpose of this

work was to determine what additional factors were required in an adequate description of the magnetostatic mode linewidths. It was found that substantially the same process as in the uniform precession takes place, but that consideration of the configuration of the fields associated with these modes is required to provide a general theory of surface dependent linewidth broadening of magnetostatic modes by degenerate spinwave scattering.

II. THEORY

The surface dependence of the magnetostatic mode linewidths is associated with a transfer of energy via surface irregularities from the resonant mode into degenerate spinwave modes. Once in the form of spinwaves, the energy is dissipated by other processes. The transfer of energy from the resonant mode appears as loss mechanism, thus the resonance line appears to be broadened.

Both the magnetostatic resonance modes and the spinwaves are solutions of Maxwell's equations coupled to an equation for magnetic motion. The equation of motion is linearized by restricting it to small excitation of the resonance. The separate behavior of the magnetostatic modes and the spinwaves is developed in the choice of appropriate approximations.

The magnetostatic mode description was developed by Walker (2). Dipolar fields resulting from the termination of the magnetization at the surface are significant in determining the resonant frequency of the mode. Since the sample is small compared to the wavelength of ordinary electromagnetic waves at the resonant frequency, the magnetostatic approximation can be used: Curl $\vec{H} = 0$. The lowest order mode of this system, the uniform precession mode, was explained much earlier by Kittel (3). The wave functions used here are those for spherical samples given by Fletcher and Bell (4). The observable magnetostatic modes are described by functions that vary slowly over the sample.

The spinwaves are magnetic waves of very short wavelengths compared to those of the ordinary electromagnetic wave of the same frequency (5). The dispersion equation for classical spinwaves was derived by Polder (6) and the properties of exchange, a quantum mechanical effort, were inserted later. These semiclassical spinwaves are described by a similar dispersion equation. The wave function for these spinwaves are given by Auld (7) and are used here in order to include the exchange effects. The dispersion equation, plotted in fig. 1, is useful to show schematically the relationships between the various waves. The long waves, with small k, correspond to magnetostatic modes and are observed as discrete resonances. The short wavelengths correspond to spinwaves. The extremely short waves, associated with very large k, are the exchange dependent spinwaves.

Magnetostatic modes are coupled to spinwaves by the dipolar fields that result from termination of the magnetization at the irregular surface. Perturbation theory expansions of the effects of the irregular surface include two first order terms. These correspond to the dipolar field associated with termination of the static magnetization and the magnetization associated with the resonant mode. Both cases are treated in detail in an earlier paper (1).

The calculated surface dependent linewidth is given in eq. (1).

$$(\Delta H)_{surface} = \frac{(4\pi M_s)}{(2\pi/r^2)Z} \times$$

$$\times \left\{ \tfrac{1}{2}(\mu''+\kappa'')_{res} \int \frac{W(\vec{k})_s \, k_s^{\,3} \, |m(r,\theta,\varphi)|^2 \, k_s^{\,3} \, d\varphi}{k^2+k_s^{\,2}[(4\pi M_s)/(2H)]/2+(4\pi M_s)/(2H)]} \right.$$

$$\left. + \int dk_s \int d\theta \int d\varphi \frac{|\cos\theta \cos\varphi|(1+\sin\theta \sin\varphi)^2 \sin^2\theta}{(\sin\theta+\omega/\omega_r \sin\varphi)^2 + \cos^2\theta \cos^2\varphi} k_s \, W(\vec{k}_s) |m(r,\theta,\varphi)|^2 \right\} \qquad (1)$$

where $W(\vec{k}_s)$ is a spectrum function resembling a power spectrum. It is derived from a Fourier analysis of the surface in the two dimensional surface wave vector $\vec{k}_s$. The integration over $\vec{k}_s$ is restricted to values corresponding to propagation of spinwaves $k_s \leq k_{max}$. M_s is the saturation magnetization of the material, r is the radius of the sphere. The transverse magnetism associated with the resonant mode is $m(r,\theta,\varphi)$. The angular frequency of the resonance is ω and $\omega_r = \gamma[H + (D/h)k^2]$ in which γ is the gyromagnetic ratio, H is the magnetic field in the material, D is the exchange parameter and k is the wave number of the spinwave where $k_s/k = \sin\theta$ in both integrals. The Zeeman energy integral contributes $Z = \int |m(\rho,\theta,\varphi)|^2 \, dv$.

The linewidth calculation, Eq. (1), requires an evaluation of the surface spectrum function $W(\vec{k}_s)$. This is obtained by performing a Fourier analysis of the surface. Experimental data (1) have shown that certain surface preparations allow considerable simplification. Incompletely polished spheres (0.5 to 2.0 oersted linewidths) have been analyzed with an interference microscope. Insertion of the spectrum function, thus obtained in Eq. (1), showed that the integral corresponding to static dipolar fields was negligible. The integral corresponding to periodic fields could be written as a product of two separate integrals.

$$(\Delta H)_{surface} = \frac{4\pi M_s}{(2\pi/r^2)Z} \left\{ \int k_s \, dk_s \, W(k_s) \right\} I(\omega, M_s) \qquad (2)$$

where

$$I(\omega,M_s) = \int d\theta \int d\varphi \, \frac{|\cos\theta \cos\varphi \, (1+\sin\theta \sin\varphi)^2 \sin^2\theta| \, m(r,\theta,\varphi)|^2}{(\sin\theta + \omega/\omega_r \sin\varphi^2 + \cos^2\theta \cos^2\varphi}$$

Numerical evaluation of $I(\omega,M_s)$ was made by automatic computer at the National Bureau of Standards. The integral over k_s reduced to a single number describing the surface.

The surface dependent linewidth, however, is not a complete evaluation of the linewidths as observed. In addition to coupling by the surface irregularities, crystal imperfections distributed throughout the volume of the sample may provide additional coupling to the degenerate spinwaves (8). Loss mechanism by which the magnetic energy is transferred directly to nonmagnetic excitation of the solid may prove significant. Observations by Nemarich (9) indicate, nevertheless, that when such contribution is important, the direct relaxation process is observed to be nearly independent of other parameters at a particular frequency; thus, it is constant for a set of magnetostatic modes at one frequency. The several linewidth contributions are additive and the general linewdith may be written

$$(\Delta H)_{total} = (\Delta H)_{surface} + (\Delta H)_{volume} + (\Delta H)_{direct}.$$

III. RESULTS AND CONCLUSION

Observations of the linewidths of a number of the magnetostatic modes were taken from a report given by R. L. White (10). Because detailed surface measurements were not available, an appropriate value was obtained by means of a best fit by least squares of three components: $(\Delta H)_{surface}$ the surface linewidth, $(\Delta H)_{volume}$ where a similar volume irregularity constant is selected, and $(\Delta H)_{direct}$ the linewidth component constant for all modes. The first coefficients depend on the magnetostatic mode, but in different ways because of differences in the mechanism by which they occur.

The calculated linewidth contribution of degenerate scattering by volume-distributed imperfections was negligible. The other two parameters were found to be typical of similarly prepared spheres (1). Comparisons with two sets of data are given in

figures 2 and 3. These linewidths are obtained from one sphere in two different orientations and they are treated independently. The pairs of points for each mode show very good agreement between linewidths conforming to the theoretical model and those observed.

The close conformity of the observations to theoretically expected behavior indicates that the semiclassical degenerate spin-wave model adequately accounts for the seemingly erratic behavior of the magnetostatic mode linewidths. In addition, one interesting possibility lies in a potential method of determining the extent to which a given specimen may have its resonance narrowed by polishing without the need of actual final polishing. This would be based on the relative linewidths of several magnetostatic modes observed while the sample surface is still in an unfinished state of polish.

IV. REFERENCES

(1) G. R. Jones, The Surface Dependence of Ferromagnetic Relaxation, Harry Diamond Laboratories Report, TR-1143 (1963)
(2) L. R. Walker, Phys. Rev. 105, 390 (1957)
(3) C. Kittel, Phys. Rev. 73, 155 (1948)
(4) R. C. Fletcher and R. O. Bell, Journ. Appl. Phys. 30, 687 (1959)
(5) J. Smit and H.P.J. Wijn, Ferrites, John Wiley and Sons, New York (1959)
(6) D. Polder, Phil. Mag. 40, 99 (1949)
(7) B. A. Auld, Journ. Appl. Phys. 31, 1962 (1960)
(8) A. M. Clogston, H. Suhl, L. R. Walker and R. W. Anderson, J. Phys. Chem. Solids 1, 129 (1956)
(9) J. Nemarich, Bull. Am. Phys. Soc. 9, 25 (1964)
(10) R. L. White, Fourth Conference on Magnetism and Magnetic Materials (1958)

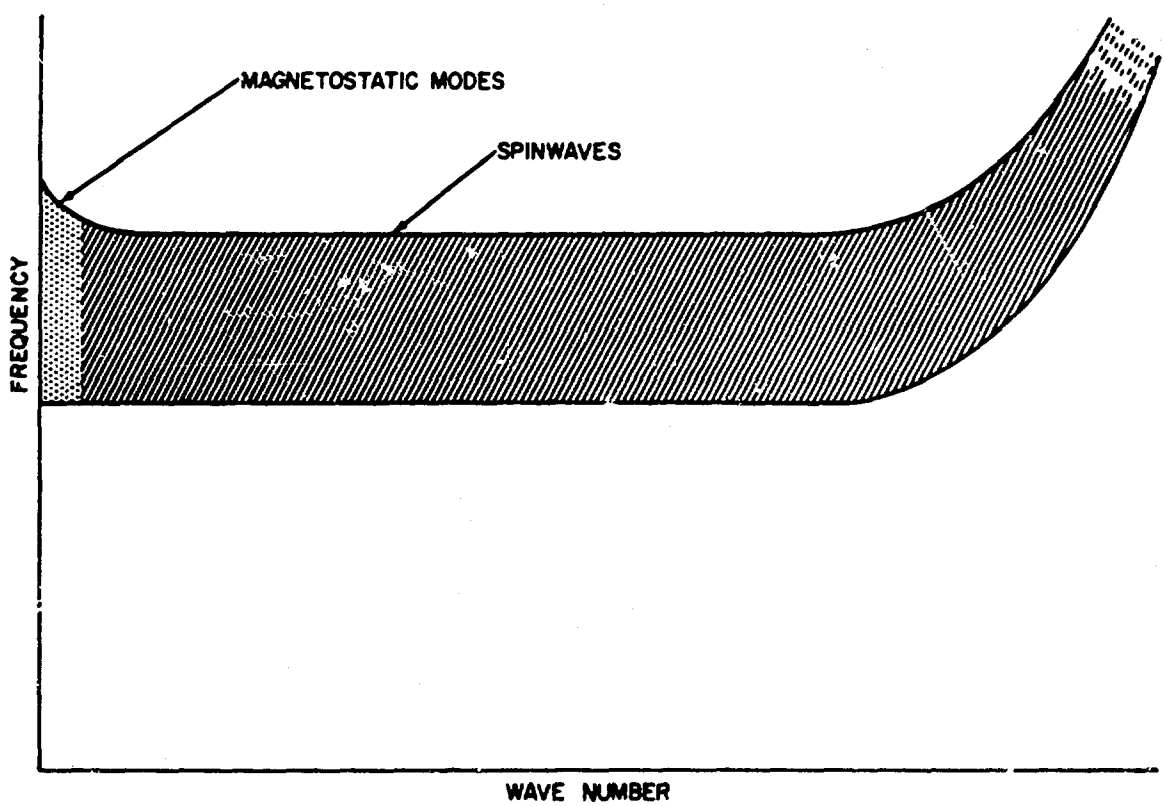

Fig. 1 Magnetic Dispersion Relation for Fixed Magnetic Field Showing Spinwaves and Magnetostatic Modes.

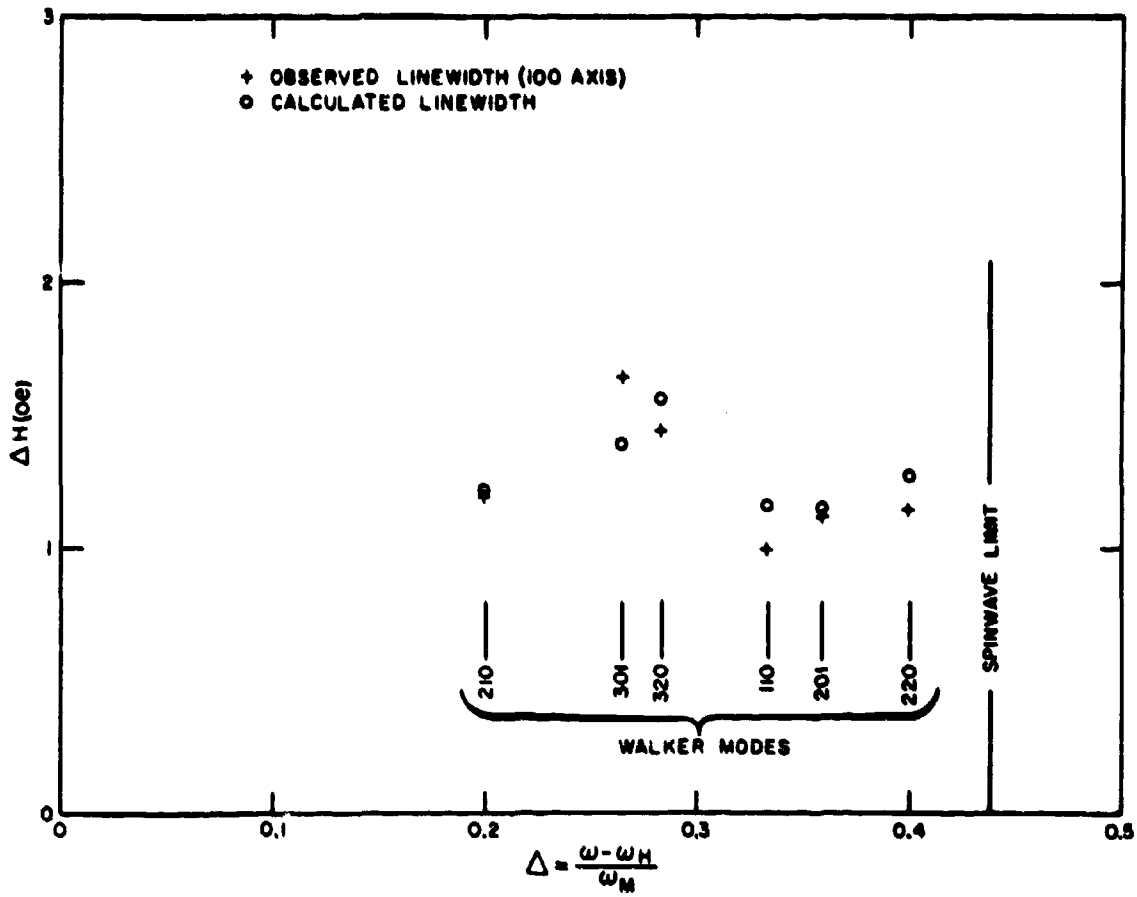

Fig. 2 Calculated and Observed Linewidths of Low Order Magnetostatic Modes: (100) Axis Magnetization.

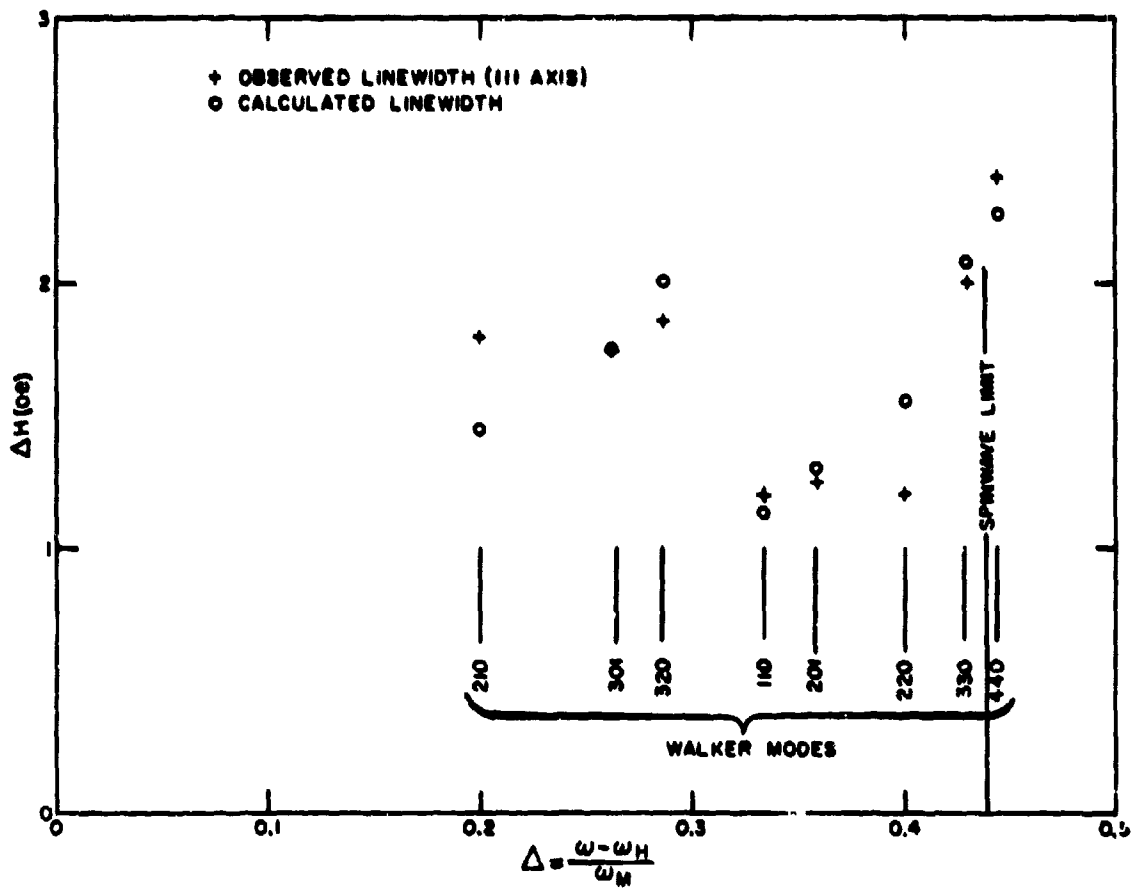

Fig. 3 Calculated and Observed Linewidths of Low Order Magnetostatic Modes: (111) Axis Magnetization.

A NEW GRAVITY METER

HENRY P. KALMUS
HARRY DIAMOND LABORATORIES
WASHINGTON, D. C.

THE NEW METHOD

For the absolute determination of gravity, methods employing Kater's reversible pendulum are usually employed. Relative measurements are made with pendulum or spring type gravity meters. Pendulum observations are time consuming and the equipment is bulky. An accuracy of 1 part in 10^6 is obtainable. Spring type gravity meters deliver fast and easy to make readings with an accuracy of 1 part in 10^{-8}, but the meters have to be compared frequently with pendulum type instruments.

The unit of acceleration due to gravity is the gal where 1 gal = 1 cm per sec^2. Hence, 1 g = 980 gal.

The change of gravity with height gives us a physical picture of the required accuracy.

$$g_h \doteq g\left(1 - \frac{2h}{R}\right)$$

g is the sea level value
h is the altitude in meters
R is the earth radius ($6370 \cdot 10^3$m)
for h = 3m, we obtain a reduction of g by about 1 milligal. Hence, if we lift the gravity meter from the floor to the ceiling of a room, the instrument should give a definite reading.

A new method for the determination of gravity will be described which is rapid and easy to apply and still has a sensitivity of at least 1 mgal. After the instrument has been calibrated once, measurements are repeatable without further calibration. It is hoped that future advances in the art will make a sensitivity of .1 or even .01 mgal feasible. The method should be applicable at sea and in airplanes because the output of the instrument is obtained as an AC voltage, the average of which can easily be obtained by integration.

The acceleration due to gravity is continually compared with centripetal acceleration by means of an AC null method whereby a single transducer is exposed to equal pressure amplitudes from g and from the centripetal acceleration. In this way, the transducer characteristic is rendered non-critical.

In figure 1, a long arm with length r_1 is shown, rotating around A with angular velocity ω_1 and carrying at its end a mass m_1. Around m_1 two short arms with length r_2 are rotating with ω_2 and $-\omega_2$ relative to the first arm, carrying masses m_2. A strain gage type transducer T is inserted in the long arm, generating a voltage proportional to the radial stress existing in the arm. The axles through A and B are horizontal. The rotations are produced by motors and maintained at constant angular velocities.

Let $|\omega_1|$ be equal to $|\omega_2|$. This means that, while the long arm performs one revolution, the short arms revolve once around the long arm. As shown in figure 2, the phase of the revolutions is adjusted in such a way that, for the long arm pointing vertically up, the two masses m_2 are together at their highest point. While the long arm points vertically down, the two masses are again together and pointing upwards.

One can guess intuitively how the system works: For the long arm pointing up, gravity compresses the transducer. For the arm pointing down, gravity expands the transducer. The centrifugal force, however, works just in the opposite direction. The long arm is lengthened by the short arms in its up position and shortened by its down position so that the centrifugal force expands the transducer more in the up position than in the down position. For a certain value of m_1 and m_2 and for a certain $\omega = \omega_1 = \omega_2$, complete cancellation of the AC output occurs so that g can be determined by measuring ω.

The transducer together with a high gain amplifier and detector are used as a null indicator. Only two elements have to be controlled with high accuracy, namely ω and r_2. This will be explained later after the equations of motion have been established and after an error analysis has been performed.

ANALYSIS

The design as shown in figure 1 is just one special arrangement. In order to keep the treatment as general as possible, it will be assumed that $\omega_1 \neq \omega_2$. The problem is defined by the determination of the acceleration of a particle P on a moving curve. This acceleration is the resultant of: a_1 - the acceleration of constraint; a_2 - the relative acceleration (found as if the curve were at rest); a_3 - the Coriolis acceleration (twice the product of the relative velocity of the particle along the curve by the angular velocity of the curve); a_1 - the acceleration of constraint of any point P on a moving curve is the resultant of: a_{11} - the acceleration of point A

around which the curve rotates; $a_{12} - r\omega^2$ from P to A, due to the rotation of AP about A; $a_{13} - r\omega^2$ perpendicular to AP.

Assuming that only one mass m_2 is rotating and further assuming that ω_1 and ω_2 are uniform and that all elements are rigid (no bending of the arms), we can determine the radial acceleration along r_1: (the centripetal accelerations are assumed positive for directions towards A and, for t = 0, the initial position of m_2 is at its highest point).

For mass m_2: $a_{11} = 0$

$$a_{12} = \omega_1^2(r_1 + r_2 \cos \omega_2 t)$$

$$a_{13} = 0$$

$$a_1 = \omega_1^2(r_1 + r_2 \cos \omega_2 t)$$

$$a_2 = \omega_2^2 r_2 \cos \omega_2 t$$

$$a_3 = 2\omega_1 \omega_2 \cos \omega_2 t$$

$$a_r = \omega_1^2 r_1 + (\omega_1 + \omega_2)^2 r_2 \cos \omega_2 t$$

For mass m_1: $a_r = a_1 = \omega_1^2 r_1$ ($a_2 = 0$, $a_3 = 0$).

For two masses m_2 counter rotating, the Coriolis term a_3 disappears because of mutual cancellation of the two accelerations. We obtain for m_2 and m_2':

$$a_r = \omega_1^2 r_1 + (\omega_1^2 + \omega_2^2) r_2 \cos \omega_2 t.$$

It is interesting to show that, if radial acceleration is considered, the function of two counter-rotating masses m_2 is equivalent to the function of a single mass $2m_2$, swinging radially along the large arm with sinusoidal motion as shown in figure 3.

$s = r_2 \cos \omega_2 t$; $\dot{s} = - \omega_2 r_2 \sin \omega_2 t$; $\ddot{s} = - \omega_2^2 r_2 \cos \omega_2 t$.

Because we assume the acceleration towards A is positive, the relative acceleration of $2m_2$ is:

$$a_2 = \omega_2^2 r_2 \cos \omega_2 t.$$

Hence: $a_{11} = 0$; $a_{12} = \omega_1^2(r_1 + r_2 \cos \omega_2 t)$; $a_{13} = 0$;

$a_2 = \omega_2^2 r_2 \cos \omega_2 t$; $a_3 = 0$; $a_r = \omega_1^2 r_1 + (\omega_1^2 + \omega_2^2) r_2 \cos \omega_2 t$.

This is the same value we obtained before for two counter-rotating masses.

We are now ready to write the equation for the radial force in our idealized (not bending) system.

The sign for the forces directed outward from A are assumed to be positive. $F_r = 2m_2[\omega_1^2 r_1 + (\omega_1^2 + \omega_2^2) r_2 \cos \omega_2 t] + m_1 \omega_1^2 r_1$

$$-(m_1 + 2m_2)\, g \cos \omega_1 t = F_{DC} + F_C + F_G.$$

In figure 4, F_r is plotted versus time. It consists of three parts: F_{DC}, a constant force, F_C at frequency $\frac{\omega_2}{2\pi}$ and F_G at frequency $\frac{\omega_1}{2\pi}$. F_{DC} and F_C only would exist if the axes were vertical. F_G is caused by gravity. For clarity, it is assumed that $\omega_1 < \omega_2$. The value of gravity could now be determined if F_C is compared with F_G. In order to compare two voltages with different frequencies, however, rectifiers are necessary. In addition, the same transducer sensitivity would be required for ω_1 and ω_2. These drawbacks can be avoided by making $\omega_1 = \omega_2$ so that the transducer is driven by two periodic forces with the same frequency and the same amplitudes with opposite phases. A real null method can now be applied for the measurement of gravity.

If $\omega = \omega_1 = \omega_2$ and if only AC voltages with the frequency $\frac{\omega}{2\pi}$ are derived from the transducer, we obtain:

$$E = K\,[4m_2\, \omega^2\, r_2 - (m_1 + 2m_2)\, g] \cos \omega t \qquad (1)$$

K is the voltage produced by the transducer per unit force. For E = 0, we obtain:

$$g = \frac{4m_2\, \omega^2\, r_2}{(m_1 + 2m_2)} \text{ cm/sec}^2 .$$

r is measured in cm and ω in radians per sec.

We can now determine the required accuracy of the components for a non-bending system. If g has to be measured with an accuracy of 1 part in 10^5, m_1, m_2, and r_2 have to be stable to 1 part in 10^6. ω has to be controlled to one part in $2 \cdot 10^6$ because $\frac{\Delta g}{g} = 2\frac{\Delta \omega}{\omega}$. It should be noted that the g-reading is independent of r_1. For a non-rigid system, it will be shown that r_1 has to be controlled to 4 parts in 10,000.

For a g of 980 cm/sec^2, the equation supplies also the correct relation between ω_1, r_2, m_1 and m_2:

$$\omega^2\, r_2 = 245\, \frac{m_1 + 2m_2}{m_2}$$

For the design of the instrument, the following constants will be chosen: r_1 = 30 cm, r_2 = 10 cm, $\omega = 2\pi \cdot 10 = 62.8$, m_1 = 159 grams, m_2 = 1 gram.

THE BENDING OF THE LARGE ARM

Because the new method is based on the comparison of two AC-voltages, their waveforms should be as free from distortion as possible. This is indeed the case if all elements of the apparatus are rigid. In a practical machine, however, bending of the arms will occur, causing phase-modulation of the angular velocity. Again, in order to keep the equations as general as possible, it will be assumed that ω_1 and ω_2 are not equal.

The moment of inertia I of the total system changes periodically with frequency $\frac{\omega_2}{2\pi}$ because of the rotation of the small arms. The angular momentum tends to remain constant so that ω_1 will be modulated with frequency $\frac{\omega_2}{2\pi}$. If the motor would drive the long arm through a heavy flywheel and if the shaft between flywheel and arm were not flexible, the arm would be driven with essentially uniform velocity.

Now, the flywheel and the unflexible shaft can be replaced by an arrangement as shown in figure 5. By extending the long arm to the other side of the main bearing and by rotating two additional masses as shown, the angular momentum will remain constant.

For 2 small masses as shown in figure 1:

$$(\omega_1 I)_{2m_2} = \omega_1 \cdot 2m_2 \ (r_1^2 + r_2^2 + 2r_1 \ r_2 \cos \omega_2 t).$$

For 4 small masses as shown in figure 5:

$(\omega_1 I)_{4m_2} = \omega_1 \cdot 2m_2 \ (r_1^2 + r_2^2 + 2r_1 \ r_2 \cos \omega_2 t + r_1^2 + r_2^2 -$

$2r_1 \ r_2 \cos \omega_2 t)$. Therefore: $(\omega_1 I)_{4m_2} = \omega_1 \cdot 4m_2(r_1^2 + r_2^2)$.

It can be seen that the angular momentum is constant. We can assume, therefore, that the long arm is driven with the uniform angular velocity ω_1. Due to the ω_2 rotation of the small arms, tangential forces on point B are produced, bending the long arm periodically with an angle excursion γ and causing a new angular velocity $\omega(t)$ of B. Neglecting second order effects, $\omega(t)$ will be a sinusoidally phase-modulated wave. The tangential acceleration is caused by the Coriolis term (a_3). $a_t = -2\omega_1 \ \omega_2 \ r_2 \sin \omega_2 t$

The acceleration is assumed to be positive in clockwise direction. The force acting on the long arm is: $F_t = +2m_2 \cdot 2\omega_1 \ \omega_2 \ r_2 \sin \omega_2 t$. F_t can also be computed by deriving the torque which is the time derivative of the angular momentum $\omega_1 I$. The torque acting on the system is:

$$T = \frac{d}{dt}(\omega_1 I) = \frac{d}{dt} \ \omega_1 \cdot 2m_2(r_1^2 + r_2^2 + 2r_1 \ r_2 \cos \omega_2 t).$$

$$T = -4m_2 \ \omega_1 \ \omega_2 \ r_1 \ r_2 \sin \omega_2 t.$$

Hence, the tangential force acting on B is:

$$F_t = \frac{T}{r_1} = 4m_2 \ \omega_1 \ \omega_2 \ r_2 \sin \omega_2 t.$$

For: $m_2 = 1$ gram, $\omega = \omega_1 = \omega_2 = 2\pi \cdot 10$ and $r_2 = 10$ cm

$$F_t^{max} = 158000 \text{ dynes} = 160 \text{ gram force.}$$

Assuming that this force acts on a beam with a length $\ell = 20$ cm (2/3 or r_1), the bending angle γ can be computed. A beam with rectangular cross-section (a = b = 3) is assumed although a tubular

design with similar stiffness will probably be chosen for a practical design. The deflection: $h = \frac{4}{E} \frac{\ell^3}{a^3 \cdot b} F_{t_1} = 3 \cdot 10^{-5}$ cm.

E is Young's modulus ($2 \cdot 10^6$ Kg/cm^2 for steel)

$\gamma = \frac{h}{\ell} = 1.5 \quad 10^{-6}$ radians.

Actually, the bending angle will be smaller because the constant centrifugal force increases the effective stiffness of the beam. A value of $\gamma = 10^{-5}$, however, will be assumed for further computations in order to accommodate any additional bending which may be caused by the transducer mounting. Hence, the long arm is periodically bent back and forth with a maximum angle $\gamma = 10^{-5}$ radians. The phase angle of B is: $\phi = \omega_1 t + \gamma \sin \omega_2 t$

$\omega = \frac{d\phi}{dt} = \omega_1 + \omega_2 \gamma \cos \omega_2 t$

THE TORQUE EXERTED ON THE SMALL ARMS

The torque exerted on each short arm is caused by accelerations of m_2, perpendicular to r_2. The only term to be considered is a_{12}, the acceleration of m_2 due to its rotation around A. There is no perpendicular component of the terms a_2 and a_3.

Figure 6 shows the vector diagram.

$a_{12} = \omega_1^2 \ell$; $\frac{\ell}{\sin \omega_2 t} = \frac{r_1}{\sin (\omega_2 - \omega_1)t}$; $\ell = r_1 \frac{\sin \omega_2 t}{\sin (\omega_2 - \omega_1)t}$;

$a_{12} = \omega_1^2 r_1 \frac{\sin \omega_2 t}{\sin (\omega_2 - \omega_1)t}$; $a_p = a_{12} \sin (\omega_2 - \omega_1)t = \omega_1^2 r_1 \sin \omega_2 t$;

$F_p = -a_p m_2 = -m_2 \omega_1^2 r_1 \sin \omega_2 t$.

For $m_2 = 1$ gram, $\omega_1 = 2\pi \cdot 10$ and $r_1 = 10$ cm.

$F_p^{max} = 39500$ dynes $= 40.5$ gram force.

The torque $T^{max} = F_p \cdot r_2 = 405$ gram cm.

This value is so low that the bending angle of the small arm can be neglected. Still, the torque has to be considered for the design of the motor, driving the two small arms so that excessive periodic phase excursions can be avoided. Second order effects caused by $\dot{\omega}$ are so small that they do not have to be considered.

THE EFFECT OF BENDING OF THE LARGE ARM ON THE RADIAL CENTRIFUGAL FORCES

It was shown before that, because of the Coriolis acceleration, the angular velocity of B is not uniform. Hence, in order to compute the radial forces with greater accuracy, ω_1 has to be replaced by $\omega(t)$. $\omega = \omega_1 + \omega_2 \gamma \cos \omega_2 t$.

The analysis of the rigid system has led to the equations:

For masses m_2: $a_{r_{st.}}^{m2} = \omega_1^2 r_1 + (\omega_1^2 + \omega_2^2) r_2 \cos \omega_2 t$.

KALMUS

For mass m_1: $a_{r_{st.}}^{m_1} = \omega_1^2 r_1$.

Replacing ω_1 by ω we obtain:

For masses m_2: $a_r^{m2} = r_1(\omega_1^2 + \omega_2^2\gamma^2\cos^2\omega_2 t + 2\omega_1\omega_2\gamma\cos\omega_2 t) +$

$+ r_2(\omega_1^2 + \omega_2^2\gamma^2\cos^2\omega_2 t + 2\omega_1\omega_2\gamma\,\omega_2 t)\cos\omega_2 t +$

$+ r_2\,\omega_2^2\cos\omega_2 t.$

Because: $\sin^2\alpha = \frac{1}{2} - \frac{\cos 2\alpha}{2}$; $\cos^2\alpha = \frac{1}{2} + \frac{\cos 2\alpha}{2}$; $\cos^3\alpha = \frac{\cos 3\alpha}{4} +$

$\frac{3\cos\alpha}{4}$; $a_r^{m2} = r_1(\omega_1^2 + \frac{1}{2}\omega_2^2\gamma^2 + \frac{1}{2}\omega_2^2\gamma^2\cos 2\omega_2 t + 2\omega_1\omega_2\gamma\,\omega_2 t) +$

$r_2(\omega_1^2\cos\omega_2 t + \frac{1}{4}\omega_2^2\gamma^2\cos 3\omega_2 t + \frac{3}{4}\omega_2^2\gamma^2\cos\omega_2 t +$

$\omega_1\omega_2\gamma + \omega_1\omega_2\gamma\cos 2\omega_2 t) + r_2(\omega_2^2\cos\omega_2 t).$

The DC term: $r_1\omega_1^2 + \frac{1}{2}r_1\omega_2^2\gamma^2 + r_2\omega_1\omega_2\gamma.$

The term at the fundamental frequency:

$\cos\omega_2 t[r_2(\omega_1^2 + \omega_2^2) + \frac{3}{4}r_2\omega_2^2\gamma^2 + 2r_1\omega_1\omega_2\gamma].$

At the second harmonic: $\cos 2\omega_2 t(\frac{1}{2}r_1\omega_2^2\gamma^2 + r_2\omega_1\omega_2\gamma).$

At the third harmonic: $\cos 3\omega_2 t(\frac{1}{4}r_2\omega_2^2\gamma^2).$

For mass m_1: $a_r^{m1} = r_1(\omega_1^2 + \omega_2^2\gamma^2\cos^2\omega_2 t + 2\omega_1\omega_2\gamma\cos\omega_2 t).$

$a_r^{m1} = r_1(\omega_1^2 + \frac{1}{2}\omega_2^2\gamma^2 + \frac{1}{2}\omega_2^2\gamma^2\cos 2\omega_2 t + 2\omega_1\omega_2\gamma\cos\omega_2 t).$

The DC term: $r_1\omega_1^2 + \frac{1}{2}r_1\omega_2^2\gamma^2.$

At fundamental frequency: $\cos\omega_2 t(2r_1\omega_1\omega_2\gamma).$

At the second harmonic: $\cos 2\omega_2 t(\frac{1}{2}r_1\omega_2^2\gamma^2).$

Neglecting all terms containing γ^2, we finally obtain the radial forces: (radial forces are assumed to be positive in outward direction).

$F_{DC} = (m_1 + 2m_2)r_1\omega_1^2 + 2m_2 r_2\omega_1\omega_2\gamma.$

$F_{\omega 2} = \cos\omega_2 t[2m_2 r_2(\omega_1^2 + \omega_2^2) + (2m_1 + 4m_2)r_1\omega_1\omega_2\gamma].$

$$F_{2\omega_2} = \cos 2\omega_2 t(2m_2\ r_2\ \omega_1\ \omega_2\ \gamma).$$

F_{DC} and $F_{2\omega_2}$ are rejected by frequency selective means. For $\omega = \omega_1 = \omega_2$: $F^{max}_{\omega_2} = 4\omega^2\ m_2\ r_2 + 2\omega^2(2m_2 + m_1)\ r_1\ \gamma$.

For $m_1 = 159$ gram, $m_2 = 1$ gram, $r_1 = 30$ cm, $r_2 = 10$ cm and $\gamma = 10^{-5}$, the second part of this expression is 400 times smaller than the first part. Hence, for a required accuracy of 1 part in 10^6, the second part has to be kept stable with an accuracy of 400 parts in 10^6 or 4 parts in 10^4. This means that if the bending of the large arm is considered, r_1 and γ have to be kept within four parts in 10000.

THE EFFECT OF BENDING OF THE LARGE ARM ON THE RADIAL GRAVITY FORCE

It has been shown that, for the rigid system, the gravity force is: $F_G = (m_1 + 2m_2)\ g \cos \omega_1 t$

$$a_g = g \cos \phi\ (t).$$

It was also shown that, for the system with the bending arm:
$\omega = \omega_1 + \omega_2\ \gamma \cos \omega_2 t$

$$\phi(t) = \int_o^t \omega dt = \omega_1 t + \gamma \sin \omega_2 t.$$

$$a_g = g \cos (\omega_1 t + \gamma \sin \omega_2 t).$$

because: $\cos (\alpha + \beta) = \cos \alpha \cos \beta - \sin \alpha \sin \beta$;

$a_g = g[\cos \omega_1 t \cos (\gamma \sin \omega_2 t) - \sin \omega_1 t \sin (\gamma \sin \omega_2 t)]$

$\cos (\gamma \sin \omega_2 t) = J_0(\gamma) + 2J_2(\gamma) \cos 2\omega_2 t + 2J_4(\gamma) \cos 4\omega_2 t +$

$\sin (\gamma \sin \omega_2 t) = 2J_1(\gamma) \sin \omega_2 t + 2J_3(\gamma) \cos 3\omega_2 t + \ ...$

($J_n(\gamma)$ is the Bessel function of the first kind of the nth order. γ is the argument of the Bessel function in question).

$a_g = g[J_0(\gamma) \cos \omega_1 t + 2J_2(\gamma) \cos \omega_1 t \cos 2\omega_2 t - 2J_1(\gamma) \sin \omega_1 t \sin$

$\omega_2 t - 2J_3(\gamma) \sin \omega_1 t \cos 3\omega_2 t]$

because: $\cos \alpha \cos \beta = \frac{1}{2} [\cos (\alpha - \beta) + \cos (\alpha + \beta)]$

$\sin \alpha \sin \beta = \frac{1}{2} [\cos (\alpha - \beta) - \cos (\alpha + \beta)]$

$a_g = g\ [J_0(\gamma) \cos \omega_1 t - J_1(\gamma)\cos(\omega_1 - \omega_2)t + J_1(\gamma)\cos(\omega_1 + \omega_2)t +$

$+J_2(\gamma)\cos(\omega_1 - 2\omega_2)t + J_2(\gamma)\cos(\omega_1 + 2\omega_2)t - J_3(\gamma)\cos(\omega_1 - 3\omega_2)t$

$+J_3(\gamma)\cos(\omega_1 + 3\omega_2)t - ...]$

For a small argument, the following approximations can be made:

$$J_0(\gamma) = 1 - \frac{\gamma^2}{4} \; ; \; J_1(\gamma) = \frac{\gamma}{2} \; ; \; J_2(\gamma) = \frac{\gamma^2}{8} \; ; \; J_3(\gamma) = \frac{\gamma^3}{48} \; .$$

Only the fundamental AC component of the transducer voltage is utilized. The bending of the arm produces a reduction of this voltage by the factor $J_0(\gamma)$. For a γ of 10^{-5}, this reduction is $\frac{\gamma^2}{4} = \frac{10^{-10}}{4}$ and represents an error in the reading of gravity of 2.5 parts in 10^{11}.

Hence, the bending of the long arm will practically not modify the transducer output. As shown before, this output consists of a wave with a frequency of 10 cps. ($\omega = \omega_1 = \omega_2$).

THE INSTRUMENT

Figure 7 shows a schematic design of the apparatus. The small masses m_2 and m_2' are carried by two thin aluminum disks. For the control of speed these disks support on their periphery a magnetic recording signature of 100,000 waves. Assuming a radius of 11 cm, the circumference of the disks is 69 cm. The recorded wavelength is, therefore, $.69 \cdot 10^{-3}$ cm, a value which is actually used in good recorders. The disks are driven by two motors M and M' with 10 revolutions per second. Two magnetic heads H and H' are arranged on the long arm.

The speed control of the long arm is carried out the same way. A disk D with magnetic recording on its rim is coupled to the arm. Magnetic head K is employed to pick up the recorded wave. Hence, while the disks rotate with 10 rps, the heads will deliver waves with a frequency of 1 Mc/sec. Disk D carries an additional magnetic signature on its surface which produces in the magnetic head L a wave with a frequency of 10 cps. The long arm together with disk D are driven by motor N.

Figure 8 shows a block diagram of the servo-loops. Motors M and M' are slaved to motor N by comparing the waves from K with the waves from H and H' in the phase detectors P and P'. Whenever M or M' advance or retard with respect to N, a positive or negative voltage is developed in P and P'. These voltages are employed in the motor control devices MC and MC' to produce exact speed and phase synchronism between N and M and M'. The slaving operation could, of course, be performed mechanically. It is, however, believed that an electronic system is more exact and has the advantage that less weight has to be supported by the moving parts.

The 10-cycle wave derived from transducer T is used to control the speed of motor N. Inspecting equation 1, it can be seen that the expression for E consists of two parts: The centrifugal wave and the gravity wave. For E = 0, their amplitudes are identical

and, if ω is measured, g can be determined. If ω is too high or too low, the phase of E will be either 0° or 180° compared with the phase of the gravity wave alone. This phase reference is delivered by transducer L. The amplified wave from T is compared with the output from L in the phase-sensitive rectifier Q. If its output is positive or negative, N is speeded up or slowed down by action of motor control NC.

Finally, the 1 Mc wave from the magnetic head K is compared with the output from a master clock CL in the mixer MI. The difference frequency is measured in the counter CC. Because $\frac{\Delta g}{g} = 2\frac{\Delta \omega}{\omega}$ and assuming that the master clock delivers 1 Mc and that this frequency corresponds to a certain g, a deviation of g by 1 milligal will produce a beatnote of $\frac{1}{2}$ cps. Observation of this beatnote for a period of 10 seconds should be sufficient to determine the exact value of the beat-frequency.

Actually, it will take longer to perform a measurement of g. The output of T will contain a certain amount of noise due to an unavoidable amount of bearing-roughness so that the bandwidth of amplifier A has to be restricted. The same effect can be achieved by introducing a low pass filter after the phase-sensitive detector Q. Whichever method is used, the time of response of the instrument will be increased. If the instrument is used on a periodically accelerated platform, additional integration networks have to be applied after Q.

Variations of the torque that the motor N has to deliver are reduced by extending the long arm to the other side and by the addition of 2 more motors for the rotation of two additional small masses as explained before. These motors are driven in phase-synchronism with M and M'.

Figure 9 shows the transducer mounting.* It is very important that the transducer should respond only to radial forces. It should be as insensitive as possible to any lateral stress of the arm. The long arm consists of parts 1 and 2. They are connected by means of thin flexible membranes 3, permitting free radial but impeding lateral motions. The transducer is connected between part 1 and 2' which is connected to part 2 by a flexible part 4. Part 2' can again be subdivided into parts 2", 2"', etc. This way, a "filter" is formed, eliminating any undesired bending of the transducer by a tilting action of part 2.

The alignment of the instrument, i.e., any deviation from the horizontal, is not critical. Let us assume that the instrument is tilted about the axis of the large arm by an angle α. The centrifugal wave will now be phase shifted by α with respect to the gravity wave. A phasor diagram is shown in figure 10. It is assumed that for correct alignment $P = K\, 4m_2\, \omega^2\, r_2 = K(m_1 + 2m_2)g$. (See equation

* Suggested by Mr. B. M. Horton.

1). After the two waves have been compared in the phase sensitive rectifier Q, an error voltage ΔE will be produced which is proportional to $P(1 - \cos \alpha) \doteq P \cdot \frac{\alpha^2}{2}$. For an accuracy of 1 part in 10^6, ΔE has to be kept smaller than $P \cdot 10^{-6}$. Hence:

$$P \frac{\alpha^2}{2} < P \cdot 10^{-6} \text{ and } \alpha < \sqrt{2} \cdot 10^{-3} \text{ radians.}$$

This means that α has to be smaller than 25 arc seconds, an adjustment which can easily be performed by conventional means.

ACKNOWLEDGMENT

The author wishes to express his appreciation to Mr. H. A. Dropkin and Mr. Arthur Hausner for their assistance in developing the analytical model.

He also acknowledges the stimulating discussions with Mr. B. M. Horton which were invaluable for the development of the new system.

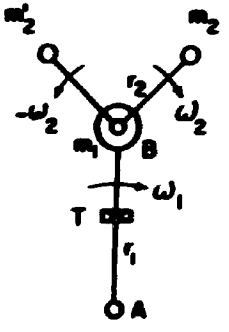

FIGURE 1

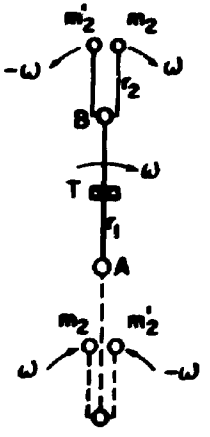

FIGURE 2

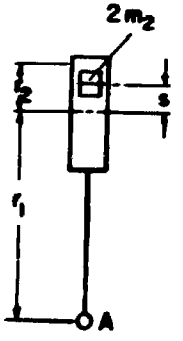

FIGURE 3

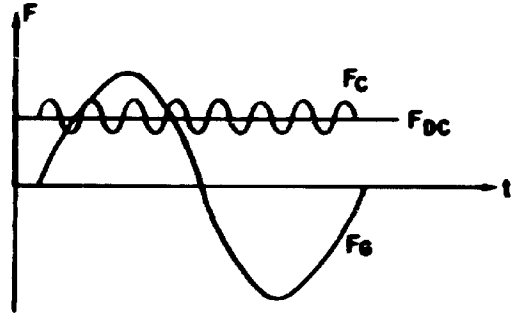

FIGURE 4

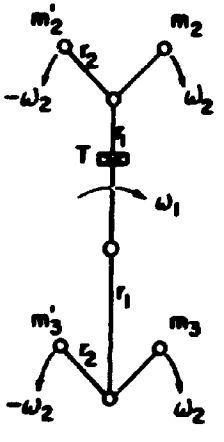

FIGURE 5

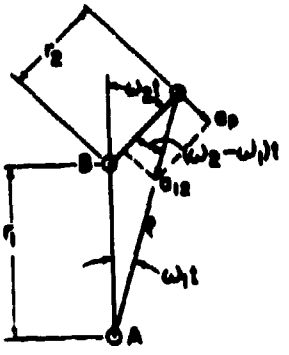

FIGURE 6

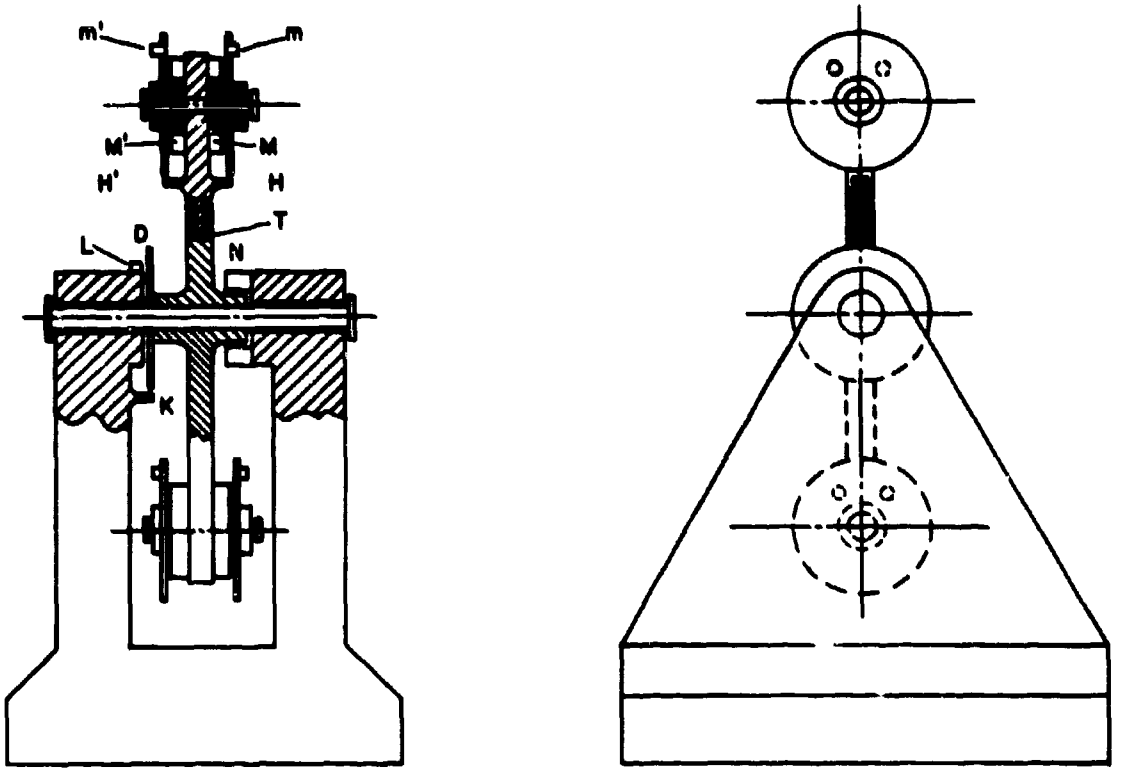

FIGURE 7

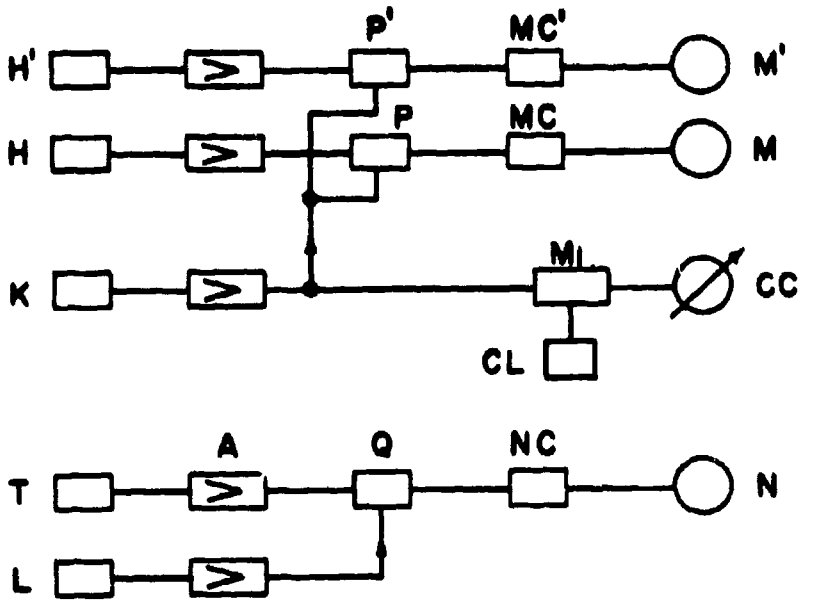

FIGURE 8

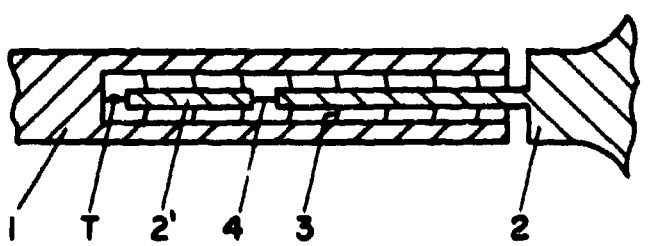

FIGURE 9

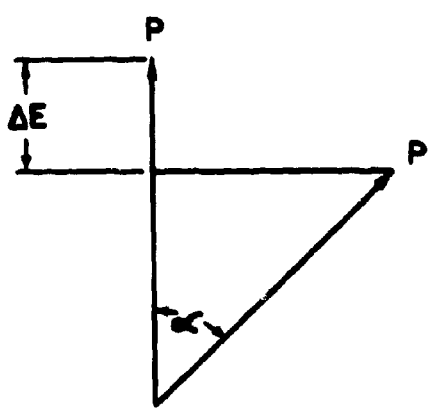

FIGURE 10

THE MAXIMUM DISSOCIATION ENERGIES OF DIATOMIC MOLECULES OF TRANSITION ELEMENTS

Part I. Upper Limits for Titanium, Chromium, and Manganese

ARTHUR KANT and BERNARD STRAUSS
U. S. ARMY MATERIALS RESEARCH AGENCY
WATERTOWN, MASSACHUSETTS 02172

INTRODUCTION

The dissociation energies for most of the homonuclear diatomic molecules (dimers) of the main group elements[1,2] (periodic groups) IA to VIIA and groups IB and IIB are known. The dissociation energies of the main group dimers when plotted against atomic number (Figure 1)[1] show a periodicity which allows for approximate estimations of dissociation energies of unknown dimers within these groups. However, no dissociation data has been reported for the transition elements and no empirical or theoretical means of prediction of the energetics of these molecules are currently available.

A consideration of the equilibrium between a solid element and its vapor shows that the ratio of dimers to atoms in the vapor will increase with temperature if the heat of sublimation of the element* is greater than the dissociation energy (bond energy)† of the corresponding dimer. For if H_s is the heat of sublimation and D_2 the dissociation energy, then the heat of reaction for the process $M(s) + M(g) = M_2(g)$ is $H_s - D_2$; the equilibrium constant is P_2/P_1 (P_1 and P_2 are partial pressures of monomer and dimer respectively); and $\partial \ln (P_2/P_1)/\partial T = (H_s - D_2)/RT$ so that P_2/P_1 increases with temperature if $H_s > D_2$. Kant[3] has shown that the heat of sublimation is greater than the dissociation energy for all elements forming non-molecular crystals. Table I is a summary of available data and it is seen that all the metallic elements, with the exception of arsenic and antimony, possess a positive $H_s - D_2$. Neither of these elements has a metallic crystal structure and it is a reasonable deduction from this table that the gaseous phase of all metals will be largely polymeric (dimers and perhaps higher polymers) at sufficiently high temperatures.

*Process $M(s) = M(g)$; M is the element and s and g refer to solid and gas respectively.
†Process $M_2(g) = 2\,M(g)$.

TABLE I

Heat of Sublimation - Dissociation Energy
$H_s - D_2 = \Delta H_r$

Group	Element	ΔH_s* kcal/mol atom	D_2** kcal/mol	ΔH_r kcal/mol
IA	Li	38.4	26.0 (6)	12.4
	Na	26.0	18.0 (6)	8.0
	K	21.5	12.0 (6)	9.5
	Rb	20.0	11.0 (6)	9.0
	Cs	18.7	10.0 (6)	8.7
IB	Cu	81.1	46.1	35
	Ag	68.4	37.5	31
	Au	84.7	52.0	33
IIA	Mg	36.0	7.1	27
	Ca	42.2	5.5	37
IIB	Zn	31.0	5.5	27
	Cd	27.0	2.0	25
	Hg	15.0	1.4	13.6
IIIA	B	141.0	69 (7)	72
	Al	78.0	46 (2)	32
	Ga	65.0	32 (2)	33
	In	57.0	23 (2)	34
	Tl	43.0	14 (2)	29
IVA	C	171	143	28
	Si	104	74	30
	Ge	90.0	66.5	24
	Sn	72.0	46	26
	Pb	46.8	23	24
VA	As	69	90.8	-22
	Sb	63	69	-6
	Bi	48	46	2
Transition	Ni	101.3	57 ($^1\Sigma$) (8)	44

*Values from Reference 4.

**Values from Reference 1 unless otherwise noted.

Accordingly, we are attempting to identify the dimers of the transition elements and estimate their bond energies by using a combination of Knudsen equilibrium effusion techniques with mass spectrometric analysis at high temperatures. In this paper, the first of a series, the results for titanium, chromium, and manganese are described. Although no diatomic molecules of these elements have been found, from the limits of detectability of our instrumentation and statistical thermodynamics it is possible to establish their maximum dissociation energies.

EXPERIMENTAL

The measurements were obtained with a time of flight mass spectrometer. Figure 2 is a schematic representation of the effusion cell and high temperature source assembly. The effusion cell was a tantalum crucible containing a thoria liner in which the metal sample was placed. This liner was used because of its relative chemical stability toward the metals under investigation. Both the tantalum

crucible and the thoria liner had 1 mm holes in their covers. The holes were designed in such manner (c, Figure 2) that the perimeter of the hole was effectively of zero thickness. The crucible was heated by electron bombardment. Two 8-mil tungsten filaments were used for this purpose, each forming a semicircle on the side of the crucible opposite that on which the optical pyrometer was sighted in order to minimize reflection of light into the pyrometer. One filament was placed in the upper half of the crucible (above the cover junction) and the other filament in the lower half. The filaments were maintained at a fixed desired level of about 800 to 3000 volts negative with respect to the crucible, and the electron emission from each filament could be varied independently by varying the current through each filament.

Temperature measurements were made by sighting an optical pyrometer alternately on two blackbody holes (1 mm diameter by 5 mm depth) located on the upper and lower halves of the crucible. Light from the blackbody holes passed through a plane Pyrex sighting window prior to impinging on the optical pyrometer. Temperature corrections for the window were made by prior calibration against a Bureau of Standards calibrated lamp with and without the window in the path of the light. The correction increases with temperature, being about + 20°K at 2000°K and + 30°K at 2500°K. The window was provided with a magnetically operated shutter so that the corrections did not vary during a run as a result of deposition of material from the hot surfaces. It was found experimentally that by using two filaments (upper and lower) it was possible to adjust the current in each filament so that the temperatures of the upper and lower blackbody holes were as close as desired. By making the upper and lower blackbody hole temperatures the same, temperature gradients in the crucible were minimized. The temperatures recorded are the mean of the upper and lower holes. A maximum difference of 0.5% of the temperature (°K) was considered acceptable but in most cases the temperatures of the holes were as close as could be read on the pyrometer (± 3° at 2000°K).

The ratio of surface area of the metal sample to that of the effusion cell hole was kept high (approximately 100) in order to establish equilibrium within the crucible. Unless the value of the sticking coefficient (fraction of molecules or atoms that strike and stick to the metal surface) is exceptionally low, equilibrium will be attained in the crucible.

Molecules effusing from the cell hole pass through the 1-mm water jacket slit (a, Figure 2) and beam-defining source slit (b, Figure 2) and then through the electron beam of the mass spectrometer. The intensity or ion current of the particular species under investigation of the ions thus formed is recorded by means of standard techniques.

To insure that the ion current for a particular mass originated in the crucible, the crucible was moved by means of a brass

bellows-micrometer arrangement so that the molecular beam no longer impinged on the mass spectrometer electron beam. The heating filament posts and filament move with the crucible so that little temperature perturbation of the crucible occurs during the motion. The ion current resulting from a particular species originating from the crucible is then determined from the difference of the ion currents when the beam is in the ON position (crucible centered) and in the OFF position. Temperatures were read simultaneously on the optical pyrometer. The fact that a lateral displacement of the crucible of approximately 1 mm decreases the ion current intensity to zero shows that the species under investigation actually originate from effusion through the 1-mm crucible hole.

The pressure in the volume surrounding the crucible is maintained between 10^{-6} to 10^{-7} mm of Hg. This insures that the molecules in the molecular beam suffer no deactivating collisions and allows, as described under "Calculation", for the estimation of partial pressures of the species under study from their recorded ion currents.

As a check on the apparatus the existence of Ag_2 was confirmed and its dissociation energy determined. A value of D(Ag-Ag) of 37 ± 4 kcal/mol was obtained, which is in agreement with that of the literature.[1,8]

CALCULATION

The molar free energy of an n atomic molecule M_n in terms of its partial pressure and partition junction Q_n is given by[8]

$$F_n = -RT \ln Q_n kT + PT \ln P_n + H_n^0 \qquad (1)$$

where H_n^0 is the heat content of M_n at absolute zero. The dissociation energy D_2^0 ($D_2^0 = 2 H_1^0 - H_2^0$) of the diatomic molecule at absolute zero may be obtained by equating twice the molar free energy of the monomer to the molar free energy of the dimer. The result is in kcal/mol

$$\frac{D_2^0}{2.303\ RT} = -\log P_1 + \log(P_2/P_1) + \log \frac{T^{3/2}\ M^{1/2}}{r^2} + \log \frac{g_2^2}{g_1^2} - \log v + 2.8247 \qquad (2)$$

where P the pressure is in millimeters of Hg_1, and

P_2, P_1 = pressure of dimer, monomer in Knudsen cell

M = mass of monomer in atomic mass units

r = interatomic distance of dimer in angstroms

g_2, g_1 = electronic partition function of dimer, monomer

v = vibrational partition function of dimer = $\left[1 - \exp.\left(-\frac{h\omega c}{kT}\right)\right]^{-1}$

T = temperature, °K in Knudsen cell

ω = vibrational frequency in wave numbers (cm^{-1})

The partial pressure of the monomers is taken from the data of Stull and Sinke.[4] The ratio of pressures P_2/P_1, provided the molecules in the beam suffer no deactivating collisions, may be obtained from the known relationship between pressure in the Knudsen cell and ion intensity in the mass spectrometer[8] and is $P_2/P_1 = (I_2^+/I_1^+)(\sigma_1/\sigma_2)(\gamma_2/\gamma_1)$, where I_2^+/I_1^+ is the ratio of ion intensity of dimer to monomer in the mass spectrometer, σ_1/σ_2 the ratio of ionization cross sections, and γ_2/γ_1 the ratio of multiplier detection efficiencies. For a monoisotopic element the ion intensity ratio is directly measured from the observed ion currents of the dimer and monomer. Otherwise the ratio is calculated from the ion currents of a particular monomer and dimer mass, determined mass spectrometrically, using the known isotopic abundances and the fact that the mass distribution of the dimer is random. Although Otvos and Stevenson's[10] theoretical estimate of σ_1/σ_2 is 0.5, experiments indicate that the ratio is expected to be between 1 and 0.5[8] and the ratio γ_2/γ_1 varies between 1 and the $\sqrt{2}$.[8] Accordingly, a value of unity is chosen for the product ratio and P_2/P_1 is taken equal to the I_2^+/I_1^+ with an estimated uncertainty of a factor of 2. This leads to an error in D_2^0 of 3.3 kcal at 2400°K and 1.7 kcal at 1200°K. The maximum ion intensity ratio is estimated from the limits of detectability of the dimer (i.e., from the noise level of the recorder, the minimum signal that can be ascertained is determined at the mass position of the dimer) and the observed intensity of the atomic specie. The electronic partition function of the latter is calculated from the known atomic energy levels.[11] The molecular constants, vibrational and electronic partition functions, as well as the interatomic spacing for the ground state, must be estimated since the molecular Ti_2, Cr_2, and Mn_2 are unknown. Interatomic distances in diatomic molecules do not differ much from crystal spacings of the corresponding element and Pauling's[12] estimates of single covalent radii are for known molecules good to a few percent. In any case the error arising from this source is not expected to be more than 0.5 kcal and thus is negligible. Vibrational frequencies were taken as 1.25 times the Debye frequency of the corresponding metal crystal. A comparison of Debye frequencies and known symmetric diatomic molecule frequencies showed that the factor 1.25 gives somewhat better correlation than a previous assumption of approximate equality of these two frequencies.[13] Frequencies calculated by Badger's rule[14] are within 25% of the Debye calculated values. An uncertainty of 30% in the estimated frequencies corresponds to an uncertainty in the dissociation energy of approximately 1 kcal.

An inspection of Equation 2 shows that the maximum calculated dissociation energy occurs if the diatomic molecule is in $^1\Sigma$ state.[15] Provided that there are no low-lying electronic molecular states that contribute to the partition function* the lowest maximum dissociation energy that can be calculated involves a molecular state of $\Lambda > 0$

*It is expected that degenerate and closely lying atomic levels will be widely separated because of the large electric field at small internuclear distances.

(multiplicity of 2) and maximum spin. The maximum spin occurs when one electron from each atom is paired in a single bond and the remaining electrons fill the d shells of each atom in the molecule according to Hund's rule. Higher spins are possible if promoted electrons in the 4p or 4d shell exist in an unpaired manner but such states are considered improbable. According to these considerations, the electron configuration of the d shell of each atom (nonbonded part) is $3d^3$, $3d^5$, and $3d^8$ for Ti, Cr, and Mn respectively and the corresponding molecular states of maximum multiplicity are $^7\Lambda$, $^{11}\Lambda$, and $^9\Lambda$ ($\Lambda > 0$).

RESULTS AND DISCUSSION

The upper limits to the dissociation energy for both $^1\Sigma$ and the maximum multiplicity molecular states are given in Table II along with the data and molecular constants used in their computation. The position of these transition dimers in the fourth period based on a $^1\Sigma$ state is also shown in Figure 1. It is perhaps improbable that the ground state of molecules of this type would be singlets and a maximum value between those given for both limits is to be preferred. An upper limit of 40 kcal for dissociation energy of chromium based on $^1\Sigma$ state has been reported previously.[18]

Reference to Table I shows that the difference between the heat of sublimation and dissociation energy ΔHr is almost constant for many of the main and subgroups of the periodic table. The average differences for the various groups are: IA, 10; IB, 35; IIB (excluding mercury), 26; IIIA (excluding boron), 33; and IVA, 26. It is also to be noted that the ΔHr for most of the elements in Table I, except for the alkalis and boron, is between 25 and 40 kcal/mol, while the corresponding values for Ti, Cr, and Mn are much higher, being greater than 68, 51, and 45, respectively. Work currently being done in this laboratory[5] indicates that the dissociation energy (calculated according to Equation 2 and assuming a $^1\Sigma$ molecular ground state) of Ni_2 is 57 kcal/mol yielding a ΔHr of 42 kcal/mol. The larger difference for these transition elements results from the relatively high stability of the transition element solids (large heats of sublimation).

TABLE II

Dissociation Energies, Data and Molecular Constants

Element	Temperature (deg K)	I_2^+/I_1^+	Monomer			Dimer			Maximum Dissociation Energies (kcal/mol)	
			Vapor Pressure (mm)	Electronic State	g_1	ω (cm^{-1})	ν	r (A)	$^1\Sigma$	Maximum Multiplicity
Ti	2451	2.8×10^{-5}	0.73	^3F	19.28	331	5.68	2.65	58.1	45.1
Cr	1901	3.9×10^{-5}	0.27	^7S	7	400	3.82	2.34	43.6	31.9
Mn	1500	3.1×10^{-6}	0.87	^6S	6	348	3.52	2.34	21.2	12.4

Verhaegen *et al*[8] have shown that a, the ratio of the heat of sublimation to the dissociation energy, H_s/D_g^0, falls into three categories: Category 1, $0.5 \leq a \leq 1.0$ consisting of the elements of group VA (s^2p^3 outer electron configuration), VIA (s^2p^4), and VIIA (s^2p^5); Category 2, $1.2 \leq a \leq 2$ consisting of elements in groups IA (s^1), IB ($d^{10}s^1$), IIIA (s^2p^1, In a is 2.5, Tl a is 3), and IVA (s^2p^2); Category 3, $a \geq 5$ consisting of elements in group IIA (s^2) and IIB ($d^{10}s^2$). Category 1 consists of molecules forming, at least in part, molecular crystals, and category 3 consists of elements which, because of the s^2 configuration form very weak diatomic molecules (either promotional energy is required to form a binding state such as s^1p^1 or the low bond energy results from Van der Waal forces). Category 2 consists of all elements forming nonmolecular crystals and having available bonding electrons in the ground state. The heat of sublimation of titanium, chromium, and manganese are 113.3, 95.5, and 67 kcal/mol, respectively, and the corresponding minimum a's are 1.93, 2.2, and 3.2, so that at least the latter two elements and probably titanium do not belong to Category 2. Nickel, although a transition element, is in Category 2, having an a value of 1.75.[8] It is interesting to note that this value is very close to that of copper ($a = 1.78$[2]).

The following model of binding qualitatively explains the limited results thus far obtained for the dissociation energies of the transition element. It is assumed that the dimers are single bonded and that bonding arises from overlap of an s electron from each atom. The ground state electron configuration for the first group of transition elements is $3d^{a-2}4s^2$ (with the exception of chromium which is $3d^{a-1}4s$) and the lowest lying state above the ground state has a configuration $3d^{a-1}4s$ from which bonding is assumed to arise. States involving the configuration $3d^{a-1}4s4p$ are of much higher energy than $3d^{a-1}4s$. The lowest lying level for the configuration $3d^{a-1}4s$ is, according to Hund's rule, a state in which the s electron is aligned parallel to the remaining unpaired electrons in the d shell. Bonding theory[17] shows that in the binding state (valence state) the bonding electron spin must be random with respect to the spins of the remaining electrons. Thus the valence state is a state consisting of part s spin parallel to remaining spins and part antiparallel, the parts being weighted in such manner as to make the spin of the bonding electron random. Moffet[17] has shown how to calculate valence states. In the case of the configuration $3d^{a-1}4s$ the result is particularly simple since in altering the spin of the s electron the total orbital momentum number L does not change and it is found that the random state is simply a mixture of the s parallel and antiparallel case weighted according to their spin multiplicity. As an example the case of manganese is considered. The ground state configuration is $3d^54s^2$ with a level designation ^6S. The promoted configuration is $3d^54s$, the lowest state of which is ^6D (s spin parallel to remaining spins) and the corresponding higher state of antiparallel spin is ^4D. The energy of the valence state above the ground state is then $3/5(E_{^6D}) + 2/5(E_{^4D})$

where E_{6D} and E_{4D} are the energies of these states above the ground state. In Table III the ground state, the promoted states, the valence states, and their corresponding energies are listed. The values are taken from Moore's Atomic Energy Levels.[11]* The dissociation energy is, in terms of the valence state energy $E_{v.s.}$, $D_e = (D_e)_{v.s.} - 2E_{v.s.}$, where $(D_e)_{v.s.}$ is the dissociation energy of the dimer to atoms in the valence state (process $M_2 = 2M_{v.s.}$, $\Delta E = (D_e)_{v.s.}$). It should be noted that the treatment given here is somewhat similar to that used by Griffith[18] in correlating cohesive energies of transition elements.

The dissociation energy to atoms in the valence states corresponds to the energy to break an s bond. Thus nickel with a valence state energy of 3 kcal/mol atom should have a dissociation energy of only 6 kcal/mol less than for s bonding, while the manganese dissociation energy should be 112 kcal lower than for s bonding (i.e., if any bonding for manganese exists it would, according to these assumptions, be due to Van der Waal forces). The maximum dissociation found for manganese (12.0 to 21.0 kcal) and the dissociation energy of Ni [57.0 ($^1\Sigma$), or 50.0 ($^3\Lambda$)] are in agreement with predictions from this model. The nickel values correspond to an s bonding energy of 63 to 56 kcal/mol which may be compared to the dissociation energies of the somewhat similar molecules of Cu_2, Ag_2, and Au_2 (atomic states $3d^{10}4s$, $4d^{10}4s$, and $5d^{10}4s$; $E_{v.s.} = 0$) of 46, 38, and 52 kcal/mol respectively.

TABLE III

Valence State Energies for Configuration

$3d^{n-1}4s$

Element	Ground State	Lowest Lying (Parallel) State		Antiparallel State		Valence State	
		Term	Energy (kcal)	Term	Energy (kcal)	Term	Energy (kcal)
Ni	$3d^8 4s^2 (^3F)$	^3D	0.58	^1D	9.7	$3/4(^3D)+1/4(^1D)$	3.0
Co	$3d^7 4s^2 (^4F)$	^4F	10.0	^2F	21.3	$2/3(^4F)+1/3(^2F)$	14.0
Fe	$3d^6 4s^2 (^5D)$	^5F	20.0	^3F	34.0	$5/8(^5F)+3/8(^3F)$	26.0
Mn	$3d^5 4s^2 (^6S)$	^6D	49.0	^4D	67.0	$3/5(^6D)+2/5(^4D)$	56.0
Cr	$3d^5 4s (^7S)$	^7S	0.0	^5S	22.0	$7/12(^7S)+5/12(^5S)$	9.0
V	$3d^3 4s^2 (^4F)$	^6D	6.0	^4D	24.0	$3/5(^6D)+2/5(^4D)$	13.0
Ti	$3d^2 4s^2 (^3F)$	^5F	19.0	^3F	33.0	$5/8(^5F)+3/8(^3F)$	24.0

*Spin orbit coupling is negligible in computing valence states. The lowest spin orbit term J was taken as the appropriate energy. Other choices give valence state energy differences which are insignificant.

From the known dissociation energies of AuCr (50.4 kcal/mol[18]) and of Au_2 (51.5 kcal/mol), it is possible to make a rough estimate of the dissociation energy of Cr_2 using Pauling's relationship between electronegativity X and dissociation energies.

$D_{v.s.}(AuCr) = 1/2\,[D_{v.s.}(Cr_2) - D(Au_2)] + 23.06\,[X_{v.s.}(Cr) - X(Au)]^2$ where the v.s. subscript refers to the valence state (subscripts for Au and Au_2 omitted because Au valence state is the same as ground state). It is readily seen from the relationships $D(AuCr) = D_{v.s.}(AuCr) - E_{v.s.}(Cr)$ and $D(Cr_2) = D_{v.s.}(Cr_2) - 2E_{v.s.}(Cr)$ that $D(AuCr) = \frac{1}{2}[D(Cr_2) + D(Au_2)] + 23.06\,[X_{v.s.}(Cr) - X(Au)]^2$. The electronegativities are estimated by Pauling's method[20] $X = (I_p + E_a)/130$ where I_p and E_a are the ionization potentials and electron affinities in kcal respectively. The electronegativity values, obtained using Moore's Tables[11] for ionization potential and assuming $E_a = 0$, are $X_{v.s.}(Cr) = 1.12$ and $X(Au) = 1.63$, and the estimated dissociation energy of Cr_2 is $D(Cr_2) = 37$ kcal. This is in agreement with our maximum value. Chromium bonding energy should be 18 kcal (Table III) less than for the valence state bonding energy which thus corresponds to 55 kcal/mol. This is not far different from the corresponding $d^{n-1}s$ bonding for nickel and copper of approximately 50 kcal, and points to the possibility that the dimers of the transition element may have approximately the same valence state bonding energy. It is evident that the remaining Group I transition elements (Cu, Fe, and V), provided the model is approximately correct, should have rather low dissociation energies and thus dimers will be found only at temperatures substantially higher than used in the present work.

REFERENCES

1. DROWART, J., and HONIG, R. E. A Mass Spectrometric Method for the Determination of Dissociation Energies of Diatomic Molecules. Journal of Physical Chemistry, v. 61, 1957, p. 980-985.

2. VERHAEGEN, G., STAFFORD, F. E., GOLDFINGER, P., and ACKERMAN, M. Correlation of Dissociation Energies of Gaseous Molecules and of Heats of Vaporization of Solids. Transactions of the Faraday Society, v. 58, July - December 1962, p. 1926-1938.

3. KANT, A. Formation of Gaseous Polymers. Watertown Arsenal Laboratories Technical Report, WAL TR 821.6/1, July 1962. AD 283134.

4. STULL, D. R., and SINKE, A. C. Thermodynamic Properties of the Elements. American Chemical Society, Washington, D. C. 1958.

5. KANT, A., and STRAUSS, B. U. S. Army Materials Research Agency. Work in Preparation for Publication.

6. GAYDON, A. G. Dissociation Energies and Spectra of Diatomic Molecules. Dover Publications, New York, 1945.

7. CHUPKA, W. A., et al. Thermodynamic Studies of Some Gaseous Metallic Carbides. Journal of Physical Chemistry, v. 62, 1958, p. 611-614.

8. SCHISSEL, P. Dissociation Energies of Cu_2, Ag_2, and Au_2. Journal of Chemical Physics, v. 26, no. 5, 1957, p. 1276-1280.

9. MAYER, J. E. W., and MAYER, M. G. Statistical Mechanics. John Wiley and Sons, Inc., New York, 1948.

10. OTVOS, J. W., and STEVENSON, D. P. Cross-Sections of Molecules for Ionization by Electrons. Journal of the American Chemical Society, v. 78, no. 1, 1956, p. 546-551.

11. MOORE, C. E. Atomic Energy Levels. National Bureau of Standards Circular 467, 15 June 1949.

12. PAULING, L. Atomic Radii and Interatomic Distances in Metal. Journal of the American Chemical Society, v. 69, March 1947, p. 542-553.

13. BAUGHAN, E. C. Vibration Frequencies in Diatomic Molecules and in Solid Metals. Transactions of the Faraday Society, v. 48, 1952, p. 121-128.

14. BADGER, R. M. Atomic Valence States in Chemical Binding. Journal of Physical Chemistry, v. 2, 1934, p. 128.

15. HERZBERG, GERHARD. Molecular Spectra and Molecular Structure, Chapter VI. D. Van Nostrand, Princeton, New Jersey, 1955.

16. ACKERMAN, M., STAFFORD, F. E., and VERHAEGEN, G. Studies of the Vapors of the System Au-Cr and Au-Pd by Mass Spectrometry. Journal of Chemical Physics, v. 36, no. 6, March 1962, p. 1560-1562.

17. MOFFITT, W. Reports on Progress in Physics, v. 17, 1954, p. 173-200.

18. GRIFFITH, J. S. The Cohesive Energies of Transition Metals. Journal of Inorganic and Nuclear Chemistry, v. 3, 1956, p. 15-23.

19. ACKERMAN, M., STAFFORD, F. E., and DROWART, J. Mass Spectrometric Determination of the Dissociation Energies of the Molecules AgAu, AgCu, and AuCu. Journal of Chemical Physics, v. 33, no. 6, 1960, p. 1784-1789.

20. PAULING, L. The Nature of the Chemical Bond. Cornell University Press, Ithaca, New York, 1948, p. 58-67.

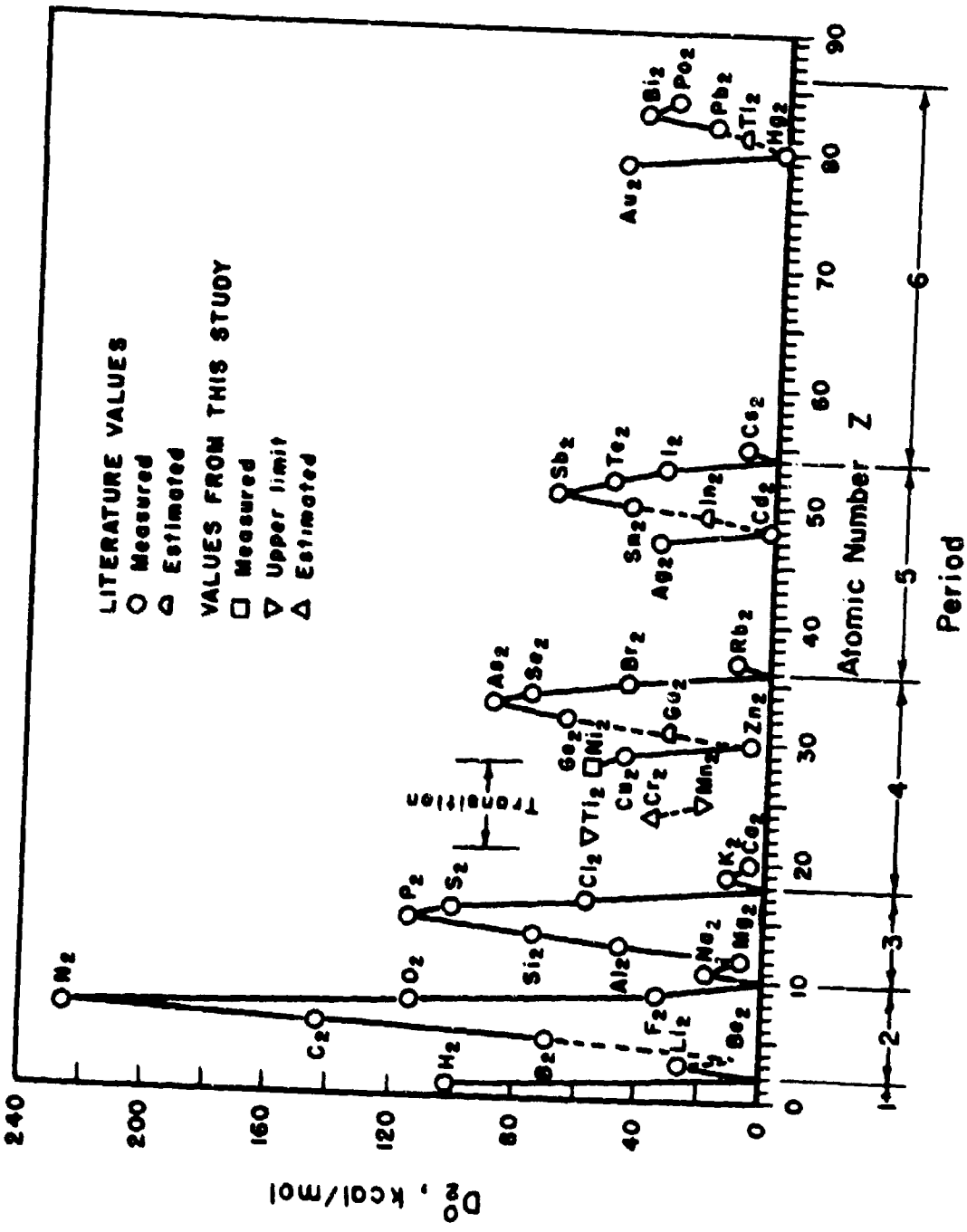

Figure 1. DISSOCIATION ENERGIES OF DIMERS VERSUS ATOMIC NUMBER Z
(Figure 1 Modified from Reference 1)

U. S. ARMY MATERIALS RESEARCH AGENCY

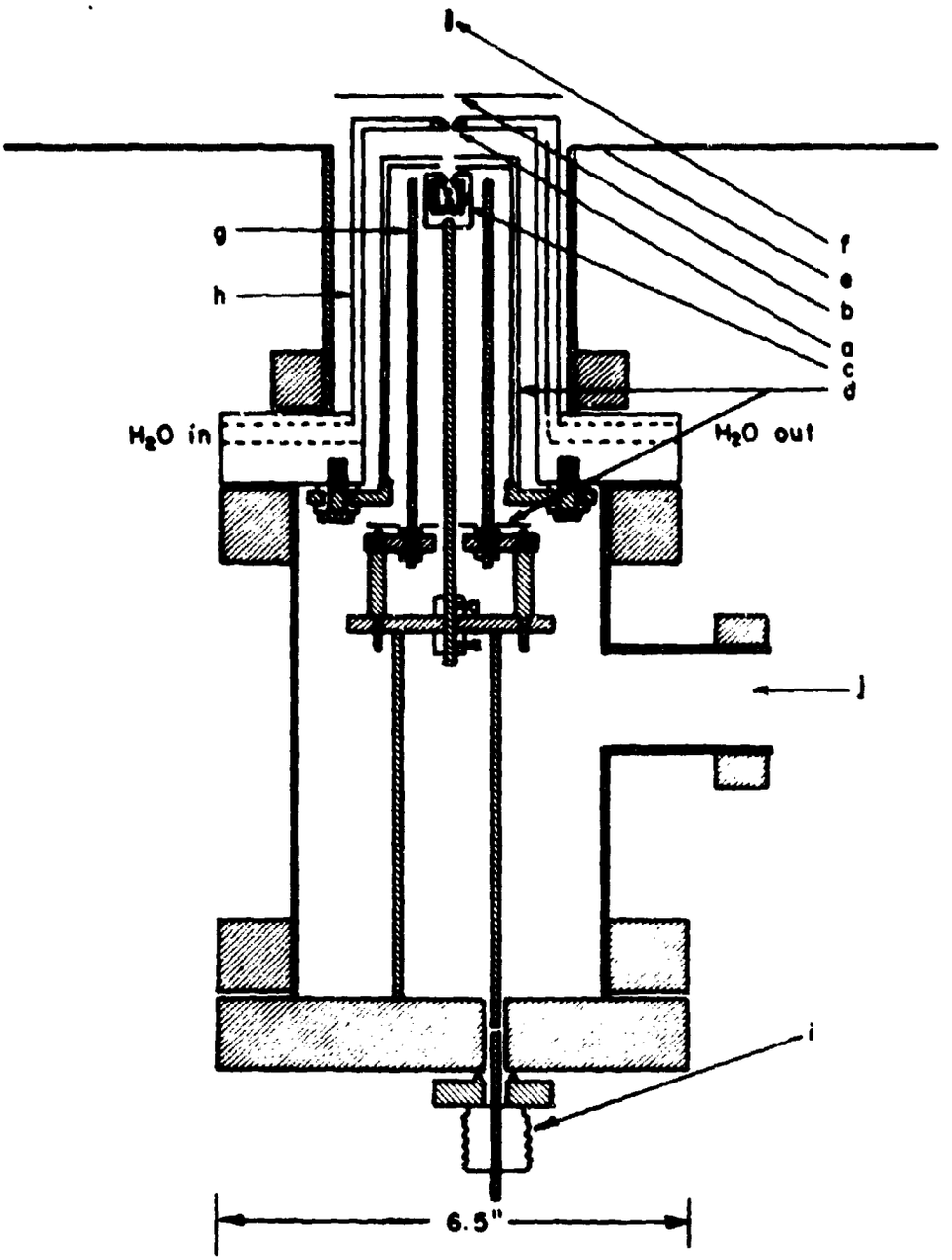

Figure 2. EFFUSION CELL AND HIGH TEMPERATURE SOURCE ASSEMBLY. a. Water jacket slit; b. Beam defining slit; c. Tantalum crucible, thoria liner, and blackbody holes; d. Tantalum radiation shields; e. Mass spectrometer housing; f. Mass spectrometer ionizing electron beam; g. Filament supporting post (tantalum); h. Water cooled jacket; i. Micrometer - bellows arrangement; j. High temperature assembly pumping port.

U. S. ARMY MATERIALS RESEARCH AGENCY

19-066-288/AMC-64

THE RELATION BETWEEN CLOUD CHARGES PRECIPITATION AND LIGHTNING DISCHARGES

HEINZ W. KASEMIR
U. S. ARMY ELECTRONICS RESEARCH AND DEVELOPMENT LABORATORIES
FORT MONMOUTH, NEW JERSEY

An extensive thunderstorm research is carried out by USAELRDL as "In-House Laboratory Director's Program" which, in collaboration with "cloud physics and cloud modification experiments", aims to correlate the meteorological and the electrical features of a thunderstorm in a qualitative and as far as possible quantitative way.

To obtain an adequate set of data of the electric condition of an individual storm from a ground network, the following idea was pursued: The electric field of a lightning discharge, which is easily measured at the ground, will reflect the stationary field of the cloud charges inside the thunderstorm. Each lightning flash may be considered as a probe which senses the stationary field along its path. Therefore the records of the lightning discharges will furnish a series of flashlight pictures of the electric condition as it develops during the life cycle of the storm.

First it was necessary to develop a theory, which links together the different electric parameters of a thunderstorm such as precipitation charge, stationary electric fields, and lightning discharges. This theory serves a dual purpose. It determines the physical quantities to be recorded and hereby helps to plan an effective measuring network, and it shows how the recorded data shall be evaluated to obtain basic electric quantities, which cannot be measured directly. As this theory deviates from and in some respect even contradicts the present ideas of the mechanism of the charge generation in the thundercloud and the lightning discharge, it seems worthwhile to formulate and discuss it as a separate entity even though the experimental part of the research is not yet completed.

1. CHARGE DISTRIBUTION IN THE THUNDERCLOUD

Investigations of the electrification of precipitation started as early as 1885.(1) Since then, a steady stream of theories

(2-9) on the charge generation in thunderstorms has been proposed and discussed. None of them explains all of the different observations on thunderstorm electricity; and objections have been raised from different points of view such as polarity, charge-generating power, efficiency of liquid as well as solid precipitation, laboratory experiments, and many others.

There is general agreement that the thunderstorm has a positive polarity, meaning that the main positive charge is located in the top and the main negative charge in the bottom of the thundercloud. Below the negative charge exists a smaller positive-charge pocket. This tripolar charge distribution is clearly depicted in the thunderstorm model of Simpson and Robinson (1) (Fig. 1a). Other models have been proposed by Schonland (11), Wichmann (12), and Vonnegut (9), as shown in Figs. 1b, c, and d, respectively. The first three models (a, b, and c) are based on charge separation by precipitation, and the last model, d, on charge separation by convective aircurrents. The positive polarity of the storm is common to all of them, but they differ from each other in the shape, size, and arrangement of the individual charge centers.

The amount of charge for the positive and negative main charge center is given by Simpson and Robinson as +24 coulombs and -20 coulombs. Schonland assumes the values of ±40 coulombs. The author (13) calculated a positive charge of +60 coulombs and a negative charge of -340 coulombs for the main charge centers.

The striking difference between these values results from the fact that Simpson and Robinson as well as Schonland calculated the cloud charges from measured field data according to the electrostatic theory, while the author based his calculation on the theory of current flow. This introduced the conductivity λ of the cloud and the surrounding air as a deciding factor in the thunderstorm theory, made it possible to connect the cloud charge Q and the conduction current I through the simple relationship $Q = \frac{\epsilon}{\lambda} I$ with each other (ϵ is the dielectric constant) and, as Tamura (20) has shown, explains the mystery of the recovery curve. (The recovery curve is the rapid regeneration of the electric field after a lightning flash to its preflash value.) The larger amount of the negative cloud charge makes it easier to understand that a thunderstorm is able to produce lightning discharges which destroy each 20 coulomb of the cloud charge every 20 seconds on the average without exhausting itself.

2. THE CLOUD DISCHARGE

If the charge accumulation in the thundercloud reaches such a value that the generated electric field exceeds the breakdown value, a lightning discharge will occur. It is not necessary that the breakdown value of the field extends over the entire distance of the flash. It is sufficient when this value is surpassed in a small area, which

we may call the starting point of the flash. This and other features of the lightning discharge can be easily deduced from Figs. 2a, b, and c. In the thunderstorm model (Fig. 2a), two equally large spheres are placed one above the other. The upper sphere is filled with positive charge and the lower sphere with negative charge of the same amount and of constant density. Figure 2b shows a graph of the potential function ϕ (solid line) through the center of the model against altitude h. The field $F = -d\phi/$ is represented by the dashed line. The maximum field strength F_{max} is at the midpoint between the spheres. This will be the starting point of the flash. Near the center points of the spheres, the field strength F passes through the value zero (marked F = 0 in Fig. 2b) and reverses its sign on the way further up or down. A lightning flash, which starts at F_{max} and grows upwards and downwards, will find an adverse field for further growth after passing through the centers of the space charges. The lightning will stop growing when the field strength at its tips no longer exceeds the breakdown value F_b. The corresponding potential value of ϕ_b (Fig. 2b), defined as the difference between the lightning potential and that of the potential function ϕ at the location of the lightning tips, is given by the approximate formula (14)

$$\phi_b = 2.5\ m \cdot F_b. \qquad (1)$$

An important conclusion can be drawn from Figs. 2a and b. The lightning flash, represented by the heavy vertical line in Fig. 2b, will never reach the ground. The field strength at the tip will be less than the breakdown value when the tip reaches the base of the cloud. The lightning will remain a cloud discharge. A ground discharge cannot be generated by a charge distribution such as given in Fig. 2a. To produce ground discharges, the lower positive space charge has to be present, as will be shown later. Therefore, if thunderstorms are recorded which produce only cloud discharges, a charge distribution in the cloud as given in Fig. 2a can be assumed.

The lightning channel can be considered as a conducting rod exposed to the electric field generated by the cloud charges. Therefore, influence charges are induced in the upper and lower ends of the channel of opposite polarity to the cloud charges. This would be for a cloud flash negative influence charge at its upper end, and positive at its lower end. The net charge of a cloud flash is zero and its polarity is negative.

The charge per unit length q on the lightning channel is shown in Fig. 2c (dashed line). It is the mirror image of the potential function ϕ with regard to a vertical line representing the lightning channel. An approximate formula (14) connecting q and ϕ is given by

$$q = -c\,\phi. \qquad (2)$$

The proportionality factor c can be interpreted as the capacity per unit length of the lightning channel. It has the approximate value of 25×10^{-12} F/m (14).

It may be worthwhile to point out some differences between the commonly used concept of the lightning discharge and that developed here. In general, it is assumed that the lightning flash starts in the center of, say, the negative space charge. By the development of a large network of fine streamers, the lightning collects the cloud discharges and transports them along its channel, either to the ground (ground discharge) or to another space-charge center of opposite polarity (cloud discharge). The lightning stops if the supply of cloud charge is exhausted. After the completion of the flash, the cloud, as well as the lightning channel itself, is discharged.

In the concept proposed here, the lightning starts between two charge centers, where the electric field has a maximum value. (In the center of the space charge, the field would be approximately zero.) The direction of channel growth is up as well as down under the influence of the field. The lightning does not collect cloud charges, and therefore it is not necessary to introduce a hypothetical network of fine streamers. There is only a separation of ions and electrons in the highly ionized lightning channel itself to build up the necessary influence charges. The concept is that of an uncharged conducting rod exposed to an electric field. The lightning flash stops, not because the cloud charges are exhausted, but because the field strength at its tips does not exceed the breakdown value. After the lightning stops, the lightning channel is filled with influence charges. Each half of the channel carries influence charges of opposite polarity to the surrounding cloud charges. The net charge of the whole channel is zero. After the cloud flash is completed, a slow neutralization process begins between the influence charges of the lightning channel and the surrounding cloud charge of opposite polarity. Only this process should rightly be called the discharge of the cloud by the lightning.

3. THE GROUND DISCHARGE

If we add the lower positive charge pocket to the positive and negative main charge centers, we obtain the charge distribution of the Simpson-Robinson thunderstorm model. This is shown in Fig. 3a, side by side with the corresponding potential function ϕ in Fig. 3b. We see that two areas with strong electric fields exist, marked sc and sg in Fig. 2b. The upper one, sc, is the starting point for cloud discharges, and corresponds to the point F_{max} in Fig. 2b. The lower one, sg, is due to the presence of the positive pocket charge and is the starting point for ground discharges. In a similar manner as the

cloud flash, the ground flash grows from its starting point to both sides until its lower end reaches the ground. This will happen only if the field strength F_b at the lower tip remains greater than or equal to the breakdown field, or $\phi_1 - \phi_o$ is always greater than ϕ_B (see Fig. 3b), where ϕ_1 is the potential of the lightning channel, and ϕ_o the potential of the ground. If the breakdown field could not be maintained on the downward travel of the lower tip, the lightning would stop growing and end up as an air discharge. The equation

$$\phi_1 - \phi_o = \phi_b = 2.5 \text{ m } F_b = -7.5 \times 10^6 \text{ V/m} \qquad (3)$$

gives the minimum potential difference against ground, which the leader stroke of a ground flash must have to reach the ground. In Eq. 3 is set $\phi_1 = 0$: $F_b = -3 \times 10^6$ V/m.

It is easy now to imagine the conditions for the charge distribution of a thunderstorm that produces predominantly ground discharges and few or no cloud discharges. They are as follows: 1) The upper positive charge center should be weak, 2) the lower negative charge center should be strong, and 3) the lower positive pocket charge should exist. Figure 3c shows the potential function of such a charge distribution.

If the lower end of the lightning channel touches the ground, the lightning will assume ground potential ϕ_o. This is accomplished during the phase of the main, or return, stroke. With respect to the h - ϕ graph in Fig. 3b, it means that the lightning channel (heavy vertical line) shifts to the right from the ϕ_1 to the ϕ_o value. The new position and the new charge distribution (broken line) are shown in Fig. 3d. We see that after the completion of the main stroke the lightning channel carries, on its upper part, a large amount of positive influence charge, and on its lower part a smaller amount of negative influence charge. The net charge on the channel is no longer zero, but positive. This means that during the main stroke the channel has acquired positive charge from the ground or that negative charge has been conducted into the ground. The amount of this charge Q_m is represented in Fig. 3d by the rectangular hatched area. It can be easily calculated from the capacity c of the channel and the potential difference $\phi_1 - \phi_o$ before and after the main stroke.

$$Q_m = c\,(\phi_1 - \phi_o). \qquad (4)$$

If we assume that the length of the channel is 4 km, that the capacity per unit length has the previous value of 25×10^{-12} F/m, and $\phi_1 - \phi_o$ has the minimum value of -7.5×10^6 V, we obtain for the minimum charge brought to earth by the first main stroke $Q_{min} = -0.75$ coulomb. This value may have to be doubled or tripled according to the number of branches of the considered lightning flash, as each branch would increase the capacity. But even so, the value of Q_{min} has the right order of magnitude, as compared to measured data available in the literature. This is a remarkable result insofar as

Q_{min} is based only on the value of the breakdown field strength at the ground and the length of the lightning channel, but does not imply any data from the thunderstorm. For successive main strokes in a multiple flash, the value of Q_{min} would, in general, be lower because the breakdown field in the pre-ionized channel is lower, and only the length added to the channel by the considered multiple stroke has to be taken into account.

Each successive leader main stroke sequence will extend the channel higher up or sideways into the cloud until the whole negative charged area of the cloud is penetrated by the flash. Therefore, ground discharges with a large number of multiple strokes indicate a large area of the negative cloud charge. Flashes with one main stroke indicate a small region of the negative charge center. It is interesting to review the different thunderstorm models in Fig. 1 from this point of view. Schonland's and Vonnegut's models, Fig. 1b and d, are apt to give high-order multiple strokes. Simpson-Robinson's and Wichmann's model, Fig. 1a and c, will generate ground flashes with only one or a low-order of multiple strokes.

4. RELATION BETWEEN PROPERTIES OF THE ELECTRIC FIELD OF A LIGHTNING DISCHARGE AND THUNDERSTORM PARAMETERS

The large number of charge-generating theories and the failure to explain all the electrical features of different types of thunderstorms by one of them suggest the idea that several kinds of charging mechanism are at work in different parts of the thunderstorm. Kuttner(15) observed on the mountain observatory at the Zugspitze that strong electric fields are always associated with graupel precipitation. This correlation was so pronounced that it led him to the introduction of the graupel dipole, with a negative polarity, which produces part of the negative cloud charge and the positive space charge pocket at the base of the cloud. Kuttner attributed the upper positive charge and the other part of the negative charge in the higher level of the cloud to the snow dipole.

The author (13) pointed out that it is doubtful that any of the three cloud charges can be identified with the charge riding on the precipitation particles. The precipitation charge lacks the ability to accumulate and concentrate in a certain cloud volume. The cloud charges can be better interpreted as the charges left behind, while the precipitation carries away the charge of opposite sign. This leads to the conclusion that either two sign reversals in the precipitation-charging mechanism are required to account for a tripolar thundercloud or that at least two, if not three, different charge mechanisms are present which may work on different precipitation particles. The second alternative would then agree with Kuttner's snow and graupel dipole. With respect to the lightning discharge, this would mean that the number of cloud discharges reflect the efficiency of the charging mechanism in the upper part, and the number of ground discharges the efficiency of the charging mechanism in the lower part

of the cloud. A record of the polarity of the flashes at the ground (negative for cloud and positive for ground discharges) would give an easy means to follow the development of the respective charge centers and their corresponding precipitation particles during the life history of the storm.

With the strong tie between the lower positive space charge pocket and ground discharges, the following relation may be stated as a working hypothesis. Thunderstorms with ground discharges contain precipitation in the form of graupel; those without ground discharges do not. It is not necessary that the graupel pellet reaches the ground still as graupel; it may be melted to a raindrop on the way down. But its existence at the base of the cloud is required.

As shown earlier, the positive polarity of the ground discharge and the negative polarity of the cloud discharge follow from the positive polarity of the thundercloud charges. Falconer and Schaefer (16) and Vonnegut and Moore (17) report measurement of strong negative electric fields, indicating a negative charge overhead, from the cirrus deck accompanying the Worcester tornado. If this implies that a tornado is topped with a negative charged anvil above the upper positive charge center, cloud flashes with positive as well as negative polarity would be produced. This would make a tornado easily identifiable from the polarity records of lightning flashes alone.

A characteristic feature for the activity of a thunderstorm would be the number of lightning discharges produced in a given time interval. Brook and Kitagava (18) defined as activity index A the frequency of lightning occurrence in a period of five minutes. The time interval of lightning discharges in weak, intermediate, and heavy storms is about 5 minutes, 30 seconds, and 3 seconds, respectively. An activity index of 1, 10, and 100 would then result. One could develop this method further by differentiating between the number of cloud and ground flashes. The cloud flash index A_c would then indicate the activity of the upper positive charge center, and the ground flash index A_g that of the lower positive charge center. Jones (19) used the number of spherics per second emitted from a tornado for his tornado identification and warning system. From his data we may infer that a tornado produces about six lightnings per second. This would result in a tornado activity index of 1800.

References

1. Elster, J., Geitel, H.: "Uber die Elektrizitats-entwicklung bei der Regenbildung," Ann. Phys. n. Chem., 25, 121-131, 1885.

2. Sohnke, W.: "Der Ursprung der Gewitter-elektrizitat und der gewohnlichen Elektrizitat der Atmosphere," Ann. d. Phys., 28, 1886.

3. Lenard, P.: "Uber die Elektrizitat der Wasserfalle," Wied. Ann. d. Phys., 46, 584-636, 1892.

4. Simpson, G. C.: "On the Electricity of Rain and Its Origin in Thunderstorms," Phil. Trans. Roy. Soc., A 209, 397-413, 1909.

5. Wilson, C. T. R.: "Some Thundercloud Problems," F. Franklin Inst. 208, 1-12, 1929.

6. Findeisen, W.: "Uber die Entstehung der Gewitterelektrizitat," Meteor. Z., 210-215, 1940.

7. Frenkel, J.: "Influence of Water Drops on the Ionization and Electrification of Air," J. Phys., Moscow 10, 151-158, 1946.

8. Workman, E. J., Reynolds, S. E.: "A Suggested Mechanism for the Generation of Thunderstorm Electricity," Phys. Rev., 74, 1948.

9. Vonnegut, B.: "Possible Mechanism for the Formation of Thunderstorm Electricity," Proc. Conf. Atmos. Elec., 1954, Geophys. Res. Paper No. 42, 169-181, 1955.

10. Simpson, G. C., Robinson, G. D.: "The Distribution of Electricity in Thunderclouds," Proc. Roy. Soc., A 177, 281-329, 1940.

11. Schonland, B.: "Progressive Lightning IV. The Discharge Mechanism," Proc. Roy. Soc., A 168, 455-469, 1938.

12. Wichmann, H.: "Grundprobleme der Physik des Gewitters," Wolfenbuetteler Verlagsanstalt, 1948.

13. Kasemir, H. W.: "The Thundercloud." Paper given at the Third International Conference on Atmospheric Electricity (in print), 1964.

14. Kasemir, H. W.: "The Lightning Discharge," USAELRDL Technical Report 2401, Fort Monmouth, New Jersey, Dec 63.

15. Kuttner, J.: "The Electrical and Meteorological Conditions Inside Thunderclouds," J. of Met., 7, 322-332, 1950.

16. Falconer, R., Schaefer, V.: "Cloud and Atmospheric Electrical Observations of the Formative Stages of the Worcester, Massachusetts, Tornado," Bull. Amer. Met. Soc., 35, 9, 1954.

17. Vonnegut, B., Moore, C.: "Giant Electrical Storms," Naval Research Contract NONR-1684(00), 1958.

KASEMIR

18. Brook, M., Kitagawa, N.: "Some Aspects of Lightning Activity and Related Meteorological Conditions," J. Geophys. Res., 65, 4, 1203-1210, 1960.

19. Jones, H.: "Research on Tornado Identification," Signal Corps Research Contract DA 36-039 SC-64493, 1956.

20. Tamura, Y.: "An Analysis of Electric Field after Lightning Discharges," Proc. Conf. Atm. Electr, 190-200, 1955.

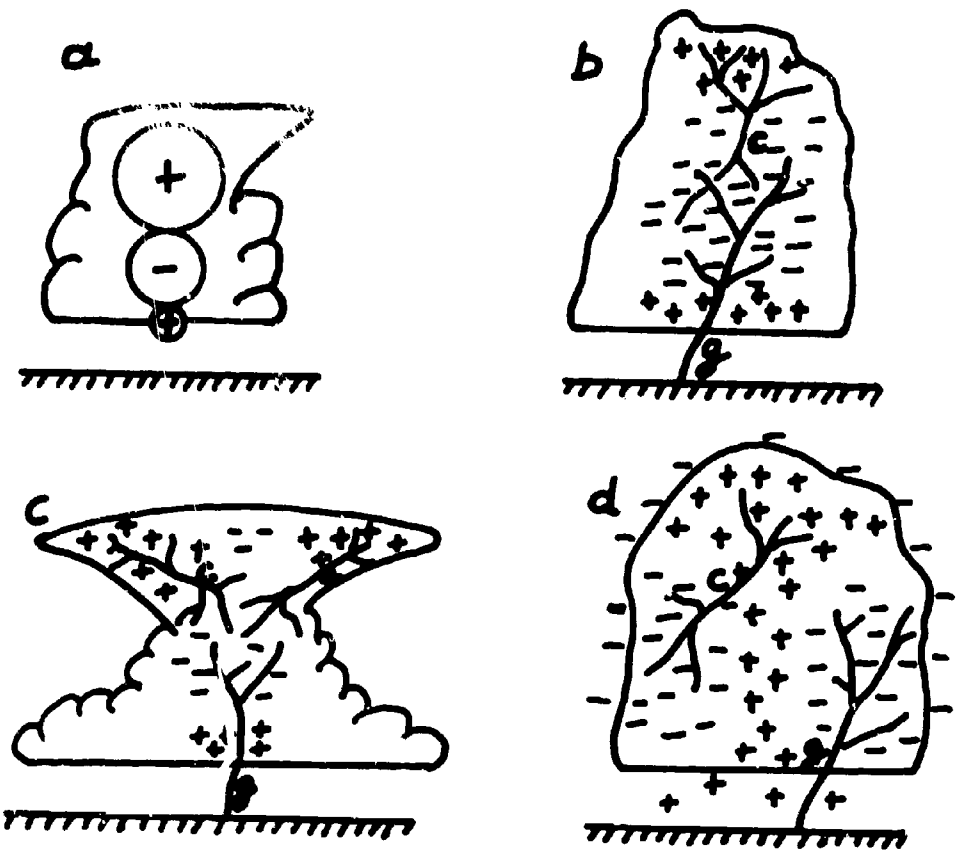

Figure 1. Thunderstorm Models of

a. Simpson-Scrase
b. Schonland
c. Wichmann
d. Vonnegut

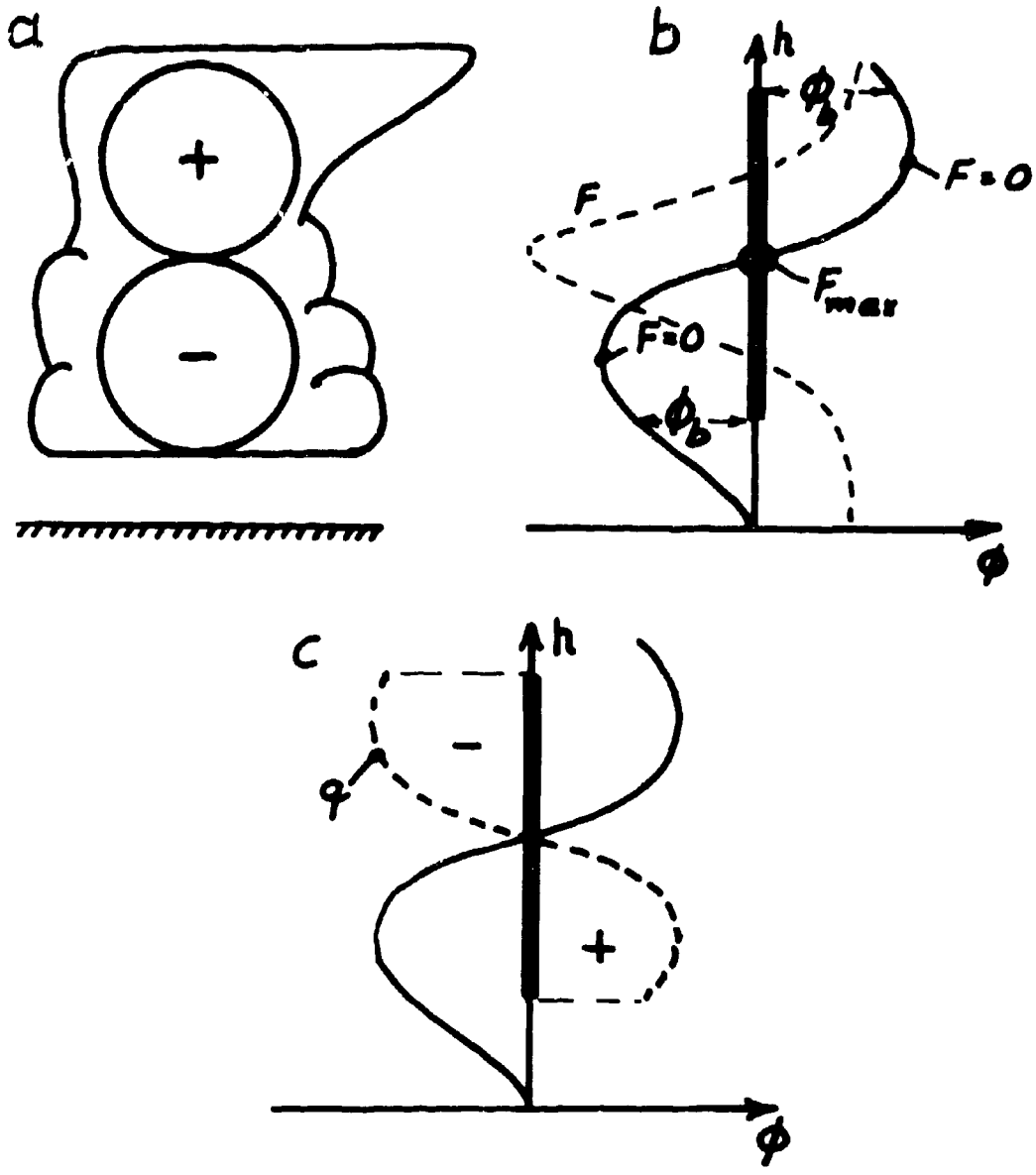

Figure 2.

a. Thunderstorm with equal positive and negative charge
b. Potential function ϕ aginst altitude h with cloud discharge
c. Chage density g of cloude discharge

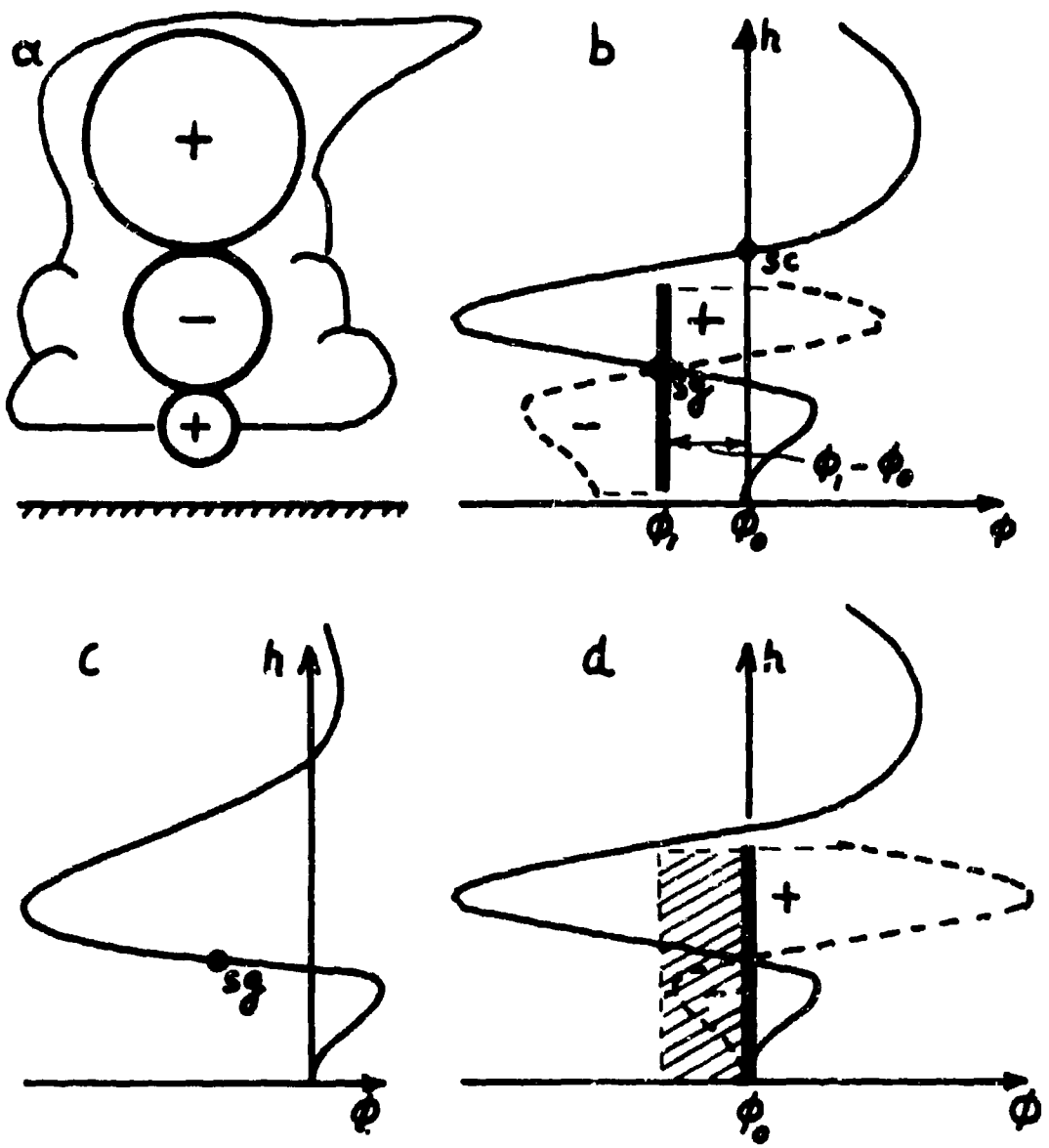

Figure 3.

a. Tripolar thunderstorm model after Simpson and Scrase
b. Potential function ϕ against altitude h with ground discharge leader
c. Potential function ϕ for ground discharges only
d. Potential function ϕ and main stroke

THE EFFECT OF STRAIN RATE ON YIELDING CHARACTERISTICS OF HIGH STRENGTH ALLOY STEELS

D. P. KENDALL
WATERVLIET ARSENAL
WATERVLIET, N. Y.

INTRODUCTION

The effect of rate of loading or strain rate on the flow characteristics of metals has long been of interest. The effect was first studied in tin by Ludwik[1] who proposed a linear relationship between the flow stress and the logarithm of the strain rate. Subsequent investigations by Nadai and Manjoine[2] showed that yield and tensile strengths are not continuously linear with logarithmic strain rate for several pure metals and low alloy steel. These materials exhibit specific ranges of strain rate sensitivity but are virtually insensitive to strain rate effects outside these ranges. The range of rate sensitivity and the strength increase are very dependent on material and temperature.

Clark and Wood[3] reported increases in the tensile strengths of several engineering materials at strain rates in excess of 100 in/in/sec including increases of from 0 to 23 percent for heat-treated alloy steels. Due to the nature of the impact type test used they did not determine the variation in strength as a function of strain rate.

There have been many recent investigations, using various techniques, into the effects of strain rate on mechanical properties. Much of this work was presented at two symposia on high rate deformation[4],[5]. Virtually all of this work, however, was limited to mild steel and relatively low strength metals and alloys. For medium strength alloy steels Abbe[6] and Hammer and Cadle[7], using pressurized cylinder techniques, have reported increases in yield strength of approximately 15 percent at strain rates of 2 and 6 in/in/sec.

It is the purpose of this current work to determine the relationship between yield strength and strain rate for a series of high and ultra high alloy steels at strain rates in the range from 10^{-4} to 10 in/in/sec.

APPARATUS AND PROCEDURE

A special high rate tensile testing system developed at Watervliet Arsenal was used to obtain the majority of data presented in this work. This machine is capable of developing forces in excess of 60,000 pounds in less than one millisecond. It operates on the principle of rapid fluid transfer from a high pressure, liquid charged accumulator to a hydraulic cylinder which rapidly loads a standard tensile specimen. The test system is shown in Figure 1 with a schematic diagram in Figure 2.

The operation of the system is as follows: The high speed valve is closed by introducing a gas (nitrogen) pilot pressure of 1500 psi beneath the plunger. The accumulator is then charged with water to a pressure of 10,000 to 15,000 psi. The system is fired by opening the electro-pneumatic trigger valve allowing high pressure to be exerted over the top of the valve plunger causing the valve to open slightly. High pressure fluid directly from the accumulator will then flow into the space above the plunger forcing it rapidly downward, thereby uncovering the outlet port of the valve and permitting rapid fluid transfer from the accumulator to the hydraulic cylinder. This results in a rapidly applied tensile load on the specimen. The volume and compressibility of the water in the accumulator is sufficient to allow up to one half inch of specimen elongation without a significant decrease in load. The strain rate is controlled by means of adjustable throttle valves in the line connecting the high speed valve and hydraulic cylinder.

The instantaneous load on the specimen is measured by means of a strain gaged loading bar or load cell into which the specimen is threaded. The load cell is instrumented to cancel any effects of bending and its output is connected to one channel of a Sanborn, light beam type, oscillographic recorder having a frequency response of DC to 5,000 cps. The entire load recording system is calibrated periodically in a conventional Riehle 60,000 pound tensile testing machine. The instrumentation is calibrated electrically before each test by shunting a standard resistor across one arm of the load cell bridge circuit. The maximum total error of load measurement is estimated to be plus or minus two percent.

To measure strain the specimen is instrumented with two, one inch gage length, high elongation strain gages which are connected to other channels of the oscillographic recorder. One load-time and two strain-time curves are thus obtained. In addition, the amplified load and strain signals are simultaneously fed into the Y and X axes, respectively, of an X-Y storage type cathode ray oscilloscope to obtain a stress-strain curve directly.

MATERIALS AND SPECIMENS

The materials investigated in this work are two moderately high strength and two ultra high strength alloy steels. The former are a standard 4340 steel (static yield strength of 158,000 psi) and a modified 4330 steel (static yield strength of 148,000 psi). The latter are a type H-11 high chromium steel (static yield strength of 250,000 psi) and an 18 percent nickel mar-aging steel (static yield strength of 275,000 psi).

All specimens except the modified 4330 were machined from one inch diameter bar stock. The modified 4330 specimens were cut from a large gun tube forging in the transverse direction. The chemical composition and heat treatment for all specimens are shown in Table 1.

DISCUSSION OF RESULTS

In order to compare some results of the experimental procedure used in this work with those of other investigations the upper yield strength of an annealed 1018 steel was determined as a function of elastic strain rate. These data are shown in Figure 3A along with results previously reported by Krafft and Sullivan[8] for a similar material. The agreement between the two investigations is quite good.

The yield strengths at 0.2 percent offset for 4340 steel and for modified 4330 steel are shown in Figures 1B and 1C, respectively. The 4340 steel shows a slight linear increase in strength over the range of strain rates investigated. The overall increase in strength is 4½ percent. The modified 4330 steel appears to exhibit no significant increase in strength up to a strain rate of about 1.0 in/in/sec. Above this rate a linear increase is seen with a strength increase of about 11 percent at a strain rate of 10 in/in/sec.

The yield strengths of two ultra high strength alloys are shown as a function of strain rate in Figure 4. Data for H-11 steel are shown in Figure 4A. Very little increase in strength is seen for strain rates up to about 0.1 in/in/sec after which the strength increases approximately linearly up to a total increase of 10 percent at 10 in/in/sec.

Figure 4B shows the yield strength of the mar-aging steel as a function of strain rate. This material shows a linear increase in strength over the entire range of strain rates with an overall increase of about 9 percent.

In the above figures each data point represents a single test specimen. The short vertical line representing plus or minus two percent of the strength level indicates the range of estimated experimental error for the data. This represents a range of points

TABLE 1. SPECIMEN CHEMISTRY AND HEAT TREATMENT

MATERIAL	C	Mn	Si	Ni	Cr	Mo	V	Co	Ti	Zr	B
4340	0.44	0.75	0.30	1.65	0.85	0.21					
Mod. 4330	0.35	0.69	0.26	2.68	1.05	0.44	0.18				
H-11	0.40	--	--	--	5.00	1.30	0.50				
Mar-Aging	0.02	0.08	0.08	18.5	--	5.0	--	9.0	0.6	0.01	.003

HEAT TREATMENT (TEMPERATURES IN ^{o}F)

	AUSTENITIZE	QUENCH	TEMPER	
4340	1550	Oil	1025	
Mod. 4330	1550	Water	1050	
H-11	1850	Air	1050	(Double Temper, 1 Hour Each)
Mar-Aging	1500	Air	900	(3 Hour Aging)

through which a line may be drawn which will truly represent the data within experimental accuracy.

Although not considered as part of this investigation, it was also observed that the ultimate tensile strength increases in the same manner as the yield strength maintaining about the same difference between yield and tensile strength. The plastic strain rate at the ultimate tensile strength differs significantly from the elastic strain rate due to the elasticity of the test system. A comparison of both yield and tensile strengths as a function of elastic strain rate would therefore be highly questionable.

It should also be noted that no variation in ductility, as measured by reduction in area, could be seen for any of the materials investigated over the full range of strain rates.

Most metals exhibit a decrease in yield and flow stress with increasing temperature over ranges in which no structural or phase changes occur. It might also be expected that strength would be affected by strain rate, but in the opposite sense (increasing strength with increasing strain rate). However, prediction of what the precise effect of strain rate would be based on some model of yielding and flow for an alloy steel would not be possible at this time since the actual yielding mechanisms in iron-carbon martensitic alloy structures have not been determined with any degree of certainty. The existence of regions of relative insensitivity to strain rate and regions of linear increasing strength and of some "critical" strain rate or transition zone at the boundary between these two regions do not fit into any conventional model of yielding and flow.

It is obvious that further work in this area is required. Extension of the range of strain rates to both higher and lower rates and testing of more specimens will be accomplished to establish the exact shape of the curves with greater confidence. The effect of temperature will also be considered along with studies in fatigue and fracture toughness.

CONCLUSIONS

For the four representative high and ultra-high strength alloy steels investigated, the increase in yield strength over a range of strain rates from 10^{-4} to 10 in/in/sec varies from 4½ to 11 percent depending on the material.

As is the case with pure metals and lower strength alloys, the increase in yield strength is linear with logarithmic strain rate over some specific increment of strain rate.

The extent of this linear range varies with the material and may be as narrow as one order of magnitude or may extend over

more than five orders of magnitude. For all cases the maximum rate investigated is still within the range of linear strength increase, indicating further increases in strength at strain rates greater than 10 in/in/sec.

REFERENCES

(1) Ludwik, P., "Elemente der Technologischen Mechanik," pp.44-47, Verlag Julius Springer, Berlin, 1909.

(2) Nadai, A., & Manjoine, M. J., "High Speed Tension Tests at Elevated Temperatures," Part I, Proc. ASTM, 40; Parts II & III, J. Applied Mechanics, June 1941.

(3) Clark, D. S., & Wood, D. S., "The Tensile Impact Properties of Some Metals & Alloys," Trans. ASM, 42, 45 (1949).

(4) Shewmon, P. G., & Zackay, V. F., eds., "Response of Metals to High Velocity Deformation," Met. Soc. AIME, 1960.

(5) Proc. Conf. on The Properties of Materials at High Rates of Strain, IME, London, 1957.

(6) Abbe, E. H., "Determination of Yield Strengths of Engineering Materials at High Loading Rates," Proc. Conf. on Dynamic Behavior of Materials & Structures, Springfield Armory, 1962, pp.242-250.

(7) Hammer, A., & Cadle, H., "The Effect of High Rate Loading on the Mechanical Properties of Ordnance Materials," Proc. Conf. on Dynamic Behavior of Materials & Structures, Springfield Armory, 1962, pp.222-241.

(8) Krafft, J. M., & Sullivan, A. M., "On Effects of Carbon & Manganese Content and of Grain Size on Dynamic Strength Properties of Mild Steel," Trans. ASM, 55, 101 (1962).

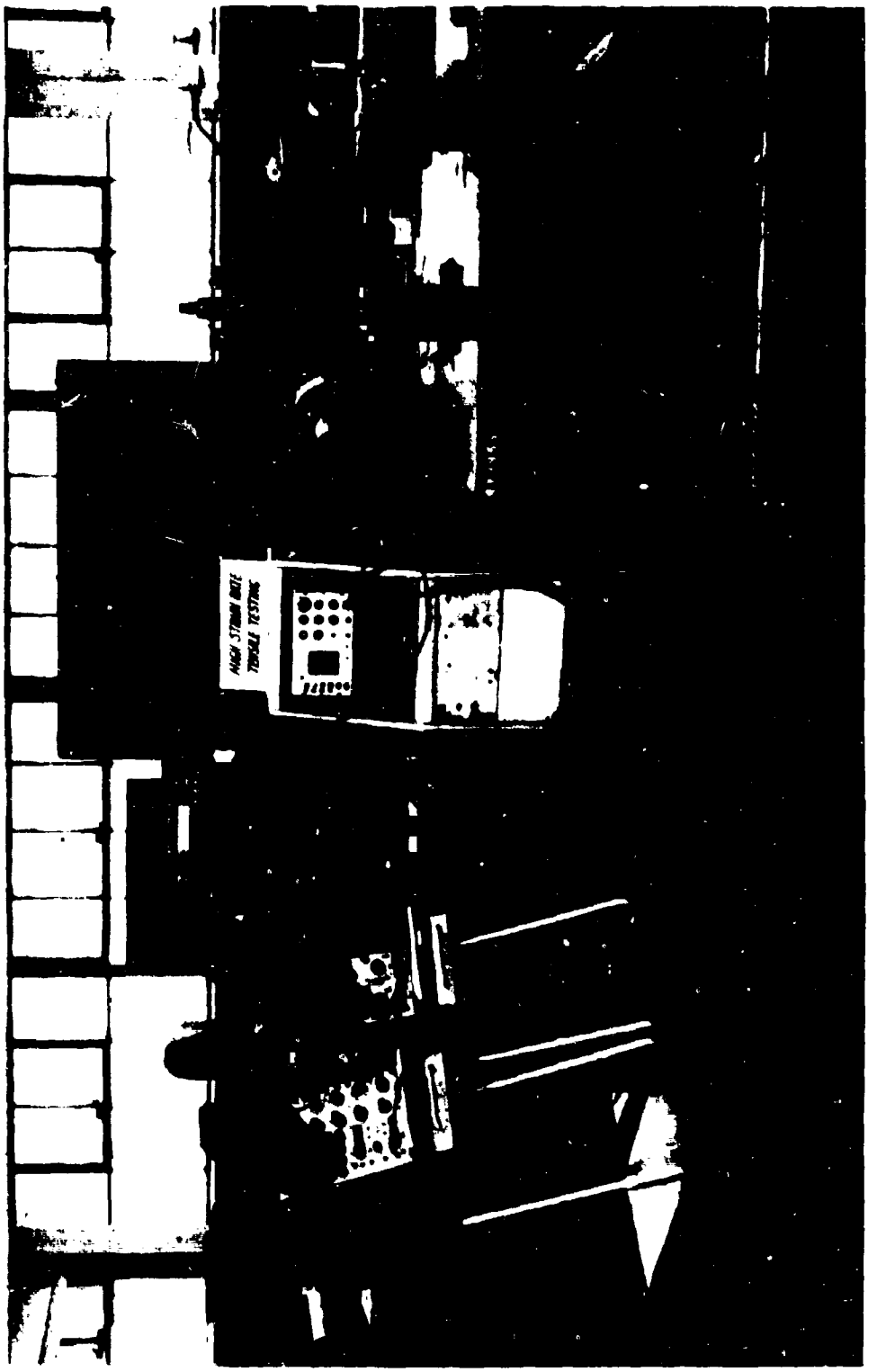

Fig. 1 HIGH STRAIN RATE TENSILE TESTING SYSTEM

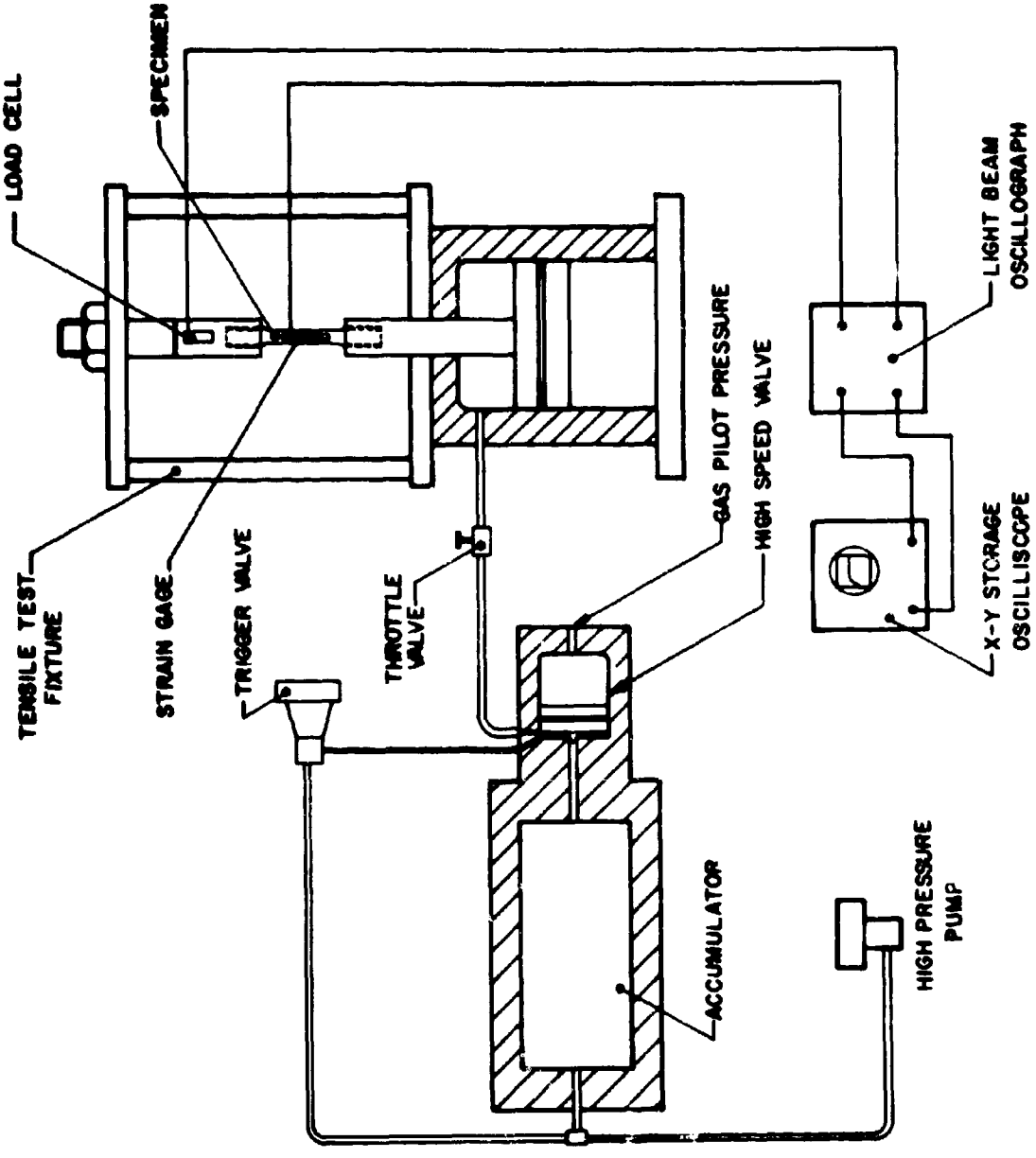

Fig. 2 SCHEMATIC DIAGRAM OF HIGH STRAIN RATE TESTING SYSTEM

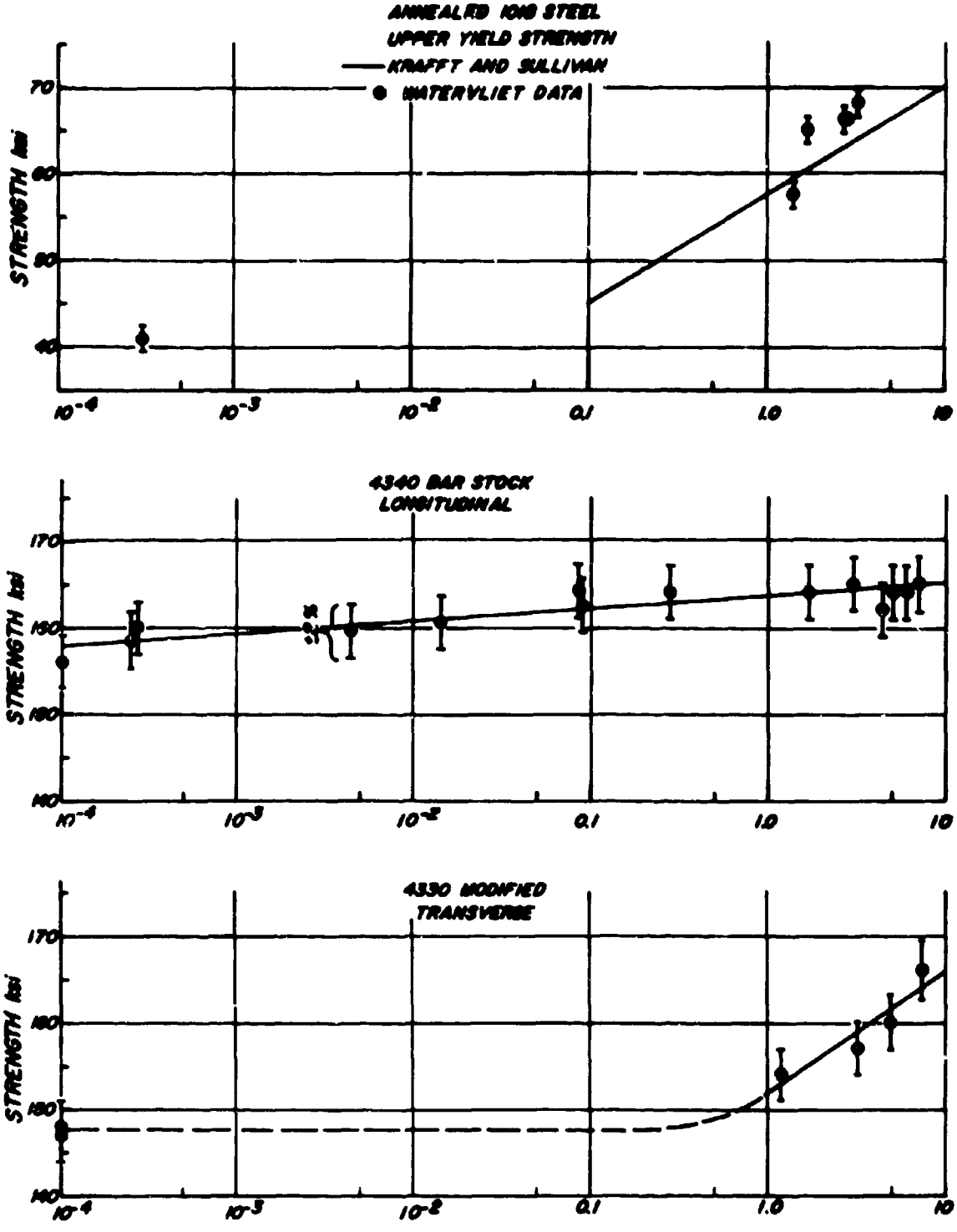

Fig. 3 YIELD STRENGTH VERSUS STRAIN RATE FOR MILD STEEL AND TWO HIGH STRENGTH STEELS

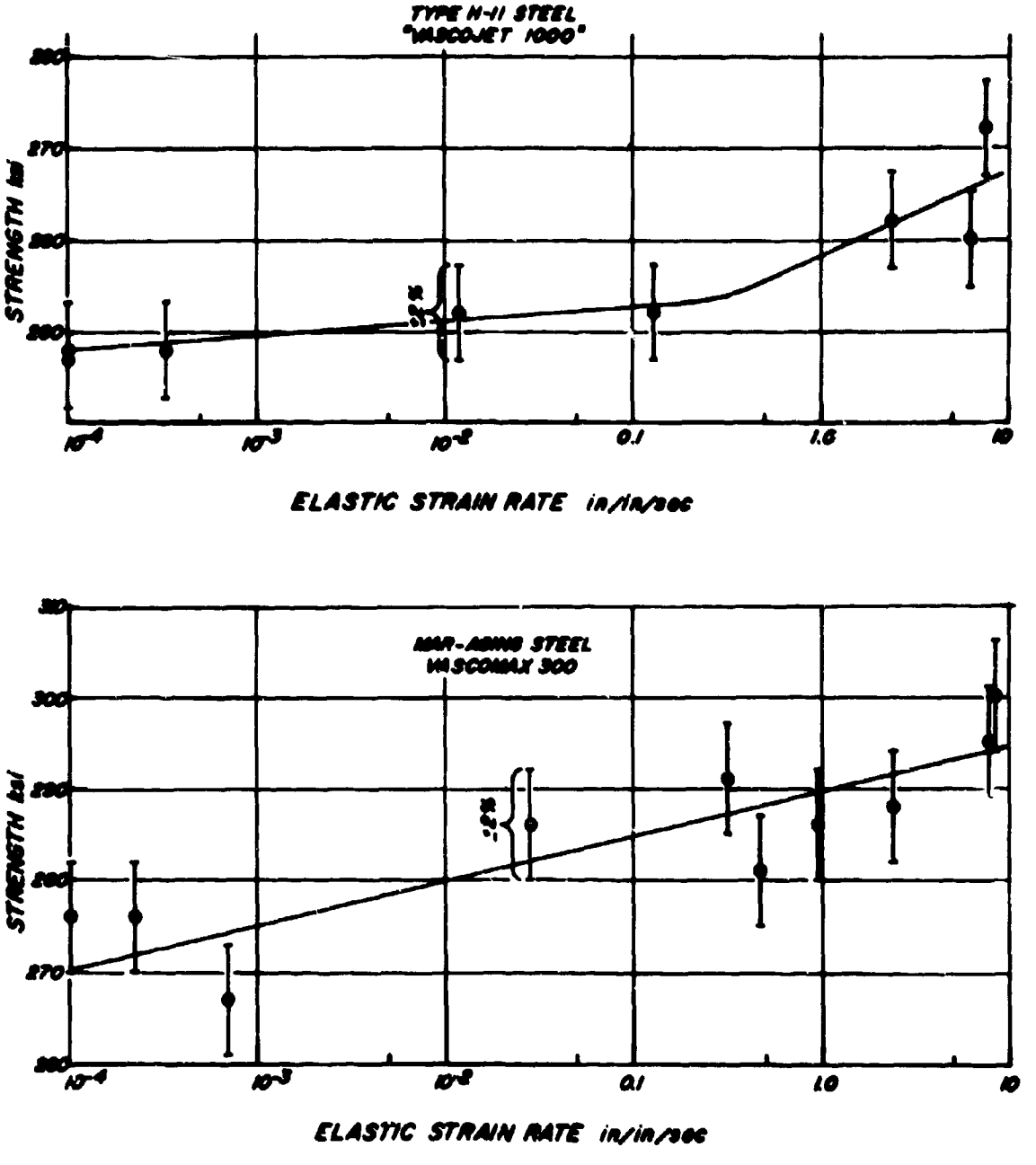

Fig. 4 YIELD STRENGTH VERSUS STRAIN RATE FOR TWO ULTRA-HIGH STRENGTH STEELS

THE DYNAMIC STRESS-STRAIN RELATION FOR A SAND AS DEDUCED BY STUDYING ITS SHOCK WAVE PROPAGATION CHARACTERISTICS IN A LABORATORY DEVICE

T. E. KENNEDY AND 1ST LT. A. J. HENDRON, JR.
WATERWAYS EXPERIMENT STATION
VICKSBURG, MISSISSIPPI

INTRODUCTION

When an instantaneous pressure is applied to a solid, it is known that either elastic waves, plastic waves or shock waves will be propagated by the solid away from the location of the disturbance or area of pressure application. The type and velocity of wave propagated will of course depend on both the magnitude of the pressure and on the equation of state of the material at the level of stress applied. Thus, when a material is taken through a stress cycle by a passing wave front, the form of the wave that is allowed to exist is dependent on the shape of the stress-strain (σ-ϵ) curve followed during the stress cycle.

Consider a solid column of material that is semi-infinite in length, of circular cross-section and has an instantaneous pressure (an impulse) applied to its free surface, Figure 1. This column is further confined in such a manner that the strain perpendicular to the direction of wave propagation is zero. It is now assumed that the solid material of the column will initiate and support the propagation of a shock wave. Thus, under the action of the applied impulse $p(\tau)$ a shock wave is initiated and propagates down the column with a velocity of propagation V_s. At a time $t = \tau$ this front will have reached a position $x = V_s \cdot \tau$ as shown in Figure 1. During a very small time, $d\tau$, the shock front will have moved to the position $x = V_s \cdot (\tau + d\tau)$ and the infinitesimal volume of material $A \cdot V_s \cdot d\tau$, shown shaded in Figure 1, will attain a particle velocity U_p. Figure 2 gives a representation of the volume being acted upon by the shock front where ABCD is the original volume of the column material traversed by the shock in a time $d\tau$ and EBCF is the volume of the shocked material after the particles behind plane BC have acquired a particle velocity U_p. Therefore, from Newton's first law, the relation for impulse-momentum across the shock front is expressed as:

$$P \cdot A \cdot d\tau = V_s \cdot d\tau \cdot A \cdot \rho_o \cdot U_p$$

$$P = V_s \cdot \rho_o \cdot U_p \qquad (1)$$

where ρ_o is the initial density of the material and A is the cross-sectional area of the column.

The work done by the shock on the element shown in Figure 2 during the time $d\tau$ is equal to the kinetic energy, the energy of deformation and any heat energy which arises due to the dissipative nature of the material in the column. Therefore, for conservation of energy

$$P \cdot A \cdot U_p \cdot d\tau = V_s \cdot d\tau \cdot A \left(\Delta Q + \Delta\delta + 1/2 \ \rho_o U_p^2\right)$$

$$P \cdot U_p = V_s \left(\Delta Q + \Delta\delta + 1/2 \ \rho_o U_p^2\right) \qquad (2)$$

where ΔQ is the change in heat energy which may be reflected in a change in temperature and $\Delta\delta$ is the energy of deformation.

The strain in the infinitesimal volume illustrated in Figure 2 is given by

$$\epsilon = \frac{U_p}{V_s} \qquad (3)$$

Combining Equation (3) with Equation (1), the velocity of shock wave propagation can be expressed as:

$$V_s = \left[(P/\epsilon)/\rho_o\right]^{1/2} \qquad (4)$$

Therefore, it is concluded from Equation (4) that the shock velocity is a function of the secant modulus, P/ϵ, of the material which is concomitant with the pressure level of the shock. Since a particular shape of the stress-strain curve was not assumed in the derivation of Equation (4), the results of Equation (4) are valid for any material which can sustain a true shock. By combining the relationships stating the conservation of momentum and energy as given by Equations (1) and (2) respectively, the following relation is obtained

$$P \cdot V_p = \frac{P}{\rho_o \cdot V_p} \left(\Delta Q + \Delta\delta + 1/2 \ \rho_o V_p^2\right)$$

$$1/2 \ \rho_o \cdot V_p^2 = \Delta Q + \Delta\delta \qquad (5)$$

Thus, one-half of the work done by the shock on an element as shown in Figure (2) is realized as kinetic energy and the other half is

manifested in the energy of deformation as reflected by the area enclosed under the stress-strain curve up to the shock pressure, P, and as energy dissipated from the shock into the medium as heat.

By combining Equations (3), (4), and (5), it can be shown that

$$1/2 \; P \cdot \epsilon = \Delta Q + \Delta \delta \qquad (6)$$

Therefore, the energy represented by the area under the stress-strain curve must be equal to or less than $1/2 \; P \cdot \epsilon$ if a shock wave is to be propagated. Figure (3) shows three types of stress-strain curves which a real solid may manifest under dynamic loading.

If a column of linearly elastic material is subjected to a shock of magnitude P, then the energy of deformation is equal to the area OAB in Figure (3a). Since the area OAB is also equal to $1/2P \cdot \epsilon$ then, from Equation (6), ΔQ is obviously zero and a shock should continue to propagate undiminished down the column at the same velocity as an elastic impulse.

Let us now consider the case of a material which has a concave upward stress-strain curve as shown in Figure (3b). If this material is traversed by a shock wave of magnitude P, the energy of deformation, $\Delta \delta$, plus the energy dissipated as heat is equal to the quantity $1/2 \; P \cdot \epsilon$ which is the area of the triangle ABC in Figure (3b). Since the shaded area beneath the stress-strain curve is the energy required to deform the material, then the unshaded area between the line AB and the stress-strain curve represents that portion of the energy, ΔQ, which is dissipated into the medium as heat as the shock traversed the material. Since this process is physically possible, there is no reason to believe that the shock will not continue to propagate as a shock in such a material. The velocity of propagation of the shock would be directly proportional to the secant modulus, P/ϵ, commensurate with the stress level of the shock as given by Equation (4).

Consider a column of material with a stress-strain curve as shown in Figure (3c) which is initially subjected to a shock loading of magnitude P, then by Equation (6) the energy of deformation, $\Delta \delta$, plus the energy flux, ΔQ, must be equal to the quantity $1/2 \; P \cdot \epsilon$ as given by the area of triangle ABC in Figure (3c); the shaded area beneath the stress-strain curve, AB, is obviously greater than the area of the triangle ABC. Therefore, in order for Equation (6) to be satisfied, the quantity, ΔQ, would have to be negative and equal in absolute magnitude to the area between the line AB and the stress-strain curve in Figure (3c). A negative value of ΔQ however, implies that the shock wave would have to draw energy out of the material to propagate which is not physically possible and the initial shock loading therefore would not continue to propagate as a shock. In such

a medium the front lengthens with distance along the bar because each level of stress propagates at a velocity proportional to the square root of the tangent modulus of the stress-strain curve, (8). One would therefore expect that a decreasing frequency would be apparent in the particle velocity-time curves as well as an attenuation of peak velocity.

In the discussion presented above, it has been tacitly assumed that the stress-strain relation is known for a given material. This is true only if the static relation can be used as a basis of analysis. However, if the dynamic stress-strain curve under shock loading is different from the static relation, the above analysis can be used as a framework for analyzing the experimental data acquired in shock loading materials in order to deduce the dynamic stress-strain relations.

EXPERIMENTAL APPARATUS AND EXPERIMENT DESIGN

In 1963, a device for conducting tests pertaining primarily to underground protective structures was put into operation by the Waterways Experiment Station, Vicksburg, Mississippi. This device, the Small Blast Load Generator (SBLG), is capable of developing dynamic loads of 250 psi or less with a rise time of less than 0.005 seconds on a soil test sample having an exposed circular surface of 12 square feet, Figure 4. The dynamic loading function P(t) is developed by detonating PETN (pentaerythritol tetranitrate) in two firing tubes mounted in the bonnet.

The test configuration was essentially a confined column of sand thirteen and a half (13.5) feet in length and 4-feet in diameter. The base of this column had a sand-clay interface which was blended by mixing the final 6-inches of the sand in the column with the clay. This transition area was provided to minimize any reflections that might occur because of the interface. The sand was placed in the lower 9.5-feet in 6-inch lifts and vibrated to obtain a uniform dense condition. The upper 4-feet of sand was placed using a "sprinkling" technique which gives near maximum density without vibrating and thus, without the danger of displacing or damaging the buried gages, (2). Density measurements indicated that an in place density of 110 lb/cu. ft. with a variation of 0.8 lb/cu. ft. was achieved by employing this placement technique. In order to eliminate the penetration of gases into the sand, a problem which caused great difficulty during earlier testing, a neoprene diaphragm was placed across the surface of the column.

A locally available sand called "Cook Creek Sand," obtained near Culkin, Mississippi, was used in all the tests. The sand is a uniform, fine sand as shown by the grain size distribution curve

given in Figure 5 and is classified as SP in the Unified Soil Classification System. The effective grain size D_{10}, of the sand is 0.02 mm, the uniformity coefficient, C_u, is 1.6 and the specific gravity is 2.65. The Cook Creek sand has particle shapes varying from round to angular, with subrounded shapes predominating. Maximum and minimum laboratory dry densities were determined as 110.8 and 93.3 lb/cu. ft. respectively by standard WES laboratory procedures as given in (6). The static, one-dimensional stress-strain curves for Cook Creek sand in one-dimensional compression are shown for various densities in Figure 6. The effective angle of internal friction for Cook Creek sand at the test density of 110 lb/cu. ft. is 42^{o}.

The over-all objective of the study was to evaluate the free-field response of sand in the SBLG in order to facilitate the evaluation of the response of test structure configurations tested in sand. This objective was achieved by measuring the stress and acceleration throughout the sand column. To obtain the acceleration measurements, 500g range strain-gage type accelerometers manufactured by the Consolidated Electrodynamics Corporation, were used. These were placed at various depths down the center line of the sand column to obtain particle acceleration and by integration, particle velocity and particle displacement. They were weighted in such a manner that the weight of displaced sand was equal to the weight of the accelerometer. The stress gages used were piezo-electric type gages supplied by the Road Research Corporation in England. The locations of these were changed in the top 4-feet every five firings to obtain complete stress coverage of this area with a minimum number of gages. One of these gages was placed at a depth of 8.5-feet and over-pressure was monitored by means of two PT-110 blast pressure gages mounted in the SBLG bonnet. The PT-110 gages were purchased from the Dynisco Corporation and were of the strain-gage type.

A total of thirty-eight (38) firings were made on the test configuration during the test series. Three initial firings were made to calibrate the gages for range and then seven groupes of five firings each were made with the stress transducers at seven depths. These depths were at the surface, 0.5-feet, 1.0-feet, 1.5-feet, 2.0-feet, 3.0-feet and 4.0-feet deep. It was found necessary to pre-load any test specimen three times before repeatable conditions existed. For this reason, the data obtained in the last two firings in each group were the only data used in evaluation of the results. An over-pressure of 70 psi was used during all firings with the exception of one, two and three. These were fired at 190 psi, 100 psi and 100 psi respectively. It was found that these higher over-pressures over-ranged the accelerometers within the upper part of the column; thus, the lower over-pressure (70 psi) was used to avoid damage to the instrumentation.

RESULTS AND CONCLUSIONS

Based on the shape of the static, one-dimensional stress-strain curve for the sand, it was assumed that the wave form would exhibit shock characteristics. This assumption was shown to be correct with "shocking up" taking place within the first few inches of wave travel and with the shock front continuing to propagate, Figure 7. It was noticed that the stress record at the 8.5-foot level showed that the front had lost the characteristics of a shock front and now was typical of a plastic wave. This implied that in the region between 4.0-feet and 8.5-feet, the stress cycle went through a point of reversal of curvature or inflection on the stress-strain curve. The assumption that the static stress-strain curve does not differ significantly from the dynamic curve, (3), appears to be valid only in the high stress region. Thus, the observed loss of shock characteristics at lower stress levels was suspected prior to testing, especially in view of the data presented by (9).

In order to obtain the location of this point of inflection on the dynamic stress-strain curve, the arrival time of the wave front was examined, Figure 8, in conjunction with the shape of the wave observed at different depths, Figure 7. Figure 8 shows that the plot of time arrival versus depth becomes non-linear at a depth of about 7.0-feet. It is also apparent from the shape of the wave form at 8.5-feet on Figure 7 that the wave is no longer a shock wave, but exhibits the characteristics of a plastic wave. The wave has therefore been transformed in shape as it traveled from a depth of 4.0-feet, where it was last recorded as a shock, to a depth of 8.5-feet, where it was next recorded as a plastic type wave shape. The fact that the rise time of the pulse increased between the depths of 4.0-feet and 8.5-feet indicates that the dynamic stress-strain relation of the sand up to the pressure level of the peak stress propagated in this region is concave about the strain axis. Since a shock was observed in the upper 4.0-feet the dynamic stress-strain curve must be concave about the stress axis for the peak stress levels experienced in this region. Figure 9 shows that the peak stress at the 4.0-foot level was 40 psi while the peak stress at the 8.5-foot level was 18 psi (The stress gage at 8.5-feet registered a stress of 20 psi and after correction for burial, 10% over-registration under non-shock loading, a stress of 18 psi was obtained.). Therefore, it is concluded that the point of inflection joining the two portions of the stress-strain curve with opposite curvature is located between 18 psi and 40 psi. In developing Figure 9, it was assumed that the over-registration for shock conditions in the region of stress above the 4-foot depth was a constant factor. Thus, it was assumed that the over-registration of the near surface gages was the same percent over-registration as that of the other shock loaded gages. The region between 4.0-feet and 8.5-feet is a region in which this correction factor would not apply because of the transition from shock to non-shock conditions.

To further locate the inflection point, the accelerometer records were integrated at the 9.8-foot and at the 7.0-foot depths to obtain particle displacement (The particle velocity was forced to zero to correct the zero drift in the acceleration records.). The difference between these two displacements was then used to compute the average strain between the 7.0 and 9.8-foot depths. A value of 6.0×10^{-5} was obtained for the axial strain.

Figure 10 shows an approximation of the dynamic stress-strain curve for Cook Creek sand which was constructed on the basis of the information discussed above. The portion of the stress-strain curve between 40 and 80 psi is located approximately along a secant modulus of 48,500 which was calculated from the shock velocity in the upper 4-feet of 1500 feet/second. The value of the axial strain and stress at 8.5-feet (6.0×10^{-5} and 18 psi respectively) gave a point, A, on the curve. It is emphasized however, that the value of the strain for point A can be in considerable error since the calculated value of the strain is dependent upon the difference between the double integration of two accelerometer records. The authors feel however, that these data contribute significantly toward pointing out the general qualitative shape of the dynamic stress-strain curve for Cook Creek sand. The initial slope of the stress-strain curve should be related to the sonic velocity through sand. The initial slope of 82,000 psi shown in Figure 10 corresponds to a sonic velocity of 2000 ft/sec observed for Ottawa sand at a confining pressure of 10 psi by (10). Sonic velocity data were not available for Cook Creek sand. The smooth curve shown in Figure 10 is the dynamic stress-strain relation inferred for dense (110 lb/ft^3), Cook Creek sand from the data presented above and the static stress-strain curve is shown for comparison. Although there appears to be a considerable difference between the dynamic and the static stress-strain curve at the lower pressure levels, it is apparent that the difference becomes less significant with pressure level. For example, the difference between the two curves at 70 psi is less than 15 percent, which definitely demonstrates a strain-rate effect, but one which is not as significant as at the lower stress levels. The strain rate effect observed for Cook Creek sand at 70 psi is of the same order of magnitude as the strain rate effect observed by (9) for Ottawa sand at 200 psi which showed that the dynamic strain was 2/3 the static strain.

In this paper, the propagation of a shock wave through various types of materials has been considered and the behavior unique to each type of material has been discussed. While the theoretical relationships could not be used to predict behavior without prior knowledge of the dynamic stress-strain relation for the sand, the relationships derived were useful in deducing the dynamic stress-strain relation from the observed behavior. The data observed from a series of tests indicate that the dynamic stress-strain relation for Cook Creek sand is concave about the strain axis at lower stress levels and concave about the stress axis at higher

stress levels. It appears that the point of inflection on the dynamic stress-strain curve is between 18 and 40 psi. The available data also indicates that the difference between the static and dynamic stress-strain relations becomes less significant at higher pressures. Further experiments are needed to establish in more detail the quantitative, dynamic stress-strain for Cook Creek sand, but the results of these pilot tests indicate the general shape of the curve and have yielded information which will aid in planning future sand column experiments.

REFERENCES

1. Kolsky, International Symposium on Stress Wave Propagation in Materials, Davids ed., Interscience Publishers, Inc., New York, 1960.

2. Getzler, and Hoeg, The Response of Soils to Dynamic Loads, Report 12, "Static Tests Upon Thin Domes Buried in Sand" MIT, December 1963.

3. Heierli, Inelastic Wave Propagation in Soil Columns, Journal of the Soil Mechanics and Foundation Division, ASCE, Vol. 88, No. 3M6, December 1962.

4. Operation Manual for 250-psi 4-foot Diameter Dynamic Load Generator, by Boynton Associates for U. S. Army Engineer Waterways Experiment Station, CE, Vicksburg, Mississippi,. November 1960.

5. Kolsky, Stress Wave in Solids, Oxford University Press, London, 1953.

6. Manual of Laboratory Tests for Soil for Use on Civil Works Projects, WES Publication, June 1963.

7. Sendon and Hill, Progress in Solid Mechanics, Vols. I and II, North-Holland Publishing Co., Amsterdam, 1960.

8. White and Griffis, The Propagation of Plasticity in Uniaxial Compression, Journal of Applied Mechanics, Vol. 15, No. 3, September 1948.

9. Mason, U. R. S., Inc., Burlingame, California, Private Correspondence, March 1964.

10. Lawrence, Propagation Velocity of Ultra-sonic Waves Through Sand, MIT, R63-8, March 1963.

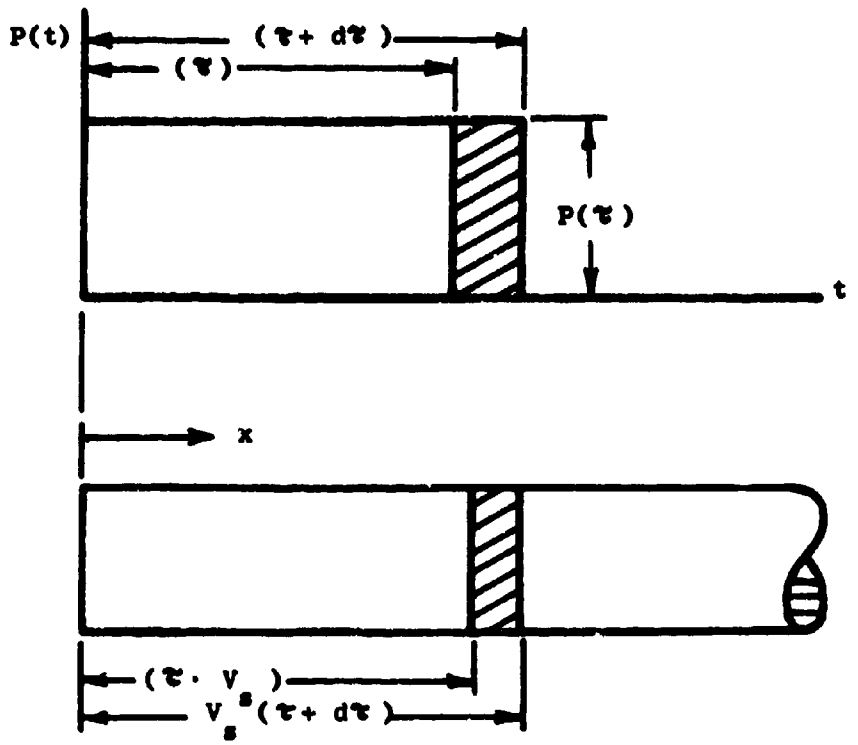

Fig. 1 Shock Front at Time $d\tau$.

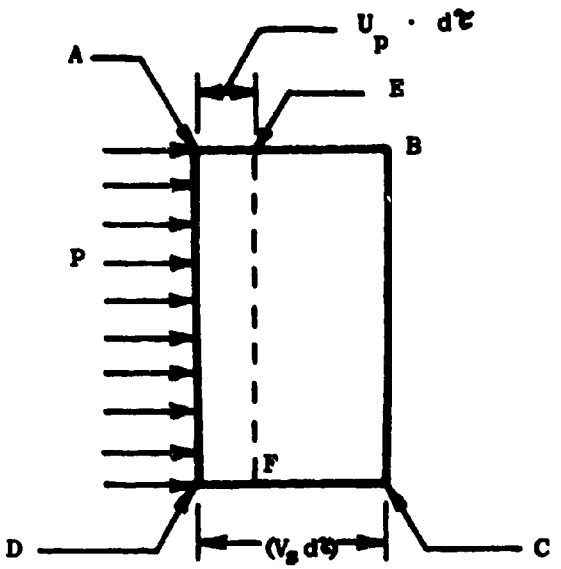

Fig. 2 Volume Being Acted Upon.

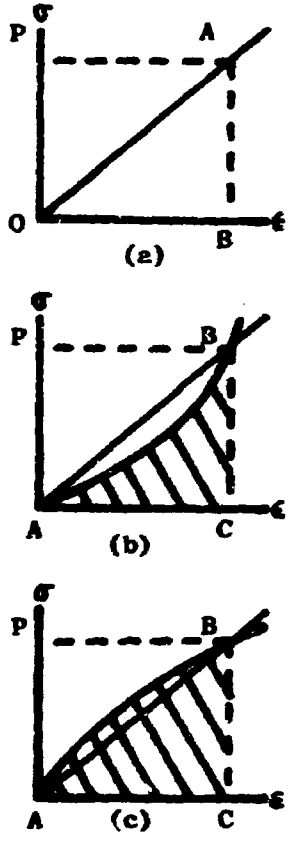

Fig. 3 Types of stress-strain curves.

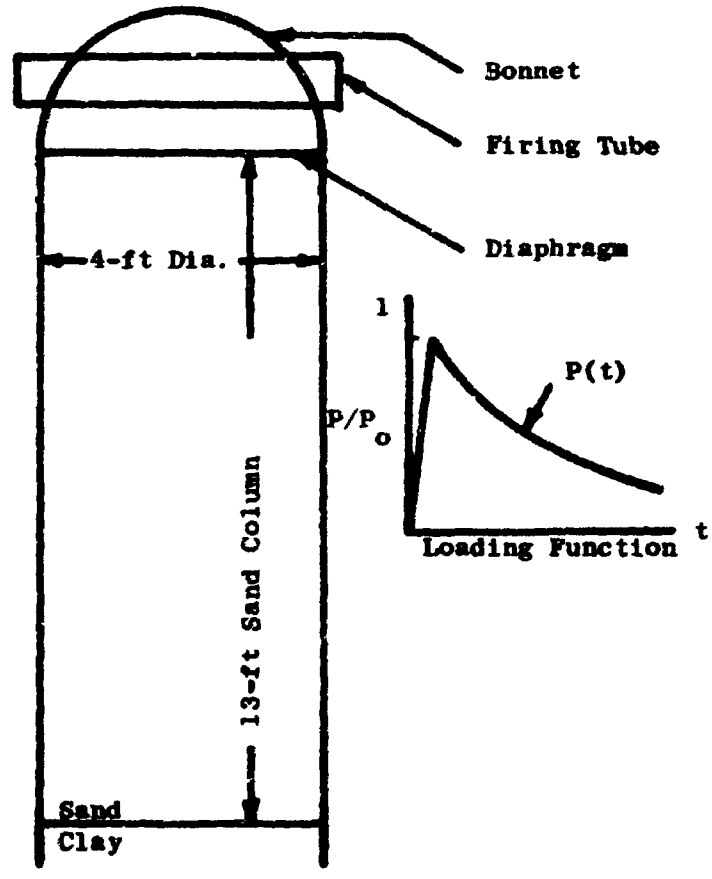

Fig. 4 Experimental Apparatus.

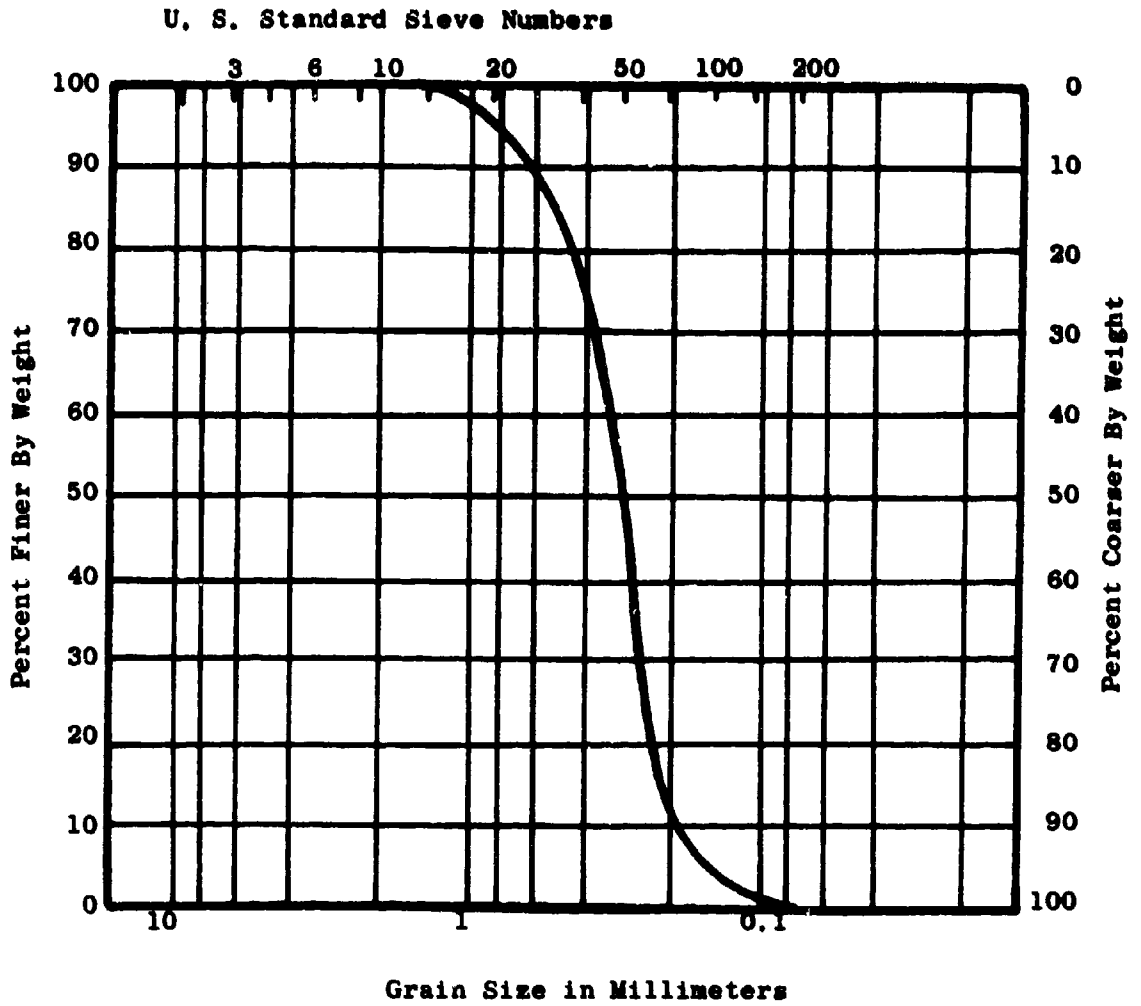

Fig. 5 Grain-Size Distribution of Cook Creek sand.

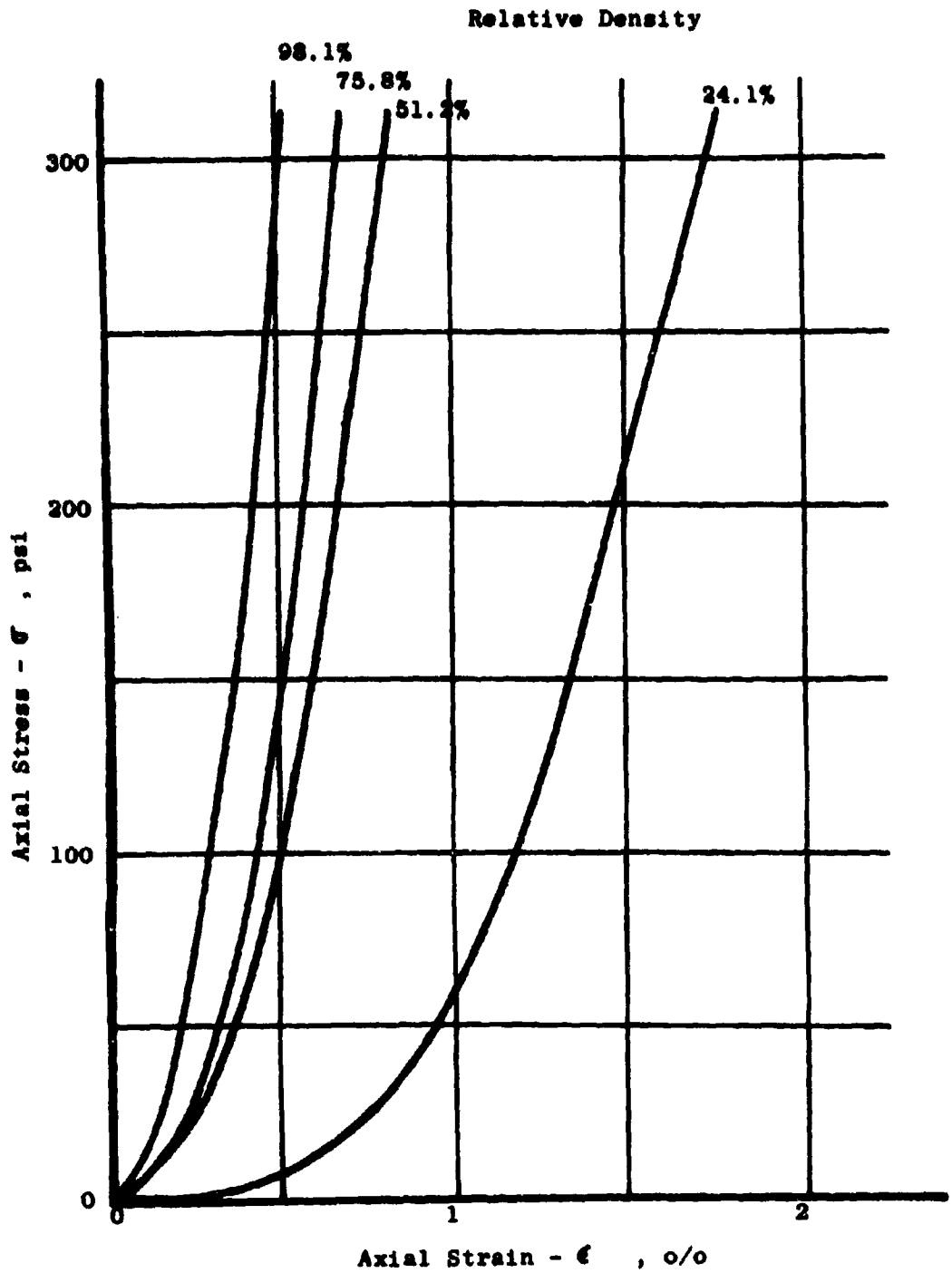

Fig. 6 One-Dimensional Stress-Strain Curves for Cook Creek Sand.

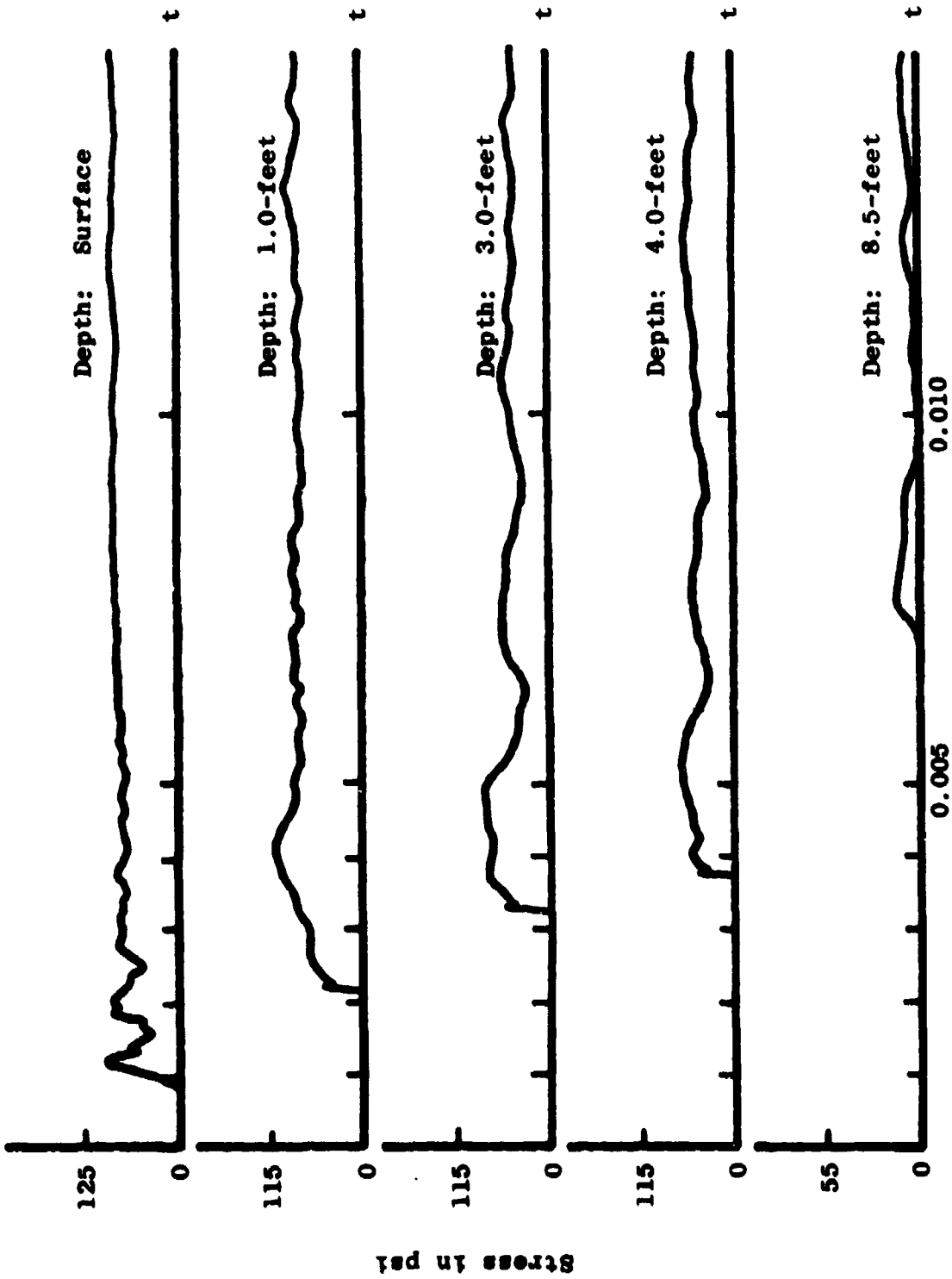

Fig. 7 Typical Stress Records.

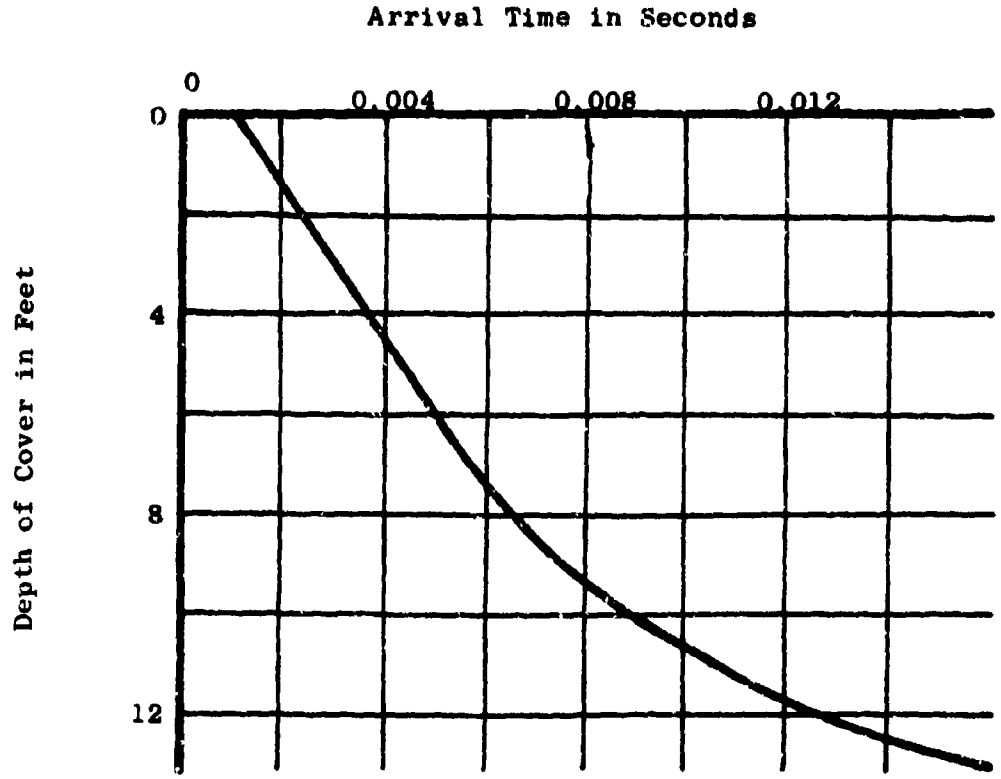

Fig. 8 Inflection Point Curve.

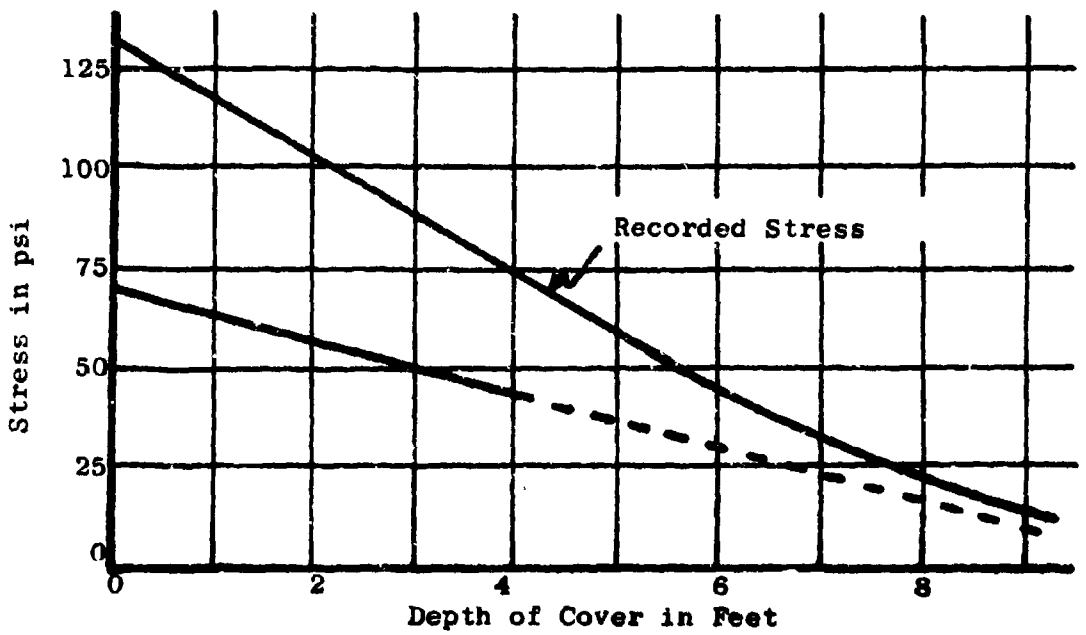

Fig 9. Stress Correction Diagram.

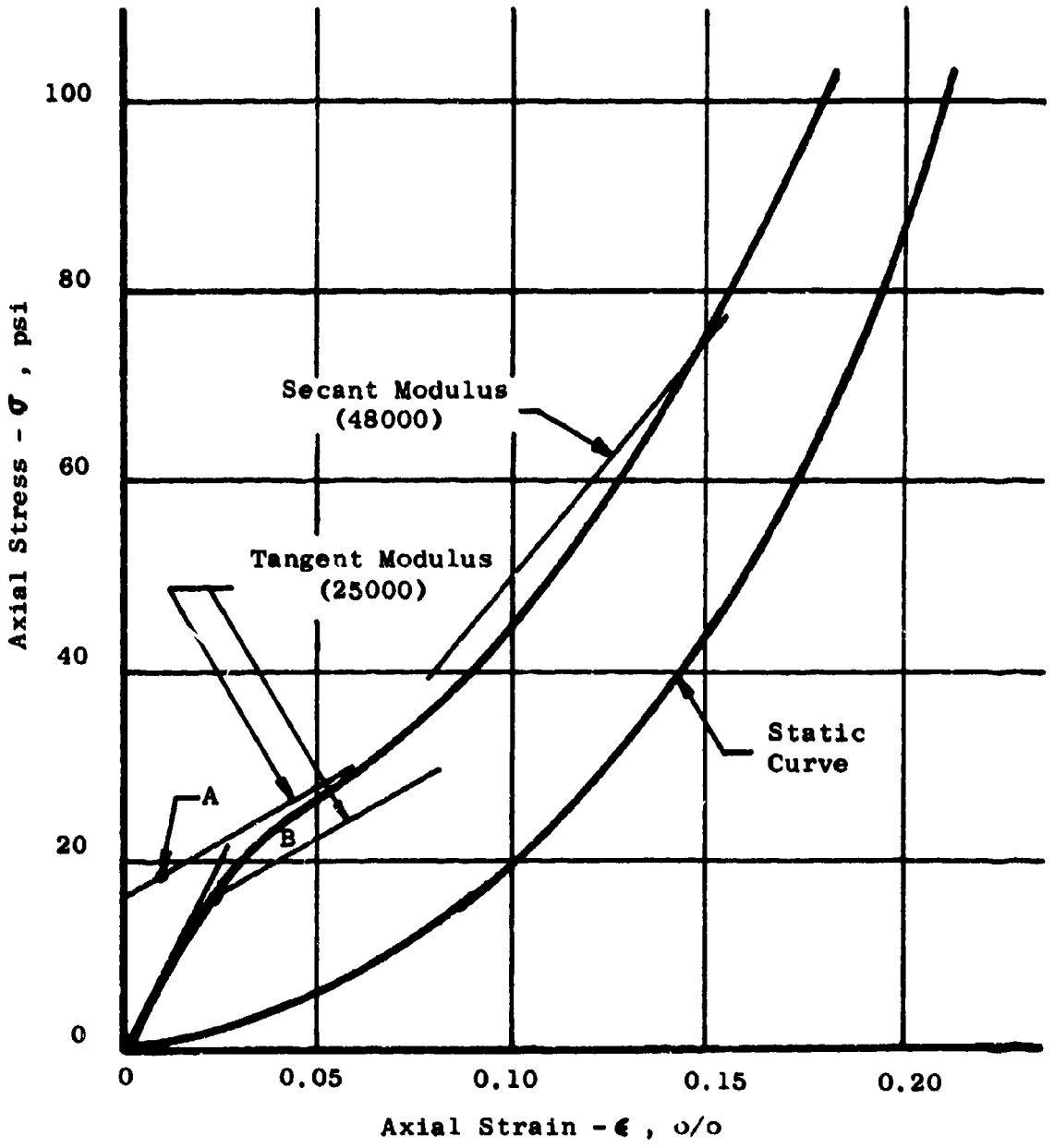

Fig. 10 Dynamic Stress-Strain Curve for Cook Creek Sand.

PERFORMANCE OF THE GERMANIUM-PHOTOVOLTAIC CELL UNDER INTENSIVE MONOCHROMATIC LIGHT

E. KITTL, S. J. SHAPIRO and K. J. BRZONKALA
U. S. ARMY ELECTRONICS RESEARCH
AND DEVELOPMENT LABORATORIES
FORT MONMOUTH, NEW JERSEY

1. Introduction:

The theory of the photovoltaic cell which uses the built in potential of a p/n semiconductor junction for collecting charge carriers, which are created by photon interaction with the valence electrons of the semiconductor crystal, is well known and published in the literature (1) through (4). The technology for fabricating practical Si-cells has reached an optimum performance potential of approximately 15% conversion efficiency in sun light of earth environment. Although a theoretical performance potential of 22% conversion efficiency has been quoted for the single crystal Si-cell when illuminated with sun light of 135 mW/cm^2 intensity, practical limitations in processing techniques and materials control will permit only an insignificant improvement at unreasonable cost over the present 15% efficiency optimum. In this paper, we will be concerned with the two major limiting factors responsible for the low conversion efficiency: (1) The spectral energy distribution of the incident light and its relationship to the p/n junction current collection mechanism, and (2) the limitation of the junction potential on doping level and material characteristics. From the presently accepted theory two general conclusions can be drawn: (1) Monochromatic light of slightly shorter wave length than the equivalent of the energy gap in the semiconductor material should produce the highest conversion efficiency and (2) maximum doping and an abrupt junction are desirable for maximum cell output voltage but do not necessarily lead to maximum conversion efficiency because heavy doping degrades the current collection efficiency of the junction.

A third and very important consideration concerns those factors limiting the power output density of the cell when the radiation input density is increased by a factor 100 or 1000 compared to normal sun light.

Two negative effects are immediately obvious: (1) Excessive thermal heating of the cell by the losses of the conversion process, and (2) an increasing voltage-drop due to series resistance. These two problems can be solved by appropriate engineering designs. On the other hand, there are positive effects which tend to increase the conversion efficiency. The junction voltage rises with photon current density until the Fermi potential limit is reached. An increasing density gradient of the excess minority carriers will improve the current collection efficiency and make it less dependent on the diffusion controlled recombination rate. However, very little is known about the expected deviation from the electrical characteristics of the p/n junction at the quoted extreme high photon injection level. Some experimental evidence of performance at this extreme high photon injection level is presented in this paper and where possible an explanation will be attempted.

2. Criteria for Output Optimization.

a. Doping level and open circuit voltage (See Fig. 1).

A p/n junction at thermal equilibrium exhibits a potential difference between the p and n type material which can be directly derived from the different position of the Fermi Level in the p and n type materials. The diagram is drawn using the potential half-way between the energy gap as reference potential. The Fermi potential of the p type material is drawn above and of the n type material below with reference to the doping level given in atoms per cm^3 of the host material. As this figure directly relates to the resistivity of the doped material, a second scale showing this parameter is given for convenience. This diagram is drawn for Ge and shows the range of temperature dependence from 200 to 400°K. It is seen that the potential difference across the junction increases with the doping level or decreases with the resistivity of the doped material. The upper limit is the energy gap of the host material reduced by the ionization potentials of the donor and acceptor atoms in the host material. It is also seen that at low temperature, this limit can be approached at relatively low doping levels which have the advantage of preserving life time and mobility of the doped material. This junction potential represents the upper limit of the open circuit voltage. This upper limit is asymptotically approached if a sufficient number of hole-electron pairs are generated by the photons absorbed in the cell and collected by the junction. High doping levels, low operating temperature and high photon injection level are necessary for maximum output voltage. Because of the adverse affect of doping on minority carrier life time and current collection efficiency, the open circuit voltage seldom exceeds 50% of the energy gap potential at normal light intensity of solar influx. However, at extreme high light intensity and lower temperatures, 75% of the energy gap voltage may be reached.

b. Junction depth and spectral response.

The major absorption mechanism of light in a semiconductor crystal can be interpreted by a collision process between the photons and the valence electrons of the atoms forming the crystal lattice. This absorption process is described by the familiar exponential law:

$$\frac{T(d)}{I} = e^{-\alpha(\lambda)d} \qquad (1)$$

where T----------transmitted light energy to depth d
I----------incident light energy
$\alpha(\lambda)$ ----absorption coefficient
d----------penetration depth

The absorption coefficient is a strong function of the wave length and the semiconductor material. Its typical dependence on wave length is shown in Fig. 2 for Ge (5) of high resistivity. In accordance with Equation (1), 95% of the radiation is absorbed at a depth $d = 3/\alpha(\lambda)$ cm. It is seen that short wave light is absorbed near the surface; long wave light penetrates deep before it is fully absorbed. This phenomenon is very significant for the performance of the photovoltaic cell. When a photon of sufficient energy ($E_{ph} > E_g$) collides with a valence electron, it is absorbed and impairs so much kinetic energy to the electron that the latter can break the bond to the lattice atom and is free to diffuse through the lattice. It becomes a conduction electron and at the same time leaves a vacancy called a hole. This process is called hole-electron pair generation by photons. The p-n junction collects these free charge carriers and presents a useful output potential of the device as described in Paragraph 2.a. above. Electrons and holes must diffuse from their region of creation to the junction before they can do useful work in the photovoltaic cell. The process of diffusion meets many obstacles; crystal imperfections, atoms of the doping material and the thermal vibration of the lattice create a limited life time and mobility for these minority charge carriers and only a fraction will be collected by the junction potential and create useful current of the cell. It is obvious that a hole-electron pair created near the surface of the semiconductor p-n junction has less chance to reach the junction than a hole-electron pair generated right in the vicinity of the junction. This means that the photon response curve of the cell, as shown in Fig. 5, will exhibit a maximum for that wave length which corresponds to a penetration depth equal to the junction depth. Another important aspect of the absorption mechanism of the photon and the current collection mechanism of the p-n junction is the problem of quantum efficiency which will be discussed in the next paragraph in more detail.

c. Optimization for Monochromatic Light.

Usually the assumption is made that the absorption mechanism of photons in a semiconductor follows the Exponential Law (See Equation 1). In the case of monochromatic light, there is a definite distribution of the generation of charge carriers (hole-electron pairs) with respect to the depth beneath the illuminated surface. The classical photovoltaic theory assumes that charge neutrality must exist in each volume increment under steady state conditions. Therefore, it is possible to write a flow equation (6,7) and solve it yielding a current voltage relationship of the illuminated p/n junction device. While no doubt exists that the dominant absorption process in a semiconductor favors the photons with an energy close to the energy gap of the material, very little is known on the absorption mechanism of the higher energy photons up to 2-3 times the gap energy (8). The quantum mechanical concept that one valence electron can only absorb the gap energy from the incident photon and the excess energy of the photon is wasted and converted into phonon energy of the lattice is expected to hold only under the following specific conditions: (1) The number of photons, which are available to produce hole-electron pairs in a given volume of absorbing material is small compared to the number of valence electrons in the same volume. In this case, the excess kinetic energy which a valence electron may have after a collision with an energetic photon will not raise the overall electron temperature of the valence electrons appreciably and the contribution of the thermal excitation (generation) of hole-electron pairs is small. (2) The probability that the excess energy (E-Eg) of the valence electron after a collision with an energetic phonon is dissipated in the lattice is much higher than the collision probability between free conduction electrons. This again means that the electron temperature is in equilibrium with the lattice and thermal excitation is negligible. (3) The number of unfilled trapping levels with energy states inside the gap is small compared to the number of energetic photons. In this case, two step excitation processes which can produce hole-electron pairs are of negligible significance. (4) Cyclotron type resonance ionization at $\lambda_g = n\lambda$ have a gain factor lower than 1 and are non-existant. (5) Radiative recombinations produce only photons of $E < Eg$ for which the material is transparent. This energy is then lost by reradiation. If a qualitative appraisal is made of these assumptions (1) through (5) at high illumination level of monochromatic light, it follows that Condition (1) can not be considered valid if the number of excess free charge carriers p generated in a certain absorption volume of the n type material approaches the number of the valence electrons available. At a generation rate $g(\lambda)$ and a recombination rate r(p) this condition exists for: $p = [N_{ph}\, \alpha(\lambda)\, \tau_p]/3 \approx 10^{23}$

For $\alpha(\lambda) = 10^3\ cm^{-1}$, $\tau_p = 10^{-3}$ sec and $N_{ph} = 3 \times 10^{23}\ cm^{-2}\ sec^{-1}$,

$I_{ph} = 0.5 \times 10^5$ amperes/cm^2.

It is seen that this condition can not occur for long wave lengths where $\alpha(\lambda) < 10^3$, however $\alpha(\lambda)$ rises very fast if the wave length of the light is reduced and at a wave length of 1/3 of λg ($\lambda g = hc/Eg$) in Ge, the injection level approaches values which will require modification of the classical assumption of Q = 1, if the photon current reaches values of 10-100 A/cm^2.

With regard to Assumption No. 2, it is also obvious that the electron temperature of the conduction electrons will rise faster than the lattice temperature when the photon injection level is increased. This also increases the contribution of thermal excitation. Very little is known about the contribution to the carrier generation by suitable intermediate energy levels between the valence and conduction band. Cyclotron type resonance ionization seems very plausible for $n = \lambda_g/\lambda = 2$ or 3 but will diminish for higher values of n. The significance of radiative recombination has been treated in the literature (9) and shall not be discussed here. Radiative recombination will reduce quantum yield and collection efficiency.

In summarizing the expected effects of high density monochromatic photon injection in a p/n junction type photovoltaic cell, it is predicted that the cell response curve may show pronounced resonance peaks at $\lambda = \frac{1}{2}\lambda g$ and $\lambda = 1/3\,\lambda g$ and the quantum yield is expected to rise above 1 for $E > Eg$. In general, it is expected that the collection efficiency of hole electron pairs will drop toward the violet part of the spectrum but at sufficient high injection densities locally created field gradients may have the opposite effect. This should become more obvious if experiments are performed with monochromatic light of short wave length and high intensity as for instance with a ruby laser light source.

3. Experimental Study Using the 13-U Spectrophotometer.

a. Modification of Spectrophotometer.

Previous spectral response studies of photovoltaic cells have been characterized by the use of light sources of low radiant intensity and low relative beam power in the visible region of the spectrum which do not reflect the actual operating conditions of the cells. To overcome this difficulty, a Model 13 U Perkin-Elmer double beam spectrophotometer was modified to incorporate the use of a 1600 watt high pressure Xenon arc lamp (10). The arrangement of the optics is shown in Fig. 4. Single beam mode of operation is used. In simply by-passing the source and recombining optics, this arrangement allows the return of the instrument to normal double beam ratio operation without the need for optical realignment. Good ventilation of the source housing is required to eliminate the discomforting concentration of ozone produced in the vicinity of this type of lamp.

b. Beam Power Calibration.

Operation of the monochromator with a slit width of 2000 microns gave the high beam power required while retaining a tolerable degree of spectral resolution. The dimensions of the illuminated exit slit were 2 mm x 15 mm. The thermocouple ellipsoid produces an image reduced 6.27 x so that the slit image measures 0.319 mm x 2.39 mm at the thermocouple receiver plane. The receiver size is only 0.212 mm x 1.912 mm, and therefore considerable spill over of image energy occurs. Assuming the energy to be uniformly distributed over the image area for 2 mm slits, an area correction factor fa = 1.82 is applied to all measurements of beam power.

A calibration of the radiometric responsivity, R of the thermocouple was made using a 25 cm x 25 cm x 33 cm laboratory constructed blackbody with a 5 mm aperture. Measurements were made at source temperatures of 900, 1000 and 1100°C, indicated by a thermocouple in contact with the massive iron core of the blackbody source. Power input, P to the thermocouple which is to be calibrated is

$$P = \frac{W}{4}\left(\frac{d}{D}\right)^2 \cdot A_r \cdot r \qquad (2)$$

where W = source radiance, watts/cm^2; d = source aperture dia., cm; D = distance from source to receiver, cm; A_r = receiver area, cm^2; r = reflectance of t.c. diagonal at 45 degrees.

The responsivity, R is v/p where v is the detector rms output when compared to a dc test signal amplified in an identical manner. A value of 1.47 μV/μW is obtained for this detector which is in good agreement with manufacturers data. It has been assumed that the thermocouple receiver surface is "black" at least to 5 microns. Recent measurements (11) taken on thermocouple detectors of this type bear out this assumption to within a few percent, and therefore no spectral corrections to the radiometric calibration were taken.

In calculating beam power to the photovoltaic cell under test the relative transmission of the alternate beam paths is t'/r'r" where r' and r" are the reflectances of the thermocouple diagonal and ellipsoid respectively and t' is the transmittance of the fused silica lens. Since the level of beam power with 2 mm slits would cause the detector output to exceed 25 μV and saturate the preamplifier, a neutral density filter is inserted at the entrance slit when power input is measured. The filter consisted of a stack of three air spaced, density 1.15, inconel evaporated on 1.6 mm thick fused silica plates.

For an observed detector signal, v_i we may now calculate the power input to a photovoltaic cell under test

$$P_i = \frac{v_i \cdot f_A \cdot t'}{R \cdot t_f(\lambda) \cdot r' \cdot r''} \qquad (3)$$

If $\Delta\lambda$ is the spectral slit width (12) at λ and A_s is the exit slit area then the spectral irradiance at the exit slit is

$$P_{\Delta\lambda} = \frac{r_i f_A}{R A_s t_y(\lambda) \tau' \tau'' \Delta\lambda} \qquad (4)$$

Experimental curves obtained for P_i and $P_{\Delta\lambda}$ are shown in Fig. 5 for 62 amps arc current. For this wavelength region of interest we have assumed the detector to be "black".

c. Photocell detector calibration.

To obtain input power measurements for the laser light experiments described below it was necessary to employ an RCA 925 phototube as a detector capable of resolving short (< 1 μsec) pulse durations. Responsivity of this detector was determined at 0.694 and 1.055 microns in the previously calibrated beam of the spectrometer.

d. Experimental Study of Ge Photovoltaic Cells.

Spectral response measurements were performed on Germanium photovoltaic cells prepared by Delco Radio Division of General Motors Corporation. A typical cell is pictured in Fig. 3. It is an alloyed junction n^+/p cell (13) with a resistivity of 0.028 ohm-cm in p and 0.15 ohm-cm in the n region. The n Ge wafer is 150 microns thick and the p layer is only 2 microns in thickness. The n surface is illuminated and shows the gridded contact structure.

When the cells are mounted on the spectrophotometer, they are illuminated by a 1 cm x 0.3 cm image of the exit slit. The light generated current output of the cell is recorded on a strip chart recorder with wave length indicated. Illumination levels are great enough to reduce the effects of cell shunt resistance on the V-I characteristic to negligible proportions.

Applying the input spectral irradiance data to the cell output and normalizing on the basis of equal number of photons we have obtained the relative photon response characteristics shown for two Ge cells in Fig. 6. Both cells show expected response peak at 1.45 microns but also exhibit unexpected rise in response in the region between 0.8 and 1.3 microns. Previous data taken under low level illumination fail to exhibit this characteristic. Both cells show the dropping response expected at the shorter wavelengths due to the depth of the junctions. The rapid loss of response found as photon energy approaches the cut-off wavelength $\lambda g = 1.86$ μ is attributed to the fact that the cells are not sufficiently thick to absorb at the longer wavelengths and the thinner cell clearly shows this limitation.

For the cell GM-59C which gave an I_{sc} = 13.5 mA at 0.96 microns when Pi = 22.2 mW, we compute a conversion efficiency, η according to the relationship

$$\eta = \frac{0.21\,\lambda\,Q}{1.237} \qquad (5)$$

assuming an anticipated V_{oc} = 0.3 V and a V-I curve factor of 0.7. Taking the reflectance of the cell to be invariant with λ and equal to 0.34, the curve shown in Fig. 7 is drawn representing a projected conversion efficiency for this cell. Using this data and the data of Fig. 6 an absolute value for Q = 1.32 at 1.16 microns results.

We actually observed a V_{oc} = 180 mV and a curve factor of 0.5 for this cell, which gave an actual efficiency of 5.5% at 0.96 microns (uncorrected for reflectance).

4. Experimental Study Using Lasers.

The laser is the simplest, high intensity, monochromatic light source available. Selection of this type of source, particularly the fluorescent pulse of the laser, eliminated the need for complex cooling systems for selective narrow band filters and test samples. Furthermore, in the actual experimental apparatus the simplicity was enhanced by the interchangeability of the two different laser crystals, Neodymium and Ruby. However, certain problems inherent in this type of light source (e.g. Calibration of beam power, flash lamp light leakage, and millisecond pulse duration) had to be overcome or compensated for. Another problem with this type of light source is the selection of appropriate laser crystals of fixed wave length. Table I (14) gives the selection of materials and their properties.

Table I

Material	Wavelength (Micron)	Mode	Operating Temperature Max. (°K)
Cr^{+3} - Al_2O_3	.69	Pulsed	300
Nd^{+3} - glass	1.06	Pulsed	300
Er^{+3} - $CaWO_4$	1.61	Pulsed	77
Tm^{+3} - $CaWO_4$	1.91	Pulsed	77

The experimental investigation reported in this paper covers only results on Ruby and Neodymium laser experiments. Initial experiments showed that the photovoltaic cell could not resolve the individual high energy laser pulses. It was, therefore, decided to use only the fluorescent pulse output of the crystal which extends over a sufficiently long time.

Initially the cell power output densities of 1 - 3 watt/cm^2 were available from the fluorescent pulse, but upon further investigation of the pulse, it was found that some of the pump lamp

energy, which detracted from the spectral purity of the fluorescent pulse, was present in the pulse. This energy was eliminated, in the case of the ruby crystal, by using a narrow band filter, passing 0.6943 ±.0017 micron with 50% transmission at its peak, and in the case of the Neodymium-Glass rod, by using a narrow band filter, passing 1.055 ±.015 micron with 31% transmission at its peak. By eliminating the unwanted energy outside of these narrow bands, we also cut down the energy within the band, so that the maximum power density reached in these experiments was 150 milliwatt/cm^2, which is still a reasonably high power density for monochromatic light of this high spectral purity. Future experiments will be conducted with higher power fluorescent pulses and subsequent laser pulses to achieve power densities beyond 1 - 3 watts/cm^2. Input power densities were measured with an RCA 925 Phototube calibrated on the Perkin Elmer 13 U Spectrophotometer to yield sensitivities of 0.0059 microamps/microwatt for the ruby crystal and 0.0080 microamps/microwatt for the Neodymium Glass rod.

The final problem involved the tracing of a V-I characteristic at the peak of the fluorescent pulse. From a typical pulse shown in Fig. 8C it is seen that the pulse is constant to within 10% variation for at least 500 microseconds. Actual chopped traces of a photodiode output and the test cell current plotted against time, show that the V-I characteristic is traced at a constant input level. This is true because the test cell current has dropped off to zero before the photodiode output has begun to decay.

An electronic triggering circuit, seen in Fig. 9, was designed to trace the V-I characteristic curve in less than 500 microseconds. In the discharge loop, the R.C. time constant is 100 microseconds. Three time constants are enough to discharge the circuit to 5% of its initial value. Now, with the photodiode in the circuit placed in such a position as to see the same light that the test cell sees, the V-I characteristic curve is traced in the first 300 microsecond of the light pulse of Fig. 8C.

Typical results from data taken on a Ge cell are shown in Table II: (G.M. 538)

Table II

Crystal	P_{in}	$P_{out\ max.}$	η	I_{SC}	V_{OC}	a
Ruby	399 mw	27.7 mw	6.95%	224 ma	.205 V	.564
Nd Glass	18.95 mw	6.65 mw	35.1 %	55 ma	.195 V	.62

Figure 8 shows the actual data from which Table II is computed. The input power is determined from the input pulses by the formula:

$$P_{in} = \frac{V_M}{R_L \quad S_X \quad T_F}$$

where V_M is the peak voltage of the pulse, R_L is the load resistance (1 megohm), S_X is the sensitivity of the phototube at wavelength X, and f_F is the filter factor of a neutral density filter, used on the phototube so that the maximum current through the tube would not be exceeded. The output power is simply the maximum power point from Curves 8B and 8D, and the efficiency is:

$$\eta = \frac{P_{out}}{P_{in}}$$

The area factor a is defined as:

$$a = \frac{P_{max}}{I_{SC} V_{OC}}$$

5. CONCLUSIONS:

The experimental results show that maximum monochromatic conversion efficiencies occur at a wavelength of 1.5 microns and reach projected values of 30 percent assuming electrical output characteristics of 0.3 volts open circuit and 0.7 curve factor which can be achieved at current densities in the order of 1.0 amp./cm^2. Compared to low intensity results the photon response of these cells shows a remarkable improvement at these higher intensities in the region of 0.8 to 1.3 microns. Based on these results, it is obvious that spectral matching of source and photovoltaic converter cell will become less critical at high injection level. There are indications that a germanium cell for instance may perform as well as or better than the Si or GaAs cells in highly concentrated sunlight. If this is the case, there will be significant changes in the design theory of thermophotovoltaic converters and solar power converters utilizing highly concentrated sunlight. Laser experiments have yielded a conversion efficiency of 35% at 1.055 microns (Nd-Glass Laser). This higher efficiency correlates reasonably well with the data obtained from spectrometer measurements. However, it should be noted that the laser data indicates a rise in Quantum Efficiency to Q = 2.0, about 4 times the level deduced from the spectrometer measurements. Such results can be explained by the increased spectral density (about 1000 times) of this laser light, over the density realized in the monochrometer. On the basis of these experiments, further studies should be made at higher intensities and at wavelengths more closely corresponding to the region of the spectral response peak of the Ge cell. More basic studies are also encouraged to probe into the mechanisms giving rise to the Quantum efficiencies higher than 1.0 which were observed in this work.

REFERENCES

(1) Silicon Solar Energy Converters
M. B. Prince, in J.A.P. Vol. 26, No. 5 May 1955.

(2) Theoretical Considerations Governing the Choice of the Optimum Semiconductor for Photovoltaic Solar Energy Conversion
Josef J. Loferski in J.A.P. Vol. 27, No. 7 July 1956.

(3) New Developments in Silicon Photovoltaic Devices
M. B. Prince, M. Wolf in Journal Brit IRE Oct. 1958.

(4) Limitation and Possibilities for Improvements of Photovoltaic Solar Energy Converters
M. Wolf in Proc. IRE Vol. 48 July 1960.

(5) Intrinsic Optical Absorption in Single Crystal Germanium and Silicon at 77°K and 300°K
N.C. Dash, R.Newman in Physical Review Vol. 99, No. 4, Aug.1955.

(6) Quantum Efficiency of Radiant Energy Photons in Semiconductors
G. C. Jain Paper presented at 6th Agard Colloquium in Cannes, France 16-20 March 1964.

(7) Realization d'un Convertisseur Thermophotovoltaique
A. Fortini, Ph Baudin, P. Sibillot in Paper presented at 6th Agard Colloquium, Cannes, France 16-20 March 1964.

(8) Electron-Impact Ionization in Semiconductors
Jan Tauc Phys. Chem. Solids Pergammon Press 1959, Vol. 8

(9) Detailed Balance Limit of Efficiency of p-n Junction Solar Cells
W. Shockley and H. Queisser J.A.P. Vol. 32 No. 3 March 1961

(10) Lamp Type is Osram XBO 1600 obtained from MacBeth Sales Corp.

(11) W. L. Eisenman, R.L. Bates and J.D.Merriam, JOSA 53 p 733,Jun 63

(12) Data obtained from the Perkin Elmer Corp., Norwalk, Conn.

(13) Quarterly Report - Contract DA36-039-AMC-02255(E), General Motors Defense Research Labs., Santa Barbara, Calif.

(14) Maiman, T.H. "Optically-Pumped Solid State Lasers" Solid State Design Vol. 4, #11 November 1963.

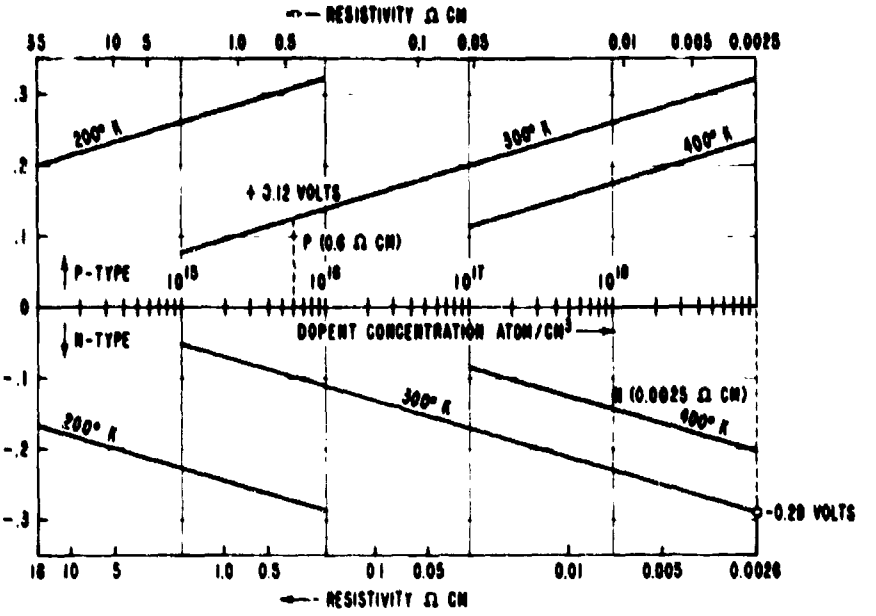

FIGURE 1. JUNCTION POTENTIAL OF GERMANIUM - PHOTOVOLTAIC CELL

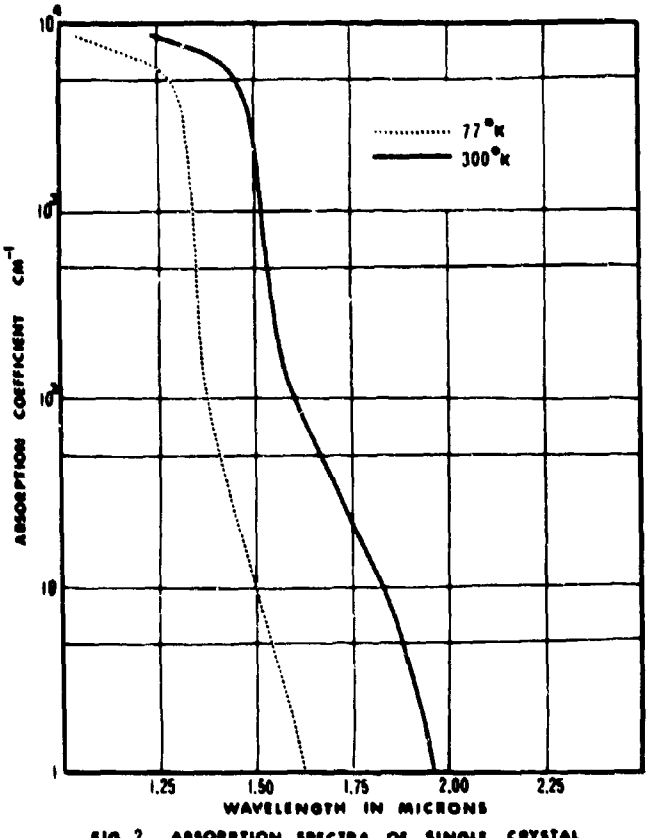

FIG 2. ABSORPTION SPECTRA OF SINGLE CRYSTAL GERMANIUM AT 77°K AND 300°K

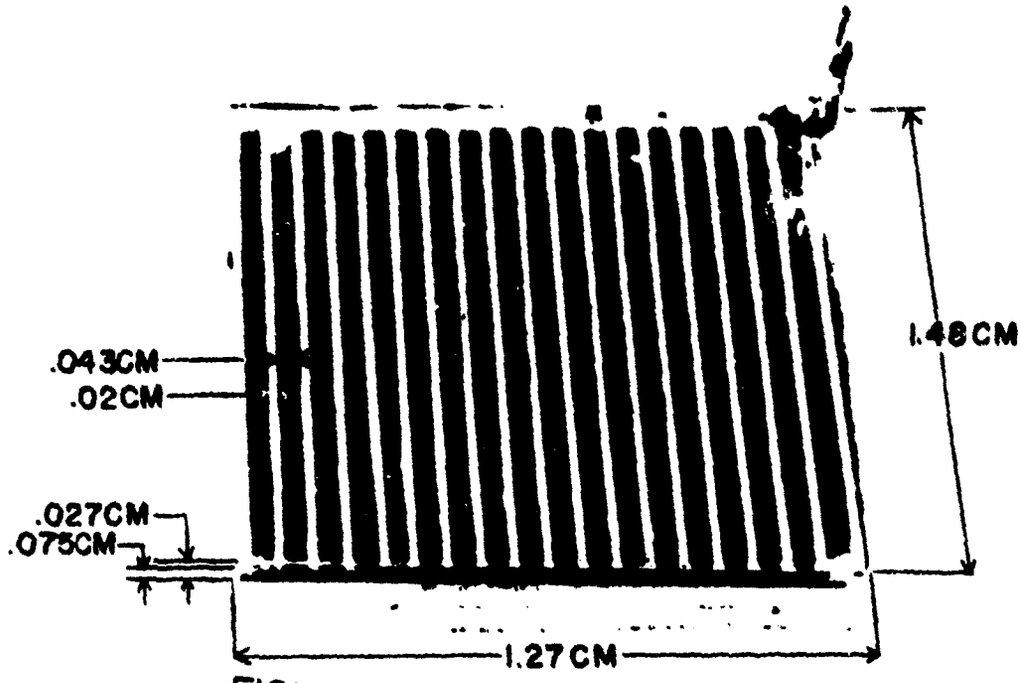

FIGURE-3.19 GRID Ge CELL

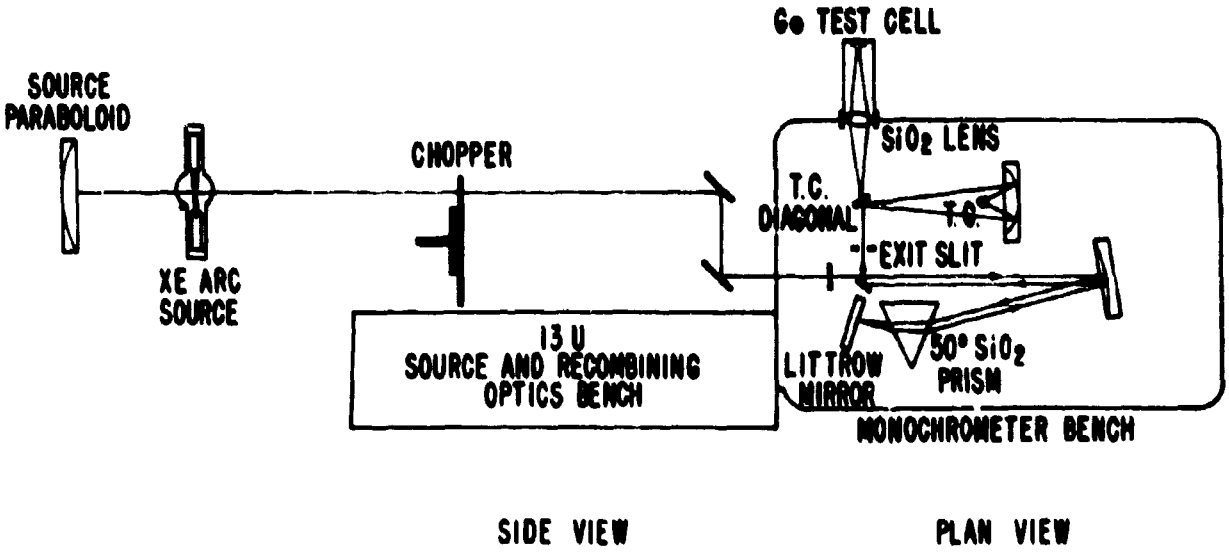

FIG. 4. SPECTROPHOTOMETER OPTICS

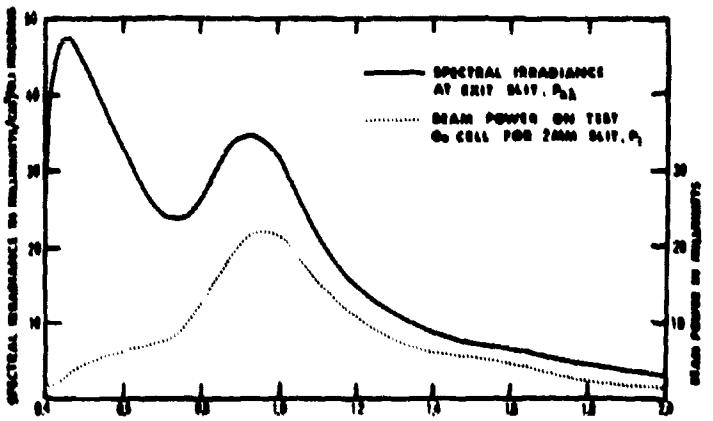

FIG 5. SPECTRAL IRRADIANCE

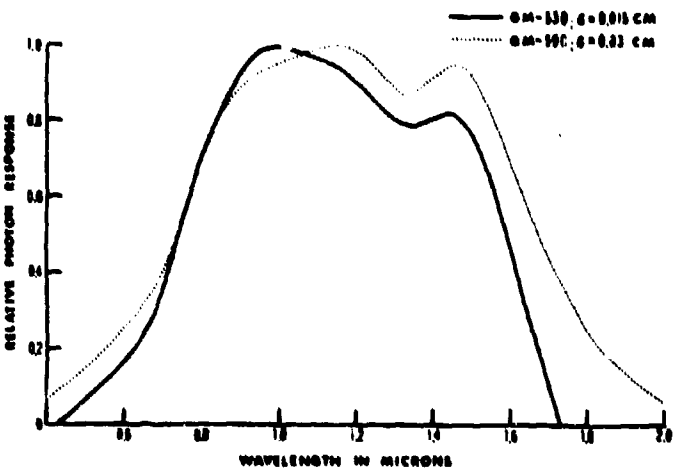

FIG 6. SPECTRAL RESPONSE CURVES

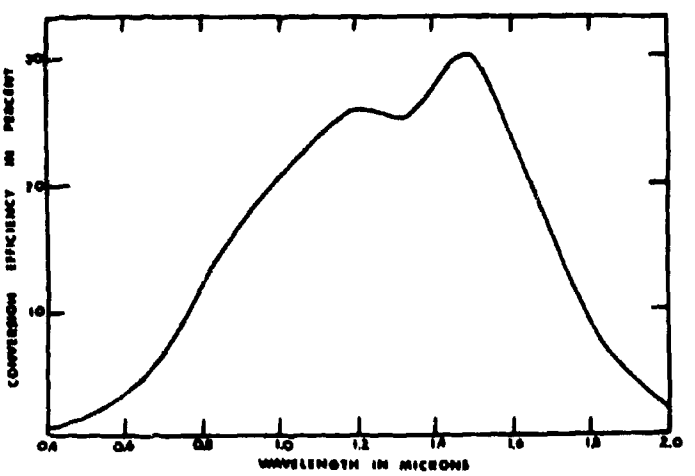

FIG 7. PROJECTED CONVERSION EFFICIENCY FOR GaAs CELL

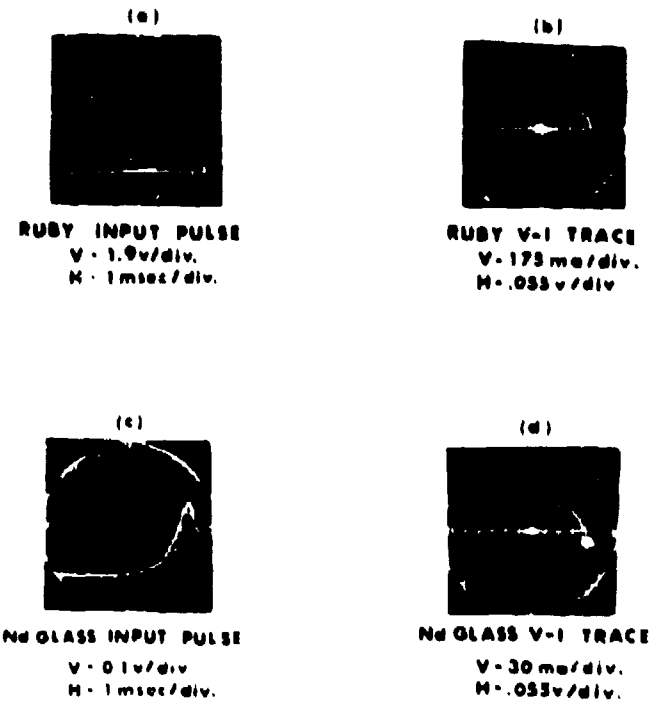

FIG 8. EXPERIMENTAL RESULTS WITH LASER

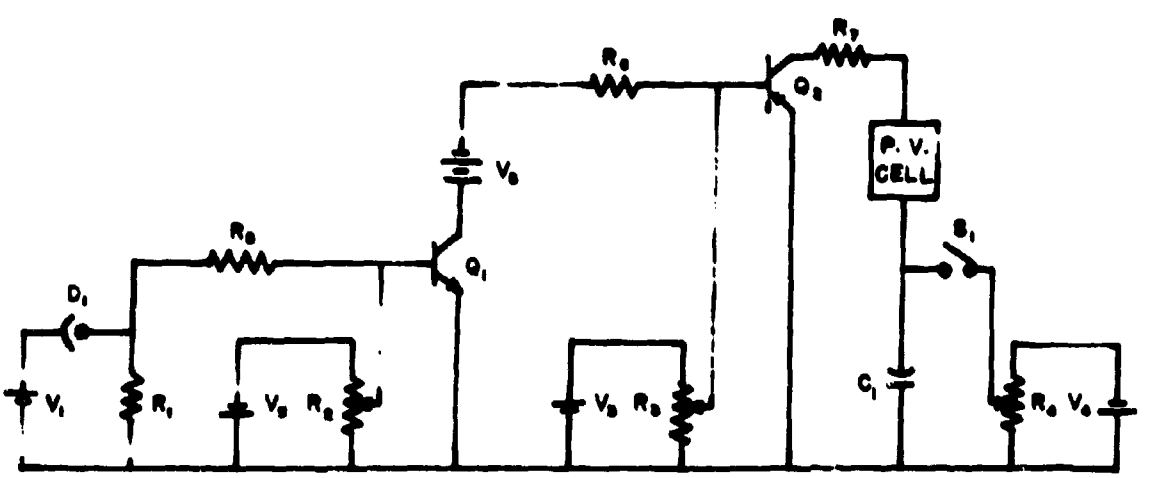

FIGURE 9 LIGHT ACTIVATED V-I CURVE TRACER

MOLECULAR STRUCTURE AND PROTEIN STABILITY: THE ACID DENATURATION OF α LACTALBUMIN

MARTIN J. KRONMAN, ROBERT BLUM, RAYMOND ANDREOTTI,
RASMA VITOLS and LEO HOLMES
U. S. ARMY NATICK LABORATORIES
NATICK, MASSACHUSETTS

Introduction

The unique properties of a protein in solution depend to a large degree on the manner in which the folded polypeptide chain determines the spatial relationships between amino acid side chains. The maintenance of metabolic functions, the organization of complex structures such as muscle, or stability of a biological fluid such as milk will ultimately depend upon preservation of the conformational integrity of constituent proteins or protein-enzymes. The wide range of functional properties that proteins exhibit is paralleled by equally wide ranges of stabilities to heat or other denaturing agents. It thus seems reasonable to ask the question - what molecular features convey stability to a protein?

Aside from the contributions made by disulfide bridges of cystine, the "bonds" which stabilize proteins are generally non-covalent in nature. They include: (a) intra-peptide chain hydrogen bonds, (b) hydrogen bonds involving amino acid side chains, (c) "hydrophobic bonds" (Van der Waals interactions) between non-polar amino acid side chains such as valine, leucine, tryptophan, etc., (d) coulombic interactions, i.e., attraction and repulsion of ionized amino acid side chains such as glutamyl, lysyl, etc. While without doubt all of these "bonds" make some contribution to the stability of a protein, their relative importance has yet to be firmly established. The investigations to be reported here represent an attempt to provide a basis for making such an assessment. Our approach has been to disrupt the protein molecule partially and then attempt to describe what molecular events have occurred during the process, i.e., which kind of bonds have been broken and which remain intact.

The protein studied, α lactalbumin, a constituent of milk whey, has a molecular weight of 16.2 x 10^3 (1). Its sedimentation constant, (1.93 S), together with the molecular weight cited, indicate that the protein molecule in its native state is nearly spherical (1). It contains 125 amino acid residues held together in a single peptide chain by four intramolecular disulfide bridges (15). Aside from the absence of any sulfhydryl groups and the high tryptophan content (5 residues) (10), the relative occurrence of the various amino acids does not appear to be out of the ordinary, e.g., the ratio of non-polar to polar amino acids is comparable to proteins with radically different characteristics (1). One of the more unusual characteristics of α lactalbumin is its extraordinary resistance to thermal denaturation, e.g., one can maintain solutions of the protein at 90° C for extended periods without producing irreversible changes.

Likewise, exposure of α lactalbumin to extremes of pH appears to produce only reversible "denaturation-like" effects. In this paper we shall describe the low pH process. By all of the generally invoked criteria of denaturation - loss of solubility (increased aggregation) and alteration of internal molecular structure (changes in molecular shape, optical rotation, ultraviolet spectra, etc.) - the changes occurring in α lactalbumin at low pH may be called denaturation.

Aggregation at Acid pH

At pH's below 4 α lactalbumin shows a marked propensity toward aggregation. This can be seen from the ultracentrifuge patterns shown in Figure 1. At pH 6 (Figures 1b and 1d) the boundaries are essentially symmetrical and unchanging with time. The sedimentation constant corresponding to these boundaries is essentially that for the native molecule of molecular weight 16.2 x 10^3. No change in molecular size occurs during the 24 hours of exposure to this pH. Observations made at pH 2, on the other hand, indicate the presence of a polymerization process. This is seen by comparison of the patterns of Figure 1b and 1d with 1a and 1c. In the latter case a new boundary, indicated as A_n appears. This boundary corresponds to a new species of molecular weight $\geq$ 300,000. The relative areas under the boundaries A (essentially unpolymerized protein)[1]

---

[1] Actually, component A corresponds to "associated" α lactalbumin, i.e., dimer or perhaps trimer. However, since its molecular weight (32,000 to 48,000) is so much lower than that of the aggregate (300,000), for our purposes we have called it unaggregated protein.

and A_n give the relative amounts of these components. Comparison of Figures 1a and 1c reveals that the amount of aggregate, A_n, increases with time. While the rate of aggregation is dependent on parameters such as protein concentration, ionic strength, pH and ionic species, at pH's below 4 (with sufficient time) aggregation will proceed to a point where all of the protein moves as component A_n or even beyond this to formation of gel. In spite of the grossness of this process, the aggregation can be completely reversed by adjustment of the pH to values above 6.

The polymerization process can be followed by measurement of solubility in ammonium sulfate solutions. In these experiments a solution of α lactalbumin at a given pH and at 25° C was rapidly buffered to pH 6.6 with immediate addition of buffered saturated ammonium sulfate to a final concentration of 2.1 M. Aggregated α lactalbumin is insoluble under these conditions and can be removed by centrifugation. The rate of insolubilization decreases with decreasing pH (Figure 2). Shown also is the rate curve for aggregation occurring at pH 2 where the supporting electrolyte was 0.15 M KNO_3 rather than 0.15 M KCl. The marked increase in the rate of aggregation in the presence of nitrate ion is the consequence of binding of the anion to the protein molecule with concomitant reduction of the molecular charge. Similar studies with other anions show that their sequence of effectiveness in promoting aggregation is the same as the sequence of binding of such ions to proteins (3).

The characteristics of the aggregation process are summarized in Table 1. Of particular importance are the effects of pH, ionic strength, and anion binding on the rate of aggregation. These demonstrate that in pH range 2 to 3.5 the rate of aggregation is essentially determined by electrostatic factors, i.e., as electrostatic repulsion between α lactalbumin molecules is reduced by an increase in ionic strength or by reducing the molecular charge by increasing the pH or by enhanced anion binding, the rate of aggregation is increased. We would anticipate, therefore, that as the pH approached the isoelectric point (4.25 to 4.5) the electric charge would tend to zero and the rate of aggregation would take on a maximal value. This, however, is not the case (Figure 3). The curve represents the percent soluble at various pH's after 24 hours. The amount soluble reaches a minimum at about pH 3.5 and then increases as we go toward the pH of minimum charge (the isoelectric point), i.e., the rate of aggregation is maximal at pH 3.5 and then decreases as we go to higher values.

The most reasonable explanation of this unexpected observation is that while electrostatic repulsive forces continue to decrease above pH 3.5, the attractive forces decrease even more drastically in this same pH interval. This could be brought about by a change in the conformation of protein molecule yielding molecular surfaces with greater mutual affinity. Evidence for such a change in conformation has been obtained by a variety of physical measurements.

Changes in Molecular Shape

A comparison of the sedimentation properties of the monomeric α lactalbumin molecule at pH 2 and at pH 8.55 reveals a difference in molecular shape. This is illustrated by the ultracentrifuge data summarized in Table 2. In the native state (pH 8.55) the frictional ratio is near unity indicating that the molecule is compact and nearly spherical with a radius of about 19 Å. In the denatured state (pH 2) the frictional ratio increases to about 1.3 corresponding to either an elongation of the molecule to yield a more ellipsoidal shape, or to isotropic swelling of the spherical molecule. In the latter case the radius would be about 23 Å.

Differential Ultraviolet Spectra

Differential ultraviolet spectra represent a sensitive means of detecting changes in the environment of aromatic amino acid residues such as tyrosine, tryptophan and phenylalanine (5). Typical curves obtained for α lactalbumin are shown in Figure 4. These are spectra of acidified solutions of α lactalbumin measured relative to identical concentrations of protein at pH 6. The spectra, characterized by peaks at about 286 and 293 mμ, are typical of tryptophan and indicate that the environment of such groups at acid pH is different from that of the reference protein at pH 6 (5). As the spectra in Figure 4 indicate, the amplitude of the maxima decrease with increasing pH. This is shown in greater detail in Figure 5 where we have plotted the amplitude of the 293 peak, ΔE_{293}, as a function of pH. The bulk of the change in ΔE_{293} occurs in the pH region 3 to 4, both at 25° C and at low temperature (2 to 4° C)[2]. Setting aside for the moment the question as to the molecular origin of these difference spectra, we can assume that the pH dependence of ΔE_{293} corresponds

[2] A gap exists in the 25° C curve since measurements cannot be made in the isoelectric region because of low protein solubility.

to the pH dependence of the conformational change identified with the denaturation. Thus, the decrease in rate of aggregation observed above pH 3.5 (Figure 3) must be the consequence of a reversion of the molecule to its native state at these higher pH's.

A scheme describing the behavior of α lactalbumin in acid solution can be written as:

$$A_N \rightleftharpoons A_D' \rightleftharpoons A_D'' \rightleftharpoons A_D''' \ldots A_D \qquad \text{(denaturation)} \quad (1)$$

these steps are instantaneous and are followed by a slow process:

$$nA_D \rightleftharpoons (A_D)n \qquad \text{(aggregation)} \quad (2)$$

Where A is the native protein and A_D', A_D'', A_D''' ... A_D represent a series of denatured forms of somewhat different structure. We have found it necessary to postulate more than one denatured form to explain the temperature dependence of the spectral change (4).

Ultraviolet Fluorescence

Further evidence for changes in the environment of tryptophan groups has been obtained from the ultraviolet fluorescence of α lactalbumin solutions. These involve wavelength shifts of the emission maxima, as well as increases in quantum yield. The pH dependence of relative intensity (R.I.) at 340 mμ, assumed to be proportional to relative yield, is shown in Figure 6. The abrupt increase in yield below pH 4 indicates that the conformational change involves separation of tryptophan side chains from other portions of the molecule which possess quenching properties. The nature of these groups is at present unknown.

Origin of Spectral Changes

While the changes in the absorption and emission spectra of α lactalbumin clearly demonstrate the existence of a conformational change at low pH, they do not in themselves tell us the nature of this change. Environmental changes consistent with these observations would include breaking of hydrogen bonds, greater mutual separation of tryptophan residues, increased separation of charges from chromophores and gross unfolding of the protein molecule with transfer of tryptophan residues from non-polar regions of the protein molecule to more intimate contact with the aqueous medium. The latter process has been frequently invoked to explain the so called "denaturation blue shift", i.e., the type of difference spectrum shown in Figure 4. Unfortunately, it is rare that direct evidence which can confirm this hypothesis is available.

In order to resolve this ambiguity we have made use of a relatively new technique which allows us to distinguish "buried" tryptophans from those in contact with water. This method, the so called solvent perturbation procedure, is based on the fact that a "molecular probe", i.e., a small inert molecule, on coming into close contact with a chromophore such as a tryptophan group will alter its spectral properties slightly (8). In practice, one determines the difference spectrum of a pair of protein solutions of identical concentration and pH, one containing the perturbant molecules, the other perturbant-free (8, 9). The magnitude of the spectral change relative to a suitable standard such as N-acetyl tryptophan ethyl ester is a measure of the extent of exposure of the chromophores. The perturbants employed are shown in Table 3. The second column of the Table gives their molecular radii (Einstein-Stokes spheres) as calculated from diffusion constants. If we imagine a protein molecule in which some tryptophans are completely buried, other project freely into the aqueous medium and still others are partially buried in "crevices" in the surface, it can be seen that the use of "probes" of various sizes should enable us to estimate the size of these "crevices".

The results obtained with α lactalbumin are summarized in Figure 7. The horizontal line marked "full exposure" represents the five tryptophans found by chemical analysis (10). As seen in the Figure, at 1° C near pH 6 all five groups are buried with respect to sucrose, glycerol and ethylene glycol (the 2.2 to 5 Å perturbants). A reference to Table 3 indicates that either all groups are completely buried or lie in "crevices" smaller than 2.2 Å - the molecular radius of the smallest probe, ethylene glycol. At this same temperature as we pass through the transition region (Figure 5) - pH 3 to 4 - the structure becomes altered such that one tryptophan residue becomes accessible to the medium. The "crevice" size for this group must be larger than 4.7 Å since it will admit a sucrose molecule.

Increasing the temperature from 1 to 25° C near pH 6 exposes two groups to the 2-5 Å perturbants. However, acidification of the protein through the transition region (pH 3 to 4) at 25° C does not involve exposure of additional groups (Figure 7), two groups still being exposed to solvent.

It is of interest to note that in 1959 Weil and co-workers (11) found that chymotryptic attack of α lactalbumin, followed by treatment with carboxypeptidase, liberated only two moles of tryptophan implying that three tryptophan groups are buried and hence

inaccessible to enzymatic attack. These results are amply supported by our solvent perturbation measurements.

Measurements employing the 1 Å perturbant (heavy water) reveal three groups exposed to solvent both at pH 6 and in the region 2 to 3 (Figure 7). Since only two groups were exposed to the 2 to 5 Å perturbants, we can conclude that one of the three buried groups must lie in a "crevice" larger than 1 Å but smaller than 2.2 Å. While the 1 Å perturbant gives slightly different quantitative results as compared to the other, it is important to emphasize the fact that no change in groups occurred on going from pH 6 to low pH, indicating that the transition does not involve increased permeability of the molecule to water.

If we now compare the results summarized in Figures 5, 6 and 7 certain conclusions can be drawn as to the nature of the alteration in tryptophan environment. Although no additional groups are exposed in going from pH 6 to pH 2 at 25° C (Figure 7), marked changes in the absorption and emission spectra occur. The latter must be due to changes in local group interactions. The increase in molecular size (Table 2) observed in acid solutions suggests that the swelling of the molecule permits greater free rotation of amino acid side chains with concomitant reduction of interactions with neighboring groups. The magnitude and directions of these spectral changes are consistent, for example, with the breaking of a hydrogen bond from tryptophan to an acceptor group, yet unknown (12). To our knowledge this is the first unambiguous demonstration that the large spectral changes associated with denaturation need not be the result of exposure of chromophores to the medium. Clearly, many previous studies of protein denaturation will have to be reconsidered in light of these findings.

The transition at low temperature is more complex than at 25 degrees. As Figure 7 indicates, acidification of α lactalbumin from pH 6 to 2 involves the exposure of one tryptophan group. Nonetheless, the magnitude of the spectral change (Figure 5) is too large to be accountable solely on the basis of an exposure of a single group. The simplest explanation of the observations at low temperature is that the transition involves more than one conformational change. This was a conclusion that was previously reached in formulating Equation 1. The total change involving tryptophan would result from both an exposure of one group and increased free rotation of buried groups in the interior of the molecule as was suggested for the 25° C transition. Direct verification of the hypothesis

unfortunately, is beyond the capabilities of present physical-biochemical methods.

Rotatory Dispersion Measurements

In addition to alterations of the environment of side chains such as tryptophan, the low pH denaturation of α lactalbumin involves a change in the folding of the polypeptide backbone. Evidence for this has been obtained from rotatory dispersion measurements. Interpretation of these data has been made in terms of the Yang-Moffitt equation (13):

$$[m'] = \frac{a_0 \lambda_0^2}{\lambda^2-\lambda_0^2} + \frac{b_0 \lambda_0^4}{(\lambda^2-\lambda_0^2)^2} \qquad (3)$$

where $[m']$ is the reduced mean residue rotation, i.e., the specific rotation reduced to mean residue weight and corrected for the wavelength dependence of the refractive index, λ is the wavelength of light and a_0, b_0 and λ_0 are parameters characteristic of the protein. λ_0 is generally taken to be 212 mμ. The parameter b_0, which can be evaluated graphically from the data using Equation 3, is very sensitive to changes in secondary structure. For example, for synthetic polypeptides, b_0 will take on values ranging from 0 to -630 degrees when the polypeptide backbone is converted to a 100% helical structure from a random coil (13). Applying the same procedure to proteins, one can estimate the percentage of the polypeptide chain in helical form from the relationship

$$\% \text{ Helix} = 100 \frac{b_0}{630} \qquad (4)$$

The results of a series of rotatory dispersion measurements made over the 313 to 578 mμ range are shown in Figure 8. Near pH 6 and below about pH 3.3, values for b_0 at 0 and 25 degrees were indistinguishable with experimental error. At pH's above 3.3 and somewhat below 5.5 solubility problems precluded measurements at 25° C. Comparison of Figure 8 with Figures 5 and 6 indicate that the spectral transition occurring below pH 4 is paralleled by a change in the folding of the polypeptide chain. The b_0 value of α lactalbumin at pH 6 indicates that the native protein has about 35% of the polypeptide chain in hydrogen bonded helical form. At low pH we find a b_0 value corresponding to about 24% helix. Thus, α lactalbumin upon denaturation at low pH loses about a third of its helical content, the transformation presumably being helix → random coil.

The close agreement of the b_0 values obtained near pH 6 at 0 and 25 degrees (Figure 8, filled and unfilled symbols) is particularly interesting in view of the burying of tryptophans observed at low temperature (Figure 7). It would appear that the conformational change associated with the latter process does not involve any change in backbone conformation.

A Pictorial View of the Low pH Denaturation

A view of the overall denaturation-aggregation process at 25 degrees is shown in Figure 9 (see also Equations 1 and 2). This picture should not be taken too literally since it is only intended to summarize visually our interpretations of the experimental observations. The symbols  represent tryptophan residues, two of which are deeply buried in the interior of the molecule in the region of certain interacting side chains (). The third buried group is in a narrow crevice at the upper right hand surface of the molecule. Two others are freely accessible to the aqueous medium.

The denaturation step at pH's below 4 (pH 2, for example) involves swelling or elongation of the molecule, together with separation of the buried tryptophan side chains from the interacting groups without, however, any additional tryptophans being exposed. At the same time about 1/3 of the helical backbone (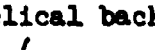) is converted to a more random structure (). During this process certain key side chains (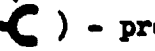) - probably non-polar in nature - are brought from the interior of the molecule to its surface where they are now available for interaction with other non-polar groups (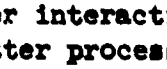). This latter process produces polymers such as those shown at the lower part of the Figure. To conserve space we have shown only a cluster of three molecules. Experimentally we find that aggregates contain an excess of 20 molecules.

This crude picture clearly represents only a first approximation to a description of the molecular changes occurring during denaturation. We expect to refine this formulation by the application of other techniques which can tell us about the environment of groups such as tyrosine, glutamic and aspartic acids, lysine and histidine. We hope in this way to come closer to an answer to our original question - what holds protein molecules together?

References

1. Inter- and Intramolecular Interactions of α Lactalbumin. I. The Apparent Heterogeneity at Acid pH, Kronman, M.J. and Andreotti, R.E., Biochem., In Press.

2. Inter- and Intramolecular Interactions of α Lactalbumin. II. Aggregation Reactions at Acid pH, Kronman, M.J., Andreotti, R.E., and Vitols, R., Biochem., In Press.

3. Binding of Ions to Proteins, Carr, C.W., Arch. Biochem. Biophys., 40, 286 (1952).

4. Inter- and Intramolecular Interactions of α Lactalbumin. III. Differential Ultraviolet Spectra, Kronman, M.J., Cerenkowski, L. and Holmes, L., Manuscript in Preparation.

5. Ultraviolet Spectra of Proteins and Amino Acids, Wetlaufer, D.B., Adv. in Protein Chem., 17, 304 (1962).

6. Inter- and Intramolecular Interactions of α Lactalbumin. V. Fluorescence of Tryptophan, Kronman, M.J., Manuscript in Prep.

7. Inter- and Intramolecular Interactions of α Lactalbumin. IV. Location of Tryptophan Side Chains, Kronman, M.J. and Holmes, L., Manuscript in Preparation.

8. Spectrophotometric Criterion for "Buried" and "Exposed" Groups in Proteins, Herskovits, T.T. and Laskowski, M., Jr., J. Biol. Chem., 235, PC 56 (1960).

9. A Cell Arrangement for Solvent Perturbation Measurements, Kronman, M.J. and Holmes, L., Anal. Biochem., 7, 124 (1964).

10. Tryptophan Content of Proteins, Gordon, W.G. and Semmett, W.F., J. Am. Chem. Soc., 76, 287 (1954).

11. Studies on the Specificity of Protaminase, Weil, L., Seibles, T.S. and Telka, M., Arch. Biochem. Biophys., 79, 44 (1959).

12. Spectral Studies of Indole and Indole Derivatives, Lumry, R., Personal Communication.

13. O.R.D. and the Conformation of Polypeptides and Proteins, Urnes, P., and Doty, P., Adv. in Protein Chem., 16, 402 (1961).

14. Inter- and Intramolecular Interactions of α Lactalbumin. VI. O.R.D. Studies, Kronman, M.J. and Blum, R., Work in Progress.

15. Amino Acid Composition of α Lactalbumin, Gordon, W.G. and Ziegler, J., Arch. Biochem. Biophys., 57, 80 (1955).

TABLE 1

Characteristics of Aggregation Reaction in pH Region 2 to 3.5

Parameter	Effect on Rate
decreasing protein conc.	decreasing
decreasing temperature	decreasing
decreasing ionic strength	decreasing
binding of anions	increasing
decreasing pH	decreasing

TABLE 2

Molecular Size of Native and Denatured α Lactalbumin[a]

pH	State	Sedimentation Constant	Frictional Ratio[b]	Spherical Radius (Å)
8.55	native	1.93 S	1.02-1.06	19
2.00	denatured	1.6 S	1.2 -1.3	23

[a] Data taken from Kronman, et al., (2), 25° C, 0.15 M KCl

[b] 20 - 30% hydration

TABLE 3

Characteristics of Perturbants

Perturbant	Effective Radius (Å)
20% Sucrose	4.7
20% Glycerol	2.7
20% Ethylene Glycol	2.2
90% Heavy Water	1

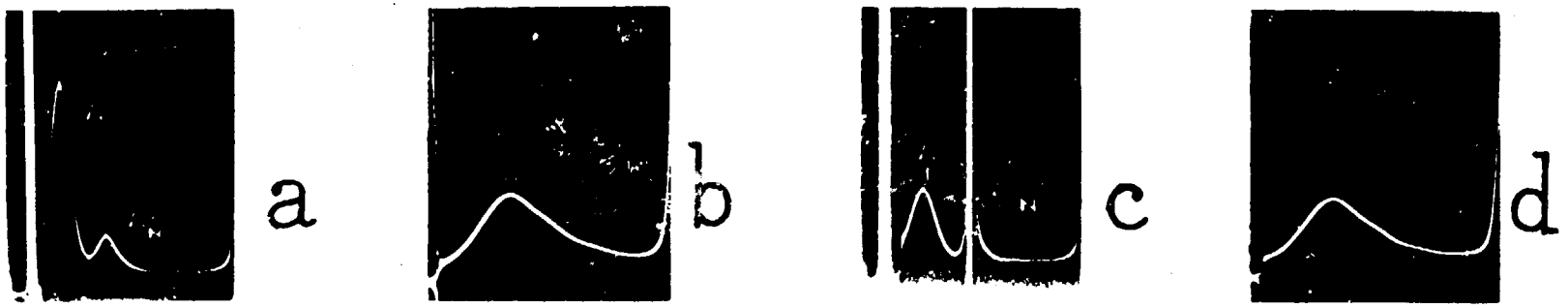

Figure 1 - Ultracentrifuge patterns of α lactalbumin solutions in 0.15 M KCl. a. pH 2.00, 5.75%, 1 hr. b. pH 6.00, 4.85%, 1 hr. c. pH 2.00, 5.75%, 24 hrs. d. pH 6.00, 4.85%, 24 hrs. All measurements made at 59,780 rpm, 0.15 M KCl, time of photography - 64 minutes. Data taken from refs. 1 & 2.

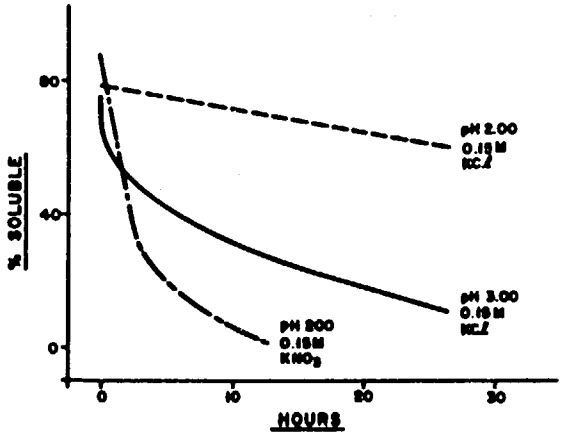

Figure 2 - Solubility changes of α lactalbumin in acid pH, 0.15 M KCl. See text for procedure. Data taken from ref. 2.

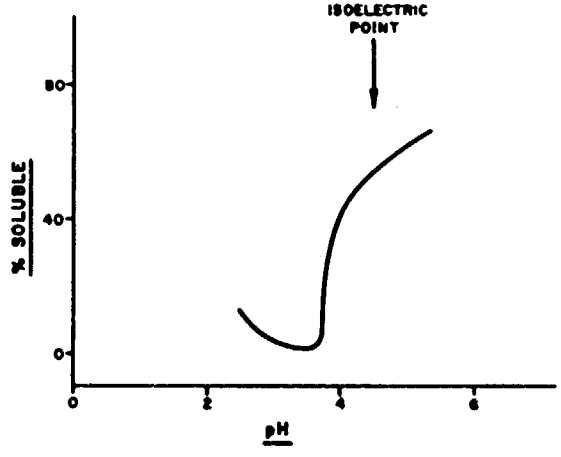

Figure 3 - Solubility of α lactalbumin after exposure for 24 hrs. to the pH indicated. See text for procedure. Data taken from ref. 2.

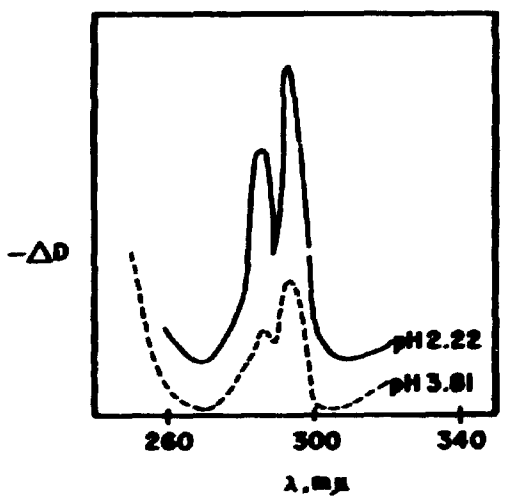

Figure 4 - Differential ultraviolet spectra of α lactalbumin at acid pH. Ref. pH - 5.8 to 6, 0.15 M KCl. Data taken from ref. 4.

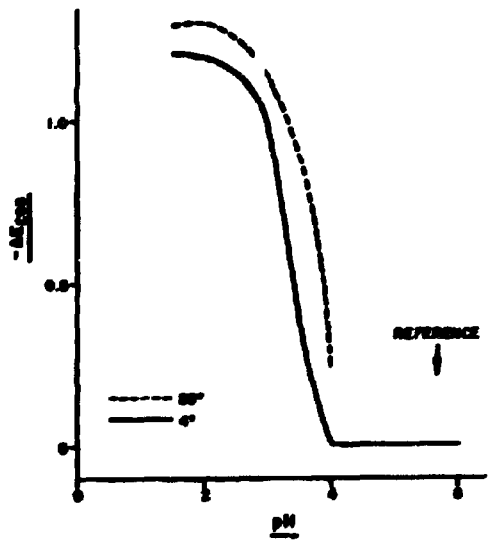

Figure 5 - pH dependence of amplitude of 293 mμ differential peak, 0.15 M KCl. Data taken from ref. 4.

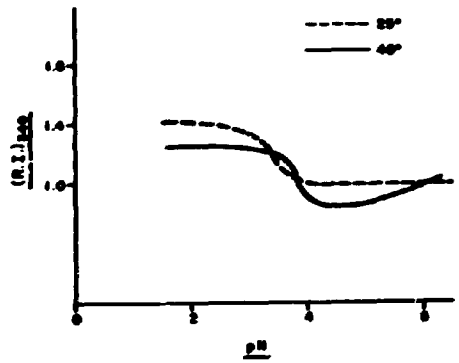

Figure 6 - pH dependence of relative fluorescence intensity (R.I.) of α lactalbumin, 0.15 M KCl. All data normalized at pH 6. Data taken from ref. 6.

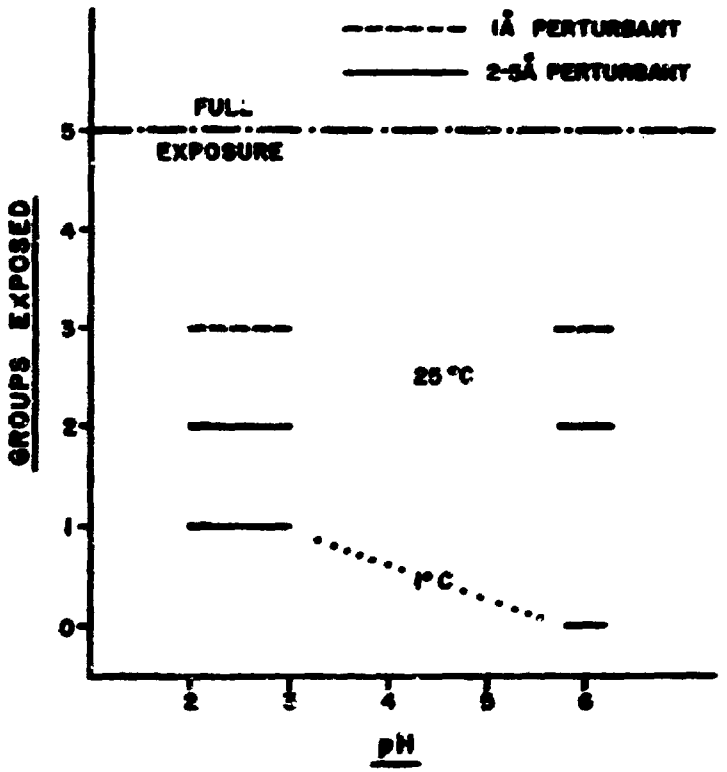

Figure 7 - Exposure of tryptophan groups in α lactalbumin as measured by solvent perturbation, 0.15 M KCl. Data taken from ref. 7.

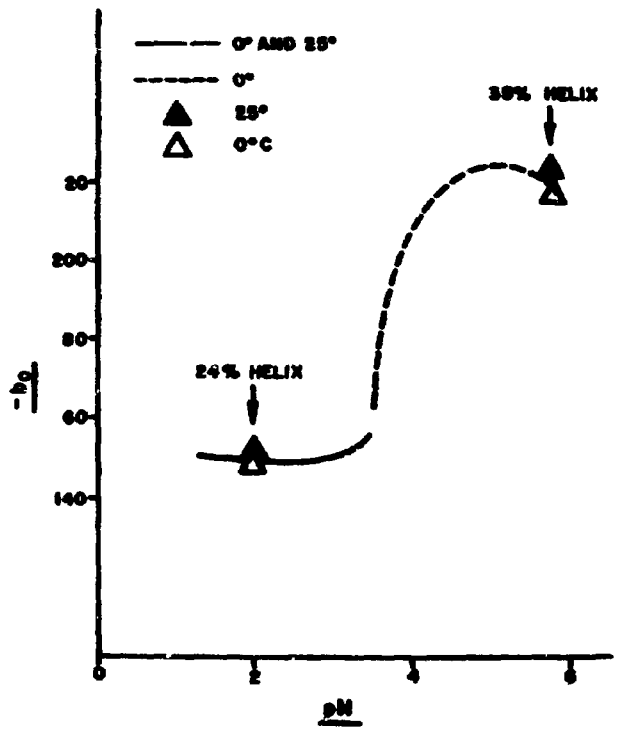

Figure 8 - pH dependence of rotatory dispersion parameter, b_o, for α lactalbumin, 0.15 M KCl. Data taken from ref. 14.

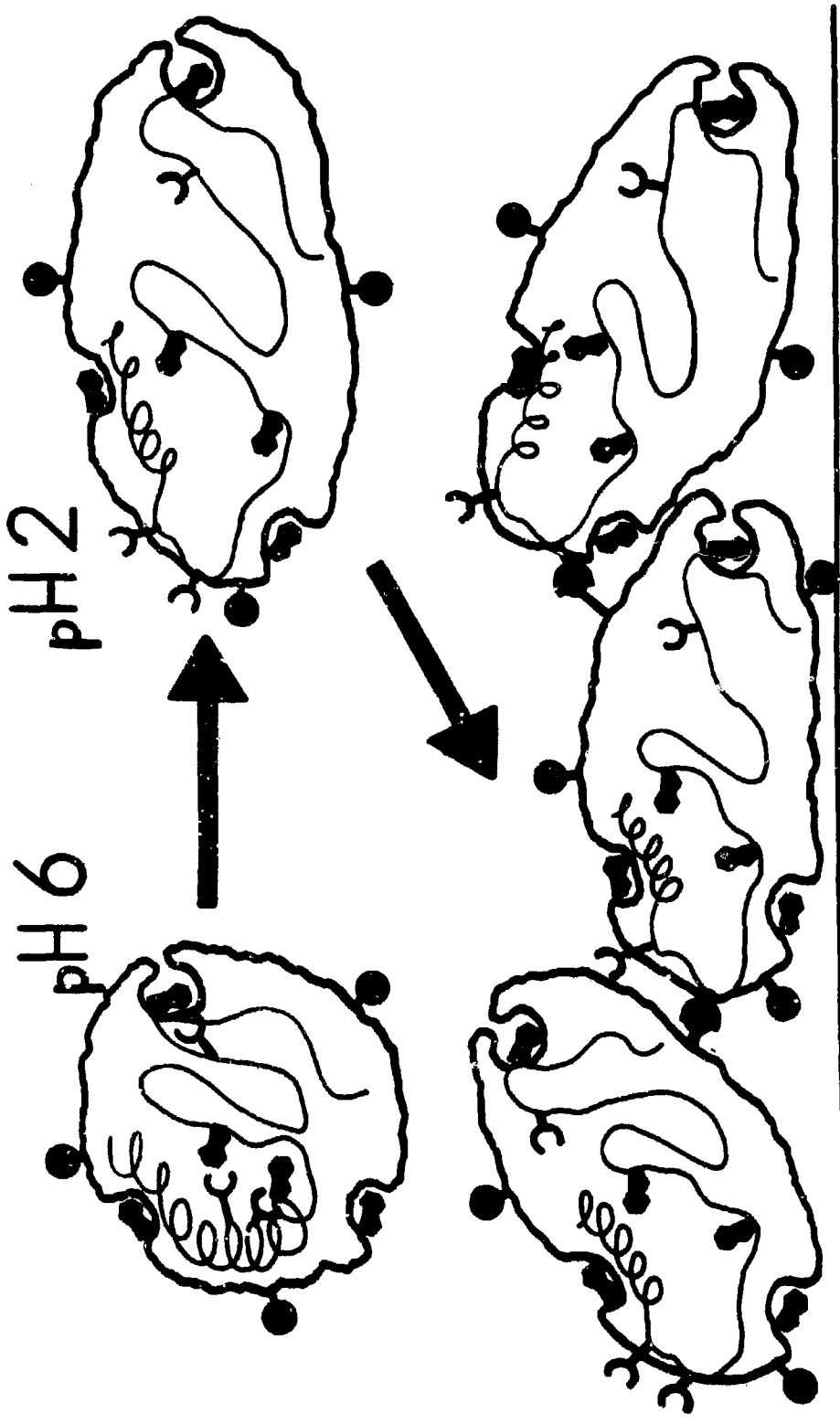

FIG. 9 SCHEMATIC REPRESENTATION OF THE DENATURATION AND THE AGGREGATION OF α LACTALBUMIN

HIGH SPEED PENETRATION OF NON-WOVEN FABRICS

ROY C. LAIBLE
U. S. ARMY NATICK LABORATORIES
NATICK, MASSACHUSETTS

At low areal densities needle-punched non-woven fabrics have proven to exhibit ballistic resistance superior to the nylon fabric presently used in personnel armor. This fact is of considerable academic and practical interest because years of research on woven fabrics have resulted in only marginal improvements over the nylon basket weave fabric.

The following study was conducted in an attempt to determine the reasons for the good ballistic resistance of felts especially as compared to the behavior of nylon fabric. High speed photography was used to follow the missile-target interaction with time while laboratory tests were conducted to study those stress-strain properties of felts which might be related to their ballistic properties.

EXPERIMENTAL MATERIALS

The major target material for the ballistic studies was a needle-punched nylon felt with the following characteristics.

Staple Length	3"
Thickness of Felt	0.1"
Areal Density	1.87oz/ft^2
Fiber Type	6 denier nylon tire cord

Method of Preparation

The felt was prepared by needling a parallel laid bat followed by pressing with a flat bed press to attain the desired thickness of 0.1".

In addition a series of felts differing in fiber type were prepared (Felters Corporation, Millbury, Mass.) in order to obtain

LA IBLE

materials with varying ballistic limit values. These felts are listed in the following Table.

TABLE I
FELT SAMPLES

Material	Fiber	Fiber Denier (dpf)*	Staple Length (in)	Felt Density (oz/in^3)	Areal Density (oz/ft^2)
FL Acrylic-1	100% acrylic-1	6	2	0.080	3.3
FL Modacrylic	100% modacrylic	50%-3 50%-12	1½	0.078	3.2
FL Polyethylene	100% polyethylene	4	1½	0.088	3.4
FL Polypropylene	100% polypropylene	6	1"	0.074	3.4
FL Nylon	100% nylon	6	3"	0.078	3.5
Nylon C-500-58 (0.60-in thick	100% nylon	6	3	0.073	6.3
Nylon C-500-58 (0.11-in thick)	100% nylon	6	3	0.134	2.1
Nylon, commercial (0.50-in thick	100% nylon	-	-	0.087	6.3

*dpf - denier per filament, where denier is the weight in grams of 9000 meters of the fiber.

The nylon C-500-58 listed for two thicknesses in the Table is the same as the major target material previously mentioned except for thickness.

EXPERIMENTAL PROCEDURES

High Speed Cinematography

The felt samples were mounted on an aluminum frame with outside dimensions of 14.5" by 11.5" and inside dimensions of 7" by 7". The felt was attached to the aluminum frame with cloth masking tape on all four sides and the aluminum frame in turn was rigidly clamped perpindicular to the camera. This method of mounting used to facilitate profile photography, was checked by V_{50} measurements and found to yield equivalent values to those obtained from the usual mounting systems. The events were recorded with a Beckman and Whitley Dynafax camera at a rate of 26,000 frames/second. Each frame was exposed for one microsecond with a total elapsed time of 38.5 microseconds between frames. A four millisecond light pulse with an intensity of 10^7 peak beam candlepower obtained from a Xenon flash tube provided the lighting for the experiments. Kodak Tri-X 35mm panchromatic film was used which, with the Dynafax camera, records two rows of 16mm frames. A 17 grain (1.1 gram) fragment simulator fired from a smooth bore .22 caliber rifle with compressed helium was used as the missile. The velocity of the missile was obtained by measuring the time re-

quired for passage between two printed circuit grids one foot apart. A Vanguard Motion Analyzer (Model M16C) was used to measure the distances representative of missile travel and transverse felt displacement. An error of only .001 inches has been attributed to the motion analyzer.

"Punch Press" Testing

The felts were subjected to a puncture test at a rate of loading averaging 6000 inches/minute. Puncture was accomplished by means of a two inch rod with a tip shaped as a .22 caliber projectile attached to the top portion of the lower part of a compression cage. The felt specimen to be tested (1-3/4" by 1-3/4") was mounted in the bottom portion of the upper part of the cage and clamped with a flat steel plate containing a 1-inch diameter hole in the center. (Fig. 1) Load was measured by a transducer of the unbonded strain - gage type while displacement was measured by a linear potentiometer-type transducer. The resulting load - deformation curve on an oscilloscope was obtained with a Polaroid Land Camera. Additional details concerning this test have been given previously (1).

Ballistic V_{50} Test

The felts to be studied were all subjected to a V_{50} test as described in "Ballistic Acceptance Test Method for Personnel Armor Material" dated 28 June 1961 (2). Essentially it is an estimate of the velocity at which one half of the missiles fired will penetrate and one half will not penetrate the subject target material.

Tensile Testing

Strips of felt 1 inch by 6 inches were tested at 12 inches/minute using the Instron Tensile Tester and at 12000 inches/minute using the Mitex high speed pneumatic tester. Both of these instruments have been described previously (1) Four inch gage lengths were used for the high speed test to insure constant rate of testing.

EXPERIMENTAL RESULTS

High Speed Penetration

High speed penetration tests were conducted at 6000 inches/minute and peak load, displacement and estimated work to rupture tabulated. The work to rupture values were obtained by triangulation to maximum load. The curve does not drop suddenly from this maximum point and an additional work to rupture of the same order of magnitude is available as force drops from maximum to nearly zero. Use of the entire area under the curve would therefore yield values for work to rupture double those listed in Table II.

LAIBLE

TABLE II
PENETRATION RESULTS ON FELT SAMPLES

Material	Average Areal Density* (oz/ft^2)	Peak Load During Penetration (lb)	Displacement During Rise (in)	Work to Rupture by Triangulation (ft-lbs)
FL Acrylic-1	3.4	214	0.23	2.0
FL Modacrylic	3.4	189	0.29	2.3
FL Polyethylene	3.4	218	0.19	1.7
FL Polypropylene	3.5	398	0.29	4.7
Nylon C-500-58 (1 layer 0.11" thick)	2.0	207	0.29	2.5
Nylon C-500-58 (2 layers 0.22" thick)	4.3	434	0.33	5.9
Nylon C-500-58 (3 layers 0.33" thick)	6.5	666	0.37	10.4
Nylon C-500-58 (1 layer 0.60" thick)	6.3	552	0.29	6.7
Nylon commercially (1 layer 0.50" thick)	6.3	345	0.31	4.4

V_{50} Test

The results of the V_{50} test on the same felt materials have been expressed as the velocity at the V_{50}, total missile energy, and missile energy corrected for the witness plate in Table III.

TABLE III
BALLISTIC V_{50} RESULTS

Material	V_{50} (ft/second)	Missile Energy (ft-lbs)	Missile Energy corrected (ft-lbs)
FL Acrylic-1	634	15.2	11.7
FL Modacrylic	695	18.3	14.8
FL Polyethylene	553	11.4	7.9
FL Polypropylene	898	30.5	27.0
Nylon C-500-58 (1 layer .10" thick)	680	17.5	14.0
Nylon C-500-58 (1 layer .11" thick)	800	24.0	20.5
Nylon C-500-58 (2 layers .22" thick)	1050	41.6	38.1
Nylon C-500-58 (3 layers 0.33" thick)	1139	49.0	45.5
Nylon C-500-58 (1 layer .60" thick)	1070	43.1	39.6
Nylon, Commercial (1 layer .50" thick)	914	31.5	28.0

LAIBLE

The last column contains the missile energy values diminished by 3.5 foot lbs. to account for the witness plate which is used in the V_{50} test. The witness plate is a 2024T-3 aluminum alloy capable of stopping a missile traveling up to 300 feet/second, which is equivalent to 3.5 foot pounds of kinetic energy.

High Speed Photography of Ballistic Impact

The thin (0.1") needle-punched nylon felt was subjected to impact by the .22 caliber 17 grain fragment simulator at velocities from 640-700 feet/second, near the V_{50} value. A cone was formed by the deformation, the height of which was used to determine the position of the missile as a function of time (Fig. 2). In Table IV the average values of missile velocity and missile energy calculated from the seven sets of photographs have been tabulated.

TABLE IV
MISSILE VELOCITY AND MISSILE ENERGY AS A FUNCTION OF TIME

Frame No.	Time Interval After Impact (Microseconds)	Missile Velocity (ft/sec)	Missile Energy (ft-lbs)
0	0	667	16.6
2	77	555	11.8
3	115	467	8.2
4	154	437	7.2
5	192	375	5.3
6	231	370	5.1
7	270	340	4.3
8	309	310	3.6
9	346	289	3.2
10	385	250	2.4
11	425	270	2.7
12	460	274	2.8

The energy extracted from the missile by the target varied quite widely for the seven experiments yielding values of 10.5, 13.1, 15.7, 16.7, 15.5, 11.6 and 13.3 foot pounds for an average of 13.8. This is the typical variation to be expected from ballistic firings near the V_{50} region where one shot at a given velocity will penetrate the target and witness plate while a second shot at the same velocity will not even penetrate the target.

Other information was also obtained from the photographs of the cone deformation. The base of the cone expands with time during and after penetration and measurements of this dimension were used to determine the "transverse wave velocity". Base radius and estimated cone weight have been also tabulated in Table V as indications of the area of maximum involvement in the deformation and of the kinetic

LABLE

energy of the felt.

TABLE V
BASE LINE VELOCITY AND CONE SIZE AS A FUNCTION OF TIME

Frame No.	Time Microseconds	Base Line Velocity (ft/sec)	Base Radius (inches)	Estimated Felt Weight in Cone (X10-3 lbs)
1	38.5	-	.25	.16
2	77.0	217	.35	.31
3	116.0	217	.45	.51
4	154.	209	.55	.77
5	192	229	.68	1.18
6	231.	180	.76	1.48
7	270.	146	.82	1.71
8	308	208	.92	2.07
9	346	208	1.02	2.65
10	385	168	1.09	3.03
11	424	174	1.17	3.49
12	461	156	1.25	3.98
13	500	154	1.32	4.44
14	540	118	1.37	4.78
15	578	128	1.43	5.20
16	618	149	1.50	5.71
17	657	132	1.56	6.20

In the time region of interest the kinetic energy of the moving felt in the cone could be estimated at about 3.5 foot-pounds as a maximum. This estimate is based upon the entire felt cone moving at the missile velocity. Higher values which could be calculated after about 10 frames are meaningless as the felt deviates from the cone shape demonstrating that the felt velocity is lagging missile velocity.

In the case of complete penetration of the felt, the missile orientation after exit from the felt could be studied. In most cases a tumbling was imparted to the missile which reached velocities as high as 1000 revolutions per second. This tumbling could be either clockwise or counterclockwise with reference to the missile's forward motion.

Tensile Tests

The results of tensile tests at two rates of testing have been tabulated for the .1 inch felt as breaking strength, elongation and estimated work to rupture. Five tests were conducted in each direction and at each speed. Four inch gage lengths were used.

LAIBLE

TABLE VI
TENSILE TEST RESULTS

Felt Direction	Rate of Testing	Breaking Strength (lbs)	Elongation (%)	Work to Rupture ft-lbs/in^2
M.D.	300%/min	130	86	4.7
C.D.	300%/min	97	84	3.4
M.D.	300,000%/min	88	78	2.9
C.D	300,000%/min	91	80	3.0

DISCUSSION

Thousands of materials such as metals, ceramics, plastics, fabrics and felts have been subjected to ballistic evaluation. In most cases this evaluation has been confined to determining the V_{50} of the material against different missiles at various orientations and inspecting the targets afterwards. Other more basic studies have been concerned with components of the target material. For example the stress-strain properties of fibers and yarns have been studied over a wide range of strain rates (3). However, there is no assurance that we can translate these yarn properties to the performance of felts and fabrics. Polypropylene yarn should have produced an excellent ballistic fabric based upon its high speed stress-strain properties but in practice proved to be considerably inferior to nylon fabric. (4,5) Felts are a particular case in point because their properties are determined as much by the interaction of the component fibers as by the properties of the individual fibers. It was hoped that by a combination of laboratory tests and photography of the missile-felt interaction, the factors responsible for the performance of felts could be uncovered.

A series of felts were subjected to various laboratory tests in order to determine some measurable mechanical characteristics which could account for their ballistic resistance. These tests have been described previously. One of these tests, the high speed penetration test, ranked the felts in order of their ballistic performance. The correlation between the two tests was quite encouraging when expressed as V_{50} as a function of laboratory work to rupture value. (1) However, when the V_{50} was expressed as an energy term also (Fig 3), the discrepancy between the actual magnitude of the energy extracted during ballistic penetration and the work to rupture values from laboratory penetration became apparent. The laboratory values were only 12 to 24% of the corresponding missile energies.

Seven years ago workers at the Army Chemical Center investigated the ballistic penetration of nylon fabric by photographing the resulting deformation. As a result of this work they estimated that up to 40% of the missile energy extracted could be due to that used in

moving the fabric rather than just stretching it (6). This work by Stewart, Petterson, Maheux and Odell furnishes an excellent comparison for the felt studies under consideration as one of the questions to be answered is why felt should show superior ballistic resistance to fabric.

The nylon needle-punched felt was selected for photographic analysis both because of its possible utilization in the ballistic armor vest and because its thinness (.1 inch) minimizes the error in estimating missile position. In Fig 4 the resultant missile velocity curve has been plotted as a function of frame number. Frame number can easily be converted to time because the frames are separated by 38.5 microseconds. Individual impacts have been studied for as many as 40 frames after impact but on the average the important extraction of energy occurs within 10 frames after impact. This means that all useful impediments to the passage of the missile must be operative within 385 microseconds for this missile velocity range of 650-700 feet/second. At this point (385 microseconds after impact) the missile energy has been reduced to about 1/6 of its original value. With one layer of nylon fabric and a missile velocity of 500 ft/second a similar reduction in missile energy was attained in one-half the time. (6)

From the base line radius of the felt at different times, the transverse wave velocity as a function of time was determined. This apparent wave velocity varies from an initial 217 ft/second 77 microseconds after impact to 168 ft/second 385 microseconds after impact (Fig 4). The low estimate of felt weight involved based upon the base circle of the cone would yield only 3.4ft.lbs. in kinetic energy of the felt. This would be 24% of the kinetic energy extracted from the missile or only one-half that found at Army Chemical Center for fabric. The major reason for this difference is the much higher transverse wave velocity of the nylon fabric compared to the nylon felt. For nylon fabric this wave velocity varied from 720 ft/second 20 microseconds after impact to 390 ft/second 180 microseconds after impact when 80% of the missile energy has been removed. At this point 29 square inches of fabric has been brought into the cone as contrasted with only 3.2 square inches of felt in the cone even 385 microseconds after impact.

Based upon the preceding one might make a sort of energy balance by subtracting 25% of the energy of the missile as converted to kinetic energy of the felt. This still would mean that the laboratory penetration values based on .77in^2 of felt would have to be multiplied by a factor of four. The penetration test values were obtained by considering the stress-strain curve to maximum load. There is roughly an equal amount of area under the curve after maximum load. Consideration of the total area would reduce the factor to two rather than four. A factor of two is not unreasonable when we compare the felt area involved in the ballistic test with that used for the labo-

ratory penetration test. However, additional experimentation will be necessary before a useful energy balance can be obtained and as yet no reason has been advanced for the superior ballistic resistance of felt as compared to fabric. In fact the slower cone formation in the felt compared to the fabric would lead to a prediction of poorer performance by the felt.

In cases where the missile penetrated the felt, observations of the missile orientation were made. The results of this study can be shown in Fig. 5 where tumbling of the missile occurs at the rate of 1000 revolutions/second. The actual energy of the tumbling is insignificant but possible use could be made of the phenomenon for stopping the missile more easily after penetration. It remains to be determined whether felt has this advantageous action even with very high speed missiles or whether it can only occur after the missile's forward motion has been decreased to a relatively harmless value. Part of this tumbling has been observed prior to exit from the felt but x-ray photographs would be necessary to observe the missile while hidden by the felt. This same ability to turn a missile has been observed by the author with other targets and other missiles.

Using most of the criteria outlined in the preceding paragraphs one might expect nylon fabric to be a more effective ballistic armor than nylon felt. The major reason for the excellent behavior of felts can be seen from the tensile stress-strain behavior at different rates of straining. The curves given in Fig. 6 are somewhat reminiscent of the generalized flow curve for single crystals. In single crystals there is an initial "easy glide" region followed first by a region due to dislocation pile up of increasing "strain hardening" and ended by a region where stresses are high enough for dislocations to escape. The corresponding regions of the felt curve are an easy glide region where fibers are realigned followed by a strain hardening region due to interaction between fiber kinks and ended with a region where fibers are pulled apart from these kinks with and without breakage. The middle region is not very strain rate dependent in perfect analogy with the single crystal flow curve.

Whereas nylon fabric exhibits an elongation of about 30% even at static speeds, nylon felt has an elongation at break of 85% at 300 %/minute and 79% at 300,000 %/minute. Furthermore this elongation is similar to a permanent plastic deformation rather than to the viscoelastic behavior characteristic of most plastic and fibrous materials. The gage length of the sample reconstructed after break is 70% longer than originally with very little elastic retraction after failure. The "strain hardening" which takes place prevents localized necking and favors maximum uniform involvement of the felt under uniform loading.

Personnel in the ballistic field have always hoped to utilise the energy absorbtion which characterizes the drawing of polymers for

defeating missiles. For this reason theoretical studies of the drawing of crystalline and amorphous polymers are of considerable interest. However it is still not known whether the information concerning the drawing of polymers in the laboratory will be applicable at the high strain rates characteristic of ballistic speeds. A polymer which draws at moderate rates of elongation may not do so in a ballistic test. The use of discontinuous media such as the nonwoven felts discussed here may be a way of capitalizing on a different type of drawing operation which is not so rate sensitive. The "drawing" operation in the case of felts involves alignment of fibers and fiber to fiber friction rather than the strain rate dependent drawing which alligns molecules. The uniform nature of the "drawing" of felts due to " "strain hardening" leads to greater energy absorbtion than would be characterized by a local "necking" of the sample.

The fiber to fiber friction which is so important in the case of felts should generate considerable heat and controlled measurements of the heat rise could lead to a better energy balance in the future. If subsequent evidence verifies the hypothesis advanced here, it should be possible to prepare improved ballistic materials based upon this principle. Plastic, ceramic or metal fibers or whiskers in a felt form or in a matrix could yield some optimum value of this friction drawing.

REFERENCES

1. Laible, R. and R. Supnik "High Speed Testing as a Measure of the Resistance to Penetration of Needle Punched Felts, High Speed Testing Symposium May 14-15, 1963, Boston, Mass.

2. "Military Standard Ballistic Acceptance Test Method for Personnel Armor Material", Standardization Division, Armed Forces Supply Center, 28 June 1961, Washington, D. C.

3. Laible, R. and Morgan, H., "The Viscoelastic Behavior of Oriented Polyvinyl Alcohol Fibers as Large Strains", J. Polymer Science 54, 53-63 (1961).

4. Laible, R. and Morgan, H. "The Viscoelastic Behavior of Isotactic Polypropylene Fibers", J Applied Polymer Science 6, 21, 269-277 (1962).

5. Laible, R. "The Dynamic Properties of High Tenacity Yarns and Their Relationship to Ballistic Resistance", Symposium on Personnel Armor, Washington, D. C., 4-5 October 1961.

6. Maheux, C. R., G. M. Stewart, D. R. Petterson and F. A. Odell "Dynamics of Body Armor Materials Under High Speed Impact I Transient Deformation Role of Deformation and Energy Absorption in Single and Multilayer Armor Panels" CWLR No. 2141, 30 October 1957.

7. Petterson, D. R., G. M. Stewart, F. A. Odell and C. R. Maheux "Dynamic Distribution of Strain in Textile Materials Under High-Spoed Impact Part I Experimental Methods and Preliminary Results on Single Yarns", Textile Research J, 30,n6, 411-421 (1960).

LAIBLE

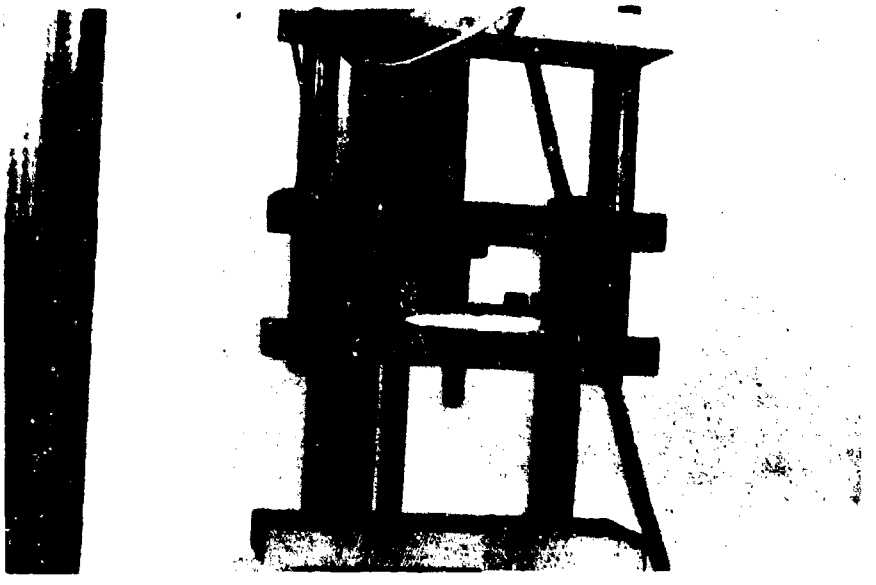

FIG. 1 LABORATORY PENETRATION TEST

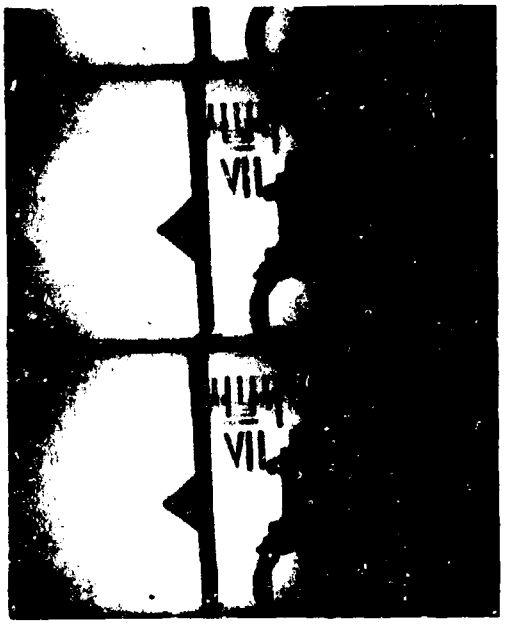

FIG. 2 CONE FORMED BY FELT UNDER IMPACT

LAIBLE

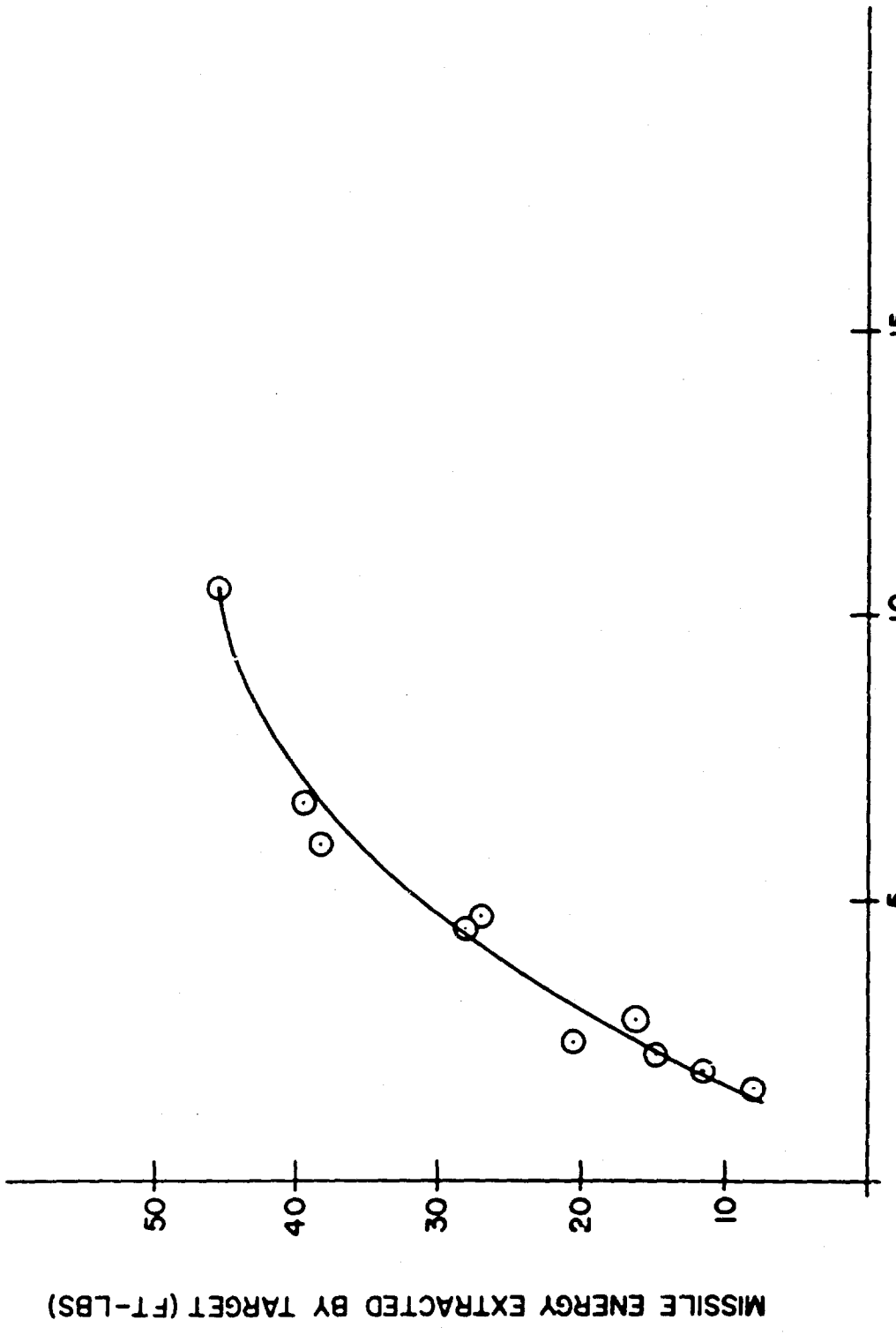

FIG 3 BALLISTIC PEFORMANCE AS A FUNCTION OF PENETRATION RESISTANCE

LAIBLE

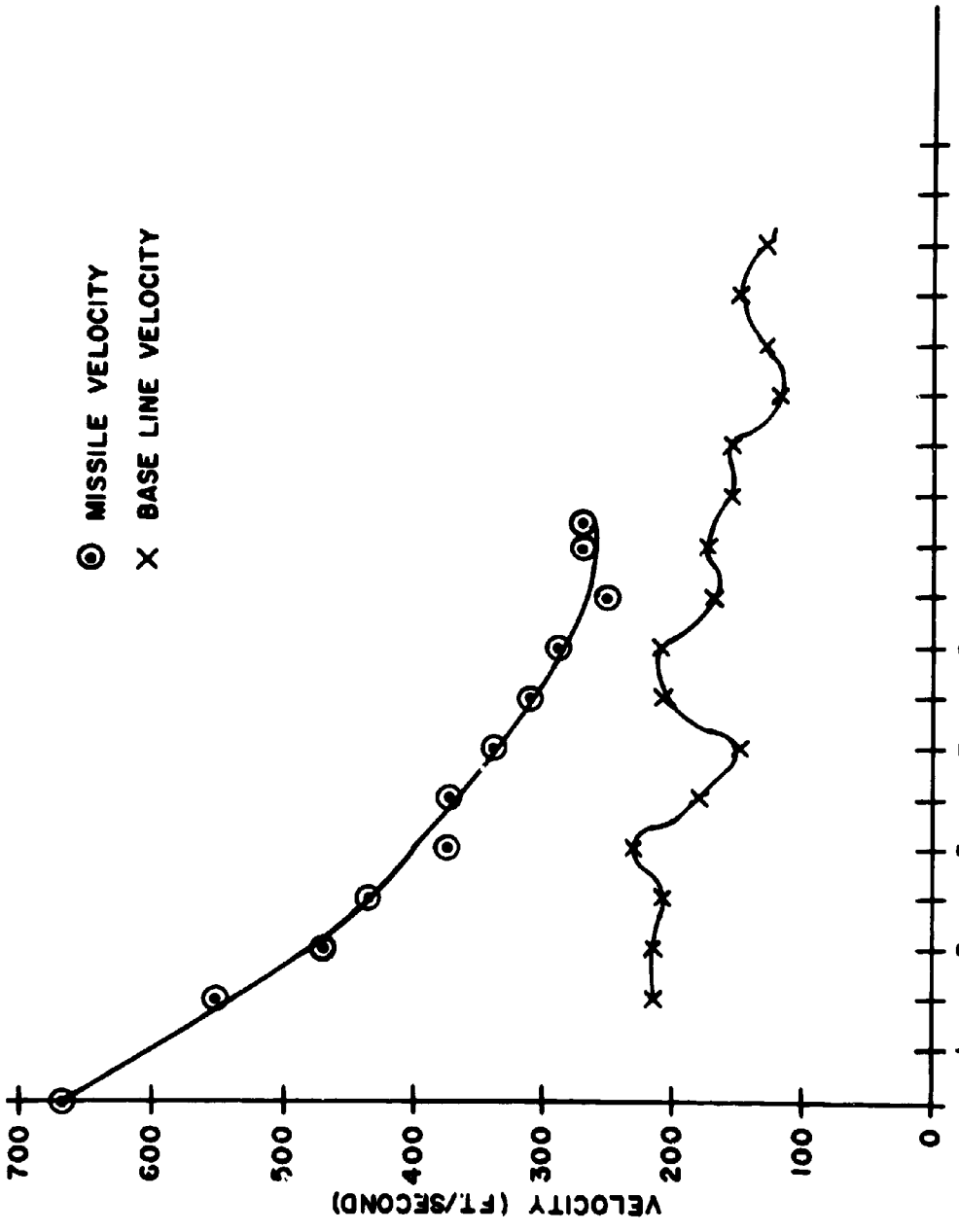

FIG. 4 MISSILE AND BASE LINE VELOCITIES AS FUNCTIONS OF TIME

IAIBLE

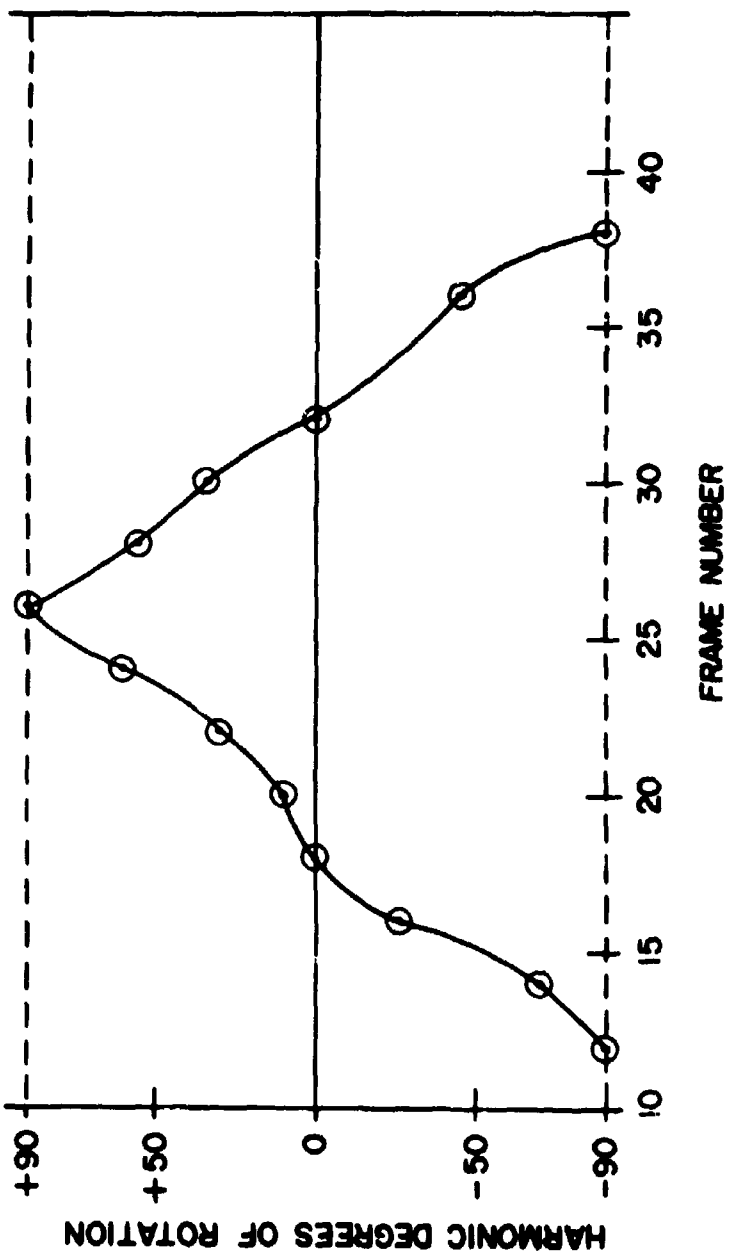

FIG-5 MISSILE TUMBLING AS A FUNCTION OF TIME(1 FRAME=38.5 MICROSECONDS)

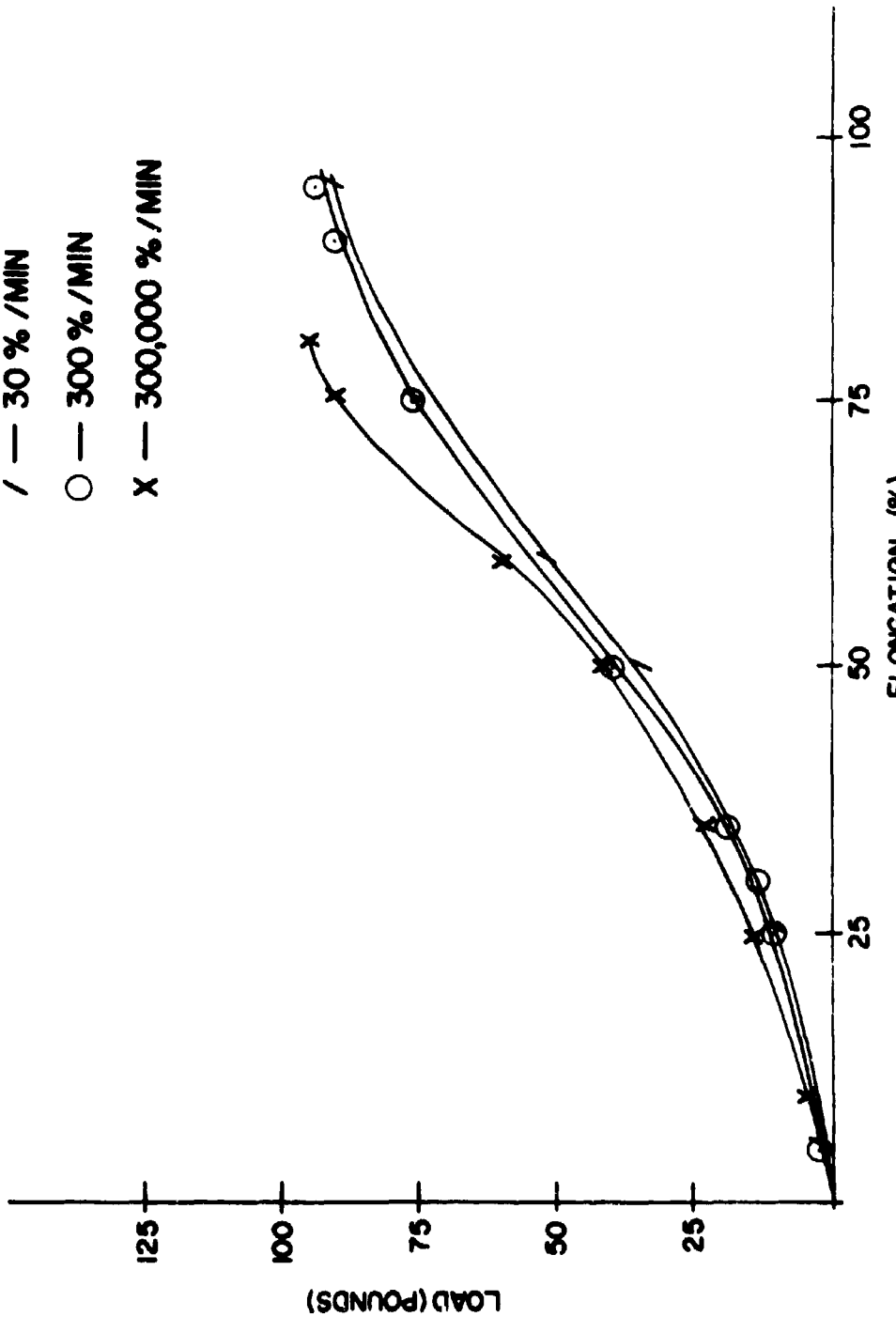

FIG 6 STRESS-STRAIN CURVES FOR NYLON FELT

AN OPTICAL SYSTEM FOR MEASURING THE ANGULAR MOTION OF THE GUN TUBE AND THE PROJECTILE IN THE BORE

STANLEY S. LENTZ
USA BALLISTIC RESEARCH LABORATORIES
ABERDEEN PROVING GROUND, MARYLAND

INTRODUCTION

The advance of technology since World War II has made it possible to reduce many of the errors associated with the accuracy of fire of direct-fired large-caliber weapon systems. Target detection equipment has helped the observer locate the target quickly and with greater accuracy than ever before. Sights and sighting techniques have been improved significantly by aiming the gun from the muzzle rather than from the breech. Fire control apparatus and computers have been developed to provide accurate data for laying the weapon. On the other hand, tanks and armored vehicles are now lighter, more mobile, and present a smaller silhouette or target. Large caliber guns mounted on these tanks and vehicles have longer, more flexible tubes, are lighter in weight, and launch projectiles at much higher velocities than their predecessors. As a result of this, the accuracy of the gun-projectile system has become a relatively large component of the resultant accuracy of fire.

In January 1955, the Army Tank-Automotive Center (ATAC) requested that the Ballistic Research Laboratories (BRL) consider a program titled "Unpredictable Inaccuracies in Primary Weapon Systems of Tanks." As a result of this program a literature survey, theoretical studies of the motion of the gun, and a number of firing programs have been carried out by BRL. In addition, several pieces of special optical apparatus have been developed, one of which is the subject of this paper.

SOME FACTORS WHICH AFFECT THE ACCURACY OF FIRE

When a number of rounds are fired at a reasonably close target, the center of impact generally falls some distance from the point of aim. This distance is a bias that may be attributed to constant factors which occur during the launch and the flight of the

projectile. A bias of this type can be determined for different rounds of ammunition and corrected in the fire control system. The random dispersion about the center of impact is produced by inconsistent factors and cannot be corrected in the fire control system. Thus, to improve the accuracy of fire the random dispersion must be reduced.

The difference between the point of aim and the point of impact is associated in part with the following phenomena:

a. Malalignment of the projectile with the axis of the bore.

b. Gross motion of the weapon produced by the powder pressure couple.

c. Impulsive disturbance transmitted by the muzzle to the projectile during launch.

d. Disturbances produced by muzzle blast on the projectile.

e. Aerodynamic jump associated with the yawing motion of the projectile in flight.

Studies of the bias or "jump" and dispersion have been in progress for many years. For example, in 1899 C. Cranz[1] * photographed the lateral vibrations of a rifle barrel and pointed out that the vibrations of the barrel and point of impact on the target varied with different powder charges.

Since 1945 there have been several major investigations of "jump". The first of these includes the theoretical investigations of barrel vibration and their influence on jump by Lee, Sneddon and Parsons (1945) and the experimental work by F. L. Uffelmann[2] (1949-1957) of England. In these studies Uffelmann developed optical systems for recording, in the vertical direction, angular displacements of the projectile and the muzzle, and also the linear displacement of the muzzle.

Another major investigation includes the cooperative efforts of Gay and Elder of BRL R-1070, May 62. (3) Their investigations consisted of a literature survey and a theoretical and experimental study of the 90mm Tank Gun, T-139. These studies included the effects of static deflection or droop of the tube, crookedness of the tube, tube bend associated with thermal gradients, and methods of calculating the motion of the gun associated with the powder pressure couple and also with unbalanced projectiles. For the firing tests the gun was mounted on an M-48 Tank and both the gun tube and tank

*Superscripts in parentheses indicate references at the end of this paper.

were instrumented to record the angular and linear displacements of the tube in the vertical direction. From the experimental data it was evident that the measured motions accounted for only a fraction of the difference between the point of aim and the point of impact. The theoretical calculations accurately predicted only the gross motion of the gun; the recorded data showed that large, high frequency, lateral forces arise from the motion of the projectile which act on the tube. These motions must affect the launching of the projectile and the accuracy of fire.

R. Thill[4] of France recently described experiments to study the motion of the 90mm Gun, 105mm Howitzer, and 155mm Gun from the time of firing until the projectile leaves the muzzle. This work was published in the Mémorial de L'artillerie Francaise and hopefully will be translated.

DEVELOPMENT OF THE APPARATUS

In view of the results obtained at BRL, it was decided to develop an optical autocollimator to measure the angular displacements of the projectile and the gun tube with respect to time. To determine the feasibility of some basic ideas for the optical system, a number of concepts were tested on an optical bench. The more promising components were incorporated into a preliminary laboratory model which was subsequently tested in firings with a 37mm Gun. A schematic diagram of the final optical system is shown in Figure 1.

The optical system has a carbon arc light source and a condensing lens which focuses the light on a pinhole located at the focal point of the off-axis paraboloidal mirror. A rotating perforated disc, just forward of the pinhole, interrupts the light to establish time marks on the trace and to furnish orientation points for correlating the various records. The mirror, set at 45° to the optical axis, has a half-silvered elliptical section at the center to pass the light from the pinhole to the paraboloidal mirror. From the off-axis paraboloidal mirror, the parallel light is directed to a front-surfaced, plane glass mirror set up forward of the muzzle to reflect the light down the gun tube. Front-surfaced, plane glass mirrors bonded to the front of the projectile and to steel brackets welded to the gun tube reflect the light back over the same optical path to the front surface of the mirror set at 45° to the optical axis. At this point the returning light is reflected to the outer surface of a rotating drum. A shutter, placed immediately in front of the drum, is used to control the exposure time of the film attached to the outer surface of the drum. Some details of the components of the system are given below:

a. Light Source

A number of different light sources were tried in the optical system including a mercury arc, zirconium arc, carbon arc and

a xenon high-speed flashing lamp. Of these light sources, the carbon arc lamp provided the best traces because of its high intrinsic brilliance and its emission in the blue region of the spectrum.

b. Condensing Lens

A Wollensak-Dumont CRO Lens, 75mm, f:1.9, was available and adequate for the condensing lens.

c. Pinhole

The pinhole was made in a thin piece of phosphor-bronze shim stock and checked with an optical comparator to insure that the hole was circular. To determine the minimum size pinhole that could be used, an investigation was conducted on an optical bench with a variety of different diameter pinholes. The results of this investigation showed that the smallest diameter pinhole, free of diffraction effects, was one with a diameter of 0.011 inch. It is important to use a small pinhole diameter because the width of the recorded traces is fixed by the diameter of the light source and the quality of the optical components.

d. Light Interrupter

The light interrupter consists of a disc with a series of equally spaced, small diameter holes drilled near the outer edge. It is turned by a constant speed motor. To minimize the cross sectional area of the cone of light cut by the interrupter and thus give sharp, well-defined breaks in the trace, the disc is located close to the pinhole.

e. Off-Axis Paraboloidal Mirror

An off-axis paraboloidal mirror with a diameter of 10 inches and a focal length of 47.9 inches is the main element of the optical system. Deviations from the mathematical figure (surface) are less than one-eighth of a wave length of the sodium D line.

A lens was first considered because it would have simplified the layout of the optical system. However, a comparable lens, corrected for chromatic aberration, cost about four times more than the off-axis paraboloidal mirror. We had to consider that the system would be exposed to muzzle blast and the lens might be broken.

f. Plane Mirror

The plane mirror which is placed several feet forward of the muzzle is a front-surfaced, first quality, 1/4-inch plate glass mirror, 10 x 10 inches square. Deviations in the flatness of the mirror are less than eight wave lengths over a distance of one

inch. The mirror must be replaced after each round because the projectile hits it.

g. Mirrors on the Projectile and Gun Tube

Front-surfaced, plane glass mirrors of either 1-1/8 inches or 2 inches in diameter are bonded to the projectiles and the brackets on the gun tube. The quality and thickness of the glass mirrors is the same as that of the plane mirrors placed forward of the muzzle.

h. Half-Silvered Mirror

The mirror consists of Borosilicate crown No. 2 glass, 8 x 6 x 1/2 inches, with deviations in flatness of less than two wavelengths. The front surface is fully aluminized and overcoated with silicon monoxide except for the elliptical area in the center which is coated with titanium dioxide. Approximately 50% of the light which strikes the elliptical area is transmitted and 50% is reflected. By designing the mirror in this way the maximum amount of light is reflected back to the film.

i. Shutter

The shutter, located on the housing for the rotating drum, has a 5-inch diameter aperture with three leaves actuated by a solenoid. Approximately 30 ms are required to fully open and fully close the shutter leaves. The operation of the shutter is controlled by an electronic sequence timer.

j. Rotating Drum

The rotating aluminum drum is 10 inches in diameter and 6 inches wide. The drum is driven by a motor and gear train from an electric drill. Power is supplied through a Variac (voltage control) to change the speed of the drum. The drum speed can be varied from 300 to 2500 rpm (film speed 160-1300 inches per sec) depending on the duration of the phenomena to be recorded.

k. Recording Film

Kodak Linagraph Shellburst Pan, Gray Base film is used to record the trace of the light spot. The film is purchased in strips that are attached to the surface of the drum with cellophane tape. This film was selected because of its high contrast, high writing speed and blue-sensitivity. Color sensitivity is important because blues are dominant in the carbon arc source and the muzzle flash, which tends to fog the film, includes reds and yellows.

The field model of the optical system, shown in Figure 2, was mounted on a heavy aluminum plate. A housing was added to keep

out extraneous light and to protect the components from muzzle blast, dust and particles of the mirror broken by the projectile. The three adjustable legs are for aligning the optical system in the field.

When the field model of the optical system was delivered to the laboratory there was a great deal of curiosity and joking among our colleagues. As a result, the coffin was named "ODD SAM"; the letters refer to Optical Device for Determining Small Angular Measurements.

The optical components were carefully aligned and checked to optimize the image quality over the entire recording plane. Next, the system was calibrated in both the vertical and horizontal directions. A graph of the calibration is given in Figure 3. The calibration shows that the system is extremely linear with a sensitivity of 0.09398 inch per mil. The sensitivity or angular deflection can also be calculated from the usual equation for an optical lever:

$$\frac{D}{\alpha} = \frac{2\ell\pi}{3200}, \quad \text{where}$$

D = deflection of the trace on the photographic record, inches.

α = angular deflection of the projectile or gun tube, mils.

ℓ = focal length of the off-axis paraboloidal mirror, inches.

$\pi/3200$ = conversion factor for changing mils to radians.

The maximum angular measurement is fixed by the radius of the paraboloidal mirror and the distance from the paraboloidal mirror to the mirror on the projectile. As the projectile travels down the bore the distance is decreased and the maximum angular measurements for the projectile are increased.

Quarter-inch, plate glass, front-surfaced mirrors are bonded to projectiles and the brackets on the gun tube with epoxy resin. Of the various adhesives that have been tested, the epoxy is best because it is strong and cures without shrinking and warping the mirrors. Images formed by a warped mirror can readily be detected since the spot is large and diffuse.

To mount mirrors at various stations along the gun tube, small, steel, triangular-shaped brackets are fabricated from bar stock and welded to the gun tube as illustrated in Figure 1. A circular, recessed portion is milled into the front of the bracket and three fine adjustment screws are set in from the rear for alignment. Epoxy resin is used to bond the small circular mirrors to the brackets.

Rubber bands are used to hold the mirrors against the ends of the adjustment screws while the cement hardens. This alignment is carried out with the gun and optical system set up in the field.

MEASUREMENTS OF THE GUN TUBE AND PROJECTILES

Measurements are made with a stargage of the diameter of the bore at fixed increments of displacement over the total length of the gun tube. These values are correlated with measurements of the projectile to determine the clearances and the maximum yaw which can take place in the bore. Previous studies indicate that yaw introduced in the bore tends to grow appreciably after emergence from the muzzle.

In accuracy studies it is desirable to minimize the transverse motions of the gun tube. This can best be accomplished by weighing and statically balancing the recoiling parts so that the center of gravity is on the center line of the bore. Under such conditions the force due to the powder pressure acts directly through the center of gravity, and transverse motion is practically eliminated. If the position of the muzzle does not change, the flight of the projectile should not be affected by transverse velocity components induced by motion of the tube during launch and by unsymmetrical gas flow around the projectile in the blast regime.

A number of physical measurements are made on the projectiles fired in the tests. These include: O.D. of the bourrelet, O.D. of the rotating band, overall length, distance from the center of the rotating band to the forward edge of the bourrelet, longitudinal position of the center of gravity, weight, static unbalance, longitudinal moment of inertia, and transverse moment of inertia. By systematic variations of these physical parameters, it is expected that their effect on accuracy can be established.

TEST PROCEDURE

The gun is set up with its trunnions horizontal and the tube accurately layed or aimed at a target several hundred feet down range with a muzzle sight. The optical system is set up so that its axis coincides with the axis of the tube at the muzzle, as shown in Figure 4. Preliminary alignment of the system is done in daylight; the final adjustments are carried out in darkness, just before firing. The tests are conducted either in daylight with a black plastic shroud built over the gun and optical system or at night. Parts of the plastic shroud must be replaced after each round because of the muzzle blast.

The projectile is loaded after the optical system is aligned. Extreme care is taken to be sure that the rotating band is properly seated and that the radius vector scribed on the base of the projectile is properly oriented. The vector marks the radial location of the center of gravity in a statically unbalanced projectile.

The radial position of the center of gravity when the projectile emerges can be calculated from the twist and the length of the rifling. To measure the angular orientation of the radius vector of the projectile in the chamber, the special optical device, shown in Figure 5, was developed. It consists of a cartridge case with a lamp mounted on the inside of the case and a level, a telescope with cross-hairs, and a protractor-eyepiece set into the base of the case. After the measurement has been made, a shortened cartridge case with the propellant and an electric primer is loaded into the chamber.

The electric primer (firing) is initiated through a micro-switch operated by the shutter on the optical system when it is fully open. Subsequent events and operation of the auxiliary instrumentation are controlled by a sequence timer composed of relays actuated by electronic counters. The traces on the optical record disappear when the projectile shatters the mirror in front of the muzzle. Immediately thereafter, the sequence timer "turns off" all the instrumentation.

A number of auxiliary measurements are made in addition to the optical measurements of the angular motions of the projectile and the gun tube. These include the following:

a. Chamber pressure vs time[5]

Strain-resistance pressure gages are mounted in the base of the cartridge case. A complete pressure-time history for each round is obtained with a cathode-ray oscillograph and its auxiliary apparatus. These records are the forcing function for the motion of the projectile and the gun.

b. Displacement of the projectile vs time[6]

Microwave interferometer instrumentation is used to measure the position of the projectile relative to a fixed point.

c. Displacement of the gun tube vs time

A displacement-time recorder is set up with a reflector attached to the recoiling parts. As the gun recoils, the displacement of the reflector is recorded with respect to time. By adding the displacement of the gun tube to the displacement of the projectile measured with the microwave interferometer, one can determine the position of the projectile in the bore at any instant in time.

d. Fiducial marks

Fiducial marks are placed on each of the auxiliary records when the electric primer is initiated and when the rotating band or front of the projectile emerges from the muzzle. The firing voltage is used to trigger one of the fiducial circuits and the other

is triggered by the projectile as it contacts several insulated metal probes located at the muzzle.

Obturation of the projectile in the bore has been one of the most difficult problems since small quantities of powder gas leaking by the projectile obscure the light. In tests conducted thus far, it has been found that obturation generally breaks down during the initial sealing period or when the projectile is within a few feet of the muzzle. As the projectile approaches the muzzle it may be exposed to high-frequency vibrations in the barrel which may break the seal. To minimize this problem, rubber base obturators or obturators at the rotating band have been used. Band obturators of rubber or fiber are preferred since they provide less constraint to the angular motion of the projectile.

Excessive muzzle flash has also been a problem with some propellants. To reduce the flash to an acceptable level, potassium sulfate may be added to the propellant, or the kind, web size, and the weight of propellant may be altered.

When the rotating band leaves the muzzle, the expanding gas and smoke surround the projectile until the gas is slowed by the air and the projectile passes through it. Since the smoke obscures the mirror, the trace is often lost during this time.

MEASUREMENTS AND REDUCTION OF DATA

A typical record obtained with the optical system is shown in Figure 6. The record consists of three separate traces: the upper one is the angular motion of the muzzle; the middle one is the angular motion of the projectile and the bottom one is a fixed reference trace from which all measurements are made. The small mirror used for the fixed reference trace is attached to a rigid support in the optical path somewhere between the off-axis paraboloidal mirror and the muzzle of the gun. The breaks in the traces do not provide an accurate time scale. To obtain this, a miniature photocell in the optical system monitors the interrupted light. Its output signal is recorded by a cathode-ray oscillograph simultaneously with that from a crystal-controlled time standard so that the distance between the breaks can be converted to true time. Long breaks and long traces on the records make it easier to orient them with the firing and muzzle contact fiducials on the cathode-ray oscillograph record.

Records made with the optical system are not restricted to three traces as shown in Figure 6. The motion at any number of stations along the gun tube can be recorded simultaneously with that of the projectile. Each mirror bracket must be welded to the gun tube so that it falls within the circular field of incident light and does not block the light to any of the other stations.

The coordinate system shown in Figure 7 is used in the measurement and analysis of the records. In this figure:

X = horizontal axis
Y = vertical axis
Z = axis of the bore at the muzzle
δ = the angle between the axis of the projectile and the axis of the bore
ϕ = the orientation of the plane containing the axis of the projectile and the axis of the bore.

Records from the optical system are placed in a Universal Telereader to measure the x and y components of each trace at the leading or the trailing edge of each break. To illustrate the procedure by which each component is read, an example is shown in Figure 8. All measurements are made with respect to corresponding points of time on the fixed reference trace. Prior to the test, the x and y components of the angle between the axis of the bore at the muzzle and the fixed reference trace are measured by placing a muzzle bore sight in the tube with a mirror aligned perpendicular to the axis of the bore.

The measurements from the Universal Telereader are tabulated by an IBM Electric Typewriter and also on IBM cards by a Printing Card Punch. To convert the raw data to actual time and angle the calculations are programmed for BRLESC, the BRL high-speed computer. The output from the BRLESC is printed on teletype paper and also punched on IBM cards. The card output provides data points for the automatic plotter.

A typical plot of the results is shown in Figure 9. Note the similarity to the exterior ballisticians' plots of yaw. Other plots of the results, such as δ, δ_x, δ_y, and ϕ versus time, can be made to study their variations.

SUMMARY

This apparatus now makes it possible to observe the very small angular motions of a projectile in the gun tube. An analysis of this motion, combined with that of the other experimental results, will provide better insight as to the forces and constraints acting on the projectile. By correlating these experimental results with theory, it is hoped that design criteria and tolerances can be established to improve the accuracy of fire.

ACKNOWLEDGMENTS

The author wishes to express his appreciation to Mr. H. P. Gay for his suggestions and assistance throughout the program, to Mr. J. R. Patchell who conducted many of the initial laboratory studies of the optical components, to Mr. R. D. Kirkendall who conducted a number of field tests with the optical system, and to Mrs. E. Wineholt who carried out most of the data reduction.

REFERENCES

1. Cranz, C. Cranz's Textbook of Ballistics, III (Part 1): Chap. 6, Sec. 1, National Defense Research Committee: Translated by C.C. Bramble, et al, 2d ed, 1927.
2. Uffelmann, F.L. The Initial Disturbances Affecting the Direction of the Trajectory of a Shot Fired from a High-velocity Gun. Proceedings of the Royal Society: No. 1350, Vol 272, 19 Mar 63.
3. Gay, H.P. and Elder, A.S. The Lateral Motion of a Tank Gun and its Effect on the Accuracy of Fire. Aberdeen Proving Ground: BRL R-1070, Mar 59.
4. Thill, R. Sur le Comportement Cinématique et Mécanique des Bouches à Feu au Départ du Projectile (Étude Expérimentale). Mémorial de L'Artillerie Francaise: Tome 37, 1er fascicule, 1963.
5. Gay, H.P. The Evolution of Gages for Measuring Pressures in Guns and Rockets at the Ballistic Research Laboratories. Aberdeen Proving Ground: BRL MR-1402, May 62.
6. Vest, D.C., et al. Ballistic Studies with a Microwave Interferometer. Aberdeen Proving Ground: Part I. BRL R-968, Sep 55. Part II. BRL R-1006, Feb 57.

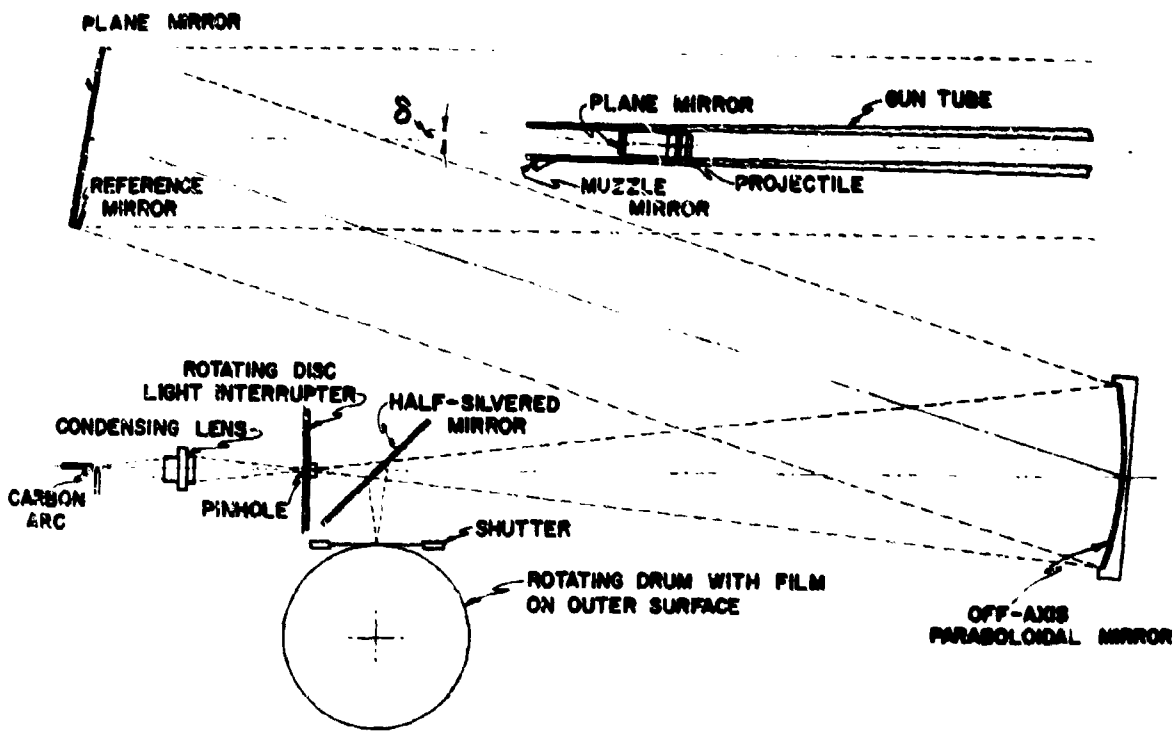

FIG. 1 OPTICAL SYSTEM

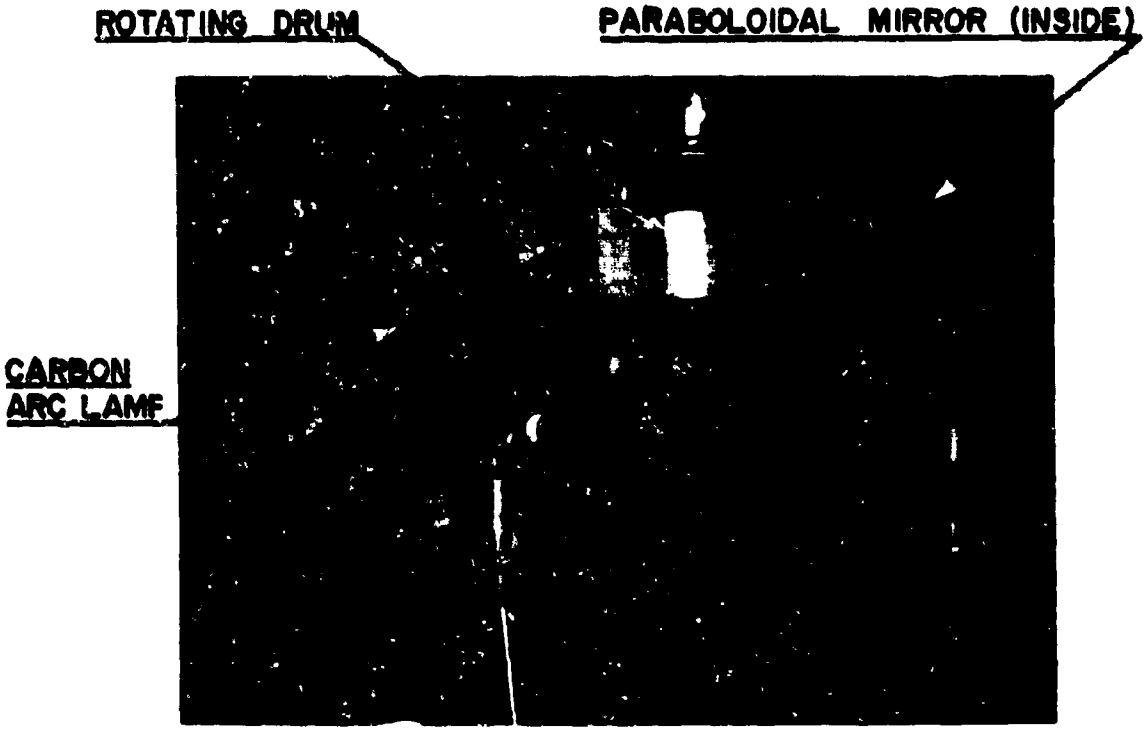

FIGURE 2 - FIELD MODEL OF OPTICAL SYSTEM

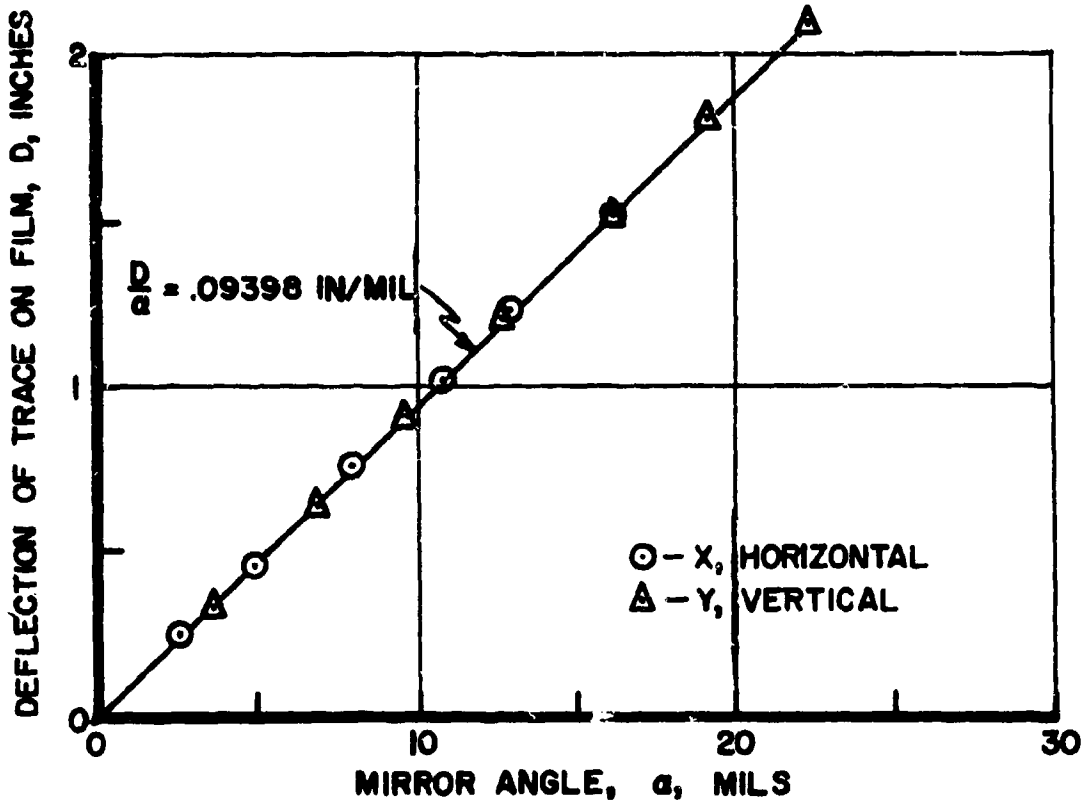

FIGURE 3 - CALIBRATION OF OPTICAL SYSTEM

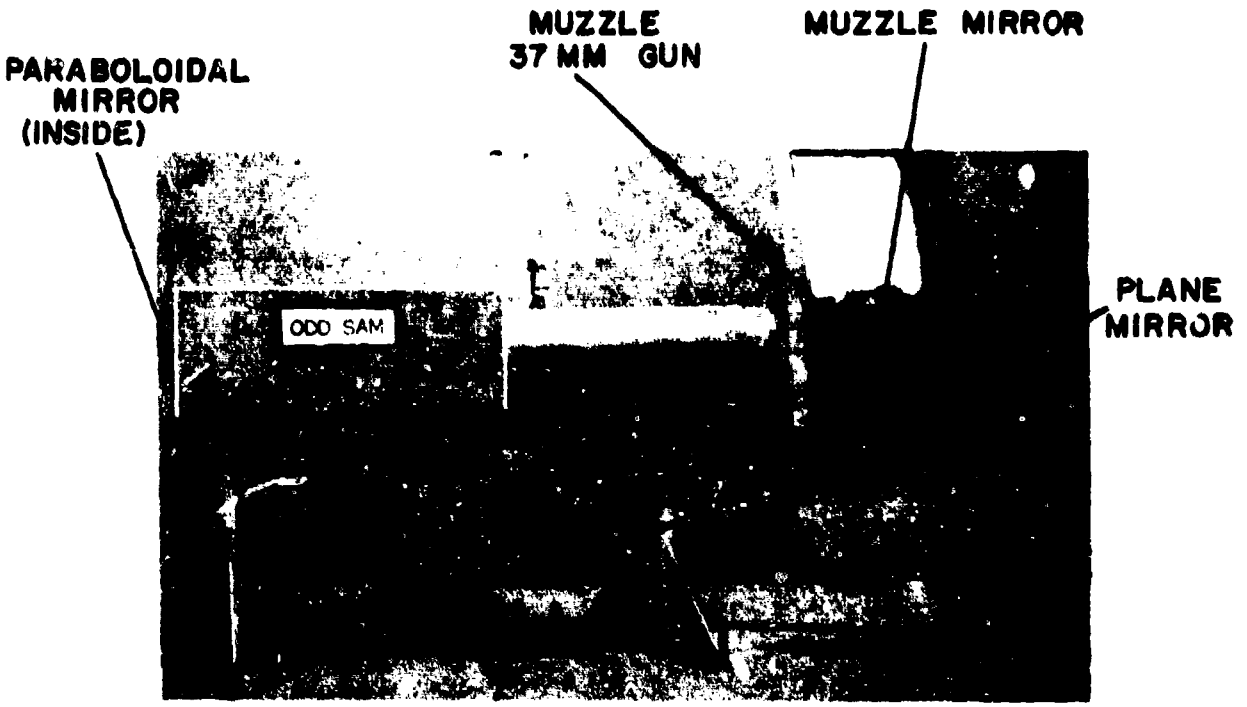

FIGURE 4-OPTICAL SYSTEM SET UP IN THE FIELD

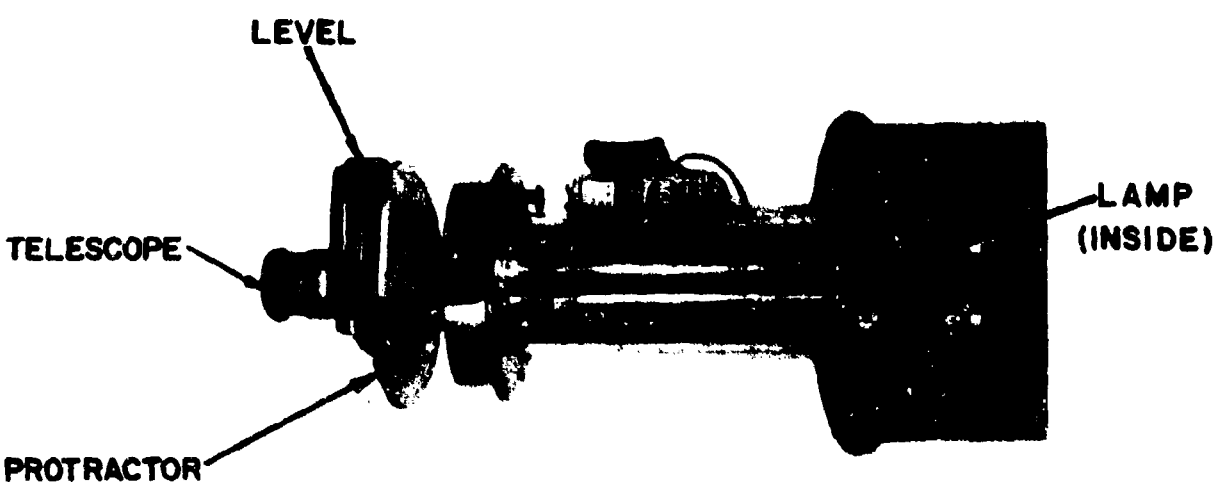

FIGURE 5-DEVICE FOR MEASURING THE
ORIENTATION ANGLE OF THE RADIUS VECTOR

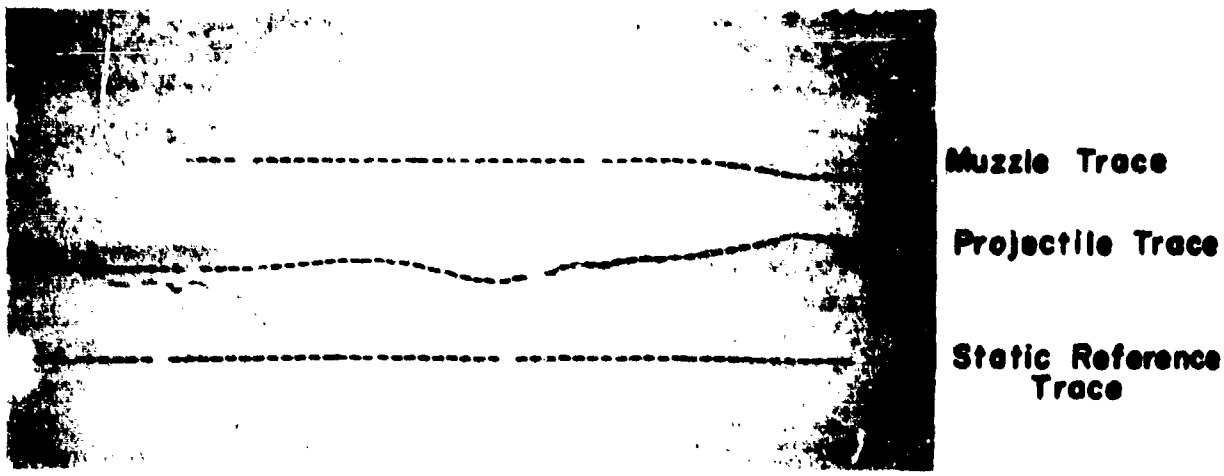

FIGURE 6 - TYPICAL RECORD

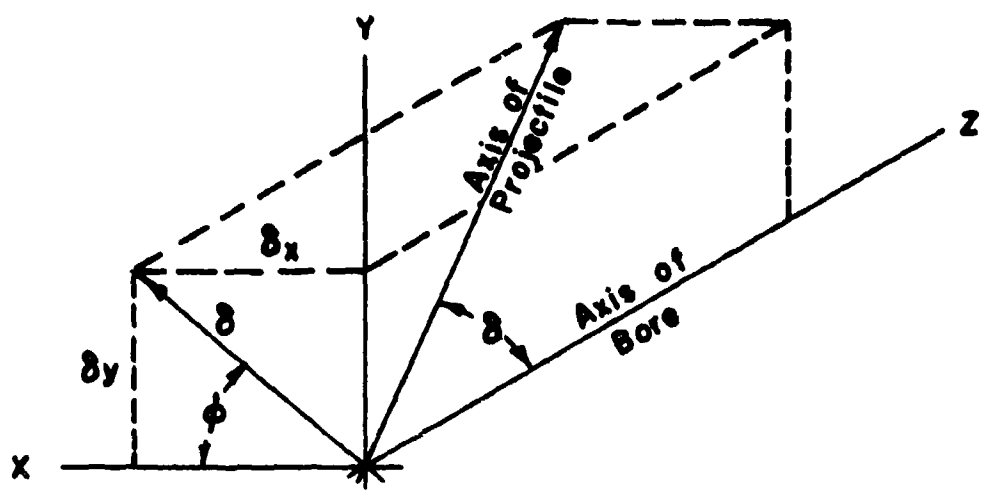

FIGURE 7 - COORDINATE SYSTEM

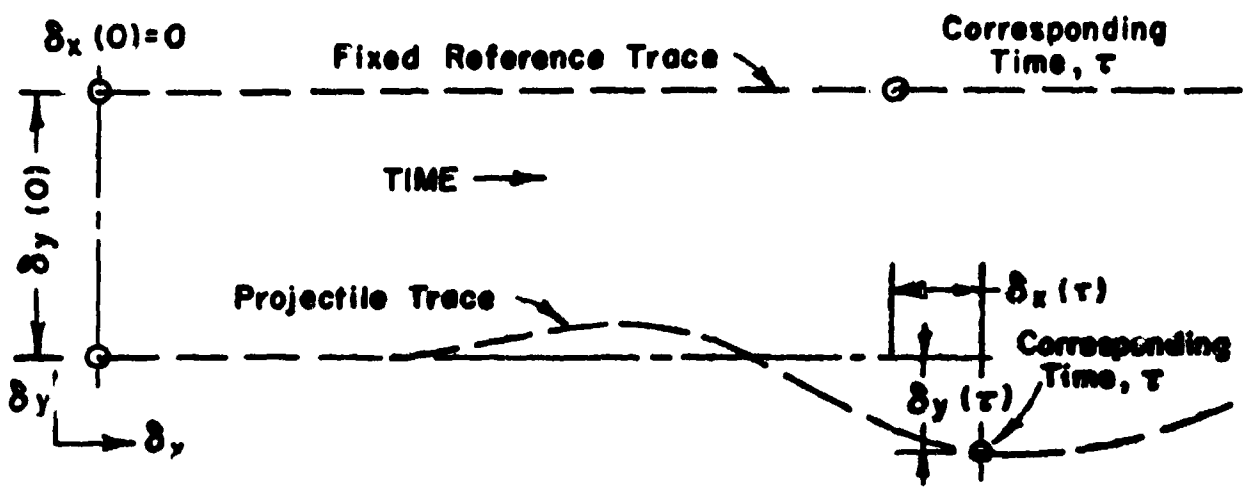

FIGURE 8 - PROCEDURE FOR READING RECORD

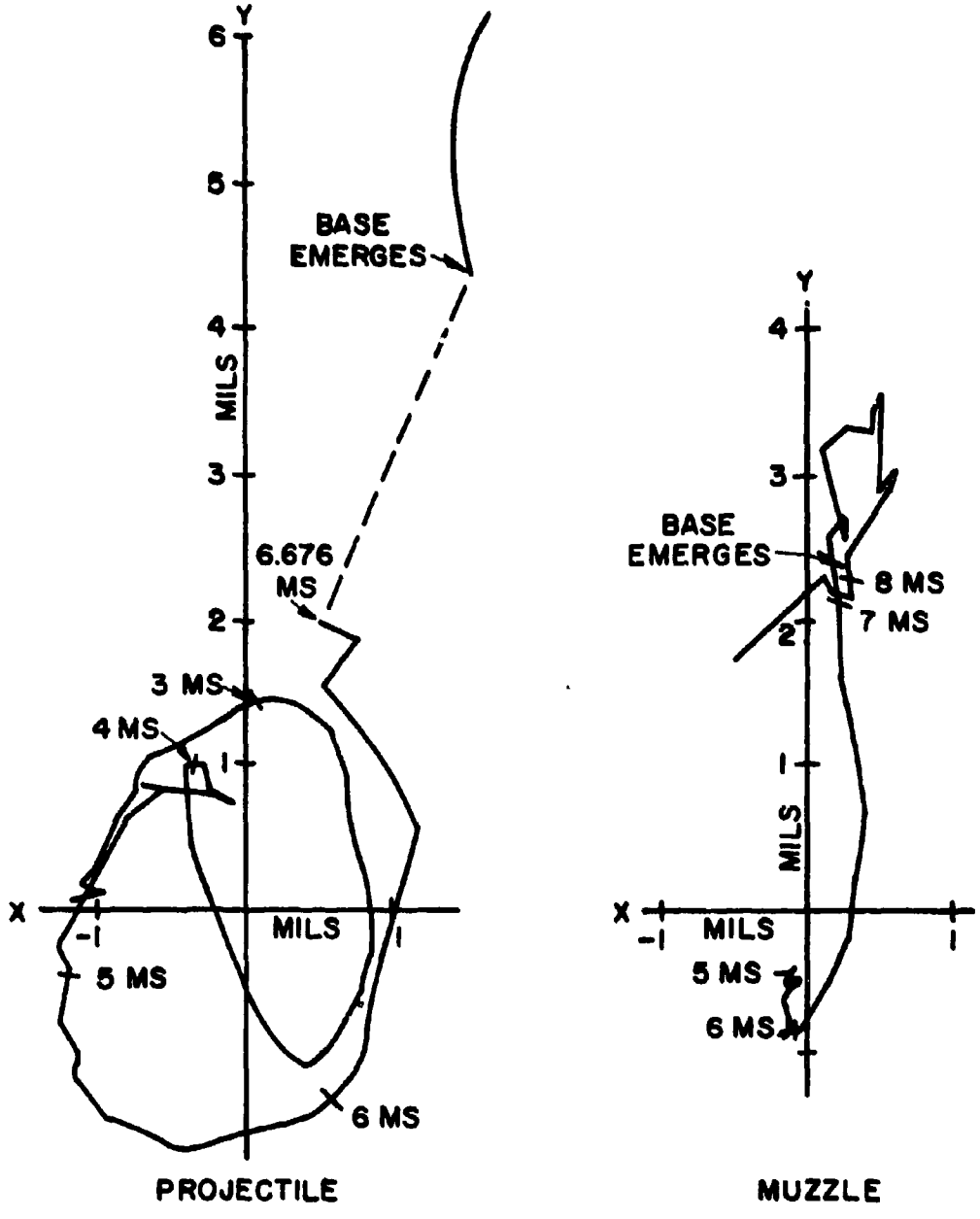

FIGURE 9 – PLOT OF ANGULAR MOTIONS

RADIATION BIODOSIMETRY AND SCREENING FOR RADIOPROTECTIVE COMPOUNDS

HILLEL S. LEVINSON and ESTHER B. GARBER
U. S. ARMY NATICK LABORATORIES
NATICK, MASSACHUSETTS

INTRODUCTION

This work has its origins in studies on bacterial spores in our laboratories (5) in which it was found that dipicolinic acid, which is usually firmly bound within the spores of Bacillus megaterium, is released from the irradiated spore. When dry spores were irradiated under the electron beam of a 2,000,000 electron volt Van de Graaff accelerator, there was a linear relationship between dipicolinic acid release and dose in the range from 8×10^5 to 1.6×10^6 rads. Spores of Clostridium sporogenes (Putrefactive Anaerobe 3679) irradiated under the same conditions, released no dipicolinic acid until the irradiation dose reached ca 2×10^6 rads and the amount of dipicolinic acid released increased with dose until ca 7.5×10^6 rads.

The present experiments were undertaken to explore the possibility that the release of intracellular substances from living cells might form the basis for a useful system of dosimetry. We felt that a "biodosimeter" in which there was a direct relationship between dose of radiation and amount of substance released would be particularly significant in experiments involving irradiation of microorganisms. Biodosimetry might be superior to chemical dosimetry for application to radiation sterilization problems because factors, such as temperature, might affect the dosimeter organism and the microorganisms under investigation similarly.

Further, we postulated that if radioprotective chemicals also protected microorganisms from loss of these intracellular substances, the method might be adaptable to the screening of radio-

protective compounds. Such a screening procedure would have obvious time and cost advantages over the usual methods involving use of laboratory animals.

MATERIALS AND METHODS

Organism - Since one object of this investigation was to devise a readily available system for radiation biodosimetry, a test organism which could be procured at a reasonable cost and in large quantity, was required. O'Brien (9), Meissel (6), Swenson (11), and Spoerl et al. (10) have reported that irradiated yeast cells undergo alterations in permeability accompanied by release of inorganic phosphorus into the suspending medium, and that irradiation effects the depolymerization of highly polymeric phosphorus containing compounds. In these exploratory investigations we have used suspensions of bakers' yeast, Saccharomyces cerevisiae, as our test organism. This organism is produced under remarkably uniform conditions and is easily and inexpensively procured commercially - we purchase our supply from a local bakery at 35 cents per pound.

On the day before irradiation or heating, approximately 50 g of fresh yeast were washed 3 times by suspending in H_2O and centrifuging. The washed yeast was resuspended in H_2O and the concentration of yeast was adjusted so that 1.5 ml diluted to 100 ml gave a reading of 145 in the Klett-Summerson photoelectric colorimeter (560 mμ). Approximately 400 ml of this double strength yeast suspension (Y_o), containing ca 30 mg of yeast (dry weight) per ml, or ca 10^9 cells per ml, were obtained from 50 g of yeast. For heating or irradiation, Y_o was mixed with an equal volume of water or of buffer.

Irradiation - Yeast suspensions (usually 15 mg of yeast per ml) were pipetted into test tubes[1] (17 x 100 mm), 7 ml of suspension per test tube. These test tubes, in wooden racks on a conveyor, were irradiated in the 1.0 megacurie Co^{60} source at the Radiation Facility, U. S. Army Natick Laboratories. For 100,000 rads, the conveyor was run through the source at a rate of approximately 3.8 feet per min.

[1] Disposable "Hi-Temp" polyethylene test tubes produced by Falcon Plastics, Los Angeles, California.

Ferrous-copper dosimeters were included with each run. After each pass through the source (generally 100,000 or 200,000 rads per pass), the test tubes containing yeast suspension were shaken and inverted to keep the yeast in uniform suspension.

Heating - In some experiments, where heating was used as a model system, yeast suspensions in plastic test tubes were heated at 60 C in a thermostatically controlled water bath for varying periods of time.

Analysis - After irradiation or heating, the yeast suspensions were centriguged, the supernatant solutions were collected and analyzed for inorganic phosphate (P) and for amino nitrogen (NH_2-N). P was determined by the method of Fiske and SubbaRow (2), using the Klett-Summerson colorimeter (660 mμ). After high doses of radiation, or after prolonged heating, addition to supernatant of ammonium molybdate - H_2SO_4 (in the Fiske-SubbaRow method) yielded a turbid solution which interfered with the test. In such cases, the supernatant was treated with trichloroacetic acid (TCA) to give a concentration of 8% TCA, centrifuged, and the TCA-soluble material tested. NH_2-N was estimated by ninhydrin reactivity in the method of Moore and Stein (8) with DL-alanine as the standard.

Other evidence for destruction of the selective permeability of cell membranes and for loss of intracellular material from yeast cells was also explored. For example, the turbidity of irradiated yeast suspensions (diluted 1:50), estimated by light transmittance in the Klett instrument(560 mμ), decreased with irradiation, but the magnitude of the change ($Klett_{560}$ of suspensions irradiated at 2×10^6 rads was 85% of $Klett_{560}$ of unirradiated suspensions) was insufficient for use in routine dosimetry. It was also found that substances with absorption maxima at 260 mμ (probably nucleic acid derivatives) were exuded from irradiated yeast. The absorbance (OD_{260}, Beckman Model DU Spectrophotometer) of supernatants increased from 0.07 for supernatants of unirradiated yeast suspensions to ca 10.0 (OD x dilution) for supernatants of suspensions irradiated at 2×10^6 rads. Work on these systems (particularly OD measurement at 260 mμ) is continuing, and we shall not discuss them further in this paper.

Survival - Appropriately diluted suspensions of yeast were plated on Mycophil Agar, pH 4.7 (Baltimore Biological Laboratory).

The agar plates were incubated at 28 C for 6 days and the number of colonies was counted. Percentage survival was calculated by comparison with similarly plated unirradiated yeast suspensions.

RESULTS AND DISCUSSION

Heating Experiments - In some of our earlier experiments, heating was used as a model system, i.e., to simulate changes that might occur on irradiation.

The choice of a suitable index for the release of intracellular material was one of the first problems to arise. Phosphorus and nitrogen-containing compounds are among the most abundant in a cell. We, therefore, tested the supernatant solutions from heated yeast for the presence of these easily detectable substances, and found that heating increased the release, from yeast cells, of inorganic P and of NH_2-N. Several factors affect the heat-induced release of these substances:

(1) Suspending fluid - The sensitivity of yeast cells to heat-induced loss of intracellular substances depends, in some measure, on the suspending fluid. Cells suspended in 2-amino-2-hydroxymethyl-1,3-propanediol [= tris (hydroxymethyl) aminomethane = Tris buffer[2]] or in water lost more P and NH_2-N than cells suspended in sodium cacodylate (dimethylarsinate) buffer (table 1). It is apparently necessary to consider the suspending fluid as a factor in investigation of the radiation-induced release of intracellular substances.

It is of some interest that 99.99% of the yeast cells in a water or Tris suspension were killed after 10 min exposure to 60 C. Practically all the release of inorganic P and of NH_2-N took place after the cells had been killed (cf table 1). The release followed soon after death in water and Tris suspension, but release of these substances from yeast suspended in cacodylate was delayed. This delay is not reflected in survival curves, the cells being killed as in water suspension. That is, although cacodylate protects to some

[2] Unless otherwise indicated, all buffers, neutralized with HCl or NaOH, were used at 0.05 M.

degree against heat-induced loss of intracellular material, it does not protect yeast against thermal destruction of the colony-forming capacity.

The release, into the suspending medium, of substances previously bound within the cell, may be due either to destruction of the semi-permeable character of the cell membrane, or to depolymerization of high molecular weight intracellularly bound substances, or to a combination of these effects. Other possibilities include alteration of the permeability of internal structures (vacuoles, mitochondria, etc.) and release of surface-bound materials. It may even be possible that release of P and of NH_2-N have enzymatic bases - the enzymes being active even though the cell's ability to divide and form colonies has been destroyed (5). Although in this work we were not primarily concerned with the mechanism of the release phenomenon, it was important to know whether release of P and of NH_2-N were both measures of the same basic mechanism. Percentage of total P released was a linear function of the percentage of total NH_2-N released after the same period of heating (Fig. 1), where total P and NH_2-N were taken as the amounts of these substances released on mechanical disruption of the cells in the Mickle Tissue Disintegrator (7). This suggested that the same fundamental mechanism operates in the release of both of these substances, and that they might be used interchangeably as indices for release of intracellular substance. Since the P assay was the more convenient, this was generally used in our radiation experiments.

(2) Protective compounds - A number of chemical compounds have been reported to be active in the protection of microorganisms from the effects of radiation. Among these, sulfhydryl compounds (4) and ascorbic acid (3) figure prominently. Since we were considering use of the release system for screening radioprotective compounds, we thought that data on possible protection against heat-induced release might prove valuable. Yeast cells were heated in Tris buffer, 0.05 M, pH 7, or in Tris containing either 0.05 M ascorbic acid or 0.05 M sodium thioglycolate (table 2). There was a suggestion that ascorbic acid (but not thioglycolate) inhibited the release of inorganic phosphate and of NH_2-N from heated yeast cells. As will be seen, both additives were effective inhibitors of the <u>radiation</u>-induced release of P.

(3) Concentration of yeast - The yeast concentration in

TABLE 1

Effect of suspending medium on heat-released yeast phosphate and amino-nitrogen

Time at 60 C	P or N released from yeast cells suspended in						
	H_2O		Tris		Cacodylate		PO_4
	P	N	P	N	P	N	N
min	µg/ml	mM	µg/ml	mM	µg/ml	mM	mM
5	0.7	0.3	3.2	0.85	1.5	0.4	0.62
10	1.5	0.63	5.3	0.87	2.75	0.8	1.1
15	4.0	0.98	15.2	3.0	5.0	1.1	1.8
20	12.8	2.4	31.0	7.1	6.9	1.4	2.5
30	34.8	6.2	39.9	8.3	15.4	2.7	4.2
45	42.0	7.15	42.9	8.8	25.0	5.7	5.7
60	43.2	7.2	43.1	8.9	43.0	6.9	8.1

Yeast cells, in H_2O or in buffer suspension, heated at 60 C. Supernatants tested for P and N. Each result is average of 3 experiments.

TABLE 2

Effect of ascorbic acid and of sodium thioglycolate on heat-induced release of yeast phosphate and amino-nitrogen

Time at 60 C	Concentration of P or amino-N released					
	Cells suspended in					
	Tris		Tris + Ascorbic acid		Tris + Sodium thioglycolate	
	P	N	P	N	P	N
min	µg/ml	mM	µg/ml	mM	µg/ml	mM
10	5.5	1.4	2.0	0.3	3.0	1.1
20	29.0	7.7	10.0	1.6	21.0	5.9
30	39.5	9.3	32.0	6.8	35.0	8.9

Yeast cells, suspended in Tris or in Tris and additive (0.05 M), were heated at 60 C. Supernatants tested for P and N.

heated suspensions markedly affected the amount of NH_2-N released. Although the concentration of NH_2-N was, of course, greater in supernatant solutions of suspensions containing 15 mg of yeast per ml than in supernatants from suspensions containing only 1 mg of yeast per ml, the NH_2-N release per gram of yeast was greater in the more dilute suspensions (Fig. 2).

Radiation experiments

(1) Suspending fluid - The higher the radiation dose, the greater the amount of intracellular material released from yeast. As with heated suspensions, the suspending fluid was important in determining the amount of P and the amount of NH_2-N released. For example, yeast cells released more inorganic P when irradiated in water suspension than in Tris suspension (Fig. 3). In either case, however, it should be noted that the amount of P released was a function of dose over an appreciable portion of the range of doses used. Aqueous suspensions of yeast cells released approximately 5 µg of P per ml of supernatant solution when irradiated with 300,000 rads; but approximately 700,000 rads were required to effect the same release from yeast suspended in 0.05 M Tris. The radiation requirement for release of intracellular P increased as the Tris concentration was increased from 0.01 to 0.5 M. However, survival (Fig. 4) was virtually identical whether water or Tris suspensions were irradiated.

(2) Protective compounds - A number of chemical compounds has been reported to be radioprotective agents for mammals and for microorganisms. These compounds, in a simple, unsophisticated view, may be said to function as acceptors of free radicals, by modification of metabolic processes, or by creation of anaerobic conditions with resulting interference with the oxygen effect (1). Sulfhydryl compounds, especially in the configuration:

$$HS-(CH_2)_x-N\begin{matrix}R_1\\R_2\end{matrix}$$

are particularly good radioprotective agents, and mercaptoethanolamine

(MEA), where x = 2, and the amino group is unsubstituted, has been widely used in studies on radioprotection. Sulfur compounds related to S-β-aminoethylisouronium Br HBr (AET)

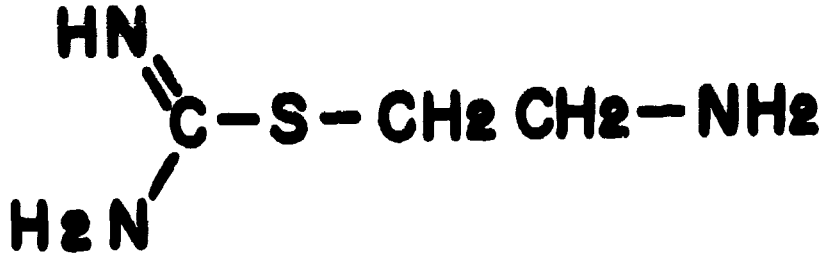

AET

have been reported to protect mammals from irradiation, and a protective effect of ascorbic acid on various bacteria has also been noted (3). As previously stated, there was no demonstrable difference in radiation survival of yeast suspended in Tris or in water (Fig. 4),nor did the addition of 0.05 M ascorbate alter survival. Sodium thioglycolate (0.05 M) and MEA (0.1 M) were also ineffective in increasing the radiation survival of the yeast. However, all of these compounds did inhibit the release of P from irradiated yeast (Fig. 5, Fig. 6). Thus far, of the reportedly radioprotective compounds which we have tested - ascorbate, MEA, thioglycolate, thiourea, and cysteine - all inhibited the radiation-induced release of P from either aqueous or Tris suspensions of yeast cells. A number of other additives - sodium chloride, sodium acetate, sodium caseinate - were ineffective in inhibiting the radiation-induced release of P. The effectiveness of thioglycolate in inhibiting the radiation-induced release of yeast P contrasts with its ineffectiveness in inhibiting the heat-induced release, suggesting different mechanisms for heat and for radiation - induced release.

Although protection from release of internal substances apparently was not correlated with radiation kill of yeast, we feel that the correlation of release with protection of mammals warrants further investigation. In spite of the obscurity of the mechanism of the P release, the system may prove useful in screening radioprotective compounds. While loss of the ability of a single-celled organism to divide and to form colonies is often equated with loss of viability, such incapacity is not necessarily equivalent to death in higher forms. Indeed, extension of these studies might reasonably be expected to lead to elucidation of differences in mechanisms for radiation kill in microorganisms and in multicellular animals. Differences in effect of radioprotective compounds might well point the way for future studies.

(3) Other dosimeters - We have used Tris and sodium caco-

dylate (dimethylarsinate) in making yeast suspensions:

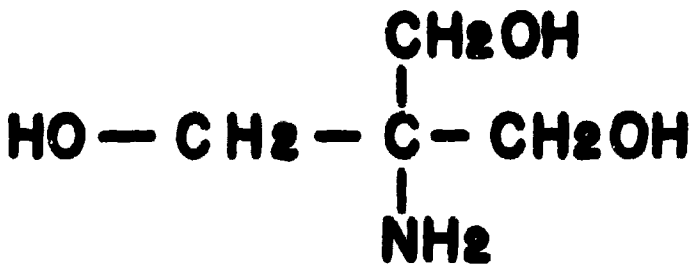

Tris

$(CH_3)_2AsOONa$ sodium cacodylate

We had planned, on the basis of heating experiments, to assay both P and amino-N released. However, when yeast was suspended in Tris or in sodium cacodylate, peculiar NH_2-N and P results were obtained. In investigation of these results, the buffers alone (without yeast) were irradiated. Irradiated Tris was assayed for NH_2-N and irradiated cacodylate was assayed for P.

There was a linear relationship between amount of ninydrin-reactive material produced from irradiated 0.05 M Tris and dose, up to at least 2×10^6 rads (Fig. 7). The usable range may extend to doses higher than 2×10^6 rads, but this has not yet been investigated.

Irradiation of sodium cacodylate yielded a substance which formed, in the Fiske-SubbaRow (2) test, an arsenomolybdate complex with a blue color similar to that of the phosphomolybdate complex formed with phosphate. The intensity of the molybdenum blue color (Fig. 8) bore a linear relation to dose up to a dose of at least 3×10^6 rads, and probably (not shown) up to 4×10^6 rads. We do not understand the mechanism of the conversion of sodium cacodylate to a compound reacting in the Fiske-SubbaRow test. However, sodium arsenate gives a positive test (forming an arsenomolybdate complex), and the mechanism may involve oxidation of the dimethylarsinate to arsenate with removal of methyl groups, perhaps through mediation of radiation-produced hydrogen peroxide. That the mechanism involves oxidation is given some credibility by the complete failure of sodium cacodylate to give a positive test when irradiated in the presence of a reducing agent such as ascorbic acid. The cacodylate system has promise as a broad range dosimeter, with perhaps its greatest potentiality where megarad doses are common, i.e., in food irradiation dosimetry. The method is rapid - we routinely run 50 cacodylate assays in less than 1 hr - and reproducible.

CONCLUSIONS

The release of intracellular materials (in particular, inorganic phosphate) from irradiated microorganisms forms the basis for using microorganisms in radiation dosimetry. We conceive of biodosimetry as being most useful where radiation inactivation of microorganisms is experimentally desirable (i.e., radiation preservation of foods), and as having its greatest advantage in the detection of changes in conditions of irradiation which might remain undetected in chemical dosimetry. We have suggested bakers' yeast, Saccharomyces cerevisiae, as one of the biodosimeter species because this organism, produced under uniform conditions at very low cost, is available commercially, and, on radiation, releases easily measurable phosphate into the suspending medium. Although with bakers' yeast, the range of the dosimeter is limited (ca 4×10^5 to 1.4×10^6 rads), the system can probably be extended by using other, more resistant, microorganisms, especially spores of bacteria.

Yeast suspensions were irradiated with several substances, reported as protecting microorganisms and mammals from the lethal effects of radiation. In every case (ascorbic acid, MEA, sodium thioglycolate, thiourea, and cysteine), these radioprotective substances inhibited release of yeast phosphate, although colony-forming capacity of yeast cells was unprotected. Our data offer promise for use of the system in a screening procedure for radioprotective compounds.

Tris and sodium cacodylate offer interesting possibilities as simple broad range dosimeters. Irradiated Tris buffer gives a positive ninhydrin test for amino-N, linear with dose from approximately 2×10^5 to 2×10^6 rads. Irradiated cacodylate gives a positive Fiske-SubbaRow test, with a linear response to approximately 4×10^6 rads.

LITERATURE CITED

(1) BRIDGES, B. A. and HORNE, T. 1959. The influence of environmental factors on the microbicidal effect of ionising radiations. J. Appl. Bacteriol., 22:96.

(2) FISKE, C. H. and SUBBAROW, Y. 1925. The colorimetric determination of phosphorus. J. Biol. Chem., 66:375.

(3) FULD, G. J., PROCTOR, B. E., and GOLDBLITH, S. A. 1957. Some microbiological aspects of radiation sterilization. Int. J. Appl. Radiation and Isotopes, 2:35.

(4) HOLLAENDER, A. and DOUDNEY, C. O. 1955. Studies on the mechanism of radiation protection and recovery with cysteamine and β-mercaptoethanol. In Radiobiology Symposium, Liege (Ed. Z. M. Bacq and P. Alexander). Butterworths, London, p. 112.

(5) LEVINSON, H. S. and HYATT, M. T. 1960. Some effects of heat and ionizing radiation on spores of Bacillus megaterium. J. Bacteriol. 80:441.

(6) MEISSEL, M. N. 1955. The biological effect of ionizing radiations on microorganisms. Proc. International Conference on the Peaceful Uses of Atomic Energy, 11:227.

(7) MICKLE, H. 1948. A tissue disintegrator. J. Roy. Microscop. Soc., 68:10.

(8) MOORE, S. and STEIN, W. H. 1948. Photometric ninhydrin method for use in the chromatography of amino acids. J. Biol. Chem., 176:367.

(9) O'BRIEN, R. T. 1958. Postirradiation release of phosphorus by yeast. Radiation Research, 9:162.

(10) SPOERL, E., NIEDZIELSKI, R. J., and BIERNAT, R. W. 1964. Permeability changes in yeast cells after x-irradiation and starvation. Radiation Research, 21:86.

(11) SWENSON, P. A. 1960. Leakage of phosphate compounds from ultraviolet irradiated yeast cells. J. Cellular Comp. Physiol., 56:77.

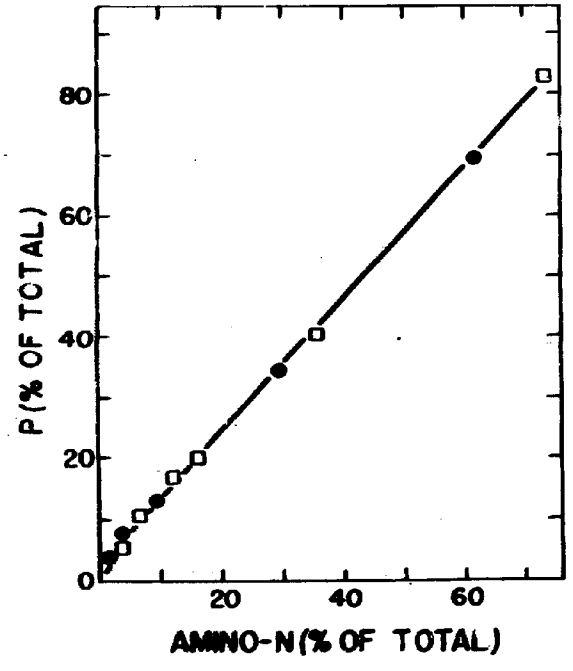

Fig. 1 Relation of heat-induced release of yeast phosphate and amino-N. Yeast cells in H_2O (○) or in sodium cacodylate (□), heated at 60 C.

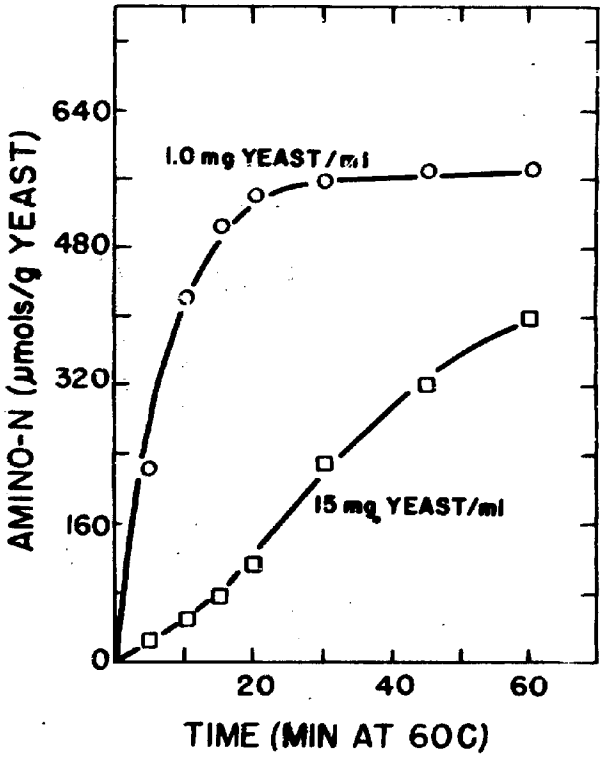

Fig. 2 Effect of yeast concentration on the heat-induced release of amino-N from yeast cells. Aqueous yeast suspensions of indicated yeast concentrations were heated at 60 C.

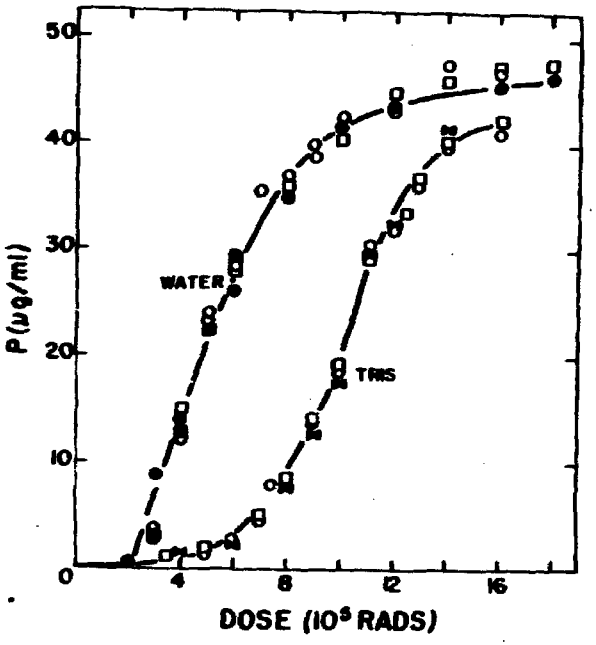

Fig. 3 Effect of suspending medium on the radiation-induced release of yeast inorganic phosphate. Symbols indicate experiments conducted at various times over a 6 months period.

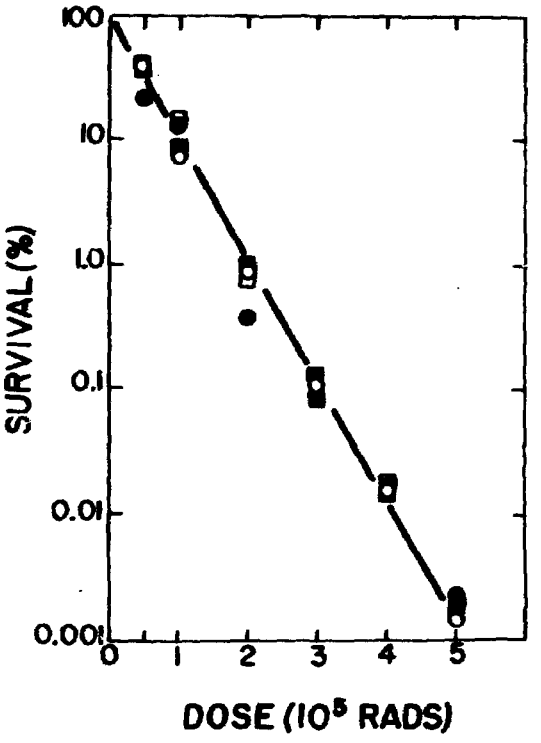

Fig. 4 Survival of irradiated yeast. Aqueous (circles) and Tris (squares) suspensions of yeast irradiated; with (●, ■) and without (○, □) the addition of 0.05 M ascorbate. Survival measured by colony formation on Mycophil agar, pH 4.7.

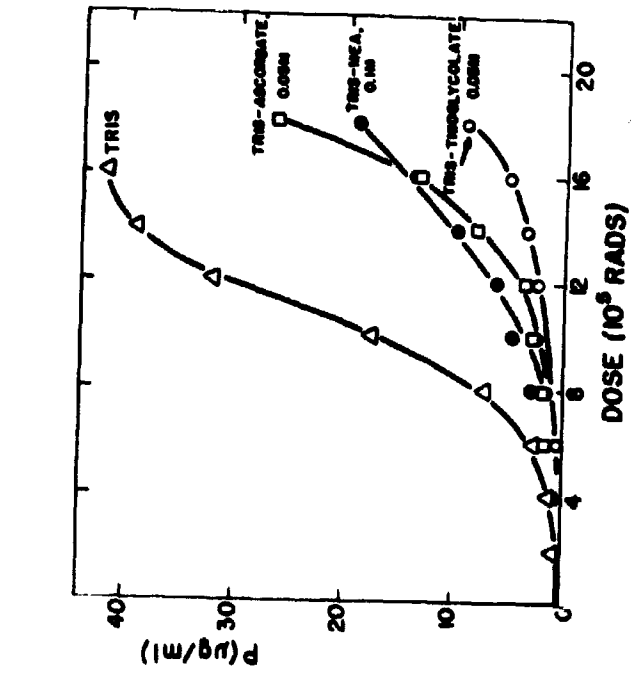

Fig. 6 Inhibition by radioprotective compounds of the radiation-induced release of inorganic phosphate from Tris suspensions of yeast.

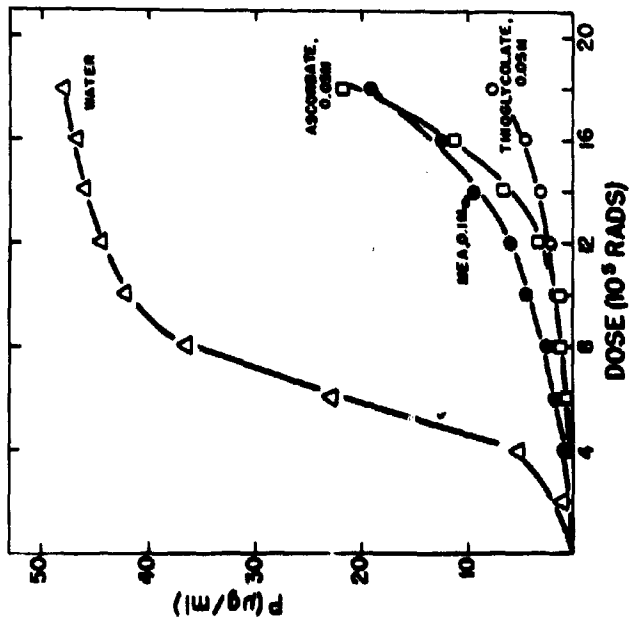

Fig. 5 Inhibition by radioprotective compounds of the radiation-induced release of inorganic phosphate from aqueous suspensions of yeast.

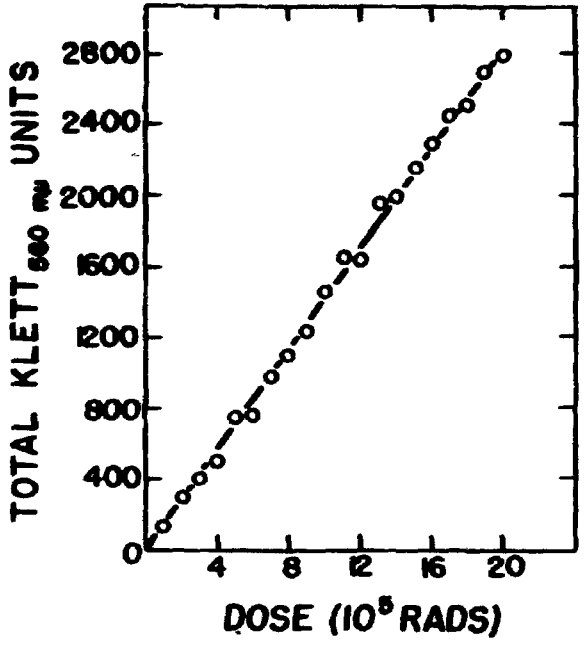

Fig. 7 Tris (hydroxymethyl) aminomethane as a radiation dosimeter. Tris, 0.05 M, pH 7, irradiated and ninhydrin-amino-N color read in Klett (560 mμ). Total Klett units = Klett reading x sample dilution.

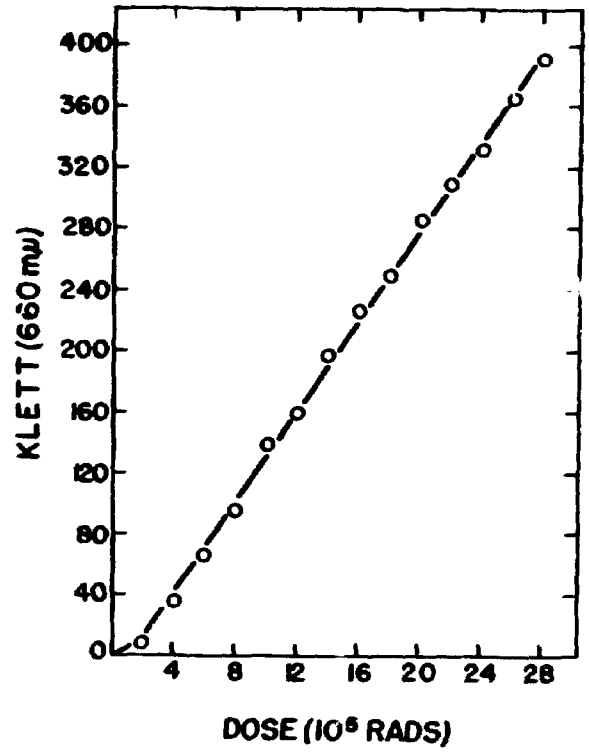

Fig. 8 Sodium cacodylate as a radiation dosimeter. Irradiated cacodylate 0.05 M, pH 5.5, tested [Fiske and SubbaRow (2)] and intensity of molybdenum blue color (Klett 660) read.

BLANK PAGE

FLUORINE HYPERFINE INTERACTION IN ELECTRON SPIN RESONANCE

ROBERT LONTZ
U. S. ARMY RESEARCH OFFICE-DURHAM
DURHAM, NORTH CAROLINA

For several years now, the technique of electron spin resonance (ESR) has been successful in providing a great deal of information concerning the structure of free radicals. This information is commonly derived from the magnetic hyperfine interaction of the unpaired electron of the free radical with various nuclei of the free radical. Since this interaction requires nuclei which possess a non-zero nuclear magnetic moment, ESR free radical analyses have usually involved the hydrogen nuclei (H^1) of organic molecules.

Only recently has the ESR analysis of a free radical using the hyperfine interaction of fluorine nuclei been carried out. The fluorine hyperfine interaction is characterized by its relatively large anisotropy of magnitude as the magnetic field is changed in orientation with respect to an axis system fixed to the free radical. For this reason, it is necessary to study fluorine hyperfine interaction using free radicals that are fixed rigidly in preferred orientations, as in a single crystal lattice.

The electron spin resonance analysis of free radicals formed by the gamma irradiation of single crystals of trifluoroacetamide (CF_3CONH_2) will be discussed. It is found that the irradiation causes a carbon-fluorine bond of some of the molecules to be broken, forming stable free radicals of $\dot{C}F_2CONH_2$. The discussion will concern the nature of the information available from the study of the hyperfine interaction of the unpaired electron (represented by the dot) with the two fluorine nuclei of this free radical.

INTRODUCTION: The study of gamma irradiated organic solids by the electron spin resonance (ESR) technique of spectroscopy provides a rich variety of information connected with the nature of radiation damage, and details of the molecular orbital. The radiation damage information is the first by-product that appears when the researcher successfully assigns the pattern of spectral lines to a particular model for the damaged molecule or "free radical." The separation between the various spectral components, or hyperfine splittings, are a measure of the unpaired electron spin density throughout the damaged molecule and is accountable by theories of the molecular orbital.

Conventional ESR spectrometers can detect a minimum number of 10^{15} to 10^{17} free radicals, a total which is frequently obtained by irradiating an organic solid for several hours. This free radical total reflects a dilute concentration of such damage centers in the bulk material, and can lead to the stability of these species for periods of years at room temperature.

The unpaired electron of the free radical often results from the breakage of a specific covalent bond, as for example a C-H bond of a carbon atom in the tetravalent bonding configuration. This same carbon atom assumes trigonal bonding following the breakage of one of its C-H bonds, with the greatest portion of the unpaired electron being concentrated in the carbon 2p orbital perpendicular to the plane of the trigonal bonds.

However, smaller unpaired electronic densities appear in localized orbitals of other atoms of the same free radical. The latter spin density is measureable as a result of the interaction energy between the magnetic dipole moment of the unpaired electron and the atomic nucleus. Carbon nuclei (C^{12}) do not possess a nuclear magnetic moment, and thus do not produce this hyperfine interaction with the unpaired electronic spin moment. Although this means that unpaired spin densities in carbon orbitals are not directly measureable from the spectral data (except by C^{13} hyperfine interaction), its absence leads to a simpler spectrum for interpretation. However, the other common element found in organic molecules, namely hydrogen, is a rich source of such hyperfine spectral lines. In fact, the spectrum due to hyperfine interaction of the unpaired electron with hydrogen nuclei will consist of 2^n lines, where n represents the number of interacting hydrogen nuclei.

The separations between various components of the spectrum are proportional to the integral $\int \psi^* A \psi \, d\tau$, where ψ is the wave function of the unpaired electron and A is the mathematical expression for the hyperfine interaction. The quantity A is a tensor, so the value of the integral is sensitive to direction of observation with respect to an axis system fixed to the free radical. (Direction of observation is defined by the large static magnetic field of the spectrometer). For example, unpaired electronic

density in hydrogen orbitals of a free radical yields an isotropic hyperfine interaction due to the spherical symmetry of the 1s orbital. It is for this reason that many organic molecules have been successfully analyzed using polycrystalline samples, particularly when the free radical is composed largely of carbon and hydrogen.

The situation for unpaired electronic density in fluorine orbitals of a free radical is quite different. Since the wavefunction of the fluorine 2p orbital does not possess spherical symmetry, the integral $\int \psi^* A \psi \, d\tau$ is sensitive to direction of observation. As in the hydrogen case, the spectrum will consist of 2^n lines for each fluorine nucleus experiencing hyperfine interaction with the unpaired electron. However, the positions of each of the 2^n lines will depend upon the direction of observation with each of the approximately 10^{15} free radicals of the sample. The net result is that the lines will be "smeared" over the spectrum in some averaging of the many possible directions assumed by the free radicals in the polycrystalline sample. Resolution of each of the 2^n fluorine lines is usually only possible through the use of an irradiated single crystal, which serves to arrange the free radicals in one or a few preferred directions.

Only recently has the analysis of F^{19} anisotropic hyperfine interaction been carried out in an irradiated organic compound (1) although analyses have been made of inorganic single crystals of salts of the transition elements (2) and of irradiated single crystals of alkali fluorides(3). This paper will be specifically concerned with the ESR analysis of irradiated single crystals of trifluoroacetamide (CF_3CONH_2), a material with a relatively simple molecular structure and of which single crystals are easily obtained.

EXPERIMENTAL: Conventional electron spin resonance spectrometers capable of operation at 9 and 24 kMc/sec were used, and spectra obtained represent the second derivative of the actual absorption. The trifluoroacetamide was purchased from the Peninsular Chemical Research Company (Gainesville, Florida) as a powder, and single crystals were grown by slow evaporation from an aqueous solution. To the best of our knowledge, the crystal structure analysis of this compound has not appeared in the literature.

ESR spectra were obtained for many orientations of the single crystal in the static magnetic field of the spectrometer. Such measurements generally describe the hyperfine interaction tensor in a non-principal plane, so that the A must be diagonalized to obtain its principal values. The arbitrary frame of reference selected for the purpose of these measurements will be known by the axes a', b, and c.

The source for irradiation of the crystals were the 1.3 MeV gamma rays of Cobalt 60. The dosage had no observable effect on the type of free radical formed, and exposures lasted several hours or more. The normally colorless trifluoroacetamide single crystals turned to a yellow color upon irradiation.

NATURE OF OBSERVED SPECTRA: Analysis of the ESR spectra shows that one of the CF bonds of trifluoroacetamide is broken as a result of the gamma irradiation. The remaining two CF bonds become reoriented so that the 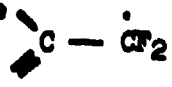 group is planar, and very probably in the plane of the CON group. The dot above is to signify the unpaired electron resulting from breakage of a CF bond. The unpaired electron spin density is in a π orbital perpendicular to the molecular plane defined by the CCF_2 group, and includes a significant contribution from lone pair 2p fluorine orbitals. The unpaired electron spin density is found to be approximately 0.11 for each of these two fluorine orbitals.

Figure 1 shows ESR spectra of the trifluoroacetamide free radical for selected orientations in the a'b plane, from which the nature of the free radical is immediately apparent. The spectrum is composed of two triplet patterns of intensity ratio 1:2:1. At the angle of 56° the two patterns coalesce when the component splittings for each of the two patterns are equivalent. However, the most general pattern has five lines representing two triplets with different component splittings, line widths, and intensities for various orientations of the crystal in the static magnetic field.

The triplet is characteristic of the hyperfine interaction of the unpaired electron with two fluorine nuclei (with nuclear spin I = 1/2), with both fluorine nuclei being coupled to the electron equally. The existence of two triplet patterns is attributed to the two distinguishable orientations for the free radical in the unit cell. Elimination of hydrogen nuclei as the source of the spectral lines is based upon the relatively large separation between component lines and their anisotropic behavior as the crystal is rotated in the static magnetic field. Therefore, the only possible free radical structure with two equivalently coupling F nuclei resulting from the breaking of a bond of trifluoroacetamide must be of the form CF_2CONH_2.

Preservation of this triplet structure for spectra of all orientations is a most important feature of the spectrum, which demonstrates the equal hyperfine coupling to the two fluorine nuclei for all orientations. This equivalence requires the 2p orbitals of the F's which give rise to the anisotropic coupling to have parallel axes and the same electron spin density. Even with equal spin densities, the two fluorine atoms would exhibit different hyperfine

interactions for non-parallel orbital axes, such as the fluorine 2p bonding orbitals in the trigonal plane. The latter situation would yield a quartet spectrum rather than the triplet as actually observed.

Figure 2 shows the component splittings for each of the two triplet patterns in the bc plane. The constant splitting observed for all angles in this plane for free radical orientation I indicates that this is the molecular plane for free radical orientation I. That is, a constant hyperfine splitting indicates perpendicularity of the magnetic field to the 2p orbital density axis. Similar behavior is observed for free radical orientation II for a plane whose normal is approximately 68° to the normal of the bc plane. This suggests that the relative positions of the two possible free radical orientations is as shown in figure 3. The angle 68° happens to coincide with the angle separating two of the external faces of the crystal.

The principal values for the nuclear hyperfine interaction tensor A were obtained using standard techniques of ESR single crystal analyses (4). Table I gives the magnitudes and directions of the tensor A for one of the two free radical orientations.

THEORETICAL ANALYSIS: The electron spin resonance spectra for all orientations may be described mathematically by the spin Hamiltonian which generally applies in free radical work,

$$H = \vec{S}\cdot\vec{g}\cdot\vec{H} + \sum_i \vec{S}\cdot\vec{A} \cdot \vec{I}(i) - g_I\beta_I \vec{H}\,\vec{I}(i) \quad , \tag{1}$$

in which the summation is over the two F^{19} nuclei of the trifluoroacetamide free radical (i = 1,2). Terms of the above Hamiltonian represent the coupling of the unpaired electron spin magnetic moment with the static field H, the interaction between the magnetic dipole moment of the unpaired electron and the two fluorine nuclei, and the direct interaction of the nuclear moments with the static magnetic field.

$$\vec{A} = g_s\beta\, g_I\beta_I \left[(\vec{U}/r^3 - 3\,\vec{r}\,\vec{r}\,/\,r^5)_{av} - 8\pi \left|\psi(0)\right|^2 \vec{U}/3 \right] \tag{2}$$

where U is the unity dyadic and r is the radius vector between the unpaired electron and the nucleus considered. The first term of A is the classical interaction between two magnetic dipoles, and the second is the isotropic "Fermi hyperfine interaction" which is applied to unpaired electron spin density at the position of the nucleus ($|\psi(0)|^2$).

Under the assumption that the electron spin is quantized along the static magnetic field, the expression (2) assumes the general form,

$$A = A_\mu (3\cos^2\theta - 1) + Af,$$

where θ is the angle between the field direction and the 2p orbital density axis, and A_μ and A_F refer to the dipole/dipole and Fermi components of the hyperfine interaction. With the observed value of A_3 = 178 gauss corresponding to orientation along the 2p density axis or θ = 0°, and $A_1 = A_2$ 24 gauss at θ = 90°,

$$\pm 178 = A_F + 2A_\mu \quad (\theta = 0^\circ)$$
$$\pm 24 = A_F - 2A_\mu \quad (\theta = 90^\circ)$$

or $A_F = \pm 75$ gauss and $A_\mu = \pm 51$ gauss.

Although the signs of A_F and A_μ cannot be determined in this experiment, these two quantities do have the same signs. These quantities represent hyperfine coupling due to unpaired electron density in spherically symmetric orbitals and non-spherically symmetric orbits respectively.

The above experimentally determined values for A_F and A_μ may be compared to equivalent numbers characteristic for a 2p fluorine electron and a 2s fluorine electron. This comparison gives the unpaired spin density present in the fluorine orbitals of the trifluoroacetamide free radical. The unpaired spin density of the 2p orbital perpendicular to the molecular plane is then,

$$\rho_{2p} = A_\mu / A_{2p}, \qquad (3)$$

where A_{2p} is the hyperfine interaction for unity unpaired spin density in a fluorine 2p orbital. A_{2p} is obtained by averaging the anisotropic dipole-dipole term of the Hamiltonian (2) over the 2p wavefunction and has the value,

$$A_{2p} = 2/5\, g_s\beta_s g_I\beta_I \langle 1/r^3 \rangle_{Av},$$

in which $1/r^3$ is still to be averaged over the p orbital. This average can be estimated theoretically or can be obtained experimentally from the fine structure in atomic spectra. Values of $\langle 1/r^3 \rangle_{Av}$ for various atoms including F have been obtained and tabulated by Barnes and Smith (5). For the p electron in $(F^{19})^-$ ions we employ the value,

$$A_{2p} = 0.044 \text{ cm}^{-1} = 470 \text{ gauss},$$

calculated by Moriya (6) and based on the $\langle 1/r^3 \rangle_{Av}$ of Barnes and Sm. . From equation (3) the unpaired spin density of the 2p orbital is therefore:

$$\rho_{2p} = 51/470 = 0.11$$

This spin density indicates that each of the CF bonds in the free radical has about 11% double bond character.

The origin of the A_F component of hyperfine coupling is not as clear as that of the $A_{\parallel}$. Although it would be expected that the 2s spin density is greater than the 1s density, the coupling of the latter unpaired density is more potent by virtue of the fact that $|\psi_{1s}(0)|^2 > |\psi_{2s}(0)|^2$. However, an upper limit for spin densities in the 2s and 1s orbitals may be obtained using calculated values of $|\psi_{1s}(0)|^2$ and of $|\psi_{2s}(0)|^2$ for F^- as calculated by Freeman and Watson (7). That is to say, upper limits to the unpaired 2s and 1s spin densities in fluorine orbitals of the trifluoroacetamide free radical are:

$$\rho_{2s} = 75/16{,}400 - 0.0045$$

$$\rho_{2s} = 75/321{,}000 = 0.00023$$

Lontz and Gordy give detailed calculations for the distribution of the remaining spin density (100% - 2 x 11%) for the trifluoroacetamide free radical. Symmetry in the hyperfine coupling leads to an assignment of a maximum of $\rho_{2p} = 0.69$ spin density to reside in the carbon 2p orbital perpendicular to the molecular plane. Since no hyperfine coupling with atoms of the amide group was detected, the unpaired spin density within this group is negligible.

CONCLUSION: This discussion has shown in outline form the information that may be obtained through the study of the anisotropic fluorine hyperfine interaction in free radicals. A similar analysis has since been carried out on the free radical $\dot{C}HFCONH_2$ (8) which is in general agreement with the data found for trifluoroacetamide. In addition, Ovenhall (9) has used the trifluoroacetamide data to interpret the fluorine hyperfine coupling in free radicals of the polymer "Teflon" ($-CF_2-\dot{C}F-CF_2$) when the polymer radicals are oriented by stretching the irradiated material.

Present efforts are being directed to the interpretation of the free radical formed by irradiation of pentafluoropropionamide, $CF_3\,\dot{C}F\,CONH_2$. The room temperature ESR spectra of this radical indicate that the CF_3 group exhibits hindered rotation about the C-$\dot{C}$ bond, and the rotation may be stopped by cooling the sample to liquid nitrogen temperature. It is expected that measurements in progress will lead to information on the potential barrier for this rotation, as well as an understanding of the orbital configurations which lead to hyperfine coupling with the fluorine nuclei of the CF_3 "methyl" group in a free radical.

REFERENCES

(1) R. J. Lontz and W. Gordy, J. Chem. Phys. 37, 1357 (1962).

(2) M. Tinkham, Proc. Roy. Soc. (London) A236, 535, 549 (1956).

(3) M. H. Cohen, W. Känzig, and T. O. Woodruff, Phys. Rev. 108, 1096 (1957).

(4) J. A. Weil, and J. H. Anderson, J. Chem. Phys. 35, 1410 (1961).

(5) R. G. Barnes and W. V. Smith, Phys. Rev. 93, 95 (1945).

(6) T. Moriya, Progr. Theoret. Phys. (Kyoto) 16, 23 (1956).

(7) A. J. Freeman and R. E. Watson, Phys. Rev. Letters 6, 343 (1961).

(8) R. J. Cook, J. R. Rowlands, and D. H. Whiffen, Mol. Phys.

(9) D. W. Ovenall, J. Chem. Phys. 38, 2448 (1963).

TABLE I

Principal Values and Directions of Nuclear Hyperfine Coupling Tensor (A) for Free Radical "I"

Magnitude	Direction
$A_1 = A_2 = 24$ gauss (498 Mc)	Perpendicular to a'
$A_3 = 178$ gauss (67 Mc)	Along a'

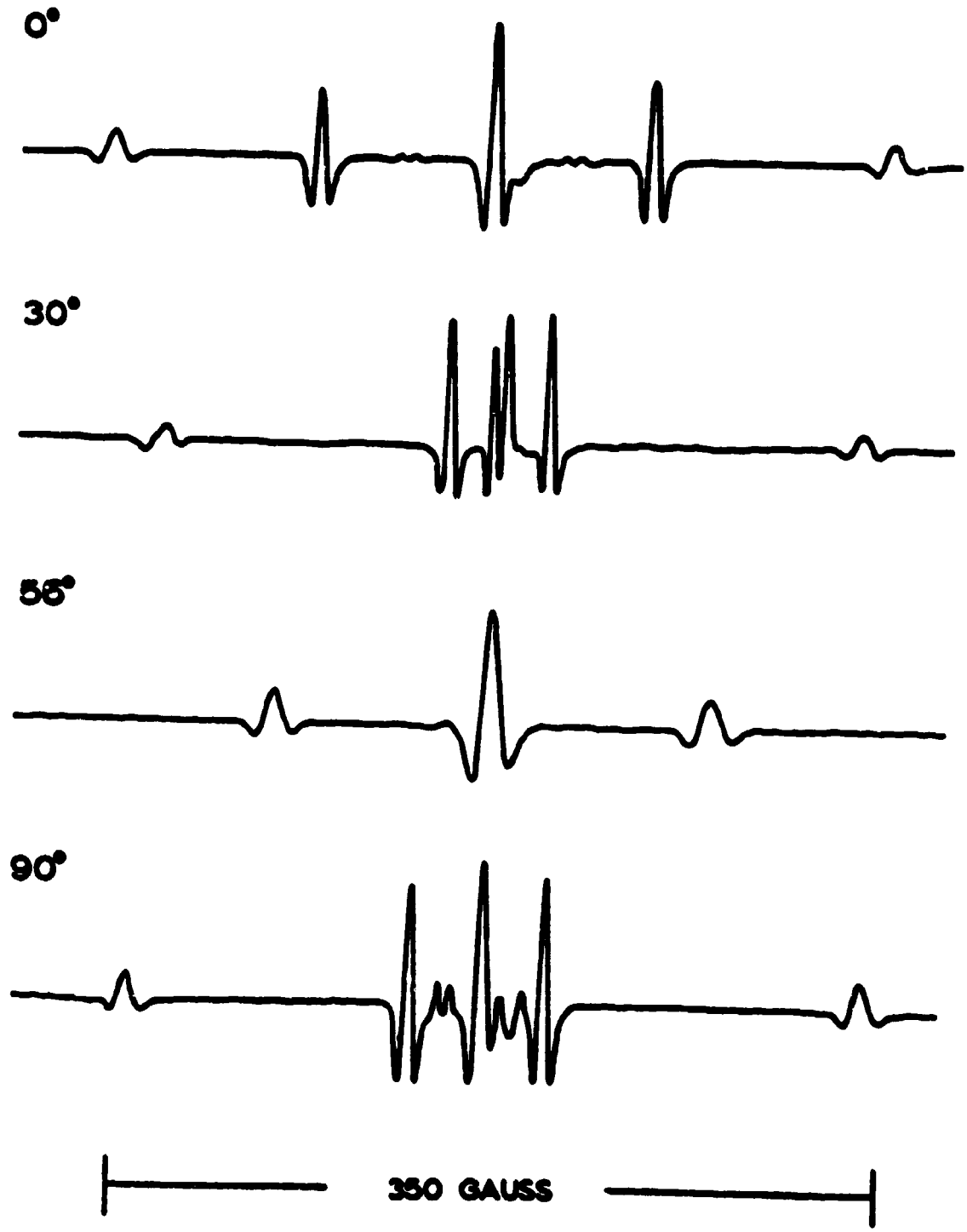

Fig. 1
ESR patterns of -irradiated single crystal of trifluoroacetamide with the static magnetic field in the a'b plane and at various angles from a'.

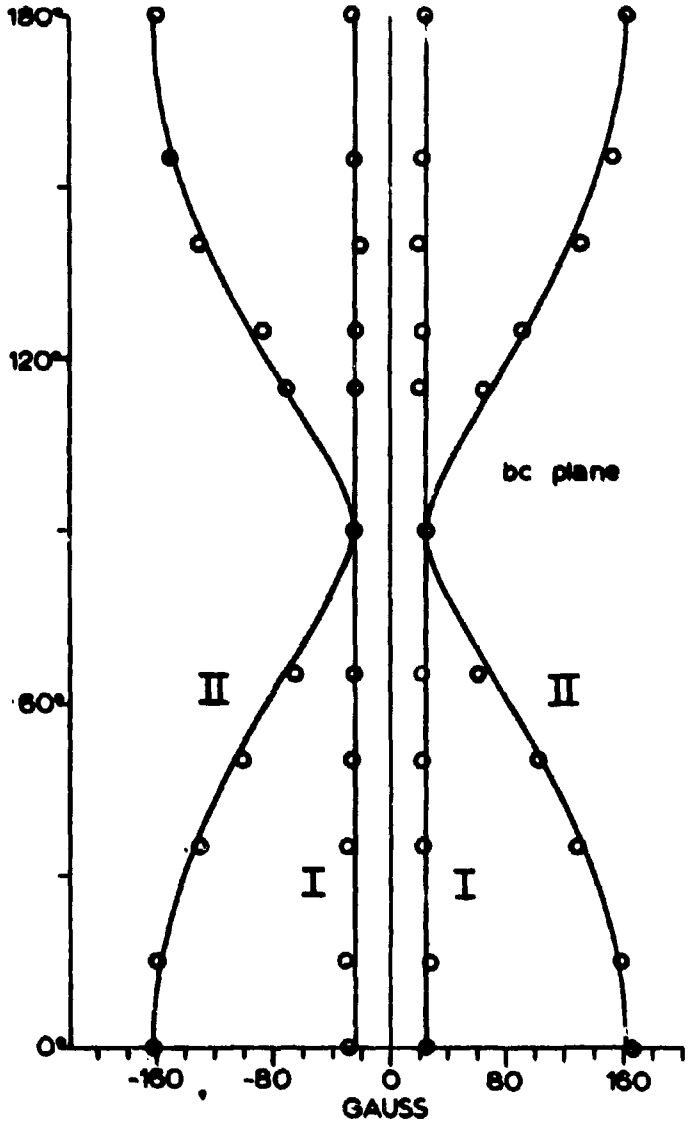

FIGURE 2. Plots of the outside components of triplets I and II for various orientations of the static magnetic field in the bc plane, with angles measured from the b axis in the direction of c.

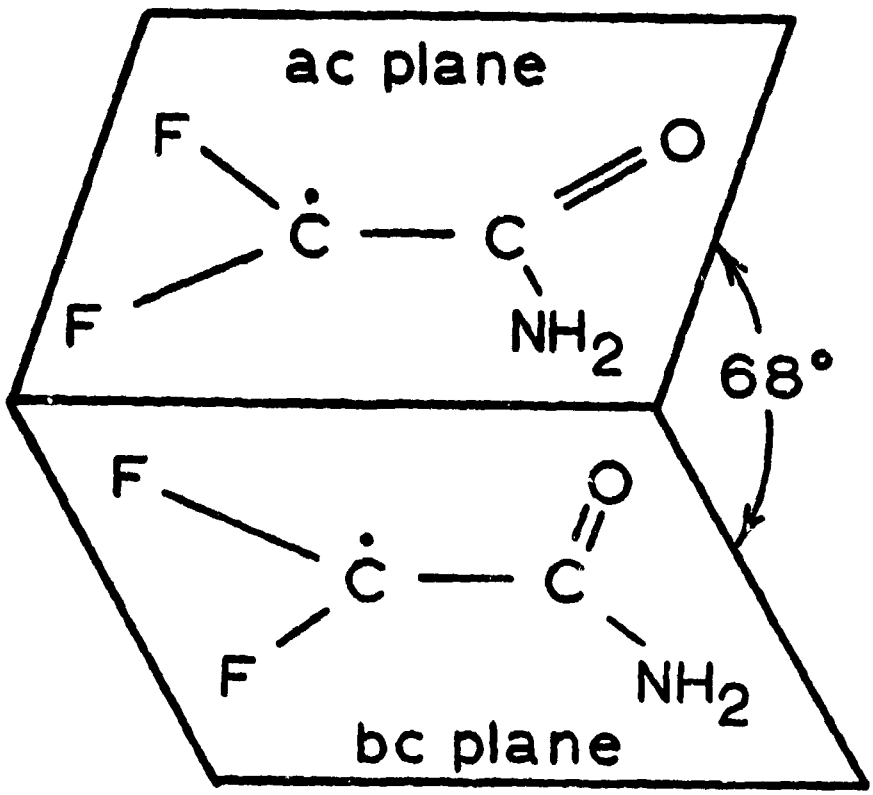

FIGURE 3. Diagram showing relative orientation of observed free radicals.

A NOVEL PROCESS FOR ULTRA-FINE CRYSTALLITES, AND THEIR THEORY AND APPLICATION IN MAGNETIC FERRITES

W. W. MALINOFSKY, R. W. BABBITT, and G. C. SANDS
U. S. ARMY ELECTRONICS RESEARCH AND DEVELOPMENT LABORATORIES
FORT MONMOUTH, NEW JERSEY

INTRODUCTION

A "single crystal" is a familiar term today, and we commonly picture its size on a scale of centimeters. But suppose such a single crystal should shrink to a millionth of this size, would its properties be the same? For the magnetic properties to be discussed here, theory answers "No". It even gives us an idea as to what to expect; what it does not do is show us how to make such materials in a form adequate for testing or practical use. Therefore, to study these properties, such a process first had to be devised. Its description is the first object of this paper.

But, why should we expect unusual properties in an ultra-fine crystallite? This can better be understood by looking first at part of a larger crystallite (Fig. 1). There it is found that the magnetic dipoles line up within a given volume (I) of the crystallite, but are commonly opposite in direction in the neighboring regions (II). Each of these regions is called a magnetic domain. In between, the dipoles go through a transition from one direction to the other, requiring some distance δw to do so. This transition region is called a domain wall. These domain walls are entities in themselves, and effective mass and inertia can be ascribed to them. For example, they can be made to oscillate in an electromagnetic field, and to go through a resonance with increasing frequency. In fact, one of the two largest schools of thought in magnetism ascribes the important technical rf properties to this wall motion. Thus, if walls were eliminated, unusual properties would be expected to result. This is precisely what is brought about in an ultra-fine crystallite.

As the crystallite diameter D is decreased, the number of domains in it gradually decreases to just two (Fig. 2b). One wall remains between them. At this stage, both wall energy and magnetostatic energy due to magnetic poles on the surface compete in contributing to the total energy. But, as the size is decreased still

further, it goes through a critical diameter D_{crit} below which the total energy becomes less with the wall eliminated than present, even though the magnetostatic energy is somewhat increased (Fig. 2a). This value of D_{crit} may be calculated (1) from the intrinsic constants of the material. Thus, for our ferrites it is calculated to be approximately 10^{-5}cm or 0.1 micron. The first requirement of this process, then, is to produce crystallites less than 1000 atom-diameters across.

At this point, it is well to introduce the second requirement on the process to be described. Although it will be shown in the next section how crystallites only 200 atom-diameters across can be obtained, it is clear that meaningfull measurements of properties on one such particle cannot be made physically. Therefore, an aggregate must be used. But, then the average properties are diluted and distorted by the spaces between the crystallites due to demagnetizing effects, unless the aggregate is compacted to a density near that of a single crystal. Known ceramic densification processes, unfortunately, increase the crystallite size well above D_{crit}, about a factor of 100 higher, which would defeat the purpose of this investigation. Thus, the second criterion of the process was to achieve near single crystal density without significant growth of the crystallites.

Subsequent sections will describe the above process, as well as the magnetic, crystallographic, and physical measurements, which show the effects of the single-domain nature of the crystallites on magnetic properties at both radio and microwave frequencies. Then these will be correlated with current theory, or the theory extended as required. Finally, the state of development of two properties for potential application will be described: 1) an increased threshold field for the onset of instability of the microwave resonance at high power levels, and 2) a temperature-stable initial permeability at radio frequencies.

THE PROCESS--COMBINED FLAME-SPRAY AND HOT-PRESS TECHNIQUES

As conceived, the process must have two steps. The first should be a reaction stage, in which ingredients of the right composition would react chemically to form the pure (single-phase) compound desired, yet which would maintain the ultra-fine crystallites well below D_{crit}. The second should be a densification stage, in which compaction to high densities would occur without crystallite growth above D_{crit}, and with no alteration of the purity of the compound. No known method could meet these requirements, so one had to be devised. We did this by using the so-called flame-spray technique for reaction, and the hot-press technique for densification.

Figure 3 is a schematic of the flame-spray apparatus, while Fig. 4 shows its principal operation. Basically, an alcoholic solution and oxygen gas sprayed a 1200°C flame out of a fine stainless steel nozzle into a vycor tube. Through this the reacted particles

were impelled into a water-spray tower and were collected. The solution consists of Ni-, Zn-, Co-, and Fe-nitrate hydrates dissolved in methyl alcohol in proportion to the ferrite formula $A_{1-x} B_x Fe_2 O_4$, where A and B along with Fe are the above metals. Since the first investigation of this technique (2) we have replaced the cyclone collection system with a water-spray tower, in order to collect smaller crystallites. Varying physical parameters, we could control the crystallite size between 0.02 - 0.12 micron. Typical ones, 0.03 micron across, are shown in an electron micrograph (Fig. 5), where they appear to be fairly well perfected. We calculated the average crystallite size (3) from broadening of five diffraction lines in the back region of x-ray diffractometer charts, and the result agreed with the electron micrograph. Using these charts, we learned to control a lossy NiFe alloy present in early runs, by increasing the oxygen pressure to the flame nozzle. The alloy did not appear above 15 psi O_2. Subsequently, the routine became to use 20 psi to allow a safety margin.

The hot-press, used for the densification stage of the process, is shown schematically in Fig. 6, while Fig. 7 shows the inductively heated die at 1100°C under 6000 psi. The basic principle of the hot-press, long-used in metallurgy, but not for ferrites, is to apply heat and pressure simultaneously to the ferrite. This results in high densification, for an unknown reason, but in little crystal growth. The latter is due to the temperatures used, 950 - 1150°C, relatively low compared to conventional sintering.

In this technique, we placed a cold-pressed pellet of the flame-sprayed powder into a cylindrical stainless steel die. ZrO_2, used as a liner and for plungers, prevented reaction with the steel. As a powder about the pellet, it aided ejection of the densified ferrite. An induction heater was controlled by a temperature programmer. Up to 98% of single crystal density could be obtained in a half-hour, with crystallite sizes of about 0.1 micron. To obtain this density in the ordinary way would require many hours, with the attendent excessive growth of the crystallites to about 100 D_{crit}.

To obtain a basic set of processing conditions, we varied hot-pressing time t, temperature T, and flame-spray oxygen pressure P. Q-meter measurements of μ_o Q at 4 Mc/s were taken as an indicator of the optimum conditions, since it is a standard merit factor for technical rf magnetic materials. μ_o is the initial permeability, and Q is a quality factor inverse to the magnetic loss. The results are shown in Fig. 8. The disadvantage in raising T indefinitely is that the crystal growth goes up rapidly, too. Low P produce a low Q, due to the high loss from a NiFe alloy previously described. Again, P cannot become too large, since it then exerts a cooling action on the flame, causing flame-out. As a result, we took P = 20 psi, t = 25 minutes, and T = 1100°C as a basic set of conditions about which to vary during subsequent experiments.

DOMAIN WALL MOTION vs. DOMAIN ROTATION

For over a decade a controversy has stimulated many workers in magnetism, as to whether domain wall motion, or domain rotation, is the magnetization mechanism underlying the technical properties in conventional materials. There are large schools of thought on each side. Briefly, the former is a change in magnetization by means of an effective translation of a domain wall through the domain; while in the latter case, it is due to rotation in unison of all the magnetic dipoles in the domain. A great deal of experimental evidence has been built up on either side. Since we could make crystallites small enough to prevent domain walls, thus allowing domain rotation only, we could compare their properties with conventional ferrites to clarify the question.

RF Peak. To do this, we measured the complex permeability μ' and μ'' (loss) to 4000 Mc/s, using appropriate bridges and slotted lines to cover the range. The results are shown in Fig. 9 for 0.10 micron Ni-ferrite as compared with a conventional one of similar density (95% of theoretical) with crystallites 500 times larger (4). The large peak in μ'', typical of conventional ferrites, is due to a resonance exhibited by the wall motion or domain rotation, whichever really exists. We reached a conclusion, thusly: if this resonance were normally due to wall motion, it should not appear for our ultra-fine wall-less ferrite. But since it did persist, we must conclude that domain rotation, instead, is the essential mechanism in Ni-ferrite for conventional, as well as ultra-fine, crystallite sizes. This was found to be true in $Ni_{1-x}Co_xFe_2O_4$ also, where $x = 0.027$, 0.030, and 0.068. In all, several dozen samples were tested, many even smaller than 0.1 micron, and the same conclusion was reached in every case. A possible argument that domain wall motion may supplement the domain rotation in the above conventional ferrite is ruled out by the finding that similar values of μ' and μ'' are found regardless of crystallite size, if the comparison is made for the same densities.

In addition, resonance frequency for domain rotation was calculated from standard theory and compared with the experimental resonance frequency in the manner of Smit and Wijn (5). Good agreement was found in all cases. In measurements on ultra-fine $Ni_{1-x}Zn_xFe_2O_4$, where $x = 0.10$, 0.33, 0.50 and 0.67, a similar rotational resonance again was found. However, because the conventional ferrite had μ' values nearly 10 times those of the ultra-fine ferrites of the same density, it was concluded that in conventional NiZn-ferrites wall motion is the predominating mechanism, while domain rotation contributes to only a minor extent.

Microwave Peak. Let us look at Fig. 9 again for Ni-ferrite, and observe the microwave frequency peak near 2000 Mc/s for the conventional ferrite. Notice that it is missing in the ferrite with $D < D_{crit}$, but that it appears again after annealing, when $D > D_{crit}$.

It is generally agreed in the standard theory that this second resonance is at too high a frequency to be accounted for on the basis of wall motion, and is due to rotation. Our evidence, too, indicates that it is due to rotation; but nevertheless, that it is directly tied to the formation of the walls.

How this can happen may be seen from the following reasoning. Polder (6) has already explained that magnetic poles will form selectively on some domain walls, i.e., those in which a component of the rf field is parallel to the walls (Y-Z plane) and perpendicular to the magnetization M_s (Z-direction). Statistically, these are important, accounting for 1/3 the total number of walls, and hence of μ''. Most important, poles on such walls result in a large demagnetizing factor N_x of 4π. This value of N_x is in sharp contrast to that when walls are not present. Without walls, N_x and N_y are effectively reduced to near zero by the susceptibility χ of the surrounding medium (7).

$$N_{eff} = \frac{N}{1 + (4\pi - N)\chi}$$

Therefore, we conclude that this large change in demagnetizing factor is related to the formation of the microwave peak as walls are formed during annealing of the ultra-fine crystallites above D_{crit}. It should be noted that this cannot be a density effect, since the anneal changed the density only about 2%.

To carry this line of reasoning further, we made a calculation of the domain rotation resonance frequency ω_{res}, starting with Snoek's general equation (8):

$$\omega_{res} = \gamma \left[(H_{an} + N_x M_s)(H_{an} + N_y M_s) \right]^{\frac{1}{2}}$$

where γ is the gyromagnetic ratio, and H_{an} is the magnetocrystalline anisotropy field. Then as explained above, without walls, N_x and $N_y = 0$, and $\omega_{res} = \gamma H_{an}$. However, upon the formation of walls, ω_{res} increases to the following value:

$$\omega_{res} = \gamma \left[(H_{an} + 4\pi M_s) H_{an} \right]^{\frac{1}{2}}$$

In the case of $NiFe_2O_4$, substituting the known values of H_{an} and using the true g-factor of 2.13 results in $\omega_{res} = 2500$ Mc/s. This is in good agreement with the observed resonance at 2000 Mc/s in Fig. 9 for the crystallites greater than D_{crit}, including the conventional sample. The slight displacement observed toward a lower ω_{res} is probably due to the superpositioning of the microwave and rf peaks.

In another composition, where one normally observes a microwave peak in the conventional material, namely $Ni_{.932}Co_{.068}Fe_2O_4$, we again obtained good agreement between our observed peak (5000 Mc/s) and that calculated from the last equation (5050 Mc/s). We estimated a true g-factor, using 2.13 (above), instead of using

the effective g-factor of 2.26. For other Co- and Zn-substituted Ni-ferrites our results were consistent with the derived theory. That is, in general, where ω_{res} calculated was low enough to fall directly under the rf peak and therefore be masked, it was never distinguishable either in our annealed samples for $D > D_{crit}$ nor in the conventional samples.

Density Theory. Finally, the theory advanced by Pippin and Hogan (9) for the microwave peak was tested. Agreeing with standard theory that this peak is due to a rotational resonance, they suggested that its distinguishability from the rf peak was a density effect, requiring a minimum value of 4.85 g/cm^3 in the case of $NiFe_2O_4$. As density increased, the rf peak would move down in frequency, exposing the microwave peak. However, we have observed numerous exceptions to this. For example, we have seen this microwave peak for $D > D_{crit}$ far below this density, in particular for 4.43 g/cm^3. Also, as was shown in Fig. 9, we could not observe it even for 5.05 g/cm^3, when $D < D_{crit}$. Moreover, we observed a strong peak in a conventionally prepared sample of supposedly borderline density (4.89 g/cm^3). Based on these results, the density theory appears to us to be inconsistent with our experimental evidence. Although density can shift the resonant frequencies, it does not appear to be a fundamental criterion for the physical existence of the microwave peak, as is crystallite size.

LOW FIELD LOSS AT MICROWAVE FREQUENCIES

An extension of the above work concerning the rf and microwave peaks was to study ultra-fine ferrites under perpendicular rf and dc fields. In this case, one expects a ferromagnetic resonance at a frequency obtained from H_{eff} given by Kittels equation (11):

$$H_{eff} = \left[\left[H_{ze} + (N_x - N_z) M_Q\right] \left[H_{ze} + (N_y - N_z) M_Q\right]\right]^{\frac{1}{2}}$$

which is a function of the external biasing field H_{ze}, (labeled H_{res} in Fig. 10) and the sample configuration. In the same figure, one can observe the low field losses, which peak at $H_{dc} = 0$. Together, the two effects add to form a loss curve with a double maxima. The source of the low field loss is known to be domain rotation resonance, as described before, which can extend up to a high microwave frequency given by (12): $\omega_{max} = \gamma (H_{an} + 4\pi M_s)$. This is because of the random orientation and shapes of the crystallites. A saturating biasing field, H_{sat} in Fig. 10, aligns all of the magnetizations, and then the sample resonates as one domain (Fig. 10, dotted curves).

We wished to compare these effects with those in an ultra-fine, domain-wall-free, ferrite. Specifically, we wanted to observe the effect on the low field losses of the absence of the second (microwave) peak in the rf dispersion discussed earlier (last section) and shown near 2000 Mc/s in Fig. 9. Instead of Ni-ferrite, however, we shall discuss $Ni_{.932}Co_{.068}Fe_2O_4$, since it exhibits this

microwave peak at a higher frequency (near 5000 Mc/s.) This makes it more evident when superimposed on the rf peak, the latter falling off to a greater extent at the higher frequency. All measurements were taken in a slotted line at 5050 Mc/s with the coaxial sample holder placed between the pole faces of an electromagnet. The sample was a small toroid, whose plane was perpendicular to H_{dc}.

For the smallest crystallites (Fig. 11a, top curve, 0.23 micron), a single large peak is observed in a range of biasing fields extending to 7000 oe. As the crystallites grow (middle curve, 0.35 micron) from several heat treatments at 1050°C, this peak divides into two peaks, and finally becomes (lower curve, > 0.35 micron) rather similar to that of conventional ferrites (compare Fig. 10, solid line). The smaller size of the resonance peak for the ultra-fine ferrite compared to that in Fig. 10 is probably due to incomplete saturation, since the demagnetizing factor is fairly large (2π, est.), and therefore H_{eff} is considerably reduced.

Figure 11b shows the rf dispersion, i.e., μ'' versus frequency for the same samples with $H_{dc} = 0$ (as in Fig. 9). Crystallite sizes are in the same order as in Fig. 11a. There appears to be a correspondence in the appearance of the microwave peak (Fig. 11b) and the increase in the low field losses at $H_{dc} = 0$ (Fig. 11a). As shown earlier, the microwave peak is due to the appearance of domain walls above a critical crystallite size, with the consequent formation of magnetic poles on them. These produce magnetic fields which, along with H_{an}, contribute to H_{eff}. Domain rotation resonance then occurs at a frequency determined by H_{eff}. Conversely, for this to occur for a given frequency, H_{eff} must equal H_{res}. At 5050 Mc/s, for example, about 1800 Oe are required, which is far more than the H_{an} of several hundred oersteds. Demagnetizing fields due to crystallite shape help make up this total, of course, but these are reduced by interaction with neighboring crystallites. So it is not too surprising that at low H_{dc} domain walls with their large demagnetizing field $4\pi M_s$ should be a major contributor to the low field loss.

Finally, we shall merely point out the possible potential inherent in the top curve of Fig. 11a (0.23 micron sample). In this curve, the point of lowest loss below resonance is at $H_{dc} = 0$. But μ'' as a function of frequency is just the rf dispersion (12), which we found is determined by H_{an} and M_s. It may be possible to tailor the second (microwave) peak to give sufficiently low loss at some frequency. It might then be practical to operate near $H_{dc} = 0$, requiring only small and light magnets for biasing.

MICROWAVE THRESHOLD FIELD AT HIGH POWER LEVELS

In this section we will describe the effect of ultra-fine crystallites on microwave properties at high signal levels. In particular, we shall deal with the instability, or degradation, of the microwave resonance beyond a specific rf signal strength, or

critical field h_c. For device applications at high powers it is desirable to increase h_c, while maintaining the losses low. An increase in h_c due to ultra-fine crystallite size will be demonstrated, and the remaining loss problem will be described.

The problem at hand is as follows. At H_{dc} equal to H_{res}, one obtains at low powers a resonance peak similar to that in Fig. 10, dotted curve. However, as the power level of the rf signal increases beyond a threshold value, the main resonance decreases. In addition, at biasing fields hundreds of oersteds lower another loss peak, the so-called subsidiary resonance, begins to appear at high powers. In applications, these two opposite trends with power degrade the characteristics of two types of devices. Those which operate at the main resonance, such as resonance isolators, require a high reverse-to-forward attenuation ratio, and they therefore suffer from the decline in X". On the other hand, such devices as circulators and phase shifters require low loss and operate below resonance, i.e., $H_{dc} < H_{res}$. The lower the H_{dc} the better, from the point of view of less magnet weight and size. Nevertheless, H_{dc} cannot be much less than H_{sat} (Fig. 10), in order to avoid low field losses, and so it usually falls in between, near a loss minimum. But this is generally in the range of the subsidiary resonance, which results in the deterioration of the merit factor of the device at high powers.

The basis for the ultra-fine crystallite approach to the above instability problem at high power levels will be discussed next. Inhomogeneities, such as ion distribution, polycrystallinity along with magnetocrystalline anisotropy, non-magnetic inclusions, and surface roughness are known (14) to broaden the uniform precession linewidth ΔH. Although h_c also increases, the greater ΔH decreases the device figure of merit. A desirable method would be to increase the linewidth ΔH_k of the important spin-waves, as can be seen from Suhl's equation (15) for the main resonance: $(h_c/\Delta H)^2 = \Delta H_k/4\pi M$. For the subsidiary resonance, Suhl obtained graphically a corresponding relationship (16). It is general practice, now, to interpret his ΔH shown on the ordinate as ΔH_k. Thus, all other variables being held constant, h_c will increase with ΔH_k.

Actually, Suhl's general spin-wave theory was derived assuming the crystallites greater than about 0.1 micron, which is certainly valid for conventional ferrites, but poses a question as to precisely what the theory predicts in the event the crystallites are below this size. At the main resonance, Schlömann (14) has found only a small improvement in the rate of degradation at medium power levels by reducing their size t to 2 microns in yttrium garnet. He attributed this to the size of pores rather than of crystallites.

We expected that ultra-fine crystallites, whose boundaries constitute inhomogeneities in the medium, would interact with spin-waves of comparable or longer wavelength λ. This, by analogy with the inhomogenity broadening of ΔH, might increase ΔH_k. Since the subsidiary resonance involves spin-waves (sp. w.) whose λ's range

between 0.15 micron to infinity, whereas the main resonance involves much shorter λ's, only the former was studied as a function of t.

Loss susceptibility X" was measured on spherical samples in a cavity with perpendicular pumping at 9200 Mc/s. $Ni_{.973}Co_{.027}Fe_{1.9}O_4$ was used, since for this Co content, the anisotropy constant K_1 is theoretically zero, which should provide a minimum ΔH. This is seen from Schlömann's equation (17): $\Delta H = \Delta H_x + |K_1/M_s| + 1.5\ (4\pi M_o)v/V$, where ΔH_x and M_o are for a single crystal, and v/V is the pore/sample volume ratio. Thus, ΔH was a function of density d, which depends on the severity of hot-pressing. The latter also affected t (Fig. 12a). The measured $4\pi M_s$ (Fig. 12b) was in fairly good agreement with that calculated (triangles) from d and $4\pi M_o = 3320$ gauss (17). On the other hand, ΔH deviated at higher t and d values from those calculated. (Fig. 12c). ΔH_x was taken as 70 Oe (17). The importance of this minimum in ΔH is seen from its correspondence with that in X" (Fig. 13d). Thus the lowest losses occurred near t = 0.18 micron.

The most important result was that the critical field h_c varied generally inversely to t (Fig. 13e). In three cases (arrows) h_c still had not been exceeded at the maximum available power in the pressurized cavity ($h_{rf} = 105$ Oe). The crosses represent conventional values; in Fig. 13e', the conventional $h_c = 16$ Oe. Subsequent annealing, which increased t, tended to reduce h_c and X" (Fig. 12c', 13d', e'; increase in t not shown). Of practical interest is a summary of peak power P attained along with the cost in X" (Table I). The highest P (> 2750 Kw) is about half the limit for an X-band waveguide.

TABLE I. POWER AND LOSS vs. CRYSTALLITE SIZE

t (micron)	Large	> .35*	> .13*	.18	.16
P (Kw)	65	225	400	> 1400	> 2750
X"	.03	.05**	.07**	.15	.6

*Annealed **At High Power Level

Finally, a qualitative explanation of the above dependence of h_c (really, ΔH_k) on t will be offered. To do this, the aforementioned graph of Suhl (16) was used, along with h_c, to determine ΔH_k for the two different biasing fields used (Table II).

TABLE II. ΔH_k vs. CRYSTALLITE SIZE

t (micron)	30	> .35	.35	.25	.18	.13
ΔH_k (1500 Oe)	32	51	79	87	111	83
ΔH_k (2000 Oe)	32	57	105	129	179	142

The general increase in ΔH_k with smaller t can be explained with the aid of Fig. 14, which shows Suhl's sp. w. spectrum (18). The solid curves indicate the sp. w. band for H_{dc} of 1500 Oe. H is the intersection of the loci for the important sp. w. frequency $\omega/2$ (i.e., half the pump frequency) and for the important sp. w. direction $\theta = \pi/4$. The vertical line ($2\pi/t$) stands for the sp. w. whose λ

equals t. As t decreases, this line moves from the left side toward the important sp. w. H. The closer it gets (for example, as shown), the greater will be the interaction between the inhomogeneity and the sp. w. (19), and this will broaden the sp. w. linewidth ΔH_k. If now the H_{dc} is increased to 2000 Oe, all the sp. w. frequencies are increased (dashed curves). At the same time, the locus of the important spin waves moves to H', i.e., even closer to $2\pi/t$. Thus, the sp. w. interaction with the inhomogeneity increases further, increasing ΔH_k more. This explanation seems to fit the general trends shown in Table II. Greater weight has been placed tacitly on the shorter sp. w. λ's, near 0.15 micron, than on the long ones, since the density of sp. w. states in k-space increases as k^2, or $(2\pi/\lambda)^2$.

TEMPERATURE DEPENDENCE OF INITIAL PERMEABILITY

Although ferrites are generally more suitable than powdered Fe for inductors above 5 Mc/s, because of greater μ' (same as μ_o) and Q, they are generally replaced by the latter in selective circuits due to the overall stability required. Tuners for military communications at this frequency commonly set overall drift limits on μ' of $\pm 0.2\%$ over -65° to 85°C. Miniaturization and stability are goals toward which we have been working. In the ultra-fine crystallite approach, we have been guided by the standard theory that domain walls can increase μ' by subdividing finer and finer with temperature T. This mechanism implies an increased temperature coefficient (T.C.) of μ'. But if the crystallites are fine enough, this mechanism should not exist. Based on many samples, this appears to be correct (Fig. 15a). For the $Ni_{.5}Zn_{.5}Fe_2O_4$ shown, t = 0.09 micron and d = 4.69 g/cm^3. Its slope is an order of magnitude less than the conventional one.

On an enlarged scale (Fig. 15b) one can see two peaks, one at T_c (which is anomalously high) and another near 0°C. If the cause of the latter were known, it might be controlled to provide T.C. = 0 by adjusting the height and separations of the two peaks. We already have evidence that increasing t increases the relative height of the Curie peak. Many samples with T.C. near 0 have been made, while 0.02%/°C is common. The one shown in Fig. 16 is $Ni_{.5}Zn_{.5}Fe_2O_4$ (t=.014 micron, d = 94% of theoretical). Its tolerance of $\pm 0.25\%$ means it does not drift more than that over -45° to 85°C. Precision in the measurements is estimated to be about $\pm 0.01\%$. Its comparison with commercial (same frequency range) and conventional ferrites (same composition) is shown. Although its T.C. is lower, its Q is also lower. Compared to stable powdered Fe, its $\mu'Q$ is 3 times higher. In an air-gapped pot-core, then it should have a miniaturization capability of about three, with greater $\mu_{eff} = 30$, similar Q = 130 and lower drift = $\pm 0.06\%$. This is less than the $\pm 0.16\%$ for the above core whose T.C. is only 0.0025%/°C. The comparison just made for our best sample can be looked upon only as an indicator of a potential for stable miniaturized inductors. Reproducibility is presently not completely satisfactory and requires some effort.

CONCLUSIONS:

A novel process was devised to obtain magnetic ferrites in previously unobtainable combinations of ultra-fine crystallite size (0.1 micron) and high density (98% of theoretical). These single domain size crystallites made it possible to show that domain rotation is the predominant magnetization mechanism in conventional Ni- and NiCo-ferrites, while domain wall motion predominates in NiZn-ferrite. Magnetic poles on domain walls accounted for the microwave peak in the rf dispersion of μ, while results for the rf peak were in good agreement with rotation theory. A more detailed analytical expression for the microwave peak was derived, which gave good agreement with experiment.

More practical results were also obtained. Greater threshold fields h_c for the non-linear instabilities at high microwave powers were found. At X-band these correspond to a factor of 40, at least, in increased power level compared to conventional ferrites. The loss is somewhat high, but continued study of the loss mechanism at low biasing fields may improve it. Eliminating domain walls reduced the temperature coefficient of μ' by an order of magnitude. In a pot-core geometry a miniaturization capability of a factor of three over powdered iron, which is currently standard in rf selective circuits, was obtained.

REFERENCES

1. J. Smit and H. P. J. Wijn, Ferrites (John Wiley & Sons, New York, 1959), p. 63.
2. J. F. Wenckus and W. Z. Leavitt, Proc. Conf. on Magn. & Magn. Matls., 1956, AIEE Sp. Public. T-91, p. 526.
3. F. W. Jones, Proc. Roy. Soc. (London) 166, 16 (1938).
4. J. E. Pippin and C. L. Hogan, Sci. Rept. No. 1, Gordon McKay Laboratory of Applied Science, Harvard Univ. (April, 1959), p. 22.
5. J. Smit and H. P. J. Wijn, op. cit., p. 274.
6. D. Polder, Phil. Mag. 40, 99 (1949).
7. J. Smit and H. P. J. Wijn, op. cit., p. 269.
8. J. L. Snoek, Physica 14, 207 (1948).
9. J. E. Pippin and C. L. Hogan, op. cit., p. 22.
10. A. S. T. M. Standard Test for Density No. C373-56, 1956.
11. C. Kittel, Phys. Rev. 73, (1948) 155.
12. J. Smit and H. P. J. Wijn, Adv. in Electronics and Electron Phys. 6, 91 (1954).
13. R. F. Soohoo, Theory and Application of Ferrites (Prentice-Hall, Inc., Englewood Cliffs, New Jersey, 1960) p. 88.
14. E. Schlömann et al, J. Appl. Phys. 31, 386 (1960).
15. H. Suhl, Proc. I. R. E. 44, 1272 (1956).
16. Ibid, J. Phys. Chem. Solids 1, Fig. 1, 218 (1957).
17. E. Schlömann, Proc. Conf. on Magn. and Magn. Matls. (1957) p. 600.
18. H. Suhl, op. cit., p. 220.
19. B. Lax and K. J. Button, Microwave Ferrites and Ferrimagnetics (McGraw-Hill Book Co., Inc., N.Y., 1962) p. 166.

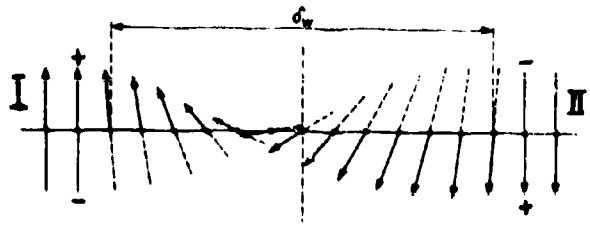

Fig. 1 Magnetic Domain Wall

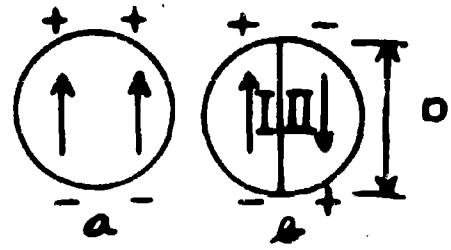

Fig. 2 Critical Grain Size

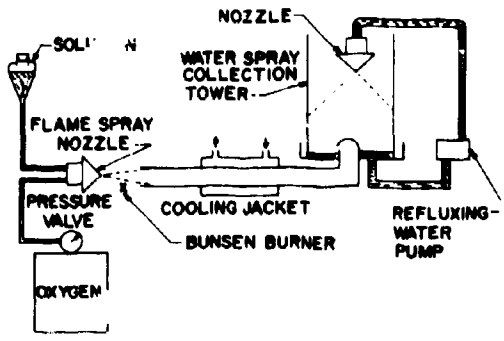

Fig. 3 Flame-Spray (Schematic)

Fig. 4 Flame-Spray Nozzle (Shown Operating)

Fig. 5 Electron Micrograph of Flame-Spray Ferrite

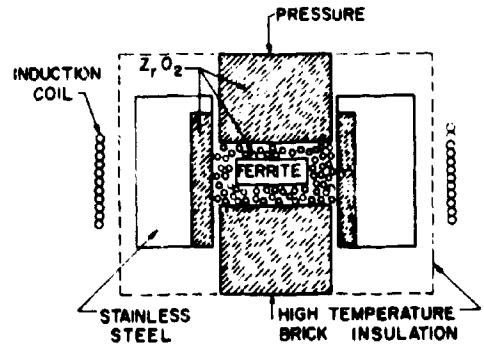

Fig. 6 Hot-Press (Schematic)

Fig. 7 Hot-Press (Shown Operating)

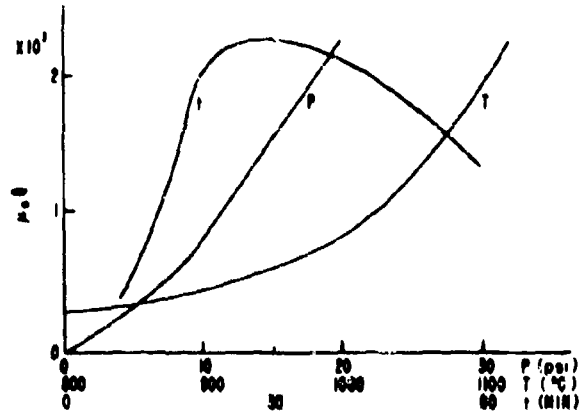

Fig. 8 $\mu_o Q$ vs Processing Parameters

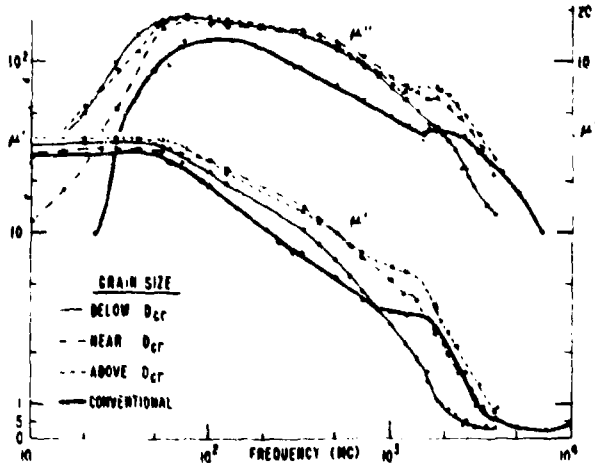

Fig. 9 R.F. Dispersion in Ultra-Fine $NiFe_2O_4$

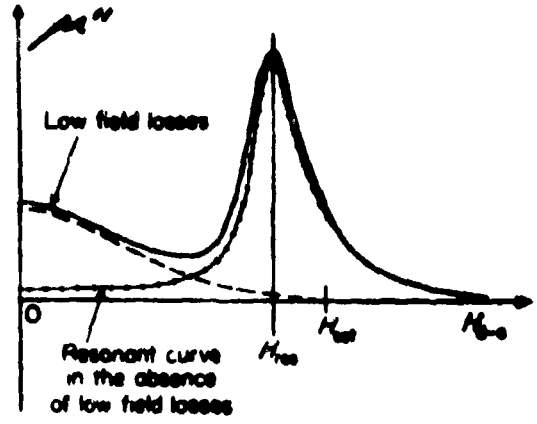

Fig. 10 Low Field Loss for Conventional Ferrites

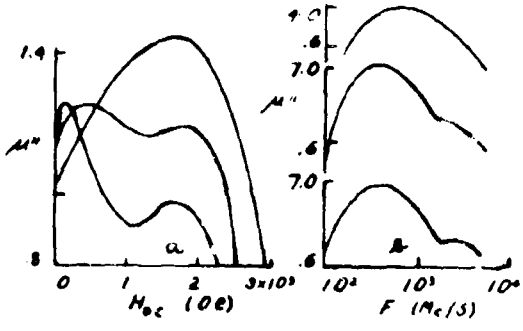

Fig. 11 a) Low Field Loss
b) R.F. Dispersion

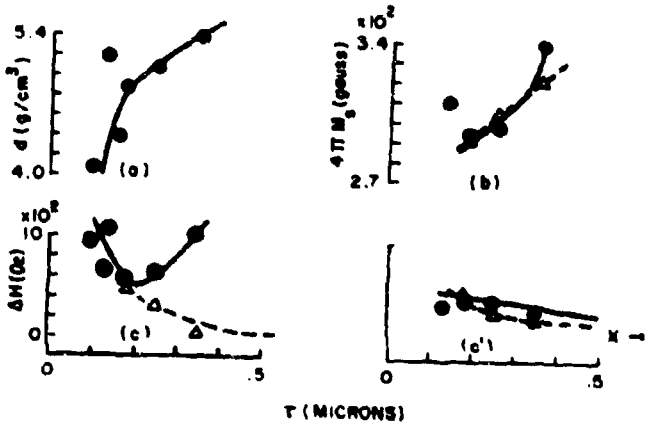

Fig. 12 ΔH, $4\pi M_s$, and Density vs. t

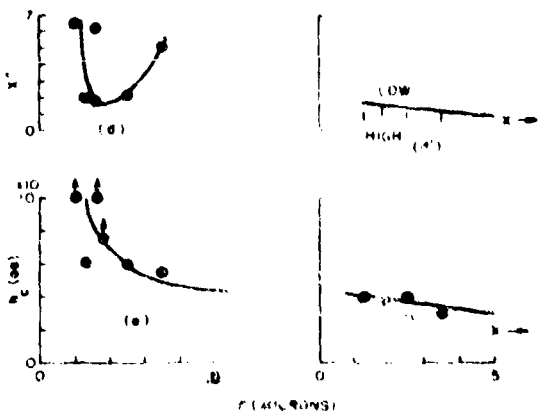

Fig. 13 h_c and X'' vs t

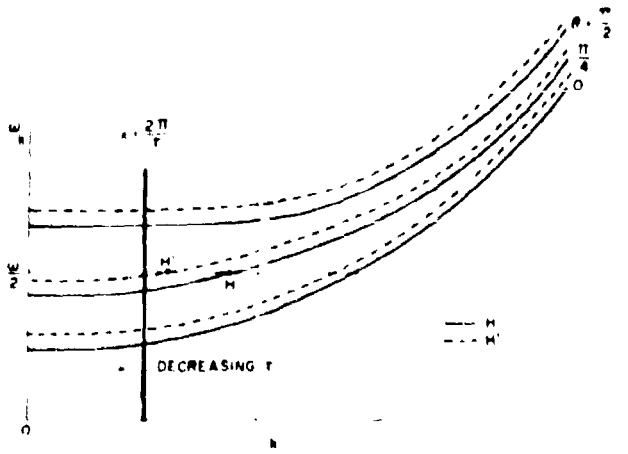

Fig. 14 Effect of H_{dc} on Spin-Wave Spectrum

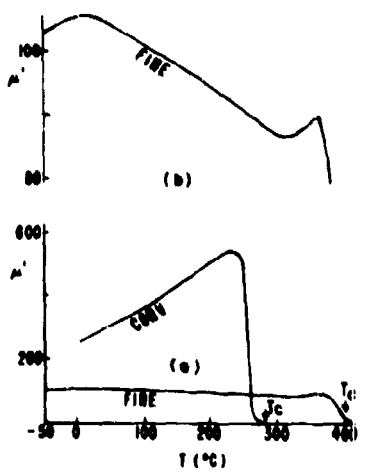

Fig. 15 Effect of t on T.C.

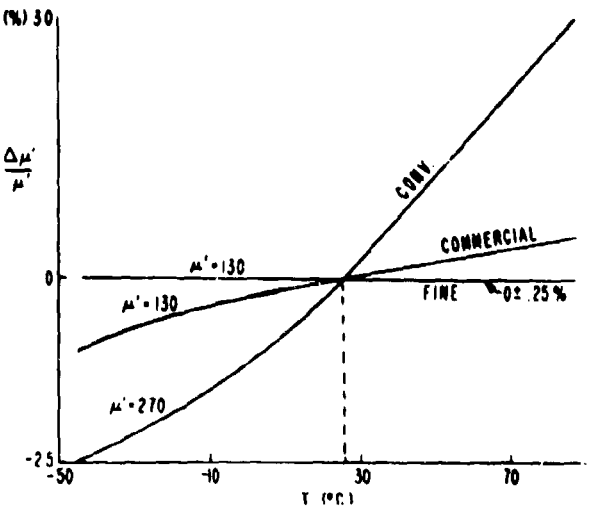

Fig. 16 Comparison of T.C. for Small vs Large t

EFFECT OF FILLER CONCENTRATION ON THE VISCOELASTIC RESPONSE OF A FILLED POLYMER SYSTEM

DONALD L. MARTIN, JR.
U. S. ARMY MISSILE COMMAND
REDSTONE ARSENAL, ALABAMA

The addition of solid inorganic filler particles to a polymeric material influences its physical response through adhesion of binder to filler particles (1), changes in crosslinked density (2,3), various hydrodynamic effects (4), and strain or stress concentrations produced about the filler particles (1). Therefore, the mechanical properties of composite solid propellants are dependent on the volume fraction of filler, the viscoelastic properties of the binder, and the interaction between the binder and filler particles. A program was conducted to determine the total effect of volume fraction of filler particles on various mechanical properties of the PBAA propellant system.

EXPERIMENTAL PROCEDURES: Five compositions of the PBAA polymeric system were prepared with filler fractions of 0, 21, 42, 63, and 84 percent, respectively, using the same lot of raw materials. The ingredients were those commonly used to make propellants. All compositions were cured at 140°F for 84 hours.

Test data were obtained with an Instron tensile tester, using end-bonded specimens approximately 1/2 in. square in cross section and 4 in. in length, and measured under uniaxial tension at constant strain rates. Crosshead rates of 0.2, 2.0, and 20.0 in./min. were used at various temperatures ranging from 180 to -90°F. As could be expected from the viscoelastic nature of the PBAA binder, the shape of the stress-strain curves was markedly affected by strain rate, temperature, and filler fraction. The strain energy density at failure was measured with an integrator used in conjunction with the Instron tester. The integrator reading, representing the area under the Instron load-time curve, was converted to strain energy density at failure by the expression

$$Q = \frac{(I)\ (F.S.)\ (C.H.S.)}{5000\ \ (V)} = \text{in.-lbs./in.}^3$$

where Q = strain energy density at failure
I = integrator reading
F.S.= full-scale load in lbs.
C.H.S.= crosshead speed in in./min.
V = volume of sample in in^3

The 5000 figure is the integrator calibration count which represents full-scale load for 1 min. The integrator method was used because the gage length remains essentially constant with bonded-end-tab specimens (5). Stress calculated on the original cross-sectional area was converted to true stress by multiplying by the principal extension ratio λ, based on the assumption that Poisson's ratio is 0.5 (6). The modulus E is the initial slope of the corrected stress strain curve. The maximum stress σ_m, strain at break ϵ_b, modulus E, strain energy density at failure Q, and reduced stress-strain data were superposed satisfactorily according to the modified W.L.F. equation (7)

$$\log a_T = \frac{-C_1 \quad (T-T_s)}{C_2 + (T-T_s)} \qquad (2)$$

where a_T = shift factor relating time to temperature
T = test temperature
T_s = reference temperature
C_1 & C_2 = empirical constants determined from experimental data (for the PBAA system and a reference temperature of 73°F, C_1 = 6.12 and C_2 = 125)

The chosen reference temperature (T_s) was 73°F, and C_1 and C_2 were determined empirically to give the best fit to experimental values of log a_T. The experimentally-determined log a_T is the shift factor required to superpose various line segments of data on the reduced time axis, each segment being measured at a different constant temperature T. In Fig. 1 the experimental values of log a_T are shown to be in good agreement with those predicted by the modified W.L.F. equation represented by the solid line.

RESULTS: The resulting data are graphically illustrated for various relationships and conditions. Figures 2,3,4, and 5 show the logarithm of maximum stress, modulus, strain energy density, and strain capacity versus the logarithm of reduced time for the 0, 21, 42, 63, and 84 percent filler fractions. Figure 6 plots the logarithm of reduced stress versus the logarithm of reduced strain for each of these filler fractions, and thus represents the stress-strain relationship in the initial portion of the stress-strain curves. Each curve was shifted by an amount A for convenience in presentation. The stress, modulus, and strain energy density data were correlated with the net cross-sectional area of the binder by dividing by $(1 - \phi)$, where ϕ represents the volume fraction of filler particles present in the system.

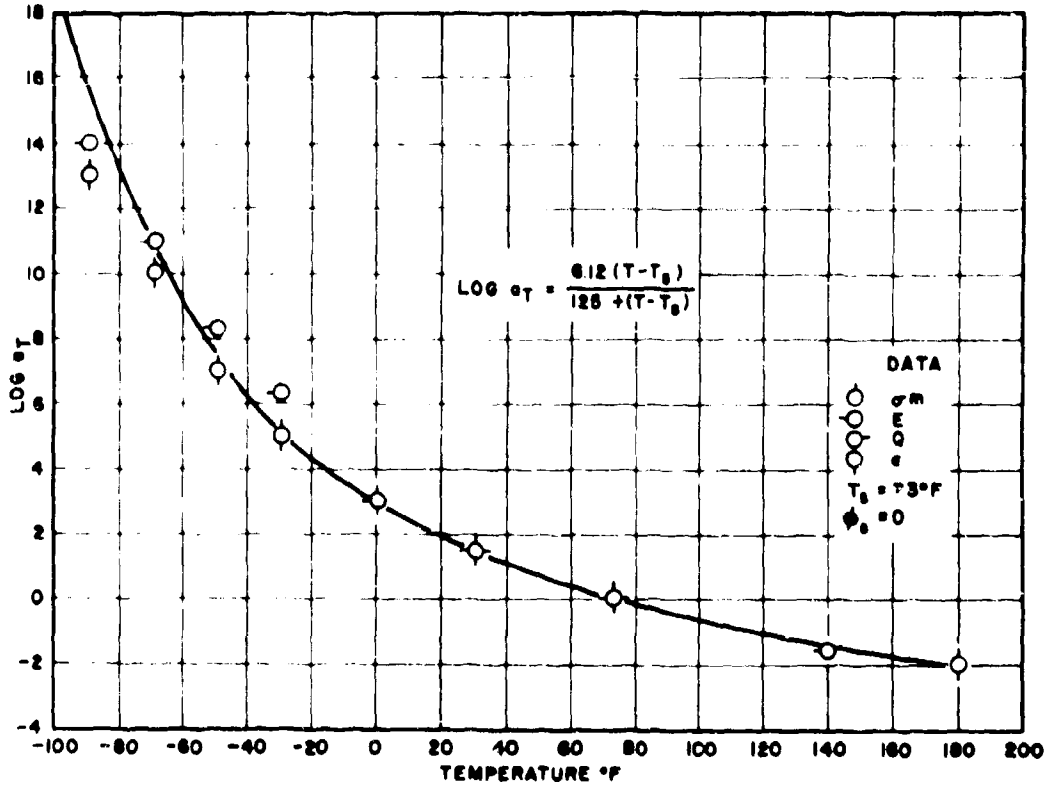

Fig. 1. a_T VERSUS TEMPERATURE

Figures 2, 3, 4, and 5 indicate the dependence of the logarithm of maximum stress, modulus, strain energy density, and strain capacity, respectively, on the filler fractions ϕ at constant values of the logarithm of reduced time, and show the variation of these properties with filler fraction at a given strain rate and temperature.

Maximum Stress, Modulus, Strain Energy Density, Stress-Strain Relationship: These four mechanical properties are affected in a similar manner by the addition of filler particles, and will be discussed as a group.

As shown in Figs. 2, 3, and 4, the addition of filler particles to the PBAA polymeric system increases the stress, modulus, and strain energy density of the binder. It was observed that a shift of the data to lower values of reduced time would permit superposition into a mechanical response spectrum representing the response of the system at some selected temperature and filler fraction over an extended time scale. The analogy noted between the shift factor relating time to temperature and the one suggested here relating time to volume fraction of filler led to the following formula:

$$\log a_\phi = \frac{B_1 (\phi - \phi_s)}{B_2 + (\phi - \phi_s)}$$

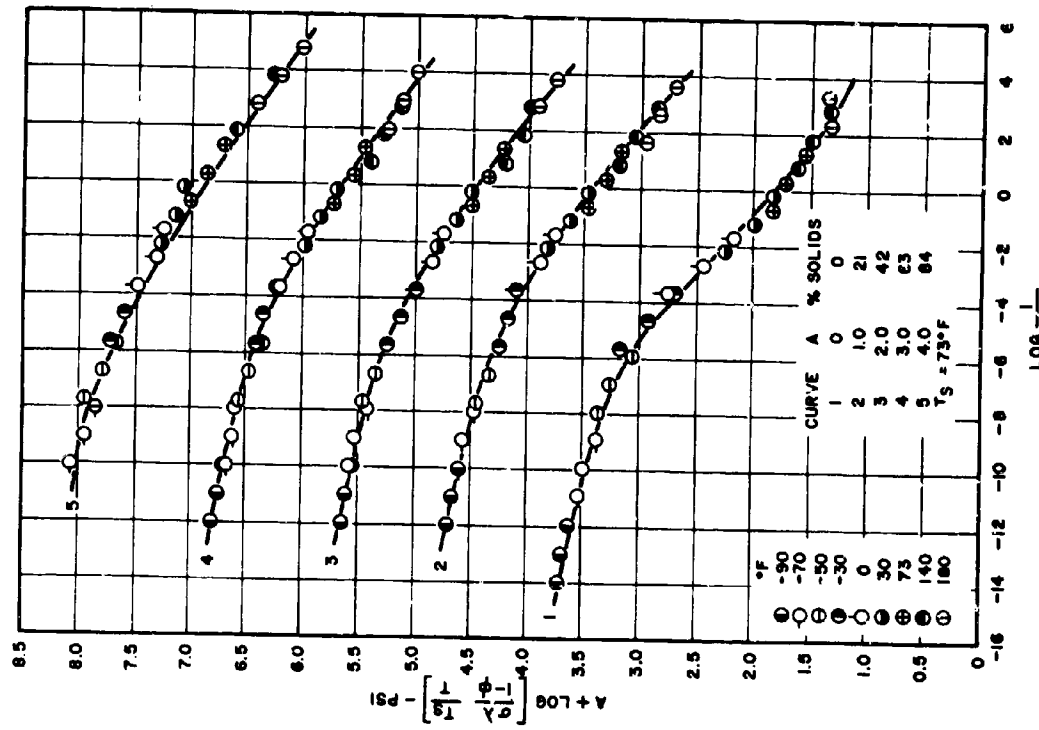

Fig. 2. MAXIMUM STRESS VERSUS REDUCED TIME

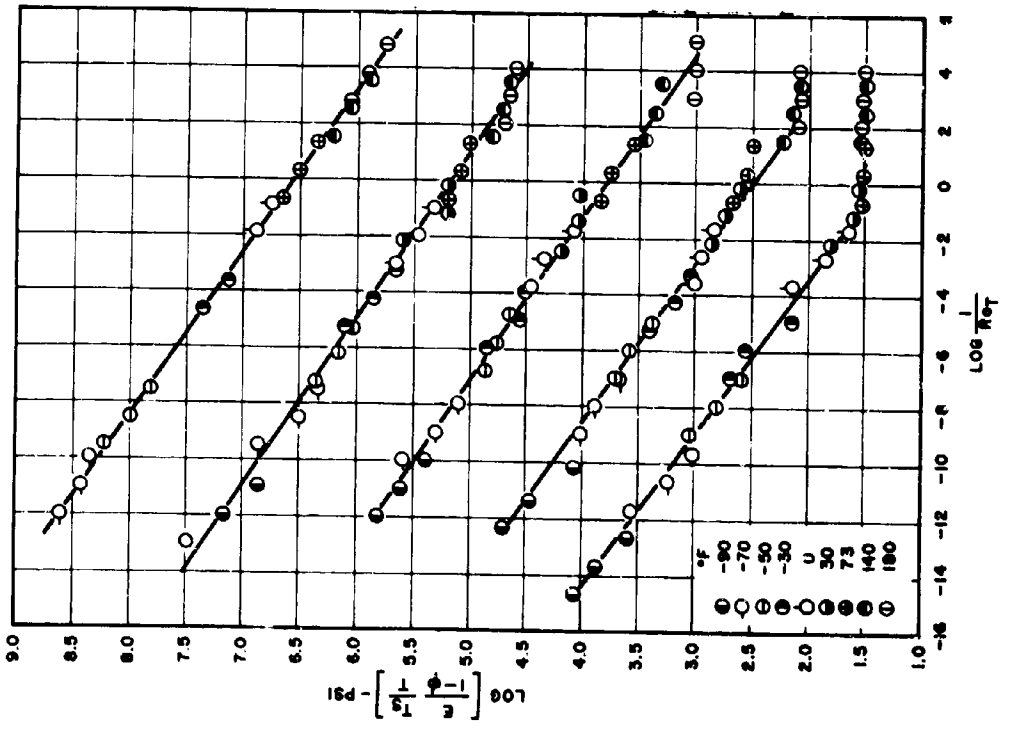

Fig 3. MODULUS VERSUS REDUCED TIME

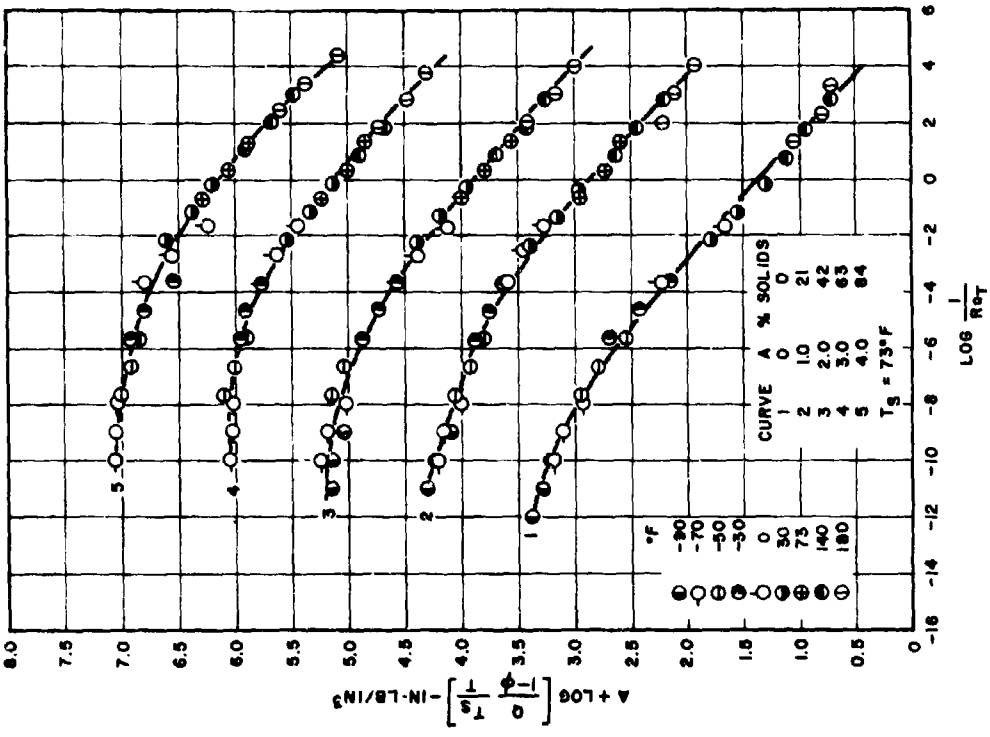

Fig. 5. STRAIN CAPACITY VERSUS REDUCED TIME

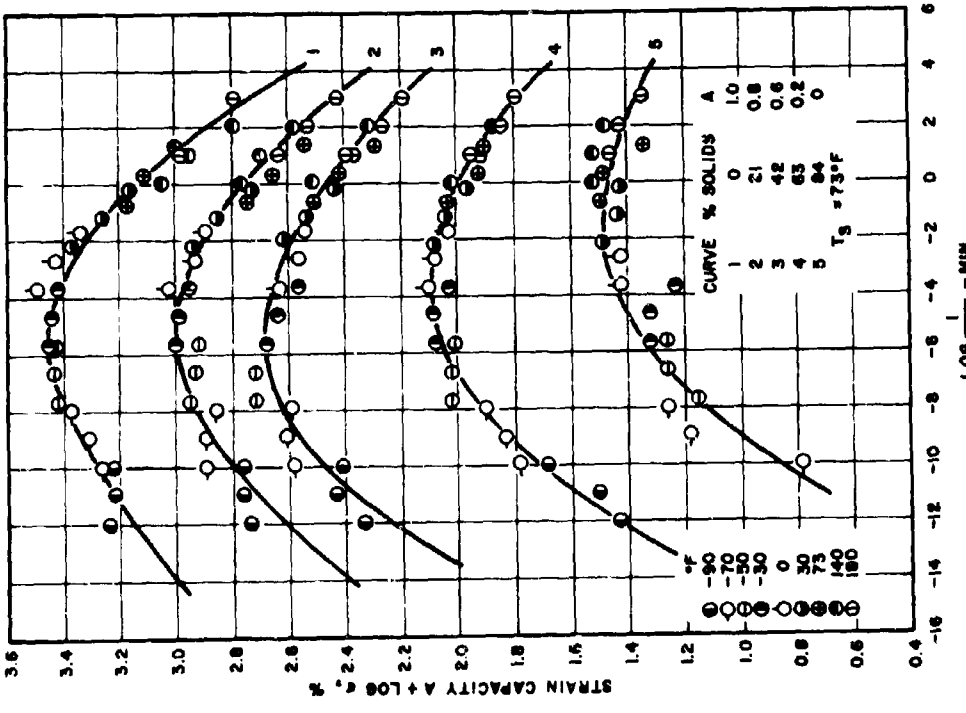

Fig. 4. STRAIN ENERGY DENSITY AT FAILURE VERSUS REDUCED TIME

where a_ϕ = filler fraction shift factor
ϕ = volume fraction of filler
B_1 & B_2 = empirical constants determined from experimental data
ϕ_s = reference filler fraction

Inverting Eq. (3) yields the following expression:

$$\frac{1}{\log a_\phi} = -\frac{B_2}{B_1}\,\frac{1}{(\phi - \phi_s)} + \frac{1}{B_1} \tag{4}$$

and the plot of $\frac{1}{\log a_\phi}$ versus $\frac{1}{(\phi - \phi_s)}$ then yields a straight line of slope $\frac{B_2}{B_1}$ and an intercept $\frac{1}{B_1}$. From Fig. 7, which treats data in this manner, the following values can be calculated for the PBAA system:

$$B_1 = \frac{1}{\text{intercept}} = 12.5$$

$$B_2 = \text{slope } B_1 = 1.45$$

Substituting these values in Eq. (3) will result in the following expression for the PBAA system:

$$\log a_\phi = \frac{12.5\,(\phi - \phi_s)}{1.45 + (\phi - \phi_s)} \tag{5}$$

Figures 8 and 9 show the maximum stress, or $\log\left[\frac{\sigma_m\,\lambda}{1-\phi}\,\frac{T_s}{T}\right]$ and the logarithm of strain energy density, or $\log\left[\frac{Q}{1-\phi}\,\frac{T_s}{T}\right]$, respectively, versus the logarithm of doubly reduced time, $\log \frac{1}{a_\phi\, Ra_T}$; Fig. 10 respresents the logarithm of modulus $\log\left[\frac{E}{1-\phi}\,\frac{T_s}{T}\right]$ versus the logarithm of doubly reduced time $\log \frac{1}{a_\phi^{2.5}\, Ra_T}$; Fig. 11 represents the logarithm of the doubly reduced stress, $\log\left[\frac{\sigma\,\lambda}{1-\phi}\,\frac{T_s}{\phi^{2.5} Ra_T}\right]$, versus the logarithm of the doubly reduced strain, $\log \frac{\epsilon}{\phi^{2.5} Ra_T}$, and is referred to as the doubly reduced stress-strain curve. These graphs illustrate dependence of the various properties on strain rate, temperature, and filler fraction. Good agreement was obtained between the experimental

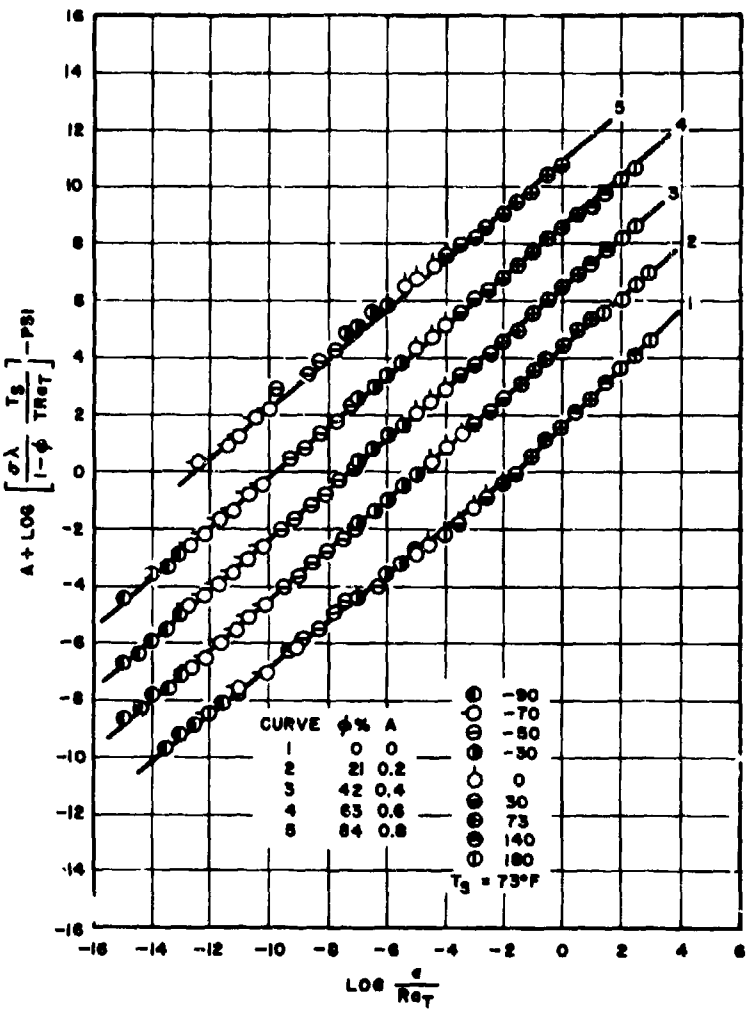

Fig. 6. REDUCED STRESS VERSUS REDUCED STRAIN

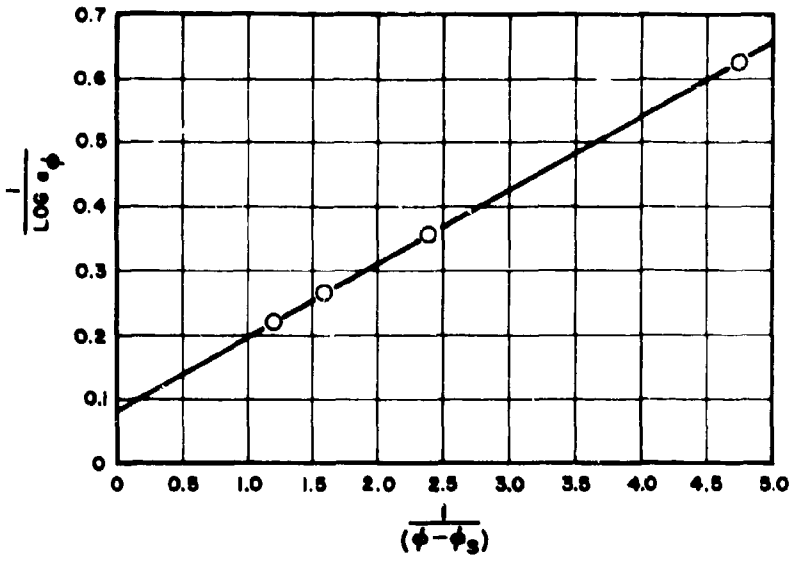

Fig. 7. $\frac{1}{\log a_\phi}$ VERSUS THE RECIPROCAL FILLER FRACTION

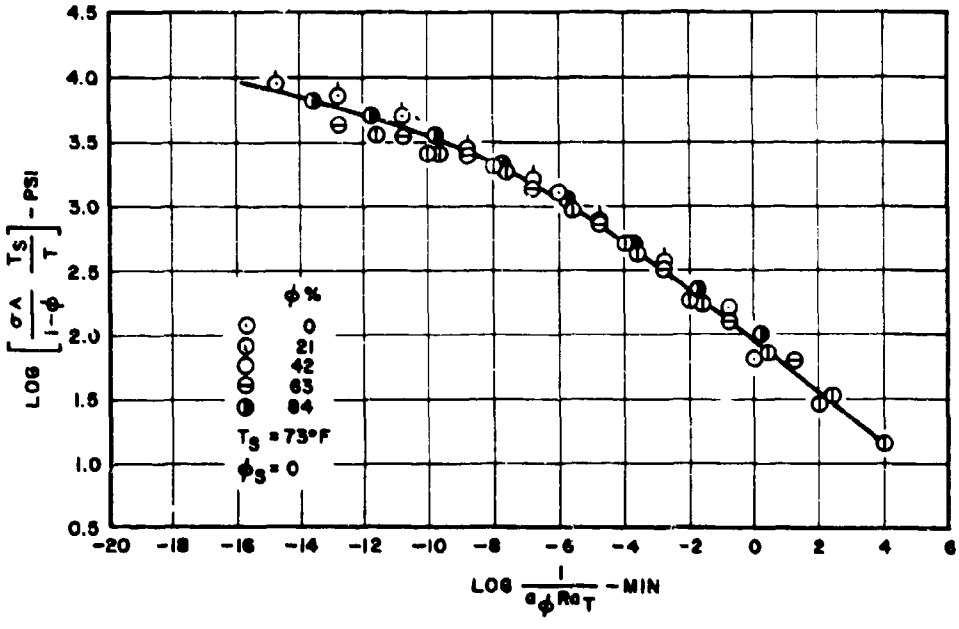

Fig. 8. MAXIMUM STRESS VERSUS DOUBLY REDUCED TIME

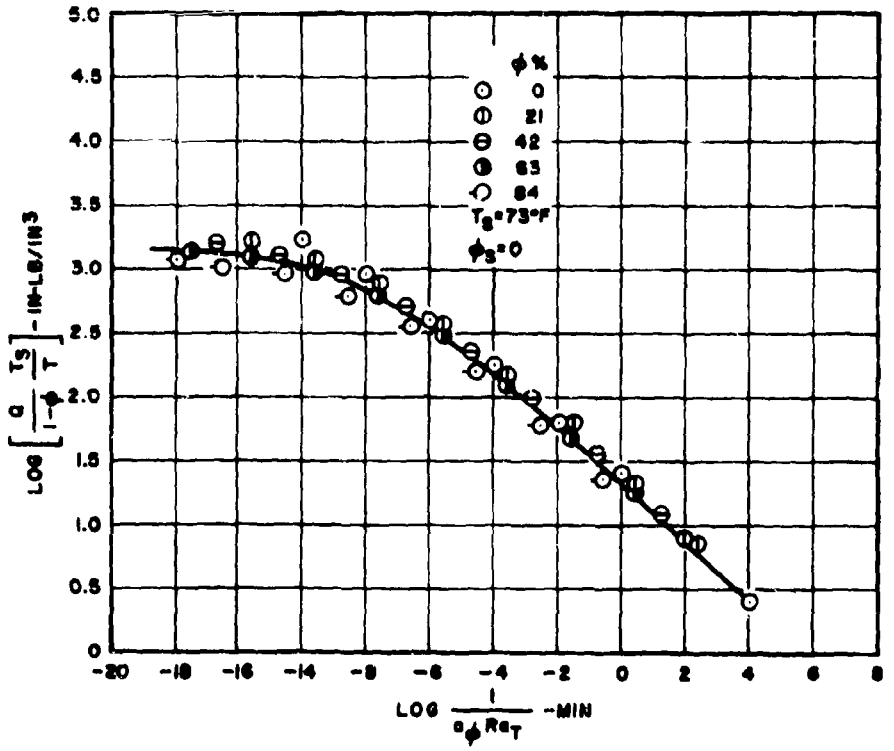

Fig. 9. STRAIN ENERGY DENSITY AT FAILURE VERSUS DOUBLY REDUCED TIME

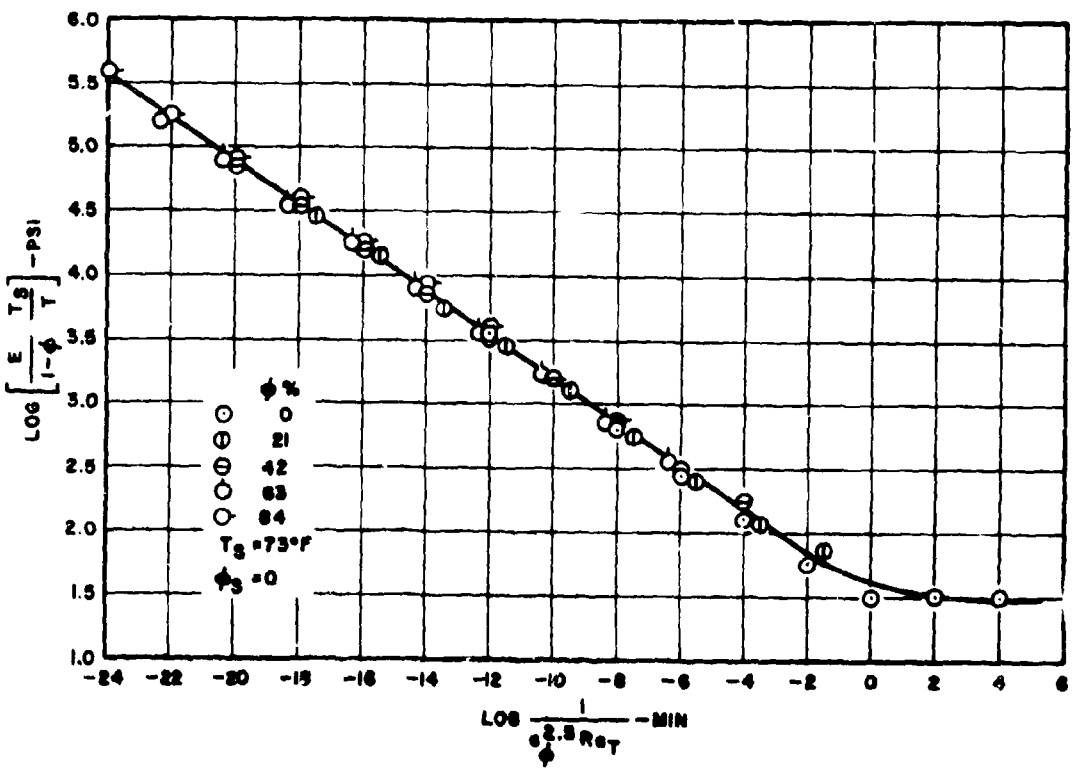

Fig. 10 MODULUS VERSUS DOUBLY REDUCED TIME

values of log a_ϕ and those calculated by Eq. (5). Figure 12 indicates the dependence of log a_ϕ on the filler fraction ϕ, with the solid line representing Eq. (5).

Superposition of the initial modulus and stress-strain data could not be achieved by applying the same shift factor as was used for the ultimate property data, because the mechanical properties of composite propellants depend on the degree of adhesion of the binder network chains to the surface of the filler particles, with the degree of adhesion in turn dependent on the extension of the sample (1). This relationship is substantiated by strain dilatometric studies which indicate that between zero and some critical strain no volume change occurs (6). At greater strains some dewetting occurs, due to failure of the adhesive bonds between the binder and filler particles, and this dewetting phenomenon is likewise dependent on extension of the sample. Therefore, as expected, the effect of filler fraction is more pronounced on mechanical properties in the initial portion of the stress-strain curve (Figs. 3 and 6) than on properties near failure (Figs. 2 and 4). The effect of filler fraction (a_ϕ^i) on the initial stress-strain properties (little or no dewetting) may be approximated by the ultimate property data a_ϕ (dewetting phenomenon believed to be completed) raised to the 2.5 power. This may be stated mathematically as follows:

$$a_\phi^i = a_\phi^{2.5} \qquad (6)$$

where a_ϕ^i is the effect of filler fraction on modulus and initial stress-strain relationship, and a_ϕ is the effect of filler fraction on the ultimate property data.

Ultimate Strain: In the literature on viscoelasticity, various mechanical models composed of springs and dashpots have been used to represent the viscoelastic properties and describe the response of different materials (7). The springs represent the elastic components, and the dashpots the viscous or time-dependent components. The addition of rigid filler particles tends to change the response of a viscoelastic medium through increased viscosity and stress and/or strain concentrations about the filler particles (1,8). Both factors tend to reduce the strain capacity of a viscoelastic medium. The decrease in the strain capacity of the PBAA system with addition of filler particles at a given strain rate and temperature is presented in Fig. 5. Although the curves (Fig 5) could not be superposed by using the a_ϕ factor, it was observed that the master curve representing the strain capacity of the PBAA system versus strain rate, temperature, and filler fraction could be achieved by use of vertical and horizontal shift factors (Fig. 14). The ratio of the horizontal shift to the vertical shift required for optimum superposition was 4 to 1, and implied the following relationship:

$$\log a_\eta = 4 \log \beta \qquad (7)$$

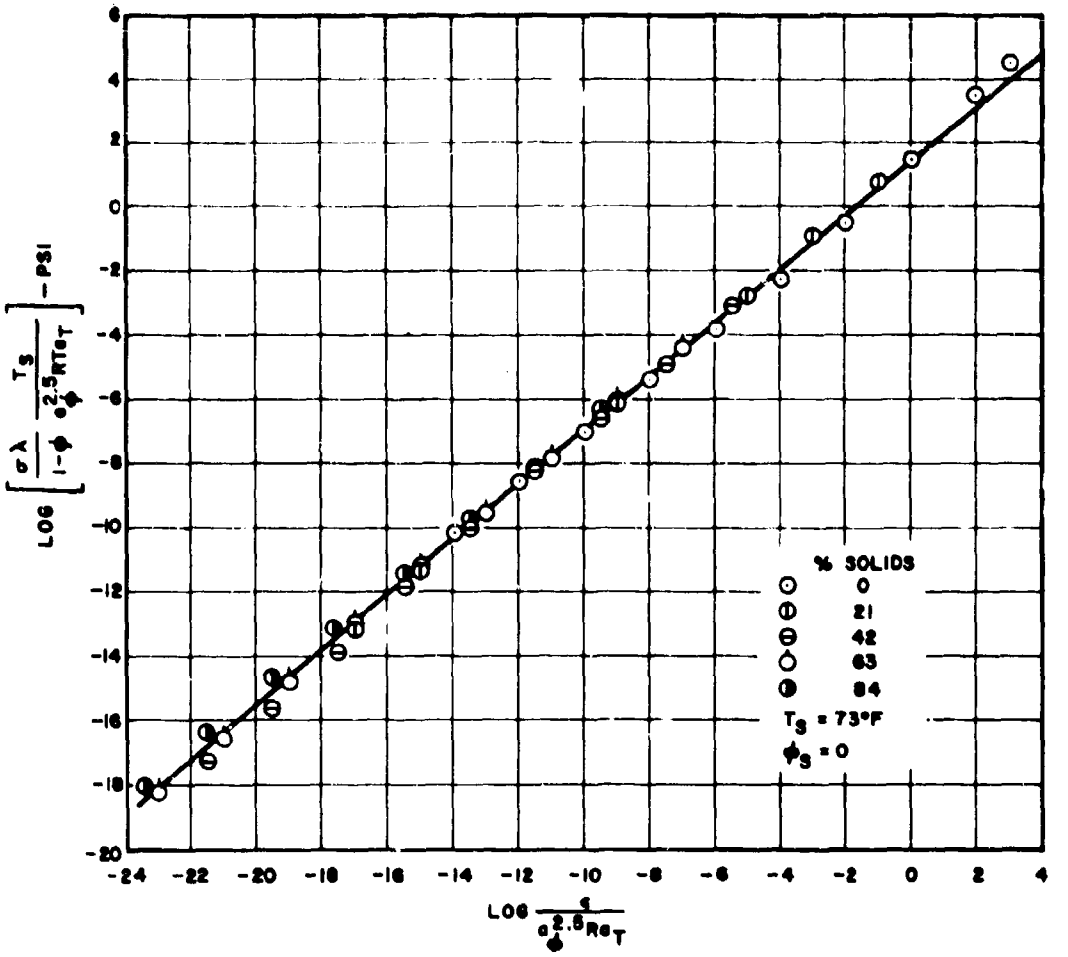

Fig. 11. DOUBLY REDUCED STRESS DOUBLY REDUCED STRAIN

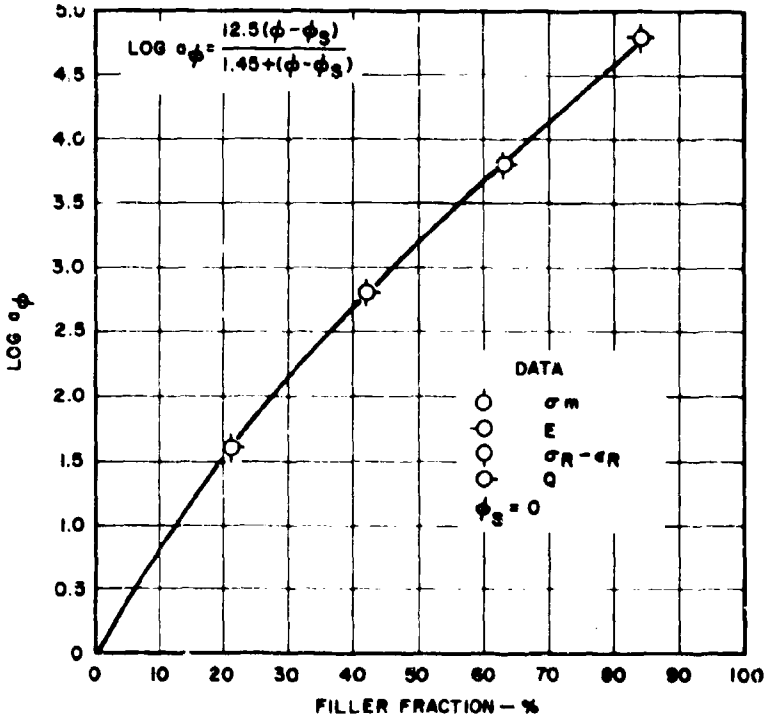

Fig. 12. a_ϕ VERSUS FILLER FRACTION

where a_η is the shift factor along the horizontal or reduced time axis, and β is the shift factor along the vertical or strain capacity axis. If we assume that a_η represents the shift factor associated with the apparent changes in the viscous component of strain which accompany changes in filler fraction, then β can represent the reciprocal of the strain concentrations induced by filler particles. This is implied in the fact that once the data have been shifted along the reduced time axis to account for changes in the viscous component with addition of filler particles, use of the factor β would superpose the strain capacity data for a given filler fraction over the full time spectrum. This can be expressed:

$$\log \epsilon_o = \log \epsilon_\phi \beta \tag{8}$$

or in terms of strain concentration factors,

$$\epsilon_\phi = \epsilon_o \left(\frac{1}{\beta}\right) \tag{9}$$

where ϵ_ϕ = the strain capacity for PBAA with a particular filler fraction, ϕ

ϵ_o = the strain capacity for PBAA gumstock at the same doubly reduced time, $\log \frac{1}{a_\eta \; Ra_T}$

$\frac{1}{\beta}$ = the strain concentration factor

The following empirical formula was derived for the dependence of the strain concentration factor $\frac{1}{\beta}$ on the filler fraction.

$$\frac{1}{\beta} = 0.780 - 0.790\ (\phi) \text{ for } \phi > 20\% \tag{10}$$

This equation will predict the strain concentration factor for PBAA composites with filler fractions greater than 20 percent. The experimental points in Fig 13 imply that with filler fractions greater than 20 percent the strain concentration factor $\frac{1}{\beta}$ is linearly dependent on the filler fraction. If this behavior is usual for PBAA composites in general, the values of $\frac{1}{\beta}$ and a_η can be estimated from Eqs. (7) and (10).

For predicting the strain concentration factor for composites ites with filler fractions of less than 20 percent, Eq. (11) proposes a relation based on a modification of Einstein's viscosity law with various shape factors. This method has been suggested by Guth (8) for other properties. The shape factor takes into account various agglomerations of filler particles and presumably could depend on the filler fraction in the system.

$$\frac{1}{\beta} = \frac{\epsilon_\phi}{\epsilon_o} = 1 - \frac{2.5\phi}{1 + 1.5\phi}$$

where $\left(\frac{2.5}{1-\phi}\right)$ is interpreted as the form factor and the other symbols have the same definition given previously. With this equation the strain concentration factor $\frac{1}{B}$ for a 20-percent filler fraction is the same as that obtained with Eq. (10), and approaches the value of 1.0 as the filler fraction approaches zero. The two equations were applied to the [illegible] from Fig. 5 to plot the master curve in Fig. 14, which thus represents the strain capacity of the PBAA binder system versus strain rate, temperature, and filler fraction, over an extended time scale.

Failure envelopes for PBAA with various filler fractions are presented in Fig. 15 as the logarithm of maximum stress, $\log\left(\frac{\sigma_m \lambda}{1-\phi}\frac{T_s}{T}\right)$, versus the logarithm of the strain capacity, $\log \epsilon_b$. These data indicate the critical stress-strain combination for uniaxial failure and the effect of filler fraction on this relationship.

CONCLUSIONS: The addition of filler to the PBAA polymeric system increases the maximum stress, modulus, strain energy density, and stress-strain properties, with a corresponding decrease in the strain capacity. The same time-temperature shift factor, $\log a_T$, can be satisfactorily applied to all formulations of the PBAA system investigated. The logarithm of maximum stress and strain energy density at failure for all filler fractions can be represented as the respective response spectrum when plotted versus the doubly reduced time. The time scale is shifted once by the amount $\log a_T$ to account for the different temperatures, and once by $\log a_\phi$ to account for the different filler fractions. The logarithm of the time-temperature shift factor and the filler fraction shift factor can be calculated by the modified W.L.F. type equations, (2) and (5). Response spectrums of the modulus and the reduced stress-strain data for all filler fractions can be constructed by use of the doubly reduced time, provided the logarithm of the filler fraction shift factor as obtained from the ultimate properties is multiplied by 2.5. This factor accounts for the difference between the binder-filler interaction at small strain, where only minor dewetting has occurred, and that at the ultimate strain, where major dewetting of the filler particles has occurred (6).

The decrease in the strain capacity due to the addition of filler particles can be empirically treated by introducing a strain concentration factor $\frac{1}{B}$ on the strain capacity axis and a viscous component factor a_η on the doubly reduced time axis. For filled PBAA systems, it is proposed that these factors be predicted by Eqs. (7), (10), and (11). Using a combination of either these equations or Figs. 13 and 14 and the appropriate strain rates for low temperature equilibrium thermal shrinkage in a large composite propellant rocket motor results in the approximate rule that an additional 1-percent increase in filler fraction will result in 2-percent decrease in the propellant's strain capacity.

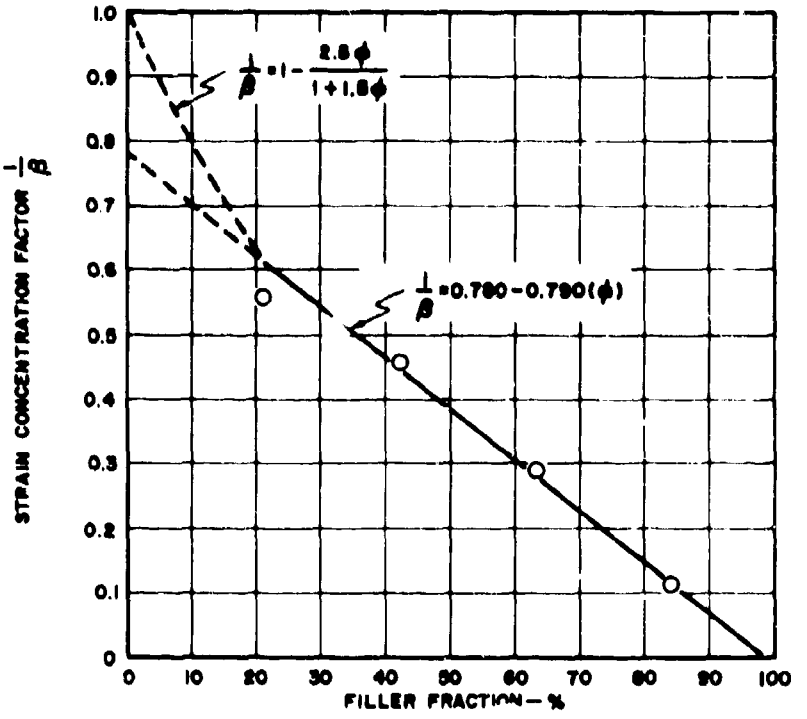

Fig. 13. STRAIN CONCENTRATION FACTOR VERSUS FILLER FRACTION

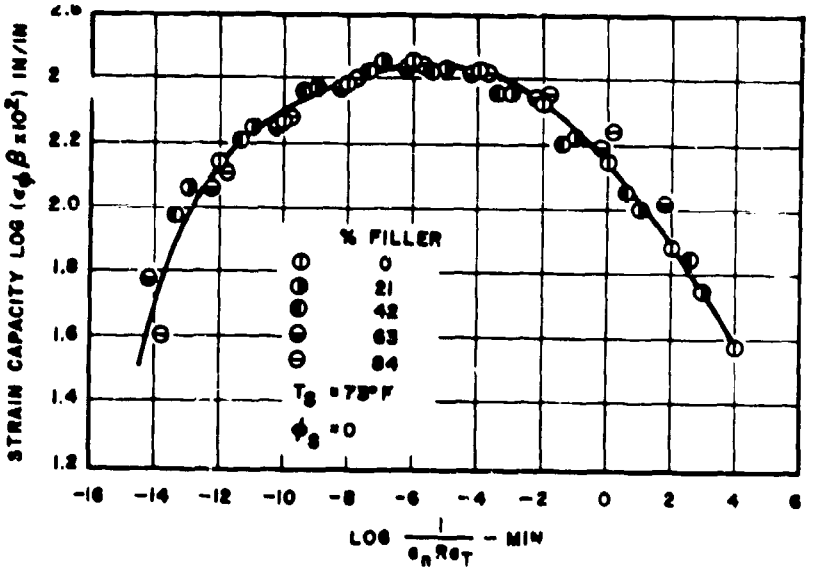

Fig. 14. STRAIN CAPACITY VERSUS DOUBLY REDUCED TIME

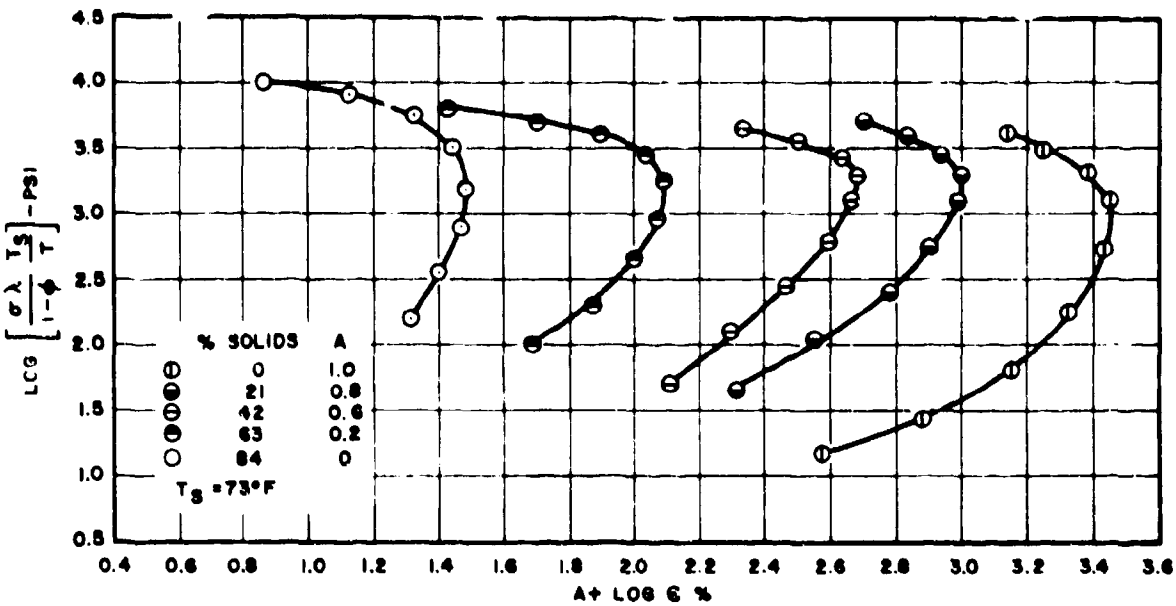

Fig. 15, STRESS VERSUS STRAIN CAPACITY

The data presented in Figs. 8, 9, 10, 11, and 13, along with Eqs. (2), (5), (7), (10), and (11), make it possible to estimate the mechanical response of the PBAA propellant system at any desired strain rate, temperature, and filler fraction within the applicable time spectrum. The ability to predict this behavior should prove extremely valuable to both the design engineer and the propellant synthesizer.

REFERENCES

1. Sato, Y., and F. Junji, "A Molecular Theory of Filler Reinforcement Based on the Concept of Internal Deformation, "Rubber Chemistry and Technology, Vol. 25, 1962, 857-876

2. Janacek, J., "Reaction of Polymers in Bulk. I., Influence of Fillers on the Degree of Crosslinking of Natural Rubber," Rubber Chemistry and Technology, Vol. 25, 1962, 563-572

3. Janecek, J., "Reaction of Polymers in Bulk II. Influence of Crosslink Density on the Mechanical Properties of Filled Vulcanizates," Rubber Chemistry and Technology, Vol. 25, 1962, 572-580

4. Payne, A.R. and W.F. Watson, "Carbon Black Structure in Rubber," Rubber Chemistry and Technology, Vol. 26, 1963, 147-155

5. Brisbane, J.J. "Effective Gauge Length of Bonded End Tensile Specimens," Rohm & Haas Co. Research Div. Memo, Redstone Arsenal, Ala., 1963

6. Landel, R.F. and T.L. Smith, "Viscoelastic Properties of Rubberlike Composite Propellants and Filler Elastomers," American Rocket Society Journal, Vol. 31, 1961, 599-608

7. Ferry, J.D., Viscoelastic Properties of Polymers, John Wiley and Sons, Inc., New York 1961

8. Guth, E., "Theory of Filler Reinforcement," Journal of Applied Physics, Vol. 16, 1945, 20-25

THE STRENGTH OF PORTLAND-CEMENT CONCRETE AS AFFECTED BY AIR, WATER, AND CEMENT CONTENT

BRYANT MATHER
U. S. ARMY ENGINEER WATERWAYS EXPERIMENT STATION
JACKSON, MISSISSIPPI

Introduction

The sedimentary rocks known as conglomerate and breccia consist of sand and gravel or of fine and coarse broken rock bound together by a cementing medium. The art of making artificial conglomerate or breccia - concrete - has been known and practiced by builders for at least two millennia. Research to discover ways of making better or more economical concrete has been carried on throughout this period. Vitruvius, in the first century A.D., reported results of research indicating advantages to the use of organic materials such as lard as admixtures in concrete.

Air Entrainment

In about 1938 it was observed that concrete pavements made with portland cements containing tallow possessed superior resistance to frost damage. Between 1938 and 1942 it was found that improved frost resistance could be imparted to concrete by the use of a variety of organic admixtures; that these materials possessed the common characteristics of producing foams when the concrete was mixed; and that the improved frost resistance was the result of the presence of air bubbles distributed throughout the cement-paste portion of the concrete mixture. Since 1942 the relation of frost resistance and air entrainment has been extensively studied, and since 1944 the Corps of Engineers has generally required that air be entrained in concrete that would be exposed to freezing. Extensive studies have indicated that the amount of air needed for frost resistance is about 9 percent of the volume of the mortar fraction of the concrete or about 4-1/2 percent of the volume of a concrete mixture made using 1-1/2-in. coarse aggregate.

Strength

The strength of concrete depends on many factors, the most important of which, normally, is the relative weight of water used per unit weight of cement. With the intentional introduction of air as an ingredient of concrete mixtures, it was found, as might have been expected, that the strength tended to be reduced, and the mobility and workability of the mixture tended to be increased as air was added. Since no increase in mobility was normally needed, it was found that by using less water when air was added, the desired amount of air could be entrained without the increase in mobility and the strength-lowering effect of the introduced air could be partially or completely overcome. In mixtures of relatively low cement content, the change to the use of entrained air permitted greater relative reductions of water content to maintain but not increase workability than were possible with richer mixtures.

Optimum Air Content

Recently the Chief of Engineers authorized the U. S. Army Engineer Waterways Experiment Station to study mass concrete mixtures of low cement content, such as are used for the interior concrete in large dams where frost action is not a factor, to develop data on what might be their optimum air content. Such mixtures are now required to contain air, but the prescribed limits on air content have been those developed for achieving frost resistance.

Previous Results

From previously reported studies it was known that the strength of any concrete mixture would be lowered or raised by about 5 percent for each 1 percent of air-void volume that was added to or removed from it. From typical curves of the relationship of water-cement ratio and strength it was observed that, for a 5 percent change in strength, a change in water-cement ratio of 0.03 by weight would be required. It was thus apparent that, when, by the introduction of entrained air into a concrete mixture of otherwise satisfactory workability and strength-gaining properties, the water content is reduced 0.03 pounds per pound of cement for each percent of air introduced, changes in air content should be accompanied by no change in strength. If, on the other hand, the reduction of water content to maintain workability is less than 0.03 pounds per pound of cement per percent of air added, the strength will be reduced as the air content is raised, and

more cement will be needed in order to maintain strength and workability by permitting a further reduction of water-cement ratio. Finally, however, if the reduction of water content to maintain workability is more than 0.03 pounds per pound of cement per percent of air added, the strength will tend to be raised, and less cement will be needed to maintain strength and workability. The change of 0.03 pounds of water per pound of cement per percent of air is 0.048 cubic feet of water per cubic yard of concrete per 100 pounds of cement. As shown in Fig. 1, this means that water must be removed in the amount of 35.6 percent of the volume of air introduced into a mixture containing 200 pounds of cement per cubic yard, if no change in strength is to occur. As the cement content of the mixture is increased, the magnitude of change in volume of water as a fraction of the change in volume of air required to maintain strength increases.

Laboratory Work

Three concrete mixtures of different cement content were proportioned without the use of an air-entraining admixture. Each of these mixtures was then modified by the introduction of an air-entraining admixture in appropriately increasing amounts to cause entrained air contents of varying amounts up to 12 percent expressed as proportional volume of that portion of the mixture finer than a 1-1/2-in. sieve. In modifying each mixture, it was required that the cement content, the coarse aggregate content, the mortar content, and the workability be kept constant. Thus it was required that, as air was added, a volume of water plus fine aggregate be removed equal to the volume of added air. What the experiment was designed to determine was: (a) what the ratio of water to fine aggregate was in the volume of water plus fine aggregate that needed to be removed to keep the workability constant; (b) whether this ratio changed with change in air content for a concrete mixture of given cement content; and (c) whether this ratio changed for mixtures of different cement content.

Results

It was found that, for the three mixtures studied, the ratio of water to fine aggregate did not change with changes in air content for a concrete mixture of given cement content but did change, apparently linearly, with change in cement content. Specifically, it was found that, for the three cement contents studied, the ratios of water to fine aggregate, in the volume of water to fine aggregate that needed to be removed as the air content was increased, were as follows:

Cement Content lb/cu yd	Ratio of Water to Fine Aggregate, by Volume
235	60:40
376	50:50
442	45:55

Discussion

These relations are shown in Fig. 1. They indicate that for a concrete mixture containing 310 pounds of cement per cubic yard the amount of water removed per unit volume of air added is 0.03 pounds per pound of cement per percent air, the value calculated to be that at which the air content could be changed with no change in strength. It is also indicated that, for mixtures of higher cement content, the amount of water that can be removed will always be less than sufficient to compensate for the effect of the added air in reducing strength. Thus, for mixtures richer than 310 pounds of cement per cubic yard, the optimum air content will be the minimum consistent with other requirements, such as frost resistance. However, for lean concretes containing less than 310 pounds of cement per cubic yard, the optimum air content to achieve the desired strength at minimum cement demand will be the maximum that it is practical to obtain. The present requirement is 4.5 $\pm$ 1.5 percent in that part of the mixture finer than the 1-1/2-in. sieve. The laboratory results also suggest that, with mixtures such as those that were studied and an air-entraining admixture of the type employed, the practical limit of air entrainment will be in the range 9-12 percent air in the portion finer than the 1-1/2-in. sieve, since it appears that the amount of air-entraining admixture required for each additional percent of air to be entrained increases sharply in this range.

Summary

The strength of a particular sample of portland-cement concrete is the result of the interaction of many factors relating to the properties of the individual constituents, the proportions in which they have been combined, and the history of the concrete prior to the time at which its strength is of interest. One of the most significant of the factors affecting strength is the ratio of the quantity of water used to the quantity of cement used. With the use of air-entrained concrete to provide frost resistance, interest in the effects of air content on strength has developed. Most of the work done, however, has concerned minimization of reduction in strength at the air content level needed for frost resistance.

Air entrainment is also employed in concrete produced for use in the interiors of large dams. A question was raised as to the most desirable air content level for such concrete. Work done at the Waterways Experiment Station indicated that, for concrete mixtures of fixed cement content, workability could be maintained unchanged as the proportions of air:sand:water were changed. It was found that this could be done by removing or adding a volume of sand and water equal to the volume of air that was added to or removed from the mixture as the amount of air-entraining admixture used was increased or decreased. The ratio of water to sand in the sand and water volume added or removed was found to vary with the cement content of the concrete, from 60:40 to 45:55 in the tests made.

Previous work indicated that, if only the air content changed, the strength might be expected to be reduced by about 5 percent for each percent of air added. It was also indicated that strength would be expected to be increased about 5 percent for each reduction of 0.03 in water-cement ratio by weight. By combining these relationships with the test data, a relation was developed which suggested that for a concrete mixture containing about 310 pounds of cement per cubic yard the air content could be changed without changing the strength, but for richer mixtures the strength would tend to be reduced as the air content was raised, and for leaner mixtures the strength would tend to be raised as the air content was raised.

The hypothesis is therefore proposed that the most desirable level of air content for concrete containing less than about 310 pounds per cubic yard of portland cement is the maximum that could be practically attained and that the most desirable level for mixtures of higher cement content is the minimum that could be practically attained. The test results suggest that it may not be practical to entrain more than about 9-12 percent by volume of air in concrete containing large aggregate due to the quantity of air-entraining admixture required. Since many concrete mixtures of higher than 310 pounds per cubic yard cement content will be used where exposure to frost will occur, the minimum practical air content for these will be that which is required to produce frost resistance.

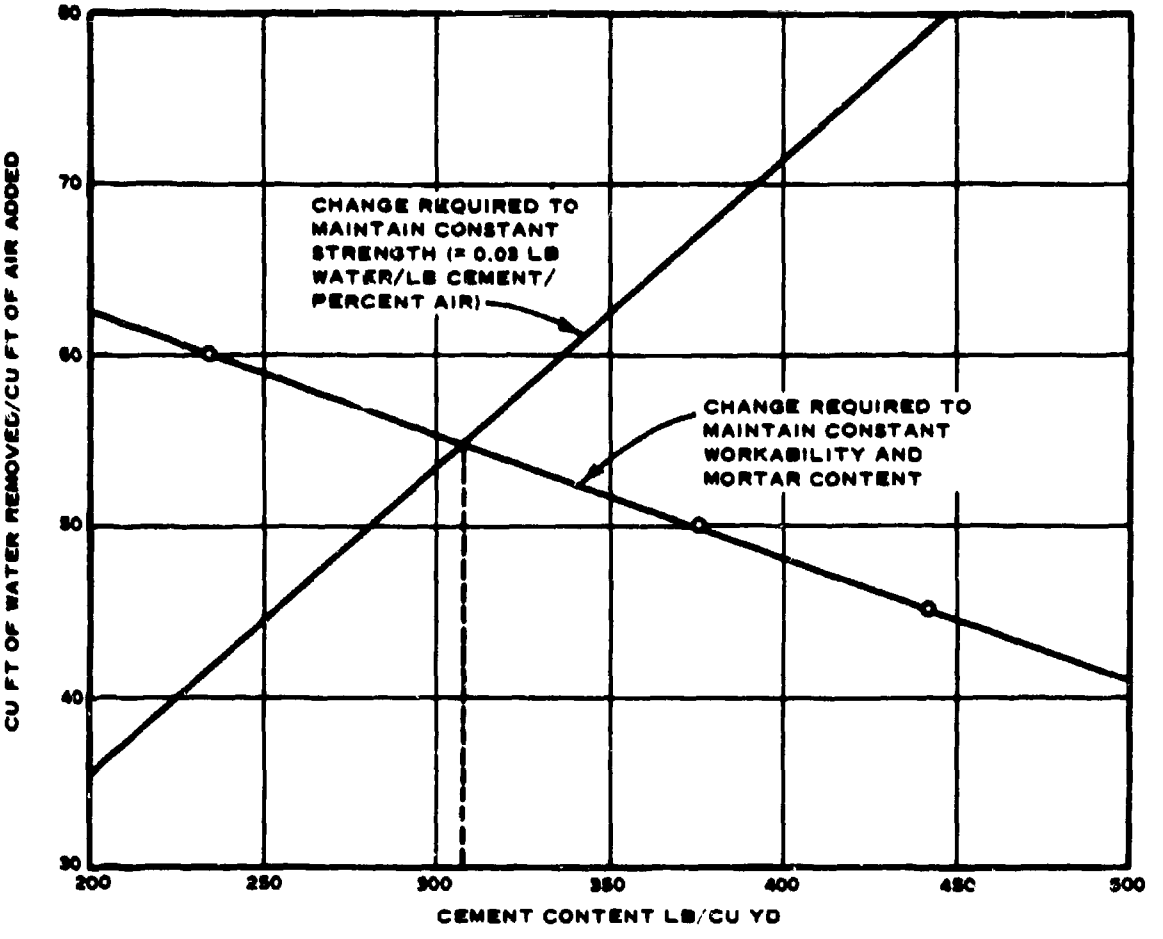

Fig. 1 - Effects of changes in air and water content on properties of concrete of different cement content.

RELAXATION PROCESSES IN FERROMAGNETIC INSULATORS

JOSEPH NEMARICH
HARRY DIAMOND LABORATORIES
WASHINGTON, D. C.

Ferromagnetic insulators such as ferrites and garnets have had wide application in many military microwave devices (1). In most of these devices the dissipative properties of these materials enter in a very important way. There has been considerable effort made during the past years to understand the details of the magnetic loss mechanism in ferromagnetic insulators. In particular there has been much discussion concerning the role of residual crystalline imperfections in the relaxation process. This latter point has special technological importance, since some measure of the role of crystalline imperfections will determine to what extent improvements in crystal growing techniques can influence device performance.

A parameter that indicates the combined effect of various relaxation processes is the linewidth of the ferromagnetic resonance absorption observed in materials of simple shapes, such as a sphere. Early calculations had indicated that direct coupling to the lattice of the long wavelength excitations induced in a magnetic resonance experiment was too weak to account for the linewidths observed. The discovery that there exists a large number of spin wave states having the same energy or frequency as (that is, degenerate with) the uniform precession of magnetization usually excited in magnetic resonance and that magnetic inhomogeneities can couple the uniform precession to these degenerate states led to the belief that coupling of the resonant mode to these degenerate spin wave states was primarily responsible for the ferromagnetic resonance linewidths observed. Several years ago, however, the experiments of Fletcher, LeCraw and Spencer (2) with the ferromagnetic insulator yttrium iron garnet (YIG) and the subsequent calculations of Kasuya and Le Craw (3) revised the notions of the magnetic resonance relaxation process in highly polished samples of this material. In figure 1 is shown a schematic representation of magnetic relaxation in YIG. The wavenumber $k = 2\pi/\lambda$, where λ is the wavelength of the spin wave. Fletcher, LeCraw and Spencer found that at room temperature if their sample

was not highly polished the primary channel of relaxation was via coupling to degenerate spin waves, whereas if the sample was highly polished the primary relaxation channel was via other processes. Kasuya and LeCraw (3) showed that with a reasonable assumption for the degree of local magnetostriction they could account for the rate of relaxation observed. The local magnetostrictive effect couples the resonant mode directly to the lattice as well as to spin waves. Subsequently it was shown (4) that at 4.2°K, coupling of the uniform precession mode to degenerate spin waves was still the predominant relaxation mechanism even in the highest polished pure YIG samples. The importance of paramagnetic impurities to the relaxation process (especially at temperatures below 100°K) has been demonstrated (5) and even in samples prepared from the highest purity material, it appears that there is a residual effect at low temperatures due to these impurities. Since relaxation rates are larger the higher the wavenumber k of the spin wave (6), no "bottlenecks" are likely to exist and one may decompose the linewidth of an observed resonance into a part ΔH_{PITS} due to coupling to degenerate spin waves by residual surface and volume pits, a part ΔH_{MS} due to local magnetostrictive effects, a part ΔH_{PI} due to paramagnetic impurities, and other terms which are usually negligible compared to the aforementioned contributions.

Prior to the above mentioned works, R. L. White had pointed out that by measuring the linewidths of other magnetic resonance modes known as magnetostatic modes one could in principle determine the relative importance of degenerate spin wave coupling to the magnetic resonance relaxation process in ferromagnetic dielectrics (7). In figure 2 a schematic diagram of the spin wave spectrum is shown together with region of magnetostatic mode excitations. The angular frequency ω_k of a spin wave of wavenumber k, is seen to be dependent on θ_k, the angle the wave vector $\underset{\sim}{k}$ makes with the direction of the static magnetic field. If a resonance with $k \approx 0$ is excited with angular frequency ω_o, then there are a large number of spin waves having the same frequency (or energy) as the resonant mode, that is, "degenerate" with this mode. It is seen that there are magnetostatic modes with $k \approx 0$ that have varying positions with respect to the spin wave manifold. If coupling to degenerate spin waves constitutes an important mechanism in magnetic resonance relaxation, then the density $\rho(\omega, k)$ of these degenerate states, should strongly affect the linewidth of the resonant mode. In particular if coupling is occurring to either medium or high k-number spin waves, it may be seen from figure 2 that the relative linewidths of the magnetostatic modes should behave quite differently on passing through the top of the spin wave manifold, ω_T. However, when the magnetostatic mode linewidths were measured in a YIG sphere (7), the variations observed were not explainable by this simple picture. Since these measurements were performed on a sample with a uniform precession linewidth of about 1.2 oersteds and highly polished samples have linewidths of 0.5 oersteds or less, it was felt that it would be of some interest

to measure the magnetostatic mode linewidths in a highly polished sample. In particular, it appeared that a measurement at room temperature and 4.2°K in the same sample might indicate how the strength of the coupling to degenerate spin waves behaved as a function of temperature.

The magnetostatic mode linewidths were therefore measured in a highly polished sample of single crystal YIG at x-band with the static magnetic field along the [111] direction. Measurements were made at both 300°K and 4.2°K. In order to make these measurements a magnetic resonance spectrometer of a particular type had to be built. Certain of the magnetostatic modes have weak intensities and measurement of their linewidths required very sensitive detection schemes. Other modes are vary intense and precautions have to be taken to decouple these modes sufficiently to measure their linewidths accurately. Since the linewidths in the samples of interest are relatively narrow (0.5 oersteds or less out of 3000 oersteds) and require certain precautions in their measurement, the problem is compounded when resonances of widely varying intensities are to be measured with high accuracy. A schematic diagram of the spectrometer used for the measurements is shown in figure 3. The YIG sphere was placed in a rectangular cavity that was resonant in the TE_{102} mode. Since the individual magnetostatic modes are preferentially excited by r.f. magnetic fields of particular symmetry and angle with respect to the static magnetic field, the angle the static field made with the r.f. field as well as the position of the sample in the cavity was made adjustable. In this way weak resonances could be optimized and resonances that were too strong could be diminished. The sample was allowed to rotate freely within the holder to permit the easy magnetic axis (the [111] direction for YIG) to align itself with the static magnetic field. The weak resonances were measured by using techniques commonly employed in paramagnetic resonance investigations (9). Magnetic field modulation and superheterodyne detection of the resonance signal was employed. The klystron was stabilized on the sample cavity. The superheterodyne detection at 30 Mc was followed by synchronous detection of the 36 cycles per second signal. The derivative of the resonance was then displayed on the Y-axis of an X-Y recorder. The X-axis was driven in proportion to the swept magnetic field.

For the stronger resonances, the superheterodyne detection system was deactivated and a self-contained stabilized klystron was used as the signal source. The linewidths were measured by means of the precision attenuator and the galvanometer detector. The resonance linewidth is the difference in the values of static magnetic field between the points where the effective imaginary susceptibility is one-half of its value at resonance. The two methods of measuring linewidths were checked by measuring several modes with both methods.

The results of the measurements on a highly polished YIG

sphere (0.058 in. diameter) at 300°K are shown in figure 4. For comparison the data of R. L. White (7) are also shown. The numbers at the top of the figures are the magnetostatic mode indices according to Walker (8). The dashed line marked $\theta = \pi/2$, $k = 0$ indicates the extrapolated top of the spin wave manifold and modes lying to the right of this line are within the spin wave manifold. H_i is the internal static magnetic field for resonance for the indicated modes and M is the saturation magnetization of the sample. Since our measurements were at 9.3 kMc and White's measurements were at 9.7 kMc, and since the parameter $\Omega_H = H_i/4\pi M$ for a particular mode is somewhat dependent on frequency, we have plotted the modes on an arbitrary Ω_H scale in order to maintain the correspondence between the various modes. It is noted that the linewidth of the uniform precession mode (the 110 mode) in this work is about 1/3 that of White's and there is considerably less variation in the mode linewidths in the narrower linewidth sample. However, there is still a residual variation of mode linewidths and the question now is whether one can conclude anything about the extent of the contribution of degenerate spin wave coupling to the linewidths from this variation. Since YIG has no disorder in magnetic sites, the primary source of degenerate spin wave interactions to be considered is scattering from volume and surface pits. In view of the fact that the exact nature of the sample surface was not known, we have used the pit scattering theory of Sparks, Loudon, and Kittel (10). These authors compute the ferromagnetic resonance linewidth due to a spherical diamagnetic inclusion in a magnetic media. The effect of surface roughness is approximated by assuming the surface is composed of hemispherical pits and that the scattering from each of the pits is additive. The linewidth calculated by these authors for a sphere of radius R_0 covered with hemispherical pits of radius R is given by

$$\Delta H_{S\text{-}L\text{-}K} = \frac{3}{4}\left\{\frac{R}{R_0}\right\} 4\pi M \int_{k_{min}R}^{k_{max}R} d(kR)\, \frac{\Omega}{\Omega r(k)} \left[J_1(kR)\right]^2 \frac{(3\cos^2\theta_k - 1)^2}{\cos\theta_k} \qquad (1)$$

where, M is the saturation magnetization

$\Omega = \omega/\gamma\, 4\pi M$ = constant for this integration

ω = angular frequency

γ is the spectroscopic splitting factor (2.80 Mc/oersted)

$\Omega_r = \Omega_H + \Omega_{ex}\, l^2 k^2$

$\Omega_H = H_i/4\pi M$

H_i is the internal static magnetic field

$\Omega_{ex} = H_{ex}/4\pi M$

H_{ex} is an effective exchange field (11)

1 is the lattice spacing

$j_1(x) = \frac{\sin x}{x^2} - \frac{\cos x}{x}$ is the spherical Bessel function of order 1 (12).

θ_k is the angle the spin wave propagation vector $\underset{\sim}{k}$ makes with the static magnetic field

$$\cos^2 \theta_k = \frac{\Omega_r^2 + \Omega_r - \Omega}{\Omega_r}$$

$$k_{min} = 0 \text{ if } \Omega^2 \leq \Omega_H (\Omega_H + 1)$$

$$k_{min} = \left[\frac{\sqrt{4\Omega^2 + 1} - (2\Omega_H + 1)}{2\Omega_{ex} l^2}\right]^{1/2} \text{ if } \Omega^2 > \Omega_H (\Omega_H + 1)$$

$$k_{max} = \left[\frac{\Omega - \Omega_H}{\Omega_{ex} l^2}\right]^{1/2}$$

If R is greater than 5×10^{-4} cm and $\pi/2 < \theta_o < 0$, equation (1) is well approximated by

$$\Delta H_{S\text{-}L\text{-}K} \approx \frac{\pi}{8} \left\{\frac{R}{R_o}\right\} 4\pi M \frac{(3 \cos \theta_o - 1)^2}{\cos \theta_o}$$

where

$$\cos^2 \theta_o = \frac{\Omega_H^2 + \Omega_H - \Omega}{\Omega_H}$$

Since highly polished YIG spheres are prepared with an abrasive with a maximum size of about 0.30×10^{-4} cm, it is expected that the residual surface imperfections would have radii somewhat less than 0.15×10^{-4} cm. Equation (1) was therefore recast into a form suitable for numerical evaluation for all values of the pit radius (13) and the results are shown in figure 5. It is seen that as the surface pit radius increases, the linewidth peak on the low field side increases rapidly and moves over to the extrapolated top of the spin wave manifold ($\theta = \pi/2$, $k = 0$). For larger pit radii the height of the peak increases roughly as the square of the pit radius and the low field side of the peak drops sharply at the top of the spin wave manifold. The other peak at the high field side also continues to increase with pit radius and moves over to higher fields until it

coincides with bottom of the spin wave manifold ($\theta = 0$, $k = 0$).

When considering coupling of magnetostatic modes to degenerate spin waves by surface imperfections, it has been pointed out by Jones (14) that one must consider the fact that the amplitude of the precession angle for a magnetostatic mode is generally larger at the surface of a sphere than it is interior to the sphere and the amount that it is larger will vary from mode to mode. It would then be expected that the contribution of degenerate spin wave coupling from surface interactions would in general vary from mode to mode. For an approximate theory such as that of Sparks, Loudon, and Kittel where the contribution of the surface interaction is independent of the angle the static field makes with the surface, this effect manifests itself in the form of a factor. We have called this factor F_{nmr} and it is easily shown to be,

$$F_{nmr} = \frac{\langle |m_t|^2 \rangle_{surface}}{\langle |m_t|^2 \rangle_{volume}} \qquad (2)$$

where m_t is the transverse component of magnetization for the mode with indices nmr, $\langle\ \rangle_{surface}$ indicates the surface average, and $\langle\ \rangle_{volume}$ indicates the volume average. The values of F_{nmr} for most of the low order modes have been computed using the published values (15) of m_x and m_y for the various modes. In most cases $F_{nmr} = (2n + 1)/3$ and is therefore independent of the field and frequency at which the mode is resonant. Table I gives the values of F_{nmr} computed for the modes on which linewidths measurements were made when $\Omega = 1.874$. The results are similar when $\Omega = 1.352$. We have assumed that the observed magnetostatic mode linewidths can be expressed by the sum of a constant contribution plus a part which depends on the mode indices and the position of the mode with respect to the spin wave manifold (in this case, the Sparks, Loudon, and Kittel result). That is,

$$\Delta H = \Delta H_o + F_{nmr}\ \Delta H_{S\text{-}L\text{-}K}\ (R) \qquad (3)$$

A best fit to the data obtained was made by varying R, the assumed effective surface pit radius and ΔH_o, the constant contribution. The value of R chosen for the best fit at both temperatures was $R = 0.10 \times 10^{-4}$ cm. Since the abrasive has an irregular shape with maximum size of about 0.30×10^{-4} cm and is probably broken down somewhat during the polishing process, the effective surface pit radius chosen for the best fit appears to be quite reasonable.

The results of this best fit to the data obtained at 300°K is shown in figure 6. It is seen that the constant contribution has been chosen as 0.350 oersteds. The uniform precession linewidth (the 110 mode) therefore appears to have a contribution of about

REMARKS

Table I. Computed values of F_{nmr}, the factor expressing the degree of relative concentration of transverse magnetization at the surface of a sphere for the magnetostatic modes with indices nmr. The F_{nmr}'s are independent of r excepting for the cases footnoted and these were computed for $\Omega = 1.874$ and the indicates values of r. N. C. indicates these F_{nmr} were not computed since measurements were not made on the corresponding modes.

Fnmr

n \ m	0	1	2	3	4	5
1		1				
2	5/3	5/3	5/3			
3	7/3	7/3	7/3	7/3		
4	7.3/3 [a]	9/3	9/3	9/3	9/3	
5	N.C.	7/3 [b]	N.C.	11/3	11/3	11/3
6	N.C.	N.C.	16/3 [c]	N.C.	13/3	13/3

a. r=2, b. r=1, c. r=0

0.05 oersteds (or 12.5% of the total linewidth) from degenerate spin wave coupling. This is consistent with the findings of Fletcher, LeCraw and Spencer (2) who found a linewidth contribution in their sample of 11.7% due to degenerate spin wave coupling.

In figure 7 are shown the results obtained at 4.2°K. In this case the constant linesidth contribution is taken to be 0.200 oersteds. It is seen that here the uniform precession mode has a contribution of roughly 0.09 oersteds out of 0.29 oersteds (or 31%) due to degenerate spin wave coupling. However, Spencer and LeCraw (4) have found that in their sample at 4.2°K roughly 56% of the total linewidth was due to degenerate spin wave coupling. The reason for this difference in contribution of degenerate spin wave coupling is probably attributable to a difference in amount of rare earth impurities in the two samples. Our sample was prepared with Y_2O_3 with rare earth impurities of 1 part in a million or less, whereas the sample of reference 4 had impurity level of 1 part in 10 million or

less. The total uniform precession linewidth at 4.2°K in our sample was 0.29 oersteds whereas in Spencer and LeCraw's (4) sample it was about 0.18 oersteds. Since rare earth impurities are known to increase the linewidth considerably for temperatures in the range of about 20°K to 100°K, as an additional check we measured our sample linewidth in this temperature range. We found that our linewidth at 77°K was 0.60 oersteds compared to 0.31 oersteds in a sample made from the highest purity of Y_2O_3 (16). Hence, we conclude that the additional 0.10 oersteds we observed in the total uniform precession linewidth at 4.2°K is probably due to rare earth impurity broadening. Our 4.2°K measurements are then consistent with the findings of Spencer and LeCraw (4).

We may therefore conclude that examination of the relative linewidths of the magnetostatic modes allows one to infer the degree to which degenerate spin wave coupling is contributing to the total linewidth of any mode. The results obtained are entirely consistent with the previous results obtained by the modulation experiments on the uniform precession mode (2,4). It therefore appears that efforts directed toward improvements of polishing techniques for spheres or toward reduction of microcrystalline volume imperfections in yttrium iron garnet will probably not result in any substantial reduction of the uniform precession linewidth in this material at x-band frequencies and room temperatures since the results of this experiment show that surface and volume imperfections do not play an important role in the determination of the uniform precession linewidth.

The author gratefully acknowledges helpful conversations with Dr. G. R. Jones, electronic computation machine programing by Mr. A. Hausner and Mr. O. Cruzan, and the assistance of the supporting staff and administration of the Harry Diamond Laboratories.

REFERENCES:

1. See for example,
B. Lax and K. J. Button, Microwave Ferrites and Ferrimagnetics (McGraw-Hill Book Co., Inc., New York, 1962); A. G. Gurevich, Ferrites at Microwave Frequencies (Consultants Bureau, New York, 1963); P. J. B. Clarricoates, Microwave Ferrites (John Wiley and Sons, Inc., New York, 1961); and references therein.

2. R. C. Fletcher, R. C. LeCraw, and E. G. Spencer, Phys. Rev. 117, 955 (1960).

3. T. Kasuya and R. C. LeCraw, Phys, Rev. Letters 6, 223 (1961).

4. E. G. Spencer and R. C. LeCraw, Phys. Rev. Letters 4, 130 (1960).

5. J. F. Dillon and J. W. Nielsen, Phys. Rev. Letters 3, 30 (1959); E. G. Spencer, R. C. LeCraw, and A. M. Clogston, Phys. Rev. Letters 3, 32 (1959).

6. R. C. LeCraw and E. G. Spencer, Journ. Phys. Soc. Japan 17, Suppl. B1, 396 (1962).

7. R. L. White, Fourth Symposium on Magnetism and Magnetic Materials (Philadelphia, 1958); R. L. White, Journ. Appl. Phys. 305, 182 (1959).

8. L. R. Walker, Phys, Rev. 105, 390 (1957).

9. G. Feher, Bell System Tech. J. 36, 449 (1957).

10. M. Sparks, R. Loudon, and C. Kittel, Phys. Rev. 122, 791 (1961); M. Sparks, Report No. 932, Microwave Laboratory, Stanford University, 1962.

11. H. Suhl, J. Phys. Chem. Solids, 1, 209 (1957); R. C. LeCraw and L. R. Walker, J. Appl. Phys. 328, 167 (1961).

12. L. I. Schiff, Quantum Mechanics, First Ed. (McGraw-Hill Book Co., Inc. New York, 1949)

13. The programing for this calculation was performed by Mr. A. Hausner.

14. G. R. Jones, Bull. Am. Phys. Soc. 9, 113 (1964).

15. P. C. Fletcher and R. O. Bell, J. Appl. Phys. 30, 687 (1959).

16. E. G. Spencer, R. C. LeCraw, and A. M. Clogston, Phys. Rev. Letters 3, 32 (1959).

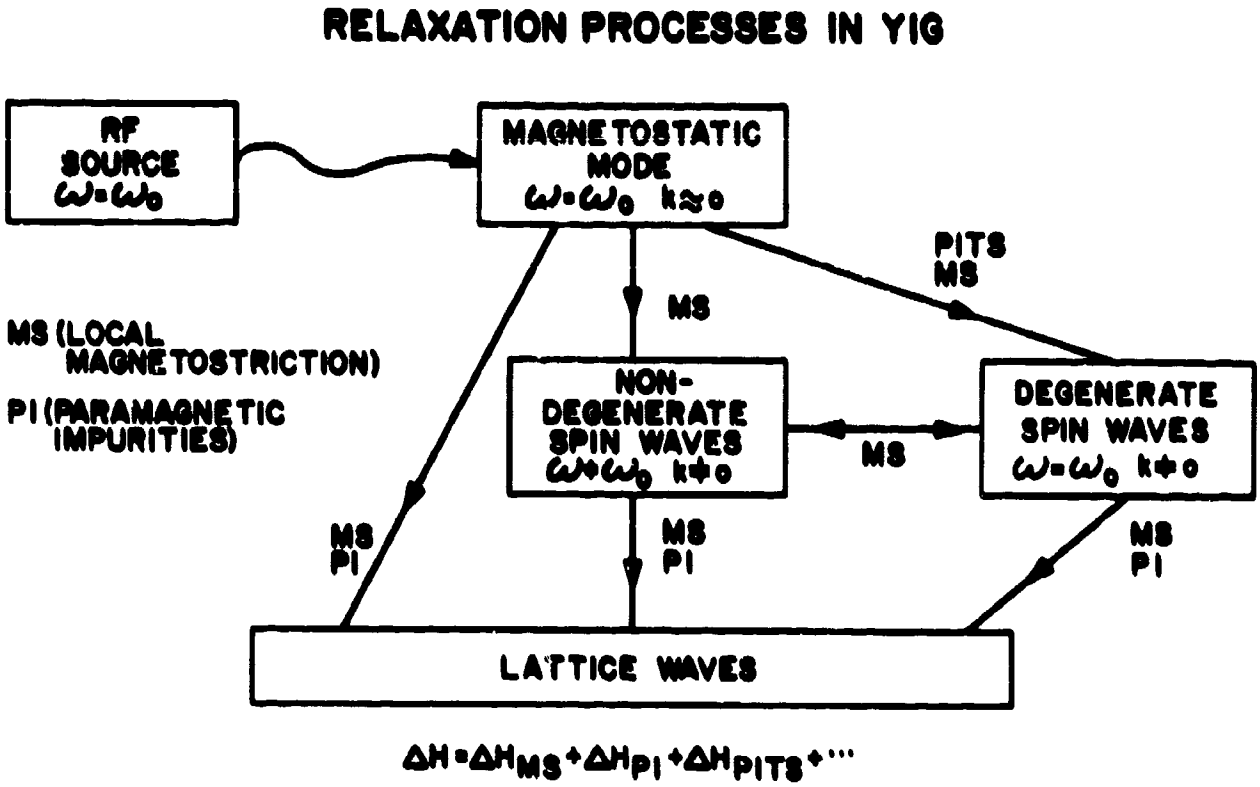

Figure 1. A schematic representation of the magnetic resonance relaxation process in yttrium iron garnet (YIG).

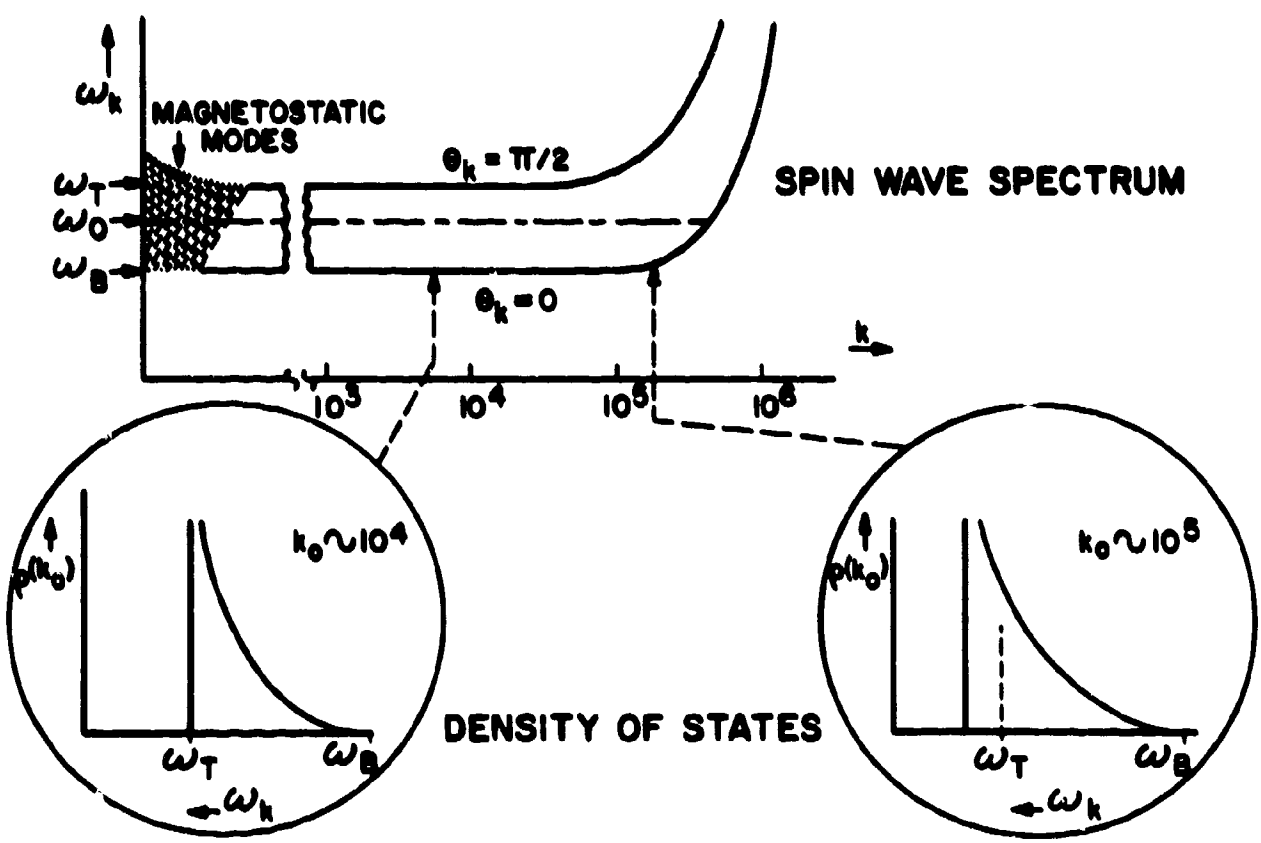

Figure 2. A schematic representation of the spin wave spectrum and density of spin wave states at two representative values of wavenumber k.

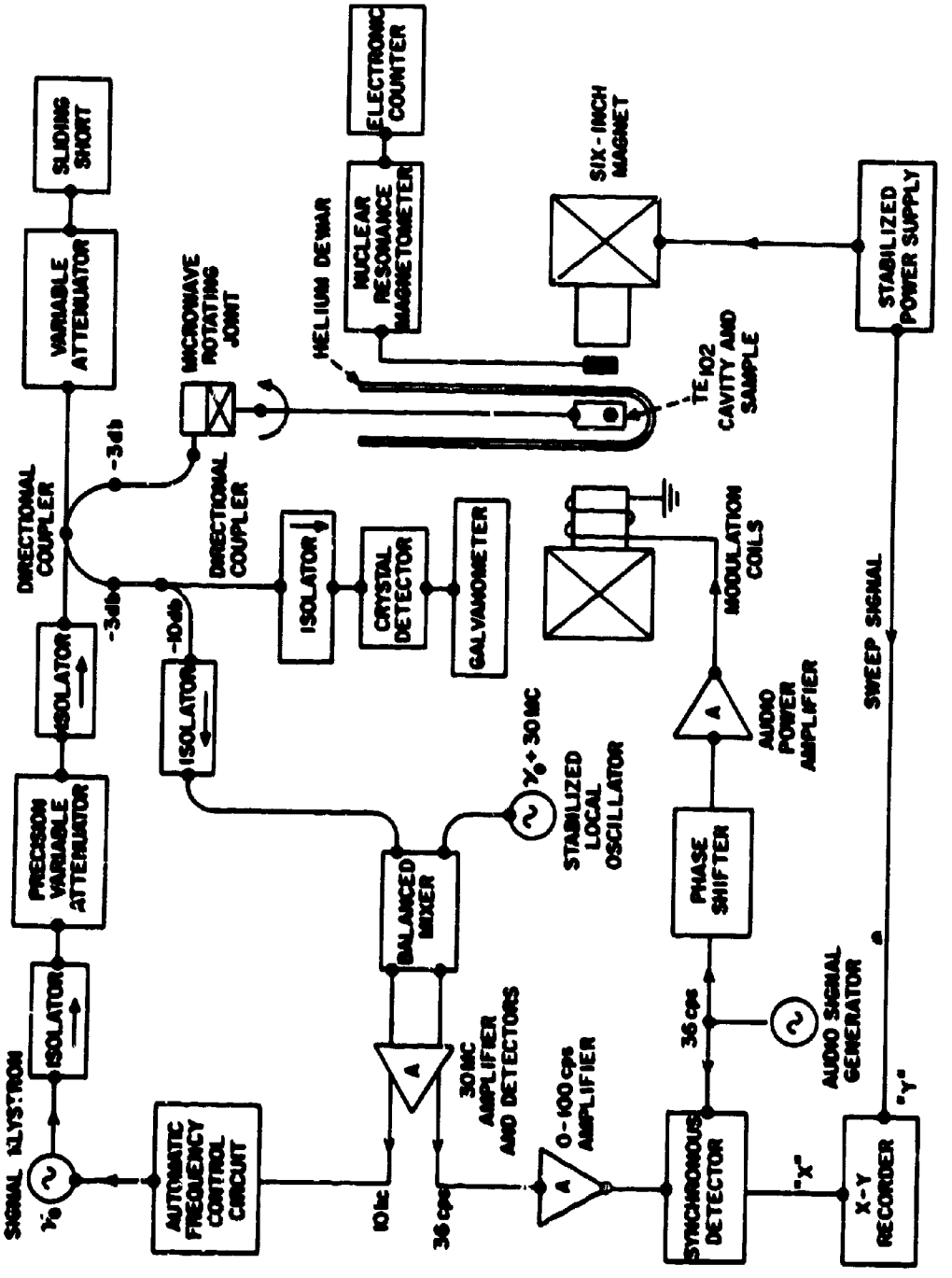

Figure 3. A schematic diagram of a magnetic resonance spectrometer used to measure magnetostatic mode linewidths.

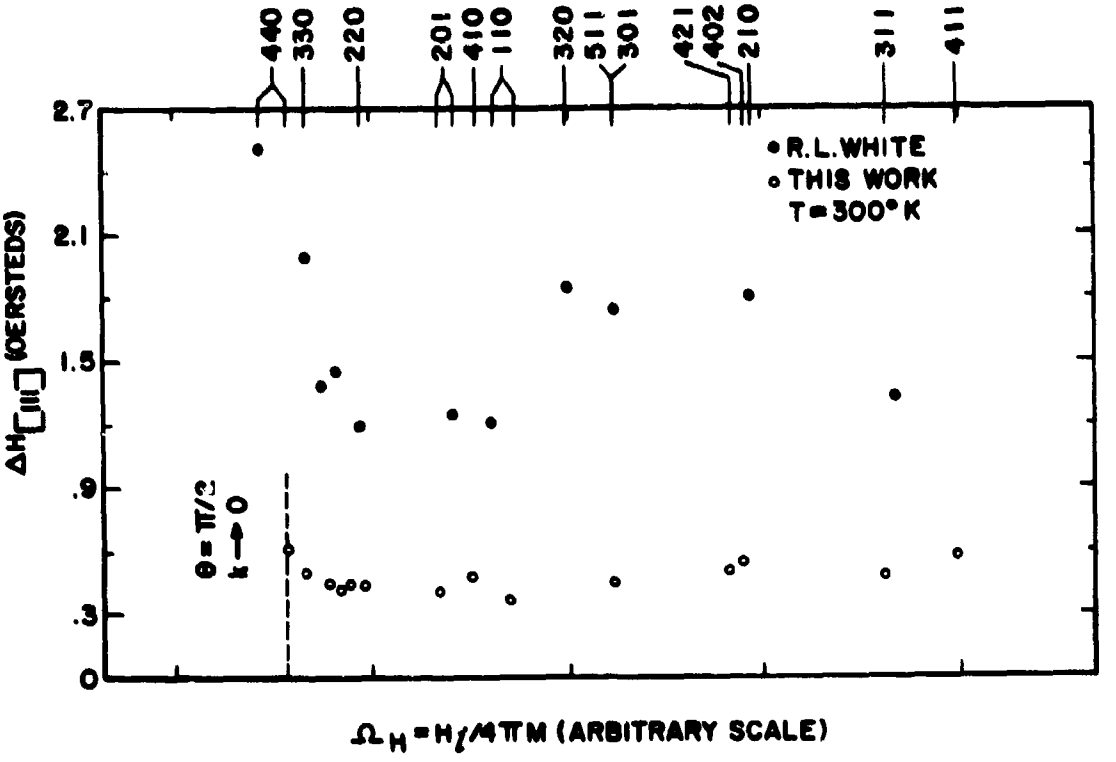

Figure 4. Magnetostatic mode linewidths in yttrium iron garnet spheres with static magnetic field along the [111] direction. The data of R. L. White (Reference 7) was taken at 9.2 kMc. The data taken at this laboratory were at 9.3 kMc.

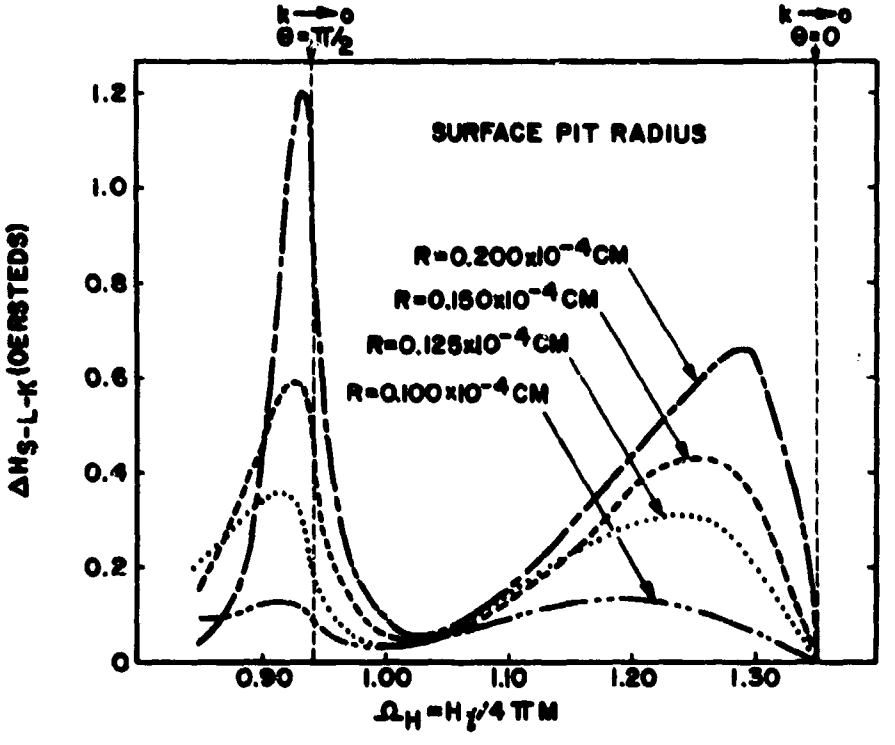

Figure 5. Ferromagnetic resonance linewidths of a sphere of radius $R_0 = 0.74$ mm covered with hemispherical pits of radius R evaluated as a function of field for resonance from the theory of Sparks, Loudon and Kittel (Reference 10). Computation performed with $4\pi M = 2481$ g, $\Omega = \omega/\gamma 4\pi M = 1.352$, and $\Omega_{ex} l^2 = 2.086 \times 10^{-12}$ cm^2.

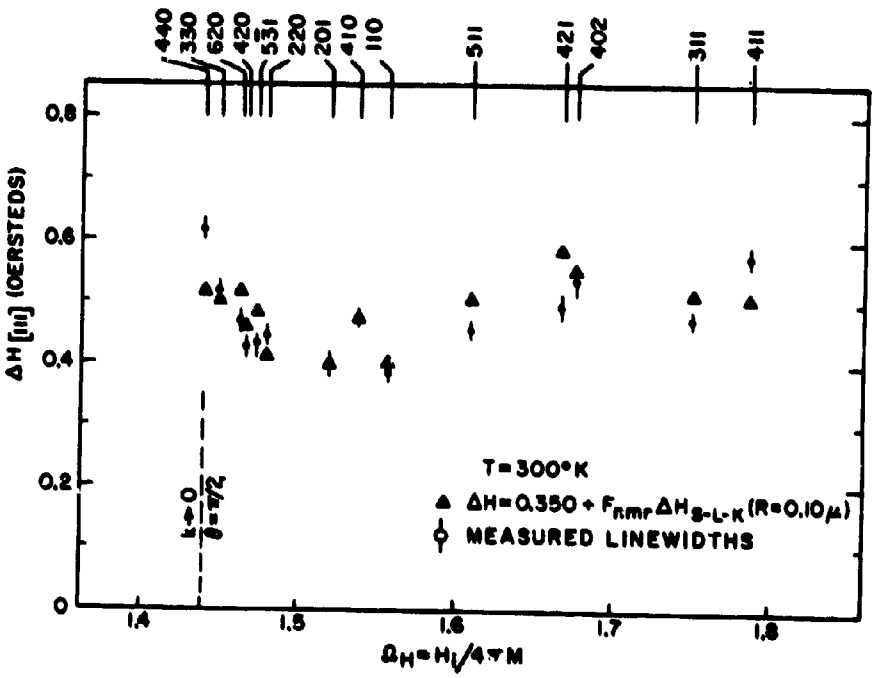

Figure 6. Magnetostatic mode linewidths at 300°K in a highly polished YIG sphere of radius 0.74 mm with the static magnetic field along the [111] direction. The mode indices according to Walker are listed at the top of the figure. Parameters used in obtaining Γ_k are $4\pi M$ = 1808 G, H_{anis} [111] = - 60 oersteds, γ = 2.80 Mc/oersted, and $\Omega = \omega/\gamma 4\pi M$ = 1.074. Data for this sample at 4.2°K are shown in figure 7.

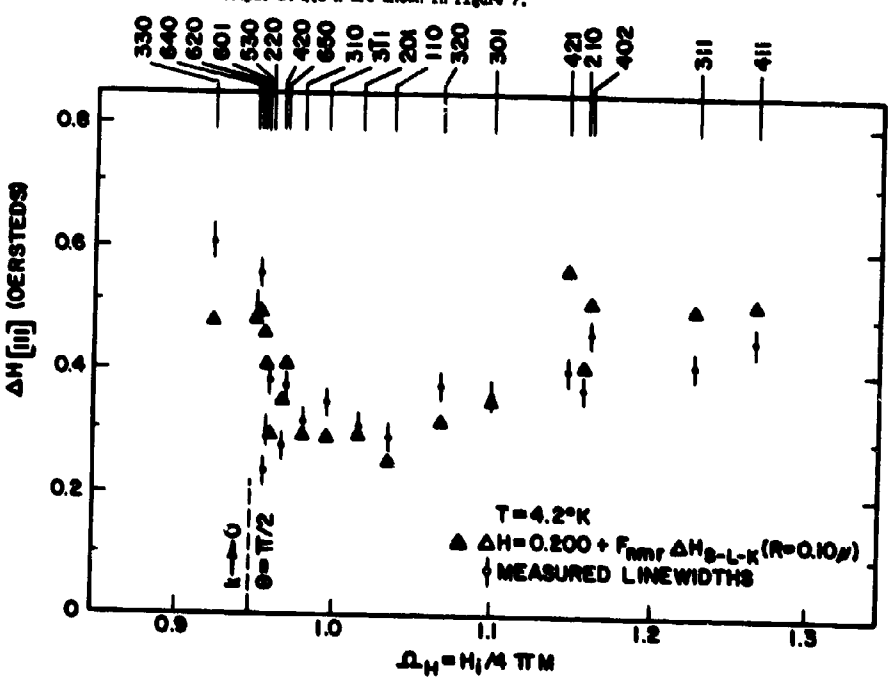

Figure 7. Magnetostatic mode linewidths at 4.2°K in a highly polished YIG sphere of radius 0.74 cm with the static magnetic field along the [111] direction. The mode indices according to Walker are listed at the top of the figure. Parameters used in obtaining Γ_k are $4\pi M$ = 1861 G, H_{anis} [111] = -176 oersteds, γ = 2.80 Mc/oersted, and $\Omega = \omega/\gamma 4\pi M$ = 1.352. Data for this sample at 300°K are shown in figure 6.

A MORPHOLOGIC STUDY OF THE PATHOGENESIS OF EXPERIMENTAL CHOLERA IN THE INFANT RABBIT

H. THOMAS NORRIS, CAPT., MC, RICHARD A. FINKELSTEIN, Ph.D.
and HELMUTH SPRINZ, COL., MC
Walter Reed Army Institute of Research
Washington, D.C.

The current spread of cholera through Southeast and East Asia with the resulting 18,400 deaths in 1963 alone (1) has re-emphasized the need for basic research on this disease as well as on all intestinal diseases affecting the combat effectiveness of our troops. The causative organism of cholera, the Kommabacillus, was discovered by Koch in 1884 (2). As early as 1894 Metchnikoff (3) was able to reproduce this enteric infection in infant rabbits by peroral inoculation. This experimental model, however, fell into disuse and it was not until very recently that Dutta modified it in an attempt to isolate the toxic portion of the vibrio responsible for the pathogenic action. The 10-day-old suckling rabbit is unique in that diarrhea and dehydration, similar to the human disease, follow intra-intestinal inoculation of cholera vibrios. However, by the 16th day of life the rabbit is markedly less susceptible to the infection.

It is the purpose of this paper to report the morphologic response of the gastrointestinal tract of the 10-day-old rabbit to intact and to ultrasonically disrupted cholera vibrios, to broth in which cholera vibrios have been grown for 18-24 hours and to cholera endotoxin.

MATERIALS AND METHODS

Intestinal infection with viable cholera vibrios was produced by introducing 10^4-10^6 living vibrios into the first loop of small bowel visualized at laparotomy using ether anesthesia on healthy 8-12-day-old rabbits. Control animals received sterile 0.1% peptone in physiological saline. Although a number of strains were tested, the majority of the work was done with V. cholerae strain 569B, Inaba serotype.

In contrast to the living vibrio experiments where laparotomy was necessary, the ultrasonically disrupted cholera vibrios, the

broth filtrates and the cholera endotoxin were all administered by polyethylene catheter into the stomach.

The complete procedure for the preparation of the suckling rabbits and the oral solution has been reported elsewhere (4). Briefly, healthy 8-12-day-old rabbits were separated from their mothers and given gastric lavage with multiple doses of tepid water until the returning solutions were free of milk and solid. The oral test materials were administered per os via a polyethylene catheter into the stomach.

In preparing the "sonicate", cholera vibrios were disrupted ultrasonically and centrifuged. The supernate was passed through millipore filters and the sterile fluid "sonicate" was administered per os in four doses of 1 ml/100 grams of body weight at 1 1/2-hour intervals. Control animals were given physiologic saline in similar doses. Brain heart infusion broth (BHIB) filtrates were prepared from aerated 18-24-hour cultures of cholera vibrios grown in that medium. The broth cultures were then centrifuged and the supernatant passed through a millipore filter. The resultant sterile filtrate was given in one dose of 1 cc/100 grams of body weight. Because of its high potency only one dose was necessary. Control animals received a similar dose of sterile BHI broth. Another cholerigenous culture filtrate, "syncase" was prepared from V. cholerae cultures in a defined medium supplemented with cas-amino acid. Cholera endotoxin was produced by the method of Ribi (5) and was administered in a dose of 2 mg/100 grams. This dose was repeated four more times at intervals of 1 1/2 hours.

Animals were sacrificed by occipital cerebral concussion and studied sequentially before and after the appearance of diarrhea. At sacrifice, tissues were immediately placed in chilled neutral buffered formalin and refrigerated for 8-12 hours. The tissues were then allowed to equilibrate with room temperature. Tissue was processed in a routine manner and stained with hematoxylin and eosin and alcian blue-PAS. In addition to the usual tissues taken for autopsy the following sections of small and large bowel were studied in every specimen: duodenum, immediately distal to the pyloric junction; jejunum, 10 cm from the pylorus; ileum immediately proximal to the ileo-cecal valve; cecum, the first several cm toward the appendix from the ileo-cecal valve; right colon, 3 cm distal to the ileal-cecal valve; left colon 2 cm above the anus. Selected tissues were also taken for histochemistry. An occasional infant rabbit developed a non-bacterial diarrhea and was excluded from this study. The principles of laboratory animal care as promulgated by the National Society for Medical Research were observed.

RESULTS

INTRAINTESTINAL INFECTION WITH VIABLE CHOLERA VIBRIOS

These animals rapidly regained consciousness after surgery, as did the controls which received sterile peptone-saline broth; and were active until approximately 18-24 hours after inoculation at which time the onset of copious diarrhea of clear to yellow fluid was noted. The animals then gradually became clammy and moribund and died by the 36-48th hour with severe dehydration. Control animals survived and demonstrated no symptoms.

Grossly (Fig. 1) at the time of onset of diarrhea the small bowel demonstrated dilation of fluid-filled loops. The cecum and right colon were massively dilated with similar fluid which resembled rice water stool. There was also marked engorgement of the intestinal vessels. The intestine remained maximally dilated with fluid from the time of onset of diarrhea until death.

Microscopically (Fig. 2), the small bowel of these animals demonstrated very severe hyperemia of all the villous and submucosal capillaries and accumulation of eosinophils in the lamina propria. The mucosa, however, was intact. The crypt epithelium demonstrated increased cytoplasmic basophilia and decrease in height. After the diarrhea had been present for several hours (Fig. 4) there was a disappearance of the eosinophils in the lamina propria, persistence of the severe congestion and in addition accumulation of proteinaceous edema fluid in the lamina propria. This latter picture persisted until death.

The large bowel, on the other hand, demonstrated only minimal congestion and mucus discharge during the same time period. The remaining organs revealed no abnormality on gross or microscopic examination. The control animals demonstrated no abnormalities (Fig. 3).

ULTRASONICALLY DISRUPTED ORGANISMS

These animals received 4 to 5 doses of "sonicate" per os via polyethylene catheter into the stomach at intervals of 1 1/2 hours.

The animals were asymptomatic until shortly before or after the last dose (6 hours after their initial dose) at which time a rather explosive movement of solid moist feces was noted. This was followed by copious and continuous diarrhea of clear to yellow-tinged fluid. Following the onset of diarrhea, the animals became clammy and moribund and died within 6-12 hours from dehydration.

Grossly (Fig. 1) at the time of onset of diarrhea the small and large bowel demonstrated a picture indistinguishable from the animals receiving the viable vibrios.

Microscopically (Fig. 5) at the onset of diarrhea there was extreme hyperemia of the villous and submucosal vessels. No eosinophils were present and the mucosa was again intact. Increased cytoplasmic basophilia and decrease in height was present in the crypt epithelial cells. After diarrhea had been present for several hours (Fig. 6), proteinaceous fluid again accumulated in the lamina propria and congestion persisted. The large bowel demonstrated only slight congestion and mucus discharge. Again, all the remaining organs were grossly and microscopically unaltered.

Tissues from several animals receiving sonicate were taken in the usual manner for histochemical examination (6) and surveyed for acid and alkaline phosphatases, monoamine oxidase, and DPNH diaphorase.

No differences were discernible in the amounts of alkaline phosphatase and monoamine oxidase between the gastrointestinal tracts of experimental animals and those of their controls. Minimal changes were noted in the amounts of DPNH diaphorase and acid phosphatase; the amount of DPNH diaphorase in the epithelial cells was decreased and the content of acid phosphatase was increased, in comparison to their controls.

BROTH FILTRATES

These animals received only one dose of BHIB filtrate or syncase and approximately 4 hours later developed diarrhea and other signs like those of the preceding two groups. The animals succumbed with dehydration within 6-12 hours after the onset of diarrhea.

Grossly (Fig. 1) the identical picture occurred as with the two preceding groups. Microscopically at the onset of diarrhea (Fig. 7) there was again severe congestion of the villous and submucosal capillaries of the small bowel, a moderate infiltrate of eosinophils and an intact mucosa. As the diarrhea continued, (Fig. 8) there was a loss of the eosinophilic infiltrate, accumulation of edema fluid in the lamina propria and persistence of the congestion. The large bowel demonstrated only congestion and slight mucus discharge. The control animals which received equivalent sterile media demonstrated none of the above changes.

CHOLERA ENDOTOXIN (RIBI)

These animals received five doses of endotoxin prepared from cholera vibrios by the method of Ribi (5). This dose was comparable in toxicity for chick embryos to the dose of sonicate used (7). None of these animals demonstrated diarrhea, although an

occasional animal succumbed. Those that died, however, demonstrated a picture dissimilar to the above. There was grossly no accumulation of fluid (Fig. 1). Microscopically there was no small bowel abnormality except for a slight amount of villous congestion. However, in the cecum (Fig. 9) there was epithelial disarray, accumulation of debris in the cecal crypts and a spotty mixed cellular infiltrate in the lamina propria.

The descending colon demonstrated marked mucus discharge. The other organs revealed no abnormality.

DISCUSSION

This experimental model duplicates several aspects of human cholera gravis; in particular, the route of inoculation, the sign of massive diarrhea, and the resulting rapidly downhill course with death from dehydration.

The striking similarity in the physiologic and morphologic response of the suckling rabbit to the viable vibrio infection, to the administration of ultrasonically disrupted cholera vibrios and to sterile broth filtrates in which cholera vibrios had been grown, indicates that the same cholerigenous moiety must be present in these inocula.

The diarrhea produced by all three challenges is quite specific and different from the occasional case of sporadic non-bacterial diarrhea seen in suckling rabbits. In this non-bacterial diarrhea there is no massive accumulation of fluid in the small or large bowel, and microscopically vascular congestion is not marked. There is, however, a slight to moderate round cell infiltrate in the lamina propria of the small bowel.

The peroral dose of endotoxin given to the suckling rabbits was approximately equal in toxicity to the dose of sonicate as measured by chick embryo assay (7). Since endotoxin failed to cause diarrhea, it is apparent that this agent by itself, is incapable of reproducing the symptomatology of cholera gravis.

It is of the greatest importance that epithelial denudation previously considered by some to be pathognomonic of cholera was entirely absent in these experiments and the other experimental models studied in this laboratory (8-12). It has been our experience that epithelial denudation is not a part of either human cholera or cholera in experimental animals and is merely a manifestation of late or improper fixation. The fact that the cholerigenous moiety has to pass through an intact epithelial lining presents no conceptual difficulties as even the absorption of whole protein molecules has now been conceded by intestinal physiologists and is a clinical fact in intestinal allergies and in botulism (13).

In addition, we see from this morphologic study that the cholerigenous moiety of the cholera vibrio also has a direct effect on the structures of the lamina propria, where there is evidence of venous stasis with marked hyperemia. This alteration presumably is associated with increased venous pressure and occurs concomitantly with the appearance and accumulation of increasing quantities of intraluminal fluid. The severe vascular response could play an important role in the prevention of absorption of water and other material from the gut lumen.

No significant changes in the epithelial lining of the small bowel were ascertainable using routine histologic methods, in particular, no necrosis of epithelial cells was seen. Histochemical techniques disclosed minor changes in the amounts of acid phosphatase and DPNH diaphorase in the mucosal epithelial cells of the small bowel. Changes similar to these have been reported elsewhere and appear to be the response of the small bowel of young or incompletely developed animals to a non-specific stress (14).

Our findings force us to discard the time-honored hypothesis that rice water stool pours forth from a denuded mucosal surface. What then is the pathogenesis of the copious diarrhea? We postulate that the cholerigenous moiety must have several actions. It must affect active transport in the mucosal epithelial cells as well as causing severe hyperemia and change in the capillary permeability of the vasculature of the lamina propria. Other important factors are the marked increase in gastrointestinal motility and the decrease in transit time with the concomitant propulsive diarrhea.

A theory relating the diarrhea of cholera to inhibition of the sodium pump has recently been advanced (15,16). This theory states that the inability to transfer sodium from the intestinal lumen into the mucosal cells is accompanied by a concomitant inability to transfer water from the gut lumen into the intestinal cells. Regardless of which theory of cellular transport of water and electrolytes is finally proven the following considerations apply to cholera. A severe disturbance of the normal electrolyte gradient is, at least initially, compatible with a structural integrity of the intestinal mucosal cell. Death from systemic effects or recovery occurs in cholera prior to the appearance of any irreversible changes in these cells.

In addition, and in extension of the sodium pump theory of pathogenesis of cholera, we believe that severe hyperemia and altered permeability of the lamina propria vasculature are also playing a role in the prevention of absorption. In this experimental model as well as the human patient, it has been shown that the gastrointestinal transit time is markedly reduced (4,17,18). This fact alone would greatly diminish the possibility of absorption or reabsorption of the intestinal contents. The ability to absorb radio-sodium is

also greatly decreased (4,19). This is probably due to a combination of decreased transit time and a direct effect of the cholerigenous toxins on the mucosal epithelial cell and its supporting lamina propria.

We, therefore, conclude that cellular, vascular and neural factors all play a role in the pathogenesis of experimental as well as human cholera.

SUMMARY

The morphologic response of the gastrointestinal tract of the suckling rabbit to viable cholera vibrios, ultrasonically disrupted cholera vibrios, and to sterile filtrates of broth in which cholera vibrios have been grown resembles the acute phase of cholera in other experimental models and the human disease. All share the same basic pathologic picture, i.e., severe vascular hyperemia early in the infection and as the animals become moribund the accumulation of proteinaceous edema fluid in the interstices of the lamina propria. Throughout the disease the intestinal epithelium remains intact. It is through this intact epithelium that the cholerigenous moiety of the inocula acts causing copious diarrhea of fluid resembling rice water, accumulation of large amounts of fluid in the lumen of the large and small bowel and death resulting from the severe dehydration. This cholerigenous moiety is absent in cholera endotoxin (Ribi).

ACKNOWLEDGMENTS

We are happy to acknowledge the collaboration of N.K. Dutta, Haffkine Institute, Bombay, India. We wish to thank H.R. Jervis, WRAIR, for the histochemical determinations.

TABLE OF FIGURES

Fig. 1. Gastrointestinal tract. Stomach (upper center of each specimen), small intestine (lower left of each specimen) and large intestine (lower right of each specimen). The large intestine of the specimen which received cholera vibrios, cholera "sonicate" and broth filtrate all demonstrate marked dilation with fluid resembling rice water stool and a slight amount of gas. In addition, the small intestine of these specimens was focally dilated. In contrast, the control specimen and the cholera endotoxin specimen demonstrate no gross abnormality.

Fig. 2. Early cholera vibrio infection. The small bowel shows moderate to marked dilation of villous and submucosal capillaries and a slight cellular infiltrate in the lamina propria. The mucosal layer is intact.

Fig. 3. Normal small bowel. The mucosal epithelium is uniformly arranged. The villous and crypt lamina propria is compact, delicate

and relatively acellular. Note that the villous capillary cannot be seen in the normal small bowel.

Fig. 4. Late cholera vibrio infection. The small bowel villous now demonstrates marked edema and persistence of the vascular congestion.

Fig. 5. Cholera sonicate-small bowel. The capillaries of the lamina propria and submucosa demonstrate severe congestion. The mucosal epithelium is intact.

Fig. 6. Cholera sonicate-small bowel. After diarrhea has been present for several hours there is accumulation of proteinaceous edema fluid in the lamina propria and persistence of the congestion.

Fig. 7. Broth filtrate-small bowel. Early response. The vasculature of the villous and crypt lamina propria is markedly dilated by red blood cells. A few polymorphonuclear leukocytes are also present.

Fig. 8. Broth filtrate-small bowel. Late response. The lamina propria now demonstrates moderate edema. The vascular congestion is still present at this stage.

Fig. 9. Cholera endotoxin-colon. There is disarray of the epithelium, accumulation of debris in the crypt and a mononuclear cellular response in the lamina propria.

Fig. 10. Normal colon. The columnar epithelium is in orderly arrangement. The lamina propria is thin, delicate and acellular.

BIBLIOGRAPHY

1. Felsenfeld, O. Personal communication.

2. Koch, R. In: Die Conferenz zur Erörterung der Cholerafrage. Dtsch. med. Wschr., 10:499.

3. Cited by Pollitzer, R. Cholera World Health Monograph, 43, p. 404, 1959.

4. Finkelstein, R. A., Norris, H. T. and Dutta, N. K. Pathogenesis of experimental cholera. 1. Observations on the intraintestinal infection and experimental cholera produced with cell-free products. J. Inf. Dis. (In press).

5. Ribi, E., Milner, K. C. and Perrine, T. D. Endotoxic and antigenic fractions from the cell wall of Salmonella enteritidis. Methods for separation and some biologic activities. J. Immunol., 82:75-84, 1959.

6. Jervis, H. R. Enzymes in the mucosa of the small intestine of the rat, the guinea pig and the rabbit. J. Histochem. Cytochem., 11:692-699, 1963.

7 Finkelstein, R. A. Observations on, the mode of action of endotoxin in chick embryos. Proc. Soc. Exp. Biol. Med. (In press).

8. Gangarosa, E. J., Beisel, W. R., Benyajati, C., Sprinz, H. and Piyaratn, P. The nature of the gastrointestinal lesion in Asiatic cholera and its relation to pathogenesis: A biopsy study. Amer. J. Trop. Med. Hyg., 9:125-135, 1960.

9. Formal, S. B., Kundel, D., Schneider, H., Kunev, N. and Sprinz, H. Studies with Vibrio Cholerae in the ligated loop of the rabbit intestine. Brit. J. Exp. Path., 42:504-510, 1961.

10. Sprinz, H. Morphological response of intestinal mucosa to enteric bacteria and its implication for sprue and Asiatic cholera. Fed. Proc., 21:57-64, 1962.

11. Sprinz, H., Sribhibhadh, R., Gangarosa, E. J., Benyajati, C., Kundel, D. and Halstead, S. Biopsy of small bowel of Thai people. Amer. J. Clin. Path., 38:43-51, 1962.

12. Sprinz, H. Personal communication.

13. Heckley, R. J., Hildebrand, G. J. and Lamanna, C. On the size of the toxic particle passing the intestinal barrier in botulism. J. Exp. Med., 111:745-759, 1960.

14. Jervis, H. R. and Biggers, D. C. Mucosal enzymes in the cecum of conventional and germfree mice. Anat. Rec. (In press).

15. Fuhrman, F. A., Fuhrman, G. J. and Burrows, W. Actions and properties of an inhibitor of active transport of sodium produced by cholera vibrios. J. Inf. Dis., 111:225-232, 1962.

16. Phillips, R. A. The pathophysiology of cholera. Bull. Wld Hlth Org., 28:297-305, 1963.

17. Beisel, W. R., Watten, R. H., Blackwell, R. Q., Benyajati, C. and Phillips, R. A. The role of bicarbonate pathophysiology and therapy in Asiatic cholera. Am. J. Med., 35:58-66, 1963.

18. Watten, R. H., Morgan, F. M., Songkhla, Y. N., Vanikiati, B. and Phillips, R. A. Water and electrolyte studies in cholera. J. Clin. Invest., 38:1879-1889, 1959.

19. Benyajati, C. Personal communication.

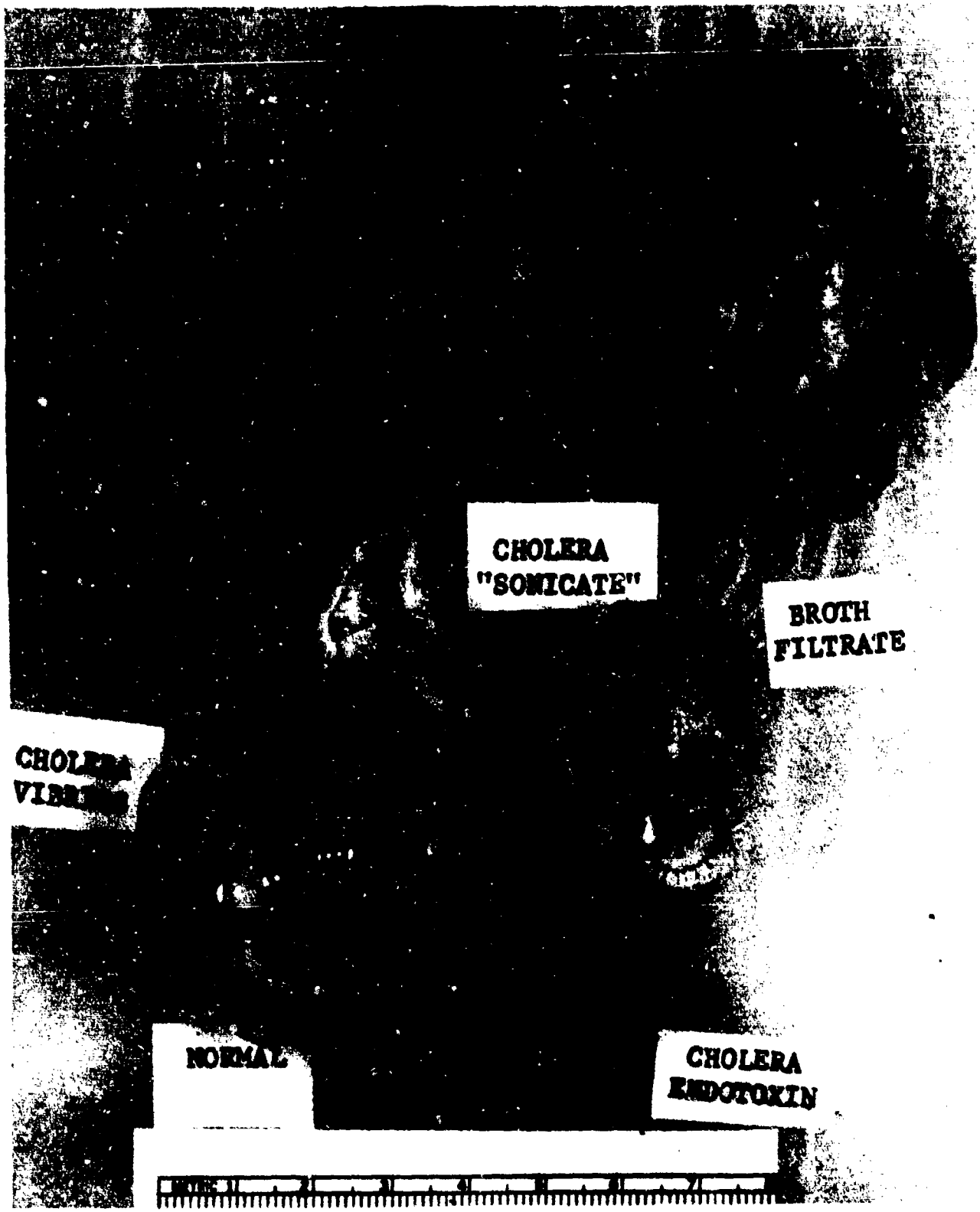
CHOLERA
"SONICATE"
BROTH
FILTRATE
NORMAL
CHOLERA
ENDOTOXIN

FIGURE 1

FIGURE 2

FIGURE 3

FIGURE 4

FIGURE 5

FIGURE 6

FIGURE 7

FIGURE 8

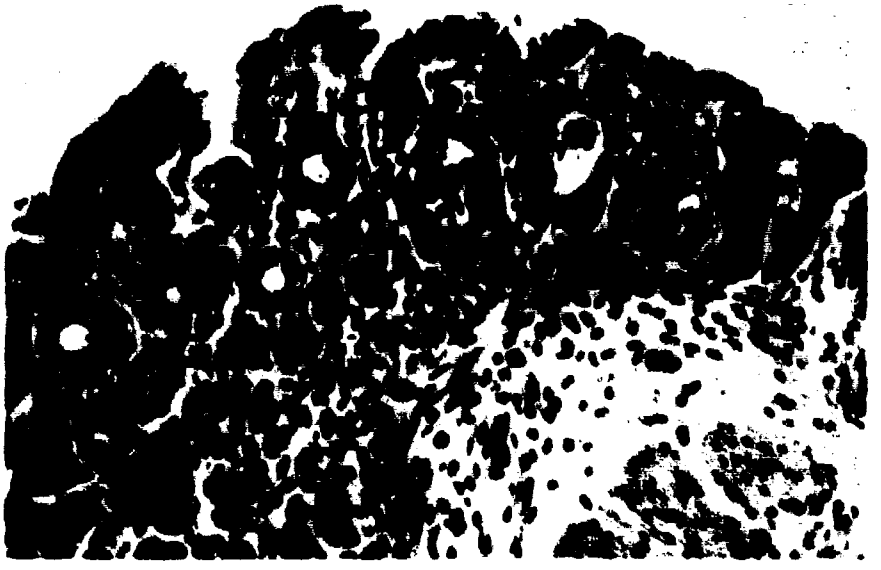

FIGURE 9

FIGURE 10

INFORMATION ASSIMILATION FROM COMMAND SYSTEMS DISPLAYS

SEYMOUR RINGEL
U.S. ARMY PERSONNEL RESEARCH OFFICE
WASHINGTON, D.C.

Technological advancements have led to increased speed, mobility, and destructive power of military operations. To permit commanders to make tactical decisions consistent with rapid and serious changes of events, it is essential that information on military operations be processed and used more effectively than ever before. To meet this need, the Army is developing automated systems for receipt, processing, storage, retrieval, and display of different types and vast amounts of military data. Witness the command control information system, conceived as a network of cross-linked highly automated, computerized systems, each dealing with specialized functions, and all feeding information to an automated tactical operations center (TOC).

One research program of the U. S. Army Personnel Research Office has been designed to provide human factors information which can be useful in enhancing the output of currently developing and future systems. The present paper summarizes the scope, rationale, and organization of the research program as well as several recently completed studies.[1]

OBJECTIVES

The objectives of the research program are to enhance the performance of command information processing systems by providing users, developers, and designers of current and future systems information concerning:

1. Objective performance measures for evaluation of system and subsystem effectiveness.
2. Effects of characteristics of the information displayed: amount, density, type, coding, updating, etc.

[1]A more complete account of the contents of this paper will appear in several separate APRO publications.

3. Capabilities, limitations, and reliability of human performance.

4. Various modes and sensory modalities of presenting information for assimilation and decision making.

5. Specification of effective individual and group work methods and techniques.

6. Allocation of functions among men and equipment.

7. Procedures for identification and assignment of appropriate personnel to critical positions.

CRITICAL INFORMATION PROCESSING FUNCTIONS IN A TOC

An automated TOC will receive vast amounts of information from many and varied sources. The information varies widely in content, form, and degree of completeness. Further, the information often affects several different staff groups. The raw data require a great deal of handling and processing by man and equipment. Personnel will work under a wide variety of conditions ranging from relatively pressure-free to overwhelmingly burdensome situations. Looking at the system as a whole, there appear to be five critical information processing operations that man and equipment have to perform (Figure 1):

1. Screen incoming data for pertinence, credibility, impact, priority, and routing.

2. Transform the raw data for input into storage devices.

3. Input the transformed data into storage devices for subsequent computations and displays.

4. Assimilate data displayed.

5. Decide on courses of action based on information displayed and information from other sources.

DELINEATING THE RESEARCH PROBLEMS

The major problems in command information processing systems emerge from a lack of experience in their use. From an examination of Army, Navy, and Air Force reports and human factors research literature, and from observation of systems and equipment in operation, a number of basic questions were identified which have to be answered before such systems can be used most effectively.

Since these automated systems are designed to assist the commander and his staff in the critical functions of information assimilation and decision making, current task activity centers about problem formulation and exploratory research in these two functions. Questions are stated from the point of view of optimizing accuracy, appropriateness, and speed of performance.

CHARACTERISTICS OF INFORMATION DISPLAYED

In the areas of decision making and information assimilation from displays of various kinds, a number of questions revolve

around (1) the amount of information it is possible to absorb, integrate, and weigh effectively; (2) the densities, formats and coding that may be best for presentation and conspicuity of information; (3) the most appropriate combinations of specific information and general information to be included in alpha-numeric and symbolic displays (maps and overlays); and (4) the relative effectiveness of alpha-numeric and symbolic display of different classes of information.

DYNAMIC ASPECTS OF INFORMATION DISPLAYED

In another category of questions, the dynamic or changing aspects of the information presented are emphasized. What combinations of rate of information updating and degree of change in an update are optimum for depicting the change that has occurred? What is the utility of hard copy to the commander and his staff for pointing up trends and providing a sense of "history", for enhancing feedback of information through comparison of current information with hard copy of past information, and for manual backup and alternate TOC purposes? When information is available at a number of levels of specificity and in the form of a number of different scales, are certain sequences of viewing this information better than others?

CERTITUDE, PROBABILITY, AND CREDIBILITY

A third category of problems concerns credibility of information presented and certitude on the part of the decision maker. Is certitude a necessary condition for good performance over time? What is the relationship between certitude and performance? If certitude is an important factor in performance, can certitude be enhanced through manipulation of characteristics of the information displayed? To what extent is it necessary or desirable to present to the commander and his staff qualitative statements as to credibility of the information and quantitative estimates of its probability? What role can the computer play here?

DISPLAY MODES

A fourth cluster of questions addresses itself to other aspects of information presentation. What display or sensory modalities are best for information assimilation and decision making purposes? Are there some combinations of sensory modalities that would enhance performance? What are the relative merits of group versus individual displays and work methods? Are both kinds necessary?

RESEARCH APPROACH

In many cases, parallel studies will be conducted with alpha-numeric and symbolic displays. The criterion or performance measures will consist of one or more measures of accuracy,

appropriateness, time, and certitude. The studies will incorporate substantive, quantitative, qualitative, formal, and conceptual aspects of information and will sample problem solving situations of different complexity levels, and situations ranging from relatively slow to rapid changes of events. Four of the following five studies have recently been completed. The first two deal with alpha-numeric displays and the remainder with symbolic displays.

I. INFORMATION ASSIMILATION FROM ALPHA-NUMERIC DISPLAYS

PURPOSE

The first study was designed to measure the effects of the following variables on speed and accuracy of information assimilation:

1. Amount of information presented (10, 18, and 25 rows).
2. Density of information presented (1:4, 1:3, and 1:2 ratio of constant letter height to space between rows).
3. Position or location of desired information (5 positions from top to bottom of slide).
4. Complexity of question asked and search required (2, 3, or 4 columns to be searched).

METHOD

Thirty subjects were used in this study. When a subject was seated, a chart or tote was projected (40" x 45") and the column headings were explained (Figure 2). Then he was given a booklet containing instructions, practice questions, and experimental questions. The subject studied a question for 15 seconds; then a slide was projected and he called out the answer as soon as he found it on the slide. The time between presentation of the information and the subject's response, and an accuracy score were obtained for each trial. There was no time limit for a response.

RESULTS

1. As amount of information increased from 10 to 25 lines, the mean search time increased approximately 4 seconds, an increase of approximately 24% (Figure 3).
2. Search time for high density of information was slightly shorter than for medium and low densities.
3. Pertinent information placed near the bottom of the displays took approximately 4 seconds longer to find than information near the top of the displays, a difference of approximately 22% (Figure 4).
4. An increase in the number of columns searched from two to four required approximately six additional seconds of search time per column, a total time increase of approximately 100% (Figure 4).

IMPLICATIONS

Amount: The four second (24%) increase in search time suggests that attention be given to the amount of information presented in displays. For those displays from which information must be rapidly extracted and assimilated, amount of information should be kept to a minimum. If time is not a critical factor, more information might be usefully presented at one time.

Density: Either an absence of differences or such slight differences as were found in search time as a function of density changes suggests that information can be packed fairly tightly into an alpha-numeric display without any loss of efficiency in assimilation. Thus, it may be feasible to present more than one tote on a slide. For example, some of the totes may ordinarily be related and contain less information than others. More than one of these low amount totes could be placed on the same slide which could result in a saving of display storage, a reduction in the number of displays called from storage during a given time period, and a reduction in the total information assimilation-decision process.

Position: The percentage differences in time between position 1 vs. position 4 and position 2 vs. position 5 reflect the procedure, as reported by most subjects, of searching the display from left to right and top to bottom. These results may have implications for operational search procedures, formatting, and placement of information in the totes. For example, it may be possible to capitalize on "natural" or optimal scanning techniques to increase conspicuity, increase confidence, and reduce search time by appropriate placement of new and important information in updated totes.

Complexity: The large percentage increases in time as a function of increased levels of complexity reflect not only the time spent in searching the displays but the time spent in referring back to the question booklet as well. With a longer, more complicated information request, subjects reported that they had to spend more time checking the original question and then rechecking their answer before they responded. Improved formats for stating information requests may reduce the amount of search time required.

The Experimental Task: The experimental task of searching for information in varying numbers of rows and columns in relatively static alpha-numeric displays may be one of the least difficult information assimilation activities that people will be required to perform in operational command systems. Other studies that will be conducted will require the recall of information no longer on display or available or the recognition that information is missing, changed or added, and the integration of information in decisions. As elements of simulation, these variations in task are expected to produce greater differences in performance.

II. CODING INFORMATION FOR CONSPICUITY IN ALPHA-NUMERIC DISPLAYS

PURPOSE

In proposed automated command information processing systems, information will be continually updated and available for display. The awareness of changes and speed with which updated information is apprehended can be an important factor in command decision making, particularly when large numbers of displays must be scanned. In this experiment, the time taken to locate updated elements of information was studied as a function of:

1. Coded and uncoded updated elements.
2. Number of updated elements (4, 8, 12, 16).
3. Total amount of elements presented (36, 54, 72, 90).
4. Group vs. individual displays.

(An element was defined as that word or number which appeared in a given cell of a chart.)

METHOD

Thirty subjects were used in this study. Sixteen pairs of charts of alpha-numeric information were presented to each subject (Figure 2). These charts consisted of two sets each of four levels of amount (36, 54, 72, and 90 elements) and four levels of number of elements updated (4, 8, 12, and 16 elements). In one set, the updated elements were size-coded and in the other set, they were not. Half the subjects received the information on a group display and half on individual displays. Each subject was given a booklet of charts arranged in the same order of presentation as the updated charts. The charts in the booklet differed from the updated charts in two respects; (a) no elements were coded, and (b) the cells corresponding to those in which updated information appeared in the updated charts contained different information. The subject's task was to compare the booklet charts with the updated charts and cross out those elements in his booklet which differed. The time between presentation of the information and the subject's response, and an accuracy score were obtained for each trial.

RESULTS

The findings concerning total amount of elements presented, number of updated elements, and coded and uncoded updated elements were parallel for group (projected) and individual displays (Figures 5 and 6).

1. Time taken to locate updated elements of information was significantly shorter for coded than for uncoded information.
2. Performance time increased with increasing total amount of elements presented and number of updated elements.
3. While time taken to locate updated elements of information increased as a function of increasing total amount of

elements presented, the rate of time increase for coded elements was substantially lower than for uncoded elements.

4. Performance time was significantly shorter with individual displays than with a group display.

IMPLICATIONS

The potential value of coding updated information in command system displays has been demonstrated. This finding lends support to the incorporation and use of coding capabilities in command information processing systems. The results on overall differences in performance between individual displays and group displays raises some doubts concerning the relative merits of group displays, at least for certain kinds of tasks. For example, group displays do not permit the viewers as much freedom to touch, trace, and mark on them as individual displays--which activities may help in the performance of the task.

III. INFORMATION ASSIMILATION FROM SYMBOLIC DISPLAYS

PURPOSE

In updating military overlays, different degrees of change occur. The purpose of this study was to determine the effects of the following variables on accuracy of information assimilation.

1. Amount of information presented (12, 16, 20, and 24 military unit flag symbols).
2. Number of symbols removed in a single updating (2, 4, 6, and 8 from each amount).

METHOD

The type of flag symbol used is shown in Figure 7. Thirty-two subjects were randomly divided into eight groups of four each. The four subjects in each group were seated 15 feet from the viewing screen and were presented the slide material simultaneously. This permitted group data collection and provided some simulation of a tactical operations center. Following the presentation of a slide with one of the four amount levels, a second slide, essentially the same as the first slide except with 2, 4, 6, or 8 elements removed, was presented. Each group received all 16 amount x elements removed combinations in different orders.

The subjects were allowed to view the first slide for one minute. At the end of this time, they were shown the second slide of the pair for one minute. Their task was to determine which flags were missing and to circle the missing flags on the appropriate page in their booklet. After they circled the missing flags, they were to show how certain or uncertain they felt about the correctness of their answer by circling one of the phrases on the eight point scale

on the bottom of the page. They were given approximately one minute to answer and had to work independently.

The subjects' responses were analyzed in terms of accuracy and types of errors (omission and commission). The accuracy scores were used as the basic data for the analysis of variance. The data collected from the eight point scale on how certain or uncertain the subject felt about the correctness of his answer was analyzed as part of another study which will be described next.

RESULTS

1. Accuracy of information assimilation decreased approximately 3 percentage points for each additional symbol included in a single slide presentation. A degradation in accuracy from 85% with 12 symbols presented to approximately 48% correct with 24 symbols presented was found (Figure 8).

2. The number of symbols removed in a single slide updating did not affect the percent accuracy of information assimilation (Figure 8).

3. The number of symbols removed did affect the type of error made. As more symbols were removed increasingly more errors of omission than errors of commission were made.

4. Individuals were found to differ appreciably in their ability to assimilate the presented information. Various methods were used in organizing and retaining the presented information.

IMPLICATIONS

1. Efforts should be made to determine the operational utility of presenting minimal numbers of military elements in a single map or overlay display by (a) informational analyses and empirical studies to determine the information needed for the commander's decisions, (b) representing logically grouped military elements as single symbols, and (c) the use of coding, multi-sensory displays, etc., to increase the informational capacity of single military symbols.

2. Ways of evaluating the relative seriousness (consequences) of misinformation represented by different types of errors in battlefield conditions should be investigated. Future studies can then include types of error as a performance measure.

3. Information assimilation may be enhanced by training in the more successful methods of organizing and retaining changes resulting from updating.

IV. CERTITUDE AND INFORMATION ASSIMILATION FROM SYMBOLIC DISPLAYS

PURPOSE

Accuracy of information assimilation may be only part of an

adequate proximate criterion for evaluating the effectiveness of various displays used in decision making. Feelings of certainty about that accuracy may ultimately play an important role in the formulation of decisions. The present study was conducted to determine the interrelationships among amount of information presented, extent of changes introduced in updating, accuracy of information assimilation, and certitude or confidence in that accuracy.

METHOD

The method is the same as outlined in the previous study.

RESULTS

1. As the number of symbols in a single slide increased, mean accuracy and mean certitude tended to decrease together in an approximately straight line fashion (Figure 8).
2. As the number of symbols removed in a single slide updating increased, certitude tended to decrease in the absence of any change in accuracy (Figure 8).
3. An individual's feelings of certitude about the correctness (accuracy) of his information assimilation from symbolic displays was not a very good indication of his actual accuracy ($r=.52$).

IMPLICATIONS

1. Certitude can be affected by a display variable which has no effect on accuracy of information assimilation. Consequently, efforts to enhance displays in command information processing systems should focus on display characteristics which increase not only accuracy of information assimilation but the confidence one has in this accuracy, pending determination of the degree of relationship of both certitude and accuracy to effectiveness of decision making
2. Both the amount of information presented and the amount of change in a single slide updating should be kept as small as feasible because this would tend to generate the highest degree of certainty and accuracy.

V. CODING, HARD COPY, TYPE, AND EXTENT OF UPDATING OF SYMBOLIC INFORMATION

PURPOSE

The purpose of this study is to determine the effect of the following on speed and accuracy of performance of information extraction and assimilation tasks:

1. Type of update (Remove, Reposition, Add units).
2. Extent of update (2, 4, 6 units).
3. Total amount of units presented (12, 18, 24 units).

4. Enhancement techniques (No aids, hard copy of previous slide to compare with uncoded updated slide, minimum coding, brightness coding).

METHOD

Each of 12 groups of 4 subjects will be presented 27 sets of slides. The first slide in a set will contain a given number of symbols systematically positioned on a map background. The second slide in a set will be identical to the first except for the changes called for by the particular type and extent of change conditions imposed. Subjects will view the slides in a set in sequence. They will have 2 questions to answer for each set of slides. Questions will relate to the updated slide. They will indicate their answers by pressing appropriate response keys as soon as they have ascertained the correct answers. They will then continue viewing the slide until 60 or 90 seconds have elapsed at which time the slide will be removed and they will indicate on their answer sheets (replicas of first slide) all changes which they observed in the second slide. Time, accuracy, and type and frequency of error will be ascertained for the extraction and assimilation tasks for each slide set.

ANTICIPATED RESULTS

While this study has not yet been conducted at this writing, the following major results are expected:

1. There will be significant decrements in performance associated with increasing amounts of units presented and extent of updating.

2. There will be substantial differences in performance as a function of enhancement techniques.

3. The decrements in performance discussed in 1 above, will be less as enhancement increases from no aids to hard copy to minimum coding to brightness coding.

IMPLICATIONS

1. Amount of information presented should be kept at a minimum consistent with operational needs.

2. Techniques for the enhancement of information presentation in terms of conspicuity, history or trends, etc. should be seriously considered in the design and development of command information processing systems.

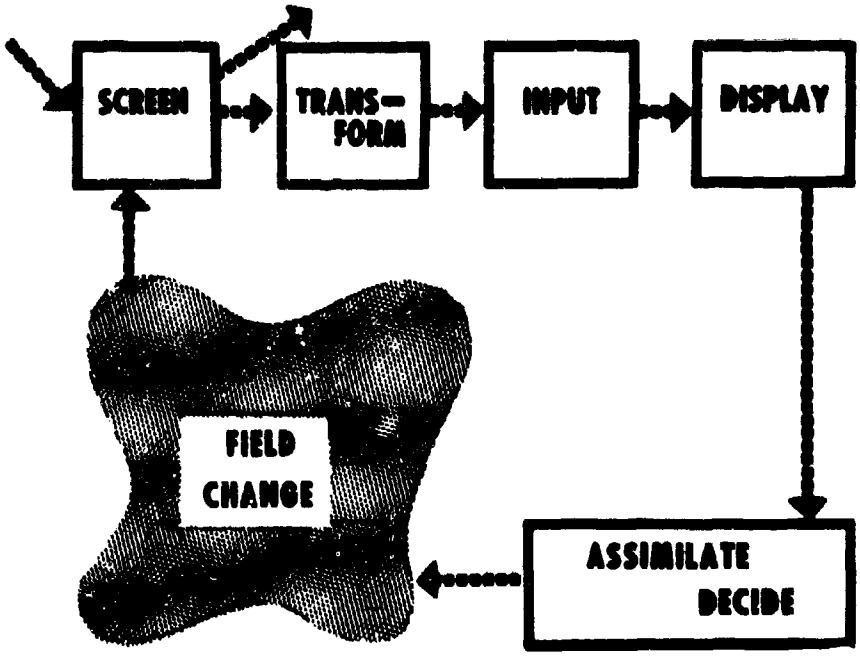

Figure 1. Schematic Representation of Operations and Information Flow in Automated TOC

FRIENDLY TACTICAL UNITS STATUS

UNIT	ACTIVITY	EFF STRENGTH	TERRAIN	ARMOR STATUS	WEATHER
36	SURROUNDING	75	VALLEY	76	SLEET
28	ASSEMBLING	72	PLATEAU	77	STORM
45	SUPPORTING	70	CLIFFS	78	DAMP
57	WITHDRAWING	82	FLATLAND	89	HOT
34	ATTACKING	86	MARSHLAND	83	COOL
99	TRAINING	83	MUDDY	95	HAIL
72	ASSAULTING	79	FOREST	70	WINDY
46	FLANKING	77	FARMLAND	80	FREEZING
53	REGROUPING	87	MEADOWLAND	96	OVERCAST
27	HOLDING	95	RIVERS	91	DRY
13	ADVANCING	78	LOWLAND	94	HURRICANE
82	REBUILDING	80	ROCKY	90	FOG
18	PLANNING	94	MOUNTAINS	72	HUMID
64	SUPPLYING	91	JUNGLE	85	DAMP
41	PENETRATING	96	LAKES	75	SUNNY

Figure 2. Coded Updated Friendly Tactical Units Status Tote

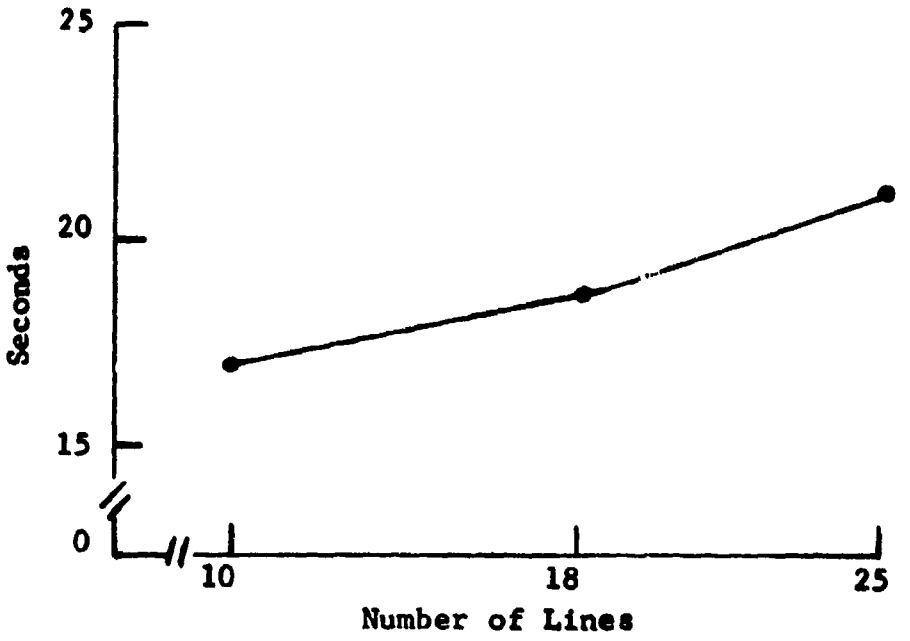

Figure 3. Mean Time at Each Amount (N = 450)

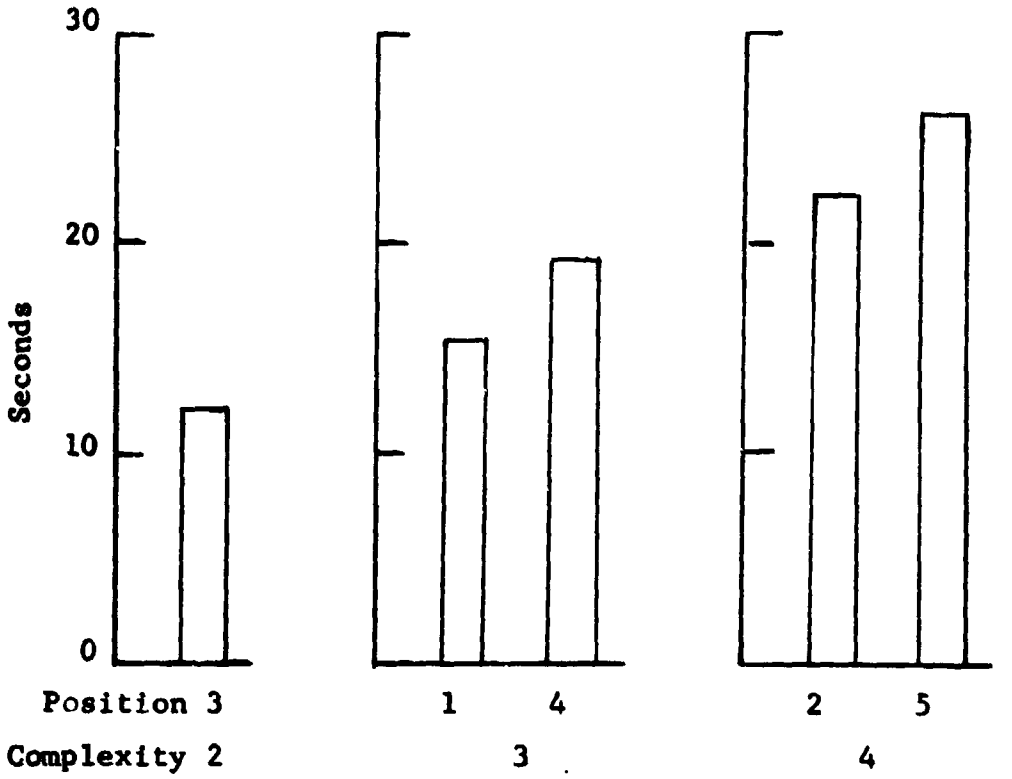

Figure 4. Mean Time at Each Complexity and Position (Each column Mean based on 270 observations)

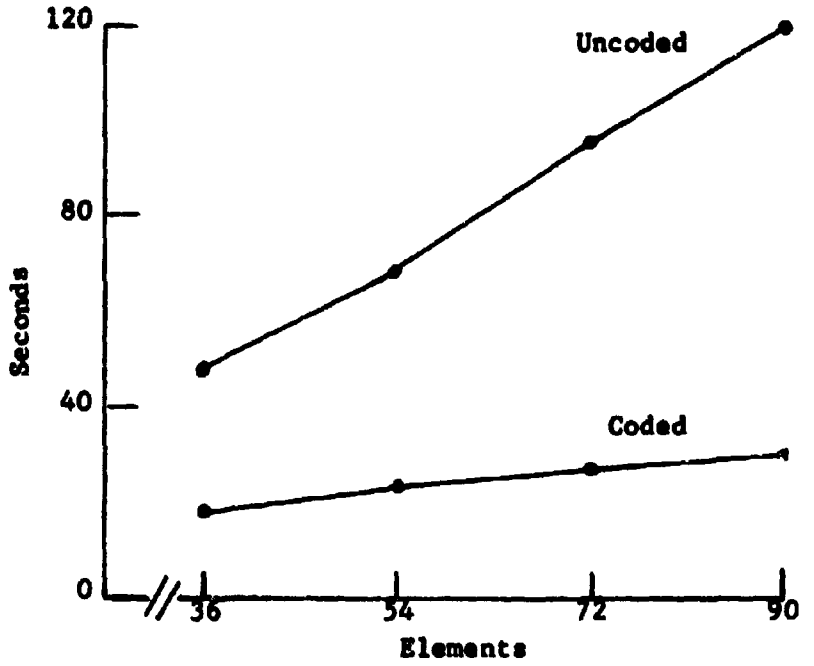

Figure 5. Mean Time at Each Amount on Projected Charts

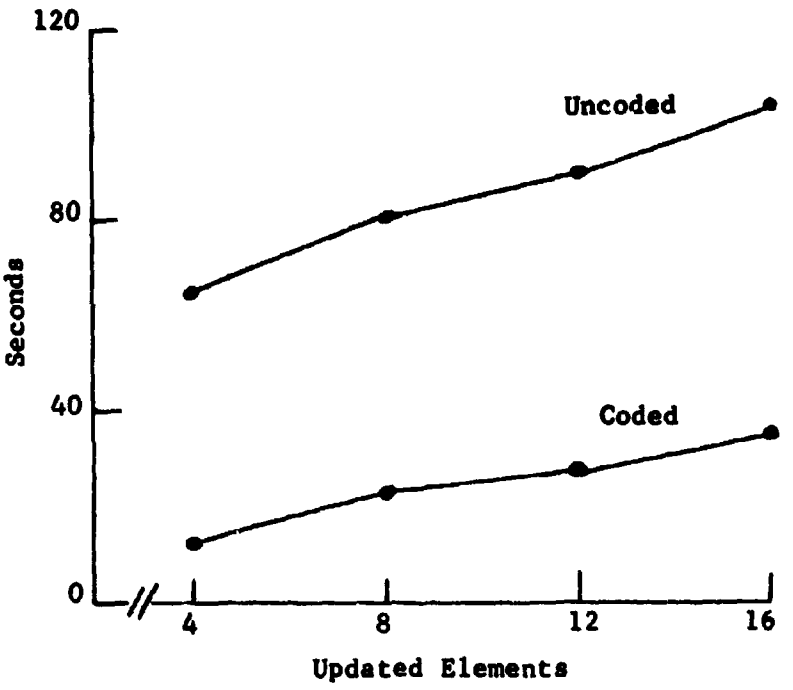

Figure 6. Mean Time for Elements Changed on Projected Charts

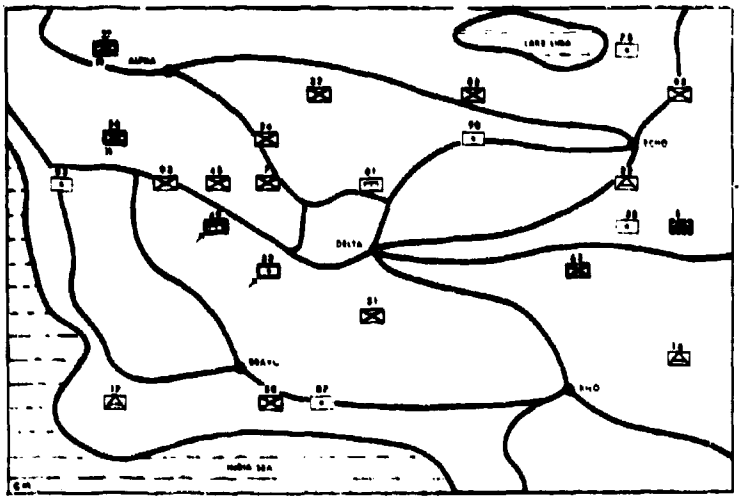

Figure 7. Coded Updated Situation Map

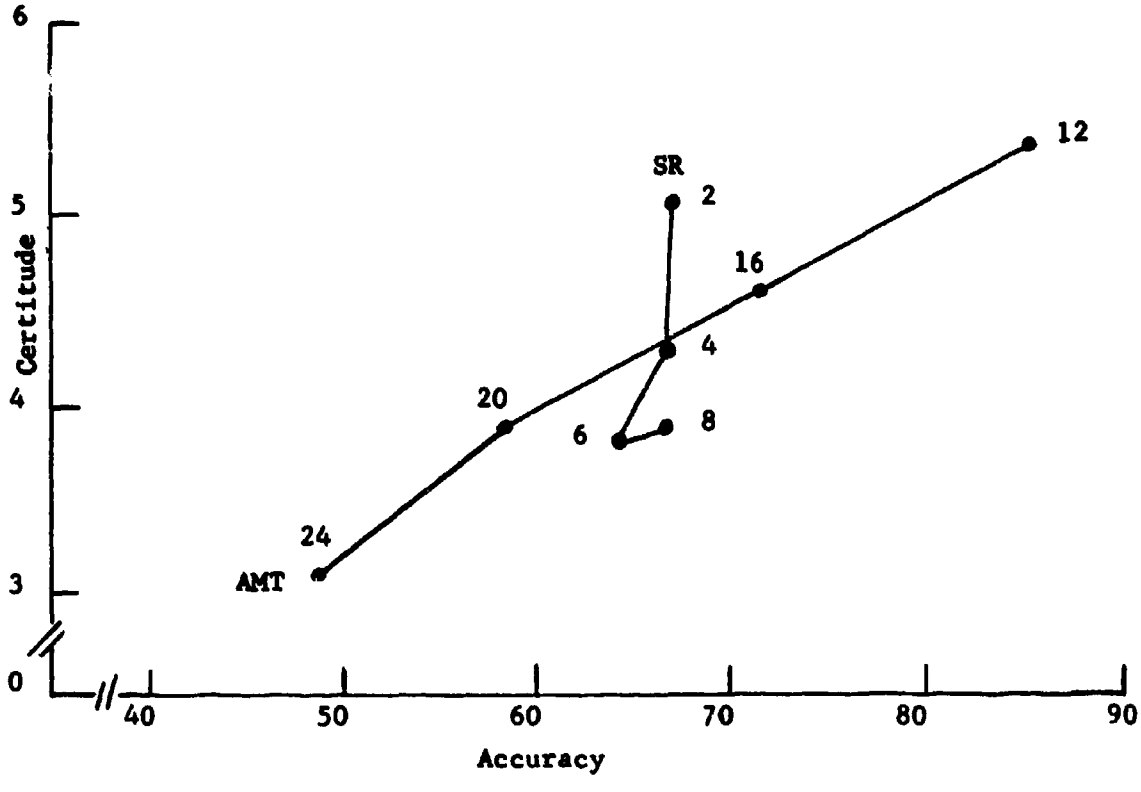

Figure 8. Relationships of Amount and Symbols Removed to Accuracy and Certitude

A DESIGN FOR ANIMAL-HEARING RESEARCH

JOHN J. ROMBA
U. S. ARMY HUMAN ENGINEERING LABORATORIES
ABERDEEN PROVING GROUND, MARYLAND

The character of hearing at any moment is generally the resultant of a large number of determinants which may be divided into two categories, stimuli impinging on the organism and the state of the organism. In hearing experiments, the organismic condition cannot be controlled in the same sense as environmental stimuli may be - the hearing mechanism is never quiescent or static, therefore, the input of stimuli is to a system which is continually active. The large variations attributable to organismic factors are one of the persisting problems in bioacoustics. If the reasons for these variations were identified, better experimental controls could be exercised. Furthermore, if a study were made of those factors of hearing sensitivity in which individual subjects differ, we might discover why some people are more susceptible to hearing impairment than others.

In our work with monkeys, we have noted relative stability of hearing sensitivity of individual subjects over time and orderly changes of sensitivity occurring when each animal was subjected to various experimental conditions. Patterns appeared which could be recognized as "belonging" to a particular animal.

First, I shall describe characteristic hearing patterns which may be found in individual subjects under normal environmental conditions; then, those which result from exposure to stressor stimuli. A characteristic feature found in individual threshold curves of most sub-human primates is the sharp tonal dip in sensitivity which occurs at about 4000 cps. This zone of low sensitivity is sufficiently universal that it is apparent even in Harris's (8) data derived from a group of monkeys (Fig. 1). Although the American Standards Association human group curve (1) appears smooth across the hearing spectrum, Gardner (5) reported finding quite a large number of 4000 cps dips in children from 10 to 18 years of age. There appears to be some relationship between this low point of acuity and further loss of hearing. Gravendeel and Plomp (7) have shown that the average location of temporary hearing loss manifested itself at the location of the dip.

Another pattern which may be worthy of study is the amount of within subject variability. The variation shown by one of our animals for a tone of 2000 cps is illustrated in Fig. 2. Ten measures were made a minute apart on each of 10 consecutive days. Threshold estimates within each test session remained relatively constant for all sessions and showed distinct differences in hearing sensitivity level from one session to another. The degree of stability revealed by the data on this animal distinguished it from other animals on this particular criterion.

Some animals show patterns of variability which differ for different parts of the sensitivity curve. There may appear a narrow distribution of values, say, about the low frequencies and a wide distribution about the highs or an animal may show consistently greater variation at only one frequency.

Additional patterns indicative of individuals can be discerned when the ear is exposed to impulse noise. An example from some preliminary research done by the author (10) is shown in Fig. 3. The curves consist of threshold measures taken before and after exposures to an impulse noise of about 150 db. The pair of curves given for each of three animals is a sample of two successive exposure periods extracted from a larger series. The short straight line at the beginning of each curve is the baseline threshold measured minutes before the noise treatment was given. The remaining points on the curve represent thresholds in transition toward another baseline. Basic similarities in character of the curves were generally observed for the data obtained from each animal. We recognized in the data stable individual patterns of change. For example, animal 50 typically continued to decrease in sensitivity up to 30 minutes following exposure. Each successive pre-exposure baseline also shifted in level, indicating a gradual decrease in hearing sensitivity. On the other hand, the curve of animal 54 regularly overshot the comparison baseline by 5 to 10 decibels 30 minutes after exposure. The curves for animal 51, are similar to the "classical curve of recovery" found in groups of subjects. It is apparent that if the data were averaged over the three animals, the result would appear as the "classical" curve. It is also clear that this group curve then would not be representative of some individual animals.

Two animals in this study displayed a systematic reduction in the amount of initial shift as a function of increasing number of exposures. It appeared that the auditory mechanism was becoming more and more resistant to the damaging effects of the loud noises. If the ear reacts by changing its structure so that it is more resistant to damage, then it becomes an important factor which must be accounted for. It is also possible that these reductions in loss may be the result of conditioning. A flash of light was programmed to immediately precede the treatment noise. Its purpose was to reduce startle in the animal. The animals may have become conditioned to activate their middle ear muscles just prior to the shot and thereby reduce the effect of the treatment. If, indeed, this happened, then the correlation between environmental stressors and the character of the shift in

hearing for each animal can be strengthened by measuring the activity of the middle ear muscles at the moment of exposure.

This is probably the best time to summarize what we have done over so far. It is apparent that there is a great deal of information lost when individual variation is not taken into account. The patterns of hearing sensitivity of individual subjects appear to correspond to stress instigated changes in their sensitivity.

The necessity for steady attention to individual subjects dictates the use of long term longitudinal studies. This type of study is seldom used in present research in this area.

In the time remaining I would like to present some variables which are important factors in hearing research.

1. Subjects. Animals are well suited for the study of hearing phenomena. Their environment may be controlled and repeated observations made over long periods of time - preferably, the lifetime of the animal. The necessity of inflicting permanent hearing losses on the subjects in order to relate some factors of pre-loss hearing behavior to factors of permanent changes in hearing condition precludes the use of human subjects. Humans can be used, under conditions of hearing losses which are only temporary to validate the principles developed with animals.

2. Noise Exposure and Organismic States. We are interested in stimulus variables such as intensity, duration, rise time, frequency spectrum, number of pulses, number of exposures and their interactions. The experimenter may also be interested in organismic states induced by such things as stress, fatigue, and ototoxic drugs.

3. Hearing Test Method. Two psychophysical techniques, the Method of Adjustment (Békésy)(2) and the Method of Limits, have been used in human audiometry. In the Békésy technique, the subject is instructed to press a button when he can hear the tone and to release it when he cannot hear the tone. The button operates a motor-driven attenuator in such a way that the intensity of the tone is decreased when the subject presses the button and increased when he releases it. As a result, the stimulus intensity oscillates up and down across the subject's threshold, and a continuous printed record of the stimulus intensity gives a picture of the threshold. In the Method of Limits, a trial sequence is first begun with an audible tone which is reduced in intensity in preselected steps on successive trials until the subject fails to respond. The next sequence is given in the ascending order, with a tone that increases in intensity until a response is obtained. Normally, programming and recording are done manually by the experimenter.

Modified forms of the Method of Limits have been used with animals in a free field situation during the past three decades, but the reliable measurement of a threshold often took an hour or longer. This method, as used, could not be considered useful for measuring most transitory shifts in hearing sensitivity. The automatic character of the Békésy technique strongly appealed to the experimenter working with animals, and not long after it first appeared the method was tried with small animals. Blough (3) successfully obtained visual

thresholds with the pigeon by using two keys. The bird was reinforced for pecking one response key when an illumination patch was visible and another key when the patch was dark. Gourevitch, Hack, and Hawkins (6) adapted the Blough two-lever technique for auditory measurement in rats. They were interested in the possibility of using the method for tracing the gradual development of hearing impairment produced by ototoxic antibiotics. Reliability of threshold level was obtained only by averaging more than 100 threshold crossings.

Clack and Harris (4) used the same technique with rats except for a minor modification in training procedure. Their results were essentially the same as those obtained by Gourevitch el al (6), but they encountered extreme difficulty in maintaining stimulus control of behavior. Good performance with this complex method seems to be beyond the ability of lower animals.

The testing of hearing in animals at the Human Engineering Laboratories is accomplished by the Method of Limits (9). Speed of threshold measurement has been improved over earlier attempts with the method through elimination of most extraneous stimuli in the test environment, extensive training of the animals, use of shock reinforcer, and minimization of variations in the sound field. Recently we worked out a completely automated program for training and testing animals, so that spurious effects caused by differences in technique among various experimenters and similar uncontrolled factors could be minimized. The machine programs material either in a fixed, predetermined sequence, or in a sequence varied according to a number of animal performance criteria.

Both the Method of Limits and the Békésy technique involve problems in need of further attention, including optimum spacing of trials, efficient scheduling of reinforcement (especially within the region of uncertainty around the threshold), reduction of the occasional disturbing aspects of negative reinforcers, and obtaining independent criteria of good performance.

4. Data Handling. A major problem in bioacoustic research is that the experiments characteristically produce large masses of data. Scientists today have analytical tools such as factor analysis, partial and multiple correlation, and analysis of variance to yield information leading to prediction. Currently, the potential of the scientist is extended through the application of electronic computer technology to carry out complex operations heretofore impractical.

We hope to develop through attention to the individual's responses a model which will predict for each individual and not simply for the average subject as has been the case previously. Obviously our efforts are directed to a problem of most immediate interest to the military - damage-risk criteria for impulse noise.

References

1. American Standards Association, American Standard Specification for Audiometers for General Diagnostic Purposes, Z 24.5 - 1951, American Standards Association, New York (1951).

2. Békésy, G. V. A new audiometer. Acta Oto-Laryngol., 411-422, 35, 1947.

3. Blough, D. S. A method for obtaining psychophysical thresholds from the pigeon, J. exp. anal. Behav., 1958, 31-43.

4. Clack, T. D. and Harris, J. D. Auditory thresholds in the rat by a two-lever technique. Journal of Auditory Research, 1963, 3, 53-63.

5. Gardner... in - Rosenblith, W. A. Establishment of criteria based on the concept of noise exposure. Laryngoscope, 58, 497-507, 1958.

6. Gourevitch, G., Hack, M. H. and Hawkins, J. E., Jr. Auditory thresholds in the rat measured by an operant technique. Science, 1960, 131, 1046-1047.

7. Gravendell, D. W. and Plomp, R. The relation between permanent and temporary noise dips, AMA Arch. Otolaryngol. no. 6, 69, 714-719, 1959.

8. Harris, J. D. The auditory acuity of preadolescent monkeys. J. comp. Psychol., 1943, 35, 255-265.

9. Martin, P., Romba, J. J. and Gates, H. W. A method for study of hearing loss and recovery in rhesus monkeys. Tech Memo 11-62, U.S. Army Human Engineering Laboratories, APG, Md., May 1962.

10. Romba, J. J. and Gates, H. W. Hearing loss in the rhesus monkey resulting from repeated exposures to identical noises. Tech Memo 3-64, U.S. Army Human Engineering Laboratories, APG, Md., Jan. 1964.

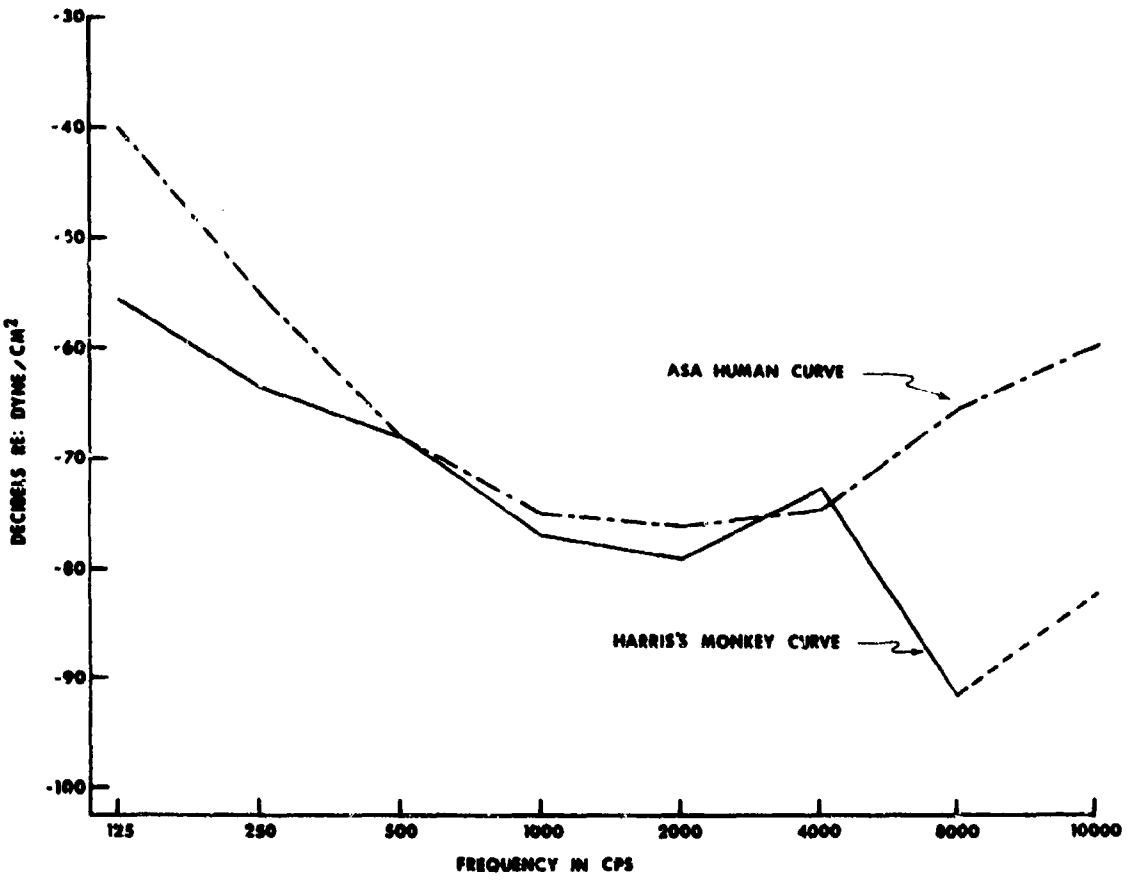

FIG. 1 SENSITIVITY CURVES FOR HUMANS AND MONKEYS

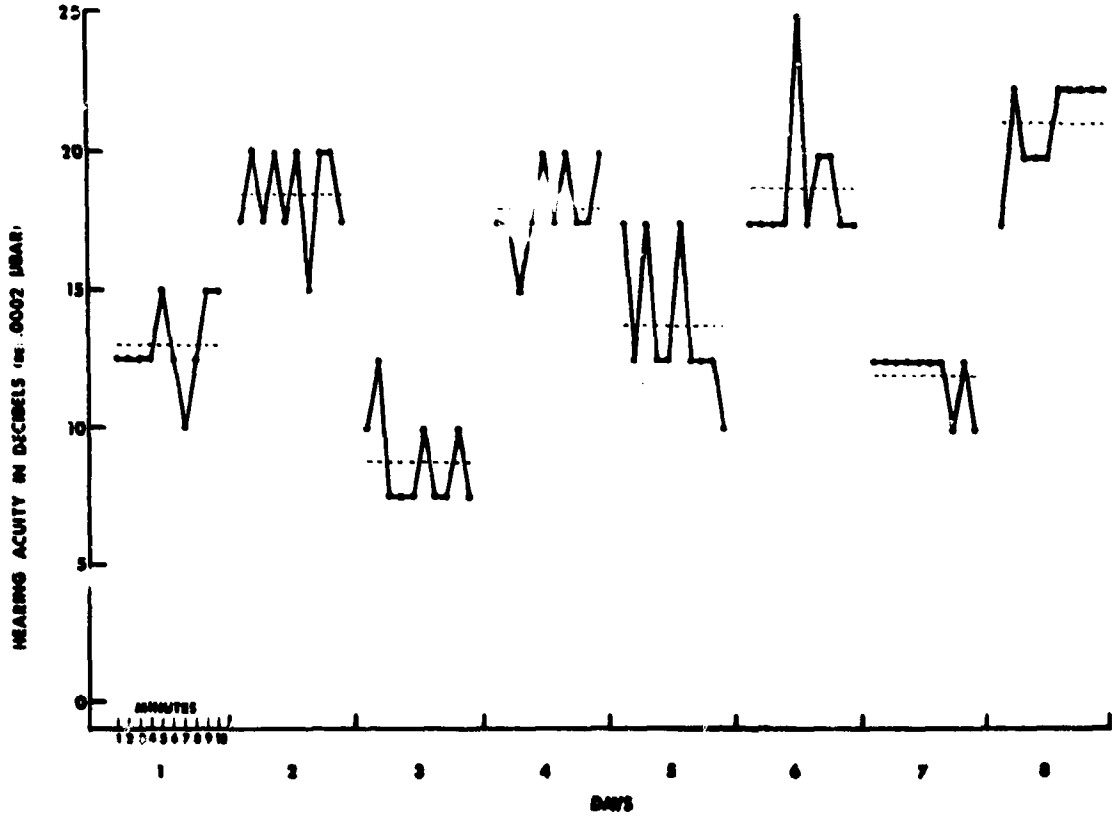

FIG. 2 WITHIN 10 MINUTE PERIODS AND BETWEEN DAYS VARIATION IN HEARING ACUITY OF ANIMAL S1 AT 2000 CPS

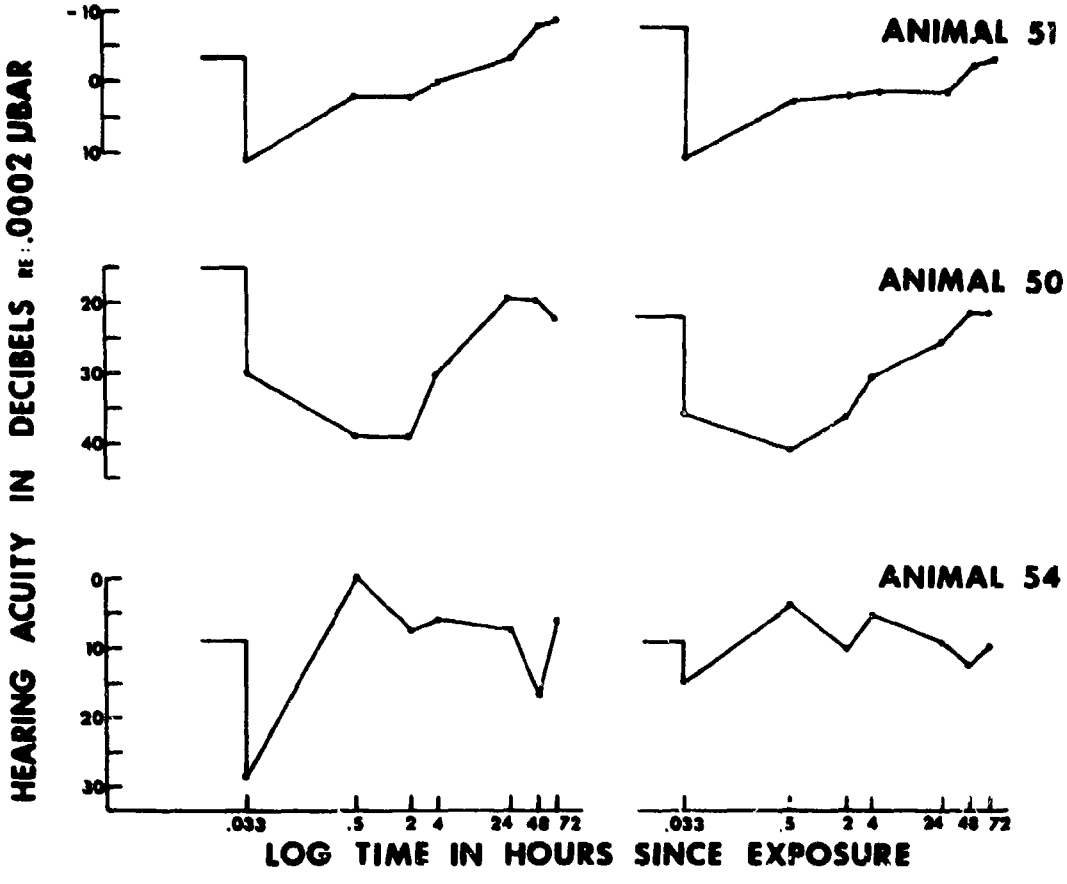

FIG. 3 SAMPLES OF HEARING LOSS AND RECOVERY TRENDS FOR THREE ANIMALS

THE EFFECT OF REACTOR IRRADIATION UPON HYDROGEN ADSORPTION BY AN ALUMINA CATALYST*

D. B. ROSENBLATT and G. J. DIENES**
U. S. ARMY, FRANKFORD ARSENAL
PHILADELPHIA, PA.

I. INTRODUCTION

The high specific surface area forms of alumina are extensively used in heterogeneous catalysis. There have been reports of enhancements in the catalytic activities of this material after exposure to reactor or gamma radiations. These enhancements were for reactions involving hydrogen, i.e. hydrogen - deuterium exchange, [1] and orthopara hydrogen conversion.[2] This suggests that there is a change in the manner in which hydrogen is adsorbed and desorbed from this material. In some preliminary work, we found substantial differences in the adsorption of hydrogen on virgin and irradiated gamma alumina.[3,4,5] These investigations have been extended and the results are given in this paper.

Changes in catalytic and gas adsorbing properties are to be expected if the surface of a solid is altered by exposure to radiation. There is a severe limitation in the choice of physical properties useful as indices of radiation damage to a surface. Electrical resistivity, mechanical measurements or optical absorption, useful in studying bulk effects, are not readily applied to a few atomic planes. Direct observation of surface effects with the field ion microscope of Muller is possible, but is limited to a few substances. Young[7] has used adsorption of krypton on alpha alumina to reveal an increase in the number of highly active adsorption sites after this material was exposed to reactor irradiation. Gas adsorption can, therefore, be used to detect surface damage, although the interpretation of results is usually not simple.

---

* Jointly supported under the auspices of the U.S. Atomic Energy Commission and the U. S. Army.

** Brookhaven National Laboratory, Upton, N. Y.

II. EXPERIMENTAL PROCEDURE

The material used in these experiments was Linde Alumina Type B, reported to consist chiefly of gamma alumina particles of about 80Å although a few relatively large (3500Å) alpha alumina grains are also present.[8] Electron diffraction results correspond to the gamma structure.[9] It is known that complex changes occur in gamma alumina if it is exposed to an increasing sequence of temperatures above 300°C. After such treatment, reduction in surface area (largely due to sintering), crystallographic changes and loss of some residual water all take place.[10] Moreover, infrared studies have shown that OH groups are bound to the surface and that the details of this binding are sensitive to sample history.[11] It is hardly surprising that observed catalytic activities vary greatly with the exact method used in calcining and otherwise preparing samples. To simplify correlation of the present gas adsorption results with the catalytic properties reported by others, we have avoided exceeding a temperature of 300°C during outgassing of samples. The specific surface areas of samples are then found to be constant, and great enough to be characteristic of a catalytically active substance.

After evacuation to pressures of 10-5mm of Hg at room temperature, or at 300°C, the specific surface areas of samples were determined by nitrogen adsorption at 78°K by the B.E.T. method of analysis. Hydrogen adsorption isotherms at 78°K were obtained by admitting known quantities of the gas into a constant volume apparatus containing a sample, and measuring the pressures after attainment of equilibrium. The ampoules containing the samples were then evacuated, sealed off and irradiated to doses of approximately 10^{18} nvt at 50°C in the Brookhaven Research Reactor. The seals of the samples were broken under vacuum by means of magnetically operated hammers thus facilitating the measurement of adsorption characteristics on irradiated samples without any intervening exposure to the atmosphere. After again degassing, measurements of nitrogen or hydrogen adsorption were repeated.

III. EXPERIMENTAL RESULTS

1. Effect of Irradiation on Specific Surface Area

The specific surface area of the gamma alumina, ($\sim$85 m^2/gm, using 16.2$Å^2$ as the area of an adsorbed nitrogen molecule at 78°K), was found to be independent of outgassing temperature between room temperature and 300°C and unaltered by subsequent exposure in a reactor to 10^{18} nvt. The fact that this radiation dose causes no change in specific surface area does not mean that the surface has been unaffected. Changes in the activity of adsorption sites will not affect the values obtained for the surface area, since the B.E.T. method measures the number of nitrogen molecules adsorbed in the

first monolayer, regardless of the details of the gas-solid interaction. In the case of our material, the high specific area is due to small particle size, and unless sintering or conversely the development of porosity occurs as a result of irradiation, no change in specific surface area is to be expected. Evidently such macroscopic changes did not occur in these samples, although they could certainly take place at higher radiation doses. Young, in about the same dose range, found no change in the specific surface area of alpha alumina.[7]

2. Effect of Irradiation on Hydrogen Adsorption

The isotherms obtained for hydrogen adsorption on a particular gamma alumina sample (wt. = 1.498$_{gm}$) before and after irradiation are shown in Fig. I. Irradiation affects not only the amount of adsorption but also the shape of the isotherm. However, the initial portions on both curves may be fitted by the Langmuir relationship $\theta = kp/(1 + kp)$ (where θ is coverage, p is pressure and k is a temperature dependent constant). The data, therefore, could be analyzed as follows. By algebraic rearrangement the Langmuir equation may be put into the linear form,

$$P/\left(\frac{x}{m}\right) = \frac{1}{AB} + \frac{p}{B}$$

where x is the number of molecules adsorbed at equilibrium on a sample of m grams at pressure p, B is the number of molecules required to complete a monolayer on 1 gm. of sample, and A is proportional to the ratio of the sticking probability to the evaporation rate. If $P/\left(\frac{x}{m}\right)$ is plotted vs. p the data will fall on a straight line in the Langmuir region and the constants B and A can be calculated from the slope $\left(\frac{1}{B}\right)$ and the intercept $\left(\frac{1}{AB}\right)$.

Fig. II presents several runs for the same sample as in Fig. 1, but replotted in the linear form. The data for the unirradiated sample follow a straight line up to P $\sim$ 300 mm of Hg, with B $\sim$ 24 cc/gm. After adsorption of $\sim$6 cc/gm, there is a drastic change in the manner of packing of hydrogen on the alumina surface, as indicated by the abrupt change in slope. After irradiation the sample behaves entirely differently. The initial B value is now between 5 and 6 cc/gm, i.e. $\sim$ 1/4 of the value for the unirradiated case.

Experiments with a large number of samples (see Fig. III) showed that the amounts of hydrogen adsorbed as well as the shapes of the isotherms varied greatly from sample to sample, even for unirradiated ones. These variations occurred although samples subdivided from the same original lots of powder were used. There were also differences in behavior between various irradiated samples.

However, the results are not random; the isotherms indicate that two different modes of adsorption are prevalent, with adsorption on the irradiated samples being characterized by only one of these modes. In Fig. III two different unirradiated samples (the solid lines) are shown; each sample was run twice, the curves for a single sample lie adjacent to one another. Data for several irradiated samples are also shown (the dashed curves). These curves all lie above those obtained for the unirradiated samples. Examination of curves such as those of Fig. III reveals that, in general, the results may be divided into the following three cases: Unirradiated type (1) with initial B $\approx$ 24 cc/gm, unirradiated type (2) with initial B $\approx$ 6 cc/gm, and irradiated samples for which initial B also $\approx$ 6 cc/gm.

The isotherms of Fig. IV may be compared with the linear plots of Fig. III. The changes in slope of Fig. III correspond to the changes in curvature of Fig. IV. Type (1) adsorption is represented by the points falling along the solid line in Fig. IV. As is explained later, this probably results from adsorption on a relatively clean sample, whereas the other data are influenced by nitrogen contamination. Some of this nitrogen is driven into the gas phase when hydrogen is adsorbed, resulting in a lowering in the net gas adsorption, i.e. our observations, which consist of measurements of loss of molecules from the gas phase are reduced when nitrogen is evolved. Those runs shown in Fig. IV which do not follow the solid curve belong to type (2) adsorption; where adsorbed hydrogen replaces nitrogen and a reduction in the net adsorption results.

3. Mass Spectrometer Evidence for Nitrogen Contamination

In Fig. IV the lowest curve, marked M.S., shows unusually small net adsorption and therefore substantial nitrogen release was suspected in this case. Consequently, the gas involved in this run was subjected to mass spectrometer analysis. After the last admission of hydrogen to the dead volume containing the sample (still at 78°K), (the last point shown for sample 100-I in Fig. IV) the gas was analyzed and found to consist of 88 percent hydrogen and 12 percent nitrogen. Since only hydrogen was admitted, the nitrogen must have been displaced from the sample as the hydrogen was adsorbed. The difference between the known quantity of hydrogen admitted and that remaining in the gas phase as shown by the mass spectrometer, i.e. the true hydrogen adsorption, was 4.42 cc/gm of sample. The gaseous nitrogen (by the mass spectrometer result) was 3.02 cc/gm. The net observed adsorption should therefore be 4.42 - 3.02 = 1.40 cc/gm which is close to the observed net adsorption of 1.39 cc/gm.

4. Chemical Analysis of Linde-Type B Alumina

Spectroscopic analysis cited by the manufacturer indicated that the material was relatively free from ordinary impurities, but no estimate of nitrogen content was furnished. Quantitative chemical

analysis of a number of fresh samples yielded very variable results, with a typical nitrogen content of 200 p.p.m. This amount of nitrogen, even if fully released, would not account for the sizable effect observed directly in the mass spectrometer experiment. However, surface nitrogen contamination would probably not show up in the chemical analysis. A simple calculation shows that a monolayer of nitrogen corresponds to 24,000 p.p.m. of nitrogen for the particle size of these samples.

IV. DISCUSSION

It is well known that very high temperatures and advanced vacuum techniques are required to free the surfaces of metallic oxides from all traces of original gas. Moreover gamma alumina possesses surface water which changes to bound hydroxyl groups in a complicated fashion as the temperature is increased.[11] Any effort to get a "pure" surface would result in a material totally different from those used in catalysis. The character of the surfaces after room temperature or 300°C degassing for 24 hours at 10^{-5} mm of Hg, must be regarded as unknown, and not necessarily reproducible. The radiation induced enhancements in the catalytic activity of gamma alumina demonstrated by others, and referred to here in Section I are apparently not due to an increase in surface area which remains constant at 85 m^2/gm.

In our experiments we have found (from the initial slopes of type (1) adsorption isotherms Fig. II or Fig. III) that 24 cc/gm of hydrogen would complete a monolayer, or using the measured surface area, the area occupied by a hydrogen molecule is

$$\frac{24}{85 \times 10^{20}} \quad \frac{\text{cc}}{(\text{Å})^2} = \frac{24 \times 6.02 \times 10^{23}}{22.4 \times 10^3 \times 85 \times 10^{20}}$$

$$\frac{\text{molecules of } H_2}{(\text{Å})^2} \quad \text{or} \quad \frac{85 \times 22.4}{6.02 \times 24} \quad \frac{(\text{Å})^2}{\text{molecule of } H_2} =$$

$$\frac{13.2\ (\text{Å})^2}{\text{molecule of } H_2}$$

This result is in approximate agreement with the experiments of de Boer et al[12] on the chemisorption of water on alumina. These workers showed that water molecules occupy 12.1 $(\text{Å})^2$ per water molecule. They claim that the most probable lattice plane in the surface will be the 1, 1, 1 plane of the spinel lattice, in which each oxygen ion takes in 6.74 $(\text{Å})^2$ of surface. Consequently each water molecule in the experiments of de Boer et al is chemisorbed to two oxygen ions in the alumina surface. In the hydrogen case, our experiments indicate that adsorption at low pressures occurs on all available sites and these hydrogen atoms are chemisorbed

in association with one oxygen surface ion. At higher pressures, when the coverage is about 6 cc/gm, the nature of the adsorption changes. At these pressures more hydrogen is adsorbed than indicated by the simple Langmuir isotherm valid at low pressures.

The remaining curves of Fig. III probably reflect contamination with nitrogen. This is suggested by the mass spectrometer analysis of the gas which is in contact with the powder.

From the data of Fig. IV, the differences between the solid line (type 1 adsorption) and the rest of the data is approximately linear with respect to pressure. This observation is difficult to interpret but one may speculate as follows. Let the hydrogen displace nitrogen from the sample at a constant rate. The released nitrogen will be partly readsorbed on the surface by physical adsorption. The rate of gaseous nitrogen production and destruction may be written as

$$\frac{dN_2^g}{dt} = K_1 H_2^g + K_2 N_2^s$$

$$- \frac{dN_2^g}{dt} = K_3 N_2^g$$

where N_2^g = concentration of nitrogen in gas phase

N_2^s = concentration of nitrogen on solid

H_2^g = concentration of hydrogen in gas phase

Under steady conditions

$$N_2^g = \frac{K_1}{K_3} H_2^g + \frac{K_2}{K_3} N_2^s$$

At low nitrogen pressures the nitrogen adsorption isotherm is approximately linear giving

$$N_2^s = K_4 N_2^g$$

and, therefore

$$\left(1 - \frac{K_2 K_4}{K_3}\right) \quad N_2^{\sigma} - \frac{K_1}{K_3} \quad H_2^{\sigma} \qquad \text{or}$$

$$N_2^{\sigma} - K H_2^{\sigma}$$

Thus, this speculation suggests that the major difference between type 1 and type 2 behavior is that in the latter case nitrogen is released. This release of nitrogen is facilitated by prior irradiation of the samples. The unirradiated type 2 samples appear to correspond to various degrees of nitrogen contamination.

The existence of an original layer of adsorbed nitrogen may be of significance for a qualitative understanding of the catalytic properties of gamma alumina. It is known that the unirradiated material has a variable catalytic behavior depending upon heating and outgassing procedures. Kohn and Taylor report that the choice of degassing technique affects the subsequent radiation enhancement of its catalytic activity.[1] Maurin, Ballentine and Sucher obtained no increase in catalytic activity if they irradiated in vacuum, but did obtain an increase if hydrogen were in contact with the alumina during irradiation.[2] This result appears to be in accord with our conclusions i.e. that irradiation in vacuum does not remove the nitrogen contamination but that it is replaceable by hydrogen.

ACKNOWLEDGMENTS

The experimental procedures were devised by W. L. Kosiba and R. C. Weed, and some of the surface area measurements were carried out by them. Some of the hydrogen adsorption measurements were made by J. C. Rothmann. We are indebted to D. A. Young for many suggestions concerning both the experimental and theoretical aspects of this problem. Thanks are due to L. Friedman and A. P. Irsa for the mass spectrometer measurements, to H. L. Finston for the chemical analyses of samples and to J. Jack and T. B. Flanagan for helpful discussions.

REFERENCES

1. H. W. Kohn and E. H. Taylor, J. Phys. Chem., 63, 500 (1959).
2. Maurin, Ballentine and Sucher, Brookhaven National Laboratory 3786 (1958).
3. D. B. Rosenblatt, G. J. Dienes and J. C. Rothmann, Bull. Am. Phys. Soc. 5, 167 (1960).
4. G. J. Dienes, in International Conference on Chemical Reactivity of Solids, Amsterdam, 1960, Elsevier, 416, (1961).
5. D. B. Rosenblatt and G. J. Dienes, Bull. Am. Phys. Soc. 8, 363 (1963).
6. E. W. Muller, J. Appl. Phys. 28, 1, (1957).
7. D. A. Young, J. Phys. Chem. Solids 15, 119 (1960).
8. R. G. Rudness, Linde Company (private communication).
9. H. W. Kohn (private communication).
10. A. S. Russell et al., Alcoa Research Laboratories, Technical Paper No. 10 (revised) 25 - 39 (1956).
11. J. B. Peri and R. B. Hannan, J. Phys. Chem. 64, 1526 (1960).
12. J. H. de Boer et al. J. Catalysis 2, 1 (1963).

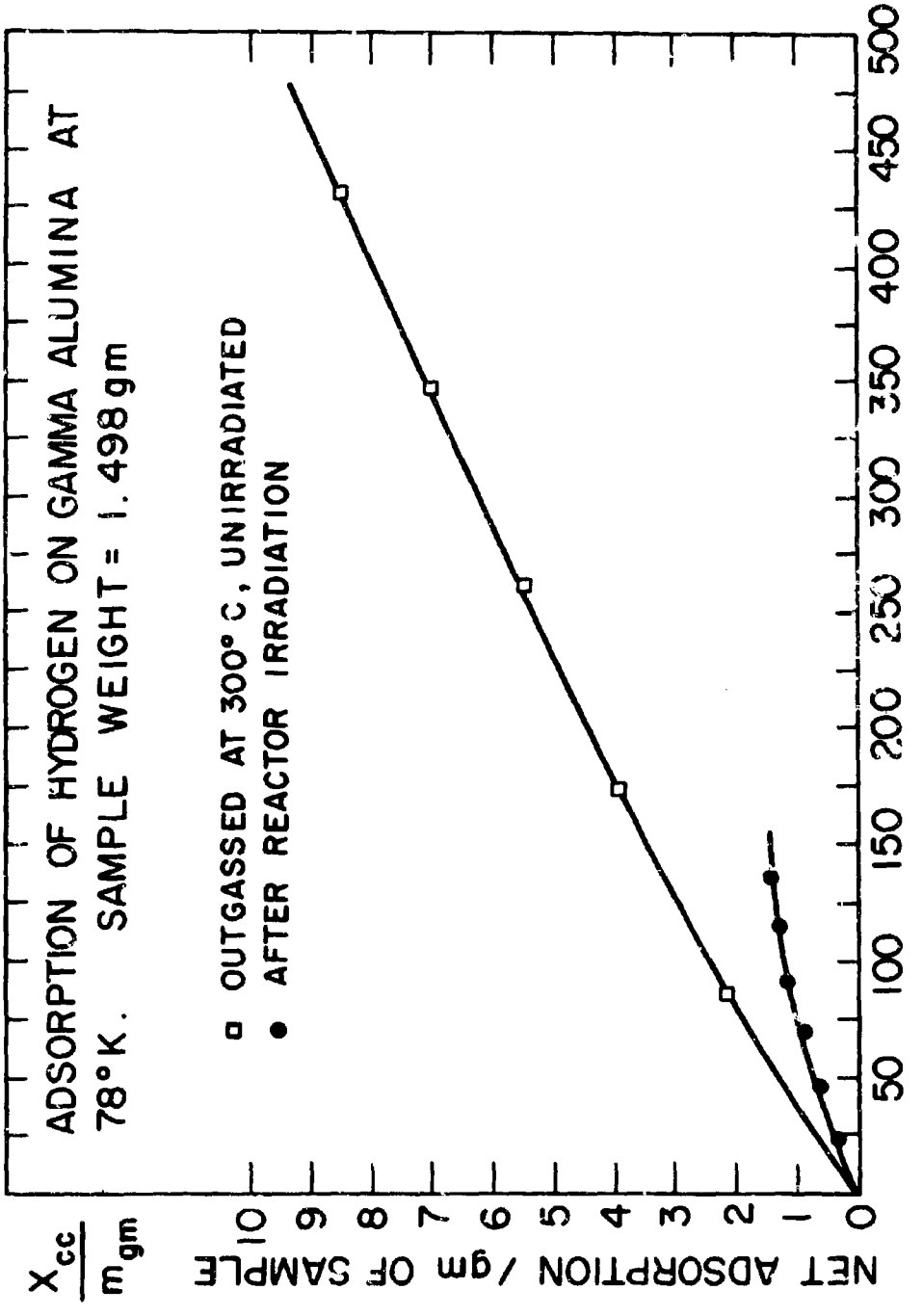
ADSORPTION OF HYDROGEN ON GAMMA ALUMINA AT
78° K. SAMPLE WEIGHT = 1.498 gm
□ OUTGASSED AT 300° C, UNIRRADIATED
● AFTER REACTOR IRRADIATION
NET ADSORPTION / gm OF SAMPLE
$\frac{X_{cc}}{m_{gm}}$
0 1 2 3 4 5 6 7 8 9 10
50 100 150 200 250 300 350 400 450 500
P mm OF Hg

FIG. 1

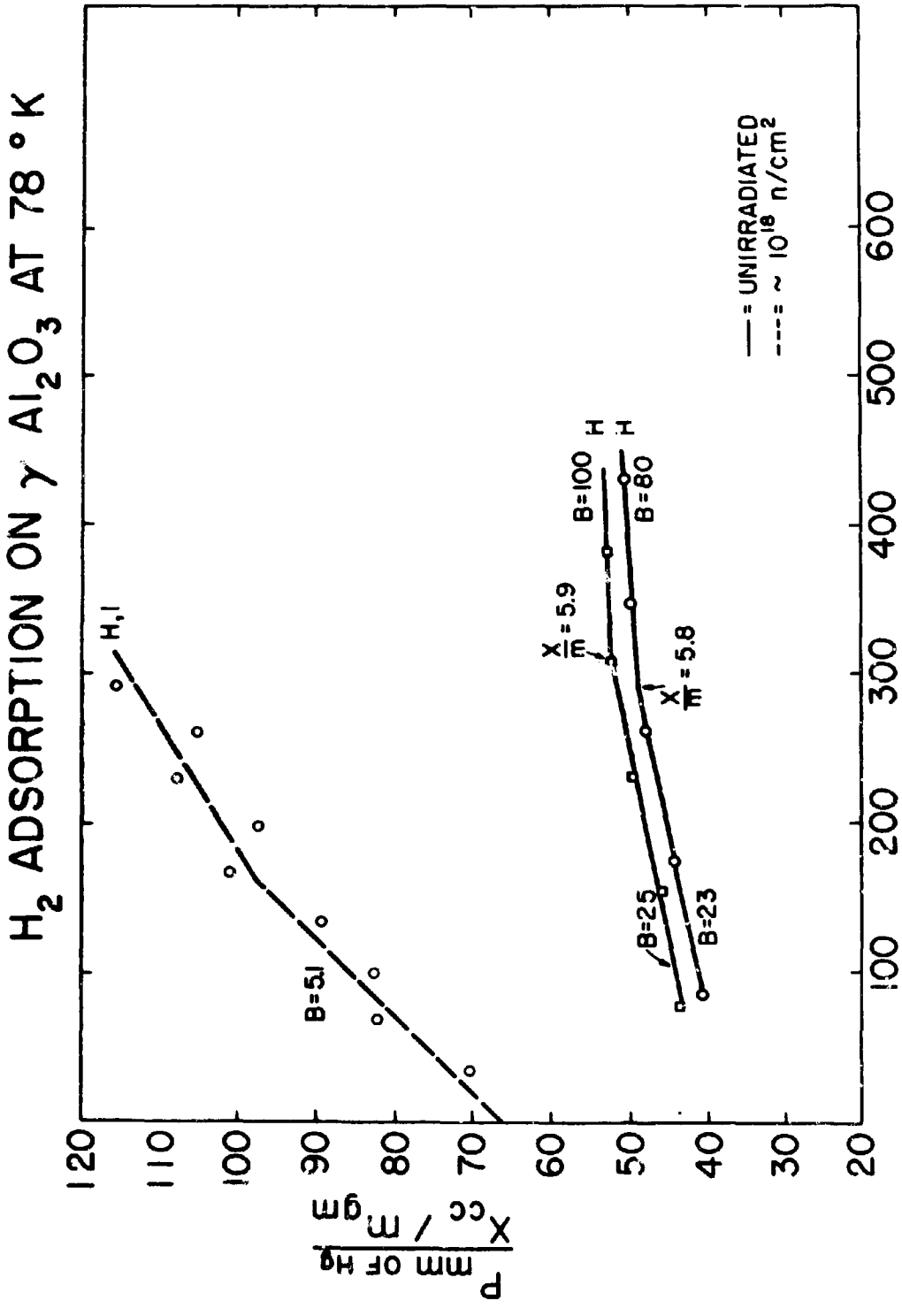
H2 ADSORPTION ON γ Al2O3 AT 78 °K
P mm OF Hg / Xcc / m gm
P mm OF Hg
= UNIRRADIATED
---= ~ 10^18 n/cm^2
H,I
B=51
B=100
B=80
B=25
B=23
X/m = 5.9
X/m = 5.8
H
H
120
110
100
90
80
70
60
50
40
30
20
100
200
300
400
500
600

FIG. 2

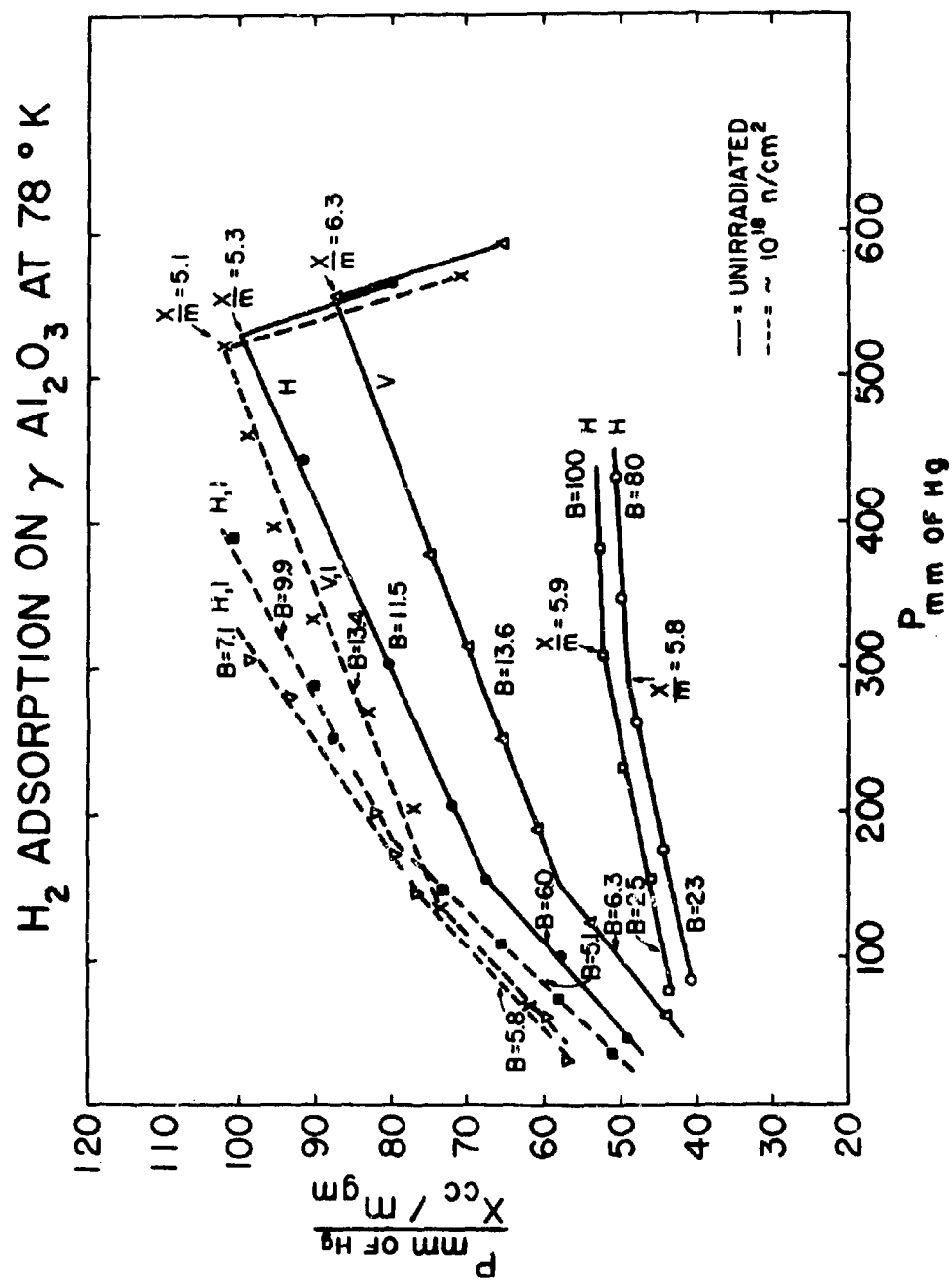
H2 ADSORPTION ON γ Al2O3 AT 78 °K
P mm of Hg / Xcc / gm
P mm of Hg
—= UNIRRADIATED
---= ~ 10^18 n/cm²
X/m = 5.1
X/m = 5.3
X/m = 6.3
X/m = 5.9
X/m = 5.8
B=7.1
B=9.9
B=13.4
B=11.5
B=13.6
B=60
B=5.8
B=5.4
B=6.3
B=25
B=23
B=100
B=80
H
V
H1
V1

FIG. 3

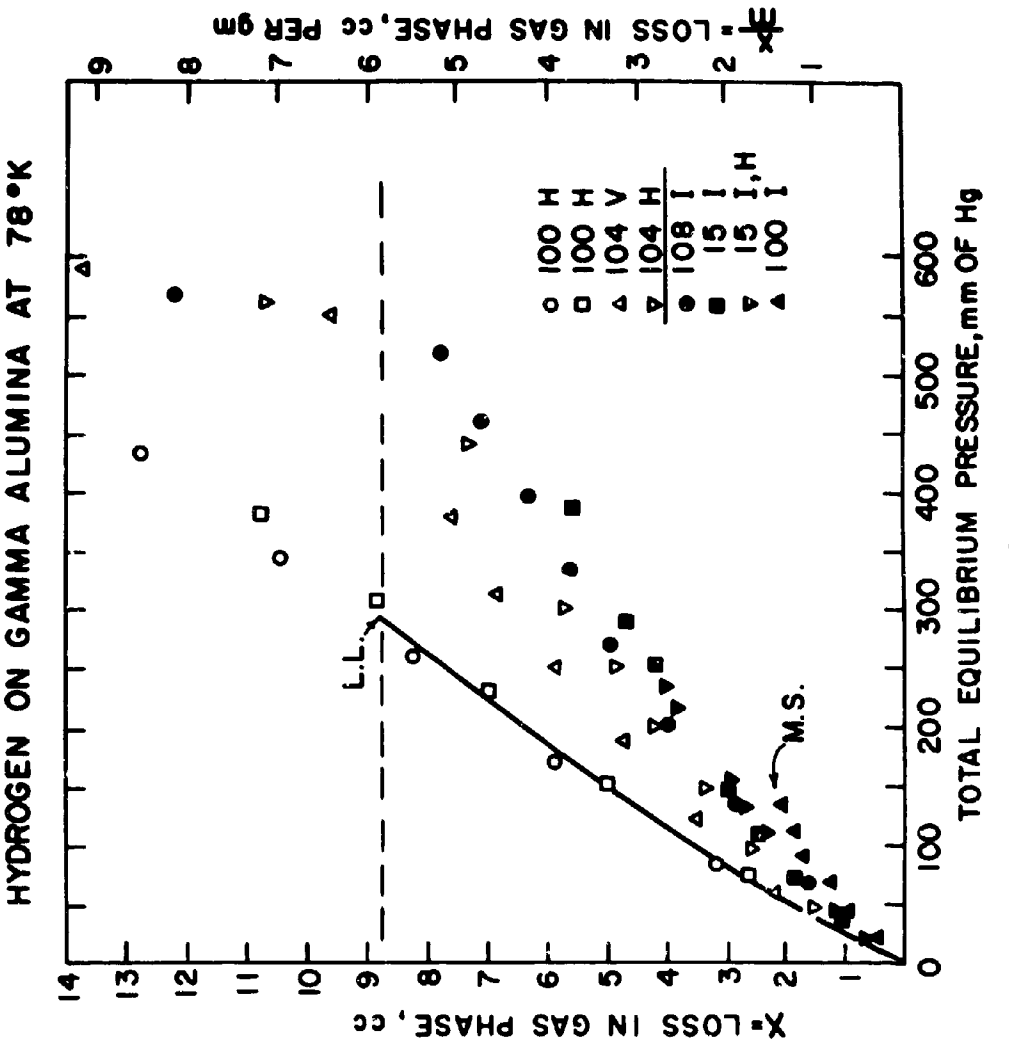
HYDROGEN ON GAMMA ALUMINA AT 78°K
X=LOSS IN GAS PHASE, cc
X/m=LOSS IN GAS PHASE, cc PER gm
TOTAL EQUILIBRIUM PRESSURE, mm OF Hg
L.L.
M.S.
100 H
100 H
104 V
104 H
108 I
15 I
15 I,H
100 I

FIG. 4

BOUNDARY LAYERS IN COUPLE-STRESS ELASTICITY AND STIFFENING OF THIN LAYERS IN SHEAR

M. A. SADOWSKY, Y. C. HSU, and M. A. HUSSAIN
WATERVLIET ARSENAL
WATERVLIET, NEW YORK

BOUNDARY LAYERS AND SKIN EFFECTS: Boundary layer effects in hydro- and aerodynamics and skin effects in high frequency alternating currents have a common general characteristic: they refer to some phenomenon like fluid flow through a pipe or alternating current flow through a wire which takes place distributed over a cross section area. The distribution over the cross section of quantities characterizing the phenomena such as velocity of flow and density of current follows some definite law over almost the entire cross section. The exception is a very thin boundary region of the cross section in which the distribution of the characteristic quantities quite suddenly changes to an entirely different law. In the example of fluid flow through a pipe, the variation of the flow velocity is shown in Fig. 1. It is practically constant throughout the cross section, except in the boundary layer, where it rapidly drops down to zero due to frictional (viscous) adhesion of the fluid to the wall of the pipe. In the example of a high frequency alternating current the distribution of the current density is shown in Fig. 2. The current density is zero throughout almost the entire cross section, except in the boundary layer (the "skin") which alone carries the (almost) entire current.

No boundary layer phenomena have been known in the theory of elasticity (in elastostatics) up to now. In elastodynamics, surface waves have been known since the time of Rayleigh. Considering elastostatics, we have, since 1962, a fundamental change of all aspects as seen in the paper by Professor R. D. Mindlin of Columbia University under the title "Influence of Couple-Stresses on Stress Concentrations." The new element introduced into elasticity are couple-stresses, and Professor Mindlin's paper contains far reaching theoretical and practical results. In the present paper the consideration of couple-stresses leads to the detection of boundary layers in elasticity. The elastic body appears wrapped up in a very thin skin displaying a formerly unheard of behavior with respect to stress distribution and deformation.

STATEMENT OF THE PROBLEM: The characteristic innovations which couple-stresses bring to the mathematical theory of elasticity can be shown within the subject of plane strain. We will limit our exposition of couple-stress theory to plane strain. Our aim is a comparison of results given by classical plane strain theory with results given by couple-stress theory. In a narrower sense, the aim is given by the title of this paper: detection of boundary layers in elasticity and stiffening of thin layers in shear.

THE INCOMPLETE SYSTEM OF 8 EQUATIONS IN 9 UNKNOWNS COMMON TO CLASSICAL ELASTICITY AND COUPLE-STRESS ELASTICITY: Before the classical and couple-stress theories diverge they establish a common ground of 8 equations in 9 unknowns. Since such a system is incomplete, it will require a completion, and this is where the couple-stress theory differs from classical elasticity. In the classical theory, the completion leads to a 9 by 9 system, in the couple-stress theory it leads to a 12 by 12 system. The completions are incompatible and mutually exclusive, which entitles the couple-stress theory to the rank of an essential modification of elasticity theory, not just an additional development.

The common ground of both theories described by means of a Cartesian system x, y is as follows: it begins with the concept of the displacements $u = u(x,y)$ and $v = v(x,y)$ from which issue the following concepts and equations:

The 3 strain components $\epsilon_x, \epsilon_y, \gamma_{xy}$, defined by

$$\epsilon_x = \frac{\partial u}{\partial x}\ ,\quad \epsilon_y = \frac{\partial v}{\partial y}\ ,\quad \gamma_{xy} = \frac{\partial v}{\partial x} + \frac{\partial u}{\partial y} \qquad (1)\ (2)\ (3)$$

The 4 stress components $\sigma_x, \sigma_y, \tau_{xy}, \tau_{yx}$, connected with the strain components by 3 stress-strain relations

$$2G\epsilon_x = \sigma_x - \nu(\sigma_x + \sigma_y) \qquad (4)$$

$$2G\epsilon_y = \sigma_y - \nu(\sigma_x + \sigma_y) \qquad (5)$$

$$2G\gamma_{xy} = \tau_{xy} + \tau_{yx} \qquad (6)$$

The stress components must equilibrate. The equilibration equations read

$$\frac{\partial \sigma_x}{\partial x} + \frac{\partial \tau_{yx}}{\partial y} = 0 \tag{7}$$

$$\frac{\partial \tau_{xy}}{\partial x} + \frac{\partial \sigma_y}{\partial y} = 0 \tag{8}$$

Eqs. (1)-(8) form a system of 8 equations in 9 unknowns

$$u, v, \epsilon_x, \epsilon_y, \gamma_{xy}; \sigma_x, \sigma_y, \tau_{xy}, \tau_{yx} \tag{9}$$

common to classical elasticity and to couple stress theory. The different meanings of τ_{xy} and τ_{yx} are shown in Fig. 3. The notation defines $\tau_{\alpha\beta}$ as the shearing stress in the direction β on a face whose outer normal is in the direction α .

COMPLETION OF THE SYSTEM IN CLASSICAL ELASTICITY: The system is completed by the equation of equilibrium with respect to rotation in the xy-plane:

$$\tau_{xy} = \tau_{yx} \tag{10}$$

The completed system consists of 9 Eqs.(1)-(8) and (10) for the 9 unknowns cited in (9).

DEVELOPMENT OF PLANE STRAIN THEORY IN CLASSICAL ELASTICITY: The analytic development of the classical 9 by 9 system leads to the following result: the 9 by 9 system is reducible to a single equation

$$\nabla^4 \phi = 0 \tag{11}$$

for a single function $\phi = \phi(x,y)$ called the stress function. All quantities mentioned in (9) are derivable from the stress function as follows: The stresses are given by the partial derivatives

$$\sigma_x = \phi_{yy} \quad , \quad \sigma_y = \phi_{xx} \quad , \quad \tau_{xy} = \tau_{yx} = -\phi_{xy} \tag{12}$$

the strains follow from the stress-strain relations Eqs.(4)-(6). The displacements are obtained from Eqs. (1)-(3) by integration. We note that $\nabla^2\phi$ is a potential function on account of Eq. (11). We determine by integration a pair of conjugate potential function H and f_y connected to $\nabla^2\phi$ by the Cauchy-Riemann equations

$$\frac{\partial H}{\partial x} = \frac{\partial f_x}{\partial y} = \nabla^2\phi \tag{13}$$

$$\frac{\partial f_x}{\partial x} = -\frac{\partial H}{\partial y} = \text{potential function conjugate to } \nabla^2\phi \tag{14}$$

The displacements are given by

$$\begin{aligned} 2Gu &= (1-\nu)H - \phi_x \\ 2Gv &= (1-\nu)f_y - \phi_y \end{aligned} \tag{15}$$

The determination of a specific ϕ from Eq. (11) depends on boundary conditions.

COMPLETION OF THE SYSTEM IN COUPLE-STRESS THEORY: Three new unknowns ω_z, μ_x, μ_y are introduced. This extends the set (9) of unknowns to 12:

$$u, v;\ \epsilon_x, \epsilon_y, \gamma_{xy};\ \sigma_x, \sigma_y, \tau_{xy};\ \omega_z, \mu_x, \mu_y \tag{16}$$

ω_z is the rotation of the element defined by

$$\omega_z = \frac{1}{2}\left(\frac{\partial v}{\partial x} - \frac{\partial u}{\partial y}\right) \tag{17}$$

μ_x and μ_y are couple-stresses (Fig. 4). There are two equations of stress-strain relations type involving ω_z, μ_x, μ_y:

$$\mu_x = 4Gl^2\frac{\partial \omega_z}{\partial x} \tag{18}$$

$$\mu_y = 4Gl^2\frac{\partial \omega_z}{\partial y} \tag{19}$$

The quantity l appearing here is the third (third independent) constant of elasticity (Mindlin's couple stress constant). The equation of equilibrium with respect to rotation in the xy-plane is

$$\frac{\partial \mu_x}{\partial x} + \frac{\partial \mu_y}{\partial y} + \tau_{xy} - \tau_{yx} = 0 \tag{20}$$

The 12 equations (1)-(8), (17)-(20) constitute a complete set with regard to the 12 unknowns (16).

We note that Eq. (10) of classical elasticity and Eq. (20) of the couple-stress theory are incompatible, which is characteristic of an essential progress involved in the couple-stress theory.

DEVELOPMENT OF PLANE STRAIN IN COUPLE-STRESS THEORY: The analytic development of the 12 by 12 system of the couple-stress theory leads to the result that two stress functions $\phi = \phi(x,y)$ and $\psi = \psi(x,y)$ are needed from which all of the unknowns (16) can be derived. These stress functions are governed by two Cauchy-Riemann equations

$$\frac{\partial}{\partial x}\left[2(1-\nu)\ell^2\nabla^2\phi\right] = \frac{\partial}{\partial y}\left[\psi - \ell^2\nabla^2\psi\right] \tag{21}$$

$$-\frac{\partial}{\partial y}\left[2(1-\nu)\ell^2\nabla^2\phi\right] = \frac{\partial}{\partial x}\left[\psi - \ell^2\nabla^2\psi\right]$$

We see that $2(1-\nu)\ell^2\nabla^2\phi$ and $\psi - \ell^2\nabla^2\psi$ are conjugate potential functions. We consequently have individual equations

$$\nabla^4\phi = 0 \tag{22}$$

$$\nabla^2\psi - \ell^2\nabla^4\psi = 0 \tag{23}$$

We note that Eq. (22) is identical with Eq. (11) and thus is again a potential function. All 12 quantities mentioned in (16) are derivable from the stress functions as follows: the 6 stresses and couple-stresses are given by partial derivatives

$$\sigma_x = \phi_{yy} - \psi_{xy} \qquad \sigma_y = \phi_{xx} + \psi_{xy}$$

$$\tau_{xy} = -\phi_{xy} - \psi_{yy} \qquad \tau_{yx} = -\phi_{xy} + \psi_{xx} \tag{24}$$

$$\mu_x = \psi_x \qquad \mu_y = \psi_y$$

The 3 strains follow from the stress-strain relations Eqs. (4)-(6). The rotation ω_z is given by

$$\omega_z = \frac{\psi}{4G\ell^2} \tag{25}$$

The displacements are given by

$$2Gu = (1-\nu)H - \phi_x - \psi_y$$
$$2Gv = (1-\nu)h_y - \phi_y + \psi_x \qquad (26)$$

in which H and h_y are defined by Eqs. (13) and (14). The set of twelve unknowns in (16) is thus expressed in terms of the stress functions ϕ and ψ which in turn are governed by Eqs. (21).

BOUNDARY CONDITIONS AT INTERFACE y = const: Since a couple-stress elasticity solution depends on a system of differential equations (21) of order 6 while in classical elasticity the only governing equation (11) is of order 4, the number of boundary conditions at an interface must increase proportionately from four conditions in the classical theory to six conditions in the couple stress-theory. For the interface $y = 0$ (Fig. 5) the classical conditions require the continuity of

$$u \,,\; v \,,\; \sigma_y \,,\; \tau_{yx} \qquad (27)$$

The couple-stress theory requires the continuity of

$$u \,,\; v \,,\; \omega_z \,,\; \sigma_y \,,\; \tau_{yx} \,,\; \mu_y \qquad (28)$$

Since all of the classical continuity conditions are preserved in the couple-stress theory, and two more continuity conditions are added, it is felt that the couple-stress theory puts a higher degree of emphasis on a general preservation of continuity at interfaces.

ELASTIC SEMIPLANE IN SHEAR BONDED TO A RIGID SEMIPLANE: Let us etch a straight line across the bonded semiplanes prior to deformation (Fig. 6a). The classical solution for the state of shear (Fig. 6b) shows the line broken into two halves, each half remaining straight and both meeting at an angle at the interface. The couple-stress theory solution (Fig. 6c) shows a smooth transition from the rigid straight half to a curve which approaches the line in Fig. 6b asymptotically. The space in which the curve 6c differs appreciable from the asymptote is the boundary layer; its thickness is about 5ℓ. The stress-strain phenomena at the interface are most unusual, as illustrated by the values

$$\tau_{yx} = -\tau_{xy} \,, \quad \gamma_{xy} = 0 \qquad (29)$$

STIFFENING OF A THIN LAYER IN SHEAR: Imagine a thin layer bonded to two rigid plates which transmit a shearing stress τ_{yx} to the layer. In classical elasticity the etched line will remain straight and turn as shown in Fig. 7a. In couple-stress theory, since $\gamma_{xy} = 0$ at both interfaces, the turning will develop but gradually in the upper and lower boundary layers, reaching the value $\gamma_{xy} = \tau_{yx}/G$ in the middle space between both boundary layers. But if the layer is as thin as in Fig. 7c, there will be no in between space and the etched curve is hardly different from its original straight position. This leads to a strong reduction of the displacement of the upper face of the layer relative to its lower face, which without the knowledge of couple-stress theory may be misinterpreted as a stiffening of the shearing modulus G of the material to a high multiple when the material comes in very thin layers (10ℓ thickness) and is subject to shear.

REFERENCES: Complete mathematical analysis of the subject of the present paper is found in the following report by the Research Division of the Watervliet Arsenal:

AD WVT-RR-6320, October 1963, Boundary Layers in Couple-Stress Elasticity and Stiffening of Thin Layers in Shear, Technical Report by M. A. Sadowsky, Y. C. Hsu, M. A. Hussain, Watervliet Arsenal, Watervliet, New York.

A more detailed derivation of the constitutive equations of couple-stress theory is given in the following report by Professor R. D. Mindlin of Columbia University:

Influence of Couple-Stresses on Stress Concentrations, Office of Naval Research, Project NR 064-388, Contract Nonr 266(09), Technical Report No. 49, September 1962.

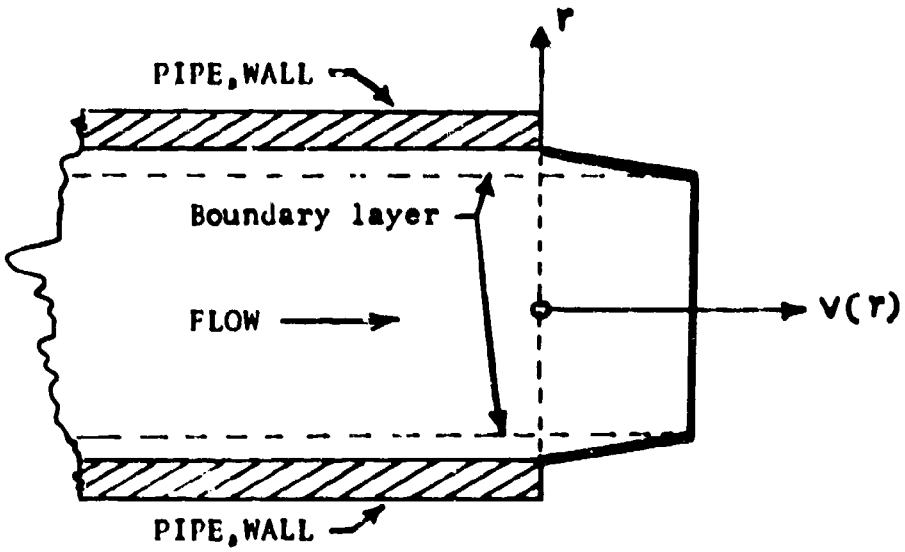

Figure 1. Velocity distribution in presence of a boundary layer

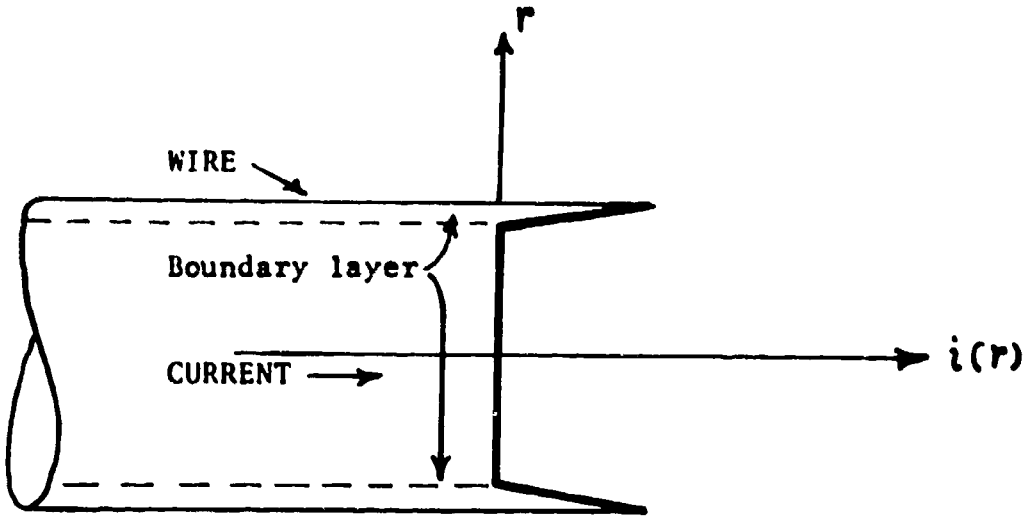

Figure 2. Current density distribution in skin effect

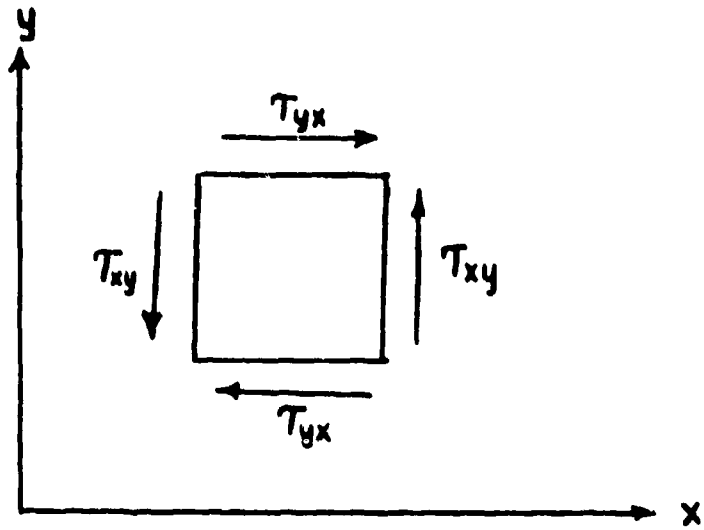

Figure 3. Conceptual difference between τ_{xy} and τ_{yx}

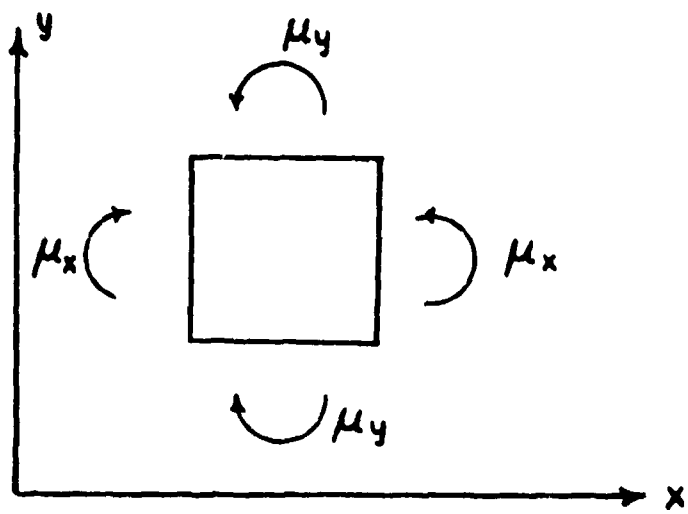

Figure 4. Couple-stresses: Cartesian components μ_x and μ_y.

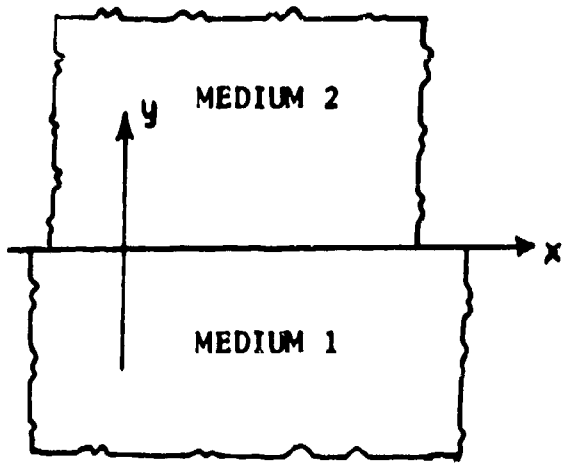

Figure 5. Interface at $y = o$

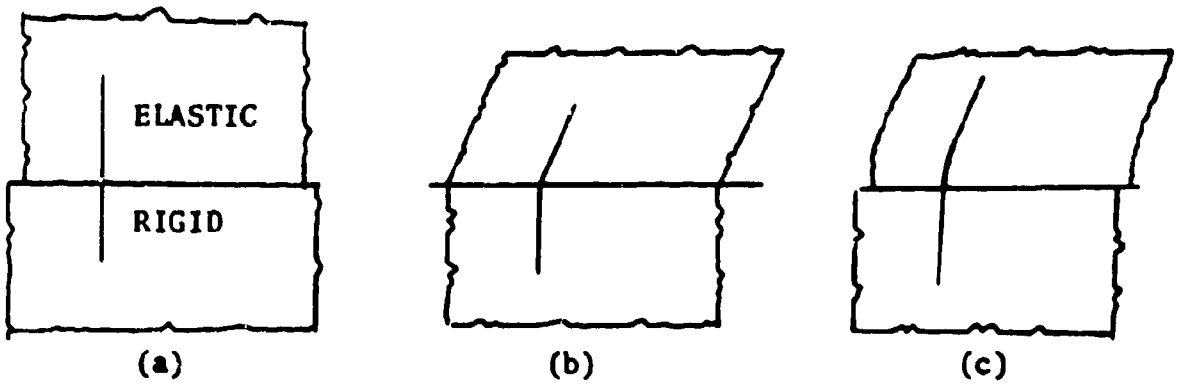

Figure 6. Bonded elastic and rigid semiplanes

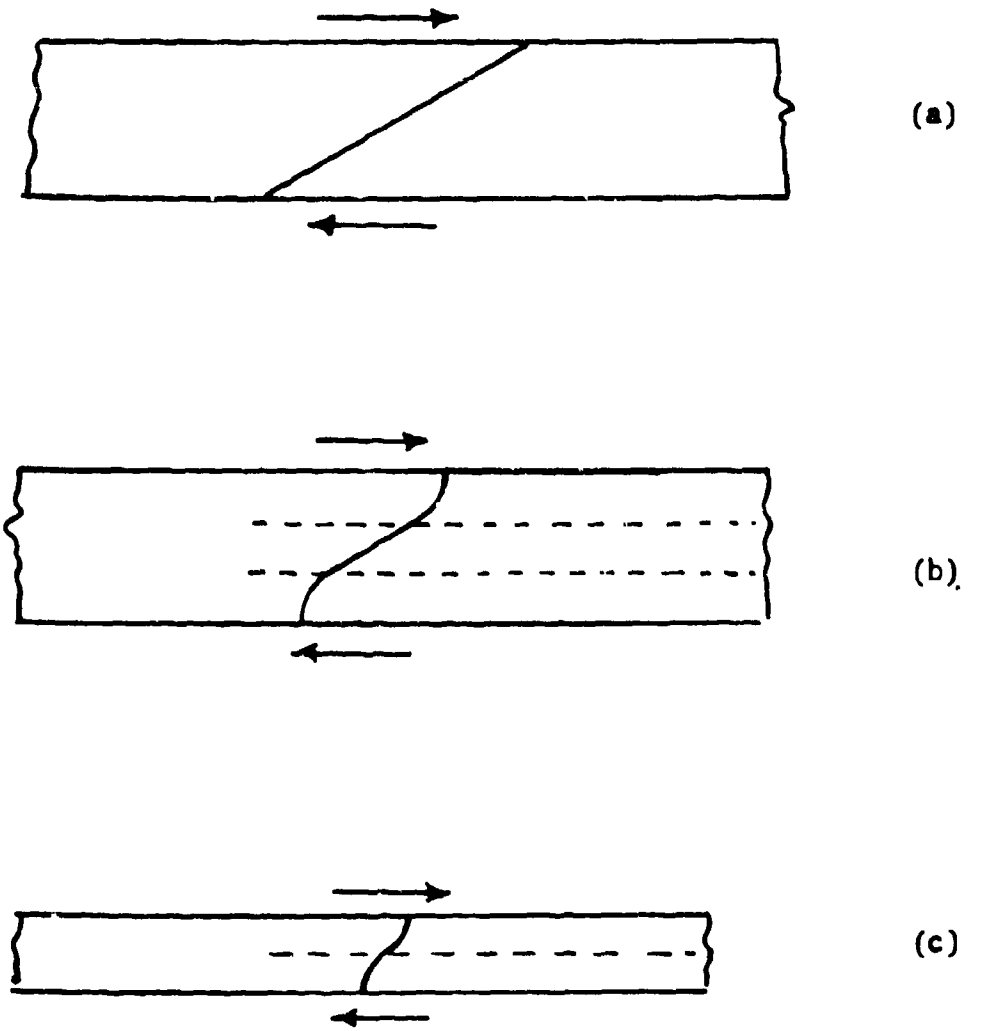

Figure 7. Thin layer in shear bonded to rigid plates at both faces.

THE PURIFICATION AND CHARACTERIZATION OF STAPHYLOCOCCAL ENTEROTOXIN B

EDWARD J. SCHANTZ, WILLIAM G. ROESSLER, JACK WAGMAN, LEONARD SPERO,
DAVID STEFANYE, DAVID A. DUNNERY, AND MERLIN S. BERGDOLL
UNITED STATES ARMY BIOLOGICAL LABORATORIES
FORT DETRICK, FREDERICK, MARYLAND

Staphylococcus aureus produces a variety of toxic substances. One of these substances is enterotoxin B, which causes emesis and diarrhea in experimental animals very similar to that caused by enterotoxin A, which is usually found in cases of food poisoning in humans (1). Bergdoll, Sugiyama, and Dack (2) reported the first significant purification of this toxin, by a combination of acid precipitation, adsorption on alumina, adsorption on IRC-50, and starch electrophoresis. Recently Frea, McCoy and Strong (3) effected a partial purification of this toxin by a combination of alcohol precipitation, filtration on Sephadex, and electrophoresis on Sephadex. Only milligram quantities of toxin were obtained by these methods. This paper describes a method of purification based on chromatographic procedures employing carboxylic acid resins that results in enterotoxin B of higher purity and in higher yields than that obtained by the above methods. The partial physical and chemical characterization of this purified toxin shows that the toxin is a simple protein composed of a single polypeptide chain with a molecular weight of approximately 35,000.

METHODS

The toxin was produced by culturing S. aureus strain S-6 for 18 hours with aeration in a medium containing 1% N-Z-Amine A (Sheffield Farms), 1% Protein Hydrolysate Powder (Meade Johnson & Co.), 0.001% thiamin, and 0.001% nicotinic acid adjusted to pH 6.5. The fermented culture usually contained between 0.1 and 0.2 mg of toxin per ml, based on Oudin tests. The toxin constituted 0.5 to 1% of the total organic solids in the culture. The culture was passed through a Sharples centrifuge to remove the bulk of the cells. The carboxylic acid exchange resin, used for the first and second steps in the purification, was Amberlite CG-50, 100-200 mesh (Rohm and Haas Co.). This resin was exchanged with sodium at least once and

partly neutralized as specified in the purification procedure by suspending the resin in 3 to 4 volumes of 0.05 M monosodium phosphate and titrating to the desired pH with sodium hydroxide. Before use the partially neutralized resin was washed thoroughly with water to remove the buffer. The carboxymethyl cellulose (CM) (Carl Schleicher and Schuell Co.), used in the final step in the purification, was Selectacel Ion Exchange Cellulose, No. 77, Type 20. It was used as purchased after washing thoroughly with water. The linear gradient buffer system used to elute the toxin from the carboxymethyl cellulose was patterned after that described by Mikes (4). Assays for the toxin were carried out by a modification of the Oudin serological technique (5). In this technique, the rate of diffusion of the toxin into a tube of agar gel containing antisera to the purified toxin serves as a measure of the toxin concentration (6). These assays require 24 to 72 hours for completion, but are serologically specific for the toxic protein and served as a reasonably accurate means for a quantitative determination of the toxin throughout the purification procedure. The results are expressed as mg of toxin per ml or, with the Kjeldahl nitrogen value, as mg of toxin per mg of nitrogen. Theoretically, when the Oudin assay shows 6.25 mg of toxin per mg of nitrogen, the toxin is pure. However, the variability of the Oudin test is ±10% and additional tests were necessary to measure small amounts of impurities. Ouchterlony tests (7), employing antisera from crude toxin preparations in the agar gel, were used for this purpose. Although the serological tests (Oudin and Ouchterlony) do not measure toxicity per se, they correlated well with toxicity tests in monkeys. The absorbance at 277 mμ was used also as a rapid but nonspecific assay to follow the proteins through the chromatographic fractionations. These measurements were made with a Model DU Beckman spectrophotometer. The results are expressed as mg of protein per ml, using an extinction value of 1.3 for 1 mg per ml at 277 mμ in a 1-cm cell. The absorbance could not be used as a measure of purity because the contaminating proteins contributed to the absorbance along with the toxin. Final preparations of the toxin were assayed by intravenous injection or feeding to rhesus monkeys to obtain the specific biological activity characterized by emesis or diarrhea. In conducting this research the animals were maintained in compliance with the principles established by the National Society for Medical Research (8).

Sedimentation studies were carried out on a Model E Spinco ultracentrifuge. Amino acid analyses were carried out on a Phoenix Amino Acid Analyzer by the method of Spackman, Stein, and Moore (9). Terminal amino acids were determined by N-dinitrophenylation with 2,4-dinitrofluorobenzene followed by acid hydrolysis for the N-terminal acid (10) and hydrazinolysis followed by treatment with benzaldehyde and identification on the automatic amino acid analyzer for the C-terminal acid (11).

PURIFICATION PROCEDURE

The method of purification is outlined in Figure 1 and involves the following steps:

Step 1. The centrifuged culture containing up to 0.2 mg of toxin per ml with an Oudin assay value of 0.04 mg toxin per mg of nitrogen was diluted with two volumes of water and the pH adjusted to 6.4. The toxin was removed from the diluted culture with CG-50 resin partly neutralized to pH 6.4 by stirring for about 30 minutes at room temperature. Two grams of this resin were sufficient to remove the toxin from one liter of diluted culture. Usually about 50 liters of diluted culture, or sufficient culture to isolate one gram of purified toxin, were processed at one time. The resin containing the toxin and impurities was filtered into a column (about 3 x 30 cm for resin from 50 liters), washed with one column volume of water, and the toxin fractionally eluted with 0.5 M sodium phosphate at pH 6.8 in 0.25 M sodium chloride. The fractions containing the peak of protein material were selected on the basis of the absorbance at 277 mμ and more precisely selected on the basis of Oudin tests and pooled. At this point the pooled fractions amounted to about one per cent of the culture volume; the Oudin test showed about 4.5 mg of toxin per mg of nitrogen, and the yield was 70 to 80%.

Step 2. The pool of fractions from Step 1 was dialyzed to remove the salts and the toxin was readsorbed on a column of CG-50; this time the CG-50 was partially neutralized at pH 6.8. Twenty grams of resin were used per gram of protein (column about 3 x 30 cm for 20 g resin). The partial neutralization of the resin at a higher pH reduced the adsorption of the impurities but still allowed complete adsorption of the toxin. Thus, the bulk of the impurities passed through the resin. After the resin was washed with water the toxin was fractionally eluted with 0.15 M disodium phosphate, and the fractions containing the peak of toxin with an Oudin value of about 5 mg of toxin per mg of nitrogen or more were selected and pooled for further purification. At this point the pooled fractions showed an Oudin value between 5.5 and 6 with a purity of 85 to 90%. The yield was 65 to 70%.

Step 3. The combined fractions from step 2 were dialyzed to bring the salt below 0.01 M and the toxin was adsorbed and chromatographed on a column of carboxymethyl cellulose. Twenty grams of this resin were used per gram of protein as measured by absorbance at 277 mμ. A linear gradient phosphate buffer from 0.02 to 0.07 M, pH 6.8, was passed through the column at a rate of 0.3 ml per minute per square cm of area on the column. The purified toxin usually came off in the fractions between 0.035 and 0.045 M, but the exact peak was located by measuring the absorbance at 277 mμ and more

accurately evaluated with Oudin tests. The fractions that had Oudin values of 6.2 or greater per mg of nitrogen and that showed only a single antigen-antibody line in the Ouchterlony tests at a level of 0.5 mg of toxin per ml were selected as the purified toxin. These fractions were pooled, dialyzed to remove most of the buffer salts, centrifuged to remove any insoluble material, and freeze-dried. The over-all yield of toxin in the purified state usually amounted to 50 to 60% based on the Oudin assay of the original culture.

PHYSICAL AND CHEMICAL CHARACTERIZATION

Table I shows some of the chemical and physical properties of the purified toxin. The freeze-dried protein is a snow-white fluffy powder that is very soluble in water and salt solutions. The dry protein also hydrates readily when exposed to an atmosphere with a relative humidity of 30% or more. Tests for carbohydrate, lipid, and nucleic acids were negative. Tests for α and β lysins, apyrase, and dermonecrotic substances, normally found in the culture, were negative in the purified preparation. The Kjeldahl nitrogen content of the protein (free of buffer salts) is 16.1%.

In velocity ultracentrifugation, solutions of the purified enterotoxin exhibit only a single symmetrical, sedimenting boundary as illustrated by the representative schlieren curves shown in Figure 2. Analyses of boundary spreading and of enterotoxin distribution at sedimentation equilibrium show that the purified material possesses a high degree of homogeneity with respect to both molecular weight and density. Its partial specific volume (0.743) and infrared spectral absorption are typical of simple proteins. The molecular weight of 35,300 obtained by sedimentation-diffusion is in good agreement with results by approach-to-equilibrium sedimentation. Stability in sedimentation behavior was observed over the pH range 5 to 10.

Electrophoretic studies showed the toxin preparation to be a single component with an isoelectric point at about pH 8.6. Deionization of a solution of the toxin on a column of mixed bed resin, M31, showed an isoionic point at pH 8.55. The toxin has a maximum absorption at 277 mμ with an extinction (E, 1%, 1 cm) of 14. The ratio of the absorption at 260 mμ to that at 277 mμ was 0.47, which confirms other tests showing that very little if any nucleic acid material is present in the preparation.

The amino acid analysis of the toxin is given in Table II. The molecule is composed of 18 different amino acids. No cysteine was found, but 2 half-cystine residues are present. High percentages of aspartic acid and lysine are indicated but, compared with most proteins, the composition of the toxin is not unusual. The recovery of the amino acid residues amounted to 102% and the nitrogen calculated from these residues in addition to the amide nitrogen amounted

to 103%. Also, the sulfur in the methionine and half-cystine residues amounted to about 102% of the total sulfur determined by the Parr bomb technique. The complete accountability (within experimental error) of the total nitrogen and sulfur shows that the toxin is composed of amino acids only and therefore is classed as a simple protein. The total of the free acid groups in the aspartic and glutamic acid residues is much greater than that of the free basic groups of lysine, arginine, and histidine, which indicates that the toxin should have an isoelectric point on the acid side of the pH range. The 30 amide groups forming asparagine or glutamine account for the alkaline isoelectric point at about pH 8.6.

The N-terminal amino acid is glutamic acid and the C-terminal acid is lysine. Quantitative estimation of the terminal acids showed 1.1 residues of glutamic acid per mole of protein for the N-terminal acid and 0.73 residues of lysine per mole of protein for the C-terminal acid. These values are within experimental error, under the circumstances of the experiments, for one mole of each terminal acid and are consistent with the representation of the primary structure of the toxin as a single polypeptide chain. No other amino acids were indicated in the analyses for the terminal acids, which lends support to the physical evidence on the high degree of purity of the toxin preparation.

This protein is unusual in many respects. The biological activity characterized by emesis or diarrhea is stable to heating at 100°C for 10 minutes without appreciable loss in activity. Under these conditions the toxin is precipitated from the solution, but when this precipitate is redissolved by cooling and raising the pH of the solution, practically all of the original Oudin activity and sickness-producing properties in monkeys are recovered. The toxin is quite stable over a pH range of 4 to 10 at room temperature. The biological activity is refractory to the action of various enzymes such as trypsin, pepsin, chymotrypsin, and papain.

BIOLOGICAL EVALUATION

Serological studies on the purified toxin using Oudin and Ouchterlony techniques also indicate a high degree of homogeneity or purity. When the toxin was employed as an antigen at concentrations of 0.5 mg or less per ml and allowed to diffuse into agar gel (Ouchterlony technique) containing antisera against crude preparations of the toxin, only a single line of antigen-antibody formed. However, by using very high concentrations of the toxin (up to 15 mg/ml) in these tests, one or two faint lines appeared, indicating that small amounts of impurity might be present. These lines disappeared completely on a 32-fold dilution of the toxin solution, but the enterotoxin line did not disappear until it had been diluted more than 8000-fold. If a minor antigen is present as an impurity, these data

indicate that it constitutes less than one per cent of the preparation. It is possible that the faint lines are artifacts and not impurities. They are not eliminated from the toxin by further chromatography on carboxymethyl cellulose. Also, when the toxin was tested by the slide immunoelectrophoresis technique, using rabbit, burro, or horse sera, only the one line, due to the enterotoxin, was formed. The toxin therefore is considered to have a purity of 99% or more.

When the toxin was tested in rhesus monkeys, emesis or diarrhea was produced in 50% of the animals (effective dose, ED_{50}) at an intravenous dose of 0.1 to 0.3 μg per kg of monkey weight and at an oral dose of 1 μg per kg.

CONCLUSIONS

In conclusion, a chromatographic method has been developed for the isolation of enterotoxin B from S. aureus cultures. Physical, chemical, and biological studies show that the toxin isolated by the chromatographic method is very pure and is a simple protein consisting of a single peptide chain with a molecular weight of approximately 35,000. Many grams of the purified enterotoxin have been prepared and this supply has allowed an extensive research program to be carried out on the characterization and determination of the structure of this protein as well as investigations on the biological effects of the toxin in host animals.

REFERENCES

(1) E.P. Casman, M.S. Bergdoll and J. Robinson, Designation of Staphylococcal Enterotoxins, J. Bacteriol. 85 715 (1963).

(2) M.S. Bergdoll, H. Sugiyama and G.M. Dack, Staphylococcal Enterotoxin, I. Purification, Arch. Biochem. Biophy. 85 62 (1959).
H.E.Hibnick and M.S. Bergdoll, Arch.Biochem.Biophy.85 70 (1959)

(3) J. I. Frea, E. McCoy and F.M. Strong, Purification of Type B Staphylococcal Enterotoxin, J. Bacteriol. 86 1308 (1963).

(4) O. Mikes, Chromatography, p. 118, Ed. E. Heftmann, Reinhold Pub. Corp., New York 1961.

(5) J. Oudin, Methode d' Analyse Immunochemique par Precepitation Specific en Milieu Gelifie Comp. Rend. Acad. Sci. 222 115 (1946).

(6) M.S. Bergdoll, M.J. Surgalla and G.M. Dack, Staphylococcal Enterotoxin. Identification of a Specific Precipitating Antibody with Enterotoxin - Neutralizing Property. J. Immunol. 83 334 (1959).

(7) O. Ouchterlony, Antigen-Antibody Reactions in Gels, Acta Pathol. Microbiol. Scand. 32 231 (1953).

(8) National Society for Medical Research. Principles of Laboratory Animal Care. Biomedical Purview 1 14 (1961).

(9) D.H. Spackman, W.H. Stein and S. Moore, Automatic Recording Apparatus for Use in Chromatography of Amino Acids, Analytical Chem. 30 1190 (1958).

(10) H. Fraenkel-Conrat, J.I. Harris and A.L. Levy, Terminal and Sequence Studies in Peptides and Proteins, Methods of Biochemical Analyses Vol II, p. 359, Ed. D. Glick Interscience Pub. Inc., New York 1955.

(11) S. Akabori, K. Ohno, and K. Narita, Hydrazinolysis of Proteins and Peptides: Method for the Characterization of C-terminal Amino Acids in Proteins, Bull. Chem. Soc. Japan 25 214 (1952).

TABLE I

SOME PROPERTIES OF PURIFIED ENTEROTOXIN B

Appearance	White fluffy powder
Solubility	Very soluble in water and salt solutions
Type of protein	Simple (contains simple amino acids only)
Nitrogen content	16.1%
Sedimentation coefficient ($s^{\circ}_{20^{\circ},w}$)	2.89 S (Single component)
Diffusion coefficient ($D^{\circ}_{20^{\circ},w}$)	7.72×10^{-7} cm^2 sec^{-1}
Partial specific volume	0.743
Molecular weight	35,300
Electrophoresis (free)	Single component
Isoelectric point	About 8.6
Extinction ($E^{1\%}_{1cm}$)	14
Toxicity, ED_{50}	0.1 to 0.3 μg/kg (rhesus monkey, IV)
Purity	>99%

TABLE II

AMINO ACID COMPOSITION OF STAPHYLOCOCCAL ENTEROTOXIN B

Amino acid	Amino acid residues per 100 g of protein	Residues per molecule to nearest integer
	grams	
Alanine	1.36	7
Amide groups		30
Arginine	2.84	6
Aspartic acid	18.33	56
Cysteine	0.00	0
Half-cystine	0.59	2
Glutamic acid	9.60	26
Glycine	1.91	12
Histidine	2.54	7
Isoleucine	3.49	11
Leucine	6.44	20
Lysine	17.25	47
Methionine	3.09	8
Phenylalanine	5.93	14
Proline	2.22	8
Serine	4.15	17
Threonine	4.56	16
Tryptophan	0.71	1
Tyrosine	10.82	23
Valine	6.10	22

FIGURE 1

SCHEME FOR THE PURIFICATION OF ENTEROTOXIN B

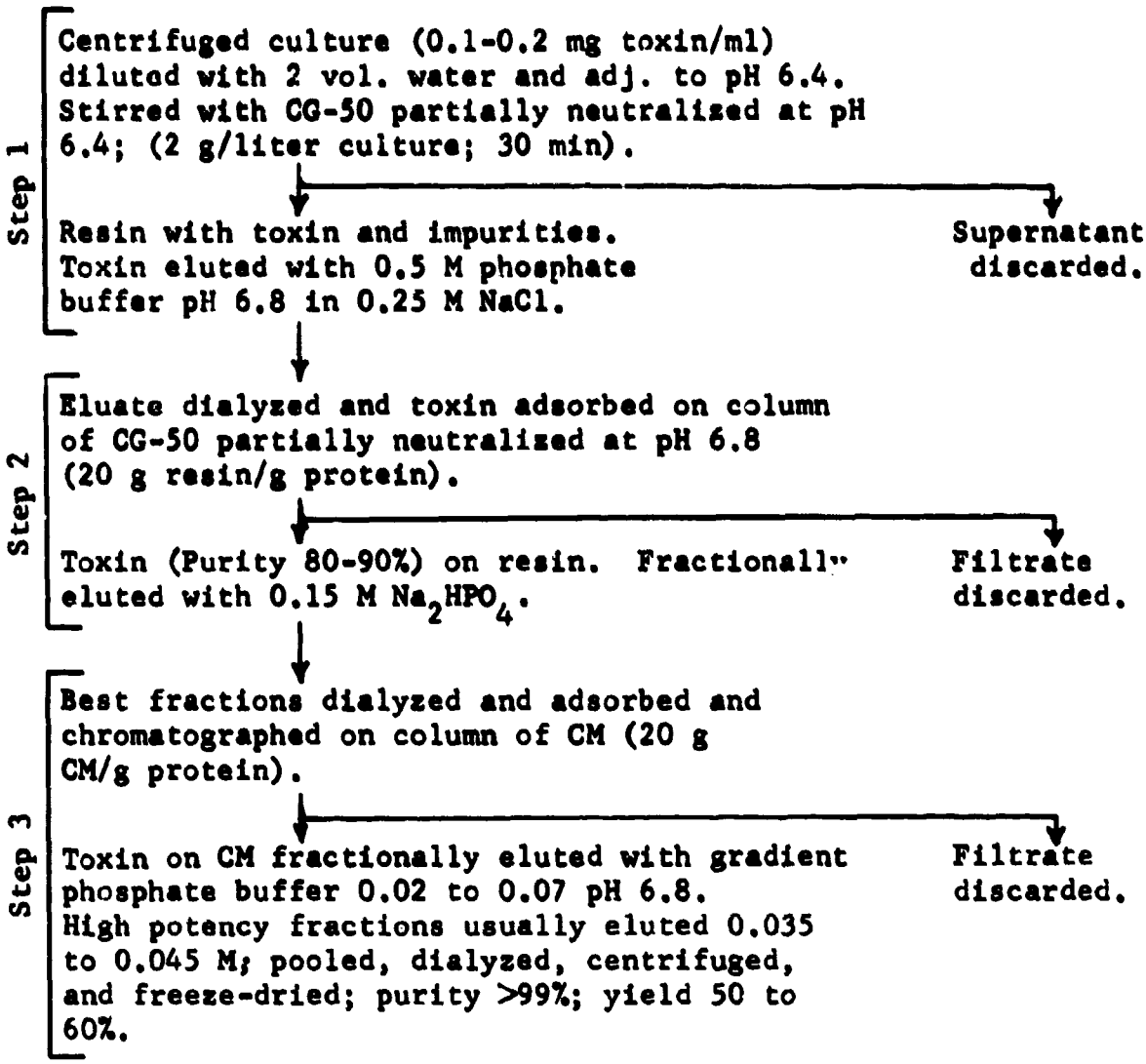

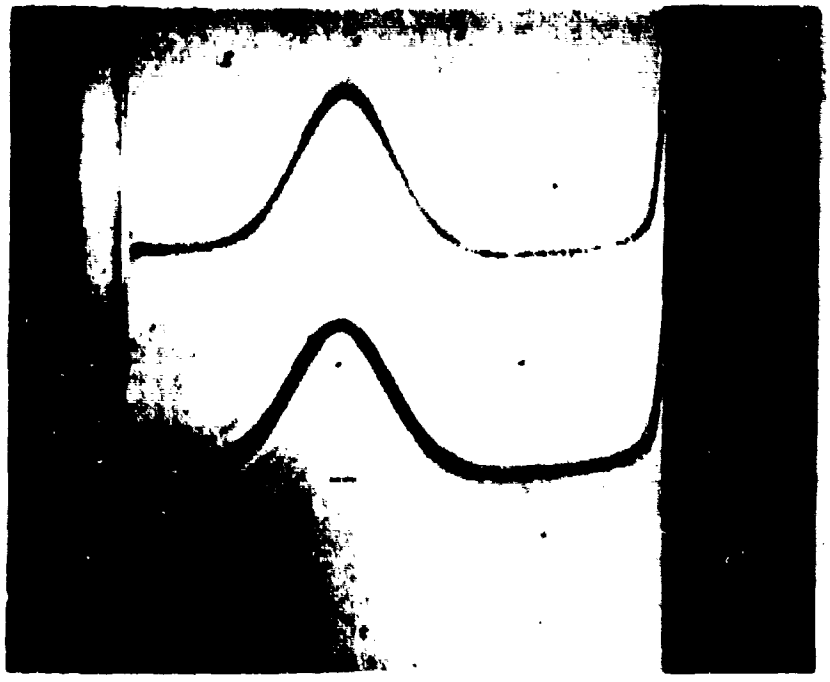

FIGURE 2. Photograph of schlieren sedimentation curves of two independently purified preparations of enterotoxin B. Concentration: 10 mg/ml in 0.05 M phosphate buffer, pH 6.8. Photograph taken 128 minutes after reaching full speed, 59,780 r.p.m. Sedimentation from left to right; temperature 20°C; schlieren angle, 60 degrees.

DIRECT MODULATION OF A HE-NE GAS LASER

ERNST J. SCHIEL
U. S. ARMY ELECTRONICS RESEARCH & DEVELOPMENT LABORATORIES
FORT MONMOUTH, NEW JERSEY

Modulation of a laser beam can be achieved either by passing the light through a modulator after the light has left the laser (indirect modulation) or by changing one of the operational parameters of a laser system, e.g., modulating the pump (direct modulation). The He-Ne gas laser lends itself very easily to a direct amplitude modulation. When the discharge in the He-Ne gas mixture is excited by an RF field, and the amplitude of the field modulated, the stimulated emission of the laser will also be modulated.

Two different types of He-Ne gas lasers were employed in our experiments. The first set of measurements was taken with a laser with confocal mirror configuration emitting in the near infrared at 11,530Å. The bore diameter of the discharge tube is 10 mm and the partial pressure of He 1 mm Hg and that of Ne 0.1 mm Hg. A Johnson Viking Valient transmitter provided the RF power to pump the laser. The power is capacitively coupled into the gas by an electrode in the middle of the discharge tube; two electrodes at ground potential are located near the two ends of the tube. The maximum achievable power output of the laser requires a pump power around 50 w. Laser power output and the length of the plasma column in which amplification occurs vs the pump power are shown in Fig. 1. Pump power threshold for stimulated emission of radiation is 17 per cent of the pump power for maximum output; the length of the plasma column is 35 cm at this point. By modulating the pump power between threshold and maximum, 100 per cent amplitude modulation can be achieved. Since the Johnson Viking Valient transmitter permits the modulation of the RF only in the audio frequency range, our experiments were limited to this range. The light was filtered by a Schott RG 10 and a Tiffen Nr. 025 filter in order to suppress the background radiation of other than the lasing Ne lines. Silicon and germanium photodiodes were used as detectors and the beam pattern was visually observed at an RCA 6914 image converter tube. The second set of measurements was taken with a Spectra-Physics (Model 112) laser with hemispherical

mirror arrangement emitting in the visible part of the spectrum at 6328Å. The bore diameter of the discharge tube is 6 mm and the partial pressure of the 0.5 mm Hg and that of the Ne 0.1 mm Hg. The same pumping techniques were used as for the infrared laser. Silicon photodiodes and an RCA 7102 photomultiplier were used as detectors, the signal was recorded on a 545A Tektronix oscilloscope.

For modulation experiments the pump power was adjusted to a certain carrier level (bias) and then a modulation of 1 kc was put on it. A completely sinusoidal light modulation resulted if only a small percentage of pump power was modulated (Fig. 2(a)). However, if the modulation of the pump was increased beyond a unique level dependent upon the bias, clipping began. A specific combination of bias and modulation gave a certain maximum instantaneous power level and a minimum instantaneous power level. At too high a maximum instantaneous power level, upper clipping occurred (Fig. 2(b)). At too low a minimum instantaneous power level, lower clipping occurred (Fig. 2(c)) since the length of the plasma column dropped below threshold. It is interesting to notice that lower clipping has never been observed to be "flat," while upper clipping is always "flat." In Fig. 3 the amplitude of the photodetector response as a function of the percentage of pump power modulation for several bias levels has been given; the dotted line indicates the division between unclipped (sinusoidal) and clipped photodetector response, since saturation limits the power output of the laser.

The dependence of the amplitude of the modulated light emitted by a gas laser on the modulation frequency reveals not only information about the frequency limitations of the direct modulator concept, but also indicates a bottleneck in the generation of excited Neon energy states which limits the power output of a He-Ne gas laser. Experiments on frequency dependence were conducted in the following manner. The modulation of the RF was adjusted at a low frequency so that a large sinusoidal modulation of the lights without clipping resulted. Keeping the RF power and modulation level constant the modulation frequency was increased and the corresponding light output observed. The results of these experiments are shown in Fig. 4.

Up to 7 kc/sec the amplitude of the modulated light of both lasers stays at a constant level, then the amplitude decays with increasing frequency. The decay of the infrared laser is much more pronounced than that of the red laser. The asymptotes of the decay characteristics are:

$$I = I_o \left(\frac{\alpha}{\omega}\right)^{1.64} \quad \text{(Infrared Laser)}$$

and

$$I = I_o \left(\frac{\alpha}{\omega}\right)^{0.606} \quad \text{(Red Laser)}$$

$$\alpha = 2\pi\, 11.1 \cdot 10^3 .$$

For comparison the amplitude vs frequency characteristic for an exponentially decaying signal is plotted in Fig. 4. This characteristic follows:

$$I = I_0 \frac{\alpha}{\sqrt{\alpha^2 + \omega^2}}$$

and the asymptote: $I = I_0 \left(\frac{\alpha}{\omega}\right)$. The time constant $\tau = \frac{2\pi}{\alpha}$ for the exponential decay has been chosen so that all the asymptotes meet at the same frequency f = 11.1 kc/sec.

The characteristics of both lasers follow a "power law" decay considering the short lifetimes of the higher laser transition Neon states ($3s_2$ for the red and $2s_2$ for the infrared laser) and also the short lifetime of the terminal state of the laser transition ($2p_4$ for both lasers) only the long lifetime of the He metastables (2^1S and 2^3S) or the 1s states of Neon can account for a slow decay. The destruction of He metastables by energy transfer to Neon is directly dependent on the partial pressure of Neon in the ground state and this pressure (i.e., the number of available Neons in the ground state) is limited by the diffusion Neon in 1s state to the wall of the discharge tube. The diffusion Neon 1s to the wall requires a longer time for a larger tube diameter and a gas laser with a large bore discharge tube will, therefore, not follow a high modulation frequency. For this reason the infrared laser (which is the one with the bigger tube diameter) has a much longer decay and does not follow at higher modulation frequencies. The red gas laser (with the small tube diameter) follows higher modulation frequencies much better. The dependence of laser operation on the tube diameter is also evident in the relation for optimum laser gain:

$$pD = \text{constant}$$

(pressure times tube diameter is constant).

Helium-Neon gas lasers with a small tube diameter (2 mm) should, therefore, have a short decay time and can follow a high modulation frequency with reasonable modulation depth of the emitted radiation. The pumping process is not directly linked to the Neon diffusion process and it is of little consequence for time dependence of light emission if the laser is pumped by an RF field or by a discharge between electrodes.

Using this modulation concept we have built an experimental communication system for one audio channel by simply modulating the Valient as it was originally designed. The receiver consists of the same photodiodes used during the experimenting backed up with sufficient amplification to drive a speaker.

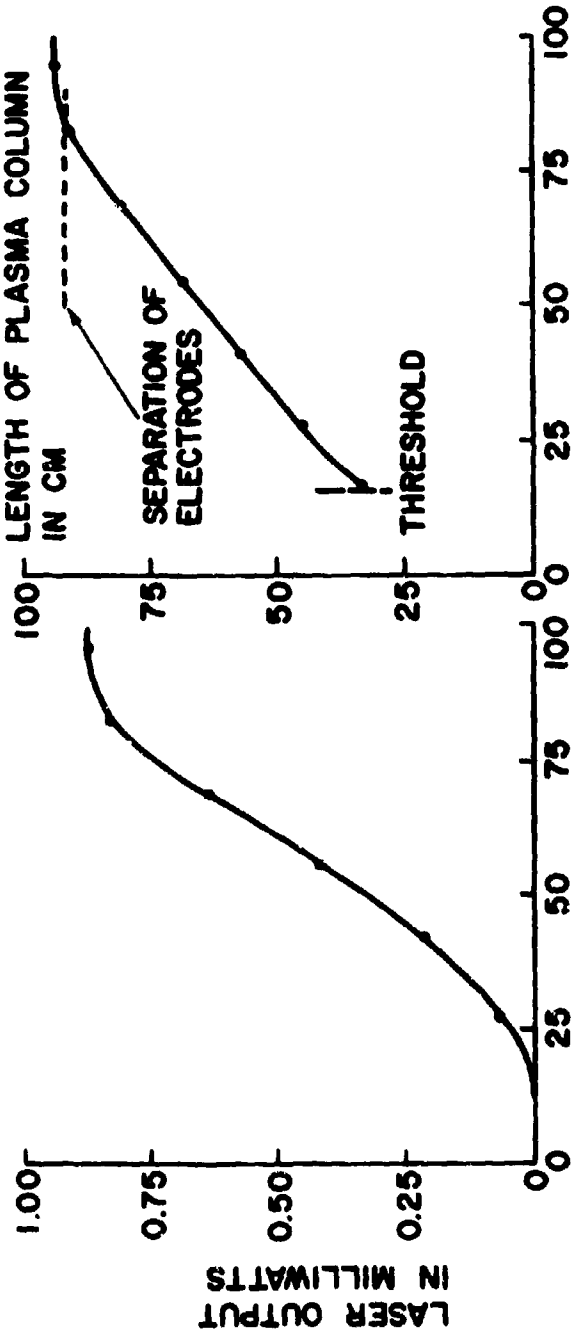

Fig. 1
LASER Characteristics (Pump Power for maximum output is around 50 w at 27.1 MC)

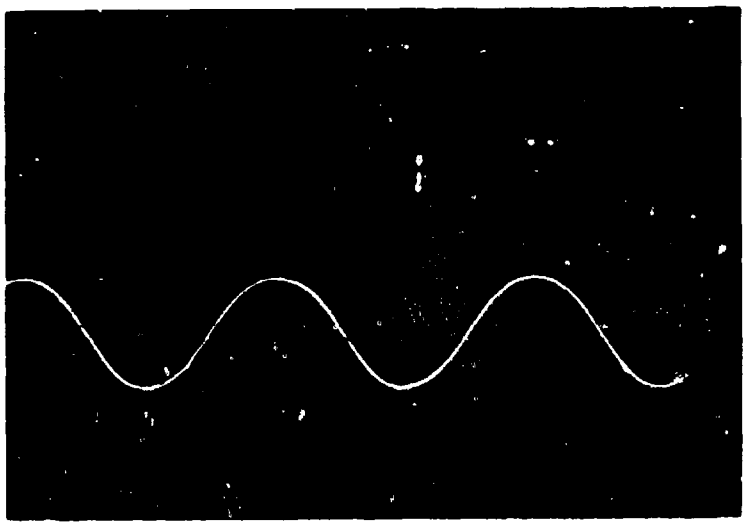

a

SINUSOIDAL MODULATION OF LASER OUTPUT.
LOWER TRACE: MODULATED LIGHT.
UPPER TRACE: PUMP MODULATION

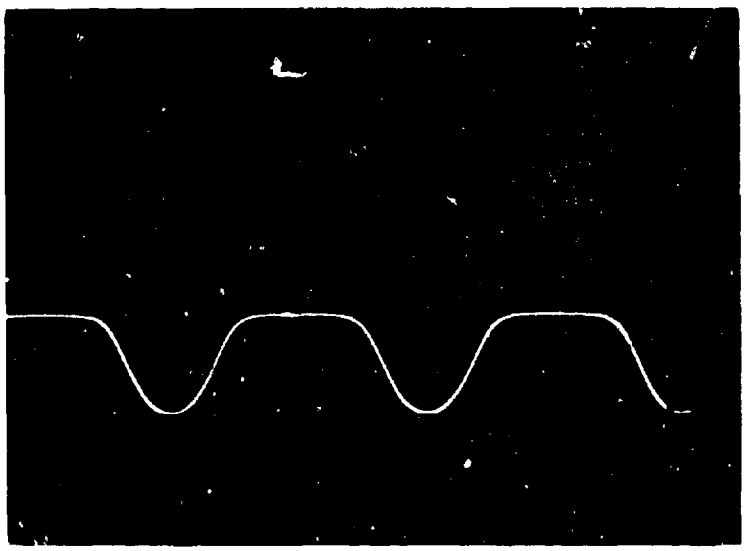

b

UPPER CLIPPING.
LOWER TRACE: MODULATED LIGHT.

Fig. 2

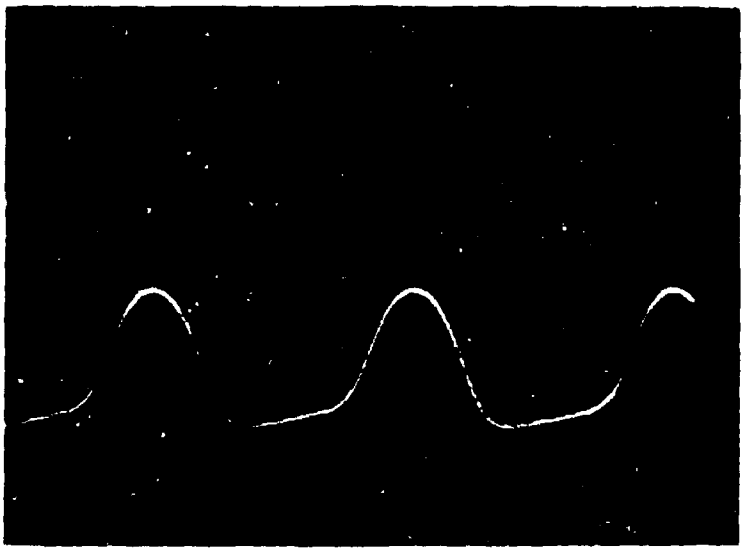

LOWER CLIPPING.
LOWER TRACE: MODULATED LIGHT.
UPPER TRACE: PUMP MODULATION.

Fig. 2

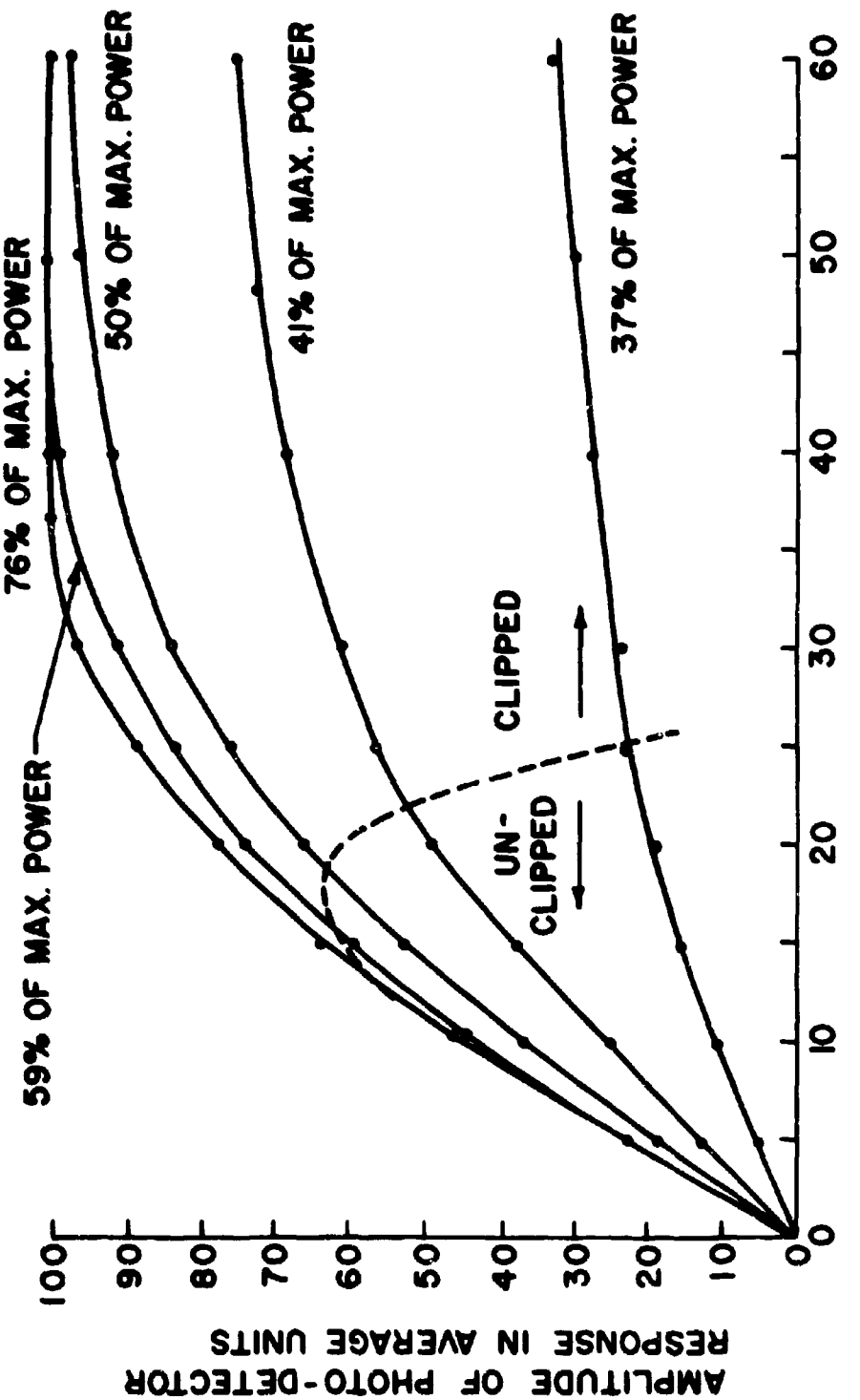

Fig. 3
Modulation Characteristics of a Gas LASER.

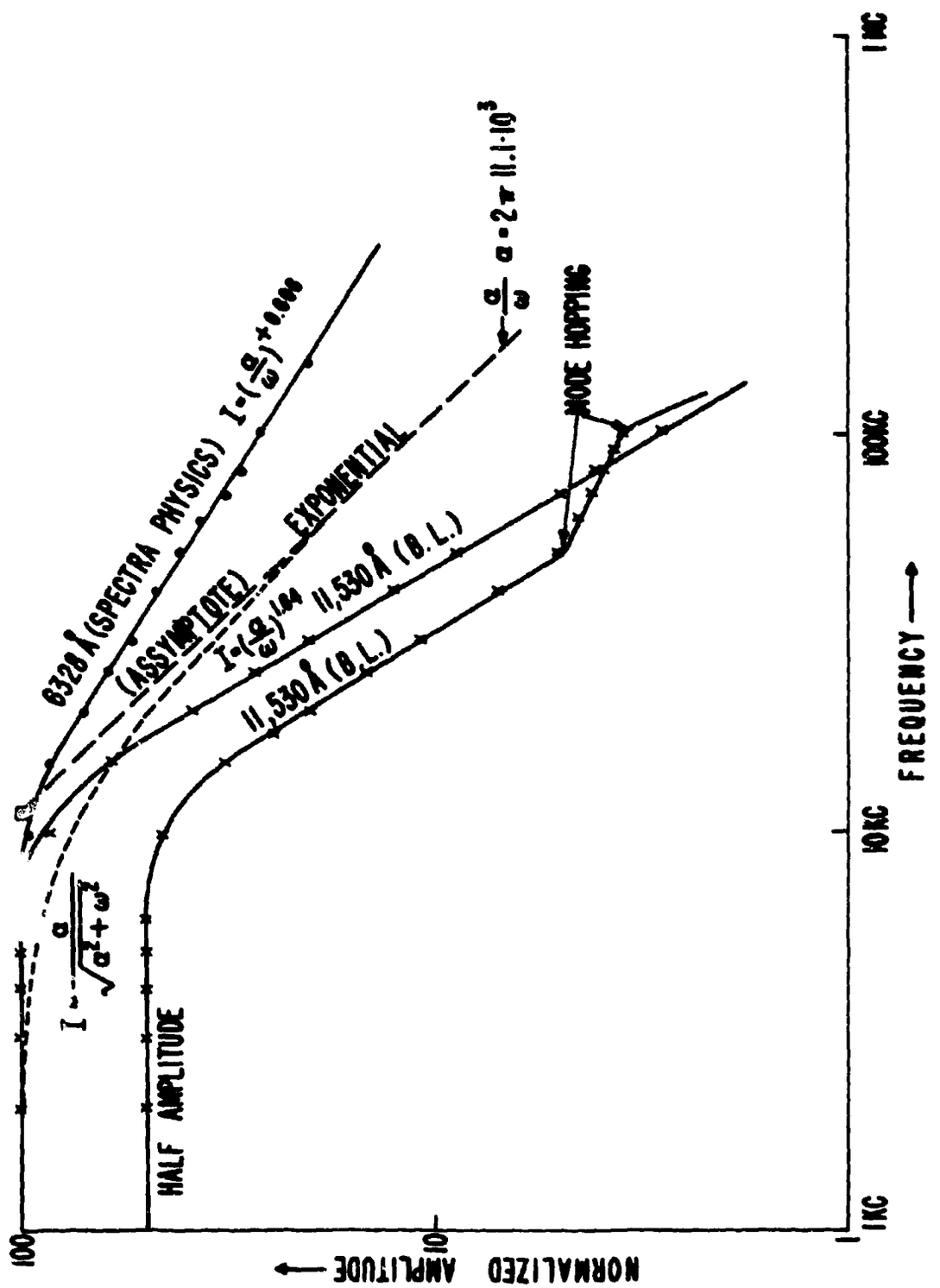

Fig. 4
Amplitude of Modulated Light VS Frequency.

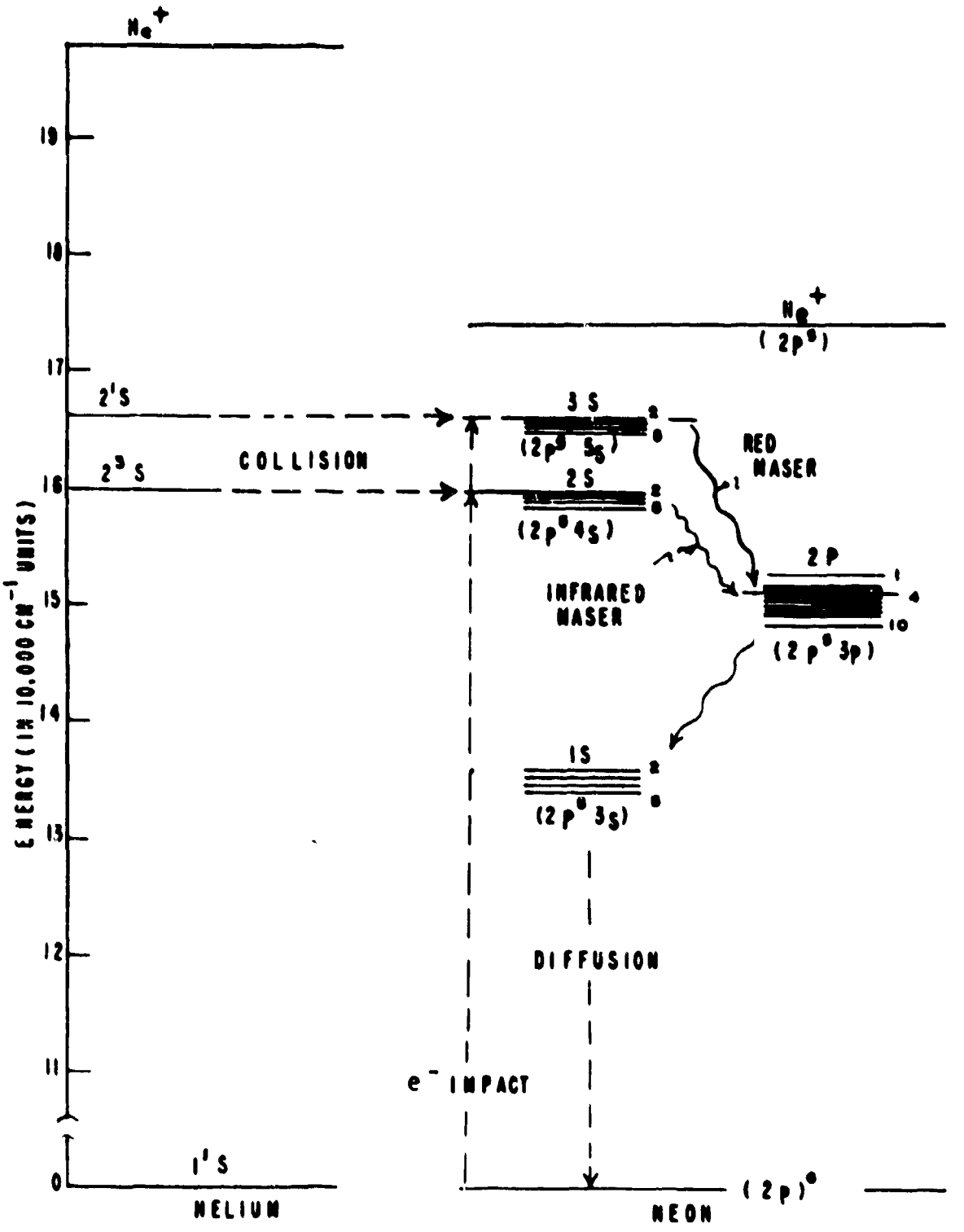

Fig. 5
HE-NE GAS LASER ENERGY STATES.

HYDROGEN SYSTEM DEPENDENCE ON DISCHARGE PARAMETERS

S. SCHNEIDER, J. E. CREEDON, and N. L. YEAMANS
U. S. ARMY ELECTRONICS RESEARCH AND DEVELOPMENT LABORATORIES
FORT MONMOUTH, NEW JERSEY

The fundamental processes of electrical discharges in hydrogen are usually pressure dependent, and many of the measured quantities are expressed as functions of pressure. Variations in hydrogen pressure influence characteristics, such as voltage hold-off, breakdown time, arc drop, deionization time, and dissipation, in hydrogen-filled devices. In designing experiments or devices utilizing hydrogen as the discharge medium, the factors affecting the hydrogen-metal system must be considered. Contrary to normal expectations, the heat of the discharge does not increase the observed gas pressure according to the equations of state for a homogenous medium. Instead, as shown in Fig. 1, a temporary pressure decrease occurs. The hydrogen-filled diode has an initial pressure of 490 microns Hg. After the filament is turned on to heat the electron source, the pressure rises in a predictable manner as expressed by the equations of state modified by normal hydrogen solubility in metal relations. When pressure stabilization occurs, the discharge is turned on and the pressure falls rapidly and then slowly rises as thermal equilibrium is established between the heat of the discharge and the container. Upon extinction of the discharge, the pressure quickly returns to its previous level. Removal of the heater voltage is followed by a small rise in pressure and a slow decay to the original cold pressure. The small rise in gas pressure is due to well-known phenomena common to endothermic hydrogen-metal systems. Many investigators (1,2,3) have studied these phenomena, and considerable information is available on the solubility of molecular hydrogen in endothermic metals as a function of temperature. With respect to the changes during and after the discharge, observers (4,5) have noted that the presence of ionization or the dissociation of molecular hydrogen by hot filaments increases the solubility of hydrogen in metals. However, no definitive work has been done to express the relationship between occlusion and discharge conditions. In 1956 (6) evidence was presented that the pressure within high-power, pulsed, hydrogen triodes varied dynamically with the peak power. On the basis of this observation, a more detailed

study was conducted to determine the relationship of the dynamic pressure change for any discharge condition and to obtain an understanding of the fundamental process involved. A series of experiments were conducted under a wide range of conditions from narrow pulses to direct current. From these experiments, the relationship between discharge conditions and the dynamic pressure variations has been determined. In addition, it has been established that the phenomenon varies directly with the production of atomic hydrogen during the discharge.

In Part I, the fundamental relationship is discussed. Part II discusses the influence of the physical state of the nickel on the dynamic occlusion of hydrogen during a discharge. It deals with the effects of plastic deformation and hydrogen loading of the metal.

PART I - FUNDAMENTAL RELATIONSHIP

This part of the paper discusses the relationship developed between the discharge conditions and the quantity of gas dynamically occluded during the discharge.

EXPERIMENTAL PROCEDURE

Since nickel is the most commonly used tube metal because of its availability, high purity, ductility, ease of spot welding, ease of outgassing, and low cost, most experiments and devices utilize it in large quantities for electrodes and shields. For these reasons and because of the availability of considerable information on its properties, such as the solubility of molecular hydrogen, nickel was selected as the basic metal component of the hydrogen-metal system to be studied. The primary type of tube built for this study contained a hot electron source as the cathode to eliminate the complication of analyzing the effect of the cold-cathode-arc mechanism. The tubes were constructed as shown in the X-ray (Fig. 2). The cathode is a cylindrical nickel base, triple-oxide-coated structure indirectly heated by a filament. The filament is completely shielded from the discharge area by the cathode structure. There are several heat shields around the cathode to conserve heat and prevent deposition of cathode material on the cylindrical collector that completely surrounds the cathode structure and shields the outer walls of the container from the discharge. To operate under conditions other than those permitted by a diode structure, a molybdenum electrode is incorporated in the tube. The molybdenum disk is surrounded by the collector and isolated from the cathode by a perforated disk and a solid baffle. This permits use of the device as a triode. Each tube is one-third of a liter in volume and contains a nominal 65 grams of nickel. Two thermocouple pressure gauges monitor the pressure in the tube. These gauges are mounted on a long appendage to minimize the influence of the discharge products and rf noise generated during pulsing.

After processing and filling the tube with hydrogen, it was placed in the experimental setup shown schematically in Fig. 3. The pressure was monitored continuously on a recorder with a response time of one second. A Bausch and Lomb 1/4 Meter Monochromator with a 7265 photomultiplier, S-20 response, was used to examine the spectral output as a function of time and operating conditions. In addition, a second photomultiplier, 1P21, S-4 response, was used to monitor total light output. The voltage and current characteristics were viewed simultaneously.

The experimental tubes were studied as diodes and triodes under dc and pulse conditions ranging from 0.25 microsecond to 12.5 microseconds wide at several pulse repetition rates.

EXPERIMENTAL RESULTS

A typical example of the experimental results is shown in Fig. 4, where the maximum percentage change in pressure is plotted as a function of the total discharge power dissipated (P_d) in the gas. ΔP is defined as the initial pressure (P_i) minus the minimum operating pressure. For comparative purposes, the ΔP values were normalized by dividing by the initial pressure. The data shown in this figure were obtained with the tube operated as a diode at several pulse widths and direct current. Empirically, the dependence of $\Delta P/P_i$ on P_d is given by

$$\Delta P/P_i = S_D (P_d)^{\frac{1}{2}} \qquad (1)$$

where S_D directly relates to the occlusive capacity of a metal for hydrogen under discharge conditions.

The square-root dependence on total dissipated power was observed in all modes of operation (triode, diode, and direct current). In extended studies on several tubes, the functional relationship of equation (1) was verified over a pressure range from 100 microns to 1000 microns.

The total power dissipated per pulse is obtained by integrating the product of the instantaneous value of the voltage drop across the tube $[v(t)]$ with the value of the current $[i(t)]$. The form of the generalized integral is illustrated in equation (2)

$$P_d/prr = \int_0^T v(t)\, i(t)\, dt \qquad (2)$$

where prr is the pulse repetition rate and T is the period. For the wave forms shown in Fig. 5, equation (2) can be integrated by parts

giving

$$P_d = P_c + P_{ss} \tag{3}$$

where P_c is the power dissipated during the breakdown period and P_{ss} is the amount contributed during the steady-state interval. Dissipation resulting from the inverse voltage and the recharging of the energy storage system during the interpulse interval was minimized so as to eliminate the effects of ion bombardment and sputtering on operating pressure.

It can readily be shown (7) that P_c and P_{ss} are given by

$$P_c = e_{py}\, i_b\, prr\, \tau_{eff} \qquad \text{(watts)} \tag{4}$$

$$P_{ss} = v_t\, i_b\, prr\, t_p \qquad \text{(watts)} \tag{5}$$

where
- e_{py} = peak forward voltage in volts
- i_b = peak current in amperes
- prr = pulse repetition rate in pulses per second
- v_t = potential in volts during the constant current interval. The value of v_t does not include the potential drop associated with the oxide-cathode-coating resistance.
- t_p = pulse width in seconds at the 50 per cent value.
- $\tau_{eff} = \tau_a^2 / 2(\tau_a + \tau_c)$
- τ_a = anode fall time constant in seconds.
- τ_c = circuit rise time constant in seconds.

Except for very short pulse widths, the steady-state contribution is generally much greater than the breakdown dissipation and, in the case of diode operation, the dissipated power is determined almost exclusively by equation (5). In both the diode and dc cases the P_d values are given by

$$P_d = v_t\, I \tag{6}$$

where I is either the average or dc current in amperes.

In view of the pressure dependence on gas dissipation, the decrease in the operating pressure in the presence of a discharge was thought to be associated with a heating of the nickel, which is known to be a good endothermic occluder (2,3). If a solubility phenomenon of this type were occurring, then the rate at which the hydro-

gen pressure changes would be governed by Fick's law (8). Fig. 6 is a typical analysis of the recordings of the pressure dependence on time, and the data are presented in a form that is related to the diffusion laws. An exponential dependence on time is observed both with respect to the rate at which the gas enters the metal (left side of graph) and the rate at which the gas diffuses out of the metal (right side of graph). These results are indicative of diffusion in a thin metal, and, therefore, support a solubility mechanism.

Prior investigations (1) have shown that the solubility (s) for molecular hydrogen is

$$s = s_o P^n e^{-b/T} \tag{7}$$

where s_o is the solubility in cm^3 per 100 grams of metal; P is the pressure; T is the temperature of the metal in ^oK; and b is a constant whose value is related to the heat of absorption. The value of n has been found to be equal to one-half for molecular gases such as hydrogen and nitrogen.

Using known solubility data for hydrogen in nickels (8) an expression can be derived for

$$\Delta P/P_i = \frac{82\ V_{Ni}\ 10^{-645/T_i}}{V_{total}\ P_i^{\frac{1}{2}}} \left[\left(\frac{P}{P_i} \right)^{\frac{1}{2}} 10^{+645\left(\frac{T-T_i}{TT_i}\right)} - 1 \right] \tag{8}$$

where V_{Ni} is the volume of nickel; V_{total} is the volume of tube; T_i and T are the initial and final temperatures of the nickel in ^oK; and P_i and P are the initial and operating pressures.

Equation (8) can be used to determine the temperature of the nickel required to give the observed phenomenon. For example, using nominal values of $\Delta P/P_i = 0.25$; $V_{Ni} = 7.3\ cm^3$; $V_{total} = 333\ cm^3$, $P_i = 0.600$ mm, and $T_i = 375^oC$, it is predicted that the final temperature of the nickel is 764^oC. Since the actual power dissipated in the tube is known to be a small fraction of that required to raise the nickel temperature to this value, a straightforward endothermic reaction is obviously not the dominant mechanism.

Earlier, it was mentioned that prior investigators had noted an increased cleanup of hydrogen gas when atomic hydrogen was produced. Since atomic hydrogen is known to be generated by a discharge, its dependence on discharge conditions was investigated.

The relation of atomic hydrogen to the pressure change phenomena was investigated by deriving its dependence on discharge conditions and correlating the magnitude with $\Delta P/P_i$. From radiation

principles, the intensity of emitted light caused by electron atom collisions is given by

$$I_\lambda = k_\lambda n_H n_e \tag{9}$$

where I_λ is the instantaneous intensity at a wavelength (λ); n_H is the atomic hydrogen concentration; n_e is the electron density; and k_λ is the probability of an electron-atom collision producing an excited atom in a given energy level. Equation (9) can be directly applied to the intensity of the alpha line of the Balmer series (6563 angstroms), since the upper energy-level population for this transition is essentially proportional to the probability of an inelastic collision. In the steady-state period of the discharge, the electron density (n_e) can be given as a function of the current (i) and the electric field (E) across the plasma by

$$n_e = \frac{i}{A\ e\ v_d} \sim \frac{i}{E/P} \tag{10}$$

where A is the cross-sectional area of the discharge; e is the electronic charge; and v_d is the drift velocity (9,10) and is equal to the product of the mobility (μ_e) and E/P. The electric field (E) is equal to the plasma drop divided by the electrode separation. The terms A, e, and μ_e are constants. Combining equations (9) and (10), the atomic hydrogen concentration is

$$n_H \sim \frac{I_\lambda\ E/P}{k_\lambda\ i} . \tag{11}$$

In this expression only the excitational probability (k_λ) has to be determined, since the other quantities are directly measurable. It is known from collision data that most excitational probabilities (11) are linearly related to the average electron energy up to the critical energy of the transition. Since the average electron energy (12) is a function of E/P, equation (11) can be rewritten for the hydrogen alpha transition as

$$n_H \sim \frac{I_\alpha\ E/P}{i\ f\ (E/P)} \tag{12}$$

where

$$f\ (E/P) \sim E/P \tag{13}$$

for $E/P < 50$ volts/cm-mm Hg

and $$f\,(E/P) \sim (E/P)^{1/3} \qquad (14)$$
for $E/P > 50$ volts/cm-mm Hg.

The latter case was experimentally studied. The hydrogen alpha intensity was measured and a relative value for the atomic hydrogen concentration was obtained from equation (12). Fig. 7 shows $\Delta P/P_i$ plotted against the values of average atomic hydrogen concentration ($n_H t_p$ prr) for the case of a low-pressure diode (P_i = 0.17 mm). This result shows that a linear dependence on the average atomic hydrogen pressure is involved in the solubility mechanism.

PART II - INFLUENCE OF THE PHYSICAL STATE OF THE NICKEL

In the course of the experiment, lateral shifts in the curve describing the behavior of dynamic occlusion under discharge conditions were observed. Since the fundamental relationships to the discharge parameters remained the same, it was assumed that the shifts were due to differences in the metal. A series of experiments were therefore conducted to determine the influence of the physical state of the nickel.

EXPERIMENTAL PROCEDURE

The basic design and procedure for constructing tubes for this part of the investigation were the same as discussed in Part I. Two variations in the construction and filling procedures were made: 1) to study the effects of plastic deformation, several of the tubes were constructed with cold-worked-nickel collector cylinders; and 2) to provide additional information on the behavior of hydrogen in metals, several of the tubes were filled with a mixture of 1% tritium (H_2^3) and 99% hydrogen (H_2^1). The procedure for filling the tubes and analyzing the results has been previously described (13). Since this part of the study was primarily concerned with the influence of the metal on dynamic occlusion rather than the effect of the discharge, the tubes were all arbitrarily operated under triode conditions at a fixed pulse width of one microsecond.

PLASTIC DEFORMATION

The literature (14,15,16) on the occlusion of molecular hydrogen in metals shows that permeability and occlusion capacity of metals varies as a function of the degree of strain or deformation. This phenomenon is attributed to a system of voids or rifts in the metallic structure. In the case of severely deformed metals, the rifts are particularly numerous or large. To determine how this applied to the occlusion of atomic hydrogen, several tubes were constructed with cold-worked-nickel cylinders, and the results were compared with those of a tube with well-annealed nickel. Fig. 8 shows

the results obtained with two tubes operated over a range of power dissipation from 2 to 13 watts. Curve a is for annealed nickel and curve b is for cold-worked nickel. The dependence between the dynamic pressure change and the power dissipated in the gas during the discharge was the same for each case and was in agreement with equation (1). The only difference between the results on the two tubes was an increased occlusive capacity of the cold-worked-nickel tube. This resulted in a value of 0.085 for S_D in the cold-worked case, an increase of 70% over the value for the annealed nickel tube. In another experiment to study the effect of cold-working, two tubes filled with a tritium tracer were operated for one hour each. Analysis of the cylindrical collectors for tritium content as a function of depth is shown in Fig. 9. Curve a and curve b represent the annealed case and the cold-worked case respectively. The curves represent the permanent occlusion of hydrogen by the nickel. Examination of the areas under the curves shows an order of magnitude increase in the quantity of tritium occluded in the deformed metal. From these results, it was concluded that plastic deformation of metal increases the occlusive capacity for both molecular and atomic hydrogen, but does not affect the basic relationship that determines their respective rates of reaction.

LONG-TERM EFFECTS

Several tubes with different degrees of deformed nickel were placed on life test at 16 kilovolts peak voltage, 175 amperes peak current, and 1000 pulses-per-second repetition rate. This operation corresponds to an average power dissipation in the gas of 13.5 watts. The triodes were checked periodically and tests were conducted up to 2150 hours. The fundamental relationship between atomic hydrogen generation and the dynamic occlusion remained the same throughout life. The observed value of S_D, however, decreased with life, as shown on Fig. 10. Curves a and b, respectively, represent the results of well-annealed and deformed nickel. To extend the results with well-annealed nickel over another order of magnitude, curve c was added to the graph. The discrepancy in the first two points on curve c is believed to be due to an initial inaccuracy in the recorded operating time. However, at several hundred hours, this error is negligible, and the data fit curve a and extend the results to 2150 hours. The observed value of S_D decreased with life according to the relationship

$$S_D = C - 0.0135 \log t \qquad (15)$$

where t is the number of hours and C is the value of S_D after one hour of operation, with the initial value of S_D determined by the degree of plastic deformation. Data on gas pressure versus life for these tubes generally obeyed the same relationship as that plotted for S_D. This led to the hypothesis that the observed S_D is a function of the degree of loading of the nickel with hydrogen and that, as the voids or rifts in the nickel are filled, the measured occlusive capacity of

the nickel is being reduced by the amount of hydrogen already absorbed. As confirmation of this hypothesis, Fig. 11 shows the results of operating tubes with a tritium mixture at this condition. Curve a and curve b represent the results after one hour and 676 hours, respectively. Examination of the area under each curve reveals an increase of almost two orders of magnitude in hydrogen content with life, thus confirming that the hydrogen content of the metal influences the apparent occlusive capacity of the metal.

CONCLUSIONS

The dependence of hydrogen-metal system behavior on discharge parameters has been studied, and a square-root dependence on the power dissipated in the gas has been established. A solubility mechanism has been established in which the concentration of atomic hydrogen was found to be the significant factor. In view of this result, hydrogen occlusion cannot be viewed as just a function of the diatomic gas but must be modified to include the generated dissociation product, the monatomic gas. The monatomic gas occlusion has been determined to vary directly as a function of its pressure, as compared to the square-root dependence of a diatomic gas on its pressure.

By the use of the discussed relationships, the effects on fundamental processes that exhibit pronounced pressure dependence can be accurately predicted. In the design of hydrogen-filled devices, particularly those needed for high-energy switching of power for microwave devices and optical pumps for lasers, the behavior under discharge conditions can now be predicted and the device can be designed to operate under the dynamically varying pressure conditions.

The influence of the physical state of the metal on the dynamic occlusion of hydrogen under discharge conditions has been studied. Plastic deformation of the metal and the production of large rifts or voids increases the occlusive capacity of the nickel for both molecular and atomic hydrogen. It does not, however, change the fundamental relationship between the gas behavior and the discharge parameters, but only increases the solubility factor in the equation. The long-term effect of exposing the metal to the discharge has been analyzed, and a relationship between the apparent change in solubility and life has been established and verified. This relationship enables the prediction of the life of hydrogen-filled devices and provides the necessary information to compensate for hydrogen-pressure losses.

REFERENCES:

1. D. Smith, Hydrogen in Metals (University of Chicago Press) 1937.

2. A. Sieverts, Z. Metallkunde, 21, 37-44, 1929.

3. M. Armbruster, Jour. Am. Chem. Soc., 65, 1043-54, 1943.

4. L. Ingersoll and J. Hanawalt, Phys. Rev., 34, 927-77, 1929.

5. W. Büssem and F. Gross, Metallwistschaft, 16, 669-77, 1939.

6. S. Schneider and S. Verner, Fourth Hydrogen Thyratron Symposium, 1955.

7. S. Goldberg, Final Report, USAELRDL Contract DA36-039 sc-52589, 1955.

8. S. Dushman, Scientific Foundations of Vacuum Techniques (J. Wiley & Sons, New York, N.Y.) 1949.

9. R. A. Nielson, Phys. Rev., 50, 950, 1936.

10. N. E. Bradbury and R. A. Nielson, Phys. Rev., 49, 388, 1936.

11. H. J. Van Vesteyn and F. Penning, Revs. Mod. Phys. 12, 87, 1940.

12. L. J. Varnerin and S. C. Brown, Phys. Rev., 79, 946, 1950.

13. S. Schneider, Phys. Rev., 48, 1951.

14. L. Kirschfeld and A. Sieverts, Z. Physik Chem., 145, 227, 1929.

15. W. Baukloh and H. Kayser, Z. Metallkunde, 27, 281, 1935.

16. G. Chaudron, Met. Abs., 12, 347, 1944.

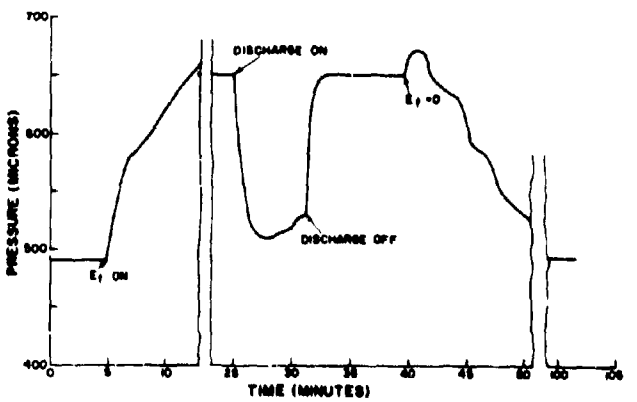

Fig. 1 Gas pressure response to an arc discharge.

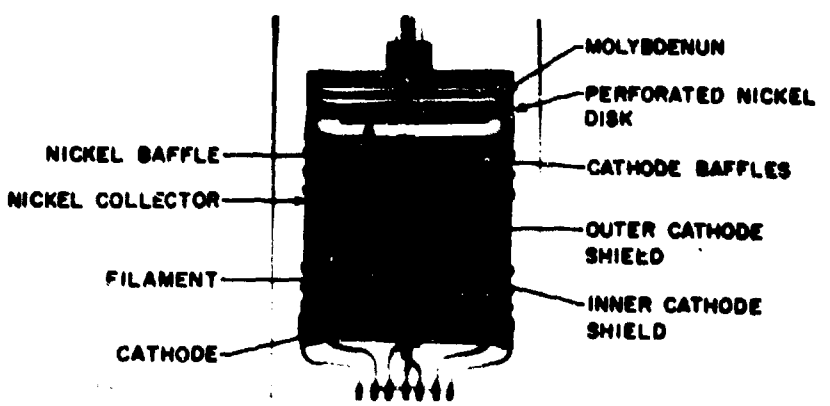

Fig. 2 Experimental Tube.

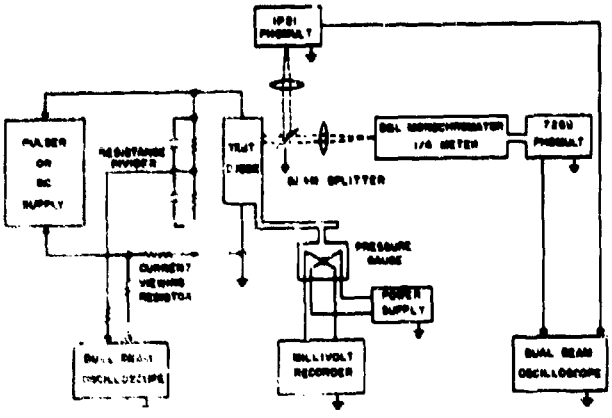

Fig. 3 Experimental setup.

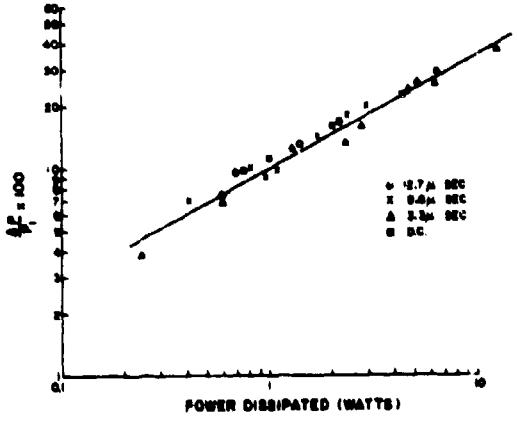

Fig. 4 Pressure variation vs. gas dissipation.

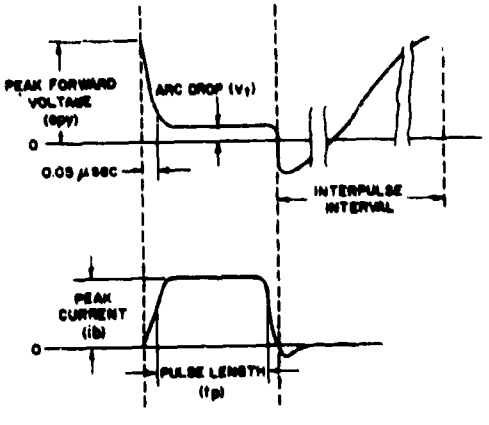

Fig. 5 Triode voltage and current wave forms.

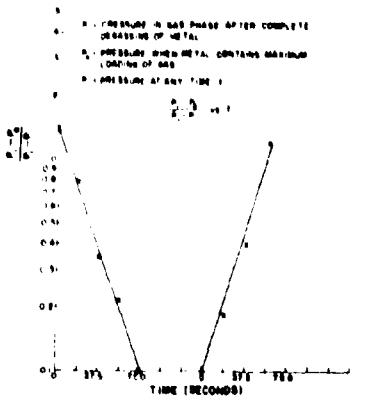

Fig. 6 Fick's law.

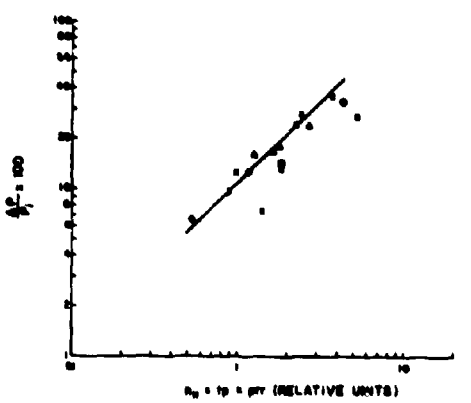

Fig. 7 Pressure variation vs. atomic-hydrogen concentration.

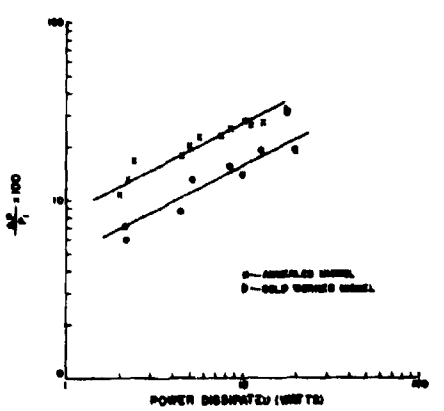

Fig. 8 Pressure variation vs. gas dissipation for well-annealed and cold-worked nickels.

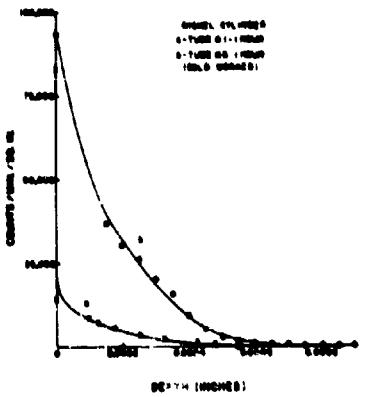

Fig. 9 Tritium concentration vs. depth for well-annealed and cold-worked nickels.

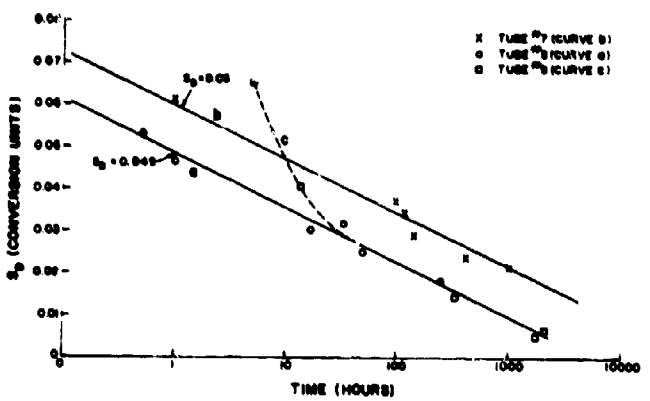

Fig. 10 S_D vs.time for well-annealed and cold-worked nickels.

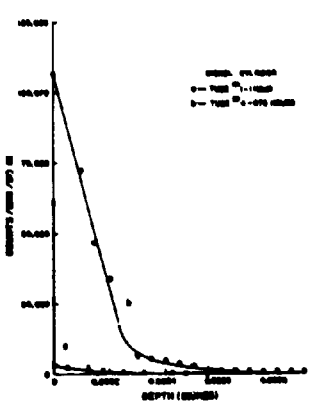

Fig. 11 Tritium concentration vs. depth as a function of time.

OPTIMIZATION OF THE ROTATING REFLECTOR Q-SWITCH

M. SCHOENFELD, D. A. REAGO* and E. GREEN
FRANKFORD ARSENAL
PHILADELPHIA, PENNSYLVANIA

I. Introduction

One of the simplest methods of switching the regeneration in an optical resonator to obtain a high power pulse of radiation is the rotating reflector Q-switch first successfully demonstrated by scientists at the U. S. Army Electronics Laboratory, Ft. Monmouth[1]. Because it is easy to instrument and is relatively immune to environmental extremes of temperature, shock and vibration, this technique - with minor differences - is the basis of both of the laser range finders being developed for the Army: one by Radio Corporation of America under contract with Ft. Monmouth, the other as an in-house effort at Frankford Arsenal.

In connection with the latter development (Range Finder XM23) a detailed study of the rotating reflector switch has been conducted at Frankford Arsenal. It is the purpose of this paper to present the experimental data and to propose a model for the rotating reflector Q-switch which is consistent with our experiments and provides, moreover, an extremely useful rationale for optimizing resonator design to obtain maximum single pulse output. The experimental data pertains specifically to a ruby laser in a cavity terminated by roof prism reflectors; this configuration was chosen for use in the range finder to avoid problems of film durability and component alignment associated with the use of dielectric mirrors. The conclusions drawn from the analysis are, however, independent of the details of the feed-out or reflection mechanism employed, and are therefore believed to have general applicability to any type of rotating reflector switch.

By appropriate choice of resonator length and switching speed, single pulse laser output can be consistently obtained with the double prism arrangement. The quality of the ruby

crystal is the least controllable element of the system; nevertheless cavity parameters can almost always be optimized to yield single pulse output in the megawatt power range. Deviation from an optimum single pulse arrangement leads initially to loss in peak power and ultimately to development of after pulses which not only rob power from the leading pulse but are extremely undesirable from the standpoint of the range finder application for which the resonator was developed. When optimum conditions are met, a relatively narrow pulse (25 nanoseconds halfwidth) with fast (10 nanoseconds) rise time can be produced with the configuration to be described below. The beam angle will be of the order of 2×10^{-6} steradians.

In addition to dependence on geometrical factors and crystal quality, single pulse output is greatly affected by temperature. Attainment of large single pulses becomes increasingly difficult at temperatures below that for which the resonator is optimized; on the other hand, at higher temperatures single pulse capabilities are excellent but only at the expense of additional input energy.

II. Q-Switch Analysis

A. The Q-switch theory first suggested by Hellwarth[2] and developed by Lengyel and Wagner[3] and others[4,5] deals with cavities of fixed geometry - usually switched electro-optically- in which build-up of a giant pulse by rapid conversion of stored energy to radiation involves consideration, in the ideal case, of only diffraction losses and feed-out losses. Furthermore, the treatment of the phenomenon of multiple pulsing as discussed by McClung and Hellwarth[5] apparently involves detailed assumptions regarding line shape, relaxation mechanisms and other intrinsic characteristics of the laser medium.

The interesting feature of the rotating reflector Q-switch is that its properties are largely dominated by geometrical factors, specifically the varying walk-off losses as the reflector rotates into parallelism. This domination is, in fact, so complete that, as will now be shown, significant conclusions in excellent agreement with experiment can be drawn from a highly artificial ray-geometric model which completely ignores the dynamics of the stimulated emission process in the laser medium.

Consider (Fig. 1) an active medium in a Fabry-Perot cavity terminated by two reflectors A and B which, at the instant of initiation of an axial plane wave, are at an initial angle θ_0. Suppose that reflector B is rotating into parallelism with A about an axis perpendicular to the plane of the diagram with an angular velocity ω. At each reflection the wave front will be deviated downwards so that the ray at its upper boundary will be displaced successively by amounts D_1, D_2, etc., as shown.

Summing up the displacements for n round-trips of the cavity gives:

$$(1)\quad D = \Sigma D_N = 2L\left[n(n-1)\theta_0 - 2n\,\frac{(n-1)(n+1)}{3!}\omega\tau\right]$$

where L is the optical path between the reflectors and τ is the round trip transit time, i.e. $\tau = \frac{2L}{c}$, c = velocity of light

For large n, we may write, approximately:

$$(2)\quad D \simeq 2L\left[n^2\theta_0 - n^3\omega\tau\right]$$

For any specific aperture, D_0, equation (2) gives the number of passes before walk-off of the marginal ray, i.e. the maximum dwell-time of the wave in the cavity. We note also that, depending on the specific values of the various parameters, walk-off may occur at the lower boundary of the aperture (before mirror parallelism) or, since D can change sign, may occur at the upper boundary after the mirror has passed through parallelism.

Assume now, on this simple model, that in order to build up a sizeable single pulse output, a wave must survive for n round trips of the cavity; n would depend on all the factors which affect gain per pass in the laser (inversion, linewidth, scattering, diffraction, feed-out loss, etc.) but would be a specific number for a given ruby at a given temperature and pumping level.

We now adopt as an optimization condition for survival of an n-pass wave the requirement that the marginal ray reach the edge of the aperture when the displacement D reaches a maximum, i.e.

$$(3)\quad \frac{\partial D}{\partial n} = 0$$

This leads to the relation:

$$(4)\quad n' = \frac{2\theta_0}{\omega\tau}$$

where n' is the number of transits the wave has made at maximum displacement. Since this maximum displacement may not exceed the available aperture D_0, insertion of (4) in (2) gives:

$$(5)\quad L^2\omega \simeq \frac{3cD_0}{2n'^3}$$

This can be expressed in terms of the total number of passes n before walk-off at the upper boundary of the aperture if we note that $n = \frac{3\theta_0}{\omega\tau} = \frac{3n'}{2}$ as is evident from setting d = o in equation (2).

We finally obtain the following simple optimization condition:

$$(6)\quad L^2\omega \simeq \frac{81cD_0}{16n^3}$$

We note, parenthetically, that in spite of the naivete of the assumptions used in its derivation, equation (6) checks well with our experiments in the following sense: if we insert the specific values of L, ω and D_0 used in the optimized cavities to be described later, the calculated value of n agrees within a factor of two with the observed pulse width. We regard this agreement, however, as somewhat fortuitous and prefer to discuss the qualitative implications of equation (6) as regards the functional relations between cavity parameters necessary to optimize single pulse output. For this reason we rewrite it as a proportionality:

$$(7)\quad L^2\omega \sim \frac{cD_0}{n^3}$$

The quantity $L^2\omega$ is inversely related to the dwell time of the spinning reflector in the cavity; similarly the number of passes n required for build-up of a "giant" pulse is inversely related to the gain per pass of the resonator. Equation (7) can therefore be interpreted as follows: for optimum single pulse generation the dwell-time should be matched to the gain per pass. If there is a mismatch between dwell-time and gain, then we have two possibilities.

(1) If the dwell-time is too long, i.e. $L^2\omega$ is too small, peak power is reduced; if the mismatch is sufficiently great, double or multiple pulsing will result. The mechanism can be visualized as follows: with high gain, the spinning reflector closes the cavity at an angle θ_0 greatly removed from parallelism, since a relatively small number of passes before walk-off suffice to produce a highly amplified wave. This premature walk-off will clip peak power before the available inversion is exhausted; furthermore, if the intrinsic gain is sufficiently high, enough inversion may be left in the ruby to produce an after pulse (or pulses) as the reflector approaches parallelism.

(2) If the dwell-time is too short, i.e. intrinsic gain per pass is too low to match the given L and ω, monopulse output will be maintained but power in the single pulse will be clipped. This happens essentially because the amplified wave walks out of the cavity <u>after</u> parallelism, but before the available inversion has been optimally exhausted. Note particularly that unlike the case of the static electro-optical Q-switch, faster switching may actually reduce peak power. This, as well as other conclusions drawn from the optimization condition, will be illustrated in the experimental data presented below.

For example, if double pulsing occurs at some particular pumping level, it follows from the above that it can be eliminated by increasing resonator length, switching speed or feed-out loss. Since dwell time varies inversely as the square of resonator length, adjustment of this parameter should be more effective than faster switching. However, increase in the pumping level, and therefore in stored inversion and gain per pass, will eventually result in power fall-off and again multiple pulsing. Since crystals vary greatly in intrinsic gain, it follows that no set of cavity parameters will be optimum for all rubies. In fact, in a cavity of fixed L and ω it is possible, as we have found in our experiments, for a ruby to be too "good" to single pulse. This apparent paradox should not be pushed too far; a crystal with noticeable optical discontinuities may double pulse in any cavity.

B. The foregoing analysis suggests the possibility of constructing a more complete model for the rotating reflector Q-switch based on an exact calculation of walk-off losses and including the details of the stimulated emission process in the laser medium itself. We have undertaken such a calculation and expect to report the results at a later date; for the present, we wish merely to outline a possible approach to a more exact solution.

Our starting point is the family of rate equations governing the dynamics of Q-switching in a fixed Fabry-Perot structure; this is available in the literature[3-5] and will not be repeated here. In line with what has been said, we must now add other terms to cover walk-off losses due to misalignment of the end-mirrors. Consider a plane wave launched at angle φ_m to the normal of the fixed mirror in Fig. 1 and assume, without loss of generality, that the active medium has a square cross-section. Then it can be shown that the rate of loss of photons due to walk-off is approximately:

$$(8)\quad \frac{dS_m}{dt} \simeq -\left|\frac{2c\theta t}{\tau} - \frac{c\omega t^*}{\tau} + \frac{c\varphi_m}{\tau}\right| \frac{S_m}{D_o}$$

where S_m is the number of photons in the mode m at time t and all the other symbols are as previously defined. Equation (8) is analogous to equation (1) but takes into account the continuous clipping of the wave front as it travels through the resonator, not just the fate of the marginal ray, and generalizes the launching angle of the wave, previously assumed to be $\varphi = o$.

It is necessary to include low-Q modes for which $\varphi \neq o$ in the calculation for the following reason. The high gain developed in the strongly inverted medium permits a tremendous number of low-Q modes to oscillate for at least a few passes when the mirrors are far from parallelism. Although the contribution of any one of the high-angle modes to the main pulse is trivial, their multiplicity exhausts a significant

amount of inverted population which would otherwise be available to the high-Q axial or near-axial modes which actually generate the main pulse. In order to obtain a quantitative solution it is therefore necessary to sum the contribution of all modes which can simultaneously oscillate.

In addition to the necessity of a multi-mode approach, the rate equations are further complicated by requiring the inclusion of a fluorescence term, the treatment of which is rather involved and so will not be given here. It is important, however, to recognize that it is necessary to include such a term; otherwise, upon initial mathematical launching of a family of modes at some arbitrary starting position $\theta_0 > \theta_T$, all modes would walk out of the resonator, bringing an abrupt end to the regenerative process without having exhausted the inverted population. Fluorescence must therefore be continuously applied to keep the process alive prior to mirror alignment.

On the basis of the ideas briefly outlined above, a set of iterative equations suitable for machine computation has been derived. The solution of these equations gives the Q-switched output power as a function of time for given cavity parameters. A few trial calculations have been run, with results which are reasonably consonant with observed pulse powers and rise times. One calculated pulse profile is shown in Fig. 2; this is based on an assumed stored inversion of 25% and a gain of $0.4 cm^{-1}$ in the ruby. Only a limited range of input parameters has been explored to date, so that no judgment can yet be made as to the degree of validity of the mathematical model employed.

III. Description of Laser Cavity

The two prism cavity which we have investigated is shown in Fig. 3. The ruby is 2" x 1/4" with 90° C-axis orientation. Prisms A and B are identical, with the exception that a narrow bevel, through which the laser energy is fed out, is polished along the 90° vertex of A. The width of the bevel is .020 inches, corresponding to a feed-out loss factor of approximately 10%. The effect of varying feed-out loss ratio on cavity characteristics is considered below; however, in most of the experiments it was fixed at the above value. Both prisms are of the 90°, 45°, 45° roof type. Prism A is mounted on a vertical motor shaft perpendicular to the beveled vertex. Prism A is so oriented that when the cavity is closed, its beveled vertex, the 90° vertex of Prism B, and a diameter of the ruby are mutually parallel and lie in the same plane. The distance ℓ_1 from prism B to the ruby is fixed at approximately one inch for convenience of alignment. The distance ℓ_2, the vertex to vertex distance of the prisms, is variable. Prism A may be rotated at speeds up to 1.5 milliseconds/revolution (40,000 rpm). A pulse

from a magnetic pickup triggers the lamp flash (from a standard FXS #38A lamp) at any time up to approximately one millisecond prior to the closing of the cavity. Typical delay between lamp trigger and cavity closure varies from 250 to 400 microseconds, depending on the type of capacitor employed and circuit inductance. The time between the lamp trigger position and the closed position of the spinning prism is measurable to about 5 microseconds, assuring for a given energy input that the degree of inversion will be constant when the cavity is closed. Ruby and lamp are coupled in a conventional manner by means of a small silvered cylindrical reflector.

IV. Experimental Results at Room Temperature

The following parameters were investigated for the purpose of obtaining maximum single pulse laser output power with a maximum allowable input energy of 150 joules (imposed by weight limitations on Range Finder XM23).

(1) The total length (ℓ_g) of the cavity (measured vertex to vertex in the closed position).

(2) The Q-switching rate as measured by the rotation speed of Prism A.

(3) The input energy to the capacitor.

Deliberate errors introduced in the alignment of components of the cavity (Fig. 1) verified the necessity of keeping alignments within tight, but not impractical, tolerances: approximately ±.005" and 1 minute of arc in angle. When this is done, ruby quality is the single uncontrolled factor which strongly affects resonator characteristics and, indeed, duplication of results from ruby to ruby is not possible. But the pattern of variation of output as a function of the four principle parameters (cavity length, rotation speed, input energy, temperature) is consistent.

The bulk of the data reported here was obtained for a ruby (27R) which is quite good by the criterion of uniformity and low strain. It has a fine ground rather than a polished cylinder. Both types have been used successfully, but the former finish yields more uniform pumping of the rod. Fig. 4 shows peak output power as a function of capacitor input energy or pump energy for several cavity lengths at 15,000 rpm motor speed. A solid curve indicates single pulse output; the dashed curve represents output in the form of multiple pulses. In the latter case the peak power plotted is that of the leading pulse. Note that at the shorter cavity lengths, when the rate of rise of peak power as a function of pump energy levels off, multiple pulsing begins, in agreement with the simple model previously discussed. It is then necessary to increase cavity length substantially to take advantage of the increased input, i.e.

the dwell time in the cavity must be decreased, exactly as expected from the previous analysis. Thus the 20cm cavity becomes more effective than the 13cm cavity at 107 joules, the curve for the 28cm cavity crosses the 20cm curve at 116 joules, and it might be anticipated that the curve for the 36cm cavity would eventually cross the curve for the 28cm cavity. Moreover, as the cavity length increases, the pump energy range over which a given cavity length is nearly optimum also increases.

In Fig. 5 the tendency toward an optimum cavity length at each pumping level is further illustrated. Output power is plotted as a function of cavity length for several inputs with the motor speed fixed at 22,200rpm. Note also the predicted increase in optimum cavity length to match the increased gain per pass at the higher pumping levels and the incidence of double pulsing when the dwell time (cavity length) is too short.

Fig. 6 shows curves of peak power output as a function of motor speed for the 20cm cavity. The rise of power output with increasing switch speed is predicted by basic Q-switch theory. However, the decline of output power beyond some critical switch rate is, as brought out earlier, peculiar to a rotating mirror switch. This is shown experimentally by the decay of the curves in Fig. 5 with increasing motor speed. The shift of the maxima to higher prism rotation speeds with increasing inversion is again predictable from Equation (7).

Fig. 7 shows oscillographs of output pulses. A calibrated RCA 917 Vacuum Photocell was the detector. Traces were recorded on an 85 megacycle Tektronix 585A Oscilloscope. The horizontal scale is 0.1 microsecond/square. These oscillographs show instantaneously radiated peak power; the peaks are in the several megawatt region. Rise time and pulse width are well within the capability of the monitoring instrumentation.

Trace A is that of a typical optimized single pulse, trace B shows the second pulse developing 0.1 microsecond after the first pulse as a result of over pumping; while trace C shows a complete degradation of the monopulse phenomenon, in this instance due to increased gain in the ruby at low temperature, as will now be discussed.

V. Temperature Effects

Military requirements for performance through an extended temperature range led to experimental investigation of temperature characteristics of the monopulse laser. These have been obtained for a large number of crystals at a fixed cavity length and rotation speed. In Fig. 8 peak power output vs. pump energy curves are displayed for eight temperatures ranging from 233° to 325°K (-40°K to +125°F) for a specific and quite typical ruby.

As expected, threshold decreased with temperature. However, the maximum single pulse output attainable also decreases with temperature. For inputs beyond that corresponding to the maximum, multiple pulsing occurs. At quite high temperatures, 325°K and above, the maximum broadens. The highest maximum in the case of the 20cm cavity usually occurs at about room temperature which is not surprising since this particular cavity was originally optimized at this temperature. In the cases illustrated, maximum attainable output is not seriously affected by high temperature (although higher pump energy is required).

The explanation of the low temperature behavior is quite straightforward, in terms of the foregoing model. At low temperatures, the exponential gain constant of the ruby increases, primarily because of line narrowing. Consequently, there is a mismatch of the fixed cavity dwell-time with the now higher intrinsic gain. Under these conditions, the room temperature monopulse degenerates in power and ultimately leads to double or multiple pulses. At temperatures below -40°F, most rods exhibit severe degradation in maximum attainable output power before onset of a second pulse.

The foregoing model of multipulse generation suggests that increase in peak monopulse power at low temperature can be obtained by compensating for the increased intrinsic gain in the ruby; either by decreasing dwell-time, i.e. increasing either L or ω, or by deliberately reducing cavity gain. We have verified that either increasing the resonator length to 40cm or increasing the feed-out loss from 10% to 15% by widening the feed-out bevel, results, as expected, in enhanced monopulse peak output at -40°F by a factor of about two. This is illustrated in Figs. 9 and 10. In Fig. 9 a family of power curves is shown for the same ruby as in Fig. 8, except that the feed-out slit has been widened from .020" to .030". In Fig. 10 the effect of doubling the cavity length on low temperature peak monopulse output is clearly demonstrated.

It must be recognized that the improvement in low-temperature performance which can be obtained by one or the other of the devices suggested above implies a corresponding degradation of peak power output at higher temperatures. In principle, a cavity of fixed parameters can be optimized for only a single temperature or, more realistically, for a narrow range of temperature. Optimization over a broad range of temperatures requires means of continuously varying one or more of the cavity parameters which influence dwell-time or gain. In line with what has been stated above, parameters which might be varied include resonator length and switching speed. Another promising method, the feasibility of which we have experimentally verified, is to vary the gain of the cavity by use of a variable polarization device. By one or more of these techniques

it should be possible to obtain high power monopulse operation over a wider range of temperature.

REFERENCES

1. R. Benson, R. Godwin and M. Mirarchi, "A Single Pulse Ruby Laser for Ranging Applications," Vol. 3, Proceedings of 1962 Army Science Conference, West Point, N. Y.

2. R. W. Hellwarth, "Advances in Quantum Electronics," Columbia University Press, New York, N. Y., pp. 334-341, 1961

3. W. G. Wagner, B. A. Lengyel, "Evolution of the Giant Pulse in a Laser," Journal of Applied Physics, Vol. 34, No. 7, pp. 2040-2046.

4. A. A. Vuylsteke, "Theory of Laser Regeneration Switching," Journal of Applied Physics, Vol. 34, No. 6, pp. 1615-1622, June 1963.

5. F. J. McClung, R. W. Hellwarth, "Characteristics of Giant Optical Pulsations from Ruby," Proceedings of the I.E.E.E., Vol. 51, No. 1, pp. 46-53.

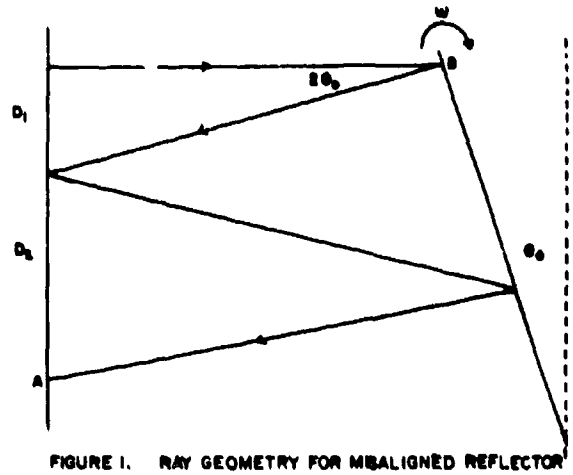

FIGURE 1. RAY GEOMETRY FOR MISALIGNED REFLECTOR

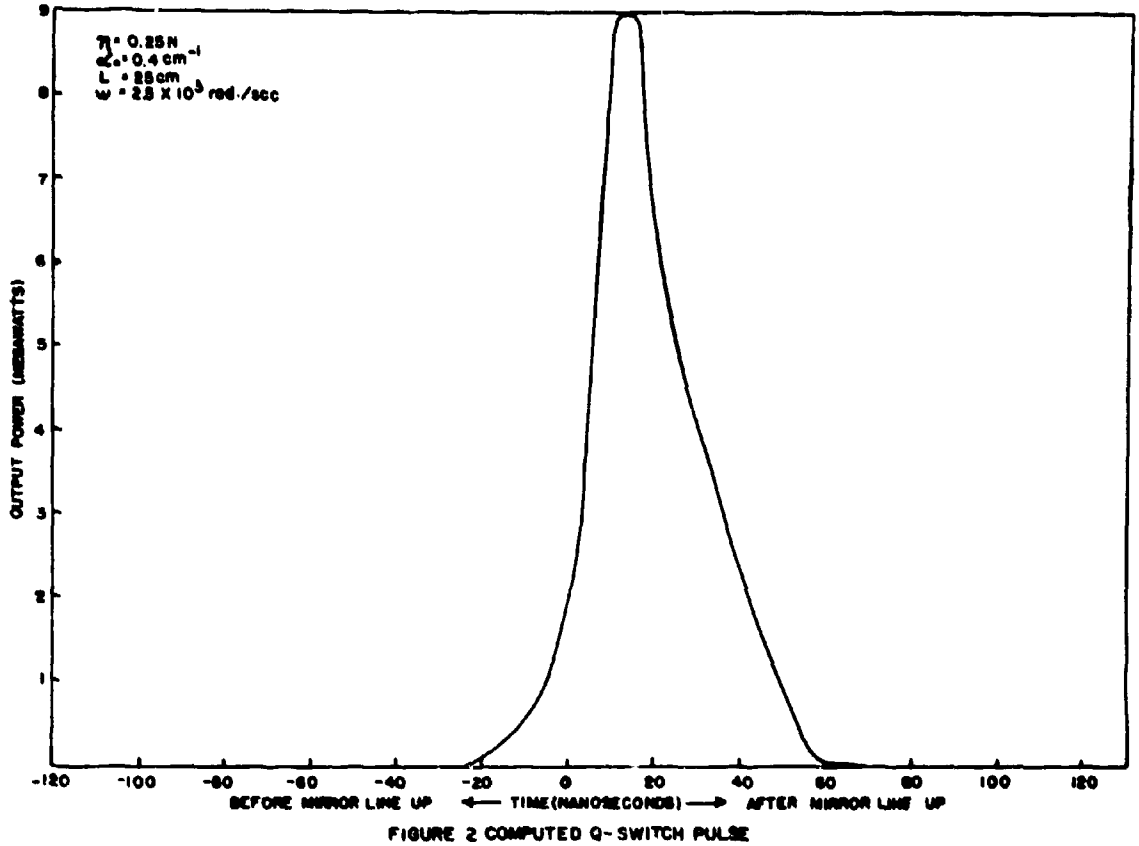

FIGURE 2 COMPUTED Q-SWITCH PULSE

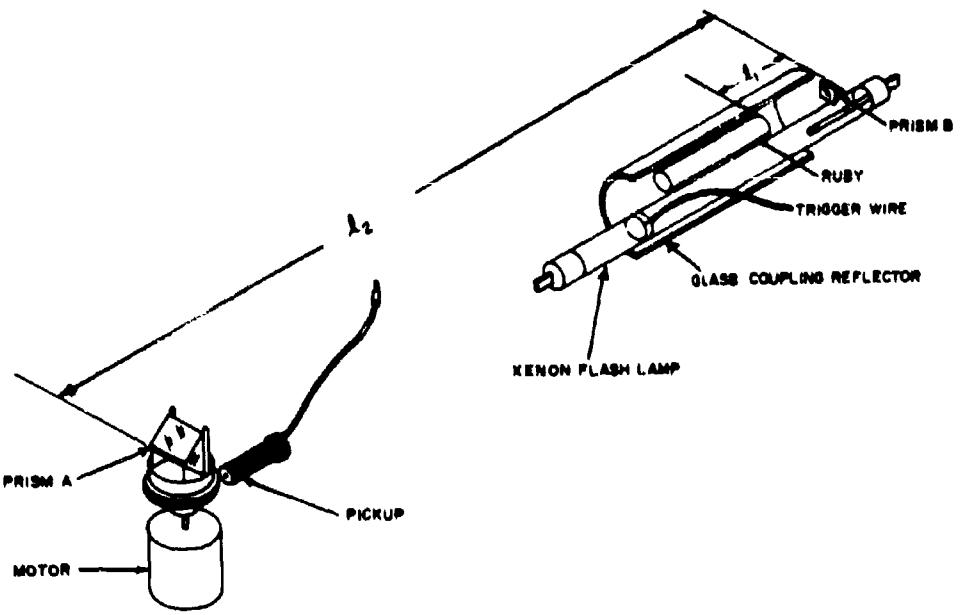

FIGURE 3. SCHEMATIC OF LASER CAVITY

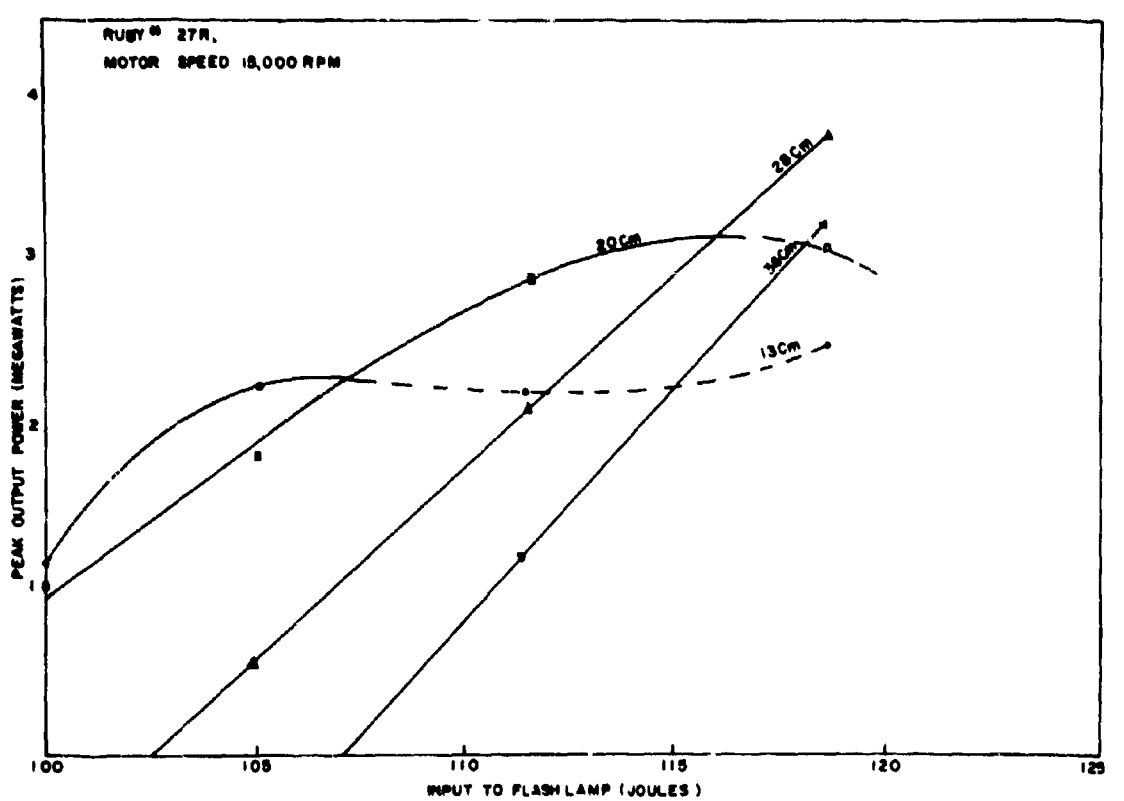

FIGURE 4. OUTPUT CURVES FOR VARIOUS CAVITY LENGTHS

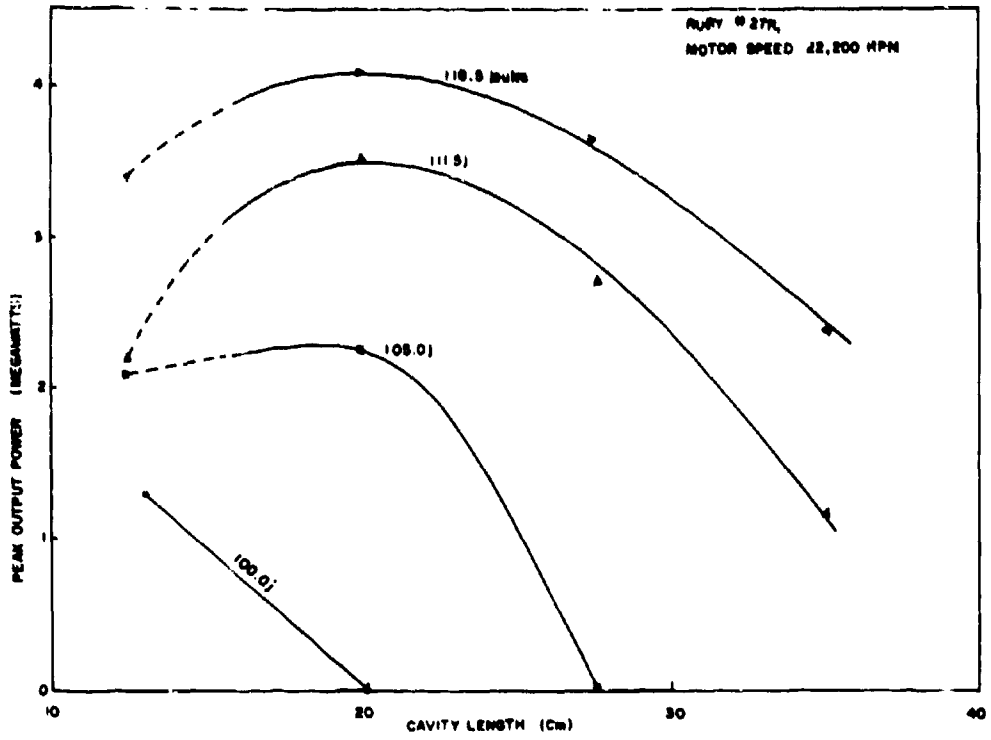

FIGURE 5. OPTIMUM CAVITY LENGTHS AT VARIOUS PUMPING LEVELS

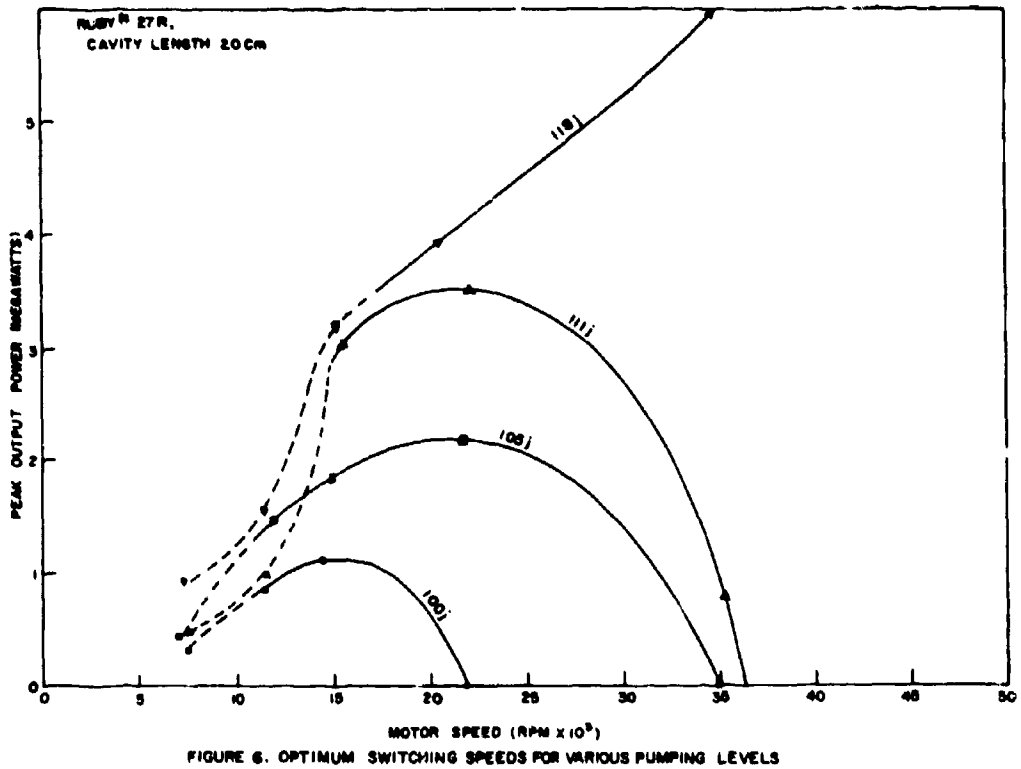

FIGURE 6. OPTIMUM SWITCHING SPEEDS FOR VARIOUS PUMPING LEVELS

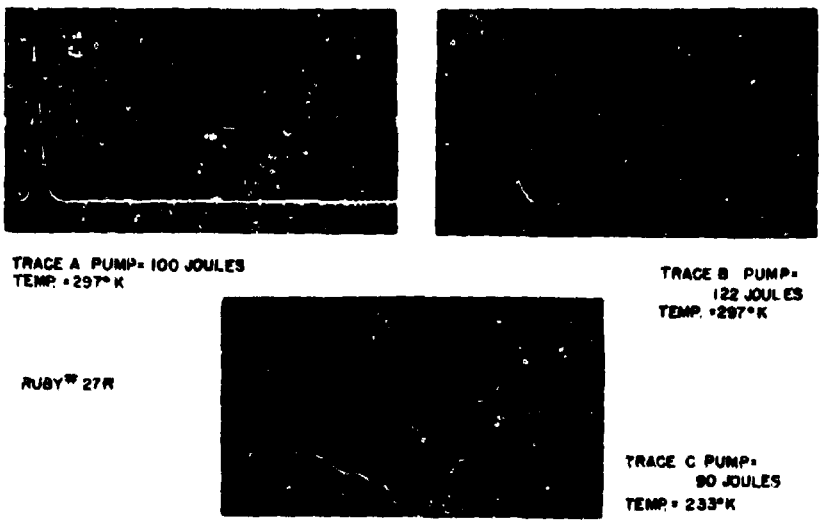

FIGURE 7. OSCILLOGRAMS OF TYPICAL OUTPUT PULSES

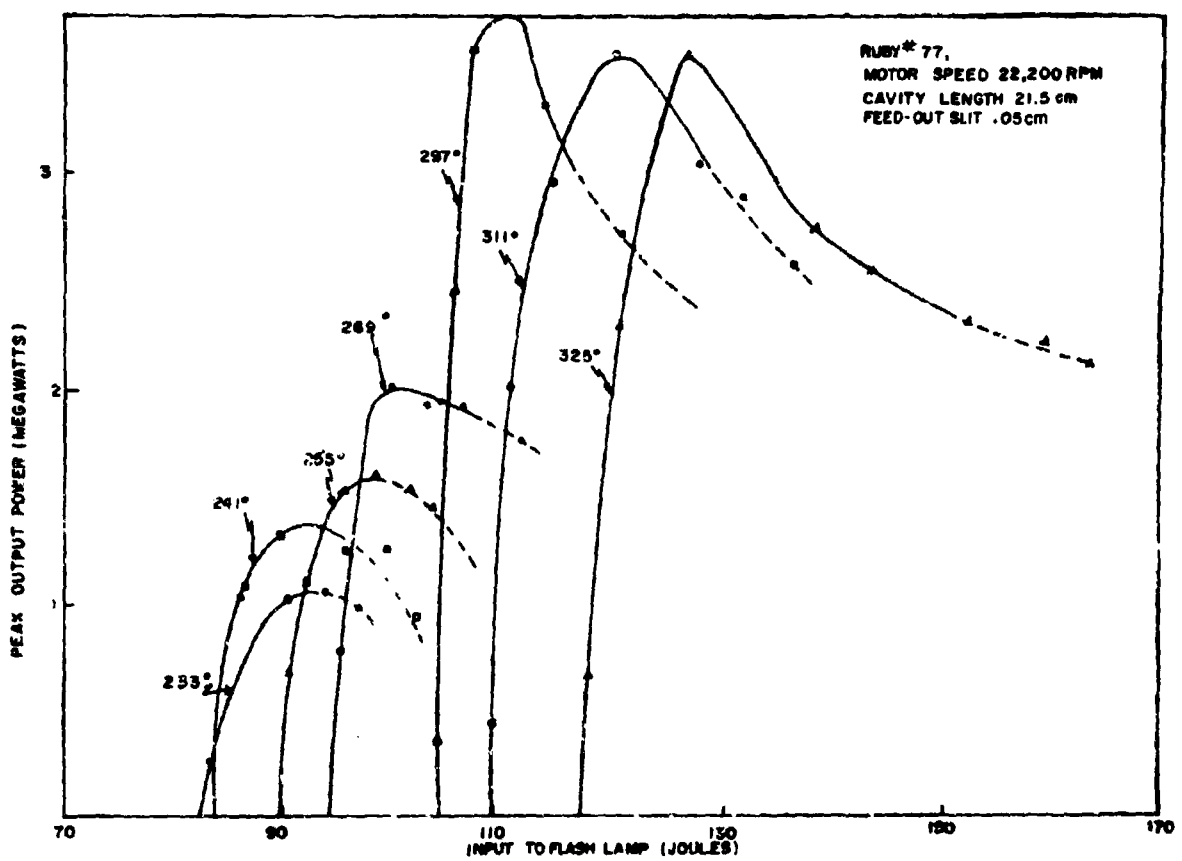

FIGURE 8. TEMPERATURE DEPENDENCE OF Q-SWITCH OUTPUT

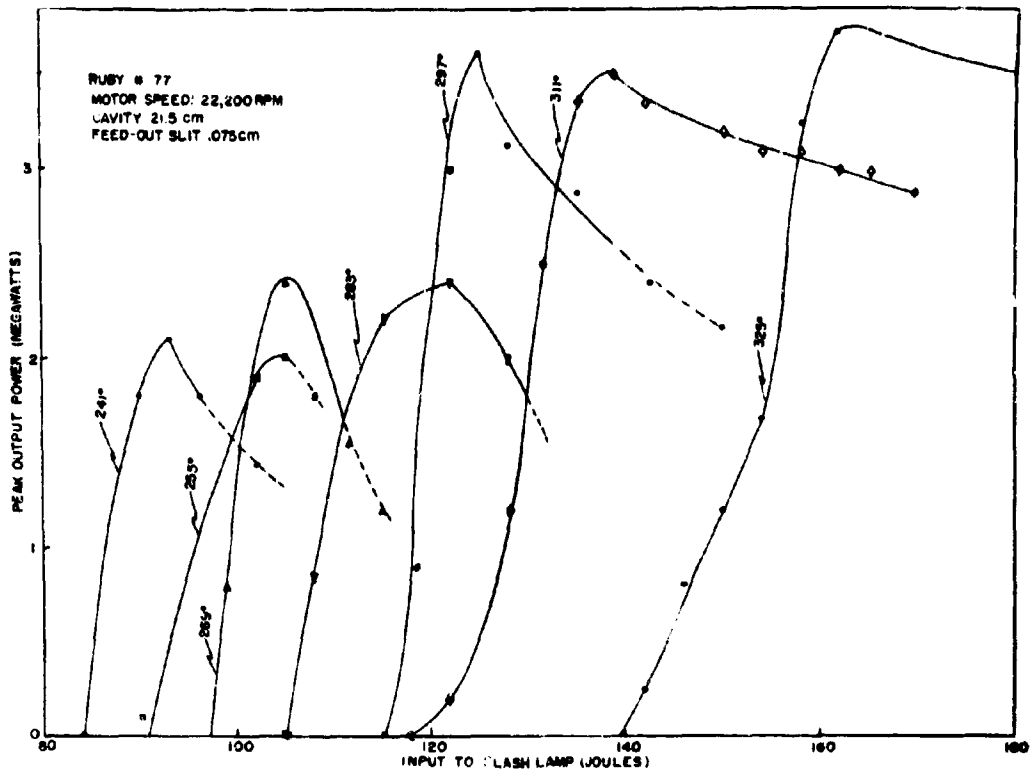

FIGURE 9. EFFECT OF INCREASE IN FEED-OUT LOSS (COMPARE FIGURE 8)

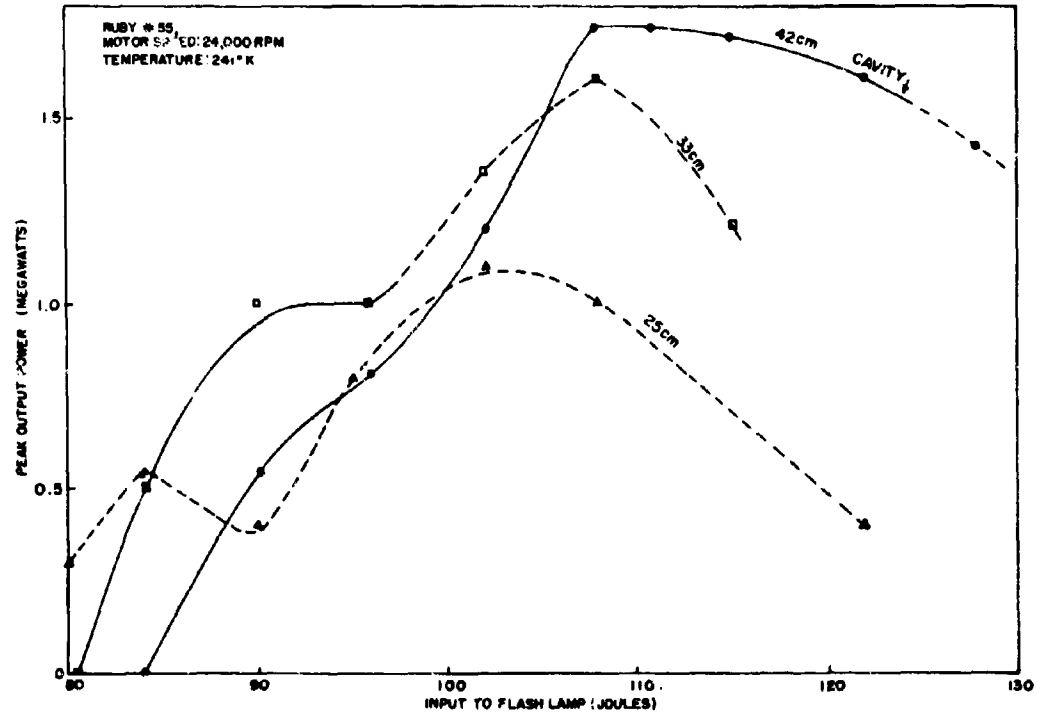

FIGURE 10. OPTIMIZATION OF CAVITY LENGTH AT LOW TEMPERATURE

NEW HIGH-ALTITUDE FAST-RISING BALLOON

MOSES SHARENOW
U. S. ARMY ELECTRONICS RESEARCH AND DEVELOPMENT LABORATORIES
FORT MONMOUTH, NEW JERSEY

SUMMARY

This paper presents the theory, design, and development of a novel type of balloon that offers promise of meeting Army requirements for a fast-rising, high-altitude meteorological balloon. The design consists of an inner high-altitude balloon and an outer streamline balloon. The assembly is so designed that it will ascend rapidly to approximately 50,000 feet. At this altitude the streamline balloon bursts and falls away from the inner balloon. The inner balloon now, by virtue of its increased free lift, proceeds to accelerate at the upper level of flight, providing a faster ascent rate throughout most of the flight than that which the individual component balloons are capable of attaining. Various techniques for successfully separating the streamline balloon from the spherical balloon during flight are discussed as well as some of the problems encountered in inflating the balloon on the ground.

BACKGROUND

The Army has a requirement for a meteorological balloon capable of rapid ascents to an altitude of 100,000 feet during both daytime and nighttime. This balloon is necessary to obtain upper-air meteorological data for artillery units, for units preparing radioactive fallout predictions, and for weather stations making forecasts for the field army. The balloon will enable data to be obtained more rapidly than is currently possible and will obtain representative data more nearly above a given station by virtue of the higher ascent rate. The balloon, together with an inflation-launching device and hydrogen generation equipment, comprises a fast-rising balloon system which is part of a larger Army Automatic Meteorological Sounding System.

The Army does not now have standard balloons which are capable of reaching both the required altitude of 100,000 feet and attaining the required ascent rate of 1700 feet per minute during

both day and night. Spherical Balloon ML-537, placed into recent use, provides the required altitude during day and night; however, its rate of rise is only 1000 feet per minute. Streamline Neoprene Balloon ML-541 provides the required rate of rise, but it is capable of rising to only 75,000 feet during the daytime alone. Attempts to extrapolate the performance of the streamline balloon by increasing its size have been only partially successful in that daytime altitudes have been lifted to around 90,000 feet. Nighttime altitudes above 60,000 feet were not attainable with this type of balloon.

Early attempts to develop fast-rising balloons by the use of streamline inexpansible plastic-type balloons having stabilizing fins have proven impractical in that excessively large balloons and therefore large volumes of hydrogen are required. In addition, expert rigging and alignment of fins are required to produce the stability required for rapid ascent. Balloons of this type did provide rapid ascent rates to 40,000 feet. Attempts to employ large, thick-wall spherical balloons having high internal pressure, or several balloons, one inside the other to prevent deformation, have provided erratic results. Also, generation of excessive amounts of hydrogen for inflation was required.

In order to understand the development discussed in this paper, some of the earlier work on the theory of the ascent rates of expansible type spherical and streamline balloons is presented.(1), (2),(3).

The equation of motion for balloons of this type is given by $L - D = m \frac{dV}{dt}$, where L is the free lift, D is the drag, and V is the ascent rate of the balloon. The mass of equipment and weight of gas carried aloft are given by m. Integration of the equation was performed by assuming a constant drag coefficient. Analysis of this theory shows that although balloons of this type should theoretically accelerate to burst, they all do not follow the theory because of the critical Reynolds number effects. Results of the theory are summarized as follows:

1. Streamline neoprene balloons accelerate rapidly to an altitude of approximately 50,000 feet. They then show a sharp deceleration in the next 10,000 feet, after which there is a slower deceleration to burst.

2. Spherical thick-wall neoprene balloons also accelerate rapidly to 50,000 to 60,000 feet, provided they have sufficient free lift (almost twice as much hydrogen as that required for the streamline balloons). They also exhibit a sharp deceleration and leveling off above this altitude unless the balloons are quite large.

3. Large thin-wall spherical balloons of the high altitude type will accelerate to burst provided they do not reach the critical Reynolds number. Their rate of rise is much lower than streamline balloons in the lower 50,000 feet and much higher in the upper 50,000 feet.

Figure 1 shows the relationship between drag coefficient and Reynolds number for theoretical spherical and streamline bodies.

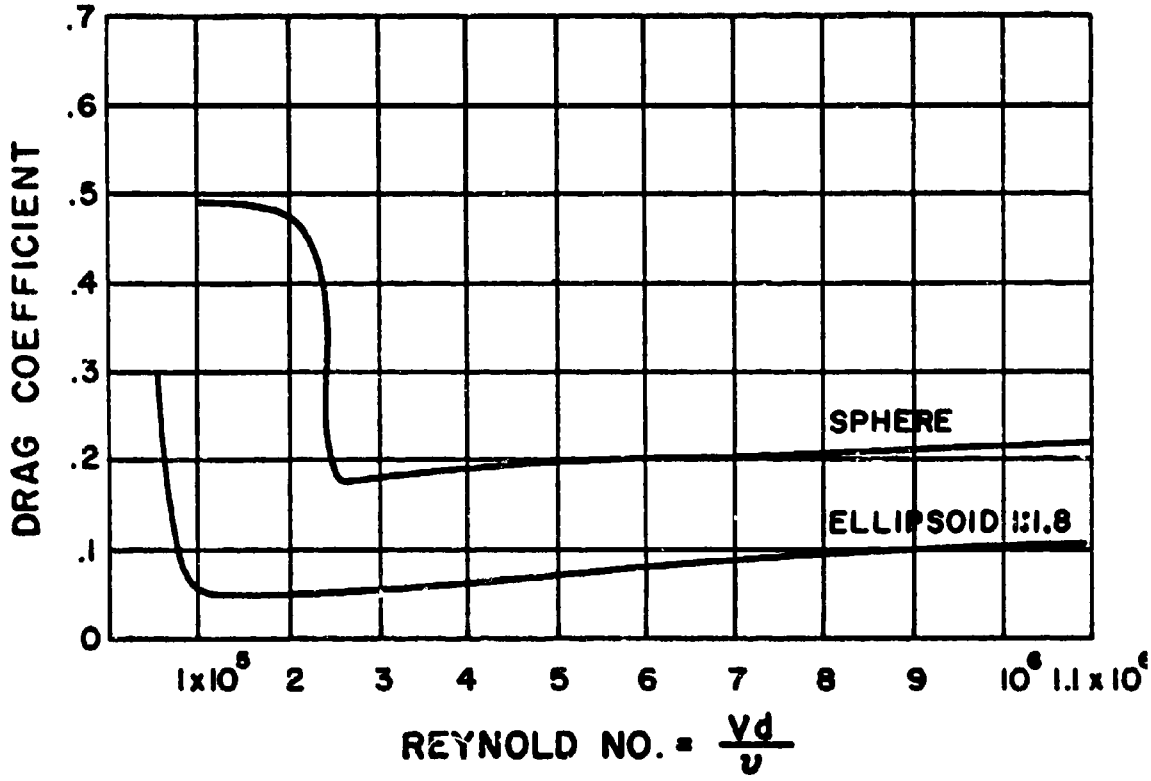

DRAG OF RIGID SPHERE & ELLIPSOID

FIG.1

Balloons generally leave the ground at the extreme right-hand side of the curve and follow it to the left as they ascend. When they reach the point near 3×10^5, the drag coefficient rises sharply and the balloon decelerates sharply. If the balloon is sufficiently large and its ascent rate is high enough, it may not reach the critical number and will continue to accelerate to burst. The

accelerative effect is more pronounced with fast-rising balloons than with the slower 1000-feet-per-minute types, since other atmospheric parameters can cause ascent-rate changes of the same magnitude as those encountered on the slower rising balloons.

DISCUSSION

The problem of obtaining a high-altitude fast-rising balloon was attacked from three angles: aerodynamic studies, neoprene latex compounding studies, and fabrication techniques. Aerodynamic studies were required to determine methods of reducing drag or air resistance of balloons to obtain optimum ascent rates. Latex compounding studies were necessary in order to develop balloons which could attain the 100,000-feet altitude with the larger volume of gas required for fast-rising balloons. The standard 100,000-feet Balloon ML-537 could not attain the altitude with the larger gas volume. Investigation of techniques for fabricating balloons was necessary in order to reduce to practice the results of both the aerodynamic and compounding studies.

A study of both known and new principles of air-flow patterns past rigid experimental models revealed that, although reduction in drag was achieved in wind-tunnel tests, attempts to apply the results to actual balloons which are semirigid failed in most instances to produce the desired results. A new approach was indicated if the problem was to be solved.

As a result of an intensive research investigation into the physical and chemical properties of balloon films (4), balloons capable of high-altitude performance both day and night (120,000 to 130,000 feet) were developed. These balloons, having a substantial margin of performance above 100,000 feet, could safely be overinflated with the volume required to produce the higher ascent rates for fast-rising balloon application. Success was achieved through the conception of a novel design known as the "combination balloon." This balloon combines an inner high-altitude balloon of the above type with an outer streamline balloon of the ML-541 type. Figures 2 through 5 show the components of the balloon as well as the configuration at launching and in flight. The inner balloon has a length of 145 inches, weighs 2200 grams, and, at launching, generally has a few folds. The outer balloon is about 145 inches long and weighs about 1800 grams. However, the inner balloon is contained entirely within the spherical part (65 inches) of the streamline balloon.

The advantage of the combination balloon is that it combines the high ascent rate of the streamline balloon in the lower altitudes with the high ascent rate of the thin-walled spherical balloon in the higher flight altitudes. The streamline balloon carries the assembly rapidly to 50,000 feet. The streamline balloon is designed to burst at this altitude, instead of its normal altitude

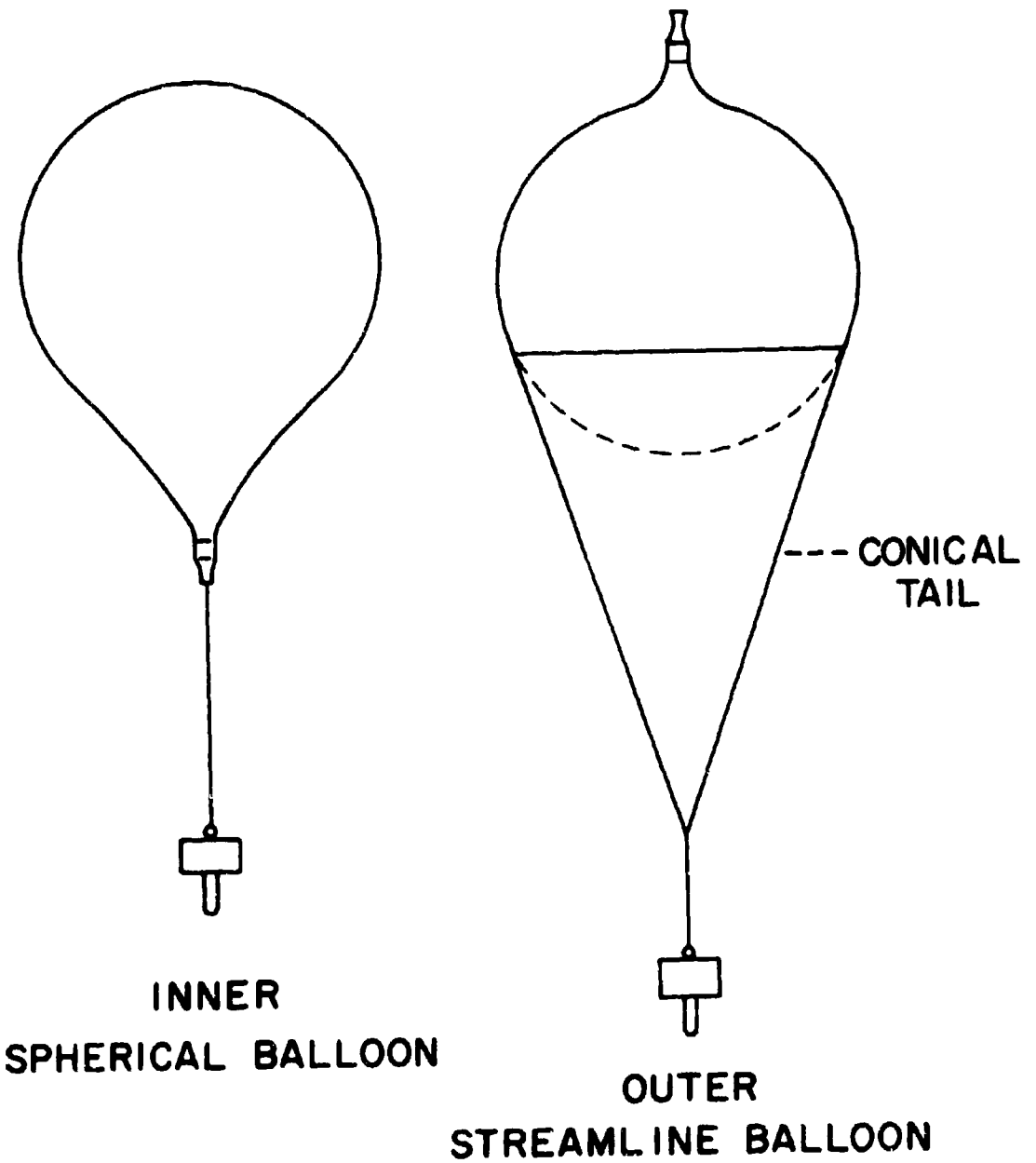

COMBINATION BALLOON COMPONENTS

FIG. 2

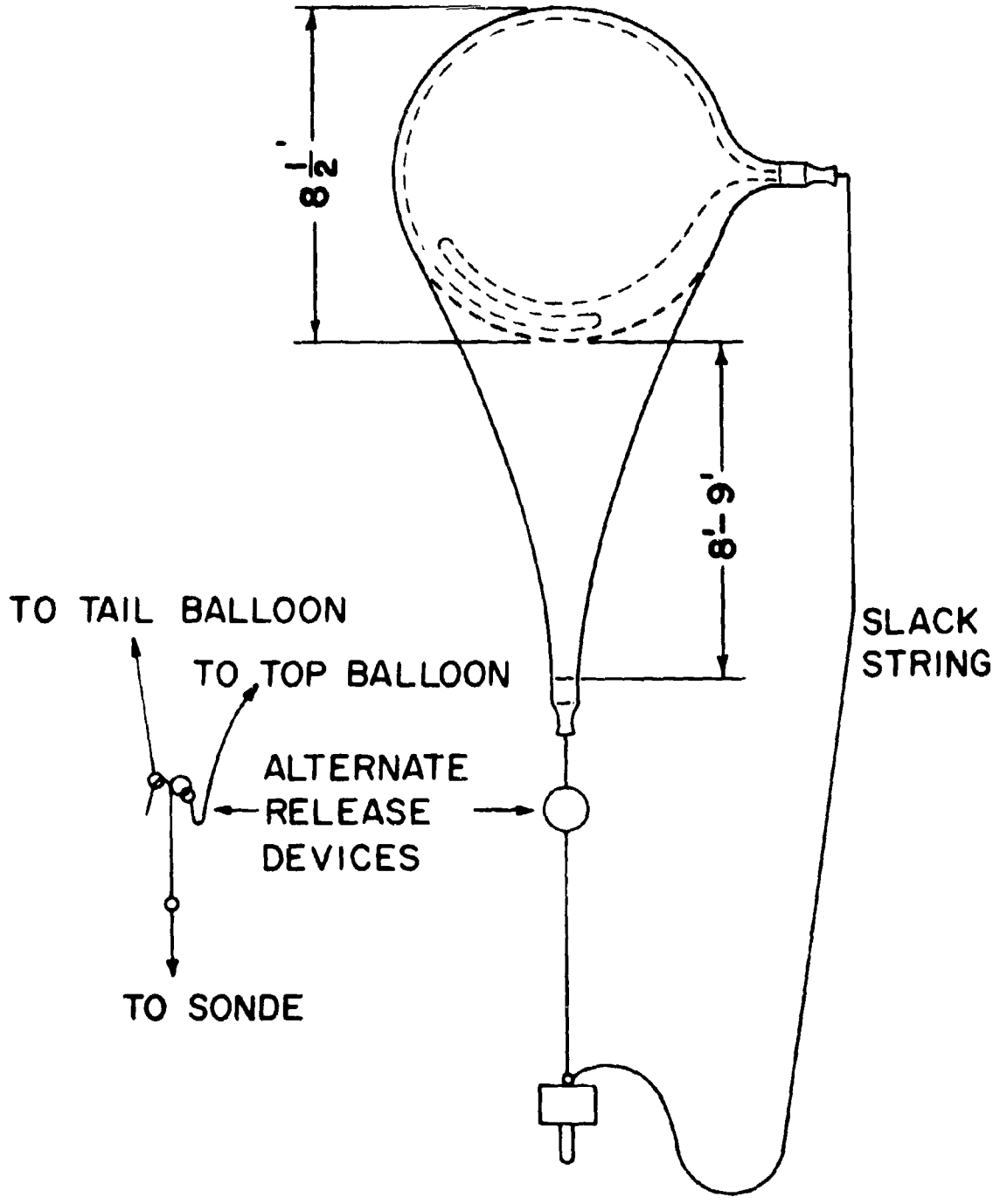

COMBINATION BALLOON ASSEMBLED
(AT LAUNCHING)
FIG. 3

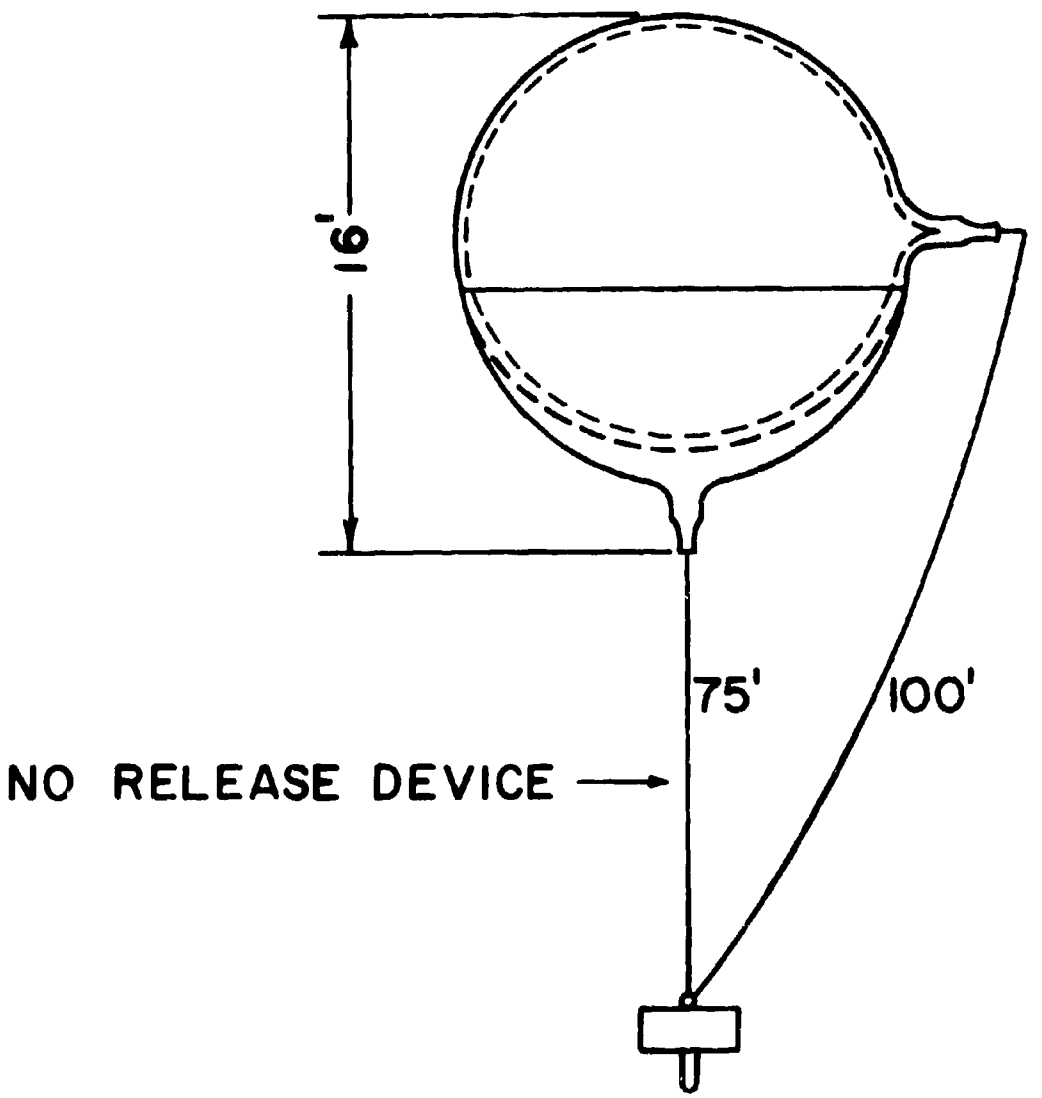

BALLOON NEAR 50,000 FEET

FIG. 4

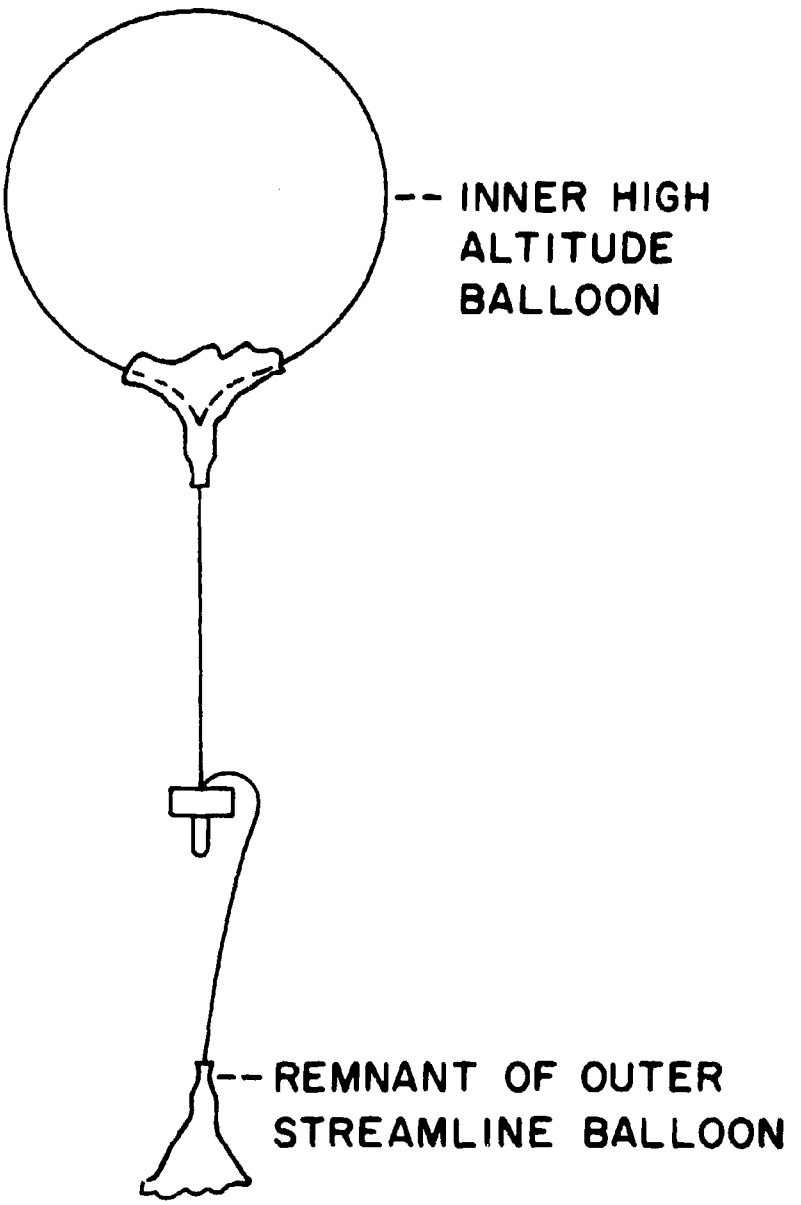

BALLOON AFTER OUTER BALLOON BURST
(NEAR 50,000 FT.)

FIG. 5

of 75,000 feet, and fall away from the inner balloon. The inner balloon, now stripped of the dead weight of the outer balloon, has increased free lift and proceeds to accelerate at the upper level of flight where normally a streamline balloon would decelerate.

Figure 6 shows how the inner spherical balloon alone starts out at the slow rate of 900 feet per minute, reaching around 1500 feet per minute near 70,000 feet. The balloon then accelerates more rapidly from 70,000 feet until burst near 100,000 feet, reaching ascent rates as high as 2100 feet per minute. On the other hand, the streamline balloon alone (Fig. 7) starts off at around 1600 feet per minute and reaches an ascent rate from 2700 to 3000 feet per minute near 50,000 feet. The ascent rate drops sharply in the next 10,000 feet, frequently by as much as 1000 feet per minute, and then decelerates further until burst. The sharp deceleration is due to the balloon's going through the critical Reynolds number, characteristic of a body of revolution, and represents a transition from turbulent to laminar flow.

The combination balloon (Figs. 8 and 9) combines the advantages of both balloons. It starts out around 1400 feet per minute, accelerating as a streamline balloon to 2200 feet per minute, with peak rates often as high as 2500 feet per minute near 50,000 feet. Its ascent rate is lower than a streamline balloon alone up to 50,000 feet, since it has to carry the weight of the inner balloon as well. The streamline balloon is compounded to burst at this altitude instead of continuing on to 75,000 feet, even though the streamline balloon might have a slight advantage over the spherical balloon between 50,000 and 60,000 feet (see shaded area). The reason for this is to prevent burst of the inner balloon upon burst of the outer balloon on a consistent basis. The inner spherical balloon moves along at around 1400 feet per minute, slowly increasing in ascent rate until it reaches 70,000 feet when it picks up to 1600 feet per minute, then accelerating more rapidly to as high as 2100 feet per minute near 100,000 feet.

The average ascent rate to 100,000 feet is approximately 1700 feet per minute in the daytime and 1600 feet per minute at night. Nighttime ascent rates are generally lower than daytime rates for the same volumes of hydrogen for all balloons. This is due to the fact that solar radiation increases the free lift of a balloon in the daytime by creating a super heat within the balloon. The temperature of the gas inside can be as much as 40°C warmer than the air outside the balloon from 50,000 feet on up to burst. At night, on the other hand, the gas temperature is 5 to 10°C cooler than the air temperature. The balloon at night therefore displaces a correspondingly smaller volume of air and has a lower free lift than does the balloon during the daytime at similar altitudes. Since the Army considers it important to have a single balloon for both day and night use, this discrepancy in performance must exist unless a

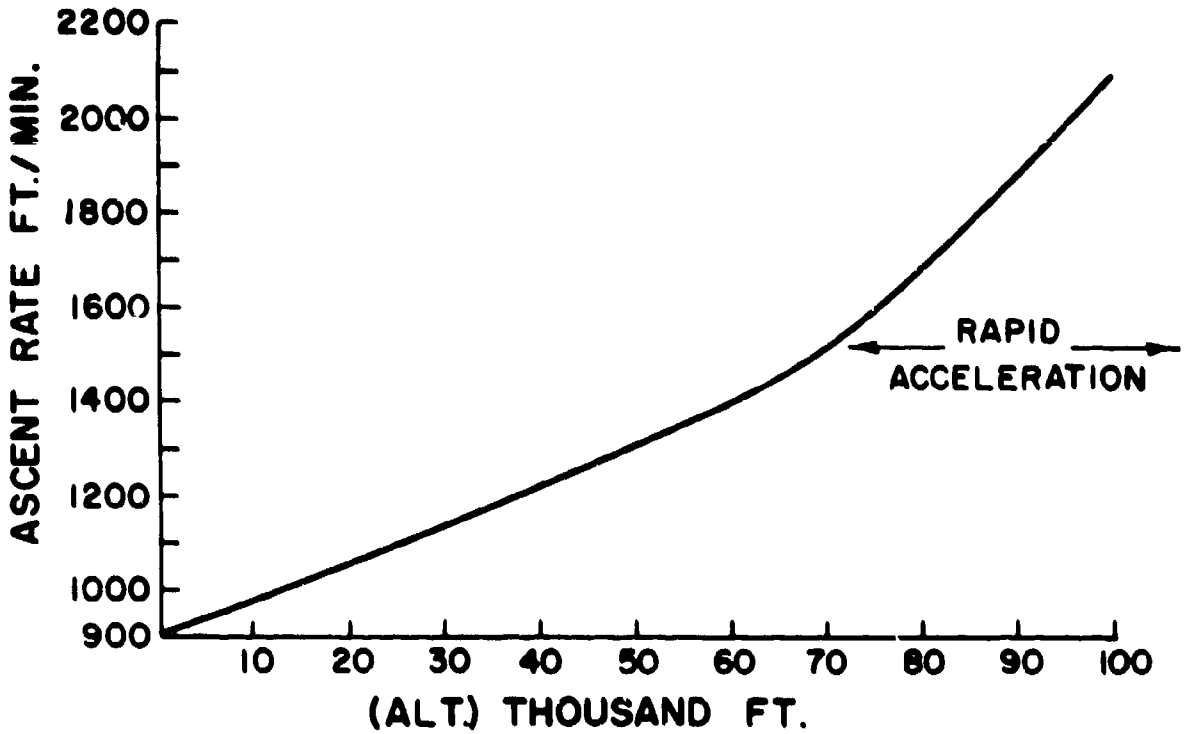

INNER HIGH ALTITUDE BALLOON

FIG.6

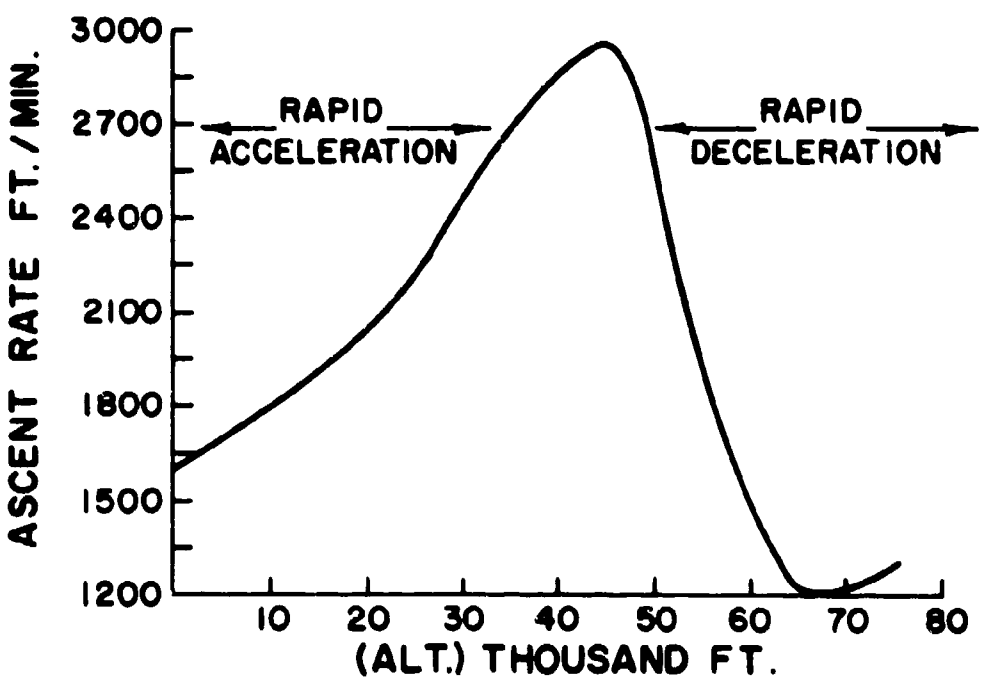

OUTER STREAMLINE BALLOON

FIG.7

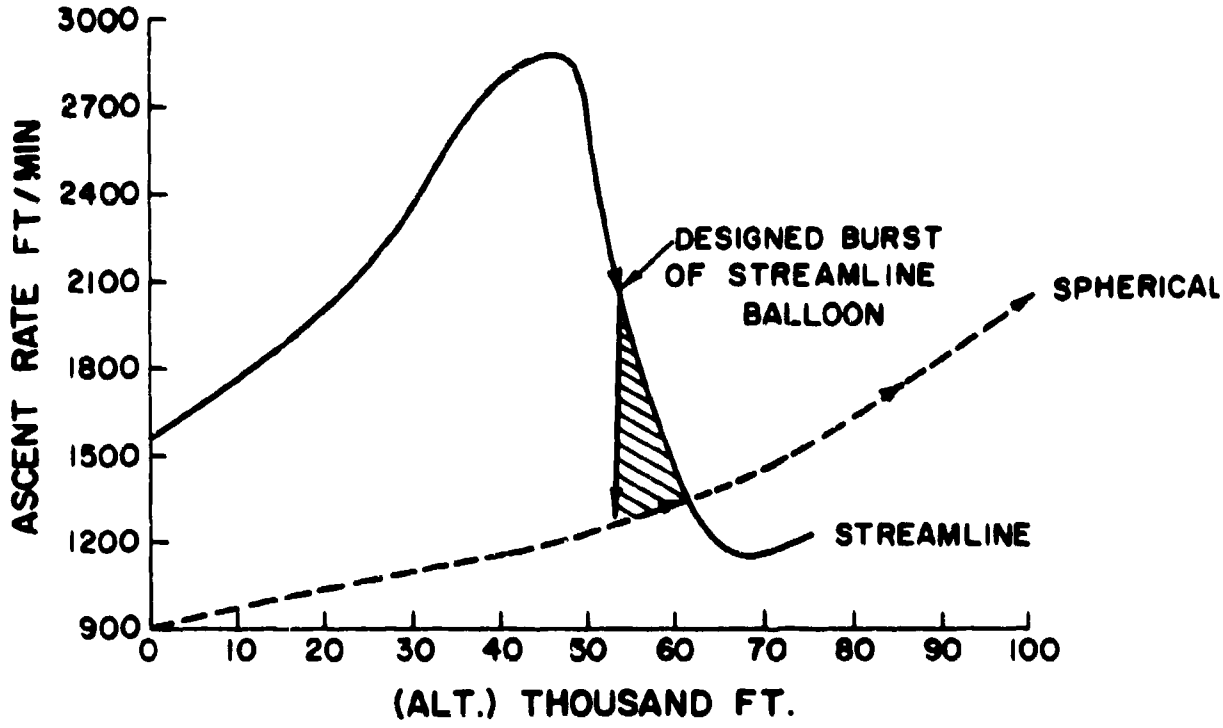

COMBINED ASCENT RATES

FIG. 8

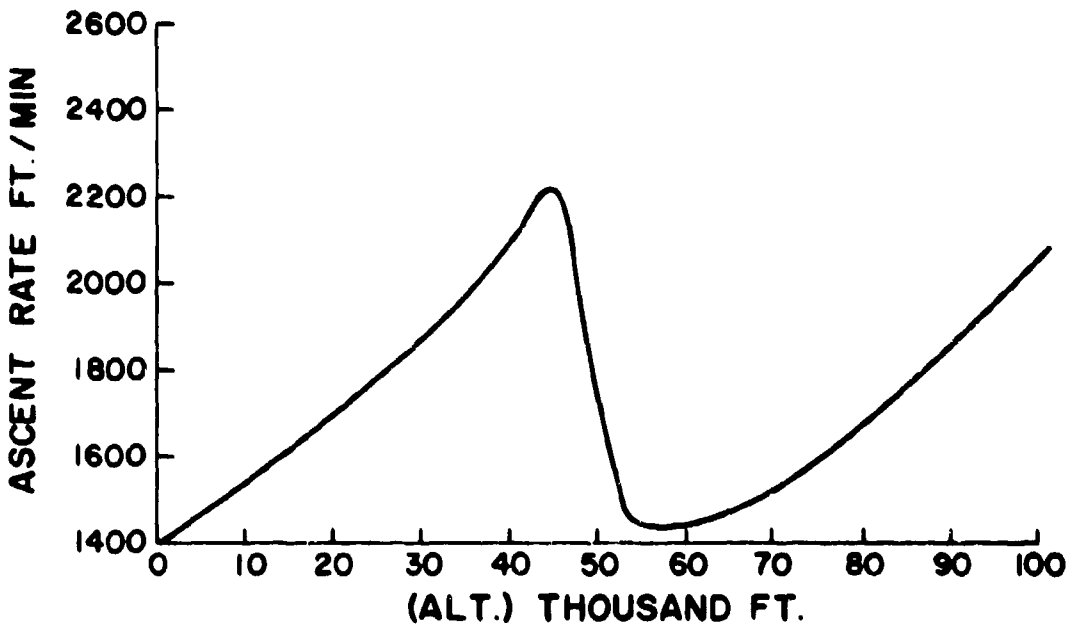

ACTUAL ASCENT RATE OF
COMBINATION BALLOON

FIG. 9

larger volume of gas can be used for nighttime performance. In order to obtain satisfactory altitudes at night, the balloon manufacturer must incorporate larger amounts of plasticizer into his compound; otherwise the balloon films would freeze. This, in turn, softens the balloon film and reduces the ascent rate in the daytime to some extent so that actually a compound designed strictly for daytime use would produce a balloon capable of ascent rates between 1800 and even as high as 1900 feet per minute rather than only 1700 feet per minute.

Problems of Balloon Inflation and Rigging

In order to make the combination balloon a practical field tool, it is necessary to provide a balloon which requires a minimum of skill in inflation and rigging. Since the inner balloon is quite a long balloon, it must be folded inside the considerably shorter streamline outer balloon. During the earlier stages of inflation, gas pockets can develop which can pinch off large sections of the inner balloon and prevent full inflation of all parts of the balloon, thus causing either premature burst on the ground, irregular shapes, or premature burst during flight. The use of a very fine lubricating dry talc between the two balloons has largely eliminated this problem and produced a very consistent performance to 100,000 feet. The talc allows the balloons to glide readily and expand without constricting the inner balloon.

Another device being considered is to have a thin one-inch polyethylene inflation tube packed throughout the inner balloon. The inflation tube has holes throughout its length, allowing the gas to escape through all sections of the inner balloon. Initial tests on this device are promising. Procedures for inflating this balloon are expected to be routine and similar to those used in inflating streamline balloon ML-541, which is inflated in a manner similar to a spherical balloon since it has two necks and is inflated from the top neck and then inverted at launching.

In order to gain maximum benefit with regard to increasing the free lift of the inner balloon at 50,000 feet where the outer balloon bursts, it is obviously desirable to discard as much of the outer balloon as possible. The manufacturer has successfully designed the outer balloon film compound to do two things: first, to allow it to burst without recovery, i.e., without a snap-back which could burst the inner balloon; secondly, to permit separation of most of the balloon from the inner balloon. These were accomplished by controling the cure or vulcanization phase of manufacture. However, to insure separation of most of the outer balloon, mechanical devices have to be employed. Both of these are illustrated in Fig. 3. In the case of the hook, when the outer streamline balloon breaks, the cord holding it to the train line slides off the hook. The other release device employs a five-inch balloon

designed to burst at a diameter of ten inches, which corresponds to approximately 50,000 feet in altitude. When this balloon bursts, the balloon inverts and the load is taken up by the neck of the inner high altitude balloon. Because the small balloon will generally not burst simultaneously with the outer streamline balloon, this device is not considered as reliable as the hook. Experiments are continuing with the hook.

CONCLUSIONS

1. The combination balloon represents not only a solution heretofore unobtainable, but also a practical solution to the problem of obtaining a high-altitude fast-rising balloon.

2. It provides the capability of meeting Army requirements in a single balloon.

3. The balloon is compatible with equipments currently under development for inflating and launching balloons and with ground tracking equipment.

REFERENCES:

1. Sharenow, M., Ascensional Rate Characteristics of Large Spherical Balloons. Paper presented at meeting of American Meteorological Society, St. Louis, Missouri, 1950.

2. Sharenow, M., Streamline Neoprene Balloon, SCEL Technical Memorandum M-1776, Fort Monmouth, New Jersey, 18 May 56.

3. Sharenow, M., Streamline Neoprene Balloons, Bulletin, American Meteorological Society, May 61.

4. Sharenow, M., and E. Nelson, Some Recent Advances in High-Altitude Balloon Technology. Paper presented at meeting of American Meteorological Society, El Paso, Texas, Nov 63.

THE EFFECTS OF MASSIVE DOSES OF IONIZING RADIATION UPON CONDITIONED AVOIDANCE BEHAVIOR OF THE PRIMATE

JOSEPH C. SHARP, CAPT, MSC and JOSEPH V. BRADY, LT COL, MSC
WALTER REED ARMY INSTITUTE OF RESEARCH
WASHINGTON, D. C., 20012

There have been few if any formal investigations into the effects of massive and acute doses of radiation on ongoing learned behavior of primates. The reports by Allen, Brown, Logie, Rovner, Wilson and Zellmer (1), Wilson (15), Pickering, Langham and Rambach (14) and Zellmer and Pickering (16) all mention "clinical observations" or "general behavior." These observations list a large number of symptoms and signs. Ataxia, nystagmus, convulsions, etc., are all listed and associated with central nervous system damage. The signs of hematopoietic attenuation include ulceration, septicemia, purpura of the skin, gastrointestinal bleeding, etc. Gastrointestinal involvements have been listed as including diarrhea, vomiting, anorexia, etc. Allen et al. (1) mentioned an amorphous symptom complex which they called "debility, consisting of an extreme loss of interest in all surroundings, disinclination or inability to move, and a tendency to sit, unmoving and huddled over with a bowed head and a ruffled fur..." (p.9). While suggestive, these observations tell little if anything about learned and highly motivated behavior following massive doses of radiation.

Several studies in the past have attempted to determine how high doses of radiation affect cognitive faculties. One of the earliest (8) radiated monkeys with 880 to 28,000 r at 1,000 r per minute and tested 3 minutes, 1 hour and 8 hours after exposure. All animals refused to respond to all tests. The loss of motivation because of nausea and vomiting probably accounted for the animals' refusal to be tested. Langham et al. (8) concluded, among other things, that it was not justified "...to draw specific conclusions as to their inability to respond under duress (radiation exposure) as would apply to a military situation" (p.3). These investigators also stated that "general observations" suggest that about 5,000 r produced "incapacitation within a few minutes." Riopelle, Grodsky and Ades (13) tested rhesus monkeys following exposure to 350 to 2,000 r. In tests of delayed response, avoidance conditioning and visual discrimination only the latter test was able to distinguish between

radiated and control animals. Rats given 5,000 r to the head learned a T maze 60 days, 30 days or immediately after exposure in fewer trials than non-irradiated rats (2) and a retention test demonstrated equal or superior performance for the radiated rats 3 to 80 days post exposure (3). Pickering, Langham and Rambach (14) reported on work by Kaplan and his group showing results which failed to yield "clear-cut differences between pre and post radiation error scores for any of the dose levels" (p. 34) in a maze experiment using shock to motivate monkeys to make visual discriminations. One of the important conclusions made by Kaplan was the existence of a wide range of individual reactions to radiation exposure. It was hard to discern, however, whether the differences between individual monkeys were greatest for radiation effects, the behavior being tested, or some complex interaction of the two.

In studies reported by Casey (6) goats received mixed neutron and gamma radiation and were then transported from the reactor site to the behavioral test site and immediately subjected to testing in an obstacle course. The incentive to run this obstacle course was social. Social incentives have been shown to be more motivating than food incentives in certain physiological states (10). Casey reported it impossible to test any goat after receiving 50,694 rads, five out of seven animals being unable to respond in any way after 24,347 rads.

Exposure of the whole body of mammals to large doses of ionizing radiation at high rates results in performance decrements. The time course and the quality of the behavioral decrements is still obscure. This is especially true for highly motivated tasks which call for simple but continuous performances.

With the advent of modern techniques of behavioral control and the development of a primate-restraining apparatus (12) it is now possible to test a wide variety of behaviors before, during and after irradiation. In addition, methods of programing and recording on-going behavior can be remote and automatic.

It was the purpose of this study to investigate how a relatively simple, highly motivated task which required periodic responding would be affected by massive and acute doses of whole body x-irradiation.

Procedures

Adult male primates (macaca mulatta) procured by the Department of Laboratory Animals, Walter Reed Army Institute of Research, were used. Weight ranged from 3.8 to 5.2 kg. Throughout all experiments the principles of laboratory animal care as promulgated by the National Society for Medical Research were observed.

All monkeys remained in the restraining apparatus throughout all experiments. Attached to the restraining apparatus were a bank of multicolored stimulus lights, a hand response key (modified telegraph key), and a pair of wires, one to the foot rest and one to the metal seat, for administering electric shock. Also located in the monkey's environment was a loud speaker wired to a "white noise" generator to attenuate cues and noises from outside the small booth

in which the monkey lived. Automatic timing and switching circuits located outside the booth programed each event during each session.

After 3 to 6 weeks' habituation to the chair, avoidance behavior was conditioned in the following manner. While in the restraining apparatus the animal was shocked. If the animal did not respond to this first shock by depressing the response key he continued to receive shocks at the rate of one every 2 seconds (shock-to-shock interval or S-S interval). Each time the monkey pressed the lever he postponed the next shock for 10 seconds (response-to-shock interval or R-S interval). The shock duration was fixed at 350 ms; the intensity was approximately 10 mA. Initially the behavior was "shaped" to the correct response, i.e., any movement in the vicinity of the response key resulted in postponement of the next shock for 10 seconds. This phase of training usually required 1 to 2 hours. Finally, only a downward movement of the key served to postpone shock; holding the key down did not delay the shock for more than the 10-second interval.

As soon as the monkey began to press the key sufficiently often to indicate to the experimenter that some conditioning had occurred, the following change was made. The R-S interval was progressively shortened until a response was required every 2 seconds. The S-S interval remained at 2 seconds. An animal making avoidance responses 30 times per minute could avoid all shocks if the responses were evenly spaced. This final schedule was chosen to provide a stable response rate to compare against post-irradiation effects. In order to avoid undue fatigue a schedule of working for 30 minutes and then resting for 30 minutes was employed; this 1-hour period was called a session. The work period (S^D) was signaled to the monkey by a red light, the rest period (S^Δ) by a green light.

As the animal's performance became more proficient the number of consecutive sessions was gradually increased over a period of 3 to 4 weeks, to a total of 50 or 72 sessions. That is, an animal would be on schedule either 50 or 72 hours. At the completion of a run 24 to 28 hours would intervene before the beginning of the next run. Water and food were available at all times.

When the animals were radiated an automatic safety circuit was added to the program. This circuit was so designed that if the monkey did not respond after six consecutive shocks he was given a brief 2-minute "safety-break." At the end of this 2-minute period the regular avoidance schedule was continued. This procedure prevented the animal from receiving large numbers of shocks during states of incapacitation.

After thorough training the animals were moved to the National Institutes of Health and habituated to the procedures of irradiation. The habituation consisted of moving the monkey, in the restraining chair, from the living booth to a position directly under the Van de Graaff shutter. A cable connecting the programing and recording apparatus to the equipment on the chair in the exposure room made it possible to record responses during habituation and irradiation. Because the opening and closing of the shutter made

considerable noise, a transient but marked increase in response rates always followed shutter operation. It took several weeks to habituate the animals to these noises. After complete habituation, however, it was impossible to detect any change in response rate upon operation of the shutter. While in the exposure room the monkey was monitored via closed circuit television at all times.

After complete habituation three sham irradiation runs were made. These served to provide baselines to which post-irradiation behavior could be compared. These sham runs were identical to the irradiation runs in every way but for radiation.

On the day of irradiation two normal sessions were completed. During the second S^{Δ} period the monkey was moved under the Van de Graaff with the center of his head 42 cm below the center of the x-ray target; the connecting cable was attached to the chair, the television monitors turned on and the exposure room closed. The moving and adjustments interrupted the S^{Δ} period for from 5 to 10 minutes. At the appropriate time the next S^{D} period was started. After 3 minutes the shutter opened and irradiation continued for periods of from 6 to 22 minutes depending upon the total dosage desired. After completion of irradiation and the S^{D} period the monkey was moved back to his living booth and the programed schedule continued until death. The 3 mev Van de Graaff unit at the National Institutes of Health was used. It was operated at 2.5 mev x-rays (HVL = 9.6 mm Pb.); and current values of 0.6 to 0.8 mA. Exposure rate varied from approximately 1,500 to 1,900 r per minute. Focal distance was 42 cm and coincided with the center of the brain. Dosimetry was done with a standardized ionization chamber placed in the same position as the brain (42 cm). This chamber was used to calibrate a current integrator connected to a transmission ionization chamber to determine total dosage.

Results

Figure 1 shows the average number of responses per minute plotted against sessions for monkey X-955 and demonstrates that a stable response rate prior to irradiation was achieved. Note that after 215 hours of successive 30-minute work and 30-minute rest periods there was no diminution in responding. The average of the first 20 and last 20 sessions was 163 $\pm$ 2 responses per minute. The overall S^{D} response rate averaged almost six times that required to avoid all shocks. The S^{Δ} responses, or responses during the rest period, show only occasional bursts and these usually coincided with disturbance of the monkey for cleaning or feeding. Only this monkey was worked for 215 hours, all the rest worked for either 50- or 72-hour periods.

10,000 r

Figure 2, plotted in the same way as Figure 1 but with the mean and standard deviations from the previous control runs indicated, shows the debilitating effect of 10,000 r. Prior to irradiation monkey C-546 responded at an average rate of 223 responses per minute. Ninety-nine percent of the time his normal rate was between

180 and 266 responses per minute. The entire range of S^{Δ} responses was between 0 and 109 responses.

Ten thousand roentgens delivered during the third S^{D} period appeared to have a transient effect on the following session, and within 2 hours post-irradiation there was complete recovery. Following the recovery there was a slow irregular decline in the response rate but not until the forty-sixth session was the rate below the minimum level required to avoid all shocks. From the forty-ninth session until death in the seventy-seventh session, C-546 made only spasmodic responses. The animal died 78 hours after irradiation. It can be said that he performed within three standard deviations 20 to 25 hours after irradiation and successfully avoided most shocks for about 40 hours post-irradiation. There seemed to be little change in S^{Δ} responding following irradiation.

General behavioral observations included the usual signs of vomiting and diarrhea during and immediately following irradiation, followed by vertical nystagmus (15 hours) with increasing ataxia (17 to 20 hours). There was no sign of loss of interest in his surroundings or inability to move as reported by Allen et al. (1) until 33 to 38 hours post-irradiation.

Radiation affected the performance of two additional monkeys in much the same way as it did C-546. There was a transient decline in responding during or shortly following exposure and then a return to normal or near normal for several hours. When behavioral disintegration did occur it was marked, severe, rapid and relatively permanent. Death followed irradiation in 58 and 89 hours, respectively.

The general observations recorded for these two monkeys were quite similar to those for C-546. One animal did show ataxia beginning during session 31 (29 hours post-irradiation). Ataxia was first noted 25 hours post-irradiation in the other animal.

Monkey C-545 showed a marked decline in response rate following irradiation, this suppressed response rate persisting until death at 181 hours. The performance was reliably and consistently below normal levels even though he lived twice as long as the three animals reported above. The S^{Δ} response rate was uniformly low suggesting the continuing discrimination of the work and rest periods.

The last two animals in this series exhibited responses to the irradiation not seen in the first four animals. After responding adequately for 63 and 34 hours, respectively, there was the usual sudden and marked cessation of responding which in all other monkeys heralded death. However, after 30 or 13 hours a dramatic "recovery" was made and for a period of either 35 or 50 hours they responded at below normal levels but with rates high enough to avoid most shocks (see Figure 3). During the period of spasmodic or no response the animals continued to receive shocks at the rate of one every 2 seconds. If there was no response for six consecutive shocks the 2-minute "safety break" was introduced; at the end of the 2-minute period the shocks were again delivered. During these hours of no recorded responding the animals were alert and responded to the shocks with vocalizations and attempts to hit the response lever,

but because of severe ataxia seemed unable to do so. Muscle strength and tonus were near normal as tested by grasping the paws and judging the vigor of the resultant reaction.

The clinical observations for these two animals followed a time course similar to that for all the other animals with the exception of time of death (170 and 123 hours, respectively). The first signs of ataxia were noticed between 24 and 32 hours after exposure; one vomited while in the exposure room and again 40 minutes after removal from the room. Vertical nystagmus was present 42 and 37 hours after irradiation. Diarrhea was present in both animals 24 hours post-irradiation.

20,000 r

Irradiation of the whole body with 20,000 r effectively compressed the time course of various behavioral events. All animals were dead 21 hours after irradiation; all effective responding, i.e., an average response rate above 30 per minute, ceased after 11 hours and in some cases after only 2 hours. For an example of the debilitating effects of 20,000 r on this form of behavior, see Figure 4. This figure is presented in the same manner as the previous data for the 10,000 r monkeys.

All monkeys exhibited severe vomiting during and for an hour after irradiation. Two appeared to have vestibular involvement for a short time during irradiation but did not manifest this while being moved from the exposure room or at any time after. One animal appeared on the television monitor to have become somewhat stuporous and the response rate decreased to a point where a few shocks were delivered. However, after 6 minutes the rate of responding increased and was maintained at an adequate level for the balance of the session. The response of this monkey prompted a change in the data collection and analysis which was used on all animals receiving 40,000 r.

40,000 r

After only 1 hour, behavior was severely disrupted following a whole body dose of this magnitude. All animals were dead 7 hours after irradiation and effective response rates were not maintained for longer than 2 hours.

Because some animals appeared to lose consciousness during radiation exposure, a modified method of recording S^D responses during the irradiation session was introduced. The number of responses for each minute was recorded in addition to the total for the entire S^D period. The minute-by-minute response rates were plotted for the session immediately before irradiation and for the irradiation session for each monkey as illustrated in Figure 5 for monkey C-397. Note that after only 3 minutes of exposure all responding had stopped, but before the total dose had been delivered the response rate had started to return to normal. Before the full 30-minute session was completed, the monkey was responding at normal levels. Even after the loss of consciousness and severe vomiting, C-397 was motivated by the electric shocks to find the response lever and press it at a high rate. Two additional animals stopped responding

during irradiation and then returned to near normal levels by the end of the radiation session.

Figure 6 summarizes the findings of the present experiment. The dose-time relationships for time of death, last recorded response, the start of complete behavioral disintegration (which is that point where response rates dropped to near zero levels), and when the last response fell within three standard deviations of control values are plotted as a function of total dosage. For the 10,000 r group there was a period of at least 60 hours between the last "normal" sessions and death. As the total dose increased, the difference between these two points became less, but there was still about 15 hours at 20,000 r and 5 or 6 hours at 40,000 r.

Discussion

The results of this experiment indicate quite clearly that the use of behavioral indexes, as opposed to survival times, should result in a marked readjustment of the time lines for a realistic evaluation of the effects of ionizing radiation in military and civil defense situations. The primates used in this experiment were highly motivated to perform a relatively simple task yet the behavior was markedly deficient as much as 60 hours prior to death (in the 10,000 r group). The variability in both survival time and the onset of deterioration of behavior for the 10,000 r group is difficult to explain. The survival times reported by Langham, et al. (8), Langham, Rothermel, Woodward, Lushbaugh, Storer and Harris (9), Allen, et al. (1), Wilson (15) and Pickering, et al. (14) all show considerable interanimal and interexperimental variability. Some of the variability is probably due to the quality and rate of radiation used in the reported experiments. Apparently, the response of rhesus monkeys to ionizing radiation of doses in the neighborhood of 10,000 r is highly variable. This is true whether survival time or behavioral parameters are used as the reference dependent variable.

The variability at 10,000 r introduced into these experiments could be due to the "mode" of debilitation. With a total whole body dose slightly less than 10,000 r death has been attributed primarily to gastrointestinal dysfunction, while at greater doses, a central nervous system death is induced (14). There was a certain amount of inaccuracy in measuring the dose rate in the present experiments. It was estimated that this error was about 0.7 percent. Sitting in the restraining apparatus was an experimental variable not previously used in studies of behavioral radiology and conceivably could have had an effect on survival times. The monkeys were forced to sit in an upright position throughout the experiment and were subjected to an occasional electric shock. These shocks, the necessity of working to avoid shocks, and the actual restraints placed on the animal are all known to be effective stressors as indicated by reported elevations of the 17-hydroxycorticosteroids (5) and the production of gastrointestinal disorders (4).

It has recently been reported that monkeys injected with a neurotrophic virus, type I poliovirus, are protected from the debilitating effects of the virus if the injection follows a period of

psychological stress (11). The monkeys were stressed by placing them on a 24-hour avoidance regimen similar to that used in the experiments reported here. If poliovirus and radiation can be considered neurotrophic agents and if the stress produced by an avoidance schedule protects from the effects of poliovirus, then this form of stress may protect monkeys from radiation-induced CNS deaths.

In the experiments with 10,000 r the intervals between the last control period and the start of the experimental session varied from 62 to 228 hours. There was a perfect rank correlation between length of rest and survival time. That is, the "rested" animals lived longer than the less "rested" animals. Table I shows the actual values. Although this is in direct disagreement with the hypothesis that the stress associated with avoidance behavior may be radioprotective, it is suggestive of a stress-protection mechanism. Certainly more work is needed in this area.

Table I

Data Showing the Amount of Rest Prior to Irradiation and Survival Times

Animal Number	C-126[a]	C-140	C-546	X-541	X-418	X-955	X-545
Survival Time (hours)	40	58	78	89	123	170	181
Time between Last Control Period and Irradiation (hours)	62	98	120	210	216	225	228

[a]. The behavioral data for this animal were not reported because of an equipment failure.

It should be remembered that the behavioral test used in this experiment was under strong motivational control. Animals would continue or attempt to continue to respond even though very sick. The loss of motor control and the resulting inability to accurately direct responses towards the response lever occurred in all animals. However, the motivational properties of the resulting shocks were marked and probably even intensified as radiation illness progressed. A large amount of energy was expended vocalizing and "pawing" in the area of the response lever. Only during the terminal stages of the experiments did the shock lose its intense motivational property. Studies in other fields have shown that monkeys will continue to effectively press the response lever even during the initial stages of uremic coma (unpublished data, this laboratory). Uremia has little effect on motor abilities. It was felt that monkeys used in the experiments reported here would have responded for longer periods of time if their motor apparatus had not been so seriously debilitated. A less demanding response could be conditioned and would probably remain functional for a longer period of time. Of more interest,

however, would be the effects of massive doses of ionizing radiations on sensory and the so-called cognitive abilities.

One of the important conclusions to be drawn from the results of the present experiment is that for practical military purposes survival time, following a lethal exposure to ionizing radiations, will be less useful than behavioral indexes for future military planning. This is particularly true following doses below 20,000 r. At 10,000 r the difference between survival time and the time when the animal last performed within "normal" limits averaged about 70 hours. At higher doses this difference became progressively less, so that at 40,000 r there was a 6-hour difference. Doses of this order of magnitude resulted in marked behavioral disintegration within 30 minutes.

In conclusion, it seems safe to assume that: (1) Complicated or intricate motor manipulations will be severely attenuated by radiation. (2) The shock avoidance paradigm is a powerful motivator and probably should continue to be used in preference to other forms of motivation for animal experimentation in behavioral radiology. (3) The use of behavioral indexes will result in a more valid and pragmatic evaluation of the role of ionizing radiations in military and civil defense situations (7). (4) The techniques of long-term behavioral control and the quantitative nature of the recorded behavior are valuable new tools for behavioral radiology. (5) Much more work on the effects of massive and acute doses of ionizing radiation on behavior is necessary. (6) The radioprotective effects of psychological stress should be carefully explored.

References

1. Allen, R. G., Brown, F. A., Logie, L. C., Rovner, D. R., Wilson, S. G., and Zellmer, R. W.: Acute effects of gamma radiation in primates. School of Aviation Medicine, USAF, Report No. 59-41, 1959.

2. Blair, W. C.: The effects of cranial x-irradiation on maze acquisition in rats. J. comp. physiol. Psychol., 51: 175-177, 1958.

3. Blair, W. C., and Arnold, W. J.: The effects of cranial x-radiation on retention of maze learning in rats. J. comp. physiol. Psychol., 49: 525-528, 1956.

4. Brady, J. V., Porter, R. W., Conrad, D., and Mason, J. W.: Avoidance behavior and the development of gastroduodenal ulcers. J. exp. Anal. Behav., 1: 69-72, 1958.

5. Brady, J. V., Mason, J. W., Mangan, G., Conrad, D., and Rioch, D.: Concurrent plasma epinephrine, norepinephrine, and 17-hydroxycorticosteroid levels during conditioned emotional disturbances in monkeys. Psychosomat. Med., 23: 344-353, 1961.

6. Casey, A.: Incapacitation of the goat following massive doses of mixed neutron and gamma radiation. Quarterly progress report, Air Force Project 29 (601)-5211 (TAM RF Project 312), Brown, O. S., project coordinator, 1963.

7. Gerstner, H. B.: Military and civil defense aspects of the acute radiation syndrome in man. School of Aviation Medicine, USAF, Report No. 58-6, 1957.

8. Langham, W. H., Kaplan, S. J., Pickering, J. E., Lushbaugh, C.C., Haymaker, W., Storer, J. B., and Harris, P. S.: The effect of rapid massive doses of gamma radiation on the behavior of subhuman primates. Los Alamos Scientific Laboratory, Report LA 1558, 1952.

9. Langham, W. H., Rothermel, S. M., Woodward, K. T., Lushbaugh, C. C., Storer, J. B., and Harris, P. S.: Studies of the effect of massive, rapid doses of gamma rays on mammals. Los Alamos Scientific Laboratory, University of California, Report LA 1643, 1953.

10. Liddell, H. S.: The effect of thyroidectomy on some unconditioned responses of sheep and goat. Amer. J. Physiol., 75: 579-590, 1953.

11. Marsh, J. T., Lavender, J. F., Chang, S. S., and Rasmussen, A. F.: Poliomyelitis in monkeys: Decreased susceptibility after avoidance stress. Science, 140: 1414-1415, 1963.

12. Mason, J. W.: Restraining chair for the experimental study of primates. J. Appl. Physiol., 12: 130, 1958.

13. Riopelle, A. J., Grodsky, M. A., and Ades, H. W.: Learned performance of monkeys after single and repeated x-irradiations. J. comp. physiol. Psychol., 49: 521-524, 1956.

14. Pickering, J. E., Langham, W. H., and Rambach, W. A.: The effects from massive doses of high dose rate gamma radiation on monkeys. School of Aviation Medicine, USAF, Report No. 60-57, 1960.

15. Wilson, S. G.: Radiation-induced central nervous system death. School of Aviation Medicine, USAF, Report No. 59-58, 1959.

16. Zellmer, R. W., and Pickering, J. E.: Biological effects of nuclear radiation in primates. School of Aviation Medicine, USAF, Report No. 60-66, 1960.

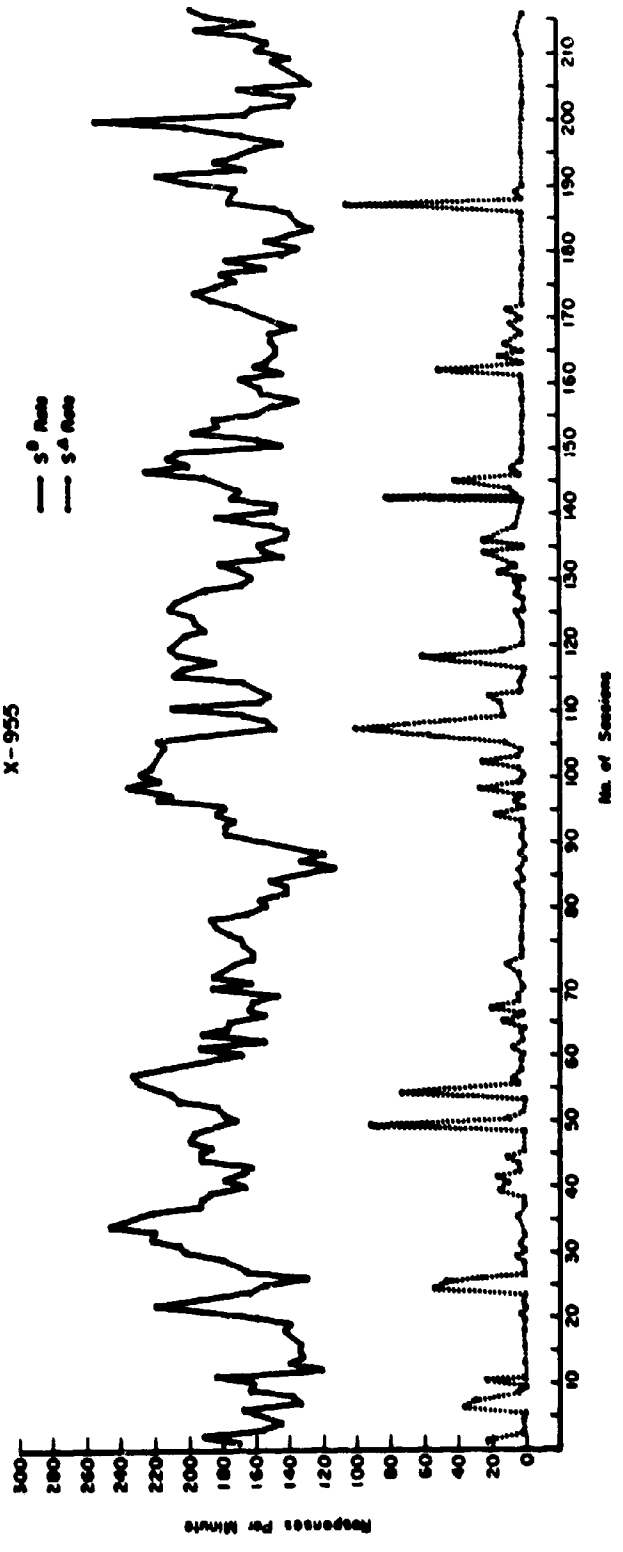

Fig. 1. A plot of control data for monkey #X-955. Note the response rate remains constant, even after 215 hours of avoiding, and that except for occasional bursts of responding during the S^{Δ} periods he makes effective use of rest periods.

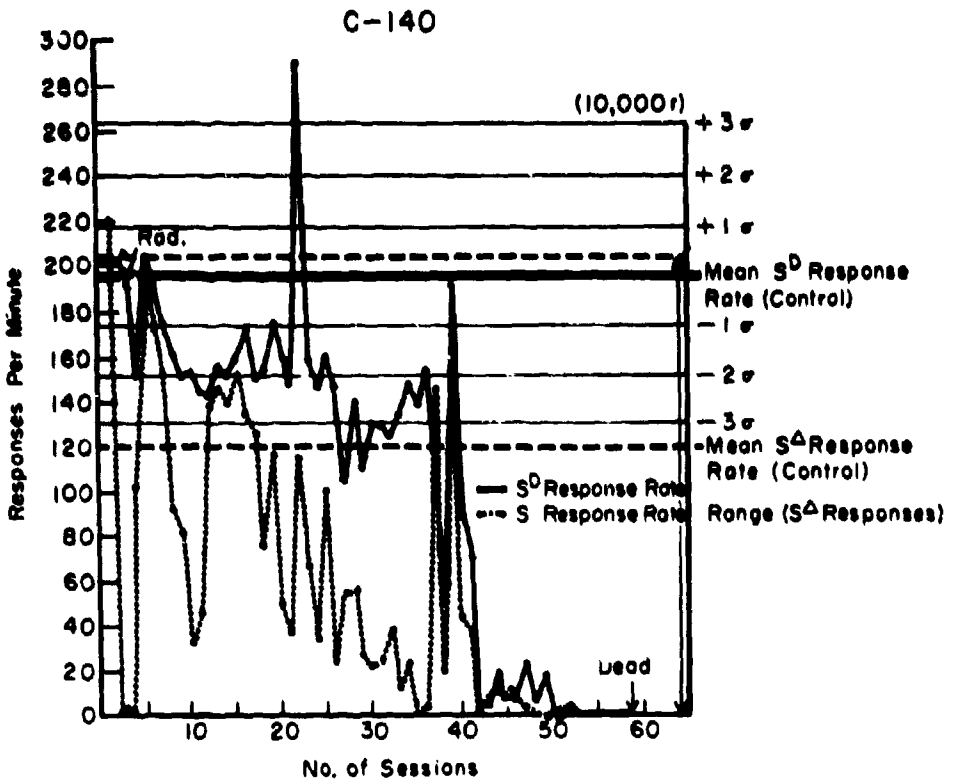

Fig. 2. A plot of the post-irradiation data for monkey # C-140. The mean control rates of responding with their standard deviations (σ) are plotted for comparisons. The complete range of responding during rest (S^{Δ}) periods is also indicated. Note radiation during third S^{D} session.

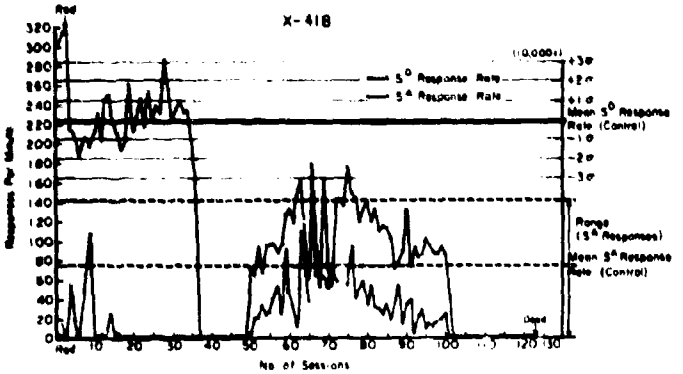

Fig. 3. A plot of the post-irradiation data for monkey #X-418. The data are plotted in the same manner and with the same comparisons to control periods as in Fig. 2. Note the return of a low response rate following a period of no responding for 10 hours.

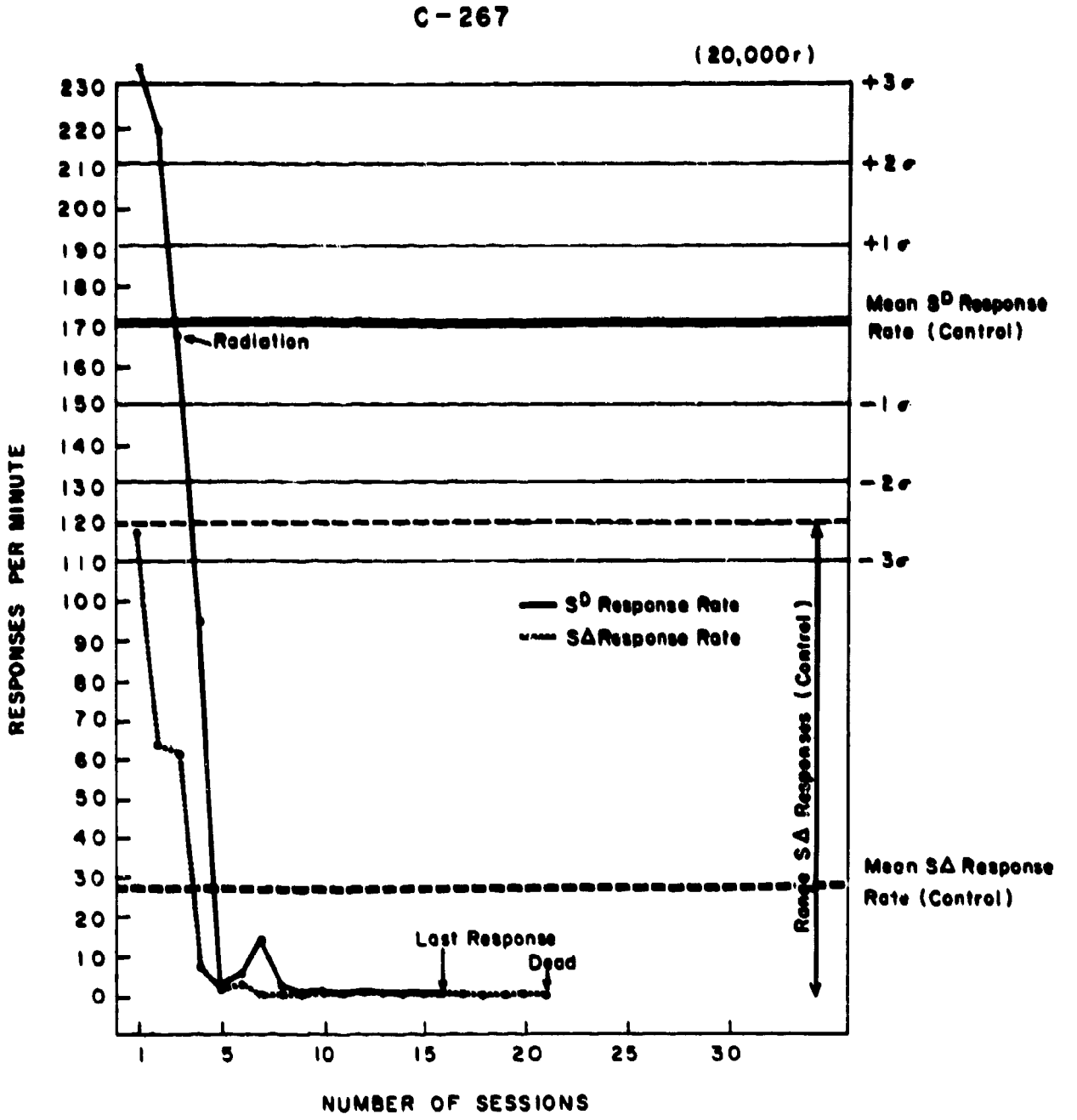

Fig. 4. A plot of the post-irradiation data for monkey #C-267. The data are plotted in the same manner and with the same comparisons to control periods as in Fig. 2.

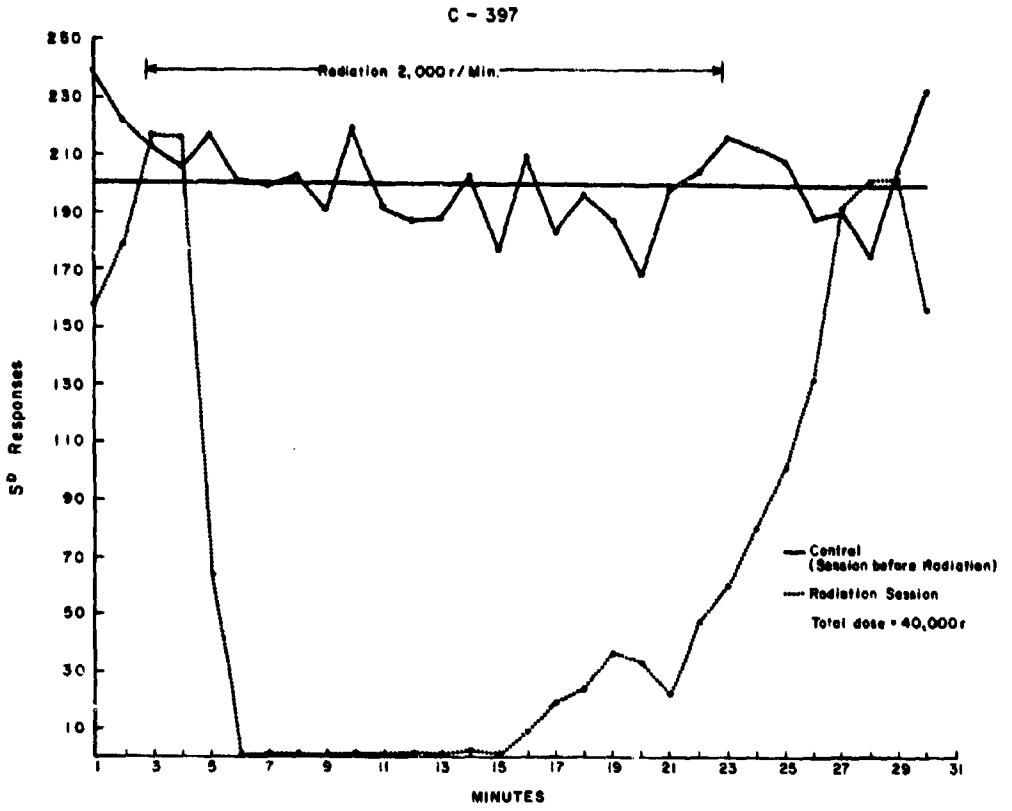

Fig. 5. A plot of the pre and irradiation S^D session of monkey # C-397. Each point represents the total S^D responses made during each minute of irradiation. For comparison, the data immediately prior to irradiation are given (the solid line) along with that session's mean. Note the complete cessation of responding during irradiation and the "recovery" of responding -- even while being irradiated.

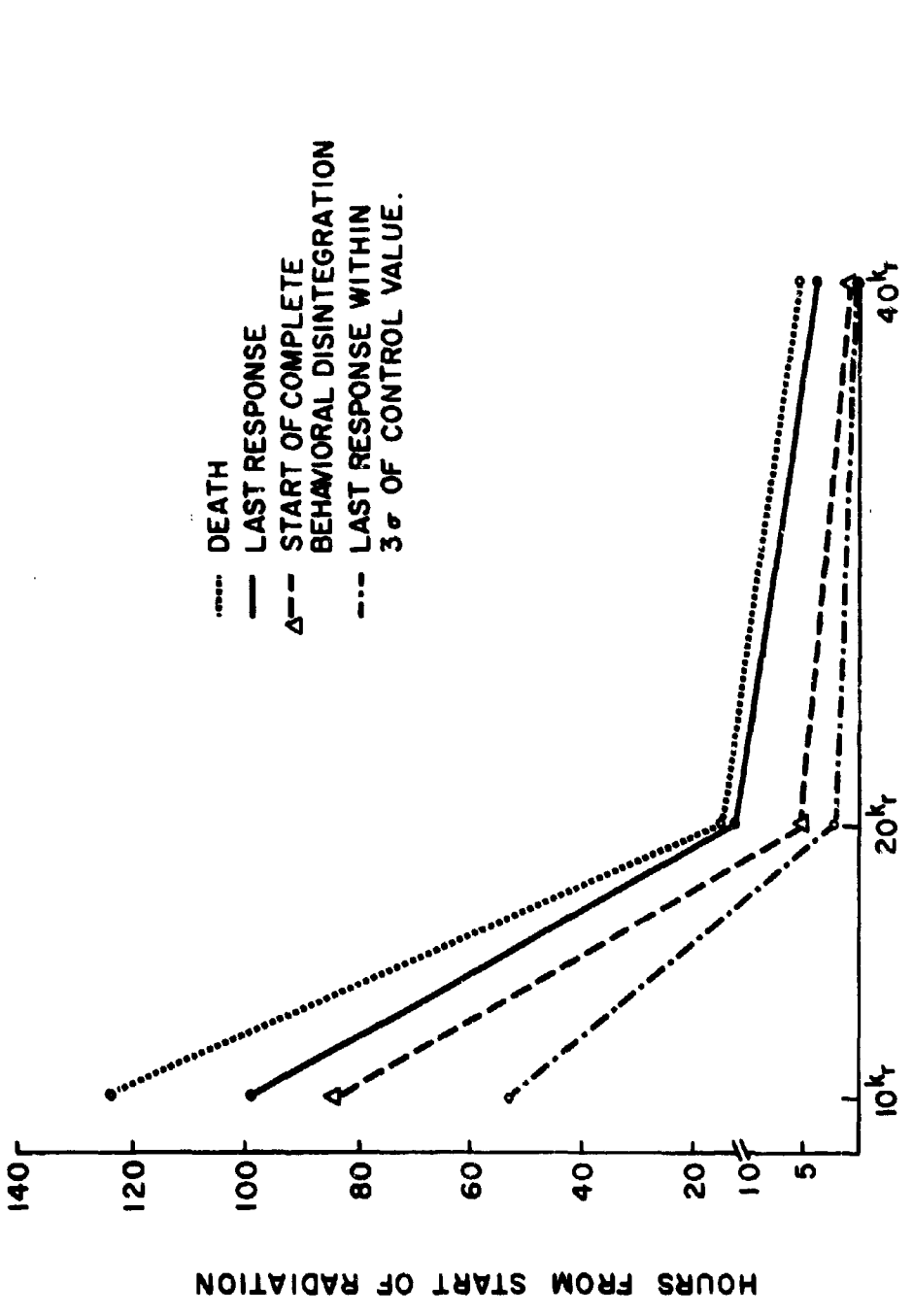

Fig. 6. A summary of the time-dose relationships between survival times and various behavioral indexes.

PREDICTED BLAST PROPERTIES OF PENTOLITE AND THEIR COMPARISON WITH EXPERIMENT

R. E. SHEAR
U. S. Army Ballistic Research Laboratories
Aberdeen Proving Ground, Maryland

INTRODUCTION: The prediction of the magnitude of several significant parameters of the blast wave generated by explosions at high altitudes (or at reduced ambient pressures) is a problem of current interest to the aircraft and missile designer, and to those engaged in the study of damage to such vehicles. Incident and reflected pressures, and their variation with distance from the explosive source, are readily calculated and useful in the prediction of damage caused by blast waves.

It has been demonstrated that the Brinkley-Kirkwood shock propagation theory[1] adequately predicts the variation of peak incident shock pressure with distance for TNT and Pentolite bursts under sea-level atmospheric conditions[2]. For example, Shear and Wright have shown that if the initial values required by this theory are obtained from appropriate detonation calculations, then the resulting pressure-distance relation is in excellent agreement with experimental observations. The thesis of the present report is to determine if a similar agreement is obtained for bursts in air at reduced pressures.

Initial shock pressures for Pentolite explosions in air at ambient pressures p_o of 1, 1/10 and 1/100 atmospheres are computed and used as initial values in the Brinkley-Kirkwood Theory to obtain peak pressure-distance curves. The reflected peak pressure for normal incidence can then be obtained as a function of distance from the charge center if one knows the incident shock pressure-distance relation and the equation of state for air. The reflected pressure-distance curves for Pentolite bursts in air at 1 and 1/100 atmospheres are presented and compared with available experimental measurements.

THE BRINKLEY-KIRKWOOD THEORY AND INITIAL VALUES: The Brinkley-Kirkwood shock propagation theory[1] is based on a similarity constraint imposed upon the energy-time curve of the shock flow. The use of this constraint and the Hugoniot

relations enabled Brinkley and Kirkwood to reduce the system of partial differential equations describing the flow process to a system of ordinary differential equations for the shock front pressure and energy as functions of distance from the charge. These equations are:

$$\frac{d(p/p_o)}{d(R/R_1)} = \frac{(p/p_o)}{(R/R_1)} \left[-1 + L - \frac{M(R/R_1)^2}{Q} \right], \quad (1)$$

$$\frac{dQ}{d(R/R_1)} = \frac{Q}{(R/R_1)} \left[-L + \frac{N(R/R_1)^2}{Q} \right], \quad (2)$$

where p/p_o is the incident excess peak pressure ratio and R/R_1 the distance in units of the charge radius R_1. Q is a reduced energy defined by

$$Q = \frac{49}{15} \frac{\rho_e q}{(R/R_1)\,(p/p_o)\,p_o}, \quad (3)$$

where ρ_e is the explosive density (1.65 g/cm^3) and q is the specific total energy in the flow field. The functions L, M and N (Equations 1 and 2) depend upon the shock Hugoniot relations and can be tabulated as functions of p/p_o, p_o and the ambient temperature T_o. In this work T_o shall be taken to be 300°K. For the range of ambient pressures considered here it suffices to use the polytropic gas relations in determining L, M and N. The use of the polytropic gas Hugoniot relations simplifies L, M and N and sample calculations indicate that the solutions of (1) and (2) are relatively insensitive to the change. With this simplification L, M and N become functions of p/p_o only.

Equations (1) and (2) are to be solved subject to the specification of the peak pressure ratio p_1/p_o and the specific energy of flow q_1 at the charge surface $R/R_1 = 1$. The determination of p_1/p_o and q_1 requires knowledge of the detonation state of the explosive, of the equation of state for the explosion products, of density, pressure and energy as functions of distance behind the detonation front, and of the isentropic expansion of the explosion products. These calculations have been performed for Pentolite[3] so that the initial conditions required for the integration of Equations (1) and (2) can be obtained readily if one assumes that the detonation process is independent of the ambient pressure p_o. With this assumption the detonation front values of pressure p_d, detonation velocity D, etc., remain unchanged and the distributions of pressure, density and energy behind the detonation front are invariant with respect to p_o. In particular, the specific total energy q_1 in the flow field at the time when the detonation front has

reached the surface of the charge is constant. For the present work this value is taken to be 47568 cm^3atm/g (1152 cal/g), as reported by Shear[3].

The remaining value to be determined is the initial shock pressure ratio p_1/p_o in air, i.e., p/p_o at $R/R_1 = 1$. The initial conditions at the time of formation of the shock wave resulting from the explosion of the spherical charge of Pentolite must be determined from the boundary conditions. One such condition is that the initial shock pressure in air must equal the pressure in the explosion products. This initial pressure is that which results from the equalization of pressure resulting from the outgoing compression wave and the ingoing rarefaction wave. In addition, the boundary conditions require the equalization, at the interface, of the particle velocity in air and in the explosion products. Furthermore, the pressure and particle velocity in air are related by the shock Hugoniot relations. These conditions determine the initial velocity and pressure at the boundary by the simultaneous solution of the Equations[4]:

$$u = u_d + \int_p^{p_d} \frac{dp}{\rho c} \qquad \text{(rarefaction condition for explosion products)}, \tag{4}$$

$$u = u\,(p,\ p_o,\ T_o) \qquad \text{(Hugoniot condition for air)}, \tag{5}$$

where p_d and u_d are respectively the pressure and flow velocity at the detonation front, and ρ and c are respectively the density and sound speed in the explosion products.

The integral in Equation (4) has been tabulated by Shear[3] for the explosion products of Pentolite. Equation (5) has been computed for air at different p_o from the data of Hilsenrath and Beckett[5]. The simultaneous solution of Equations (4) and (5) yield

$$\begin{aligned} p_1/p_o &= 669 \quad \text{for} \quad p_o = 1 \text{ atm}, \\ p_1/p_o &= 840 \quad \text{for} \quad p_o = 1/10 \text{ atm}, \\ p_1/p_o &= 1000 \quad \text{for} \quad p_o = 1/100 \text{ atm}. \end{aligned} \tag{6}$$

The initial excess pressures (6) and the value of the specific energy, $q_1 = 47568$ cm^3atm/g, at $R/R_1 = 1$ are the desired initial values. The initial values of Q can be determined from (3). These initial conditions have been used to solve Equations (1) and (2) for the incident shock pressure as a function of distance. The calculated pressure-distance curves corresponding to $p_o = 1$, 1/10 and

1/100 atmospheres are plotted on Figure 1. The experimental data of Dewey and Sperrazza[6] for p_o = 1/10 atm are also plotted on Figure 1, as well as some experimental data corresponding to p_o = 1 atm. The latter data was extracted from Goodman's compilation[7]. The agreement between the experimental data and the computed pressures is satisfactory.

Figure 2 shows plots of the peak pressure ratio vs. the reduced distance variable, $p_o^{1/3}(R/R_1)$. These curves indicate over what region Sach's method of scaling may be appropriate and the regions where scaling must be used with caution.

NORMALLY REFLECTED PRESSURE: The shock front reflected pressure can be computed easily if the incident shock strength and the equation of state for air, relative to some assumed ambient condition, are known. The calculation merely requires the solution of the well known shock relations -- with appropriate boundary conditions -- which govern the reflected shock wave.

Normally reflected pressure has been calculated as a function of the incident pressure for the case where the ambient conditions ahead of the incident wave are p_o = 1/100 atm and T_o = 300°k. Similar calculations for p_o = 1 atm and T_o = 300°K were reported by Shear and McCane[8]. The results of both calculations are plotted on Figure 3. It is to be noted that there is a marked difference between the two calculations, indicating the influence of ambient pressure p_o on the reflected pressure. These calculations of the reflected pressure ratio p_2/p_1 and the corresponding calculations of incident pressure vs. distance of Figure 1 are sufficient to give the reflected pressure-distance relation of Figure 4. The dashed lines of these plots represent extrapolations which are based upon some preliminary calculations and estimates obtained from Ziemer's[9] calculations.

The experimental measurements of the reflected pressure made by Olson and Wenig[10], Goldstein and Hoffman[11] and Jack[12] are also plotted on Figure 4. In general the agreement between pressures given by the curve and the corresponding experimental data is excellent. The only exception is that data points of Jack in the region between 7 and 12 charge radii appear to be too low in comparison with the curve.

Some measurements of reflected pressure for Pentolite blasts at reduced pressure are currently underway at these Laboratories but are of such a preliminary nature that they have not been included here.

Reflected pressures vs. distance for p_o = 1/10 atm were not computed since only the portion of the shock Hugoniot in the neighborhood of the initial shock pressure was computed. Estimates may be obtained, however, from Figures 3 and 4 and reference (9).

SUMMARY AND CONCLUSIONS: The calculation of the initial shock pressures, resulting from Pentolite explosions in air at 300°K and at ambient pressures p_o of 1, 1/10 and 1/100 atmospheres, provides one of the initial values required for the solution of the differential equations of the Brinkley-Kirkwood propagation theory. The other required initial value is the energy in the hydrodynamic flow field at the termination of the detonation state. These initial values have been obtained from the detonation calculations performed by Shear[3]. It has been found that the computed pressure-distance curves are in agreement with experimental observations. These derived pressure-distance curves and the reflected peak pressure computed as a function of incident shock pressure were used to obtain reflected peak pressure as a function of distance. The computed reflected pressures are in excellent agreement with the experimental data of references 10-12. These experimental measurements of reflected pressure resulting from a Pentolite blast are the only direct measurements of reflected pressure known to the author. Some blast experimentation at reduced pressures is currently underway at these laboratories but this work has not been reported -- thus no comparison can be made between predicted and measured values of the incident and reflected pressures for bursts at 1/100 atmospheres.

The good agreement between predicted and measured incident pressures (p_o = 1 and 1/10 atm) is encouraging. Similar calculations for different initial conditions and for different explosives should be made to determine if similar agreement exists and to determine the limits of applicability of these methods. If calculations similar to these and the detonation calculation of Shear[3] result in reliable estimates of incident and reflected pressure, then this procedure provides a quick and economical method of prediction. For example, the Brinkley-Kirkwood computation requires about 2 1/2 minutes (input to output time) on the BRLESC. In addition, calculations such as described here, if reliable, provide input data for the numerical solution of the hydrodynamical equations governing the blast field, and provide results which are useful for comparison.

REFERENCES:

1. (a) Brinkley, S. R., Jr. and Kirkwood, J. The Physical Review. Vol. 71, 1947, page 606.

   (b) Cole, R. H. Underwater Explosions. Princeton University Press, 1948.

   (c) Makino, R. Ballistic Research Laboratories Report No. 750, Aberdeen Proving Ground, Maryland, 1948.

2. Shear, R. E. and Wright, E. Q. Ballistic Research Laboratories Memorandum Report No. 1423, Aberdeen Proving Ground, Maryland, 1962.

3. Shear, R. E. Ballistic Research Laboratories Report No. 1159, Aberdeen Proving Ground, Maryland, 1961.

4. Doering, W. and Burkhardt, G. Contributions to Theory of Detonation. Wright-Patterson Air Force Base, Dayton, Ohio, 1949 (trans. Brown University).

5. Hilsenrath, J. and Beckett, C. W. TN 56-12, Arnold Engineering Development Center, Tennessee, 1956.

6. Dewey, J. and Sperrazza, J. Ballistic Research Laboratories Report No. 721, Aberdeen Proving Ground, Maryland, 1950.

7. Goodman, H. J. Ballistic Research Laboratories Report No. 1092, Aberdeen Proving Ground, Maryland, 1960.

8. Shear, R., and McCane, P. Ballistic Research Laboratories Memorandum Report No. 1273, Aberdeen Proving Ground, Maryland, 1960.

9. Ziemer, R. W. Space Technology Laboratory Report No. TR-60-0000-09093, Los Angeles, California, 1960.

10. Olson, W., and Wenig, J. Ballistic Research Laboratories Memorandum Report No. 1347, Aberdeen Proving Ground, Maryland, 1961.

11. Goldstein, H., and Hoffman, A. J. Ballistic Research Laboratories Technical Note No. 788, Aberdeen Proving Ground, Maryland, 1953.

12. Jack, W. H. Ballistic Research Laboratories Memorandum Report No. 1499, Aberdeen Proving Ground, Maryland, 1963.

FIG. 1 – PEAK EXCESS PRESSURE RATIO vs. DISTANCE IN CHARGE RADII

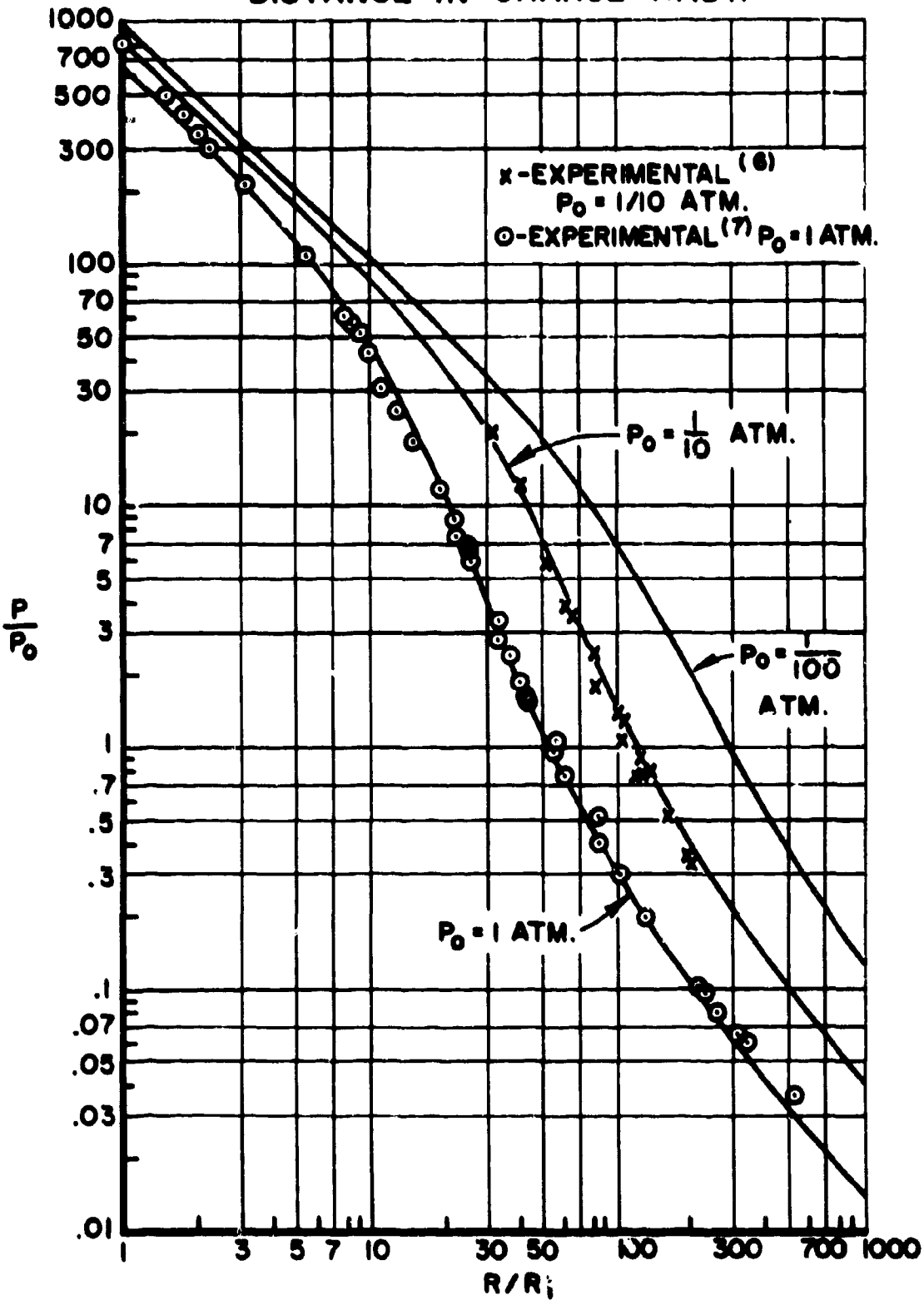

FIG. 2 – PEAK EXCESS PRESSURE RATIO vs. DISTANCE

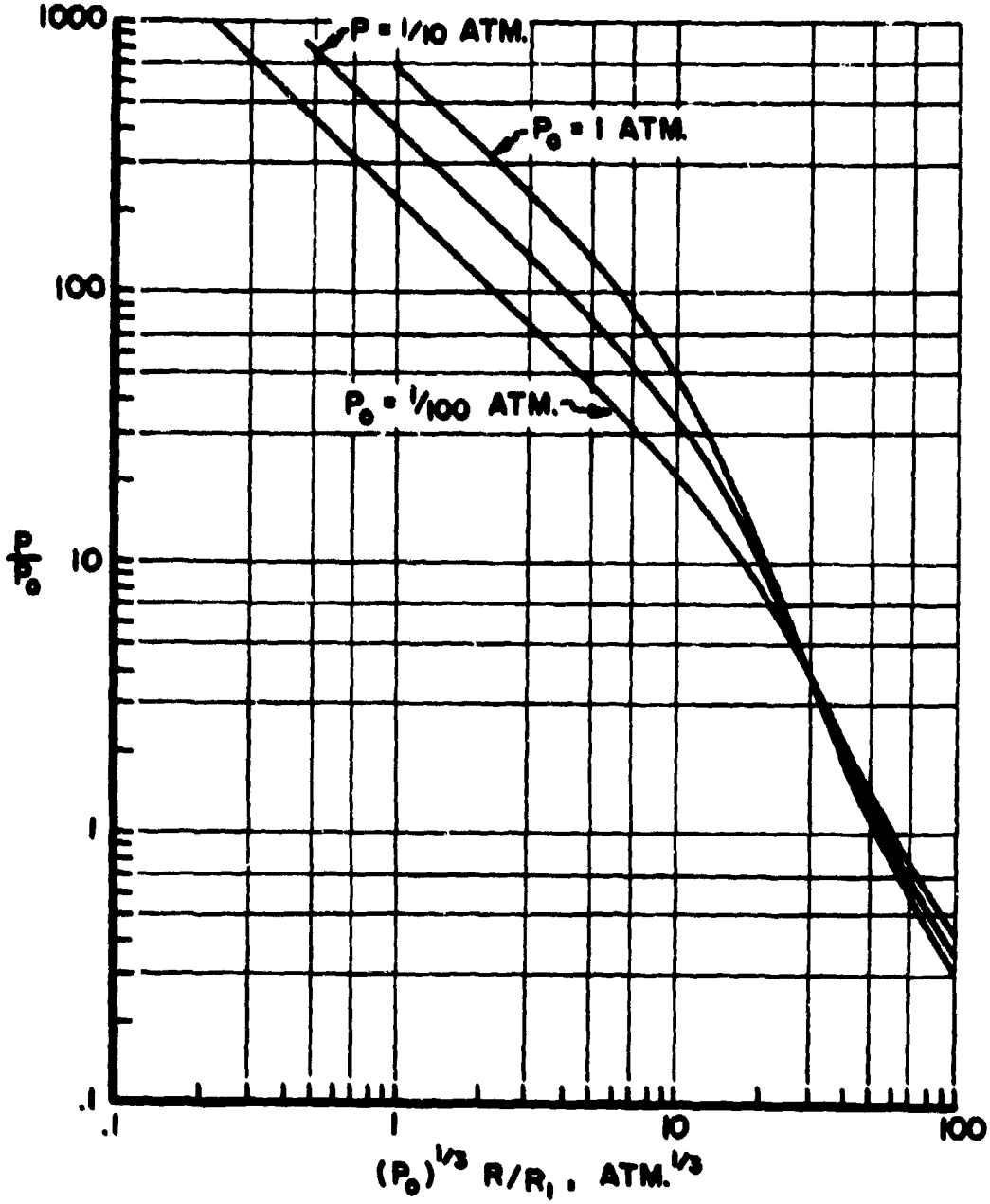

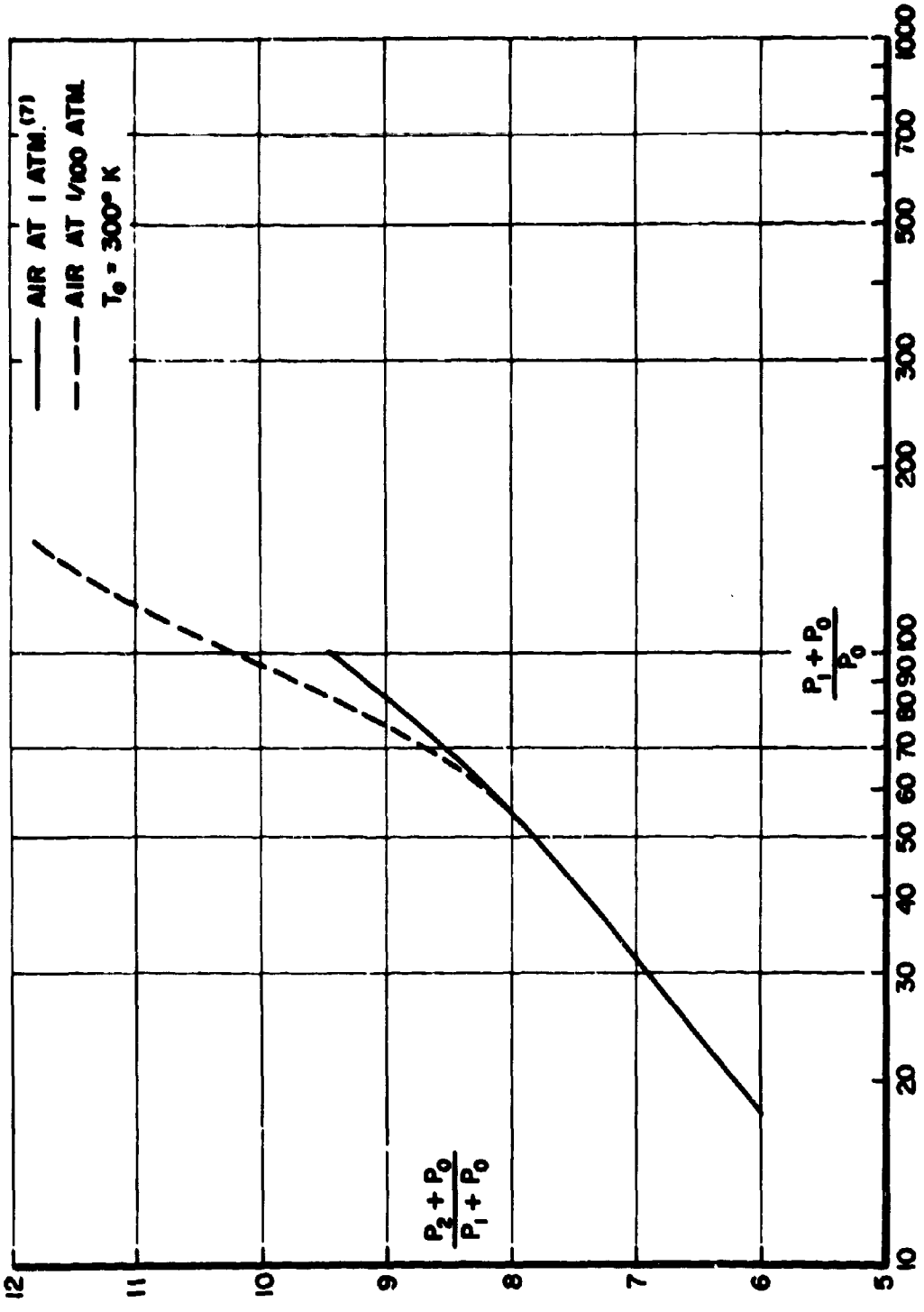

FIG. 3 — NORMAL REFLECTED PRESSURE VS. INCIDENT PRESSURE

FIG. 4 – REFLECTED EXCESS PRESSURE RATIO VS. DISTANCE IN CHARGE RADII

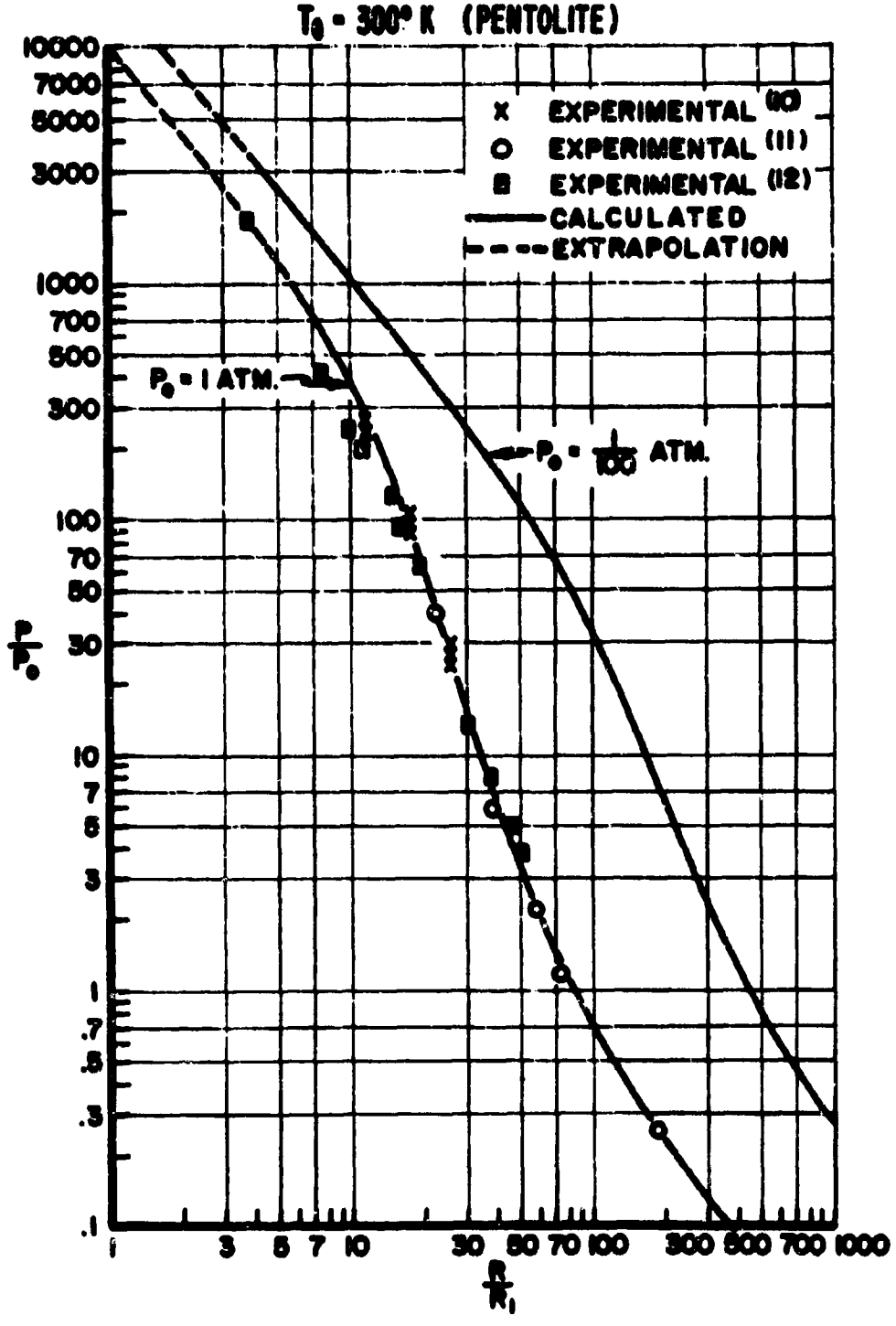

HOMOGRAFT REJECTION IN THE FETAL LAMB*

A. M. SILVERSTEIN
ARMED FORCES INSTITUTE OF PATHOLOGY
WASHINGTON, D. C. 20305

The elucidation of the fundamental nature of the immunologic response in man remains one of the important goals of both military and civilian medicine. Its importance extends into at least two areas of immediate and practical interest: the improvement of immunization technics to protect against infectious disease, and a solution of the problem of the immunologic rejection of homografts that would permit more extensive replacement of damaged skin or other organs from one individual to another. Advances in both of these areas will require new insights into the way in which the immunologic apparatus develops and the manner in which it functions.

One of the classic approaches to problems of this type that has furnished useful information in other fields of biology has been the study of the development of various structures and functions in the immature animal. Such ontogenetic studies may allow a clearer appreciation of the fundamental nature of a biologic process, since the relationships among developmental steps in the young animal are often easier to see. In the field of immunology, however, the ontogenetic approach has been very much neglected, and only recently has interest been awakened in the potentials of this approach (1, 2). The relative paucity of prior work on the development of immunologic competence, especially in the mammalian fetus, has required the preliminary development of a variety of surgical approaches to the fetus that would permit the study of the fetal response to immunization and grafting procedures.

---

*The investigations described in this report were performed in collaboration with Keith L. Kraner, Captain, USAF, VC, Chief, Veterinary Surgery Branch, Armed Forces Institute of Pathology.

The fetal lamb was chosen as the experimental animal for these investigations for several reasons. Its 5-month gestation period is long enough to permit a study of the response of the fetus to various immunologic procedures such as homografting over an extended period *in utero*. Its relatively large size, as compared with more conventional laboratory animals, permits greater ease of manipulation. In addition, the usually encountered twin pregnancies in sheep allow experimentation with one fetus, reserving the second twin as an extremely satisfactory internal control. Finally, and perhaps most significantly, the ovine placenta is such that there is no passage of gamma globulins from mother to fetus during gestation. Not only is the fetal lamb an agammaglobulinemic prior to birth, but one can be assured that any immune response observed in the fetus is of fetal and not maternal origin (3).

Earlier reports on the immunologic response of the fetal lamb have shown that this animal is capable of forming circulating antibodies *in utero* at a very early gestational age (3). This report will discuss the response of the fetal lamb to orthotopic skin homografts in terms of three principal areas: (a) the technical problems associated with extensive surgery of the fetus without interruption of pregnancy, and the solutions devised; (b) results of grafting of lambs *in utero* at different fetal ages and the events surrounding the development of their ability to reject skin homografts specifically; and (c) the very special characteristics of the fetal lamb model, which permits certain almost unique and critical experiments on the mechanism of homograft rejection, and the results of one such study.

THE SURGICAL PROBLEM

The literature contains relatively few reports of successful major surgical work on the mammalian fetus. Only one report exists on an attempt to study the fetal response to homografted skin in the mammal. This was the study of Schinkel and Ferguson (4), in which small pieces of skin were buried subcutaneously in the fetal lamb. These investigators encountered several serious difficulties in their approach, however. A number of these animals were aborted following surgery, losses of amniotic fluid resulted in difficulties in delivery of the young, and the buried skin graft proved not to be ideally suited for a satisfactory interpretation of results.

In order to study the complete range of responses of the fetal lamb to homografts, it was desirable to apply full- or split-thickness skin grafts orthotopically onto fetuses at various gestation ages. Since these grafts were to be fitted onto the fetal skin surface and sutured in place, a procedure was necessary that would permit the fetus to be removed completely from within the uterus and fetal membranes, retaining only the umbilical connection to the placenta. After the placement of several grafts, the fetus

would have to be returned to its original position, the fetal membranes and uterus closed, and the uterus returned to the maternal abdominal cavity, all without interrupting pregnancy.

As experience was gained with these approaches, a technic was finally developed to accomplish these goals that combined certain aspects of the procedure described by Schinkel and Ferguson (4), the surgical method described in our earlier immunization studies in the fetal lamb (3), and a number of other useful modifications in technique. The procedure will be described in greater detail elsewhere (5); only its principal features will be outlined here. Fluothane general anesthesia was used throughout the procedure, applied to the pregnant sheep via an endotracheal tube. The entire uterine horn was exteriorized through a midline abdominal incision, a window was incised in the uterine wall through which to work on the large fetuses, and the smaller fetuses (less than 15 to 20 cm in length) were brought completely out of the uterus. The allantois was included in the incision through the fetal membranes, since this appeared to improve the healing process. A large portion of the amniotic fluid was then removed, incubated with penicillin during work on the fetus, and replaced immediately prior to closure of the fetal membranes. Fitted skin grafts were sutured with fine silk, rather than the buried grafts favored by Schinkel and Ferguson. The fetal membranes were closed by drawing them together tightly with a silk suture, taking care not to leave tears through which amniotic fluid might be lost. The uterus and the abdomen were closed by normal procedures. The entire procedure was characterized by rigid observance of aseptic technique throughout. At an appropriate time after the original grafting procedure, the lamb was delivered by Caesarian section for histologic and serologic study.

So well did these procedures satisfy the requirements of the investigations that in 36 instances of major fetal graft surgery, only 1 fetus was aborted as a result of the surgical intervention. The fetuses appeared to tolerate the operation so well that it proved to be possible to repeat the surgical procedure more than once on the same fetus. This has led to the successful application of multiple grafts on a fetus, the ability to biopsy the graft, and even to regraft the animal at a later date, thus expanding appreciably the scope of these studies on fetal response to homografts.

(In order to indicate the extent to which surgical intervention in the fetus is possible, it is worthy of mention that in preliminary studies we have been able to perform total thymectomies upon fetal lambs at midgestation. Due to the anatomy of the fetal lamb, this has required the performance of radical neck surgery and in addition a thoracotomy with dissection of thymus in the mediastinum from the fetal pericardium and aorta. Not only did the fetuses survive so extensive a procedure as this, but it was also possible to perform additional surgery on these same animals later in gestation,

with the application of skin grafts and the immunization of these thymectomized animals in order to assess the effects of thymectomy on their development of immunologic competence. The results of these studies are, unfortunately, too incomplete to be included here. Mention is made of the technical success of these procedures, however, to call attention to the range of investigations possible in many fields, with such a fetal model).

FETAL RESPONSE TO HOMOGRAFTS

Three important questions may be asked about the fetal response to skin homografts applied in utero. They are (a) how early does the fetus develop the immunologic competence that permits it to reject the homograft specifically? (b) how does the fetal response compare with that of the mature adult? and (c) what morphologic and serologic changes accompany graft rejection in the fetus?

Graft Rejection and Fetal Age: Four fetuses between 64 and 67 days of gestation were grafted with fitted skin grafts from adult (split-thickness) and fetal (full-thickness) sources. The animals were delivered at intervals between 9 and 21 days after grafting, and the grafts and draining lymph nodes were examined. In no case was a clear-cut rejection process visible (Table I). The grafts had taken well and resembled autografts, even after remaining in place for 21 days. Only one graft (356-1, adult homograft) had a mild diffuse mononuclear infiltrate in the graft bed, which did not appear to involve interference with graft vitality. This could have resulted from the accidental introduction of exogenous contaminants with the graft. The draining lymph nodes at this early fetal age were found to be similar to those seen in ungrafted animals of the same age, again indicating that the fetuses had not responded in any significant manner to homografts applied at this stage of gestation.

A number of other fetal lambs were grafted between the 77th and the 139th day of gestation with a variety of fitted skin grafts from different sources. The grafts were examined between 7 and 15 days later, about half being checked on the 10th day (Table I). In all but one case, the autografts applied for control purposes had taken well and were undisturbed by any host reaction. In contrast, every homograft applied during this interval was found to be involved in an active and typical rejection process. Even the grafts examined at 7 or 8 days showed unequivocal evidence of rejection, indicating that the process had commenced at least 1 to 2 days earlier. By the 9th to the 14th day, the grafts were obviously at a very late stage of rejection. In all instances, the typical reaction in the draining lymph nodes confirmed the nature and stage of the rejection process.

Finally, newborn lambs were grafted by exchanging full-thickness skin among five animals on the day of birth. In each

instance, two grafts were applied on a recipient from the same donor, so that one could be taken at 7 and the other at 10 days. Examination of these tissues showed that the rejection process in the newborn lamb appeared to be no different from that occurring in the competent fetal animal. The grafts were accepted in a typical fashion, and at 7 days active rejection was evident. By the 10th day, each of the grafts was in the final stages of rejection, with vascular stasis and accompanying necrosis.

Morphology of Fetal Graft Rejection: The initial healing of grafts was similar morphologically to that described for other species (6). In those fetuses sacrificed early after implantation of the graft there was primary union between donor and host epithelial margins, regardless of the type of graft--whether of maternal, unrelated adult, or fresh or frozen fetal skin. In the case of adult tissue new hair growth was observed in a few instances. Cross section of the graft also demonstrated firm union and the establishment of vascular anastomoses between graft and recipient bed in these early cases. Histologic demonstration of this primary take was also expressed in the survival and hypertrophy of epithelium and in the presence within the graft of patent blood vessels containing formed elements. At this stage the homografts resembled autografts on animals of similar gestational age. In both instances, a few mononuclear and polymorphonuclear cells were noted in the graft bed. In maternal and unrelated adult grafts, hypertrophic follicular epithelium was also present.

The rejection of grafts, once begun, followed the pattern previously described for acute graft rejection (6). In all instances in which adult tissue was used, whether maternal or unrelated, rejection was preceded by grossly discernible edema of the graft, then hemorrhage, and later retraction of the graft bed. Vascular stasis and hemorrhage were readily apparent histologically within the graft and the adjacent graft bed. The mononuclear infiltrate was most prominent about small vessels in the graft bed and adjacent to disintegrating epithelium, especially at the junction of graft and host tissue. These cells ranged from small lymphocytes to larger mononuclear forms with indented nuclei and a more abundant cytoplasm. No evidence of formation of typical adult plasma cells was noted in the graft or graft bed, nor was pyroninophilia seen in the mononuclear cells. Varying degrees of polymorphonuclear infiltrate were present, most apparent in the later stages of rejection. Epithelial degeneration was marked at this time (after 7 days) in those animals on which the graft was placed on or after the 80th day of gestation. One curious feature, perhaps a result of the intrauterine milieu, was the apparent survival of a thin outer rim of epithelium in some cases in which the remainder of the graft had become completely nonviable. It may have been that the superficial cells of the graft, bathed in amniotic fluid, were able to retain some degree of viability even though the circulation had become completely stagnant.

Grafts of fresh and frozen fetal skin behaved in a similar fashion to adult grafts, except that epithelial proliferation about hair follicles was not so apparent. Examination of the frozen grafts early in the course of rejection showed a slough of the outer margin of epithelium, though follicular and basal layers were well preserved. It is probable that the preservation of this tissue was only partial and that the most peripheral layers of epithelium were not viable after transfer.

Protein Response Accompanying Graft Rejection: It appeared desirable to determine whether the lymphoid hyperplasia that accompanied homograft rejection in the fetal lamb was associated with the production of significant amounts of immunoglobulins. In an earlier paper (7) evidence was presented that the normal fetal lamb forms small amounts of β_{2M}-globulin but no typical 7S γ- or β_{2A}-globulins. The lymphoid response to antigenic and adjuvant injections was invariably accompanied by the formation of 7S γ- or β_{2M}-immunoglobulins, often in appreciable quantities.

Among the fetuses engaged in homograft rejection, no significant increase in circulating β_{2M}-globulin was found above normal levels. In no instance were either β_{2A}- or 7S γ-globulins detected in the sera of these animals. These data were confirmed by the absence of production of significant amounts of these proteins by the reactive lymph nodes grown in tissue culture in the presence of radioactive amino acids (8), and they accord well with the absence of immature and mature plasma cells in the nodes and graft beds.

THE MECHANISM OF HOMOGRAFT REJECTION

The ability to study the rejection of tissue homografts in the fetus furnishes a good example of the advantage of pursuing experimental immunology in this special fetal environment. Not only may valuable information be obtained on the ontogenesis of the immune response, but it may also be possible to clarify simultaneously some fundamental conceptual problems in immunology.

The nature of the immunologic mechanisms responsible for the rejection of orthotopic skin homografts has not yet been fully resolved (9). While most investigators favor the view that graft rejection involves the mechanism of delayed hypersensitivity mediated by sensitized mononuclear cells (10), the obligatory participation in this process of conventional circulating antibody has proved difficult to exclude (11).

The fetal lamb *in utero* furnishes an experimental model that may provide a suitable approach to this problem. Advantage can be taken of the ability of the fetal lamb *in utero* to reject skin grafts specifically (4, 8) and of the fact that in this unique environment the fetus is deficient or completely lacking in

immunoglobulins (7). This deficiency results from the limited production of these proteins by the fetus, and also from the inability of maternal antibodies to cross the ovine placenta.

It has already been indicated that the rejection of homografts by the lamb fetus is not accompanied by the formation of plasma cells, either in the graft or graft bed, or in the lymph nodes draining the site of the rejection process. These observations suggest that the formation of circulating antibodies may not be of critical importance in the process of homograft rejection. In order to test this suggestion more critically, four fetuses were grafted between the 120th and the 139th day of gestation. In addition to the grafts, however, each fetus received an intraperitoneal or intracardiac injection of 10 ml each of rabbit antisheep 7S γ-globulin and rabbit antisheep β_{2M}-globulin at the time of grafting. In addition, two fetuses were similarly grafted, but injected with 20 ml of normal rabbit serum as an experimental control. Ten days later the fetuses were delivered, bled, and autopsied.

The rationale behind this experiment was as follows: If the fetus could be shown to reject a skin homograft in the normal way in the presence of persisting rabbit antisheep globulins, then the conclusion would be almost inevitable that circulating antibody does not play an obligatory role in this process. Under these conditions, fetal antibody globulins, even if produced, should be unable to reach the graft site. If, on the other hand, graft rejection is inhibited or altered by the rabbit antisheep globulins, then circulating antigraft antibody must be implicated in the rejection process, according to a similar line of reasoning.

In every instance, the grafts were rejected in an apparently normal fashion. In addition, each fetus showed a persisting level of circulating rabbit γ-globulin at the end of the 10-day period. Of the animals that had received rabbit antisheep globulins, only one showed persistence of detectable antisheep 7S γ-globulin and antisheep β_{2M}-globulin activity in its serum by tanned cell hemagglutination assay. Although the titers were only moderate (1:8 in each case), satisfactory negative controls and standards render the data significant. It became apparent that at this point (10 days after injection) the rabbit antisheep globulins were being cleared rapidly from the fetal circulation, and that we were fortunate in finding persisting antiglobulin activity even in the one fetus.

It is highly probable, however, that during the earlier stages of graft rejection, circulating antisheep globulins were present in all four animals. In future experiments, more highly purified rabbit globulin preparations will be employed, and the animals will be delivered earlier than the 10th day after grafting.

DISCUSSION

The data presented in this paper confirm and extend the earlier observations of Schinkel and Ferguson (4) that the fetal lamb *in utero* is able to reject allogeneic skin grafts. Orthotopic skin homografts applied to fetal lambs about the 65th day of gestation were accepted and retained for up to 21 days without signs of the intervention of an active rejection process. In contrast, all grafts applied after the 77th day of gestation were accepted initially and then effectively rejected within 7 to 10 days. The rate of rejection and the histologic picture in the graft and its bed and in the reactive draining lymph node were similar to those described for specific homograft rejection in adults of other species.

In an earlier paper (3), it was made clear that the fetal lamb did not suddenly accede to full immunologic competence after an earlier "null" state. Rather, the fetus was observed to respond to antigenic stimuli in a stepwise fashion, related in some unknown manner to the nature of the antigen involved. Thus, there seems to exist a "hierarchy" of antigens. The response to some, such as bacteriophage ϕX and ferritin, occurs at an early stage of gestation long before the fetus manifests any response to other antigens such as ovalbumin. Antigens such as diphtheria toxoid and *Salmonella typhosa* were not observed to elicit a fetal response at any time during gestation. Antibody formation to these substances did not appear until many weeks after birth. In this respect, ovine histocompatibility antigens appeared to occupy an intermediate position in the antigenic hierarchy. It is thus apparent that no special case can be made in ovine ontogeny between the homograft reaction as one form of immunologic response and antibody formation as another.

The absence of homograft rejection in those animals grafted at about 65 days' gestation raises a problem similar to that posed by the antibody response of the fetal lamb. Does the inability to form antibody to a given antigen or to reject the skin graft prior to some critical time reflect the induction of tolerance to these antigens? Or is it possible that the immature animal is merely immunologically incompetent to respond to the antigen and, in fact, does not "recognize" it in an immunologic sense? The retention of a graft in position for 21 days on fetus 304-1 (sacrificed on the 88th day) is certainly significant, for at the same gestation age fetus 305-2 was already rejecting a graft applied 11 days previously. This result could reflect either immunologic tolerance of the graft on the part of this animal or decreased susceptibility to rejection of a graft that has been well accepted and retained for a period of time (12).

While the fetal lamb is able to form antibody in response to certain antigens, as has been shown earlier (3), there is little question that in most instances this initial intrauterine response

is somewhat less efficient than that of the adult. It is therefore surprising that once the fetus develops the ability to reject homografts, it does so with the rapidity and apparent competence of the adult, furnishing the full range of cellular events, graft invasion, and breakdown within 7 to 10 days of application. In this respect, the acquisition of competence by the fetus appears to be complete despite its relatively abrupt appearance. This was true regardless of whether the graft came from an unrelated fetus or adult, or from its own mother.

A final point may be raised relative to the mechanism of homograft rejection and its possible dependence on circulating antibody (13). In other species, the appearance of plasma cells in the reactive draining lymph node and in the graft bed itself has been cited in support of the notion that circulating antibody is produced during and ultimately participates in the rejection process. The fetal lamb offers a unique opportunity to study this question, since the ovine fetus is to all intents and purposes an immunologic virgin with extremely immature lymphoid tissue and little or no immunoglobulins in its circulation.

It is therefore of special significance that when care was taken to transplant sterile skin from a fetal donor, no plasma cells could be found in either the draining nodes or the graft bed at any time prior to, during, or after rejection. Neither could any increase in circulating immunoglobulins be observed in these fetuses, a fact confirmed by tissue culture experiments performed on various organs. The suggestion that the homograft reaction is a cellular form of response is further borne out by the preliminary results, which indicate that the fetal lamb is able to reject a homograft in a normal fashion despite the presence of excess rabbit antisheep β_{2M}- and 7S γ-globulins in its circulation at the time of rejection. All of these data point to the possibility that conventional circulating antibodies do not play an <u>obligatory</u> role in the rejection of solid-tissue homografts.

SUMMARY

Procedures have been developed that permit orthotopic skin grafting of the fetal lamb <u>in utero</u> without the interruption of pregnancy. The fetus was found to reject orthotopic skin homografts applied at any time after the 77th day of gestation. Prior to this gestational age, grafts remained in place without stimulating any detectable immunologic response. Once the fetus achieves the ability to reject the graft, the process occurs with the same competence and rapidity as in the adult. Graft rejection in the fetal lamb is unaccompanied by formation of plasma cells or by the production of typical immunoglobulins, thus supporting the suggestion that circulating antibody does not play an obligatory role in the process.

BIBLIOGRAPHY

1. Miller, J. F. A. P., and Davis, A. J. S., Ann. Rev. Med., 15, 000, 1964.

2. Silverstein, A. M., Science (in press).

3. Silverstein, A. M., Uhr, J. S. Kraner, K. L., and Lukes, R. J., J. Exp. Med., 117, 799, 1963.

4. Schinkel, P. G., and Ferguson, K. A., Aust. J. Exp. Biol. Med. Sci., 6, 533, 1953.

5. Kraner, K. L., and Silverstein, A. M. (in preparation).

6. Medawar, P. B., J. Anat., 78, 176, 1944.

7. Silverstein, A. M. Thorbecke, G. J., Kraner, K. L., and Lukes, R. J., J. Immunol., 91, 384, 1963.

8. Silverstein, A. M., Prendergast, R. A., and Kraner, K. L. (in press).

9. Hasek, M., Lengerova, A., and Hraba, J., Adv. Immunol., 1, 1, 1961.

10. Medawar, P. B., in "Cellular and Humoral Aspects of Hypersensitivity States," H. S. Lawrence, Ed., Hoeber-Harper, New York, 1959.

11. Stetson, C. A., in "Mechanisms of Hypersensitivity," J. H. Shaffer, G. A. Lo Grippo, and M. W. Chase, Eds., Little Brown, Boston, 1959.

12. Woodruff, M. F. A., in "Biological Problems of Grafting," F. Albert and P. B. Medawar, Eds., Blackwell, Oxford, 1959.

13. Converse, J. M., and Rogers, B. L., Eds, "Fifth Tissue Homotransplantation Conference," Ann. N. Y. Acad. Sci., 99, 335, 1962.

TABLE I

Response to Orthotopic Skin Homografts in Fetal and Newborn Lambs

Lamb No.	Gestation age at grafting (days)	Interval before graft removal (days)	Source of graft	Stage of rejection	Remarks
356-1	64	9	Frozen fetal Adult	No rejection Very early (?)	
357-1	65	14	Frozen fetal Adult	No rejection No rejection	
312-1	65	15	Maternal	No rejection	
304-1	67	21	Frozen fetal Adult	No rejection No rejection	
305-2	77	11	Frozen fetal	Late rejection	
343-1	82	12	Maternal Autograft	Late No rejection	
350-1	82	15	Frozen fetal Autograft	Late No rejection	
344-1	97	9	Maternal Autograft	Late No rejection	
323-1	122	14	Fresh fetal	Very late	
34,-1	120	10	Fresh fetal	Late	Rabbit antiglobulins*
342-1	122	10	Fresh fetal	Late	Rabbit antiglobulins
332-1	122	10	Fresh fetal	Middle	Normal rabbit serum

TABLE I cont'd.

319-1	125	10	Newborn lamb Autograft	Late No rejection	Rabbit antiglobulins
355-1	125	10	Fresh fetal	Middle	Normal rabbit serum
311-2	130	8	Fresh fetal	Late	Rabbit antiglobulins
307-1	136	7	Fresh fetal	Late	
309-2	139	10	Fresh fetal	Very late	
359-1	Birth#	7 12	Newborn Newborn	Middle Late	
359-2	Birth	7	Newborn Newborn	Middle-late Late	
345-1	Birth	7 10	Newborn Newborn	Middle-late Late	
345-2	Birth	7 10	Newborn Newborn	Middle-late Late	
341-1	Birth	10	Newborn	Middle-late	

* After grafting, lambs were injected with 20 ml of whole rabbit antisheep B_{2m}- and γ-globulins, or with 20 ml of normal rabbit serum.

Gestation period in sheep is about 150 days.

BIAXIAL TENSILE BEHAVIOR OF ANISOTROPIC TITANIUM SHEET MATERIALS

JOSEPH L. SLINEY
U. S. ARMY MATERIALS RESEARCH AGENCY
WATERTOWN, MASSACHUSETTS

INTRODUCTION

The mechanical behavior of high strength sheet materials has been under extensive study and evaluation for several years, since high strength to density ratios are needed for use in high speed aircraft and missile systems. A major problem in this area is fracture toughness[1] since this property has limited the usable strength level in high strength sheet materials.

Polycrystalline structural materials are usually assumed to be isotropic; however, they may be anisotropic with respect to many types of behavior, such as thermal conductivity, electrical resistivity, coefficient of expansion, fracture toughness, and plastic deformations. A great deal of anisotropy of directionality in ordinary ferrous or nonferrous strip products is due to elongated inclusions and phase distributions. In comparison to this type of anisotropy, there is also mechanical anisotropy which arises from preferred crystallographic textures which influence the yielding and plastic deformation properties of certain materials. This paper will deal with the influence of a biaxial stress field on the biaxial tensile strength of certain anisotropic titanium alloy sheet materials and the advantages to be gained through the use of mechanical anisotropy. A review of a recently proposed anisotropic yield criterion[2,3] is presented with experimental data on two commercially produced titanium-base alloy sheet materials.

ISOTROPIC YIELDING CRITERIA

Two of the most widely used yielding criteria for isotropic materials under conditions of combined stresses are those of Tresca and Von Mises.[4] Tresca's yield criterion is:

$$(\sigma_x-\sigma_z)^2 + 4\tau_{xz}^2 = Y^2 \qquad (1)$$

or if we consider only principal stresses:

$$\sigma_1 = \sigma_3 = Y \qquad (2)$$

where $\sigma_1 \geq \sigma_2 \geq \sigma_3$ and Y is the uniaxial yield strength.

The Von Mises yield criterion is

$$(\sigma_x-\sigma_y)^2 + (\sigma_y-\sigma_z)^2 + (\sigma_z-\sigma_x)^2 + 6\tau_{yz}^2 + 6\tau_{zx}^2 + 6\tau_{xy}^2 = 2Y^2 \qquad (3)$$

or if we consider only principal stresses as in Equation 2

$$(\sigma_1-\sigma_2)^2 + (\sigma_2-\sigma_3)^2 + (\sigma_3-\sigma_1)^2 = 2Y^2. \qquad (4)$$

A comparison between the plane stress ($\sigma_3 = 0$) yield locus of the Tresca and the Von Mises yield criteria is presented in Figure 1. The maximum difference between these two criteria occurs under a two-to-one biaxial tensile or compressive stress state. A 15% yield strength increase is predicted by Von Mises' yield criterion under these conditions, and experimental data has indicated excellent agreement[5] for ductile materials. Inherent in these two failure criteria is isotropy, i.e., identical mechanical properties in all directions.

ANISOTROPIC YIELDING CRITERIA

Hill[5] has modified Equation 3 for anisotropic materials by introducing anisotropy parameters. Backofen, Hosford and Burke[2,3] have applied Hill's equation for plane stress loading which is of particular interest for long, thin-wall pressure vessels. For the particular case for material having rotational symmetry (i.e., $X_o = Y_o \neq Z_o$ where X_o, Y_o, and Z_o are the uniaxial yield strengths in the longitudinal, transverse, and thickness directions which are considered to be the principal planes of anisotropy), the yield equation is given by:[2]

$$\sigma_x^2 + \sigma_y^2 = \sigma_x \sigma_y \left[\frac{2R}{1+R}\right] = X_o^2. \qquad (5)$$

This yield equation relates the conventional uniaxial yield strength (X_o), the anisotropy parameter R*, and the principal stresses. For the case of a long, thin-wall, closed-end pressure vessel: ($\sigma_x = 2\sigma_y$) the maximum principal stress for yielding is

$$\sigma_x = X_o\sqrt{\frac{4(1+R)}{5+R}}. \qquad (6)$$

---

*$R = \frac{d\epsilon_w}{d\epsilon_t}$. This is the ratio of the rate of change of the width-to-thickness plastic strains.

Larson and Nunes[6] have measured R values greater than 7.0 for Ti-4Al-3Mo-1V alloy sheet. Substituting R=7 into Equation 6 yields $\sigma_x = 1.63\ X_o$. This means that the maximum principal stress needed for yielding (under a 2:1 biaxial stress field) is 63% greater than the uniaxial yield strength. Also, if R=1 (isotropic material), $\sigma_x = 1.15\ X_o$, which is the same result as that predicted by the Von Mises yield criterion.

Improvements in strength similar to that predicted by Equation 5 for a two-to-one biaxial tensile ratio are also predicted for other biaxial tensile stress conditions. The plane stress biaxial yield loci for R values between 0 and 5 are presented in Figure 2. Maximum texture hardening[7] in a biaxial stress field occurs under plane strain loading conditions. The biaxial stress ratio for plane strain loading is related to R by the following equation:

$$\frac{\sigma_x}{\sigma_y} = 1 + \frac{1}{R} . \qquad (7)$$

Substituting Equation 7 into Equation 5, the relationship between the maximum principal stress, the uniaxial yield strength, and the anisotropy parameter R is obtained for maximum strengthening:

$$\frac{\sigma_x}{X_o} = \frac{R+1}{\sqrt{2R+1}} . \qquad (8)$$

An equation similar to Equation 5 may be derived for sheet materials which exhibit nonrotational symmetry ($X_o \neq Y_o \neq Z_o$):

$$\sigma_x^2 + \frac{(P+1)R}{(1+R)P}\,\sigma_y^2 - \frac{2R}{1+R}\,\sigma_x\,\sigma_y = X_o^2 . \qquad (9)$$

This equation relates the uniaxial yield strength X_o, the anisotropy parameters P and R (measured 90° apart), and the principal biaxial stresses. However, for the experimental work described in this paper, the material will be considered to have rotational symmetry (P=R). (While this is not exactly the case, it may be a reasonable approximation).

REVIEW OF CRYSTALLOGRAPHIC TEXTURES

The mechanical anisotropy in polycrystalline aggregates of the body-centered cubic (bcc) or the face-centered cubic (fcc) systems is minimized by the high degree of symmetry in the crystallographic structure. Most of the present candidate solid propellant motor casing materials are of these crystallographic types. However, alpha titanium base alloys have a hexagonal close-packed (hcp) crystal structure. X-ray diffraction studies[8] indicate that upon cold-rolling and a low temperature anneal (800 to 1000 F) textures of the type (0001) [10$\bar{1}$0] are obtained in alpha titanium sheet materials. Hosford and Backofen[3] have described these textures as the ideal case for maximum anisotropy.

This ideal texture is shown schematically in Figure 3. The most common slip systems for titanium are basal plane-slip (0001), pyramidal $\{10\bar{1}1\}$, or prismatic $\{10\bar{1}0\}$, which occur in the densely packed directions $\langle 1\bar{2}10\rangle$. Consideration of these flow mechanisms for a material having a perfect (0001) texture indicate that a tensile test in the plane of the sheet will deform by thinning in the width direction but not in the thickness direction. If a biaxial stress is applied in the plane of the sheet, then flow must occur on other slip planes and directions. If this is the case, then very high biaxial yield strengths will result as indicated by the theory.

Titanium processing textures[8,9,10] for alpha alloys are not far from the ideal case, except that the basal plane is inclined toward the transverse direction. If the basal plane is rocked 90° to the transverse direction, then texture softening will result. That is, the material will have an R value less than one, and yielding will occur as indicated in Figure 2. Of course, the actual behavior of alpha titanium sheet is not as simple as implied here, since other slip and twinning systems may be operative. However, it is apparent that commercial titanium sheet which has a hexagonal close-packed crystal structure may have a built-in resistance to thinning and thus offer biaxial strength improvements.

MATERIALS

One sheet of Ti-5Al-2.5Sn alloy and one sheet of Ti-4Al-4Mn alloy were employed in this study. The Ti-5Al-2.5Sn is an all-alpha alloy and the Ti-4Al-4Mn is an alpha-beta alloy. The sheet thicknesses and chemistry are listed in Table I.

TABLE I

Chemical Analysis

Alloy	Thickness (inches)	ELEMENTS (weight %)							
		C	Al	Sn	Fe	N	O	H	Mn
Ti-5Al-2.5Sn	0.112	0.021	5.64	2.30	0.18	0.024	0.11	0.007	-
Ti-4Al-4Mn	0.070	0.046	4.25	-	0.19	-	-	-	3.49

EXPERIMENTAL PROCEDURE

Test Specimens

A biaxial tensile specimen of the type which was developed previously by Corrigan[11] for isotropic materials was used for experimental verification of the proposed yielding criteria for texture-hardened materials. This specimen, Figure 4, has a simple machined transverse slot and uses the restraint of a large elastic bulk to produce a condition of plane strain ($\epsilon_y = 0$). In isotropic materials,

this specimen produces a two-to-one tensile stress after a plastic strain of approximately one percent. In anisotropic materials considered to have rotational symmetry, the biaxial tensile ratio is the same as Equation 7. The degree of biaxiality in this specimen is governed by the degree of anisotropy. Pin-loaded biaxial tensile specimens were used for the low temperature tests. This modification to the biaxial tensile specimen is presented in Figure 5. In addition, uniaxial and edge-notched sheet tensile tests were conducted, specimens for which are presented in Figure 6.

Testing Procedures

Conventional wedge-type grips were employed for the room temperature biaxial tensile tests, and pin-loading grips were employed for the uniaxial tensile, edge-notched tensile, and the low temperature biaxial tensile tests. There is an order of magnitude of difference in the gage lengths of the uniaxial and biaxial tensile specimens. Therefore, if the same head speed is used for testing these specimens, the same difference would exist in the strain rate. In order to minimize the strain rate effect, head speeds of 0.05 inch per minute and 0.005 inch per minute were used on the uniaxial and biaxial test specimens respectively.

Rosette foil gages (FABX 12-12) were used to measure the width strain (ϵ_w) and the longitudinal strain (ϵ_ℓ) which were plotted continuously on a Moseley X-Y recorder. In addition to the strain gage measurements, a deflectometer was used to obtain a load deflection curve for yield determination. The anisotropy parameter (R) for each tensile specimen was calculated by assuming constant volume after yielding in order to determine the plastic thickness strain ($\epsilon_\ell + \epsilon_t + \epsilon_w = 0$). A typical recording of the longitudinal and width strains with sample calculations is presented in Figure 7. These calculations are for material with no strain hardening as indicated by the load-deflection curve. If the load increases during plastic deformation, the elastic strain increase during plastic deformation must be considered in the calculations.[12]

Sheet Test Program

The bulk of the mechanical tests were conducted on the Ti-5Al-2.5Sn alloy. The yield strength at 0.2%, tensile strength, anisotropy parameter (R) and the biaxial tensile strength (specimen presented in Figure 4) were determined at 15° intervals in an arc of 165° from the longitudinal direction. Additional longitudinal mechanical tests were conducted over a temperature range of room temperature to -312 F. These tests consisted of tensile, edge-notched tensile, and pin-loaded biaxial tensile (Figure 5) tests.

Limited tensile and biaxial tensile tests were conducted on the Ti-4Al-4Mn (RS130B) alloy. The yield strength at 0.2%, tensile strength, anisotropy parameter (R) and the biaxial tensile strength

were measured in both the longitudinal and transverse directions on this sheet in the annealed condition. These same parameters were determined on this material in the longitudinal direction in the solution-treated and aged condition (1450 F 2 hr, WQ + 900 F 24 hr, AC).

Pressure Vessel Tests

Two closed-end cylindrical pressure vessels were fabricated from the Ti-5Al-2.5Sn alloy. The longitudinal direction of the sheet was oriented in the transverse direction of the cylinders. Longitudinal MIG welds were employed, and thickened ogive end closures, forged from Ti-6Al-4V alloy billets, were welded on each end. Cylinder 1 was welded with an unalloyed filler wire, and Cylinder 2 was welded with a Ti-6Al-4V alloy filler wire. Longitudinal and transverse strain measurements were recorded using Type PA7 strain gages, 90° from the longitudinal weld and at the mid-length of the cylinders. Both vessels were hydrostatically tested to failure by pressurizing at a uniform rate. A pressure time and strain time history was obtained for each cylinder with a Visicorder.

RESULTS AND DISCUSSION

Mechanical Tests

The mechanical test data, 0.2% yield, tensile, biaxial tensile strength, and the anisotropy parameters R which were obtained from the various orientations on the Ti-5Al-2.5Sn alloy, are presented in Table II. No significant variation of yield and tensile strengths was obtained with specimen orientation.

TABLE II

Tensile and Biaxial Tensile Properties of Ti-5Al-2.5Sn Alloy

Test Direction (degrees from rolling direction)	Yield Strength, 0.2% (ksi)	Tensile Strength (ksi)	Biaxial Tensile Strength (ksi)	$\frac{BTS}{TS}$	R	$\frac{\sigma_x}{X_o} = \frac{R+1}{\sqrt{2R+1}}$
0 Longitudinal	123.0 123.0 124.0	128.4 125.4 126.9	201.8	1.59	3.36 3.10 2.86	1.56 1.53 1.50
15	122.0	125.0	203.3	1.62	2.86	1.48
30	121.0	124.0	209.5	1.69	3.25	1.55
45	123.0	120.9	204.1	1.69	3.17	1.54
60	121.0	123.2	186.2	1.51	4.25	1.70
75	119.0	121.5	206.7	1.70	3.36	1.56
90 Transverse	125.0 126.0 124.0	129.8 131.2 131.1	208.4	1.60	2.57 2.57 2.78	1.44 1.44 1.46
105	125.0	127.6	206.2	1.61	2.85	1.48
120	124.0	127.4	149.5	1.17	3.46	1.58
135	124.0	126.3	205.4	1.63	3.17	1.54
150	123.0	125.8	205.7	1.63	3.40	1.58
165	122.0	127.0	161.9	1.27	3.54	1.60

The theoretical biaxial tensile strength ratios have been calculated using Equation 8 for the measured R values, and these data are also presented in Table II. In order to compare the biaxial tensile strength to ultimate tensile strength (BTS/UTS) ratios determined by tests with the theoretical σ_x/X_o ratios calculated from the anisotropy parameters, it is necessary to extrapolate the yield theory to maximum load and plastic instability.[11] Recognizing these limitations and also the assumptions in the derivations, there is good agreement between these two ratios with a few exceptions. These exceptions occur at orientations where low biaxial tensile strengths were obtained, i.e., 120° and 165°. These inconsistencies may be attributed to wedge grip misalignment and/or grinding marks in the transverse slot. Typical uniaxial and biaxial test specimens are presented in Figure 8. The type of fracture on both of these specimens should be noted. Specimen misalignment was evident on the biaxial tensile specimen from the wedge grip marks. Some difference between the calculated strength ratios and the measured strength ratios may be due to the assumption of rotational symmetry which is not exactly the case. The theoretical ratio of the maximum principal stress to the uniaxial yield strength for the case of nonrotational symmetry may be obtained by substituting $\sigma_x/\sigma_y = 1 + \frac{1}{P}$ into Equation 9. The resultant stress ratio for a test in the x direction is:

$$\frac{\sigma_x}{X_o} = \sqrt{\frac{(1+P)(1+R)}{1+P+R}} \qquad (10)$$

A comparison between the strength increases predicted for the cases of rotational and nonrotational symmetry may be obtained by the use of Equations 8 and 10 respectively and Table II.

Rotational	Nonrotational
R = P = 3.14	R = 3.14 P = 2.64
$\frac{\sigma_x}{X_o} = 1.53$	$\frac{\sigma_x}{X_o} = 1.49$

The small differences between the two σ_x/X_o values indicate that, for the small difference in magnitude of the anisotropy parameters measured in this material, the assumption of rotational symmetry does not appreciably affect the results.

The 0.2% yield, tensile, biaxial, and edge-notched tensile strength data obtained from the longitudinal direction of the Ti-5Al-2.5Sn alloy as a function of test temperature are presented in Figure 9. These tests were conducted to determine if the biaxial strength increases obtained at room temperature would also be obtained at low temperature, where the uniaxial strength increases rapidly. The ratio of the BTS/UTS obtained for the various test temperatures decreases from 1.53 at room temperature to 1.41 at -112 F. Below this temperature, the strength ratio is approximately constant. This parallelism

between the BTS and UTS may be seen in Figure 9. It should also be noted in this figure that the edge-notched tensile strength is equal to the ultimate tensile strength at -110 F, indicating a tough, notch-ductile material. For test temperatures of room temperature and -312 F, strength to density ratios of 1.25×10^6 inches and 1.75×10^6 inches, respectively, were obtained with the biaxial tensile specimen.

The limited measurements of yield, tensile, biaxial tensile strengths, and the anisotropy parameter R obtained on the Ti-4Al-4Mn alloy are presented in Table III. These tests were conducted to determine if heat treating an alloy that exhibited anisotropy in the

TABLE III

Tensile and Biaxial Tensile Properties of Ti-4Al-4Mn Alloy

Test Direction	Yield Strength 0.2% (ksi)	Tensile Strength (ksi)	Biaxial Tensile Strength (ksi)	R	$\frac{BTS}{UTS}$	$\frac{\sigma_x}{X_o} = \frac{R+1}{\sqrt{2R+1}}$
Ti-4Al-4Mn (RS130B) Mill Annealed						
L	134.3 135.7	134.3 136.0	181.2 185.6	5.0	1.38	1.81
T	128.6 128.6	135.1 136.3	188.8 200.0	4.0	1.45	1.67
Ti-4Al-4Mn (RS130B) 1450 F 2 hr. WQ + 900 F 24 hr. AC						
L	142.5 140.6	155.3 155.0	205.7 220.8	5.5	1.37	1.88

annealed condition would increase or decrease the amount of anisotropy. In comparing the longitudinal tensile and biaxial tensile strength in the heat-treated conditions with the annealed condition, it is observed that both values increased by 20 ksi.

Pressure Vessel Tests

The physical dimensions, burst pressures, burst strengths, and strain observations on the two test cylinders are presented in Table IV. Both test vessels failed by opening up along the longitudinal weld. Photographs of these two vessels are presented in Figures 10 and 11. A pressure-time and strain-time trace recorded on Cylinder 2 is presented in Figure 12. All traces recorded are essentially straight lines, indicating that the base metal had not yielded when rapid failure occurred in the weld. The burst strengths were approximately 25% greater than the uniaxial yield strength of the base metal. It should not be expected that a longitudinal weld would exhibit anisotropy and biaxial strength increases. Therefore, in order to utilize mechanical anisotropy, pressure vessel fabrication methods other than rolling and welding are needed. One method of reducing the maximum principal stress on the weld in a cylinder would be by the use of a spiral weld. If the weld was oriented at 30° from the transverse axis, the normal stress would be reduced to 63% of the tangential stress in the cylinder. Other methods of fabrication which may be

TABLE IV

Pressure Vessel Data

	Cylinder 1	Cylinder 2
Diameter (in)	8.82	8.72
Length (in)	21	25
Thickness (in)	0.118	0.118
Weld Filler	Unalloyed	Ti-8Al-4V
Type of Weld	MIG	MIG
Sheet Alloy	Ti-5Al-2.5Sn	Ti-5Al-2.5Sn
Burst Press (psi)	5100	5100
Yield Strength (psi)	123,000	123,000
Tensile Strength (psi)	132,500	132,500
Burst Stress ($\frac{PD}{2t}$) (psi)	156,000	183,000
Strain L	----	600 μ in/in
Strain T	800 μ in/in	7500 μ in/in

possible, if processing techniques can be developed to produce proper textures, are shear spinning and ring rolling. Also, wrapping a motor case with thin strips is a possibility. The wrapping method is particularly intriguing since the strips may be oriented so that the principal planes of anisotropy are oriented to the principal stress directions. The principal planes of anisotropy are not always oriented in the longitudinal and transverse directions of the sheet. Note that the R values in Tables II and III vary slightly as a function of test direction.

GENERAL DISCUSSION

Data has been presented on an alpha and an alpha-beta titanium alloy which have exhibited mechanical anisotropy and biaxial strength increases of 50% and greater. The assumption should not now be drawn that all alpha titanium sheet and all alpha-beta sheet will exhibit anisotropy and biaxial strength increase. Many titanium sheet alloys have been tested at this Agency.(12) Some of these alloys exhibit anisotropy and some do not. The all-beta alloy, which has a bcc crystal structure, does not exhibit anisotropy. Whether or not an alloy will exhibit anisotropy is dependent upon the chemistry and the thermal processing history. Therefore, controlled processing research must be performed to determine how to obtain the proper texture in titanium sheet alloys before this mechanism may be fully utilized. Research is presently being conducted on this subject both at our Agency and other laboratories.(13) Whether or not textured material will obey the exact mathematical analysis described in this paper is open to question since, as in most other deviations, certain assumptions are made. However, the advantage of using a nominally low-strength, weldable, extremely tough material for rocket motor casings or other pressure vessel applications is obvious. Fracture toughness problems have plagued the rocket motor case industry for some time, and these problems will be magnified as strength levels are increased by the conventional methods, i.e., heat treating, cold working, and/or alloying.

REFERENCES

1. IRWIN, G. R., et al. Fracture Strengths Related to Onset and Arrest of Crack Propagation. NRL Report 5222, November 1958.

2. BACKOFEN, W. A., HOSFORD, W. F., and BURKE, J. J. Texture Hardening. Transactions Quarterly, ASM, v. 55, March 1962, p. 264.

3. HOSFORD, W. F., JR., and BACKOFEN, W. A. Strength and Plasticity of Textured Metals. Sagamore Conference, August 1962. Also Massachusetts Institute of Technology Preprint 261.

4. GENSAMER, MAXWELL. Strength of Metals Under Combined Stresses. American Society for Metals, Cleveland, Ohio, 1941.

5. HILL, R. The Mathematical Theory of Plasticity. Clarendon Press, Oxford, 1956.

6. LARSON, F. R., and NUNES, J. Strain Hardening Properties of High Strength Sheet Materials. Watertown Arsenal Laboratories, WAL TR 834.2/2, March 1961.

7. WHITELEY, R. L. Anisotropy in Relation to Sheet Processing. Sagamore Conference, August 1962.

8. DEFENSE METALS INFORMATION CENTER. Flow Properties, Deformation Texture, and Slip Systems of Titanium and Titanium Alloys. TML Report No. 30, January 1956.

9. MAYKUTH, D. J., HOLDEN, F. C., WILLIAMS, D. N., OGDEN, H. R., and JAFFEE, R. I. The Effects of Alloying Elements in Titanium. DMIC, Battelle Memorial Institute, DMIC Report 136B, v. B, 29 May 1961.

10. LEACH, A. E. Titanium Directionability Program. ASD Technical Report 62-7-675, Crucible Steel Co. of America, January 1962.

11. CORRIGAN, D. A. The Bi-Axial Strength of Heat-Treated Alloy Steel Sheets and Weldments. Watertown Arsenal Laboratories, WAL MS-42, July 1961.

12. LARSON, F. R. Anisotropy of Titanium Sheet in Uniaxial Tension, U. S. Army Materials Research Agency, AMRA TR 63-36, December 1963.

13. HATCH, A. J. Effects of Processing Variables on Texture Hardening of Ti-5Al-2.5Sn and Ti-6Al-4V. Titanium Metals Corp. of America, Project 48-5, August 1963.

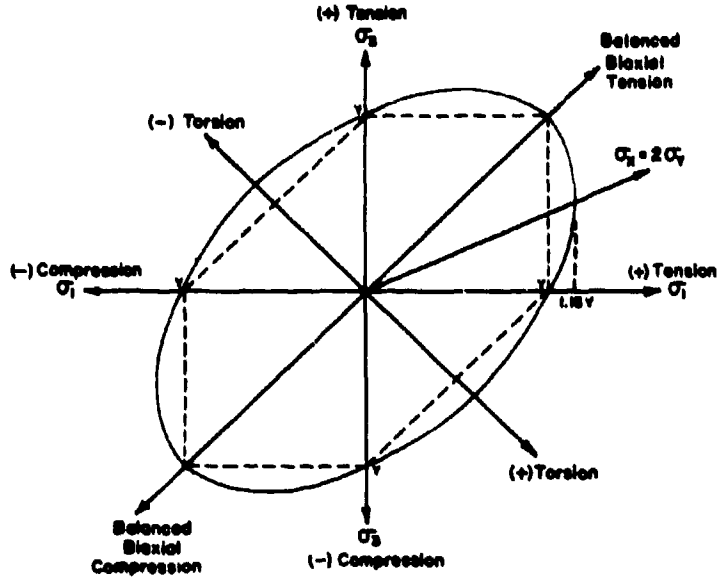

Hexagon – Tresca yield criteria
Ellipse – Von Mises yield criteria

Figure 1. YIELD LOCUS FOR TRESCA AND VON MISES YIELD CRITERIA UNDER PLANE STRESS LOADING

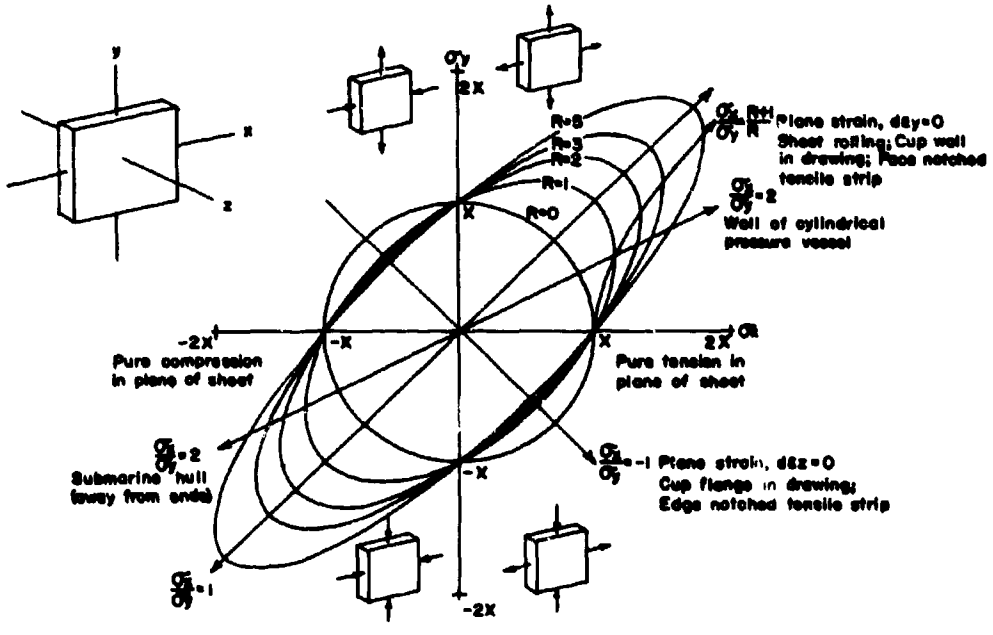

Figure 2. PLANE STRESS YIELD LOCI FOR SHEETS WITH TEXTURES THAT ARE ROTATIONALLY SYMMETRIC ABOUT THE THICKNESS DIRECTION, Z. VALUES OF R INDICATE THE DEGREE OF ANISOTROPY. AFTER BACKOFEN (Reference 3)

U. S. ARMY MATERIALS RESEARCH AGENCY

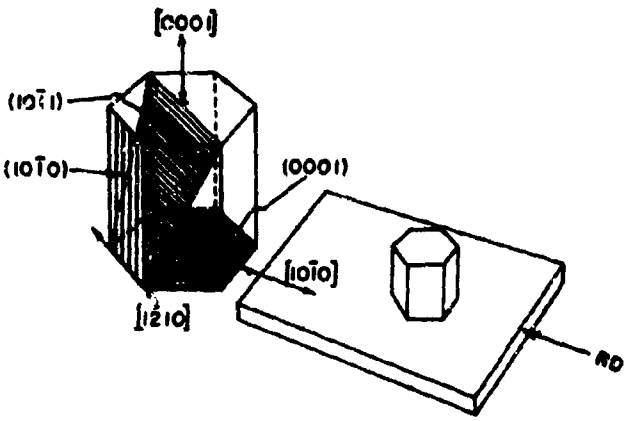

Figure 3. COMMON SLIP SYSTEMS FOR HCP METALS. (Reference 3)

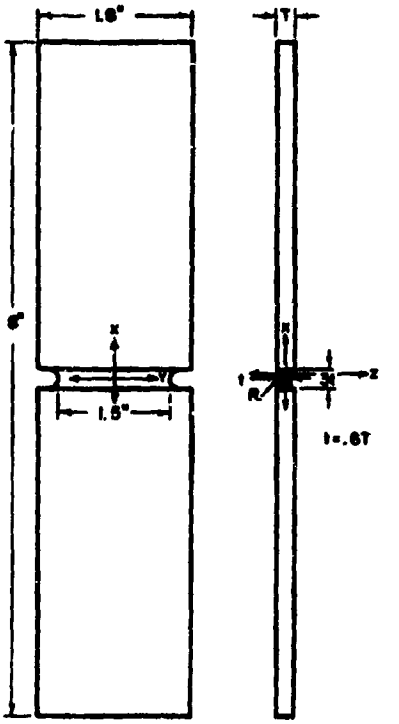

Figure 4. PLANE STRAIN BIAXIAL TENSILE SPECIMEN

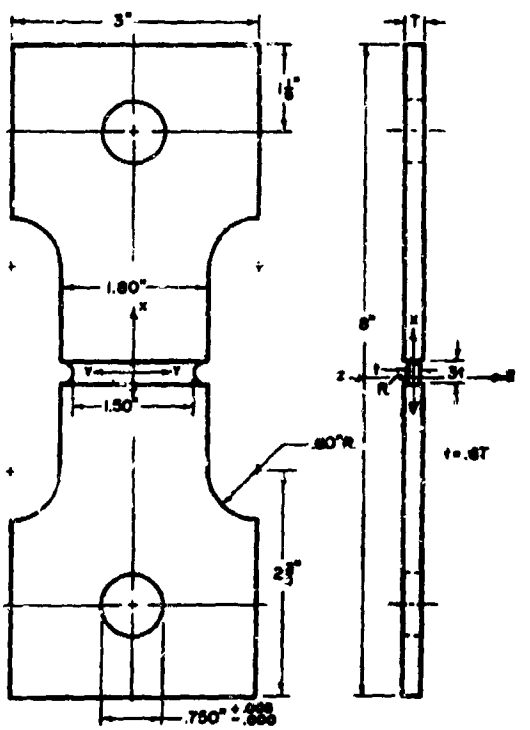

Figure 5. LOW TEMPERATURE PLANE STRAIN BIAXIAL TENSILE SPECIMEN

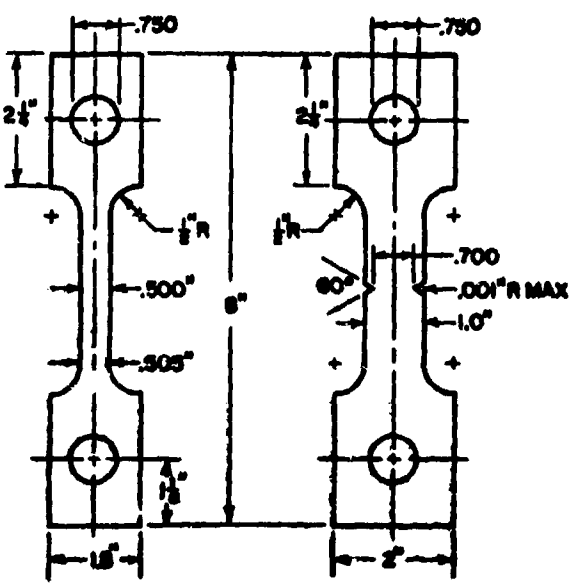

Figure 6. NOTCHED AND UNNOTCHED TENSILE SPECIMENS

U. S. ARMY MATERIALS RESEARCH AGENCY

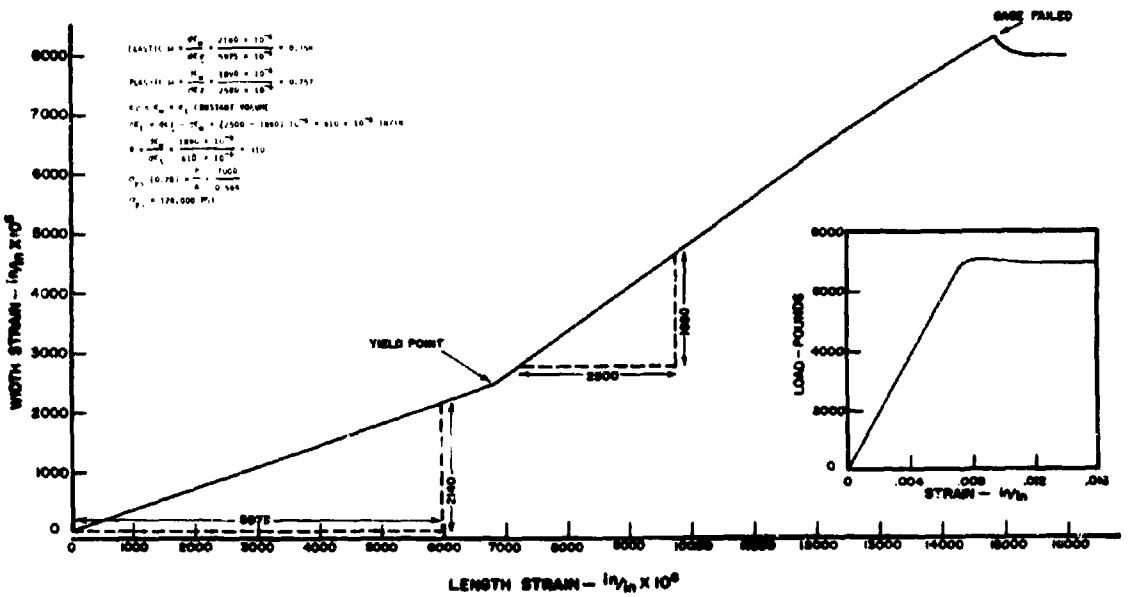

Figure 7. STRAIN CURVE FOR ANISOTROPIC SHEET MATERIAL (Ti-5Al-2.5Sn-LONGITUDINAL)

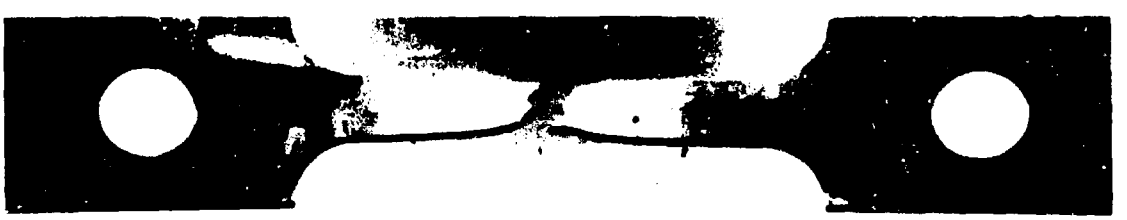

Uniaxial Tensile Specimen

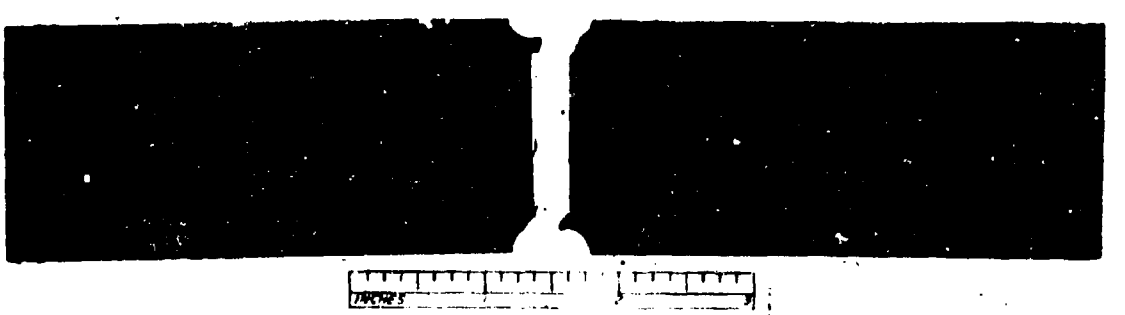

Biaxial Tensile Specimen

Figure 8. FRACTURES IN TITANIUM ALLOY (Ti-5Al-2.5Sn) SHEET IN UNIAXIAL AND BIAXIAL TENSILE SPECIMENS

U. S. ARMY MATERIALS RESEARCH AGENCY

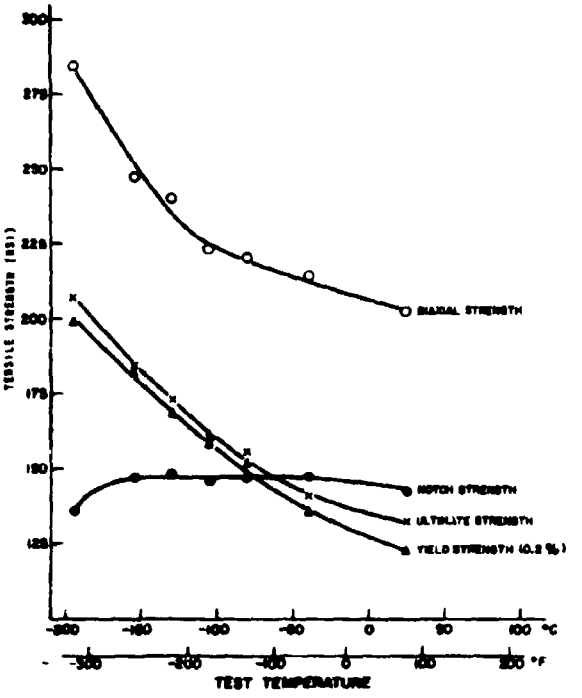

Figure 9. TENSILE, EDGE-NOTCHED TENSILE, AND BIAXIAL TENSILE DATA FOR Ti-5Al-2.5Sn ALLOY, SHEET B

Figure 10. Ti-5Al-2.5Sn TEST CYLINDER 1

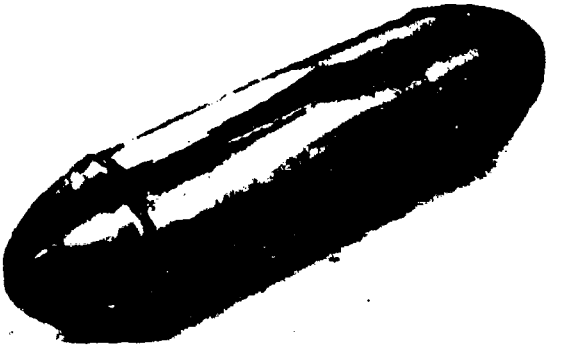

Figure 11. Ti-5Al-2.5Sn TEST CYLINDER 2

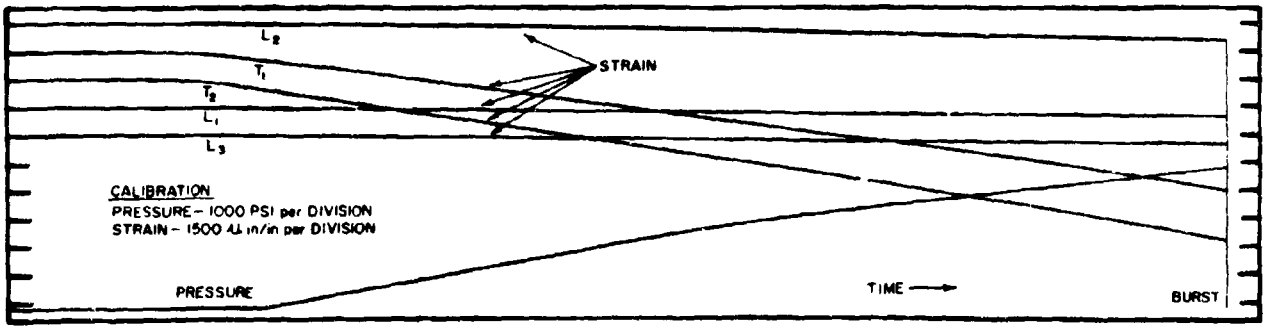

Figure 12. PRESSURE TIME - STRAIN TIME CURVE FOR Ti-5Al-2.5Sn CYLINDER 2

U. S. ARMY MATERIALS RESEARCH AGENCY

OPTICAL-ELECTRONIC AZIMUTH AND RANGE BETWEEN NON-INTERVISIBLE DISTANT GROUND STATIONS

EMANUEL M. SODANO
G. I. M. R. A. D. A.
FT. BELVOIR, VIRGINIA

1. INTRODUCTORY BACKGROUND

A frequent problem in geodesy, especially in remote areas, is the determination of direction and distance between two ground positions that are located several hundred miles apart. Due to the curvature of the earth, such positions are not intervisible. To further complicate matters, extensive bodies of water or impassable terrain often intervene. The connection is therefore made through measurements to a high intermediary object. Radar and similar electronic distance measuring instruments supplied the initial impetus to the use of airplanes as the aerial link. However, the application was confined to distances because the distortion of electromagnetic waves by the earth's atmosphere principally affected the accuracy of azimuth measurements. The requirement for measuring such azimuths between non-intervisible distant stations persisted, however, because (a) trilateration nets were weakly oriented in spite of many redundant lines and (b) positions of islands lying almost in a straight line could not be intersected from distances alone.

In 1952, the writer published an optical azimuth solution which in 1958 was combined in [1] with an alternate method. Although both proved accurate to better than 1 second in tests, the one requiring only two simultaneous observations of an airborne light proved less vulnerable to intervening clouds. Its essential role in the connection of numerous Pacific islands up to 240 miles apart is described in [2] by the U. S. Army and Air Force. Nevertheless, difficulties and postponements due to persistent cloud cover are also noted.

The present paper proposes two new methods that advantageously combine all-weather electronic distances with optical observations. In one case, the azimuth of the airplane's light is observed from only one of the two ground stations, thus eliminating the optical simultaneity. Sufficient data is therefore provided even through heavily scattered clouds, as illustrated in Fig. 1. When the cloud cover is complete, the method of Fig. 2 uses two airplanes to relegate

the electromagnetic and optical paths entirely beneath the clouds. When clouds are higher or gone, this second method also gives a greatly extended solution. Both procedures provide determinations of the range as well as azimuth. Variations in aircraft course are not critical. The method of Fig. 2 is ideally suited— in fact, more economical -- for small low-altitude Army type aircraft.

2. DERIVATION OF BASIC RELATIONSHIPS

With reference to Fig. 3, the object is to determine the distance and azimuth from a to b. Point p' represents the aerial position of a vehicle which, although shown on the circumference of a circle, may actually be assumed at no special location if unguided. Let the vehicle record its electronic distances to a and b at the same instant that its horizontal and vertical directions are recorded by a tracking theodolite (or camera) at a. Let D_a and D_b be the geometrical chords of the atmospherically refracted lines just recorded. Draw a plane through b and perpendicular, at o, to the extension of the normal through a. From p', drop a line perpendicular to the plane at p and complete the rectangle p'poao'. D_a then lies in the plane formed by the rectangle and projects into r, while D_b projects into d. Let α_Z represent the zenith angle o'ap'.

When (due to the motion of p') point p intersects the straight line $\overline{ob}$, angle bpo becomes 180° and the two planes through p'p become coincident. Since the resulting single plane passes through the normal $\overline{ao}$ and through b, it represents the normal section azimuth (α_N) from a to b. This azimuth projects along line N. Correspondingly, the projected direction (o to p) of the airplane will be denoted as α. For any arbitrary position of the vehicle, p', the variable angle bop can therefore be expressed by:

$$\alpha - \alpha_N = \angle \text{ bop} \tag{1}$$

Applying the law of cosines to the plane triangle bop:

$$d^2 = r^2 + N^2 - 2rN \cos (\alpha - \alpha_N) \tag{2}$$

By means of the Pythagorean theorem and a few trigonometric relationships, d^2 can be also expressed successively as follows:

$$d^2 = D_b^2 - (E + V)^2 = D_b^2 - (D_a \cos \alpha_Z + V)^2$$

$$= D_b^2 - D_a^2 (1 - \sin^2 \alpha_Z) - V^2 - 2VD_a \cos \alpha_Z$$

$$= D_b^2 - D_a^2 + r^2 - V^2 - 2VD_a \cos \alpha_Z \tag{3}$$

Equating (2) to the last form of (3) and eliminating r:

$$D_b^2 = (N^2 + V^2) + D_a^2 + 2VD_a \cos \alpha_Z - 2ND_a \sin \alpha_Z \cos (\alpha - \alpha_N) \tag{4}$$

where the square of the required chord length from a to b of Fig. 3 is given by

$$L^2 = N^2 + V^2 \tag{5}$$

and its angle of depression relative to the horizontal at station a is obtained from

$$\tan \alpha_L = V \div N \tag{6}$$

Formula (4) is a theoretically rigorous three-dimensional relationship that is independent of the size and shape of the earth. In practice, it is limited only by the degree of accuracy with which the input -- D_a, D_b, α_Z and α -- can be obtained from the associated measured distances and azimuths, corrected for atmospheric refraction and electromagnetic wave velocity. The output -- N, V, and α_N -- consists of exact constants which can be determined best by least squares. Up to this point, it should be noted, formula (4) is general enough for application to any horizontally or vertically uncontrolled path of an airplane, balloon, rocket or satellite.

3. SIMPLIFICATION OF ATMOSPHERIC CORRECTIONS

Numerous formulas are available for computing the difference between an electronically measured arc length (S) and the corresponding geometric chord (D), in order to correct for refraction and velocity changes induced by atmosphere on electromagnetic waves. For the purpose of the present paper, the form of such mathematical expressions is even more critical than the actual numerical magnitude of the correction, because the literal formula must permit convenient substitution into subsequent derivation equations. From applicable literature it was determined that, even for some of the more accurate formulas, the relationship between chord and arc could be reduced rigorously to the following simple form of power series:

$$D = S(K_0 + K_2 S^2 + K_4 S^4) \tag{7}$$

By transforming formula (89) of [3] into terms corresponding to (7) above, the following expressions for the K coefficients were deduced:

$$K_0 = 1 + n_0 - \frac{\Sigma n}{2} + \frac{\Delta h\, \Delta n'}{12} \tag{8}$$

$$K_2 = \frac{\Sigma n'}{24R} + \frac{\Delta n\, \Sigma n'}{12\, \Delta h} + \frac{(\Delta n')^2}{96} - \frac{(\Delta n)^2}{8(\Delta h)^2} \tag{9}$$

$$K_4 = \frac{(\Delta n)^2\, \Delta n'}{48\, (\Delta h)^3} + \frac{\Delta n\, \Delta n'}{48R(\Delta h)^2} - \frac{\Delta n\, \Delta n'\, \Sigma n'}{144(\Delta h)^2} - \frac{\Delta n'\, \Sigma n'}{144R\, \Delta h} \tag{10}$$

where

R = Radius of spherical approximation to earth beneath ray path

n_0 = Index of refraction designed into electronic distance instrument, or Electromagnetic velocity in vacuum ÷ Velocity designed into instrument

n = Index of refraction as a function of height = $a_0 + a_1 h + a_2 h^2$

$n' = \frac{dn}{dh}$, $\Delta(*) = (*)_A - (*)_G$, $\Sigma(\#) = (\#)_A + (\#)_G$, and subscripts G and A denote evaluation at ground and at aerial station.

The numerical example given on page 53 of [3] can therefore be represented by the following:

$$D = S(1.0000\ 8857 - .0000\ 8242 \times 10^{-5} S^2 - .0000\ 0294 \times 10^{-10} S^4) \tag{11}$$

where S is the given slant range of 194.18493 nautical miles (about 223 statute miles) from ground to air.

Equations (8) through (10) and associated definitions show that the K's for (7), independently of S and its powers, approach constancy under the following conditions: a fixed ground station elevation, a substantially constant aerial vehicle height, and a relatively stable atmosphere over the area of operation. In such case, the square of (7) can be represented by means of another set of constants as follows:

$$D^2 = S^2 \ (K_x + K_y \ S^2 + K_z \ S^4) \qquad (12)$$

In addition, if S varies by a limited extent only, the sum of the parenthetical terms of (7) will approach constancy because of the smallness of the coefficients of S^2 and S^4 as shown by (11). Therefore by using an airplane, which can fly at a fairly constant elevation and can approximate a circular arc around one of the ground stations by means of substantially equal slant range measurements S, equation (7) can be reduced to:

$$D = SK \qquad (13)$$

The geometry of this circular arc flight is illustrated in Fig. 3. It can be shown that if poor piloting were to cause the radial slant range S to vary by as much as $\pm$ .25 nautical mile (about $\pm$ 1520 feet), D computed by (13) would differ from (11) by only 1 inch in spite of the false assumption that its only K remain absolutely constant. (The optical vertical refraction will be treated later, although it could also be corrected in a manner similar to (13).)

All subsequent derivations will treat K's as constants, with flights conforming thereto. Whenever feasible, such constants will express the chord D in terms of the directly measured S. This will provide accurate formulas that avoid extensive calculations of variables and, when the values of the constants can be determined by empirical solutions, will dispense with the expensive acquisition of atmospheric index of refraction data.

4. APPLICATION TO RANGE AND/OR AZIMUTH

The substitution of (12), for station b, into (4) gives:

$$K_x \ S_b^2 + K_y \ S_b^4 + K_z \ S_b^6 = (N^2 + V^2) + D_a^2 + 2VD_a \cos \alpha_Z - 2ND_a \sin \alpha_Z \cos(\alpha - \alpha_N) \qquad (14)$$

Now substitute (13) and its square -- both for station a -- into (14), and divide the result by K_a^2 to obtain:

$$K_e \ S_b^2 + K_f \ S_b^4 + K_g \ S_b^6 = (K_N^2 + K_V^2) + S_a^2 + 2K_V \ S_a \cos \alpha_Z - 2K_N \ S_a \sin \alpha_Z \cos (\alpha - \alpha_N) \qquad (15)$$

where $K_N = N \div K_a$, $K_V = V \div K_a$, (16)(17)

K_e is close to unity, and K_f and K_g are very small.

Next, let equation (15) be applied to Fig. 3 at two points, p_1 and p_2, instead of one.

$$(K_e \ S_{1b}^2 + K_f \ S_{1b}^4 + K_g \ S_{1b}^6) = (K_N^2 + K_V^2) + S_{1a}^2 + 2K_V \ S_{1a} \cos \alpha_{1Z} - 2K_N \ S_{1a} \sin \alpha_{1Z} \cos (\alpha_1 - \alpha_N) \qquad (18)$$

$$(K_e S_{2b}^2 + K_f S_{2b}^4 + K_g S_{2b}^6) = (K_N^2 + K_V^2) + S_{2a}^2 + 2K_V S_{2a} \cos \alpha_{2Z} - 2K_N S_{2a} \sin \alpha_{2Z} \cos (\alpha_2 - \alpha_N) \quad (19)$$

Bearing in mind that K_f and K_g are very small, it is apparent that if S_{1b} is chosen nearly equal to S_{2b}, the following corresponding products in equations (18) and (19) will be essentially equal:

$$K_f S_{1b}^4 \approx K_f S_{2b}^4 , \qquad K_g S_{1b}^6 \approx K_g S_{2b}^6 \quad (20)(21)$$

The preceding assumptions correspond to the condition that for any point p_1 in Fig. 3, subsequently a p_2 will be obtained nearly symmetric to it with respect to the opposite side of line N. Now, by subtracting equation (19) from (18), the constant $(K_N^2 + K_V^2)$ as well as the terms represented by (20) and (21) will cancel out and leave:

$$K_e (S_{1b}^2 - S_{2b}^2) = (S_{1a}^2 - S_{2a}^2) + 2K_V (S_{1a} \cos \alpha_{1Z} - S_{2a} \cos \alpha_{2Z}) + 2K_N [S_{2a} \sin \alpha_{2Z} \cos(\alpha_2 - \alpha_N) - S_{1a} \sin \alpha_{1Z} \cos(\alpha_1 - \alpha_N)] \quad (22)$$

If the difference in length between any paired (S_{1b}, S_{2b}) in (22) is as much as $\pm$ .25 nautical mile because of their lack of symmetry around N or due to variations from a circular flight, the resulting error will again be only about 1 inch.

The equations that will provide the four principal solutions -- (4), (14), (15) and (22) -- will now be put into a form suitable for least squares by separating the constant azimuth α_N from the variable horizontal azimuths and joining its sine or cosine to every N or K_N:

$$D_b^2 = [(N \cos\alpha_N)^2 + (N \sin\alpha_N)^2 + V^2] + D_a^2 + 2VD_a \cos\alpha_Z - 2N \cos\alpha_N D_a \sin\alpha_Z \cos\alpha - 2N \sin\alpha_N D_a \sin\alpha_Z \sin\alpha \quad (4')$$

$$K_x S_b^2 + K_y S_b^4 + K_z S_b^6 = [(N \cos\alpha_N)^2 + (N \sin\alpha_N)^2 + V^2] + D_a^2 + 2VD_a \cos\alpha_Z - 2N \cos\alpha_N D_a \sin\alpha_Z \cos\alpha - 2N \sin\alpha_N D_a \sin\alpha_Z \sin\alpha \quad (14')$$

$$K_e S_b^2 + K_f S_b^4 + K_g S_b^6 = [(K_N \cos\alpha_N)^2 + (K_N \sin\alpha_N)^2 + K_V^2] + S_a^2 + 2K_V S_a \cos\alpha_Z - 2K_N \cos\alpha_N S_a \sin\alpha_Z \cos\alpha - 2K_N \sin\alpha_N S_a \sin\alpha_Z \sin\alpha \quad (15')$$

$$K_e(S_{1b}^2 - S_{2b}^2) = (S_{1a}^2 - S_{2a}^2) + 2K_V (S_{1a} \cos\alpha_{1Z} - S_{2a} \cos\alpha_{2Z}) + (2K_N \cos\alpha_N)(S_{2a} \sin\alpha_{2Z} \cos\alpha_2 - S_{1a} \sin\alpha_{1Z} \cos\alpha_1) + (2K_N \sin\alpha_N)(S_{2a} \sin\alpha_{2Z} \sin\alpha_2 - S_{1a} \sin\alpha_{1Z} \sin\alpha_1) \quad (22')$$

In addition to possibly some of the purely atmospheric parameters (K_x, K_y, K_z, K_e, K_f, K_g), the preceding four equations contain either of the following two sets of constants and perhaps their squares:

$$V , \; N \sin\alpha_N, \; N \cos\alpha_N \; . \quad (23)(24)(25)$$

$$K_V, \; K_N \sin\alpha_N, \; K_N \cos\alpha_N. \quad (26)(27)(28)$$

The tangent of the required normal section azimuth α_N is obtained from (24) $\div$ (25) or (27) $\div$ (28), whereupon N can be obtained by substituting α_N back into (24) or (25) only. This means that only equations

(4') and (14') can provide -- in addition to α_N -- N and V for the solution of the required chord length L from (5). Finally, the tangent of the chord's angle of depression is obtained from V + N according to (6) or, as evident from (16) and (17), using $K_V + K_N$.

In addition to their difference in number of unknown constants and in whether the distance as well as the azimuth can be obtained, the four principal solutions differ by type of flight and extent of atmospheric data requirements. For example (22'), which gives only the azimuth, has had all chords D replaced by the directly measured arcs S; therefore it requires no acquisition of atmospheric index of refraction data. Also, it is the only equation that is linear in its constants and, since it pairs off approximately equal distances from station b, systematic errors will cancel by subtraction. The other equations require atmospheric data between the airplane and both, one, or no ground stations, depending on the D's eliminated. The constants of (15') and (22') can be determined wholly empirically because of their substantially circular flight at a fairly constant elevation, whereas (4') places no constraint on flight variations but the resulting variable K's must be computed individually from terms of (8), (9) and (10). D_a for (14') is calculated using the constants of (13) or (7), depending on whether the level flight is approximately circular or not.

The zenith angle α_z, which appears in all principal formulas, can of course be replaced by the angle of elevation α_h by substituting the complimentary trigonometric function. Their optical vertical refraction can be kept fairly constant either by flying at nearly constant altitude and radius, or by relaying the theodolite's α_h reading to the pilot. Therefore α_z could be assigned an average value or, better yet, such value (including refraction) could be determined as an empirical constant from the already required least squares solution. For example, by assuming α_{1z} and α_{2z} in (22') to be equal and constant, the following parameters instead of its (26), (27) and (28) would be determined:

$$K_V \cos\alpha_z \ , \quad K_N \sin\alpha_N \sin\alpha_z \ , \quad K_N \cos\alpha_N \sin\alpha_z \ . \qquad (29)\ (30)\ (31)$$

5. GEODETIC ASPECTS OF CALCULATIONS AND FIELD PROCEDURES

In practice, observed azimuths involve plane rather than geodetic sections. Since the directions in Fig. 3 will be observed only from station a, derivations by plane sections avoids the azimuth correction for the otherwise skew normals that would have resulted if the elevated airplane position had been projected perpendicular to the spheroid rather than made parallel to the normal of a. Also, the observed plane section directions from a to p' are not to be reduced to geodetic azimuths. Thus the only azimuth corrections [4] that may be required are those due to: a large deviation of the vertical at a in the component at right angles to D_a, combined with a high angle of elevation (α_h) of D_a; a large relative skewness of the spheroid normals at a and b, combined with a large elevation of b from sea level; and of course the difference between the plane section's α_N and the

geodetic azimuth from a to b. On the other hand, if from a to b the astronomic rather than the geodetic azimuth is required, the correction to ap for the deviation of the vertical at a must be omitted. In this case the plane through station b is considered to be perpendicular to the astronomic vertical, rather than to the spheroid's normal, at station a. In fact, it is strictly with respect to this local astronomic vertical (rather than the spheroid's normal) that the zenith angle of the airplane can be directly and rigorously observed. Finally, the geodetic distance is generally obtained from the chord by calculating a corresponding circular arc based on the average radius of curvature between stations a and b, taking their elevations into consideration. A more sophisticated procedure is to consider the distance as an arc of an appropriate ellipse.

It does not matter whether horizontal theodolite directions are taken counter or clockwise, or with respect to a known or arbitrary reference line. That's because the difference $(\alpha - \alpha_N)$ in (2) can change only in sign, thus not affecting the cosine. The true reference value can be applied to the result later by addition of a constant. In fact, by adopting a reference direction that makes all the observed α have approximately equal absolute sines and cosines, the least squares observation equations can be assumed equal in weight. The accuracy of angular tracking can be improved (especially for relatively uniform, though rapid, circular motion) by the use of an electrically driven theodolite with speed controls. Camera recordings of strobe-illuminated cross hairs and of horizontal and vertical circles can be used for subsequent correction of residual tracking errors. To be sure that all recordings take place only when the airplane's light is visible from the optical ground station, the recording instants should be determined by the optical observer. (Although not treated here, star-background photography too could presumably be used for the azimuth recordings.)

6. ERROR ANALYSIS AND STRENGTH OF FIGURE

In connection with (13) and (22) respectively, it has already been noted that inequalities of the radial or paired distances produce negligible errors, even if caused by piloting variations as large as $\pm$ .25 nautical mile. That's because in (13), (22) and others, the true instantaneous recordings of the airplane's S are used. Since a large navigational tolerance is permitted, a high percentage of the measured data will meet acceptance standards -- even when distances are to be appropriately paired. Furthermore, measurements from two or more similar flights can be combined whenever the separate ones may have provided insufficient data because of clouds or technical difficulties. Finally, when the uniformity of the atmospheric profile over the area of operation is questionable, separate solutions by component areas could be performed. In view of the preceding, only the effect of the geometrical configuration upon the propagation of just the instrumental measurement errors need be analyzed.

Since the angle of elevation of the aerial vehicle will be

relatively small, the strength of the three-dimensional figure is approximated by the projected relationship (2), whose d and r may be assumed to contain their own numerical measurement errors plus small lineal components from errors in α_Z. The representation of (2) as $F(d, \alpha, r, N, \alpha_N) = 0$ gives:

$$\Delta F = \frac{\partial F}{\partial d}\Delta d + \frac{\partial F}{\partial \alpha}\Delta\alpha + \frac{\partial F}{\partial r}\Delta r + \frac{\partial F}{\partial N}\Delta N + \frac{\partial F}{\partial \alpha_N}\Delta\alpha_N = 0 \qquad (32)$$

Substitution of the partial derivatives into (32) gives, for any one point, the following error formulas WHEN α_N IS ASSUMED TO BE ZERO FOR CONVENIENCE:

$$\Delta N = \frac{d\,(\Delta d) - (r - N\cos\alpha)\,\Delta r - (r\,N\sin\alpha)\,\Delta\alpha}{N - r\cos\alpha} \qquad (33)$$

$$\Delta\alpha_N = \Delta\alpha - \frac{d\,(\Delta d) - (r - N\cos\alpha)\,\Delta r}{rN\sin\alpha} \quad \text{radians} \qquad (34)$$

$$= \Delta\alpha - \frac{\Delta d}{r\sin(bpo)} + \frac{(r^2 + d^2 - N^2)\Delta r}{2r^2 d\sin(bpo)} \quad \text{radians} \qquad (35)$$

For the two-point formula, (22'), the error is derived instead from $(F_1 - F_2) = 0$, in which the constant N^2 cancels. Since the symmetry with respect to the two points produces the same error from each, only one of them was assumed in error and the resulting $\Delta\alpha_N$ became half of either (34) or (35). (Since (22') is not designed to provide N, it is not surprising that its ΔN becomes ∞.)

In (35) the change caused by Δd becomes minimum (for a given r) when angle bpo is 90°. In the right triangle thus formed in Fig. 3, $r^2 + d^2$ equals N^2 and so the coefficient of Δr also becomes minimum -- in fact, zero. Therefore $\Delta\alpha_N$ from (35) is minimum when d is perpendicular to r, which means that d is tangent to the airplane's projected approximate circular course. The same is true for the two-point solution, (22'). For the distance error, (33), only the coefficient of Δr will be minimum when d is again assumed tangent to a circle. Analysis has shown, however, that the sum of the squares of the errors caused by Δr, Δd and $\Delta\alpha$ will be minimum at the same tangency point if the latter are assumed related as follows:

$$\Delta r = \Delta d = 2[r(\Delta\alpha)] = \Delta \qquad (36)$$

that is, Δr and Δd are each regarded as twice the size of the lineal displacement of p in Fig. 3, caused by the rotation of r through the angular error $\Delta\alpha$. Substituting (36) into (33) in terms of Δ and summing the squares of the three errors, gives finally:

$$(\Delta N)^2_{(36)} = \frac{2r^2 + 2N^2 - 4rN\cos\alpha - .75N^2\sin^2\alpha}{(N - r\cos\alpha)^2}\cdot\Delta^2 \qquad (37)$$

To check the condition that will make the coefficient of Δ^2 in (37) a minimum, obtain its derivative with respect to the variable α; equate the result to ze o; then simplify to obtain $\cos\alpha = r \div N$, which implies that d in Fig. 3 is perpendicular to r and therefore tangent to the circle as predicted. Although the specific assumptions, (36), that govern (37) are reasonable, (33) through (35) treat the more general cases. The latter can also be used to determine additional

minimization, such as by choosing appropriate relative or absolute lengths for r and N. (Of course, the airplane should also be observed at positions substantially prior to and past the two ideal points of tangency, in order to obtain independent observation equations.) By means of (33) and (34), the strength of figure for a 225 mile line has been computed at one of the points of tangency and 25 miles prior to and past it, using a flight arc of 100 miles radius. For assumed measurement errors related as in (36) -- 5 ft. in r, 5 ft. in d and 1 sec. in α -- the resulting root of the summed square errors was only about 6.3 ft. in N and 2.25 sec. in α_N, for any of the three points. (The range of the d was 201 $\pm$ 25 miles approximately.)

7. BI-AERIAL AZIMUTH & RANGE FOR ALL-WEATHER AND/OR EXTENDED SOLUTION

Fig. 4 provides the principal geometry for the derivation of the bi-aerial method that is pictorially illustrated in Fig. 2. The quadrilateral $bo_a p_a p_b$ of Fig. 4 obviously corresponds to the projected triangle bop of Fig. 3. Therefore in lieu of the conventional law of cosines used in equation (2) for the triangle, a more general law of cosines must be deduced for a plane quadrilateral. Accordingly, it can be shown that for $bo_a p_a p_b$ in Fig. 4:

$$r_a^2 + (D_b^2 - Z_b^2) + 2r_a\sqrt{D_b^2 - Z_b^2}\cos[(\alpha_a - \alpha_N) + \beta] = d_c^2 + 2N[r_a\cos(\alpha_a - \alpha_N) + \sqrt{D_b^2 - Z_b^2}\cos\beta] - N^2 \quad (38)$$

Since $\overline{p_a p_a'}$ and $\overline{p_b p_b'}$ are $\perp d_c$, while $\overline{p_a p_a'}$ and $\overline{o_a o_a'}$ are $\perp r_a$, d_c and r_a are the projections of D_c and D_a, respectively:

$$d_c^2 = D_c^2 - [(E_a + V) - Z_b]^2 = D_c^2 - (V - Z_b + D_a\cos\alpha_{Z_a})^2 \quad (39)$$

$$r_a = D_a \sin\alpha_{Z_a} \quad (40)$$

Substitution of (39) and (40) into (38) gives:

$$D_a^2 + D_b^2 - D_c^2 + N^2 + V^2 + 2VD_a\cos\alpha_{Z_a} - 2ND_a\sin\alpha_{Z_a}\cos(\alpha_a - \alpha_N) - 2(V + D_a\cos\alpha_{Z_a})Z_b - 2[N - D_a\sin\alpha_{Z_a}\cos(\alpha_a - \alpha_N)]\sqrt{D_b^2 - Z_b^2}\cos\beta - 2D_a\sin\alpha_{Z_a}\sin(\alpha_a - \alpha_N)\sqrt{D_b^2 - Z_b^2}\sin\beta = 0 \quad (41)$$

whose Z_b, $\cos\beta$ and $\sin\beta$ in the last three terms are dependent on the UNKNOWN LOCAL DEFLECTION OF THE ASTRONOMIC VERTICAL AT STATION b, and are the only remaining quantities requiring appropriate definition. For the moment, assume that in Fig. 4 the astronomic verticals E_a and E_b both lie in the plane bao_a. Due to the earth's curvature and the deflection components WITHIN plane bao_a, E_a and E_b will lack parallelism by angle θ. This is equivalent to the astronomic arc from a to b, which is computed from the spherical law of cosines using ASTRONOMIC latitudes and longitudes (ϕ, λ) as follows:

$$\cos\theta = \sin\phi_a\sin\phi_b + \cos\phi_a\cos\phi_b\cos(\lambda_a - \lambda_b) \quad (42)$$

Since E_b lacks perpendicularity to $bo_a p_a p_b$ by said angle θ, β will not equal the corresponding angle, β', measured horizontally at b. The relationship between β and β', as well as the Z_b which too is required for (41), can be determined from the coordinates of aerial position

p'_b which already have been derived in Fig. 5 successively from other points. Thus, after eliminating r_b and E_b in the manner of (40) and the end of (39) respectively, there results:

$$Z_b = D_b \sin \alpha_{Z_b} \cos \beta' \sin \theta + D_b \cos \alpha_{Z_b} \cos \theta \qquad (43)$$

$$\cos \beta = (D_b \sin \alpha_{Z_b} \cos \beta' \cos \theta - D_b \cos \alpha_{Z_b} \sin \theta) \div \sqrt{D_b^2 - Z_b^2} \qquad (44)$$

$$\sin \beta = (D_b \sin \alpha_{Z_b} \sin \beta') \div \sqrt{D_b^2 - Z_b^2} \qquad (45)$$

Since the physical direction of the reference line N is not known exactly, all the observed β' must be modified by a small empirical constant. Also, since a small deflection of the vertical in the plane normal to bao_a will actually exist, a small constant modification to β also will do if the RANGE OF VALUES OF β IS MODERATE AND SUFFICIENTLY SYMMETRIC RELATIVE TO OPPOSITE SIDES of N. Thus:

$K_{\beta'}$ = correction to β' ; K_β = correction to β . (46) (47)

Actually, if the flight is also reasonably circular and level, all quantities except β', β and perhaps Z_b in (43), (44) and (45) can be regarded as constants. (Since a to b is long, the small deflection normal to bao_a does not change θ.) Substitution of (42) through (47) into (41) -- numerically, algebraically or simplified as above when appropriate -- finally produces an azimuth and range equation corresponding to (4), but for two airplanes instead of one. Hence the further simplifications represented by equations beyond (4) can be applied to the data of EITHER or BOTH stations. The azimuth can be geodetically referenced by applying to α_N a correction for the known deflection at station a.

8. CONCLUSIONS

The three-dimensional solutions derived here for azimuth and range up to 700 miles are virtually all-weather because of their use of electromagnetic distance, non-simultaneous or under-cloud optical observations, and unexacting aerial navigation which allows measurements from different passes to be combined, if insufficient, rather than discarded. Yet the flight pattern eliminates much or all atmospheric data acquisition. For the bi-aerial procedure, small Army type aircraft are ideal. The methods are therefore more economical, rapid and accurate than contemporary ones requiring virtually straight flights, simultaneous optical observations, atmospherically stable electromagnetic interferometers, or appropriate satellite passes.

9. BIBLIOGRAPHY

1. Sodano, E.M. -"Determination of Laplace Azimuth between Non-Intervisible Distant Stations by Parachuted Flares and Light Crossings", Bulletin Geodesique, 1958, No. 49.
2. Adams, L.H. -"U.S. National Report, 1960-1963, to XIII General Assembly of I.U.G.G.", Transactions, American Geophysical Union, June 1963, pp. 310, 311, 316.
3. Schreiter, J.-"Formulas Relating Shoran Measurements to Geodetic Data", O.S.U. Mapping and Charting Research Laboratory, Technical Paper No. 194, Ohio, 1955.
4. Bomford, G. -Geodesy, Oxford, 1952, pp. 73-76.

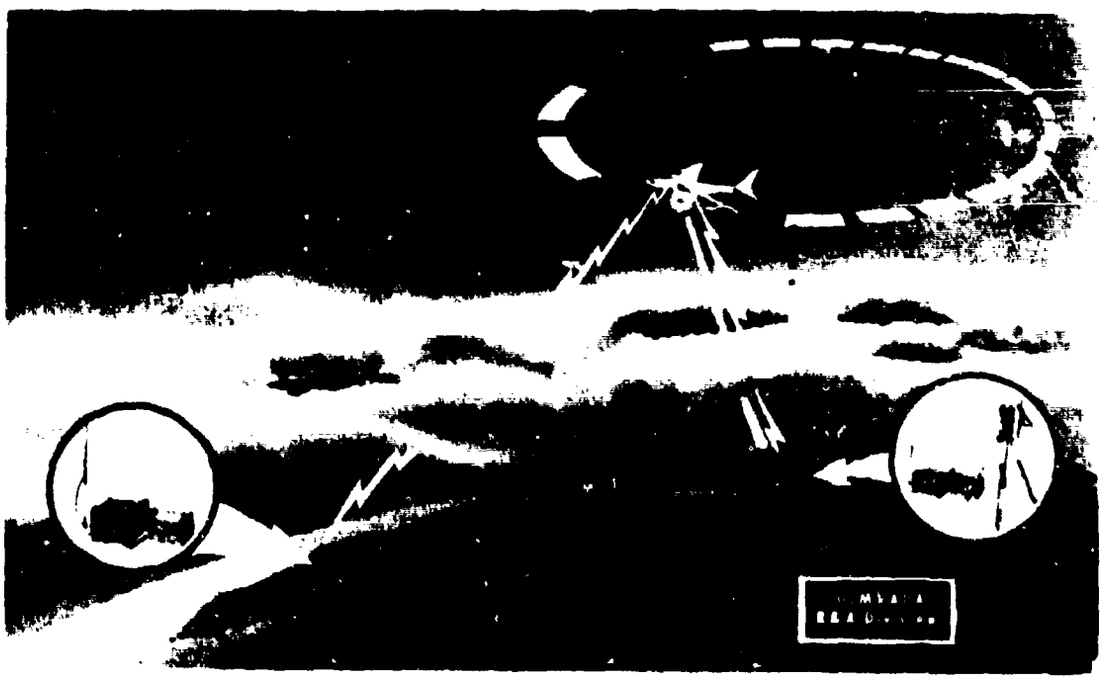

FIG. 1: OPTICAL-ELECTRONIC AZIMUTH AND DISTANCE DETERMINATION

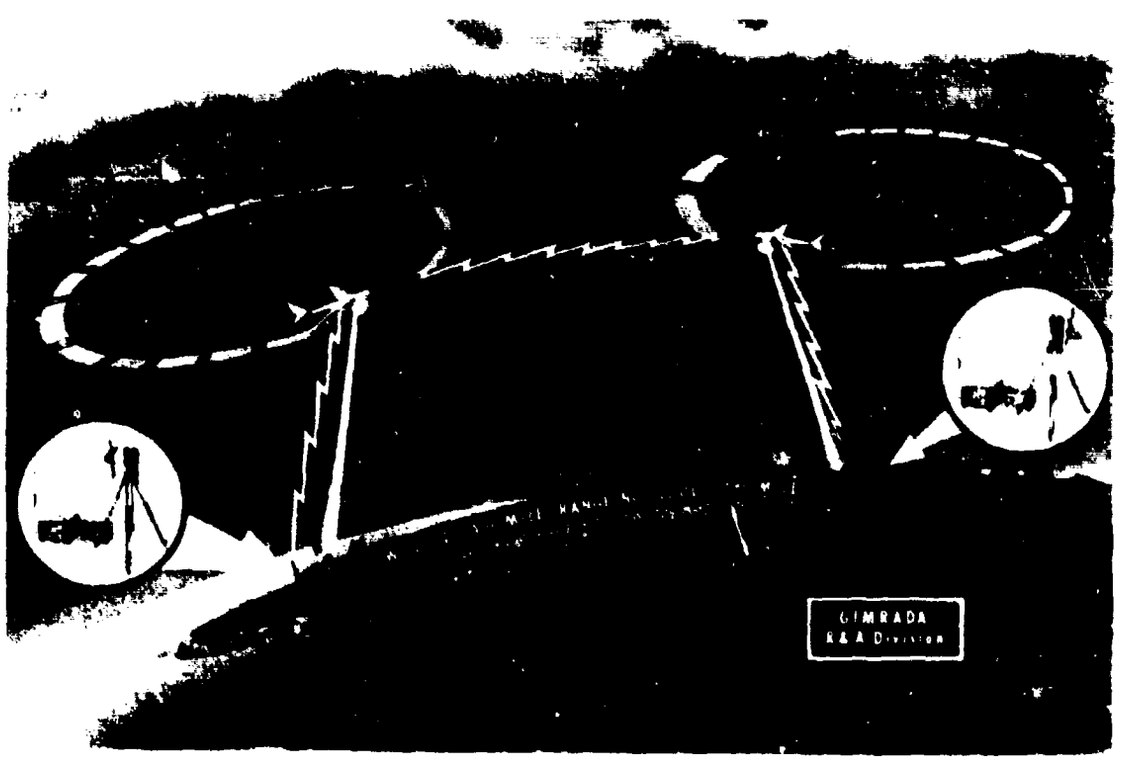

FIG. 2: BI-AERIAL METHOD FOR ALL-WEATHER OR EXTENDED SOLUTION

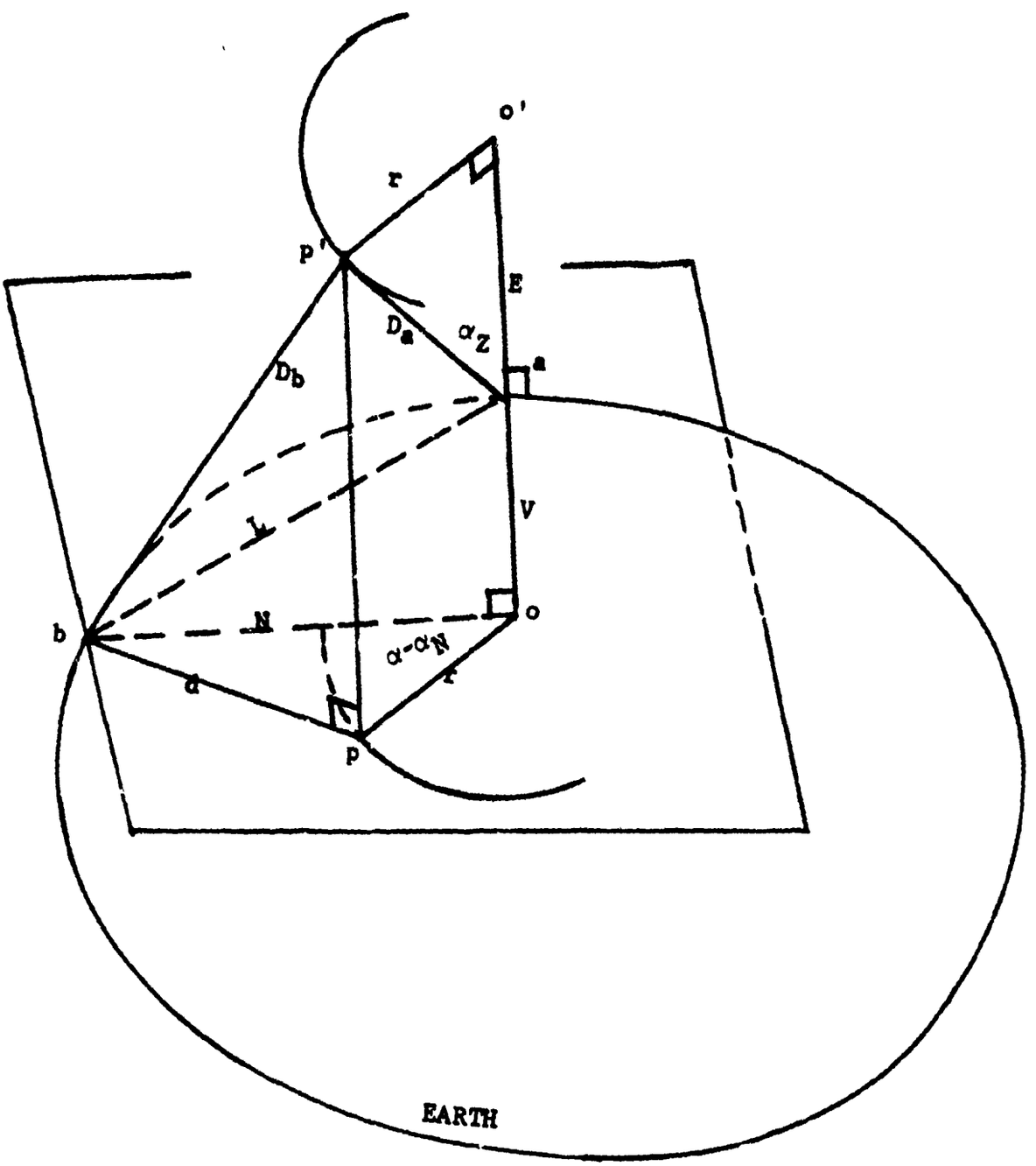

FIG. 3: BASIC GEOMETRY

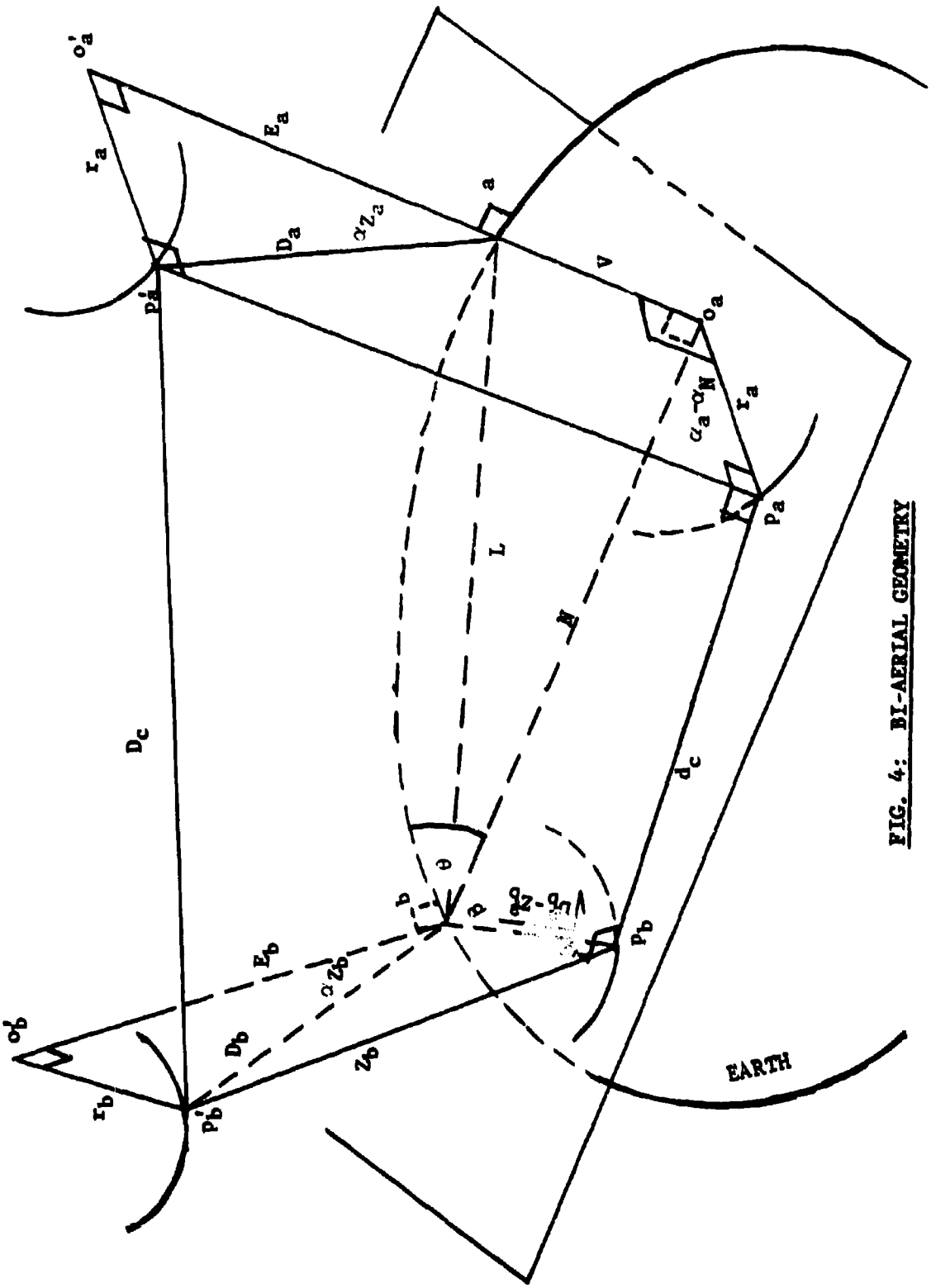

FIG. 4: BI-AERIAL GEOMETRY

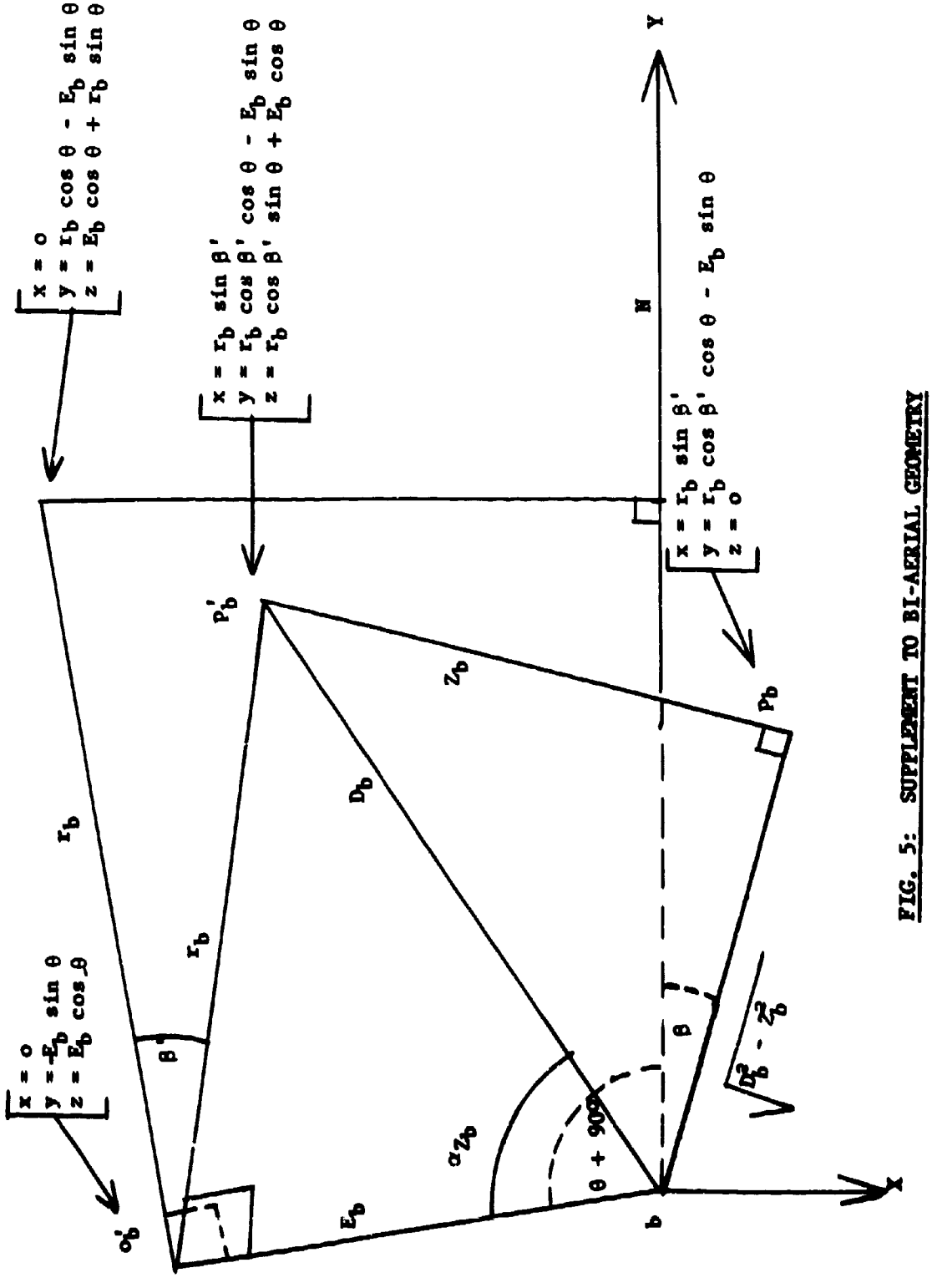

FIG. 5: SUPPLEMENT TO BI-AERIAL GEOMETRY

PHOSPHORUS, ARSENIC, AND BORON-CONTAINING FERROCENE DERIVATIVES

G. P. SOLLOTT, J. L. SNEAD, S. PORTNOY,
W. R. PETERSON, JR., and H. E. MERTWOY
FRANKFORD ARSENAL
PHILADELPHIA, PENNSYLVANIA

Previous work in these laboratories has produced the first known phosphorus-containing ferrocene derivatives, and has shown that contrary to the general behavior of aromatic compounds, ferrocene reacts with phosphorus trichloride under Friedel-Crafts conditions to give the tertiary phosphine (1).

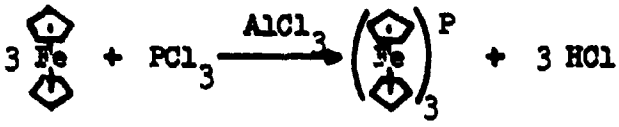

As an outgrowth of this work, it was recently demonstrated that ferrocene undergoes reactions with phenylphosphonous dichloride and diphenylphosphinous chloride in the presence of anhydrous aluminum chloride to give diferrocenylphenylphosphine and ferrocenyldiphenylphosphine, respectively (2).

$$2\ ArH + C_6H_5PCl_2 \xrightarrow{AlCl_3} (Ar)_2PC_6H_5 + 2\ HCl$$

$$ArH + (C_6H_5)_2PCl \xrightarrow{AlCl_3} ArP(C_6H_5)_2 + HCl$$

(Ar = ferrocenyl)

These compounds represent the first unsymmetrical tertiary phosphines prepared by a Friedel-Crafts process. The preparative method is facile and novel. Its usefulness lies in the fact that to produce these compounds, it is unnecessary to prepare an intermediate metallic derivative of ferrocene for interaction with the acid chlorides, as required by older methods (3).

The purpose of the present work is threefold: (a) to determine the scope of the new process for the synthesis of unsymmetrical

tertiary phosphines of ferrocene; (b) to determine the applicability of Friedel-Crafts reactions in the preparation of arsenic and boron-containing ferrocene derivatives; (c) to investigate the usefulness of lithioferrocenes in the preparation of ferrocene derivatives containing phosphorus, arsenic, and boron. This paper describes the results which have been obtained to date. The work should lead ultimately to the preparation of novel ferrocene polymers.

Results and Discussion

Unsymmetrical Tertiary Phosphines of Ferrocene by Friedel-Crafts Reactions.- Reactions of p-methoxy-, p-methyl-, p-chloro-, and p-cyanophenylphosphonous dichlorides with ferrocene under Friedel-Crafts conditions have been found to give, after thirty hours of refluxing in n-heptane, the corresponding tertiary phosphines, I, II, III, and IV, respectively, Table I, and/or phosphine oxides in yields shown in the Table.

Table I

Diferrocenyl-(substituted)phenylphosphines, 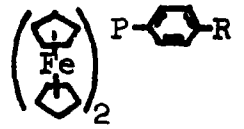

Phosphine	R =	Yield[a] %	Recovered ferrocene %
I	CH_3O	47 (17)	27
II	CH_3	73 (14)	16
III	Cl	53 (21)[b]	19
IV	CN	15 (15)	55

[a] Includes the phosphine isolated as its oxide, and recorded in parentheses.
[b] The oxide was obtained as the hemihydrate.

Formation of these compounds in this manner substantiates the mechanism suggested previously (1, 2), viz. trisubstitution on phosphorus occurs in a stepwise fashion. In the present instance, this may be represented as follows.

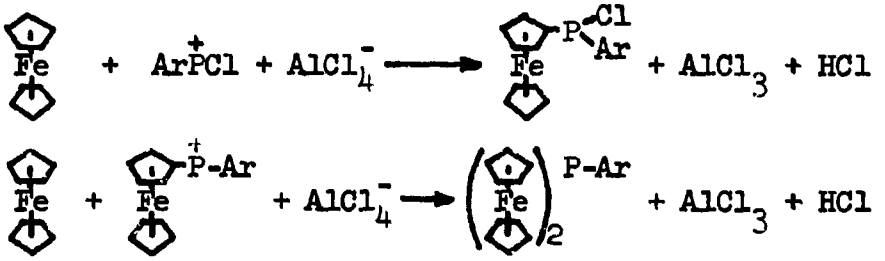

Diferrocenylphenylphosphine was previously obtained (2) in 75% yield (including 8% as the oxide) after a shorter period of reflux (twenty hours) employing the same molar ratio, 2:1:1, of ferrocene,

acid chloride, and aluminum chloride in n-heptane. It appears that chloro- and methoxyphenylphosphonous dichlorides have a significant retarding effect on the subsequent reaction with ferrocene to form the tertiary phosphine. In the case of methoxyphenyl, this retarding effect might be explained in terms of weakening of the positive charge on phosphorus in the intermediate electrophiles by resonance.

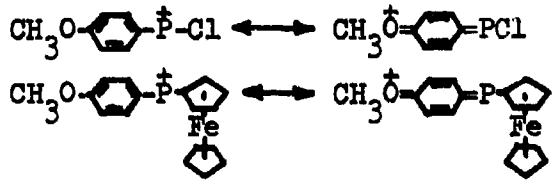

In the chlorophenyl case, although similar resonance forms can be written, the electron-withdrawing (inductive) effect of this group should also retard the initial dissociation process

by which the intermediate electrophile is produced. This latter mode of retardation should be even more pronounced in the case of the strongly electron withdrawing p-cyanophenyl group. The relatively low yield of product, and large recovery of ferrocene obtained from the reaction of p-cyanophenylphosphonous dichloride (Table I), however, is attributed in large part to experimental factors.

p-Cyanophenylphosphonous dichloride shows only slight solubility in n-heptane, and was thus added to the reaction flask (containing ferrocene in heptane) in the molten state rather than in solution. The resultant inhomogeneity of the reaction mixture may also account for the fact that only the oxide was isolated. Under more homogeneous conditions resulting from the use of an appropriate solvent, the phosphine should be isolable since in all other cases the phosphine was isolated in major amount. Like diferrocenylphenylphosphine (2), the pure diferrocenyl-(substituted)phenylphosphines are stable to air oxidation, but complexes of these are oxidized in the presence of aluminum chloride when air is not excluded from the refluxing reaction mixtures. Those phosphines which were isolated were readily converted to the corresponding quaternary salts on treatment with methyl iodide.

Substituted phenyl groups of widely divergent Hammett sigma values, -0.268 for p-methoxyphenyl to +0.660 for p-cyanophenyl (4), have been included in this investigation. The results show that the reaction of ferrocene with aromatic phosphonous dichlorides ($ArPCl_2$) under Friedel-Crafts conditions to give tertiary diferrocenylphosphines is general and of wide scope.

Friedel-Crafts Reaction of Ferrocene with Arsenic Trichloride.- That ferrocene undergoes trisubstitution on phosphorus under Friedel-Crafts conditions is strong evidence that the compound is a highly reactive nucleophile (2). It therefore seemed reasonable to

expect that reaction with arsenic trichloride under the same conditions would lead to trisubstitution on arsenic, since benzene has been reported to give the tertiary arsine (5), although not the tertiary phosphine (6).

It has been found, however, that ferrocene undergoes only monosubstitution on arsenic under a variety of experimental conditions. Ferrocenylarsenic oxide (V) was the only product obtained after hydrolysis of the reaction solids, and arose from ferrocenyldichloroarsine (VI) as precursor. Table II summarizes the results. Employing a 3:1:1 molar ratio of ferrocene, arsenic trichloride, and aluminum chloride in refluxing n-heptane for twenty hours gave the oxide in optimum, although modest yield.

When carbon disulfide was used as solvent, the product was isolated only in trace amount. With excess arsenic trichloride as solvent, the product could be isolated after heating the reaction mixture at 75-80° (Table II), but only intractable black solids were obtained after refluxing (130°). In most cases (Table II), ferrocene could be accounted for almost quantitatively.

Table II

Friedel-Crafts Reaction of Ferrocene with Arsenic Trichloride

Molar ratio, ferrocene: $AsCl_3$:$AlCl_3$	Solvent	Reflux time, hr.	Recovered ferrocene,[a] %	Yield of ferrocenylarsenic oxide (V), %
3:1:1	n-heptane	20	76 (8)	22
3:1:1	"	30	62 (6)	16
3:1:3	"	20	88 (18)	6
3:1:1.5	"	20	76 (12)	15
3:1:0.5	"	20	85 (3)	10
3:1:1	CS_2	20	90 (14)	1
1:3:0.75	$AsCl_3$	5[b]	82 (33)	5
1:3:0.75	"	20[b]	86 (30)	8

[a] Includes ferrocinium ion converted to ferrocene, and recorded in parentheses.
[b] The reaction mixture was heated at 75-80°.

— — — — — — — —

Although the structure of phenylarsenic oxide has not been established (7), ferrocenylarsenic oxide is formulated as a cyclic dimer (V) on the basis of its chemistry. Chemical transformations were performed giving ferrocenyldichloroarsine (VI), bis(ferrocenylchloroarsenic) oxide (VII), and bis(ferrocenylhydroxyarsenic) oxide (VIII) as indicated in the following scheme. The structure of oxide VII was confirmed by molecular weight determination.

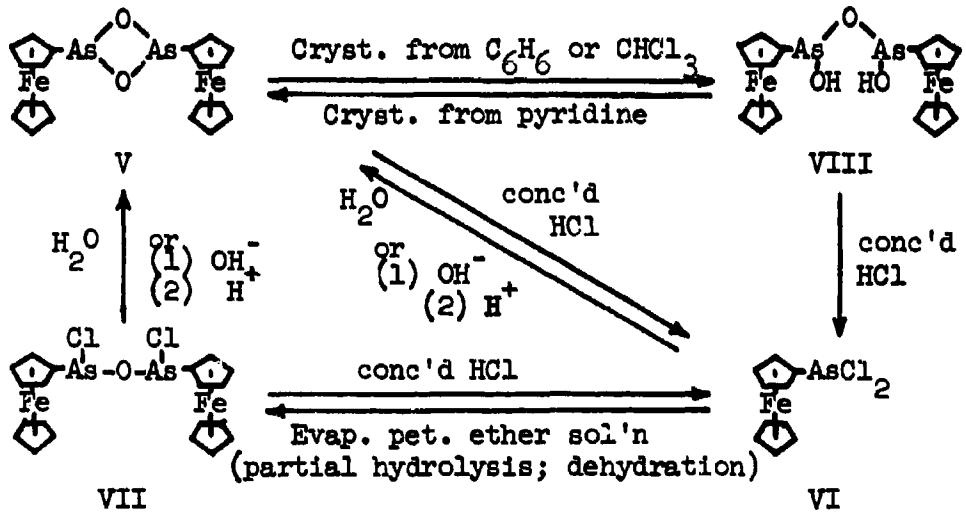

Bis(ferrocenylchloroarsenic) oxide (VII) was obtained from ferrocenyldichloroarsine (VI) by evaporation of its solution in petroleum ether (but not n-heptane), and could be hydrolyzed readily to oxide V. Oxides V, VII, and VIII were readily converted to the dichloroarsine (VI) by trituration with concentrated hydrochloric acid.

Ferrocenylarsenic oxide (V) is soluble in aqueous alkali, as is phenylarsenic oxide (7), and is probably converted to the salt, Va. Oxide V is regenerated on acidification. Prolonged heating of a solution of V in aqueous alkali gives insoluble VIII very likely via hydrolysis of the salt (Va) first formed, the equilibrium being shifted in the direction of VIII as VIII separates from solution.

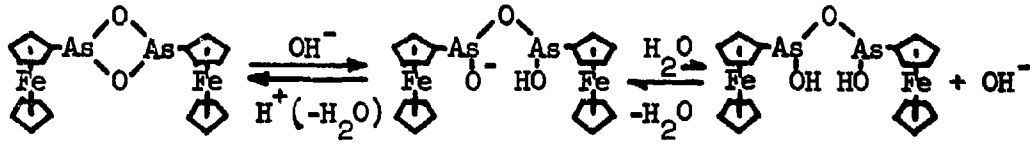

Attempts to crystallize V from chloroform or benzene, or merely heating V in ethanol produced insoluble VIII, apparently by addition of water across the oxide bridge. Oxide VIII is practically insoluble in all common solvents except pyridine. Attempted crystallization of VIII from that solvent produced oxide V by removal of a molecule of water. Freezing a solution of VIII in the same solvent, however, caused VIII to separate, indicating that in ordinary pyridine the following equilibrium exists, probably catalyzed by hydroxide ion present in the solvent.

$$V \underset{-H_2O}{\overset{H_2O}{\rightleftharpoons}} VIII$$

Compounds VII and VIII are the first examples of new classes of compounds of the type $(RAsCl)_2O$ and $(RAsOH)_2O$, respectively. The compounds discussed are the first known arsenic-containing ferrocene derivatives.

It is to be noted that the reaction of phosphorus trichloride in place of arsenic trichloride under conditions otherwise identical to the last case summarized in Table II, leads to a 10.5% yield of tertiary product and 4.2% of secondary product, besides 3.6% of primary product (1). The decreased reactivity of ferrocene in its reaction with arsenic trichloride relative to its reactivity with phosphorus trichloride, and relative to that of benzene in its reaction with arsenic trichloride (5) indicates feeble electrophilic character in the intermediate species, $C_5H_5FeC_5H_4\overset{+}{A}sCl$, due to the strongly electron-donating ferrocenyl group (8). On the other hand, the phenyl analog, $C_6H_5\overset{+}{A}sCl$, must be a relatively strong electrophile since it reacts further with benzene (5). It was therefore surprising that the reaction of ferrocene with phenyl dichlorcarsine under Friedel-Crafts conditions did not produce the ferrocenylphenylarsine. The reason for this is unclear.

Reaction of Ferrocene with Boron Trichloride under Friedel-Crafts Conditions.- Benzene has been reported to undergo monosubstitution on boron in a reaction with boron trichloride and aluminum metal (9). Both mono- and disubstitution are obtained, however, when benzene reacts with boron tribromide and aluminum chloride (10). In the case of ferrocene, mono- and 1,1'-diboronic acids have been prepared via the reaction of lithioferrocenes with butyl borate (11). However, no investigation of the behavior of ferrocene with boron trichloride under Friedel-Crafts conditions has been reported.

The aluminum chloride-catalyzed reaction of ferrocene with boron trichloride to produce hitherto unknown di- and triferrocenyl derivatives of boron appeared to be feasible from two standpoints: ferrocene is a highly reactive nucleophile; boron trichloride is a strong electrophile by virtue of the incomplete octet of electrons on boron. Unlike the phosphorus trichloride-aluminum chloride system, no interaction occurs between boron trichloride and aluminum chloride as such. The requisite electrophilic species, $\overset{+}{B}Cl_2$, appears to form under Friedel-Crafts conditions via a solvation step as follows (9).

$$ArH + BCl_3 \longrightarrow ArH{\cdot}BCl_3 \xrightarrow{AlCl_3} ArH\overset{+}{B}Cl_2AlCl_4^-$$

Ferrocene was expected to serve in the capacity of ArH.

We have now found that the reaction of ferrocene leads to monosubstitution on boron, and have found no evidence to indicate that disubstitution occurs under the conditions investigated to date. With ferrocene, boron trichloride, and aluminum chloride in a 3:1:1 molar ratio in refluxing heptane (twenty hours), ferrocenylboronic acid (IX) was obtained in 27% yield, arising by hydrolysis of the reaction product, ferrocenyldichloroborane ($C_5H_5FeC_5H_4BCl_2$). The boronic acid (IX) was dried under reduced pressure to produce ferrocenylboronic anhydride trimer (X). Boronic acids, in general, are known to give only cyclic, trimeric anhydrides (boroxoles) on undergoing dehydration (12). The trimeric structure of X was confirmed by molecular weight determination in camphor. The anhydride has not been reported

previously by Russian (11) or American (13) workers in their investigations of ferrocenylboronic acid prepared from lithioferrocene.

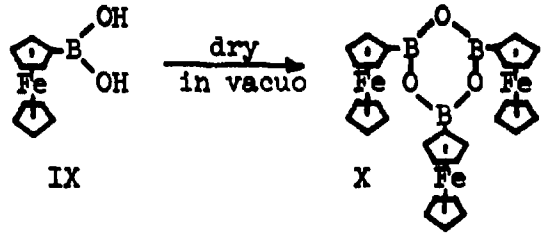

IX X

The anhydride was converted to the boronic acid by dissolving in 95% ethanol, or by acidification of its solution in aqueous alkali. Mulling the boronic acid in hexachlorobutadiene caused dehydration to the anhydride, as determined by infrared spectrum. Mulling the acid in mineral oil (Nujol) did not produce this effect.

Phosphorus and Arsenic-Containing Ferrocene Derivatives from Lithioferrocenes.- Acetylation of ferrocene with excess acetyl chloride and aluminum chloride readily leads to 1,1'-diacetylferrocene (14). Attempts to obtain ferrocene derivatives with phosphorus attached to both cyclopentadienyl rings by Friedel-Crafts reactions, however, have given only negative results. For example, ferrocenyldiphenylphosphine did not react with diphenylphosphinous chloride to give the expected biphosphine. This is attributed to formation of an interfering salt complex between the monophosphine and aluminum chloride.

1,1'-Bis(diphenylphosphino)ferrocene (XI) and ferrocenyldiphenylphosphine (XII) have now been prepared in 14% and 30% yields, respectively, by reaction of a mixture of mono- and dilithioferrocenes with diphenylphosphinous chloride.

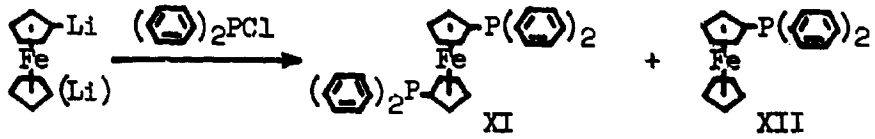

XI XII

Phosphine XII was shown by infrared spectrum and mixed melting point determination to be identical to the product prepared under Friedel-Crafts conditions (2). The biphosphine (XI) is the first ferrocene derivative containing two atoms of phosphorus. The bis-quaternary salt was readily obtained upon treatment of XI with excess methyl iodide.

Lithioferrocenes also have been employed in a reaction with diphenylchloroarsine to produce 1,1'-bis(diphenylarsino)ferrocene (XIII) and ferrocenyldiphenylarsine (XIV), compounds not preparable by Friedel-Crafts reactions.

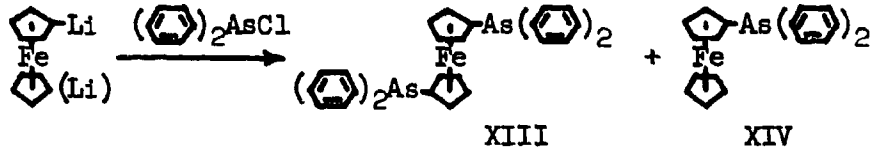

XIII XIV

Although isolated in less than 10% yield, these compounds should be obtainable in greater yield through development of improved procedures for working up the unusually complex reaction mixture. The biarsine (XIII) is the first ferrocene derivative containing two arsenic atoms.

Experimental[a]

Diferrocenyl-(substituted) phenylphosphines (I-IV) and Derivatives.- The tertiary phosphines and oxides (I, II, III, IV; Table I) were prepared from the appropriately substituted phenylphosphonous dichlorides (0.1 mole) by reactions with ferrocene (0.2 mole; 37.2 g.) and anhydrous aluminum chloride (0.1 mole; 13.4 g.) in refluxing n-heptane (30 hr.), analogous to the reaction previously reported for the preparation of diferrocenylphenylphosphine and its oxide (2). p-Methoxyphenylphosphonous dichloride was prepared by the method of Viout (15). The procedure described by Buchner and Lockhart (16) was used for the preparation of p-tolylphosphonous dichloride. p-Chlorophenylphosphonous dichloride (distilling 121-122° at 13 mm.) was prepared by a reaction modeled after this method. p-Cyanophenylphosphonous dichloride was synthesized according to the procedure outlined by Quin and Humphrey (17). Because of the limited solubility of the nitrile in n-heptane, this reactant was added dropwise in the molten state to ferrocene in n-heptane. Only the phosphine oxide was isolated in this case, and shown to be a hemihydrate. Amounts of ferrocene recovered from the reaction mixtures are listed in Table I. Quaternary methiodides usually were prepared from the phosphines and methyl iodide in benzene, as previously (2). Diferrocenyl-p-methoxyphenylphosphine (I) was crystallized from ethanol giving an orange powder, m.p. 158-160° (dec.); yield 15.4 g. (30%).

Anal. Calcd. for $C_{27}H_{25}Fe_2OP$: C, 63.81; H, 4.96; Fe, 21.98; P, 6.10. Found: C, 64.16; H, 5.58; Fe, 22.13; P, 6.17.

Phosphine I oxide was obtained as orange needles from isopropyl alcohol, m.p. 111-113°; yield 8.9 g. (17%).

Anal. Calcd. for $C_{27}H_{25}Fe_2O_2P$: C, 61.87; H, 4.83; P, 5.92 Found: C, 62.39; H, 4.91; P, 5.97.

Phosphine I methiodide, not crystallizable from alcohols, was washed with benzene; m.p. 87-89°.

Anal. Calcd. for $C_{28}H_{28}Fe_2IOP$: C, 51.73; H, 4.34; I, 19.52; P, 4.76. Found: C, 52.40; H, 4.66; I. 19.15; P, 4.66.

Diferrocenyl-p-tolylphosphine (II) was crystallized from ethanol affording a yellow powder, m.p. 165-167° (dec.); yield 28.8 g. (59%).

Anal. Calcd. for $C_{27}H_{27}Fe_2P$: C, 65.62; H, 5.51; Fe, 22.60; P, 6.27. Found: C, 66.30; H, 5.50; Fe, 22.22; P, 6.24.

Phosphine II oxide was obtained as a yellow powder from benzene-heptane, m.p. 151-153° (dec.); yield 7.1 g. (14%).

Anal. Calcd. for $C_{27}H_{27}Fe_2OP$: C, 63.56; H, 5.33; P, 6.07. Found: C, 64.36; H, 5.64; P, 5.87

---

[a] Melting points are uncorrected. The analyses were performed by Schwarzkopf Microanalytical Laboratory, Woodside, N. Y.

Phosphine II methiodide was crystallized from isopropyl alcohol giving dark orange crystals, m.p. 121-122°.

Anal. Calcd. for $C_{28}H_{30}Fe_2IP$: C, 52.86; H, 4.75; I, 19.95; P, 4.87. Found: C, 53.52; H, 5.26; I, 19.14; P, 4.82.

Diferrocenyl-p-chlorophenylphosphine (III) was crystallized from ethanol giving a yellow powder, m.p. 166-168° (dec.); yield 16.4 g. (32%).

Anal. Calcd. for $C_{26}H_{22}ClFe_2P$: C, 60.92; H, 4.33; Cl, 6.92; P, 6.04. Found: C, 60.97; H, 4.62; Cl, 6.94; P, 6.00.

Phosphine III oxide was crystallized from benzene giving orange crystalline clusters, m.p. 162-164° (dec.); yield 11.0 g. (21%).

Anal. Calcd. for $C_{26}H_{22}ClFe_2OP$: C, 59.08; H, 4.20; Cl, 6.71; P, 5.86. Found: C, 59.50; H, 4.48; Cl, 6.48; P, 5.75.

Phosphine III methiodide was prepared from the phosphine in n-heptane. Not crystallizable from alcohols, the methiodide was washed with benzene; m.p. 173-175°.

Anal. Calcd. for $C_{27}H_{25}ClFe_2IP$: C, 49.55; H, 3.85; Cl, 5.42; I, 19.39. Found: C, 49.98; H, 4.05; Cl, 5.29; I, 18.95.

Phosphine IV oxide hemihydrate was crystallized from n-heptane giving an orange powder, m.p. 207-208° (dec.)[b]; yield 7.4 g. (15%).

Anal. Calcd. for $(C_{27}H_{22}Fe_2NOP)_2 \cdot H_2O$: C, 61.40; H, 4.39; N, 2.65; P, 5.87. Found: C, 61.80; H, 4.73; N, 2.76; P, 5.76.

Ferrocenylarsenic Oxide (V) and Derivatives (VI-VIII).- The reaction of 55.8 g. (0.3 mole) of ferrocene, 18.1 g. (0.1 mole) of arsenic trichloride, and 13.3 g. (0.1 mole) of anhydrous aluminum chloride was performed in a total of 600 ml. of refluxing n-heptane (20 hr.) analogously to reactions of acid chlorides of phosphorus described previously (2). Extraction of the reaction solids with 2N sodium hydroxide, and acidification of the extract at 5° with concentrated hydrochloric acid gave 6.1 g. (22%) of ferrocenylarsenic oxide (V) as a yellow powder, m.p. 275.5-276° (dec.).

Anal. Calcd. for $(C_{10}H_9AsFeO)_2$: C, 43.53; H, 3.28; As, 27.14; Fe, 20.24. Found: C, 43.17; H, 3.52; As, 27.44; Fe, 19.97.

A solution of oxide V in chloroform (or benzene) was concentrated and cooled causing bis(ferrocenylhydroxyarsenic) oxide (VIII) to separate as a light yellow powder, m.p. 266-267° (dec.).

Anal. Calcd. for $C_{20}H_{20}As_2Fe_2O_3$: C, 42.15; H, 3.54; As, 26.29; Fe, 19.60. Found: C, 42.12; H, 3.41; As, 25.83; Fe, 18.78.

Oxide V was triturated with concentrated hydrochloric acid. Extraction with n-heptane, and evaporation of the solvent under an air stream gave ferrocenyldichloroarsine (VI) in 94% yield, in the form of golden leaflets, m.p. 63-64.5°. The product crystallized from n-heptane as an orange powder. It hydrolyzed slowly in air, or rapidly on trituration with water, to oxide V. Trituration of oxides VII and VIII with concentrated hydrochloric acid also produced the dichloroarsine (VI).

Anal. Calcd. for $C_{10}H_9AsCl_2Fe$: C, 36.30; H, 2.74; As, 22.64;

[b] The compound was first dried at 110° in vacuo for three hours.

Cl, 21.43; M.W. 330.8. Found: C, 36.95; H, 3.02; As, 22.33; Cl, 21.43; M.W. 323 (camphor).

A solution of ferrocenyldichloroarsine (VI) in petroleum ether (b.p. 30-75°) was evaporated slowly to dryness under an air stream. The residue was stirred with petroleum ether at room temperature, and the insoluble solid removed by filtration. Additional solid was obtained by repetition of this procedure, employing the filtrate each time. The solid was crystallized from n-heptane to give bis(ferrocenylchloroarsenic) oxide (VII) as a yellow powder, m.p. 118.5-120°. Oxide VII hydrolyzed slowly in air, or rapidly on trituration with water, to oxide V.

Anal. Calcd. for $C_{20}H_{18}As_2Cl_2Fe_2O$: C, 39.59; H, 2.99; As, 24.69; Cl, 11.69; M.W. 606.8. Found: C, 40.37; H, 3.33; As, 24.01; Cl, 11.06; M.W. 585 (camphor), 594 (osmotically in benzene).

Ferrocenylboronic Acid (IX) and its Anhydride (X).- The reaction of 39.0 g. (0.21 mole) of ferrocene, 8.2 g. (0.07 mole) of boron trichloride, and 9.3 g. (0.07 mole) of anhydrous aluminum chloride was run in 250 ml. of refluxing n-heptane (20 hr.) analogously to the reactions of acid chlorides of phosphorus described previously (2), with one notable exception. The reaction flask was initially cooled to -70° while gaseous boron trichloride, previously condensed in a dry-ice-acetone bath, weighed, then allowed to warm to room temperature, was led into the heptane-ferrocene-aluminum chloride mixture. After a period of warming to room temperature with stirring, the reaction mixture was refluxed. Extraction of the reaction solids with 2N sodium hydroxide, and acidification of the extract at 0° with 2N sulfuric acid gave 13.2 g. (27%) of ferrocenylboronic acid (IX) as a yellow powder, m.p. 143-145°; lit. 143-148° (11). The boronic acid was dried under reduced pressure for three days over phosphorus pentoxide, then crystallized from n-heptane giving orange, crystalline ferrocenylboronic anhydride trimer (X), m.p. 263-265°.

Anal. Calcd. for $(C_{10}H_9BFeO)_3$: C, 56.70; H, 4.28; B, 5.11; M.W. 635.5. Found: C, 57.06; H, 4.51; B, 5.31; M.W. 627 (camphor).

1,1'-Bis(diphenylphosphino)ferrocene (XI) and Ferrocenyldiphenylphosphine (XII).- A mixture of mono- and dilithioferrocenes was prepared by a method based on that of Rausch et al (18), using 0.6 mole of n-butyllithium and 18.6 g. (0.1 mole) of ferrocene in 500 ml. of a 1:1 mixture of tetrahydrofuran and ether, with 20 hr. of stirring at room temperature. After dropwise addition of the lithium reagents (2 hr. without cooling) to 122.0 g. (0.55 mole) of commercially available diphenylphosphinous chloride in 500 ml. of ether, the mixture was refluxed for 20 hr. Evaporation of solvent from the liquid phase produced a dark red oil which yielded 7.8 g. (14%) of 1,1'-bis-(diphenylphosphino) ferrocene (XI), and 11.4 g. (30%) of ferrocenyldiphenylphosphine (XII). The biphosphine (XI) was crystallized from ethanol giving yellow needles, m.p. 182-184°.

Anal. Calcd. for $C_{34}H_{28}FeP_2$: C, 73.66; H, 5.09; Fe, 10.07; P, 11.18. Found: C, 73.90; H, 5.26; Fe, 10.50; P, 11.10.

The monophosphine (XII) was crystallized from n-heptane affording

orange crystals, m.p. 122-124°, which caused no melting-point depression on admixture with an authentic sample (2). A sample of the biphosphine (XI) was dissolved in excess methyl iodide. The bis-quaternary methiodide separated as an orange powder in less than one min., and was washed with benzene; m.p. 223-228° (dec.).

Anal. Calcd. for $C_{36}H_{34}FeI_2P_2$: C, 51.58; H, 4.09; I, 30.28; P, 7.39. Found: C, 50.75; H, 4.51; I, 30.29; P, 7.50.

1,1'-Bis-(diphenylarsino)ferrocene (XIII) and Ferrocenyldiphenylarsine (XIV).- Diphenylchloroarsine was prepared by the method of Barker et al (19). Arsines XIII and XIV were prepared by the reaction of a mixture of mono- and dilithioferrocenes with diphenylchloroarsine using a procedure paralleling that employed for the synthesis of the phosphorus analogs, XI and XII, above. The red oil remaining after evaporation of solvent from the liquid phase of the reaction mixture yielded 1.3 g. (2%) of 1,1'-bis(diphenylarsino)-ferrocene (XIII), and 1.7 g. (4%) of ferrocenyldiphenylarsine (XIV). The biarsine (XIII) was crystallized from n-heptane giving a yellow powder, m.p. 145-146.5°.

Anal. Calcd. for $C_{34}H_{28}As_2Fe$: C, 63.58; H, 4.39; As, 23.33; Fe, 8.70. Found: C, 62.83; H, 4.51; As, 23.57; Fe, 9.21.
The monoarsine (XIV) was crystallized from n-heptane affording a yellow powder, m.p. 119.5-121.5°.

Anal. Calcd. for $C_{22}H_{19}AsFe$: C, 63.80; H, 4.62; As, 18.09; Fe, 13.49; Found: C, 63.75; H, 4.91; As, 18.04; Fe, 13.49.

Infrared Spectra of the Phosphorus, Arsenic, and Boron-Containing Ferrocene Derivatives.- Infrared spectra were obtained from Nujol mulls employing a Perkin-Elmer, Model 321, spectrophotometer. All spectra, except those of the biphosphine (XI) and biarsine (XIII), show the usual absorptions near 1110 and 1005 cm.$^{-1}$ characteristic of monosubstituted ferrocenes (14). All compounds show typical ferrocene bands in the regions, 3060-3100 cm.$^{-1}$, 1410-1430 cm.$^{-1}$, and 810-830 cm.$^{-1}$ (20). All ferrocene derivatives containing phosphorus and arsenic absorb in the regions, 1310-1320 cm.$^{-1}$ and 1015-1045 cm.$^{-1}$, which were assigned earlier (1) to the ferrocenyl-phosphorus group. The assignment is now extended to include the ferrocenyl-arsenic group.

Summary and Conclusions

Diferrocenyl-(substituted)phenylphosphines have been prepared by reactions of p-methoxy-, p-methyl-, p-chloro-, and p-cyanophenylphosphonous dichlorides with ferrocene under Friedel-Crafts conditions. The results show that the new process for preparing unsymmetrical tertiary phosphines from ferrocene and aromatic phosphonous dichlorides ($ArPCl_2$) is general and of wide scope.

Ferrocene has been found to react with arsenic trichloride in the presence of anhydrous aluminum chloride to give only monosubstitution on arsenic under a variety of experimental conditions. Ferrocenylarsenic oxide, formulated as a dimer, was converted to ferrocenyldichloroarsine, and bis(ferrocenylchloroarsenic) and bis-(ferrocenylhydroxyarsenic) oxides. These compounds are the first

known arsenic-containing ferrocene derivatives. The latter oxides are the first compounds of the type $(RAsCl)_2O$ and $(RAsOH)_2O$.

Ferrocenylboronic acid has been prepared via the reaction of ferrocene with boron trichloride under Friedel-Crafts conditions. The boronic acid was converted to the previously unknown ferrocenylboronic anhydride trimer.

1,1'-Bis-(diphenylphosphino)ferrocene and ferrocenyldiphenylphosphine, and their arsenic analogs, have been prepared by reactions of diphenylphosphinous chloride and diphenylchloroarsine, respectively, with mixtures of mono- and dilithioferrocenes. The biphosphine and biarsine are the first ferrocene derivatives containing two atoms of phosphorus and arsenic, respectively.

The work described herein should lead to the preparation of novel ferrocene polymers. Phosphorus, arsenic, and boron-containing ferrocene derivatives and polymers are potentially useful for applications related to lubricants, plastics, and adhesives. They should be useful for the formation of novel molecular complexes of theoretical and practical interest, and may show semi-conductive properties as well as properties of biological significance.

Bibliography

1. G. P. Sollott and E. Howard, Jr., J. Org. Chem., 27, 4034 (1962).
2. G. P. Sollott, H. E. Mertwoy, S. Portnoy, and J. L. Snead, ibid., 28, 1090 (1963).
3. G. M. Kosolapoff, "Organophosphorus Compounds," John Wiley, New York, N. Y., 1950, p. 16.
4. D. S. McDaniel and H. C. Brown, J. Org. Chem., 23, 420 (1958).
5. H. Wieland and A. Kulenkampff, Ann., 431, 30 (1923); cf. Chem. Abst., 17, 1783 (1923).
6. Reference 3, pp. 43-46.
7. E. G. Rochow, D. T. Hurd, and R. N. Lewis, "The Chemistry of Organometallic Compounds," John Wiley, N. Y., 1957, p. 207.
8. E. M. Arnett and R. D. Bushick, J. Org. Chem., 27, 111 (1962).
9. E. L. Muetterties, J. Am. Chem. Soc., 82, 4163 (1960).
10. Z. J. Bujwid, W. Gerrard, and M. F. Lappert, Chem. and Ind. (London), 1091 (1959).
11. A. N. Nesmeyanov, V. A. Sazonova, and V. N. Drozd, Doklady Akad. Nauk S.S.S.R., 126, 1004 (1959).
12. M. F. Lappert, Chem. Revs., 56, 959 (1956); W. Gerrard, "The Organic Chemistry of Boron," Academic Press, London, 1961, p. 68.
13. H. Shechter and J. F. Helling, J. Org. Chem., 26, 1034 (1961).
14. M. Rosenblum and R. Woodward, J. Am. Chem. Soc., 80, 5443 (1958).
15. M. P. Viout, J. Recherches Centre, Natl. Recherche Sci. Labs., Paris, No. 28, 15 (1954); cf. Chem. Abst., 50, 7077d (1956).
16. B. Buchner and L. Lockhart, Jr., J. Am. Chem. Soc., 73, 755 (1951).
17. L. D. Quin and J. S. Humphrey, Jr., ibid., 83, 4124 (1961).
18. M. Rausch, E. O. Fischer, and H. Grubert, ibid., 82, 76 (1960).
19. R. L. Barker, E. Booth, W. E. Jones, and F. N. Woodward, J. Soc. Chem. Ind., 68, 277 (1949).
20. E. Lippincott and R. Nelson, J. Am. Chem. Soc., 77, 4990 (1955).

THE MECHANISM OF PREFERENTIAL ABLATION

B. STEVERDING
U. S. ARMY MISSILE COMMAND
REDSTONE ARSENAL, ALABAMA

INTRODUCTION: Ablative heat shielding is a very effective means of reducing the heat transfer rate of high speed bodies. The ablation process is based on the principle that the heat flow into the body can be absorbed by the flux of material away from the body. Because it is intended to keep the interior of the body cool, the heating must be restricted to a thin surface layer and, preferentially, to the material which is to be ablated. Therefore, the heat resistivity and heat capacity of the body should be as high as possible.

In liquid ablation, material may be removed by two competitive loss mechanisms -- flow to the rear and evaporation. Actually a third loss mechanism, spattering, is possible (1), but this process will be ignored in the calculations to follow.

Because the heat of evaporation is much greater than the heat of fusion, and because the injected vapor causes the gas boundary layer to increase in thickness and thus reduces heat transfer and shear, the amount evaporated should be as large as possible. For subliming materials this condition would always be realized. However, confining the selection of materials for ablation cooling to subliming materials would unduly restrict the number of possible candidates; most materials, many of them with otherwise meritorious property spectra, liquefy before they evaporate and form a thin film on the body surface. In order to keep the fluid flow in this film to a minimum, the viscosity of the liquid should be high. The ablative process is completely automatic: with increased heat input, more material will melt and evaporate.

Because the heat conductivity of the normal insulating materials increases with the temperature, it becomes more and more difficult to provide heat shielding at very high temperatures and where heavy cross sections of the insulating material have to be avoided because of weight limitations. Fortunately the high heat-shielding capabilities which ceramics, glasses, and other insulators have at

low temperatures may be regained or even virtually improved in an ablative cooling process. This is possible because the diffusion of heat to the interior of the body is balanced by the convection of heat-absorbing material to the surface, as expressed in the following formula:

$$\frac{d}{dy}\left(k\,\frac{dT}{dy}\right) = \dot{m}c\,\frac{dT}{dy}$$

where $\dot{m}$ = ablative loss rate, k = heat conductivity, and c = heat capacity. The solution of this equation is $T = T_b + \left(T_w - T_b\right)e^{\dot{m}cy/k}$, with T_w = wall temperature, and T_b = temperature in body interior. A thickness of the thermal layer θ may now be defined as

$$\theta = \int_{-\infty}^{0} \frac{T - T_b}{T_w - T_b}\,dy = \frac{k}{\dot{m}c} \qquad (1)$$

When a material has a thermal conductivity at room temperature of k_o and at the temperature T a thermal conductivity equal to 10 k_o, the latter high conductivity can be virtually reduced to its room temperature value by making the factor $\dot{m}c = 10$. Since the value of c increases with temperature, only part of the effect must be contributed by $\dot{m}$.

The suitability of a material for effective ablation cooling depends on a wide property spectrum in which heat capacity, viscosity, heats of fusion and evaporation, and heat conductivities in the solid, liquid, and gaseous states play important roles. But there is reason to believe that the structure of this property spectrum has not been thoroughly explored, and that there are physicochemical effects which may be mobilized to further improve ablation performance. One area which has received little attention is the complex of surface and interface phenomena. Wettability and surface tension are responsible for the stability of the liquid film and its coagulation into droplets. Since ablation is to a large extent the transport of matter through surfaces or interfaces, the physicochemical constitution of these will have a great influence on ablation characteristics. The constitution of a surface is most decisively altered by surface-active ingredients. Even an ingredient with a low concentration in the bulk of the liquid can have a high concentration in the surface. Adding small amounts of a surface-active medium to a liquid ablator will leave the bulk properties such as viscosity and thermal conductivity practically constant, and will only change the surface properties. Therefore its effect, being strictly additive, is easy to estimate.

METHODS FOR IMPROVING ABLATION EFFICIENCY: Ablation efficiency A_{eff} is defined by

$$\frac{q_o}{\dot{m}} = A_{eff} \qquad (2)$$

where q_c is the rate of heat transfer to a nonablating body. Introducing the definitions of the constituent terms yields

$$A_{eff} = c_b (T_w - T_b) + L_m + \frac{2}{3} c_L (T_i - T_w) + \left[\frac{1}{3} c_L (T_i - T_w) + L_v + \bar{c}_p \left(1 - \frac{1}{3} Pr^{-0.6}\right)(T_e - T_i) \right] \frac{\dot{m}_i}{\dot{m}} \quad (3)$$

where c_b and c_L = thermal capacities of solid and liquid, respectively; L_m and L_v = latent heats of fusion and evaporation; $\bar{c}_p$ = average specific heat in boundary layer; $\dot{m}_i$ = mass loss by evaporation.

The greatest contribution to A_{eff} is from the last term. This term is multiplied by $\dot{m}_i/\dot{m}$, to indicate that ablation efficiency is decisively influenced by the relative rates of the two competitive processes, evaporation and the backward flow of the liquid film. The efficiency is high when the ratio of evaporation to flow is large. The evaporation rate or the vapor pressure of a binary system depends on the temperature and the composition of the surface. Binary phase systems in which the total vapor pressure is larger than that of ideal solutions (Fig. 1) would serve this purpose, provided that in such a system surface activity occurs. Surface activity is created when the heterophobia between the solute and the solvent is sufficient to force part of the solvent out of the solution into the surface. The increase in vapor pressure in certain phase systems is caused by the same heterophobia, so that it may be assumed that both phenomena occur in most cases simultaneously. The rate of evaporation, and therefore the ablation efficiency, can often be improved by addition of an appropriate surface-active ingredient, and the degree of improvement possible can be calculated. Since the surface-active ingredient has a high concentration in the surface and the surface layers are ablated at a faster rate than the bulk material, the surface-active ingredient will disappear at a faster rate than will the other constituents. Preferential ablation is therefore caused by surface activity.

The surface-active constituent can only be effective when its concentration in the surface is not excessively reduced by ablative loss. The transport provisions for replenishing the surface layer must be effective enough that a certain concentration Γ, which is smaller than the equilibrium value but larger than the bulk concentration, can be maintained. In a laminar layer the ingredient must reach the surface by diffusion. This diffusion flow is influenced by the thickness of the liquid layer and the evaporation rate, which in turn are functions of the stream conditions. Only with a sufficiently high diffusion coefficient can this type of transport be synchronized to the rate of ablative loss. The diffusional transport would be an especially important factor in improving liquid film cooling.

Viscous ablating materials such as glasses have a low diffusion coefficient, so that preferential ablation and the corresponding improvement of ablation characteristics are difficult to realize by diffusion transport alone. However, when gas bubbles are generated during the ablation process either by degassing, boiling, or decomposition of the substrate (fiberglass-reinforced ablation materials), the surface-active ingredient can be transported to the surface by means of the gas bubbles. As bubbles rise to the surface they collect the surface-active agent until their surface reaches equilibrium concentration and deliver this amount to the surface of the liquid film. If the released gas volume is large, the free surface may reach the equilibrium concentration Γ_o or the surface may even be somewhat supercharged so that back diffusion will occur. This transport mechanism, under the condition indicated, is independent of film thickness and evaporation rate, and consequently much simpler to treat mathematically than is diffusion in a laminar layer.

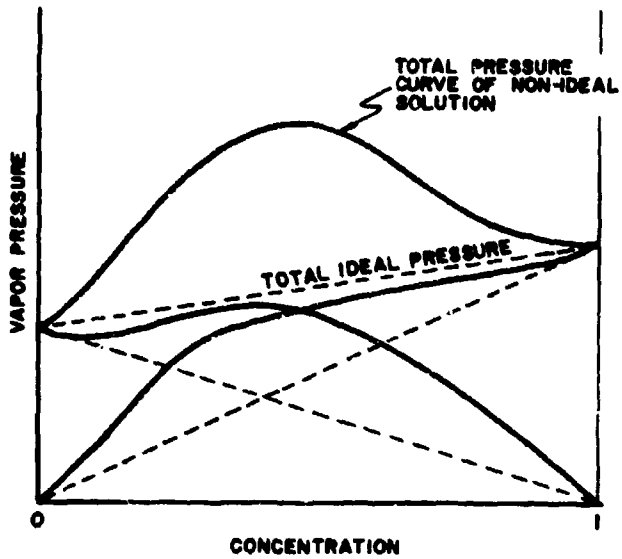

Fig. 1 BINARY SYSTEM WITH INCREASED TOTAL VAPOR PRESSURE

Preferential ablation caused by bubble formation was observed on recovered reentry nose cones (2). The component which disappeared preferentially from the silica glass was B_2O_3. Boron oxide is a competitive glass former with a different coordination number and it may therefore not easily be incorporated into the SiO_4 network. It was not determined if all glass formers with different coordination numbers exhibit surface activity when mixed with each other. In some cases the coordination number of the solute depends on its concentration and may, in diluted solutions, equal the coordination number of the solvent.

In order to calculate the degree of ablation, a value for $\frac{\partial\sigma}{\partial c}$ must be known, as will be discussed later. An approximate value

may be obtained by the sessile drop method. A small piece of silica-alumina glass of known weight was heated on a graphite plate at the estimated reentry temperature of 1700-1800°C. The glass melted and formed a nonwetting droplet. By adding a small amount of B_2O_3 powder, the droplet shape changed abruptly, the height of the droplet decreased by a factor of four, and the glass wetted the graphite surface. The surface concentration of B_2O_3 can thus be calculated from Gibbs' law.

Thermodynamic calculation showed that B_2O_3 was the only constituent of the glass which would be chemically reduced to any degree by graphite at the reentry temperature according to the reaction:

$$B_2O_3 + C \rightleftharpoons B_2O_2 + CO$$

The increase in wettability is probably due to this reaction. A high wettability stabilizes the liquid film and prevents droplet formation. The above chemical reaction is endotherm and develops gases which initiate injection cooling. Because of the high viscosity of the melt the reaction rates are small, and no substantial contribution to cooling can be expected from the endothermal effect at the indicated temperature. The addition of B_2O_3 to ablative silica glasses therefore serves a multitude of practical purposes, but only its effect on surface activity will be investigated in further detail in this paper.

Generally it may be stated that the best ablation material for a given reentry condition may still be improved by the addition of a surface-active agent which increases the total vapor pressure. The degree to which this is possible depends on how large a surface concentration of the surface active agent can be maintained despite ablation. If the extent of preferential ablation is known, the degree of improvement in performance can be calculated.

PREFERENTIAL ABLATION OF LAMINAR LIQUID LAYERS: When the equilibrium distribution of surface-active substances is disturbed by ablation, a concentration gradient will develop within the liquid layer so that the impoverished surface layer is replenished by diffusion. Figure 2 shows the development of a concentration gradient from the beginning of ablation until a nearly linear distribution is established.

The relation between the concentration in the surface layer Γ_o and the concentration in the bulk of the liquid c_o is expressed by Gibbs' law:

$$\Gamma_o = -\frac{c_o}{RT}\frac{\partial \sigma}{\partial c} \qquad (4)$$

where σ is the surface tension, T the absolute temperature, and R the gas constant.

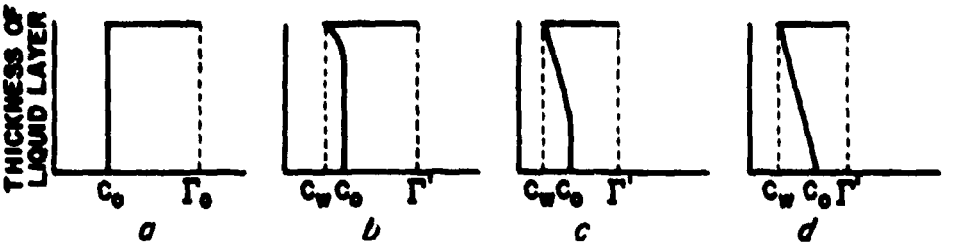

Fig. 2 CONCENTRATION

In a small cylindrical control volume (Fig. 3) around the gas-liquid surface, the mass transfer balance through the various surfaces may be expressed by the following equation, providing the height of the little cylinder is very small compared with its diameter:

$$\dot{m}_i c_w - \rho_L D \frac{\partial c}{\partial y} = \dot{m}_i \Gamma' + \frac{\partial u_i}{\partial x} \Gamma' \rho \theta \alpha \qquad (5)$$

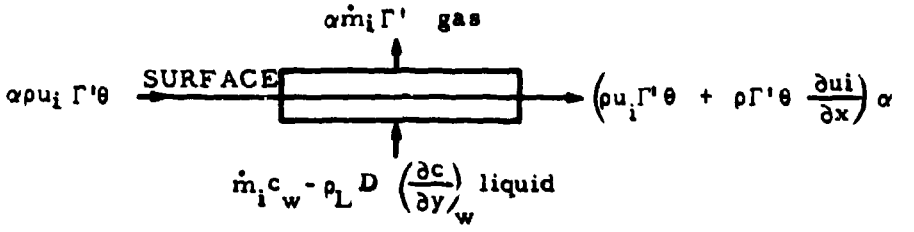

Fig. 3

where m_i = total rate of evaporation per unit area; D = diffusion coefficient; $_L$ = density of liquid; ' = surface concentration with ablation; c_w = concentration of surface active substance just below the surface; ^{w} is a conversion factor to transvert molar surface percent into weight percent. Because is in the range of intermolecular distances (10^{-8}cm), the value of the last term on the right-hand side of Eq. (5) is very small and may be ignored. The assumption is now made that c_w and Γ' are related by Gibbs' law.

$$\Gamma' = -\frac{c_w}{RT_i} \frac{\partial \sigma}{\partial c}$$

This would mean that the surface "equilibrium" concentration is established independent of the rate of ablation. This is a reasonable assumption because the transport path from the layer immediately below the surface to the surface layer is very short (in the Angstrom range), and the replacement by diffusion of ablative loss is therefore very rapid. Assuming a linear concentration gradient

$$\frac{dc}{dy} = - \frac{c_w - c_o}{\Delta}$$

where Δ is the thickness of the liquid layer, Eq. (5) may be solved:

$$\Gamma' = - \frac{\rho_L D c_o}{\dot{m}_i R T_i \Delta \left(\frac{\partial c}{\partial \sigma} - \frac{\rho_L D}{\Delta \dot{m}_i} \frac{\partial c}{\partial \sigma} - \frac{\alpha}{R T_i} \right)} \tag{7}$$

If $\dot{m}_i$ approaches zero the equilibrium distribution Γ_o should be attained in the surface. Equation (7) satisfies this condition. It is plausible that the equilibrium concentration Γ_o is also attained if Δ tends to zero. With Eq. (4) and the assumption that $\frac{T_i}{T_w} \approx 1$, which is approximated in most practical cases, Eq. (7) may be expressed

$$\frac{\Gamma'}{\Gamma_o} = - \frac{D \rho_L}{\dot{m}_i \Delta \left(1 - \frac{\rho_L D}{\dot{m}_i \Delta} - \frac{\alpha \Gamma_o}{c_o} \right)} \tag{8}$$

In order to evaluate this equation, m_i and Δ must be known as a function of the external flow conditions near the stagnation point. These relationships are known from previous investigations (1,3). In Ref. (1) it is shown that the dimensionless liquid layer thickness is almost independent of the stagnation temperature, with the exception of very small temperature values which are of no practical interest if ablation cooling is applied. A good approximation for Δ, for atmospheric pressure, is

$$\Delta \left(\frac{\rho_L K}{\mu_L} \right)^{\frac{1}{2}} \approx 0.465$$

The corresponding value for a pressure of 4 atm is 0.350. The factor K in the previous equation is given by the outer stream conditions

$$K = \frac{1}{R} \sqrt{\frac{2 p_o}{\rho_o} \left(1 + \left(\frac{\gamma - 1}{2} \right) M^2 \right)} \tag{9}$$

where R = radius of curvature of nose cap., $\gamma = \frac{c_p}{c_v}$, and M = Mach number. The value of $\frac{p_o}{\rho_o}$ is almost a constant in the atmosphere. In Ref. (4), $\dot{m}_i$ is given as a function of the stagnation temperature.

Equation (8) can now be evaluated if characteristic values for an ablation material are inserted.

Now the concentration of the surface-active agent at the free surface is known as a function of the flight conditions. The corresponding concentration in the gas boundary layer at the liquid-gas interface can be calculated by simple thermodynamic relationships. Indicating the mole fraction x of the surface-active compound by the index "1" and that of the solute by the index "2", and referring to the gas or liquid phase by the subscripts "g" and "L" respectively, the following relations exist at the surface:

$$x_{1g} = x_{1L}\gamma_1 e^{\lambda_1} \tag{10a}$$

$$x_{2g} = x_{2L}\gamma_2 e^{\lambda_2} \tag{10b}$$

where γ_1 and γ_2 are the activity coefficients in the liquid and λ_1 and λ_2 are defined by

$$\lambda_1 = \frac{L_{v1}}{R}\left(\frac{1}{T} - \frac{1}{T_{1b}}\right) \tag{11a}$$

$$\lambda_2 = \frac{L_{v2}}{R}\left(\frac{1}{T} - \frac{1}{T_{2b}}\right) \tag{11b}$$

The mole fractions and the surface concentrations are related by the following equations:

$$\Gamma_1 = -\frac{c_w}{RT_i}\frac{\partial\gamma}{\partial c}$$

$$\Gamma_2 = -\frac{(1 - c_w)}{RT_i}\frac{\partial\gamma}{\partial c}$$

it follows that

$$\Gamma_2 = \Gamma_1\frac{(1 - c_w)}{c_w}$$

Since c_w is very small we may write $\Gamma_1 = c_w \Gamma_2$. The transversion from mole fractions to surface concentration may be indicated by the factor α':

$$x_{1L} = \alpha' \Gamma'$$

$$x_{2L} = \alpha' c_w \Gamma'$$

The mole fraction of the injected gas x_g at the surface is then

$$x_g = x_{1g} + x_{2g} = \alpha' \Gamma' \left(\gamma_1 e^{\lambda_1} + \gamma_2 c_w e^{\lambda_2} \right)$$

We form the ratio x_g / x_g^o, where x_g^o is the mole fraction of the injected vapor when no surface-active agent is present:

$$\frac{x_g}{x_g^o} = \alpha' \Gamma' \left(\gamma_1 e^{\lambda_1 - \lambda_2} + \gamma_2 c_w \right) \tag{12}$$

The mole fractions x_g and x_g^o are related to $\dot{m}_i$ and $\dot{m}_i^o$, which are the rate of evaporation of the substance with a surface-active compound and the rate of evaporation of the pure substance, respectively (5):

$$x_g = \frac{\bar{M}_g \; N_{sc,w}^{0.6} \; \dfrac{\dot{m}_i}{\left(\rho_i \mu_i K\right)^{\frac{1}{2}}}}{M_g \left(\dfrac{Nu_w}{R_w^{\frac{1}{2}}} \right)_o + \frac{1}{3} \; \dfrac{\dot{m}_i}{\left(\rho_i \mu_i K\right)^{\frac{1}{2}}}} \tag{13a}$$

$$x_g^o = \frac{\bar{M}_g^o \; N_{sc,w}^{0.6} \; \dfrac{\dot{m}_i^o}{\left(\rho_i \mu_i K\right)^{\frac{1}{2}}}}{M_g^o \left(\dfrac{Nu_w}{R_w^{\frac{1}{2}}} \right)_o + \frac{1}{3} \; \dfrac{\dot{m}_i^o}{\left(\rho_i^o \mu_i^o \dot{K}\right)^{\frac{1}{2}}}} \tag{13b}$$

where $N_{sc,w}$ is the Schmidt number at the wall; Nu_w = Nusselt number at the wall for no injection; R_w = Reynolds number at the wall; M_g is the molecular weight of the injected gas for the liquid with surface-active additions; and M_g^o is the corresponding value for the pure substance. The terms $\bar{M}_g$ and $\bar{M}_g^o$ represent the corresponding mean molecular weights of the injected gases and air. It is now assumed that the Schmidt number is unity and $\rho_i \mu_i = \rho_i^o \mu_i^o$. We then obtain for $\frac{\dot{m}_i^o}{\dot{m}_i}$

$$\frac{\dot{m}_i^o}{\dot{m}_i} = \frac{1}{3\left(\rho_i^o \mu_i^o K\right)^{\frac{1}{3}}} \left(\frac{R_w^{\frac{1}{3}}}{Nu_w}\right) \left\{ 3\left[\left(\frac{Nu_w}{R_w^{\frac{1}{3}}}\right)_o \left(\rho_i^o \mu_i^o K\right)^{\frac{1}{3}} + \dot{m}_i^o\right] \frac{x_g^o M_g^o \bar{M}_g}{x_g M_g \bar{M}_g^o} - \dot{m}_i^o \right\} \tag{14}$$

The intention is to make $\dot{m}_i^o/\dot{m}_i$ as small as possible by adding a proper detergent. These possibilities shall now be investigated. Abbreviating

$$\left(\frac{Nu_w}{R_w^{\frac{1}{3}}}\right)_o \left(\rho_i^o \mu_i^o K\right)^{\frac{1}{3}} = A$$

and

$$\frac{M_g^o \bar{M}_g}{M_g \bar{M}_g^o} = B$$

we obtain from Eqs. (14) and (12)

$$\frac{\dot{m}_i^o}{\dot{m}_i} = \frac{1}{3A} \frac{3A + \dot{m}_i^o}{\alpha' B \Gamma' \left(\gamma_1 e^{\lambda_1} - \lambda_2 + c_w \gamma_2\right)} - \dot{m}_i^o \tag{15}$$

Since $\dot{m}_i^o/\dot{m}_i$ must be positive, we have a criterion for the condition under which preferential ablation is possible.

$$\alpha' B \Gamma' \left(\gamma_1 e^{\lambda_1} - \lambda_2 + c_w \gamma_2\right) - \frac{1}{\dot{m}_i} \geq \frac{1}{3}\left(\frac{R_w^{\frac{1}{2}}}{Nu_w}\right)^o \frac{1}{\left(\rho_i \mu_i K\right)^{\frac{1}{2}}} \qquad (16)$$

and since all terms of the right-hand side are positive

$$\gamma_1 e^{\lambda_1} - \lambda_2 + c_w \gamma_2 > \frac{1}{\dot{m}_i \alpha' B \Gamma'}$$

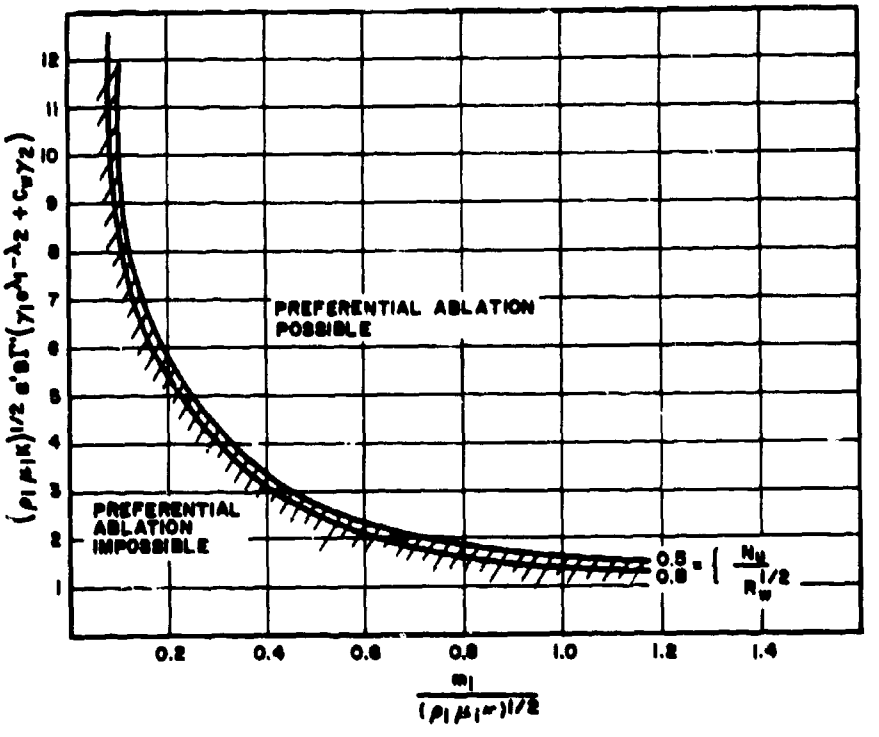

Fig. 4 POSSIBILITY OF PREFERENTIAL ABLATION

The inequality expressed by Eq. (16) is illustrated in Fig. 4, which also shows that the possibility of preferential ablation is almost independent of $Nu/R_w^{\frac{1}{2}}$. Instead of calculating the conditions which make $\dot{m}_i^o/\dot{m}_i$ a minimum, it seems more appropriate to develop a formula by means of which the experimenter will be able to optimize conditions for a given ablation system. The surface concentration appears as a factor in the previous formulas, but this is difficult to measure during an ablation test. In checking experimentally the improvement of various ablation materials by the addition of surface-active agents, it is important to have a simple method for measuring Γ'. The most convenient method is to measure the degree of preferential ablation.

If an ablation test in a plasma jet is suddenly interrupted, for instance, the liquid layer will solidify and may be chemically analyzed after the test. Such a chemical analysis can also be made of recovered reentry nose cones. The degree of preferential ablation π may be defined as

$$\pi = \frac{M_1 x_{g1}}{M_1 x_{g1} + M_2 x_{g2}} \tag{17}$$

This is the ratio of the ablated surface-active agent to the total material loss. Loss by flow to the back is hereby neglected. Combining Eqs. (10), (11), (13) and (17) we obtain:

$$\pi = \frac{\alpha' M_1 \Gamma' \gamma_1 \left\{ \left(\frac{Nu_w}{R_w^{\frac{1}{2}}} \right)_o + \frac{1}{3} \frac{\dot{m}_i}{(\rho_i \mu_i K)^{\frac{1}{2}}} \right\} e^{\left(1/T_i - 1/T_{1b}\right) L_{v1}/R}}{\bar{M} N_{sc,w}^{0.6} \frac{\dot{m}_i}{(\rho_i \mu_i K)^{\frac{1}{2}}}} \tag{18}$$

π is determined by chemical analysis; T_i is measured in the experiment, and m_i as a function of T_i may be taken from Ref. (2); K is given by Eq. (9); L_{v1} and $M_1/\bar{M}$ must be known; the Schmidt number may be assumed to be unity. The term $\left(Nu_w/R_w^{\frac{1}{2}}\right)_o$, for axisymmetric flow, is expressed by the following approximate equation (Ref. 5)

$$\left(\frac{Nu_w}{R_w^{\frac{1}{2}}} \right)_o \approx 0.765 \left(\frac{\rho_e \mu_e}{\rho_i \mu_i} \right)^{\frac{1}{2}} \tag{19}$$

The index "e" refers to values at the outside of the boundary layer. Using Eq. (19), the expression for π becomes

$$\pi = \frac{M_1}{\bar{M}} \alpha' \Gamma' \gamma_1 \left\{ \frac{0.765 \left(\rho_e \mu_e\right)^{\frac{1}{2}} K^{\frac{1}{2}}}{\dot{m}_i} + \frac{1}{3} \right\} e^{\left(1/T - 1/T_{1b}\right) L_{v1}/R} \tag{20}$$

μ_e may be calculated from Sutherland's formula for the stagnation temperature, ρ_e is given by

$$\rho_e = \rho_o \left\{ 1 + \frac{\gamma - 1}{2} M^2 \right\}^{\frac{1}{\gamma - 1}}$$

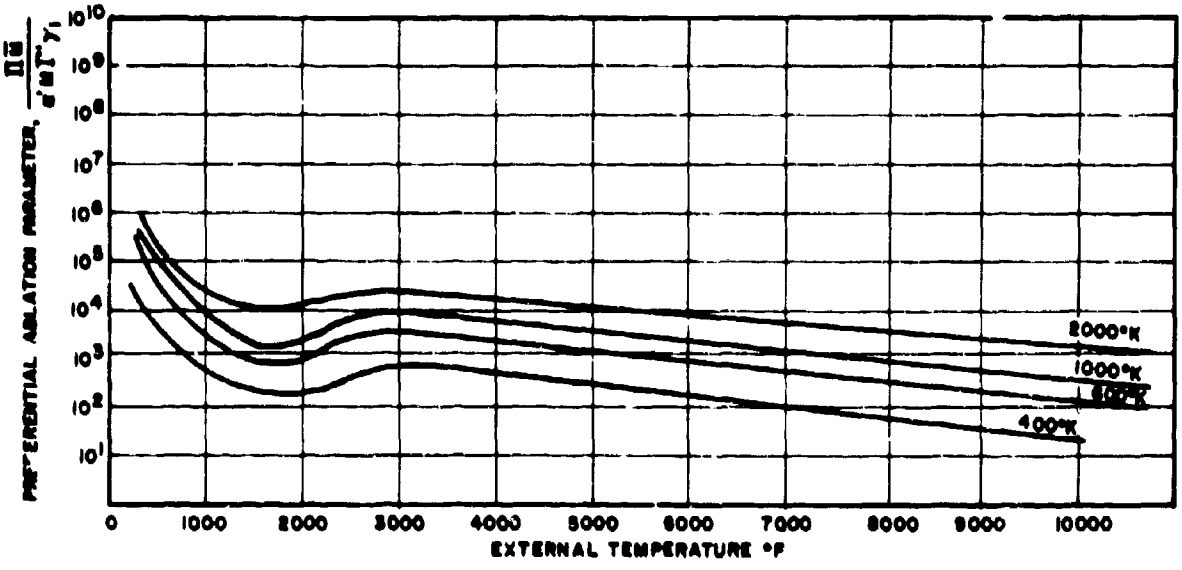

Fig. 5 DEGREE OF PREFERENTIAL ABLATION FOR A SURFACE ACTIVE SUBSTANCE WITH A HEAT OF EVAPORATION OF 1000 KCAL FOR VARIOUS BOILING POINTS AT ATMOSPHERIC PRESSURE

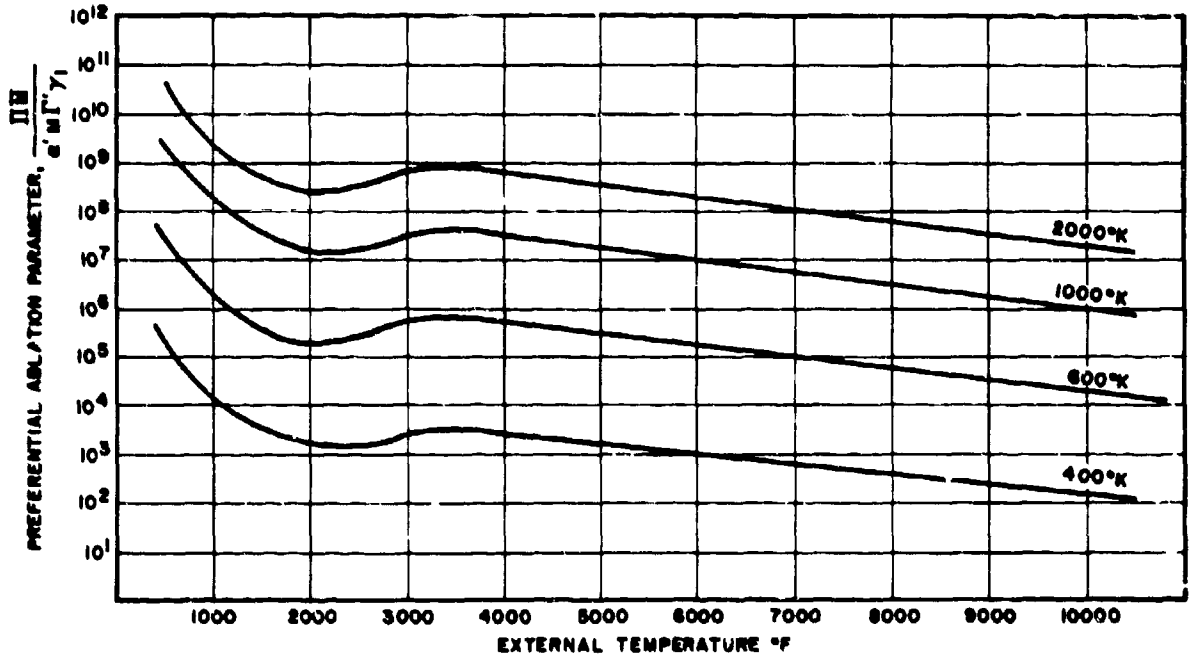

Fig. 6 DEGREE OF PREFERENTIAL ABLATION FOR A SURFACE ACTIVE SUBSTANCE WITH A HEAT OF EVAPORATION OF 3000 KCAL FOR VARIOUS BOILING POINTS AT ATMOSPHERIC PRESSURE

where $\gamma = \frac{c_p}{c_v}$, and M = Mach number. From Eq. (20) the product $\Gamma'\gamma_1$ may now be calculated and the value inserted into Eq. (15). The ablation system may be optimized for a given heat transfer condition by determining the maximum value of $\dot{m}_i/\dot{m}_i^o$ under this condition. In order to facilitate this procedure Eq. (20) is evaluated numerically. Figures 5, 6, and 7 show preferential ablation curves for surface-active media of varying boiling points and heats of evaporation. The curves have a distinct minimum around 2000°F.

The results for transport by rising gas bubbles will be published in the April issue of AIAA Journal and will therefore not be discussed here (6).

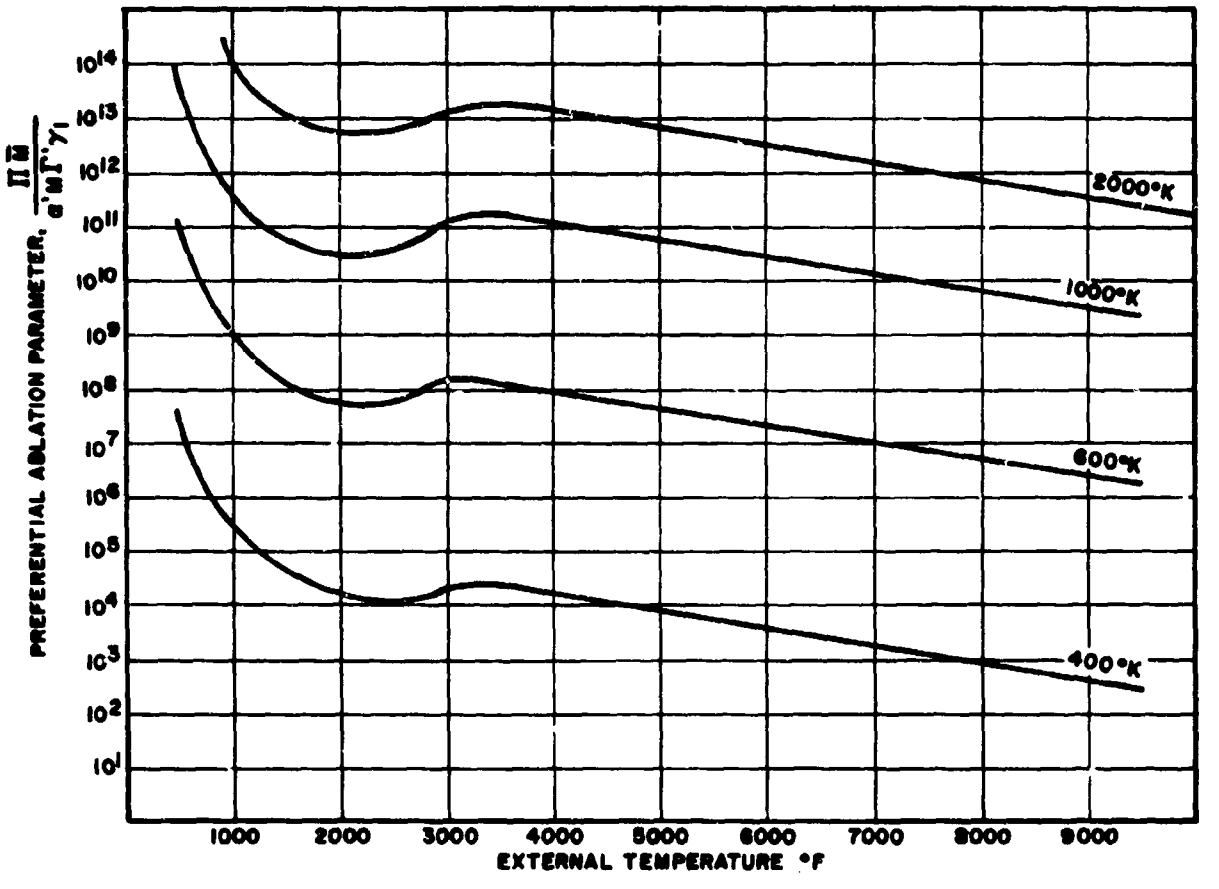

Fig. 7 DEGREE OF PREFERENTIAL ABLATION FOR A SURFACE ACTIVE SUBSTANCE WITH A HEAT OF EVAPORATION OF 5000 KCAL FOR VARIOUS BOILING POINTS AT ATMOSPHERIC PRESSURE

CONCLUSIONS: Transpiration and ablation cooling with surface-active agents may decrease the rate of heat transfer substantially.

Preferential ablation may be caused by two very different mechanisms: The surface-active agent may be transported to the surface by diffusion, in which case preferential material loss is only possible if the coefficient of diffusion is reasonably large; or the surface-active agent may be transported by gas bubbles, which transport mechanism is independent of viscosity and film thickness.

Measuring the preferential ablation rate is useful in determining experimentally whether optimal ablation conditions have been reached.

Because the addition of a small amount of a surface-active compound will not change the bulk properties of the liquid to any extent, the improvement realized by use of a detergent is strictly additive. This simplifies considerably the problems involved in selection of materials for ablation purposes.

LIST OF REFERENCES

1. Steverding, B., Fifth Intern. Symp. on Space Technol. and Science, Tokyo, Sept. 1963.

2. Roberts, L., Stagnation-Point Shielding by Melting and Vaporization, NASA Technical Report No. R-10, 1959.

3. Steverding, B., Preferential Ablation of Boron Oxide Upon Reentry of Jupiter Nose Cones., Army Ballistic Missile Agency Report No. DSN-TN-960-60, 1960.

4. Bethe, H. A., and M. C. Adams, "A Theory for the Ablation of Glassy Materials", J. Aero. Sci., 26, 1959, p. 321.

5. Roberts, L., A Theoretical Study of Stagnation Point Ablation, NASA Technical Report No. R-9, 1959.

6. Fay, T. A., and F. R. Riddell, "Theory of Stagnation Point Heat Transfer in Dissociated Air", J. Aero. Sci., 25, 1958, p. 73.

7. Steverding, B., "Surface Activity and Preferential Ablation", (Article to be published in AIAA Journal for March or April 1964).

GROWTH OF SELECTED ARBOVIRUSES IN SERUM-FREE SUSPENSION CELL CULTURES

H.R. TRIBBLE, JR., H.J. HEARN, JR., S.C. NAGLE, JR., and W.T. SOPER
U. S. ARMY BIOLOGICAL LABORATORIES, FORT DETRICK,
FREDERICK, MARYLAND

The maintenance of continuously cultured animal cells in suspension cultures that could be used for growing virus ordinarily requires the periodic addition of serum. Three major disadvantages of employing serum for this purpose, however, are that it offers the possibility of introducing (1) contaminating viruses or other microorganisms such as pleuropneumonia-like organisms, (2) antigenically active foreign proteins, and (3) protein or metabolic substances in undefined quantities. Information on the feasibility of serum-free suspension cultures for the production of virus is scant, i.e., the nutritional requirements for viral growth and the characteristics of viral populations grown in such systems have not been defined. It is the purpose of these studies to provide data in these areas. Venezuelan equine encephalomyelitis virus was selected to study viral growth in serum-free suspension cultures because it has been shown to be capable of replication in a wide variety of cell lines grown in serum-containing media and the viral growth could be assayed by several methods. Results of growth studies on a highly fastidious agent, yellow fever virus, will also be presented. In addition this report will include evidence that serum-free suspension systems are selective for viral populations possessing widely divergent genetic characteristics.

Two serum-free growth media were used in these experiments. The first, presented in Table 1, consisted of lactalbumin hydrolyzate and glutamine as nitrogen sources, vitamins, carbon sources, salts, antibiotics, and the additives methocel, insulin, and phenol red. This will be referred to as the LAH medium. The second consists of amino acids (some essential and some nonessential for the growth of these cell lines), salts, carbon sources, vitamins, antibiotics, and the same additives as in the first medium. This will be referred to as the NEAA medium and is shown in Table 2.

The experiments were conducted in 30-ml amounts in 100-ml

serum bottles in a New Brunswick Gyrotory shaker at 35 C. HeLa, cat kidney, chick embryo, and L cells were obtained from stock cultures and grown in suspension using the LAH or the NEAA medium.

The cultures were inoculated with virus by adding 10^8 mouse intracerebral LD_{50} of an egg seed preparation of a virulent strain of Venezuelan equine encephalomyelitis (VEE) virus. A sample was obtained immediately after inoculation to determine the initial virus-inoculum concentration prior to the addition of the cells. The cells were then added to final concentrations of from 5×10^5 to 1.5×10^6 per ml and the virus cell mixture was incubated for 45 minutes on the shaker. The culture was then centrifuged, washed once, and resuspended in fresh medium. At this time a 0-hour sample for virus titration and a cell count was obtained. The cell concentrations were determined by counting cells unstained after treatment with 0.5% trypan blue. The counting was performed at varying intervals, usually 24 hours apart.

Virus titers, determined by the Reed Muench method, are expressed as a mouse intracerebral or $MICLD_{50}$ obtained after the injection of 12- to 14-g mice with 10-fold diluted samples.

Figure 1 describes the replication of VEE virus in HeLa cultures grown in LAH, the growth of virus in the presence of 10% calf serum, and the rate of virus inactivation in the presence of serum-free and serum-containing media.

The initial virus inoculum in the media was 10^8 $MICLD_{50}$ per ml. After an incubation of 45 minutes and one wash, virus concentration in the LAH, shown as the open circles and solid line, beginning at 0 hour, was $10^{4.8}$ $MICLD_{50}$ per ml. A maximum titer of 10^9 $MICLD_{50}$ occurred in about 24 hours. By the 96th hour, the titer had decreased about 1 log.

The closed circles and solid line represent virus titers in the supernatant of the serum-containing medium. Starting from 10^6 $MICLD_{50}$ per ml at 0 hour, it did not reach the maximum titer of $10^{9.5}$ $MICLD_{50}$ per ml until 72 hours postinoculation. The virus remained at approximately the same level through 120 hours.

The broken lines represent the virus inactivation in cell-free media. The upper line represents the serum-containing medium, in which the virus titer did not disappear until the end of 96 hours. The lower broken line shows results in the serum-free lactalbumin medium, in which the virus titer completely disappeared by 72 hours.

In the first 48 hours the cells and supernatant fluids were titrated separately. After this time the cells and fluids were combined.

During the periods of observation, the cell-associated virus was found to be about 1/2 to 1 log lower than that in the supernatant fluid. At no time was it observed to be higher in the cells than in the fluid.

Both cultures initially contained a million cells per ml. Lysis of all but a small portion of the cell population occurred in the LAH by 72 hours. In contrast, the cell count in the serum-containing medium remained near pre-inoculation levels until 96 hours at which time approximately 60% of the cells were found to have been destroyed. The delay in cell lysis, therefore, coincided with the delay in the production of maximal titers of virus in cultures to which serum was added. It might be added that this was a consistent finding among all cultures to which serum was introduced. All uninfected cultures continued to show cell multiplication during the duration of the experiment.

The growth of VEE virus in the cat kidney cell line is shown in Figure 2. This is a fibroblast-like cell, originally isolated in our laboratory. The initial viral inoculation was 10^8 $MICLD_{50}$ per ml, and after the 45-minute incubation period and wash, the 0-hour titer was 10^4 to 10^5 $MICLD_{50}$ per ml. The virus inactivation curve presented here shows that the viral stability in lactalbumin and defined medium are essentially the same, with the virus becoming undetectable in 72 hours.

Virus growth in NEAA, represented by open circles and a solid line, and the virus growth in LAH represented by closed circles and a solid line, resulted in maximal virus titers in 24 hours. Titers in the LAH medium were 10^9 $MICLD_{50}$ per ml; those in the NEAA medium were 10^8 $MICLD_{50}$ per ml.

The serum-containing medium did not show a maximum titer until 48 hours postinoculation, at which time it contained 10^9 $MICLD_{50}$ per ml. This culture continued to be infected for an extended period of time. Observations indicated that after the 33rd day the virus lost its ability to infect mice by the intraperitoneal route and, in fact, immunized the mice against challenge with fully virulent virus. This phenomenon will be described in more detail later in this paper.

The cell population responded to the virus in the expected manner, with complete lysis in 4 to 5 days except in the serum-containing medium, in which cell multiplication continued without abatement.

Figure 3 shows VEE virus growth in L cells in NEAA, LAH, and serum-containing media. The usual patterns of growth were obtained with the serum-free medium. The maximal levels of virus was 10^9 $MICLD_{50}$ per ml with LAH (closed circles) and 10^8 $MICLD_{50}$ per ml with the NEAA medium (triangles) in 24 hours. Virus growth in

serum-containing medium was considerably delayed in this cell line and did not reach its maximum titer of 10^8 $MICLD_{50}$ per ml until 4 days postinoculation.

The previous studies suggested that virus would be produced for intervals considerably beyond the early postinoculation intervals. For this reason, these cultures were observed daily for 16 days, resulting in the disclosure of secondary peaks of viral growth at 11 to 12 days. Shortly after this time, the cultures in the LAH and the serum-containing media underwent complete cell lysis and were terminated. The culture in the NEAA medium, however, continued to demonstrate a high level of cell proliferation and a persistent production of virus for a total of 115 days. The virus that was obtained at the late intervals was found to vary considerably from that produced in the same culture at the early postinoculation intervals. For example, virus produced at the late interval was no longer lethal for mice by the intraperitoneal route, but it was highly immunogenic.

Additional experiments designed to elucidate factors associated with the chronic infection of these cultures were carried out. Time does not permit a detailed description of the results but they may be summarized as follows: (1) The interval of viral growth in the infected cultures was clearly divisible into 2 phases, an acute and a chronic, separated by a transitional phase. During the acute phase, which lasted from 1 to approximately 96 hours, large amounts of virulent virus were produced, generally in association with the destruction of the majority of the cells. This may then be succeeded by a relatively variable interval of transition that lasts from the 5th to the 10th day. The interval is characterized by a repopulation of the culture by the surviving cells, a decline in virus production, and a complete resistance of the cells to superinfection with virulent virus. The final or chronic phase of the infection usually begins after the 8th or 9th day and can persist for indefinite lengths of time unless the culture is terminated deliberately or becomes contaminated. It is characterized by the proliferation of cells that continue to be resistant to superinfection, the production of virus at levels between 10^2 and 10^4 $MICLD_{50}$, and a slow but observable selection of avirulent virus particles. As examples of this, at approximately 8 days the virus became nonlethal for rabbits, nonlethal for mice between 2 to 3 weeks, nonlethal for guinea pigs at 72 days, and nonlethal for hamsters at 112 days postinoculation when tested by the intraperitoneal route. The newly selected avirulent population was genetically stable and highly immunogenic.

The results of studies on the production of yellow fever virus in serum-free cultures will be demonstrated in the final two figures. Figure 4 shows that the growth of the virus in the chick embryo cell line propagated in the LAH and LAH - 10% calf serum cells resulted in maximal titers of 10^7 and $10^{6.2}$ $MICLD_{50}$ respectively, 6 to 8 days postinoculation. Some evidence of submaximal yields of

virus appeared at the 2nd day in both media. This was more readily apparent, however, in the culture containing LAH and calf serum. It is noteworthy that the maximal yellow fever virus yield was not delayed in medium with serum as it was in the case mentioned earlier during tests with VEE virus. Whether the serum was responsible for the temporary decline in virus production that was found 3 to 5 days postinoculation of the culture, however, is presently undetermined.

Figure 5 shows the results of propagating yellow fever virus in HeLa cultures grown in LAH and NEAA. The virus was produced to approximately the same maximal yields at 3 and 4 days of $10^{7.2}$ to $10^{7.4}$ $MICLD_{50}$ per ml. In contrast to the results of VEE virus production, cells that supported the growth of yellow fever virus failed to lyse or demonstrate any obvious signs of pathology.

An additional phenomenon of considerable interest was disclosed when the virulence of virus grown in chick embryo was compared with that of virus grown in HeLa cells. The fact that each product assayed to approximately the same titer in mice has already been shown. Tests with these products in monkeys, however, revealed a wide divergence of virulence. The chick embryo cell product after only one passage was nonlethal for monkeys when given in doses of 1000 LD_{50} by the respiratory route. It was immunogenic, however, at doses of 10 $MICLD_{50}$ and above. In contrast, between 5 and 10 $MICLD_{50}$ of the HeLa cell product were sufficient to produce lethality be the respiratory route. Infection with this preparation was almost always associated with lethality.

In summary, the ability of animal cell suspension cultures grown in three types of serum-free media to support the replication of Venezuelan equine encephalomyelitis (VEE) virus has been demonstrated. The interval of viral growth in the infected cultures was clearly divisible into 2 phases, acute and chronic, separated by a transitional phase. During the acute phase, large amounts of virulent virus were produced, generally in association with the destruction of the large majority of the cells. Titers of 10^8 and 10^9 $MICLD_{50}$ per ml within 24 hours postinoculation were obtained in HeLa, cat kidney, and L cells grown in either lactalbumin hydrolyzate medium or a defined medium containing essential and/or nonessential amino acids. Only slight individual differences in virus growth were observed among the different cell lines grown without serum. The addition of 10% calf serum, however, altered the replication pattern of the virus. This was made manifest as a delay in the attainment of the maximum titer and in the appearance of cell lysis resulting from virus growth. The observed occurrences of a chronic state of infection in the cultures and the step wise decline in virulence of the chronically produced virus for various laboratory hosts was described. Yellow fever virus replicated in HeLa and chick embryo cell lines. Titers of approximately 10^7 $MICLD_{50}$ per ml were obtained in 3 to 4 days in both cultures. A widely differing qualitative response was detected, however, because of the rapid

selection of an immunogenic population in the chick embryo cells that was nonlethal for monkeys. In contrast, HeLa cultures produced a highly virulent population that rarely failed to infect without causing lethality in monkeys.

These data indicate that serum-free suspension systems may provide a highly valuable tool for the growth of viruses by researchers engaged in a wide variety of disciplines. The production of vaccines free of foreign antigenic protein, qualitative biochemical determinations of nutritional requirements and inexpensive methods for producing viruses that are incapable of growth in conventional host systems are but a few of the areas in which serum-free suspension systems can play a highly important role.

TABLE 1

LACTALBUMIN HYDROLYZATE MEDIUM FOR SUSPENDED CELL GROWTH

COMPONENT	CONC. mg/L	COMPONENT	CONC. mg/L	
Nitrogen Sources:		**Salts:**		
Lactalbumin hydrolyzate	2500	NaCl	7400	
L-Glutamine	300	KCl	400	
		$NaH_2PO_4 \cdot H_2O$	100	
Vitamins:		$NaHCO_3$	300	
		$CaCl_2 \cdot 2H_2O$	265	
D-biotin	1.0	$MgCl_2 \cdot 6H_2O$	275	
Choline·Cl	1.0			
Folic Acid	1.0	**Antibiotics, etc.:**		
Niacinamide	1.0			
Ca pantothenate	2.0	Methocel 15 cps	1000	
Pyridoxal·HCl	1.0	N.P.H. insulin	200	units/L
Thiamine·HCl	1.0	Streptomycin	100	mg/L
i-inositol	1.0	Penicillin	100,000	units/L
Riboflavin	0.1	Kanamycin	100	mg/L
B_{12}	0.002	Phenol red	10	mg/L
Carbon Sources:				
Glucose	1000			
Sodium pyruvate	110			

TABLE 2

CHEMICALLY DEFINED MEDIUM FOR SUSPENDED CELL GROWTH

COMPONENT	CONC. mg/L	COMPONENT	CONC. mg/L
Amino Acids (essential):		**Salts:**	
L-Arginine·HCl	100	NaCl	7400
L-Cysteine·HCl	75	KCl	400
L-Histidine·HCl	60	$NaH_2PO_4 \cdot H_2O$	100
L-Isoleucine	150	$NaHCO_3$	500
L-Leucine	300	$CaCl_2 \cdot 2H_2O$	265
L-Lysine	300	$MgCl_2 \cdot 6H_2O$	275
L-Methionine	60		
L-Phenylalanine	120	**Carbon Sources:**	
L-Threonine	135		
L-Tryptophan	60	Glucose	1000
L-Tyrosine	120	Sodium pyruvate	110
L-Valine	150		
L-Glutamine	450	**Vitamins:**	
Amino Acids (nonessential):		D-biotin	1.0
		Choline·Cl	1.0
Glycine	60	Folic Acid	1.0
L-Alanine	120	Niacinamide	1.0
L-Serine	150	Ca pantothenate	2.0
L-Cystine·HCl	75	Pyridoxal·HCl	1.0
L-Aspartic Acid	270	Thiamine·HCl	1.0
L-Glutamic Acid	315	i-inositol	1.0
L-Proline	115	Riboflavin	0.1
		B_{12}	0.002
Antibiotics, etc.:			
Methocel 15 cps	1000		
N.P.H. insulin	200 units/L		
Streptomycin	100 mg/L		
Penicillin	100,000 units/L		
Phenol red	10 mg/L		

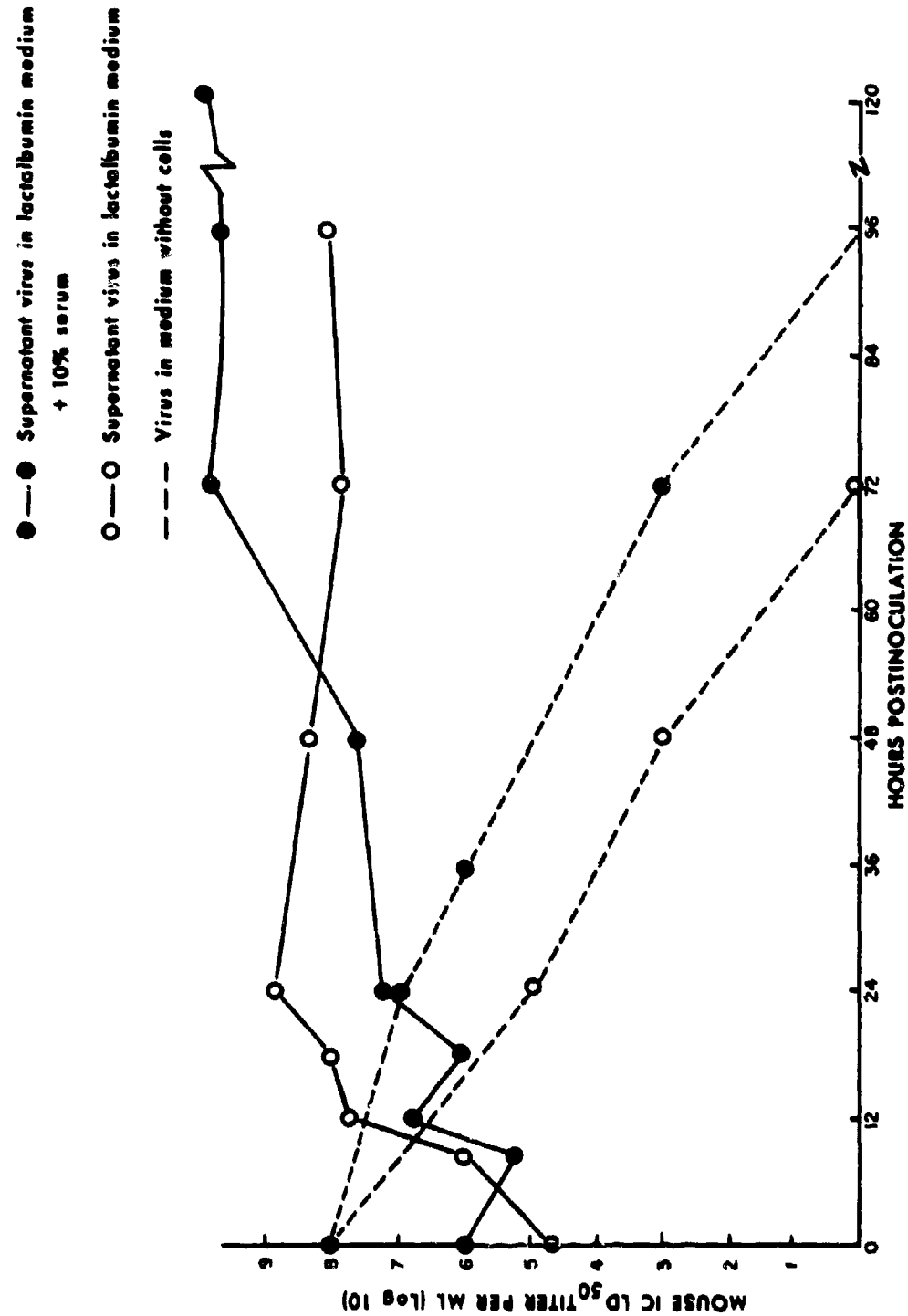

Figure 1. GROWTH OF VENEZUELAN EQUINE ENCEPHALOMYELITIS VIRUS IN SERUM-FREE SUSPENSION CULTURES OF HELA CELLS

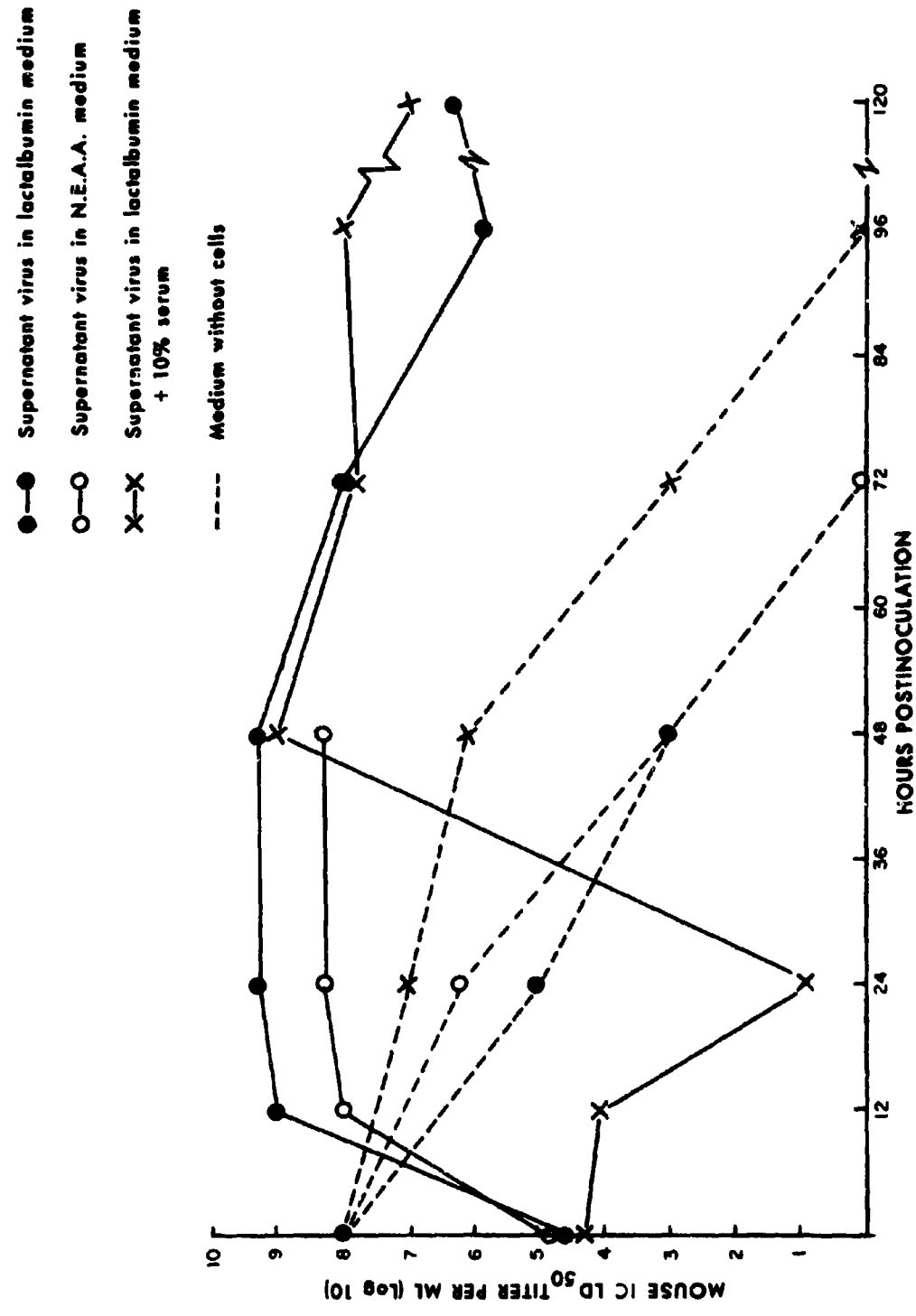

Figure 2. GROWTH OF VENEZUELAN EQUINE ENCEPHALOMYELITIS VIRUS IN SERUM-FREE CAT KIDNEY SUSPENSION CULTURES

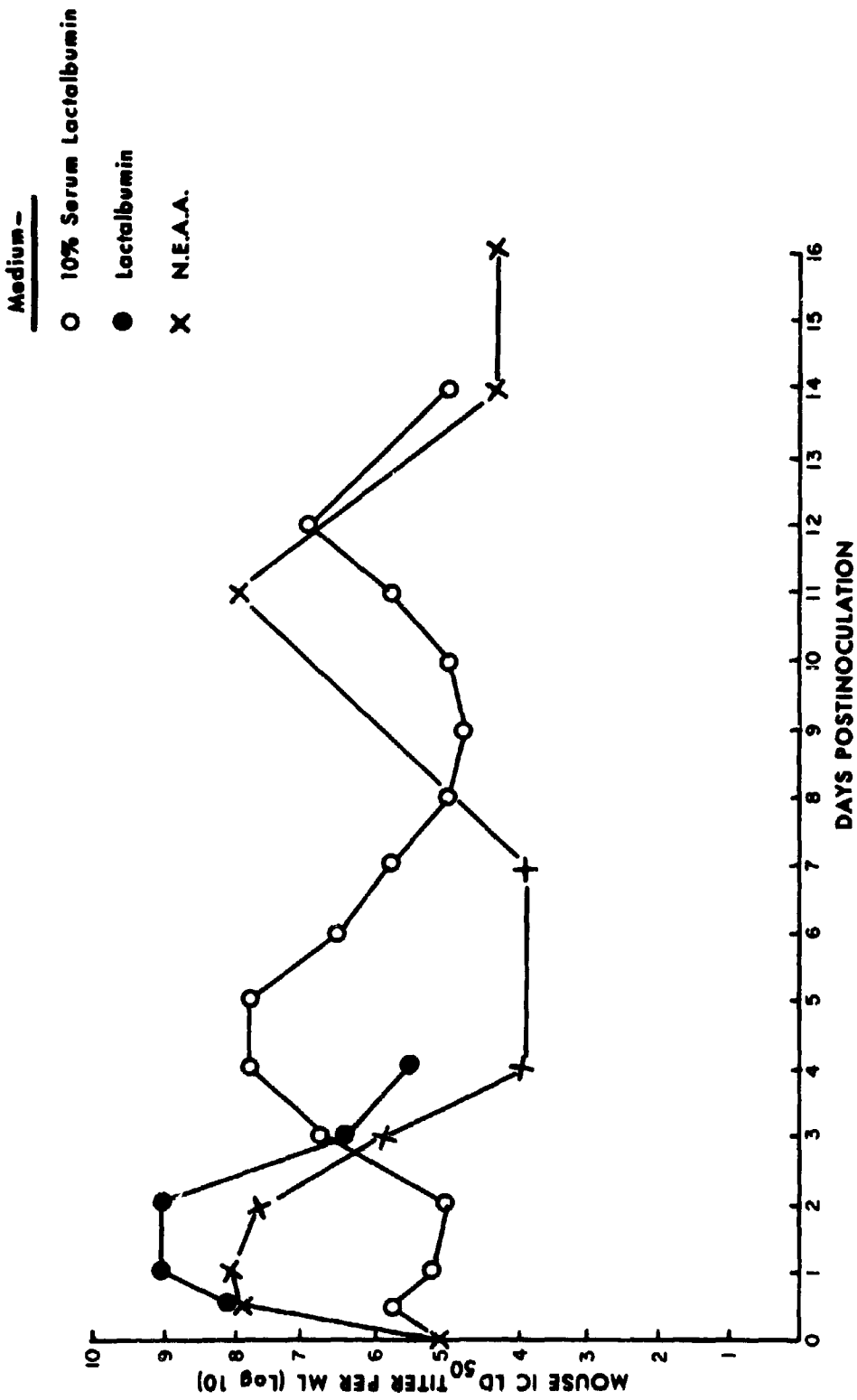

Figure 3. GROWTH OF VENEZUELAN EQUINE ENCEPHALOMYELITIS VIRUS IN SERUM-FREE L CELL SUSPENSION CULTURES

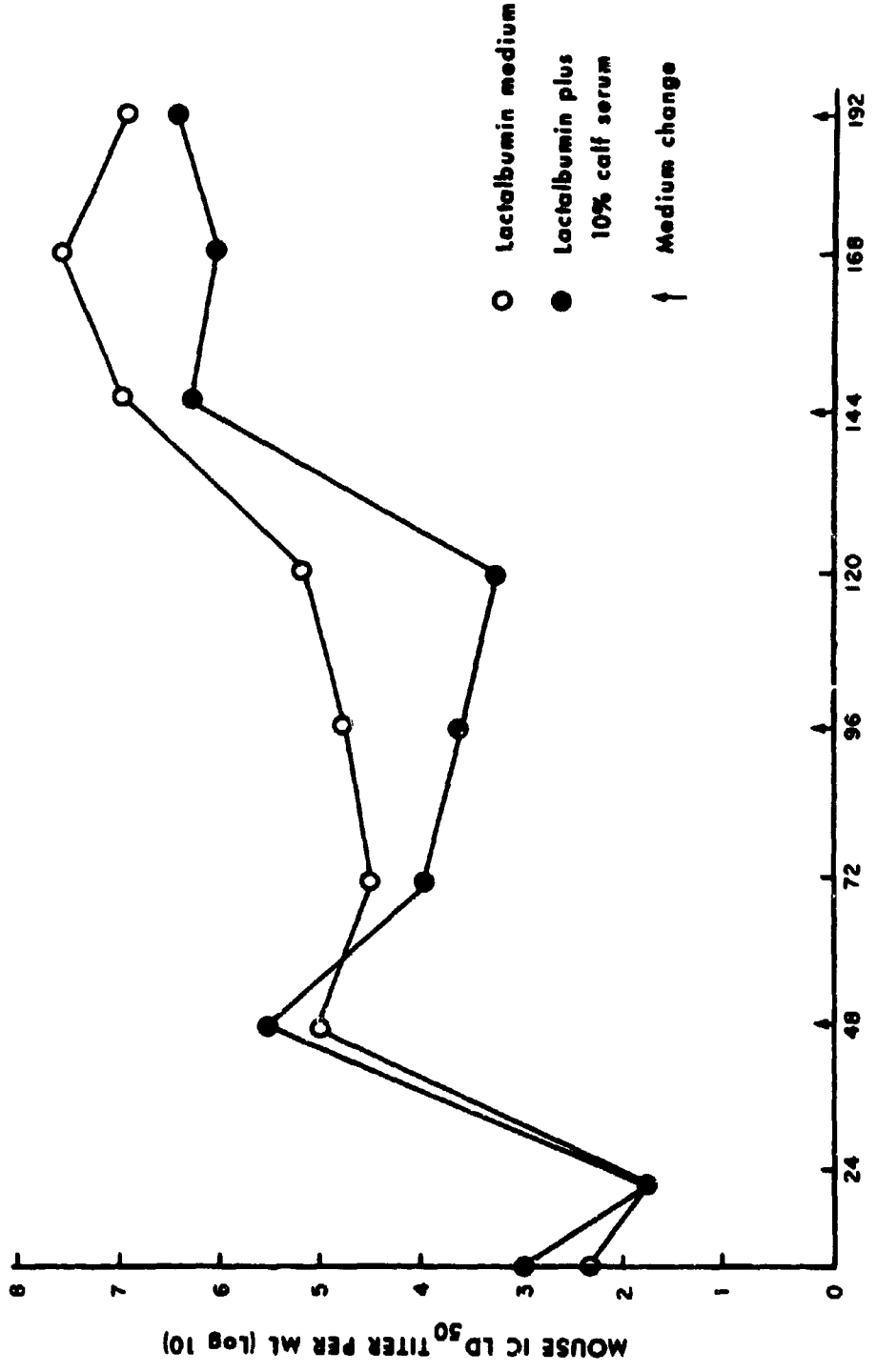

Figure 4. GROWTH OF YELLOW FEVER VIRUS IN SERUM-FREE CHICK EMBRYO SUSPENSION CULTURES

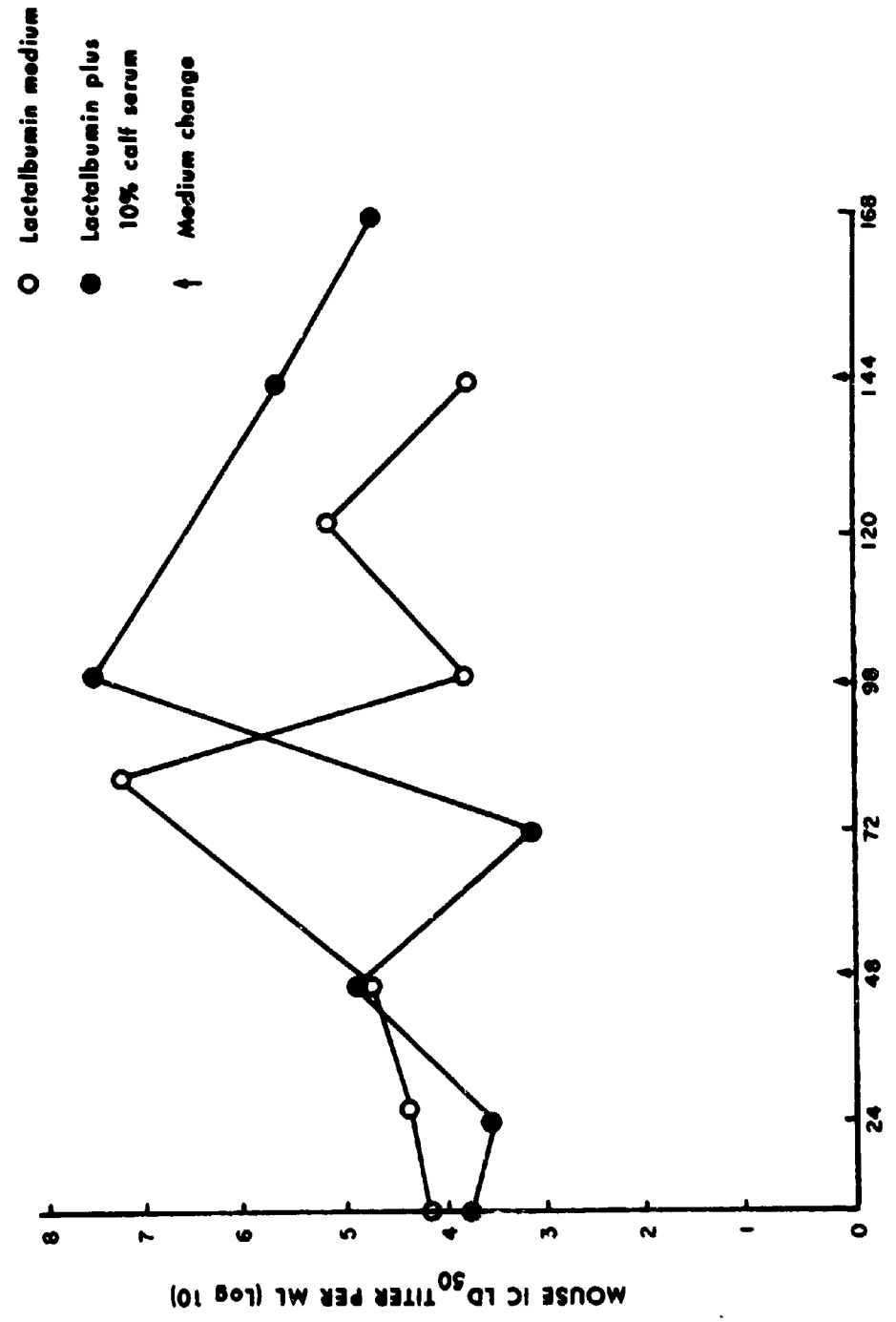

Figure 5. GROWTH OF YELLOW FEVER VIRUS IN SERUM-FREE HELA SUSPENSION CULTURES

THE EFFECT OF MIGRATING NEMATODE LARVAE AS A PROVOKING FACTOR IN VIRAL ENCEPHALITIS IN MICE

BRYCE C. WALTON, Major, MSC
U.S. Army Medical Research Unit/Panama
Balboa Heights, Canal Zone

It is well known that invariably fatal infections can result from minute quantities of certain viral agents inoculated into the central nervous system of experimental animals, while logarithmically increasing doses of the same agent administered by any other route will produce no serious ill effects. Likewise, it is also well known that a pronounced propensity for invasion of the central nervous system is exhibited by the larvae of several species of nematode parasites in the somatic migration in the vertebrate host during the early stages of their life cycle. As a consequence, it would appear that there might be considerable justification for the suspicion that an ordinarily benign infection with such a viral agent might result in a fatal outcome if it should happen to coincide with the presence of a wandering nematode which would permit its entrance into the central nervous system. The physical breaching of the blood-brain barrier by the larvae during a period of viremia could serve to inoculate the virus directly into nervous tissue as effectively as a hypodermic needle.

Innes and Shoho[1] speculated on this possibility in their review of the problem of cerebrospinal nematodiasis in horses, sheep, and goats caused by the filariid Setaria digitata. Circumstantial evidence of such occurrences is afforded by the report of Beautyman and Woolf[2] concerning the finding of an ascarid larva in the basal ganglia in a case of fatal poliomyelitis. However, evidence connecting such widely separated disease entities are rare, and it would be extremely difficult to demonstrate interaction between them in nature. Laboratory models of dual infections with migrating nematode larvae and neuropathogenic viruses will no doubt provide the best means of

* The principles of laboratory animal care as promulgated by the National Society for Medical Research were observed during the course of the experimentation reported in this study.

elucidating the basic relationships of the interaction involved in such infections. The only experimental evidence presently available concerning such a provoking effect on a neurotropic virus is that of Mochizuki et al.(3) who presented data on a small number of mice which showed a clear increase in mortality among mice inoculated subcutaneously with Japanese B encephalitis virus after a prior infection with Toxacara canis, when compared with mice receiving the virus only. Kilham and Olivier have likewise shown that concurrent trichinosis enhances the pathogenic effect of encephalomyocarditis virus in rats.(4)

The present report is concerned with the effect of intraperitoneal inoculation of mice with sublethal dosages of each of three neurotropic arboviruses, Eastern equine encephalitis (EEE), Ilheus (Ilh), and Japanese B encephalitis (JBE), to coincide with the migration of Trichinella spiralis larvae.

MATERIALS AND METHODS

Although minor variations were used in individual experiments, they were all designed to compare results among three groups of young adult male CFW mice; the Dual Infection Group which received both Trichinella and virus, the Trichinella Control Group and the Virus Control Group.

Trichinella spiralis

Infective larvae were obtained from laboratory infected mice derived from a strain maintained in rats at the USPHS Communicable Disease Center. The skinned and eviscerated carcasses of the infected mice were minced for one minute in a homogenizer and digested in pepsin-HCl artificial gastric juice (5) for two hours at 37°C with constant agitation by a magnetic stirrer. The residue was strained through two layers of gauze and the larvae allowed to settle out in conical sedimentation glasses. They were collected with a Pasteur pipette, washed with 0.85% saline solution, and then counted in the trough of a hookworm larvae counting slide* with a stereoscopic microscope to obtain the desired number for each mouse. When the correct number was determined, the worms were transferred with 0.2-0.3 ml. of saline solution to individual wells of a plastic tray of the type used for hemagglutination tests. These inocula were administered to mice with a one cc. tuberculin syringe fitted with a 1/4 inch stub of a shortened 19 ga. needle, over which was slipped a 1-1/4 inch length of flexible polyvinyl plastic tubing (premature infant feeding tube, size 5 French).** The syringe was filled separately for each inoculation, and the larvae administered to the lightly anesthetized mice by gastric intubation.

* Available from A. H. Thomas Co., Phila., Pa., Cat. #4099-A
** Available from Pharmaseal Laboratories, Glendale, Cal.

Eastern Equine Encephalitis Virus

All experiments were performed with aliquots of a single pool of 20% suckling mouse brain (SMB) suspension of the sixth mouse passage of a strain designated 3789-R6, received from the Veterinary Diagnostic Laboratory, Ministry of Agriculture, Republic of Panama, and isolated from a fatal equine case in Chame, R. P. This pool had an LD_{50} of 10^{-9} in an intracerebral titration in weanling mice.

Ilheus Virus

All experiments were with a single 20% SMB pool of Gorgas Memorial Laboratory strain BTS 3875, isolated from a bird in Bocas del Toro, Panama. This eighth mouse passage pool had a LD_{50} of $10^{-5.5}$ on intracerebral titration in weanling mice.

Japanese B Encephalitis Virus

This virus was strain #60E from the Virology Department of Walter Reed Army Institute of Research, and the pool used had a LD_{50} of $10^{-8.5}$ when titrated intracerebrally in weanling mice.

On the sixth day following infection with Trichinella larvae, the mice were separated into two groups. One half received no further inoculations and were designated Group A, or Trichinella Control Group. One half received intraperitoneal injections of 0.3 ml. of the appropriate virus suspension and were designated Group B or Dual Infection Group. An equal number of noninfected mice also were similarly inoculated with the same virus suspension to serve as the Virus Control Group, and were designated Group C.

The three groups were observed for a period of twenty days after inoculation of virus, and whenever possible, brains were secured immediately after death and frozen for subsequent intracerebral inoculation into other mice to verify presence of virus. In a few instances paralyzed, obviously moribund, mice were sacrificed.

In experiment #10 mechanical puncture of the brain was substituted for Trichinella infection to verify the effect of a rupture of the blood-brain barrier in the presence of circulating virus. An inoculum of 0.3 ml. of a 10^{-5} dilution of EEE was administered intraperitoneally to 20 mice as in the preceding experiments. On the following day these were separated into two groups, 10 received no further manipulations, while 10 were anesthetized with ether and a sterile steel pin was inserted through the lateral aspect of the skull between the ear and eye to penetrate the brain to a depth of about 1/4 inch. Ten normal mice were subjected to the same procedure to serve as non-infected controls.

For attempts to demonstrate the presence of Ilheus virus in Trichinella larvae recovered from mice from the Dual Infection Group in

Experiment #7, two mice dead on day 8 were taken immediately after death and the larvae recovered by digestion of skeletal muscle as previously described. The larvae were washed three times in sterile saline and then triturated in cold 0.85% saline solution containing 10% normal horse serum using a Ten Broeck tissue grinder. This homogenate was then inoculated intracerebrally in 0.03 ml. volumes into each of 7 hairless suckling mice. The same procedure was employed with two mice which survived dual infections in experiment #4 using EEE virus, which were sacrificed 28 days following virus inoculation.

RESULTS

Only four deaths occurred among the 115 mice receiving Trichinella. However, it should be pointed out that the two deaths recorded in Group A of experiment #6 appeared to be due to an intestinal infection unrelated to trichinosis.

The synergistic effect of dual nematode-virus infections was apparent in every experiment, as illustrated by Table 1. However, distinct differences in the level of expression of this synergism were observed between two of the agents used. The differences in the number of deaths in the dual Infection Group, as opposed to the Virus Control Group, were quite dramatic with EEE, while with Ilheus inoculation, the differences were much smaller. In the single experiment with JBE, the effect appeared to be intermediate.

In the two EEE experiments, #1 and #2, in which the i.p. virus inoculum approached the LD_{50} level, only one of thirty mice survived (97% mortality) in the Dual Infection Group, as opposed to ten of the thirty (33% mortality) in the Virus Control Group. However, when the dosage was decreased to approximately the MLD level for the Virus Control Group in Experiment #4, a corresponding reduction in percentage of mortality in the Dual Infection Group did not occur and the difference between the number of deaths in the two groups was most pronounced at this level. A parallel result is also illustrated by the virus titration experiment summarized in Table 2. A further reduction of the amount of virus inoculated resulted in no deaths in the Dual Infection Group.

There was a distinct variation in the temporal distribution of deaths between the Virus Control and the Dual Infection groups in the experiments using EEE virus (Fig. 1). With virus alone, deaths occurred between days 3 and 9, with the greatest number occurring on day 7. With the dual infection, the peak number was on day 4, and occurrences were spread over the period from day 3 to day 15. However, it must be noted that verification of viral death was not obtained in the case of the mouse dead on day 15.

A completely different relationship is apparent in the case of Ilheus virus (Fig. 2) in spite of the small numbers involved. Distribution in the two groups is essentially the same in regard to

length of the period during which deaths were observed, and the peak occurrence.

In experiment #10, wherein the brains of the mice were penetrated by a sterile pin one day after inoculation of the EEE virus, the results were comparable in every way to those of the experiments using Trichinella infection (Table 3). Four of ten died, while no deaths occurred among the mice receiving the virus alone, nor in the non-infected control group. Furthermore, the time of death coincided with those observed in the dual infections, occurring on days 4 to 6 after virus inoculation.

Attempts to demonstrate virus within the larvae recovered from mice with dual infection with trichinosis, and both EEE virus and Ilheus virus, resulted in negative findings. None of the suckling mice inoculated intracerebrally with worm homogenates developed any signs of illness.

DISCUSSION

These data, which demonstrate a pronounced synergistic effect of Trichinella spiralis infection with peripheral inoculation of arboviruses, also shed a little light on the possible underlying basic mechanism of that synergism. Infections with EEE virus are diphasic, with preliminary multiplication in non-neural tissues, and a secondary phase in which the virus invades the CNS and multiplies there.(6) It is possible that the unsuitability of non-neural tissue of older mice for virus multiplication(7) is altered to afford a more suitable milieu through changes brought about by the invasion of Trichinella larvae, as appears to happen in the case of concurrent infections with this nematode and encephalomyocarditis virus in rats reported by Kilham and Olivier.(4) If the synergistic effect was due to increase of virus multiplication in the visceral phase with a resultant "spilling over" into the CNS, it should be expected that the period until death should be at least as long as for those mice in the Virus Control Group which received lethal intraperitoneal doses. However, this proved not to be the case. Deaths occurred earlier in the Dual Infection Group, which correspond exactly to the time of death in mice inoculated intracerebrally, and indicates an early entry of virus into the CNS.

The underlying mechanism is also possibly more complex than the possible interpretation that the Trichinella merely represent a biological equivalent of the sterile pin of experiment #10 and only cause a straightforward physical penetration of the tissue which separates circulating virus from susceptible nervous tissue. Virus transport into nervous tissue by means of an intestinal tract filled with virus-containing body fluids would seem to be a possibility. Syverton et al.(8) reported that in dual infections with guinea pigs, lymphocytic choriomeningitis virus could survive long periods in Trichinella larvae and be transmitted by them. Although similar

success was not encountered in attempts to recover virus from larvae in this study, the possibilities were not fully explored and this aspect would bear further investigation.

SUMMARY AND CONCLUSIONS

Young mice given a combined infection with Trichinella spiralis and a neuropathogenic arbovirus extraneurally showed a much higher mortality rate than mice given either agent separately. Distinct differences in the degree of this synergism were apparent with different viral agents, being very pronounced with EEE, and quite minimal with Ilheus. It would appear that this synergistic effect of dual infection was not due to increased viral multiplication in visceral tissues in the initial phase of the disease caused by stress-induced changes in the host, but that it was due to early initiation of the neural phase of the disease by the introduction of virus into the central nervous system by the migrating larvae, as indicated by the time of death.

References

1. Innes, J. R. M. and Shoho, C., 1953. Cerebrospinal nematodiasis. Focal encephalomyelomalacia of animals caused by nematodes (Setaria digitata); a disease which may occur in man. Arch. Neurol. & Psychiat. 70:325-349.

2. Beautyman, W. & Woolf, A. C., 1951. An ascaris larva in the brain in association with acute anterior poliomyelitis. J. Path. & Bacteriol. 63:635-647.

3. Mochizuki, H. Tomimura, T., and Oka, T., 1954. Cerebrospinal nematodiasis as a provoking factor in Japanese B. encephalitis: an experimental approach. J. Infect. Dis., 95:260-266.

4. Kilham, L. and Olivier, L., 1961. The promoting effect of trichinosis on encephalomyocarditis (EMC) virus infection in rats. Amer. J. Trop. Med. & Hyg. 10: 879-884.

5. Larsh, J.E. and Kent, D. E., 1949. The effect of alcohol on natural and acquired immunity of mice to infection with Trichinella spiralis. J. Parasitol. 35:45-53.

6. Sabin, A. B., and Olitsky, P. K., 1938. a. Variations in pathways by which equine encephalomyelitic viruses invade the CNS of mice and guinea pigs. Proc. Soc. Exper. Biol. & Med. 38:595-597.

7. 1938. b. Age of host and capacity of equine encephalomyelitic viruses to invade the CNS. Proc. Soc. Exper. Biol. 38: 597-599.

8. Syverton, J. T., McCoy, O. R. and Koomen, J., 1947. The transmission of the virus of lymphocytic choriomeningitis by Trichinella spiralis. J. Exper. Med. 85: (6): 759-769.

Table 1.

Mortality in mice inoculated intraperitoneally with less than LD_{50} of arbovirus, with and without prior infection with 300 *Trichinella spiralis* larvae.

Inoculum / Group	1. EEE 10^{-4}	2. EEE 10^{-4}	3. EEE 10^{-5}	3. EEE 10^{-6}	4. EEE 10^{-6}
A. Trichinella	0/15	0/15	0/10		1/15 *
B. Both	15/15	14/15	9/10	6/10	13/15 *
C. Virus	5/15	5/15	0/10	1/10	0/15

Inoculum / Group	5. EEE 10^{-7}	6. JBE 10^{-4}	7. Ilh 10^{-2}	8. Ilh 10^{-2}	9. Ilh 10^{-2}
A. Trichinella	0/10	1/20 **	0/15	2/15	0/10
B. Both	0/10	8/20 **	4/15	4/15	3/10
C. Virus	0/10	1/20	1/15	1/15	1/10

Numerator denotes number of deaths, denominator number of mice tested.

** estimated 200 *Trichinella* larvae

*400 *Trichinella* larvae

Table 2.

Effect of administration of 300 Trichinella larvae 6 days prior to intraperitoneal titration of EEE virus in adult mice.

VIRUS DILUTION	WITH TRICHINELLA	WITHOUT TRICHINELLA
10^{-4}	----	3/10
10^{-5}	9/10	0/10
10^{-6}	6/10	1/10
10^{-7}	0/10	0/10
No Virus	0/10	----

Table 3.

Effect of mechanical puncture of brain of mice one day after intraperitoneal inoculation of EEE virus.

Puncture only	0/10
Virus & Puncture	4/10
Virus only	0/10

Numerator denotes number of deaths, denominator number of mice tested.

Fig. 1

Distribution in time of deaths among mice from intraperitoneal inoculation of EEE virus with, and without, prior infection with Trichinella spiralis

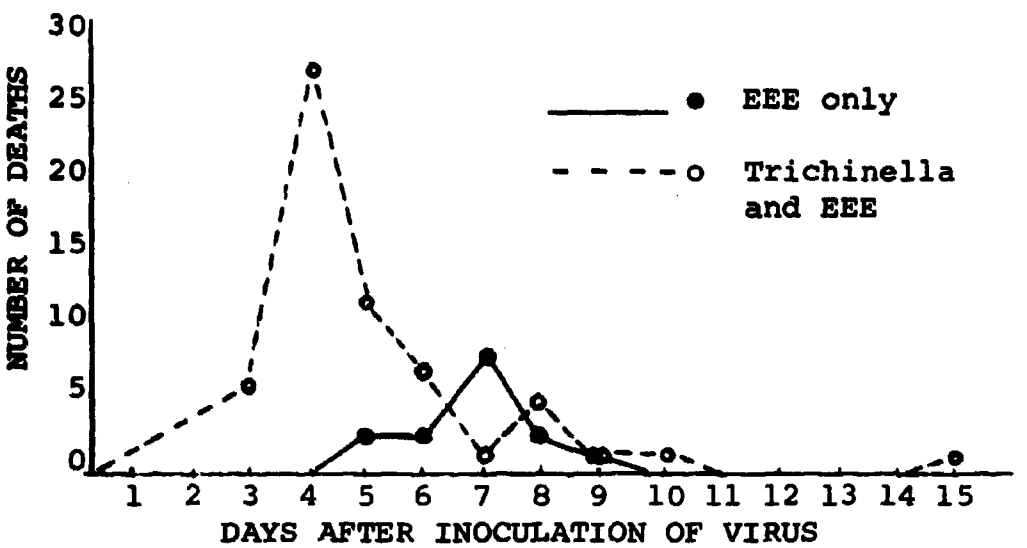

Fig. 2

Distribution in time of deaths among mice from intraperitoneal inoculation of Ilheus virus with, and without, prior infection with Trichinella spiralis

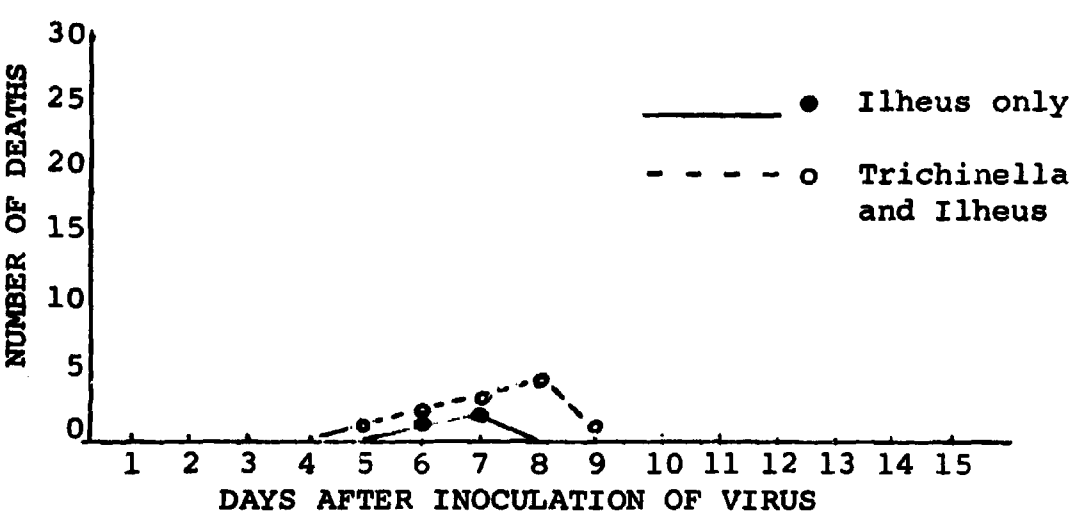

DESIGN AND REACTION MECHANISM OF SHORT-LIVED ALKYLATING AGENTS

CHARLES E.WILLIAMSON, JACOB I.MILLER, SAMUEL SASS AND BENJAMIN WITTEN*
CHEMICAL RESEARCH DIVISION, U.S. ARMY CHEMICAL
RESEARCH AND DEVELOPMENT LABORATORIES,
EDGEWOOD ARSENAL, MARYLAND

The importance of the alkylating agents in the study of basic life mechanisms is reflected in the many recent publications in this area. Exerting a wide spectrum of biological activity, these compounds are capable of producing radiation type symptoms, chromosomal aberrations, mutations, and carcinogenic as well as cancer chemotherapeutic effects (1).

In vitro experiments indicate that the primary process initiating cellular damage is the inactivation of deoxyribonucleic acid (DNA)(1). With proper understanding, it should be possible to design alkylating agents that would exert their effects almost exclusively in vital areas. Such compounds, would be expected to be extremely effective as chemical warfare agents because of the small doses required for the inactivation of DNA. Conversely, alkylating agents might be designed so that this toxic reaction with DNA occurs only in non-vital tissue as, for example, in malignant tumor tissue. Thus, short lived alkylating agents may find application in intra-arterial cancer chemotherapy. Such agents would exert their activity within the tumors but degrade rapidly to non-toxic products in the short time required to pass through the capillary bed and return to the lungs and heart. Upon arrival at the sensitive bone marrow areas only an insignificant quantity of active agent would remain.

In spite of the many studies, the basic mechanisms of chemical reactions of the alkylating agents are only vaguely understood. The current investigation was undertaken in an effort to better define the chemical actions of these compounds as they relate to the above areas of interest.

Approximately thirty new aliphatic sulfur mustards of widely varying structures were designed, synthesized (2,3), and their reactivities in aqueous media were determined. By utilization and analysis of Taft's linear free-energy relationships (4), the param-

eters controlling the reactivity of the mustards became apparent. These parameters have been formulated into a mathematical equation that can be used to aid in the design of sulfur mustards with predictable reactivities in aqueous media as measured by their half lives, which varied from fractions of a second to periods longer than five hours.

I. RESULTS AND DISCUSSION

A. Factors Influencing the Reactivity of Sulfur Mustards

The active species of sulfur mustards I is attributed to a highly reactive 3-membered ethylene sulfonium ion II (Eq.1)(5) which reacts very rapidly with water as well as with other nucleophilic reagents, such as thiosulfate, amines, proteins, thiols and nucleic acids (6). The rates of these reactions are all essentially identical and depend only upon the rate of formation of the ethylene sulfonium ion II. Because of the extremely rapid reaction between II and nucleophilic substances, the identity of the nucleophile is unimportant from a kinetic viewpoint. The rate of ethylene sulfonium ion formation (the rate controlling step) of a particular sulfur mustard thus defines its rate of reaction with all nucleophilic reagents. In accordance with eq. 1, these reactions exhibit first order kinetics.

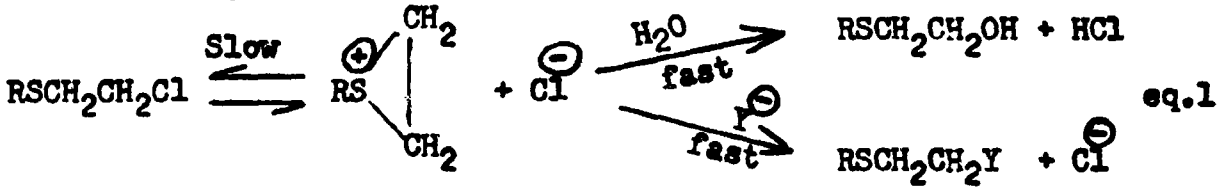

eq.1

I II where $Y^{\ominus}$ = nucleophilic reagent

Although the sulfonium ion reacts extremely rapidly, it is stable enough to exhibit selectivity toward the reacting species. Keen competition for II is observed in aqueous solutions containing small quantities of cellular constituents, such as DNA and sulfhydryl containing compounds (6).

A systematic study of the factors influencing the hydrolysis rates would, therefore, be indicative of the factors influencing the reactivity of mustards in aqueous media with all nucleophiles. In this study, the rates of cyclization of the mustards were determined by measurement of their hydrolysis rates.

The hydrolysis data were obtained by the 4-(4'-nitrobenzyl)pyridine procedure (7), pH 7.4, 37°, which measured the rate of cleavage of the carbon to halogen bond. In those instances where the reaction rates were very rapid at 37°, the rates were obtained at lower temperatures and extrapolated to 37° by means of the Arrhenius equation. The data are recorded in table 1 for the monofunctional mustards and in table 2 for the bifunctional mustards. These data indicate that the following two factors influence the rate of

cyclisation: (1) the nature of the substituent group R and (2) the type of leaving group X.

TABLE 1

Hydrolysis Rates of Monofunctional Sulfur Mustards, $RSCH_2CH_2Cl$ (pH 7.4, 37°)

S-No.	R	Experimental $t_{\frac{1}{2}}$ min.	Experimental k $min.^{-1}$	Theoretical σ^*	Theoretical $\log \frac{k}{k_0}$	Theoretical $\sigma^* \rho^*$
166	$CH_3(CH_2)_3-$	0.11	6.08	-0.130(a)	0.380	0.326
161	$(CH_3)_2CH-$	0.14	4.977	-0.190(a)	0.293	0.478
136	$CH_3CH_2CH_2-$	0.14	5.035	-0.115(a)	0.298	0.289
152	$C_2H_5OC(O)(CH_2)_4-$	0.14	4.966		0.292	
165	CH_3CH_2-	0.17	3.972	-0.100(a)	0.195	0.251
154	$(CH_3)_3C-$	0.19	3.622	-0.300(a)	0.155	0.753
153	CH_3-	0.22	3.221	0.00 (a)	0.104	0.00
124	$^{\ominus}OOC(CH_2)_2-$	0.24	2.924		0.062	
140	$C_2H_5OC(O)(CH_2)_3-$	0.49	1.409	0.091(b)	-0.255	-0.228
1	$HOCH_2CH_2-$	0.66	1.054	0.198(b)	-0.381	-0.497
6	$^{\ominus}OOCCH_2-$	0.79	0.875		-0.462	
156	$C_6H_5CH_2-$	0.81	0.859	0.215(a)	-0.470	-0.540
151	$NC(CH_2)_3-$	1.00	0.692	0.166(b)	-0.564	-0.417
171	$CH_3NHC(O)(CH_2)_2-$	1.03	0.673	0.254(b)	-0.576	-0.638
143	$C_2H_5OC(O)(CH_2)_2-$	1.09	0.634	0.254(b)	-0.602	-0.638
117	$H_2NC(O)CH_2-$	14.0	0.0496	0.71 (d)	-1.709	-1.782
100	$C_2H_5OC(O)CH_2-$	15.6	0.0445	0.71 (c)	-1.758	-1.782
146	$NCCH_2-$	308	0.00224	1.30 (a)		

(a) Values from ref. 4. (b) Derived as 1/2.8 x σ^* for substituent with one less methylene group (4). (c) 1/2.8 x σ^* for $COOCH_3$ (4). (d) σ^* value of 0.71 was assigned for the group $-CH_2CONHR$. This value best fits the data considered in this paper (2).

TABLE 2

Hydrolysis Rates of Bifunctional Sulfur Mustards,
$XCH_2CH_2S(CH_2)_nCONHCH_2CH_2NHCO(CH_2)_nSCH_2CH_2X$

(pH 7.4, 37°)

			Experimental			Theoretical		
			$t_{\frac{1}{2}}$		k			
S-No.	X	n	min.	sec.	min^{-1}	σ^*	$\log \frac{k}{k_o}$	$\sigma^* \rho^*$
46	Cl	1	17.1		0.0405	0.71	-1.797	-1.782
112	Cl	2	1.21	72.6	0.573	0.254	-0.646	-0.638
150	Cl	3	0.58	34.6	1.200	0.091	-0.325	-0.228
163	Cl	4	0.23	13.7	3.034	-0.031(a)	0.078	0.078
176	Br	1	0.28	16.6	2.506	0.71	-1.913	-1.889
179	Br	2	0.013	0.78	53.15 (b)	0.254	-0.600	-0.676
180	Br	3	0.0056	0.33	125.14 (b)	0.091	-0.253	-0.242
182	Br	4	0.003	0.18	228.51 (b)	-0.031	0.045	0.082
172	I	1	0.73	43.9	0.946	0.71	-1.986	-1.995
169	I	2	0.046	2.75	15.081(c)	0.254	-0.749	-0.714
173	I	3	0.018	0.99	42.016(c)	0.091	-0.231	-0.256

(a) Assigned value (2).
(b) Extrapolated from rate at 3.5° utilizing E_a value for S-176.
(c) Extrapolated from rate at 3.5° utilizing E_a value for S-172.

(1). Effect of Substituent Group R

Analysis of the data reveals that the reaction rate is dependent upon both the electron-withdrawing power of R and the proximity of R to the sulfur atom. As R becomes more effective in its electron-withdrawing capability, the carbon to chlorine bond becomes more stable toward hydrolysis (Table 3). Introduction of methylene groups between the sulfur atom and the polar substituent group decreases the effect of the latter due to the inductive insulating properties of methylene groups. Thus, the influence of the electron-withdrawing carbethoxy and nitrile groups on the reaction rates is markedly reduced when these groups are separated from the sulfur atom by two or more methylene units (Table 4).

TABLE 3

The Effect of Electron-Withdrawing Substituent (R) on the Hydrolysis Rates (C-Cl Bond) of Monofunctional Mustards ($ClCH_2CH_2SR$), pH 7.4, 37°

S-No.	R	$t_{\frac{1}{2}}$, min.	k, min^{-1}
136	$-CH_2CH_2CH_3$	0.14	5.035
153	$-CH_3$	0.22	3.221
156	$-CH_2C_6H_5$	0.81	0.859
100	$-CH_2COOC_2H_5$	15.6	0.0443
146	$-CH_2CN$	308	0.00224

TABLE 4

The Effect of Proximity of Electron-Withdrawing Substituent (R) to the Sulfur Atom on the Hydrolysis Rates (C-Cl Bond) of Monofunctional Mustards ($ClCH_2CH_2S(CH_2)_nR$), pH 7.4, 37°

S-No.	n	R	$t_{\frac{1}{2}}$, min.	k, min^{-1}
100	1	$-COOC_2H_5$	15.6	0.0443
143	2	$-COOC_2H_5$	1.09	0.634
140	3	$-COOC_2H_5$	0.49	1.409
152	4	$-COOC_2H_5$	0.14	4.966
146	1	$-CN$	308	0.00224
151	3	$-CN$	1.00	0.692

Consistent with eq.1, the rate of formation of the sulfonium ion II is directly dependent upon the relative basicity of the sulfur atom, which in turn, is influenced by the polar nature of nearby substituents. Thus, the presence of an adjacent electron-withdrawing group would be expected to decrease the basicity of the sulfur atom and concomitantly retard the rate of formation of II. Conversely, both the basicity of the sulfur atom and the rate of formation of II will be increased by adjacent electron-releasing substituents. The interposition of methylene units between the electron releasing or withdrawing substituent and the sulfur atom should miminize both effects.

One might expect that steric factors would also influence these reaction rates. As R becomes bulkier, the rate of cyclisation should decrease correspondingly. A series of compounds designed to test this hypothesis were prepared and their hydrolysis rates were

measured (Table 5). The rates were found not to be in the expected order if polar effects alone are considered and one might conclude that steric hindrance is responsible for the retarded rate in the bulky tertiary butyl mustard (S-154). However, a comprehensive analysis of the data, as discussed later in this report, revealed that steric considerations in the aliphatic mustards are of minor significance.

TABLE 5

Steric Considerations as Related to the Hydrolysis Rates (C-Cl Bond) of Monofunctional Mustards ($ClCH_2CH_2SR$), pH 7.4, 37°

S-No.	R		$t_{\frac{1}{2}}$, min.	k, min^{-1}
153	$-CH_3$	Increasing electron-releasing ability and steric hindrance of R ↓	0.22	3.221
165	$-CH_2CH_3$		0.17	4.972
161	$-CH(CH_3)_2$		0.14	4.977
154	$-C(CH_3)_3$		0.19	3.622

(2). Effect of the Leaving Halogen Function

One would logically predict that the substitution of the chlorine atom of the 2-chloroethyl sulfur mustards (eq. 1) by a better leaving function (e.g., $Br^{\ominus}$ or $I^{\ominus}$) would result in the more rapid formation of II and subsequent rapid hydrolysis. A comparison of the observed kinetic data of structurally related chloro-, bromo-, and iodo-mustards (Table 2) reveals that the bromo-mustards hydrolyze about three times more rapidly than the corresponding iodo-mustards and about one hundred times faster than the corresponding chloro-mustards[a]. In fact, the shortest lived mustard of the bromo series, S-182, has a half life of but 0.2 second.

B. Quantitative Correlation

Taft (4) has quantitatively correlated the hydrolysis rates of a series of aliphatic esters ($RCOOR'$) with their structures by modifying the Hammett equation. We have successfully used these relationships to correlate structure with the hydrolysis rates of the

(a)

Neither the quality of the bromine atom as a leaving group nor its electron-withdrawing power can explain the greater reactivity of the bromo-mustards as compared with the iodo-mustards. However, this anomaly is not unprecedented. It has been observed by Ross (8) that the bromoethyl nitrogen mustards hydrolyze more rapidly than the corresponding iodoethyl nitrogen mustards.

aliphatic sulfur mustards. Only polar and steric factors were considered since the mustards were so designed that resonance effects were minimal. Under these conditions, the Taft equation takes the following form (eq.2):

$$\log \frac{k}{k_o} = \sigma^* \rho^* + \delta E_s \qquad \text{eq. 2}$$

where: k_o is the hydrolysis rate of reference compound $ClCH_2CH_2SCH_3$

k is the rate of hydrolysis of the compound containing a substituent R in $ClCH_2CH_2SR$

σ^*, a constant, assesses the polar effect of substituent R

E_s, a constant, assesses the steric effect of substituent R

ρ^* is a constant describing the susceptibility of the reaction to polar effects

δ is a constant describing the susceptibility of the reaction to steric effects.

In the mustard series, eq. 2 attributes the relative reaction rates to the sum of polar and steric effects of the substituent group (R) attached to the sulfur atom. A large negative ρ^* value indicates that the cyclization process (eq. 1) is very dependent upon polar factors while a large positive δ indicates that steric effects are important. The data reported in the previous section indicated qualitatively that polar effects were the prominent factors governing the reaction rates. Accordingly, as a first approximation in the quantitative treatment, the term δE_s of the Taft equation was neglected and a graphic plot of log k versus σ^* was prepared for the monofunctional mustards (Fig 1).

The linearity observed in Fig. 1 confirms the strong dependence of the reaction rate on polar factors. Only two compounds (S-146 and S-154) deviate significantly. Compound S-146 ($ClCH_2CH_2SCH_2CN$) reacts at a rate somewhat faster than predicted by polar considerations alone. Since its first-order hydrolysis is so very slow, a complementary S_N2 reaction at the carbon-to-chlorine bond might produce a hybrid rate constant. The deviation of the tertiary butyl mustard S-154 from the linear plot cannot be readily explained. The steric constant (E_s) for the tertiary butyl group (-1.54), although large, is of the same magnitude expected for several other compounds in this series (e.g., S-100, S-117, S-143 and S-171). However, S-154 is the only member exhibiting such a markedly retarded rate. It would, therefore, appear unlikely that this retarded rate is due solely to steric hindrance. An alternate explanation was sought.

It is generally recognized that alpha hydrogen atoms adjacent to an unsaturated system produce an electronic stabilization beyond that expected from a purely inductive effect. This phenomenon, hyperconjugation, possibly plays a role in the mustards contain-

ing varying numbers of alpha hydrogen atoms. Although usually associated with the pi orbitals of aromatic, other unsaturated systems and carbonyl containing compounds, hyperconjugation may also be associated with the 3d orbitals of the sulfur atom. Both expansion of the sulfur atom's valency electron shell and stabilization by resonance into the 3d orbitals are well documented (9,10). Such hyperconjugation may occur in accordance with eq. 3.

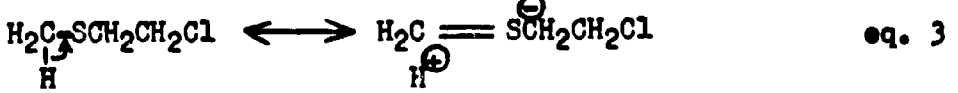

eq. 3

In conformance with the Baker-Nathan effect (11), an alpha hydrogen in the substituent group R of the mustard should impart added electron density to the sulfur atom and result in an increase in the reaction rate. Additional alpha hydrogens should intensify this effect. Such deviations are observed in these studies and may be attributed to hyperconjugation (Fig. 2). Compound S-154, which contains no alpha hydrogens, and S-161, which contains one alpha hydrogen atom, both fall outside the 95% confidence limits in the present treatment. The deviation is most pronounced with S-154.

In view of the agreement between the reaction rate and polar effects for most of the mustards, the steric susceptibility constant, δ in eq. 2, must be small and the term δE_s may properly be disregarded. For the determination of the susceptibility constant for polar effects (ρ^*) only monofunctional mustards that contained two alpha hydrogens were considered (Fig. 3). Variations due to possible hyperconjugation effects are therefore not introduced. Since it is believed that S-146 hydrolyzes simultaneously by both S_N1 and S_N2 mechanisms, this compound also was not included in the determination of ρ^*. A ρ^* value of -2.51 was obtained as the slope of the plot of log k versus σ^* (Fig. 3).

The reaction rate of the monofunctional mustard containing a methyl substituent (S-153) would normally be the reference standard from which log k_o is obtained. However, it contains three alpha hydrogen atoms. For this reason a hypothetical log k_o derived from Fig. 3 at the point where σ^* is equal to zero was considered to be more accurate. This log k_o value (0.404) was used in subsequent calculations.

Fig. 3 can be used to predict the reaction rates of 2-chloroethyl sulfur mustards. Deviations above the theoretical line are due to rate-accelerating effects, whereas deviations below the line result from steric or other retarding effects.

Employing the ρ^* and log k_o values obtained from Fig. 3 the Taft equation, $\log k/k_o = \sigma^*\rho^*$, can be applied to the reaction of sulfur mustards with nucleophilic reagents. The agreement shown in table 1 demonstrates the validity of this quantitative treatment.

Taft (4) has demonstrated that the effect of introducing a methylene group between a polar substituent and the reaction center reduces the σ^* value of the substituent by a factor of 1/2.8. Thus, the influence of n methylene groups would result in a new value, $\sigma^*/(2.8)^n$. At some sufficiently large number of methylene groups (i.e., at a point where the electron-withdrawing group no longer exerts an influence), one would expect the sign of σ^* to change from positive to a negative value. Since the term $\sigma^*/(2.8)^n$ can never be less than zero, no matter how large is n, this relationship fails at some value of n. In the mustards, this occurs when n equals 4, as in the case of S-152. Here, the hydrolysis rate is faster than predicted and is the same as S-136 (n-propyl mustard), which has no electron-withdrawing group.

From Fig. 3, σ^* values can be assigned to those substituents which do not fit the linear plot because of failure of this relationship. Such an assignment for S-152 is shown in Table 6. Included in the table are two mustards containing the carboxylate ion (S-6 and S-124), for which there are no previously recorded values. The literature σ^* value for the unionized carboxyl group (4) is not applicable to its conjugate base.

The present quantitative treatment applies to bifunctional as well as monofunctional mustards. Log k_o and ρ^* values were obtained for the structurally related bifunctional chloro-, bromo-, and iodo- sulfur mustards (Fig. 4, Table 7). Table 7 illustrates the dependence of log k_o upon the nature of the leaving halogen. The deviation of ρ^* is small.

TABLE 6

Assignment of New Polar Substituent Constants for $RSCH_2CH_2Cl$

Compound	R	σ^* for R
S-152	$-CH_2CH_2CH_2CH_2COOC_2H_5$	-0.116
S-6	$-CH_2COO^{\ominus}$	+0.184
S-124	$-CH_2CH_2COO^{\ominus}$	-0.025

TABLE 7

Taft Constants For Bifunctional Halo-Sulfur Mustards
$XCH_2CH_2S(CH_2)_nCONHCH_2CH_2NHCO(CH_2)_nSCH_2CH_2X$

X	ρ^*	log k_o
Cl	-2.51	0.404
Br	-2.66	2.321
I	-2.81	1.962

II. CONCLUSION

In aqueous buffered media or in other biological systems such as blood, the life of aliphatic sulfur mustards depends upon the rate of ethylene sulfonium ion formation. A kinetic study of this rate controlling step has led to a more comprehensive understanding of the reaction mechanism of these alkylating agents.

The major factors influencing their reactivity with nucleophilic reagents, as measured by their hydrolysis rates, have been shown to be: (1) the inductive polar effects of the substituent adjacent to the sulfur atom and (2) the nature of the leaving halogen function on the carbon atom beta to the sulfur atom. Spatial considerations (steric hindrance) are of minor significance. The concept of hyperconjugation has been useful in the explanation of a number of seemingly anomalous results.

Based on the quantitative treatment of the kinetic data, the Taft equation has been simplified. In this form, the equation can be used to design mustards of predictable reactivities. As part of this investigation, compounds have been synthesized possessing half lives at pH 7.4, 37° as short as 0.2 second to longer than 5 hours.

With the very short lived alkylating agents, the time that is required for transport to, and penetration of, the cellular membranes becomes a critical factor in determining the quantity of alkylating agent available for toxic reactions at either the cell surface or the intra-nuclear DNA. Thus, the short-lived mustards should be valuable in the study of cytotoxic mechanisms as related to cancer chemotherapy and chemical warfare.

III. LITERATURE CITED

(1) Schmidt, L.H., et al., Ann. N.Y. Acad Sci. 68, 657-1266 (1958).
(2) Williamson, C.E., et al., J. Nat. Cancer Inst. 31, 273-296 (1963)
(3) Sass, S., et al., submitted for publication.
(4) Taft, R.W., Jr., "Steric Effects in Organic Chemistry" (Newman, M.S., Ed.), New York, John Wiley and Sons, Inc., 1956, pp.559-675.
(5) Price, C.C. and Wakefield, L., J. Org. Chem. 12, 232-237 (1947).
(6) Alexander, P., Advances in Cancer Research 2, 2-72 (1954).
(7) Witten, B., et al., Cancer 15, 1041-1055 (1962).
(8) Ross, W.C.J., Advances in Cancer Research 1, 397-449 (1953).
(9) Jaffe, H.H., J. Chem. Phys. 22, 1430-1433 (1954).
(10) Price, C.C., and Morita, H., J. Amer. Chem. Soc. 75, 4747-4750 (1953).
(11) Baker, J.W., and Nathan, W.S., J. Chem. Soc. 1844-1847 (1935).

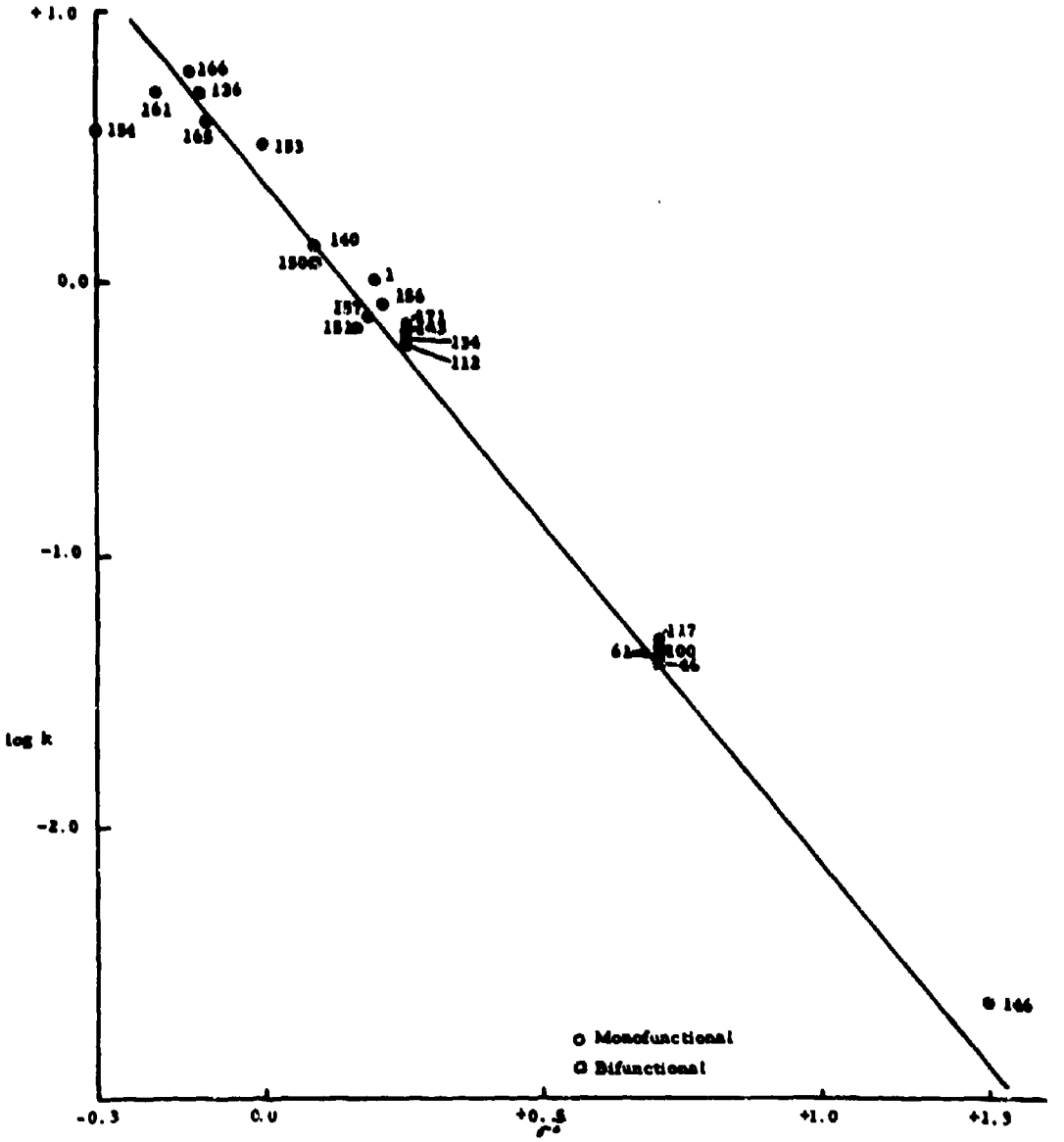

Fig 1. Plot of log k vs. σ^* For Monofunctional 2- Chloroethyl Sulfur Mustards Illustrating the Dependence of Reaction Rates on the Electron-Withdrawing Power of Substituents.

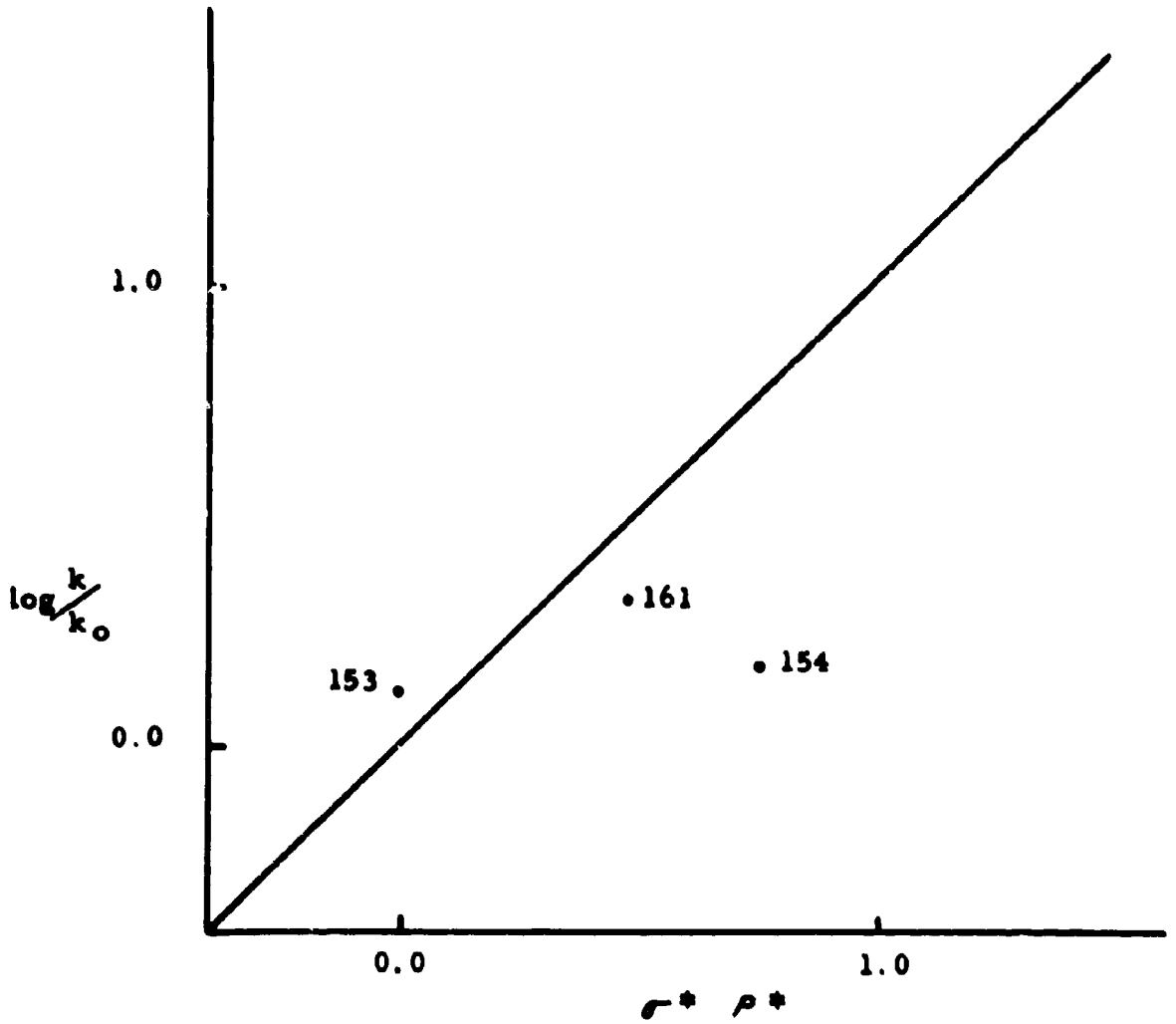

Fig. 2. Deviation from Predicted Reaction Rate with Variation in Number of α - Hydrogen Atoms. S-153 = 3; S- 161 = 1; S- 154 = 0; Correlation Line = 2.

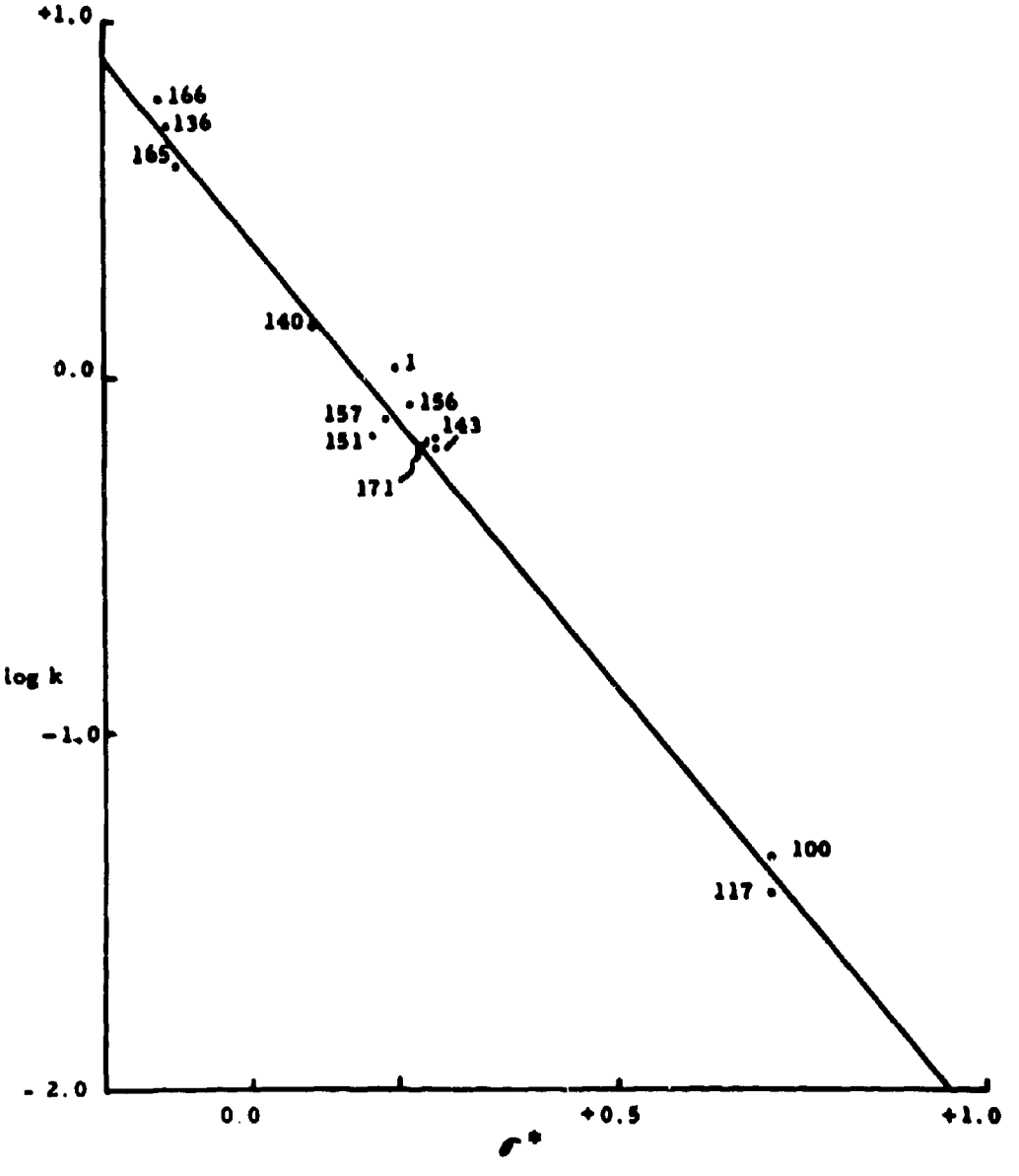

Fig. 3 Plot of log k vs σ^* For Monofunctional 2-Chloroethyl Sulfur Mustards Containing Two Alpha Hydrogen Atoms. Slope = - 2.51; log k = 0.404 where $\sigma^* = 0$.

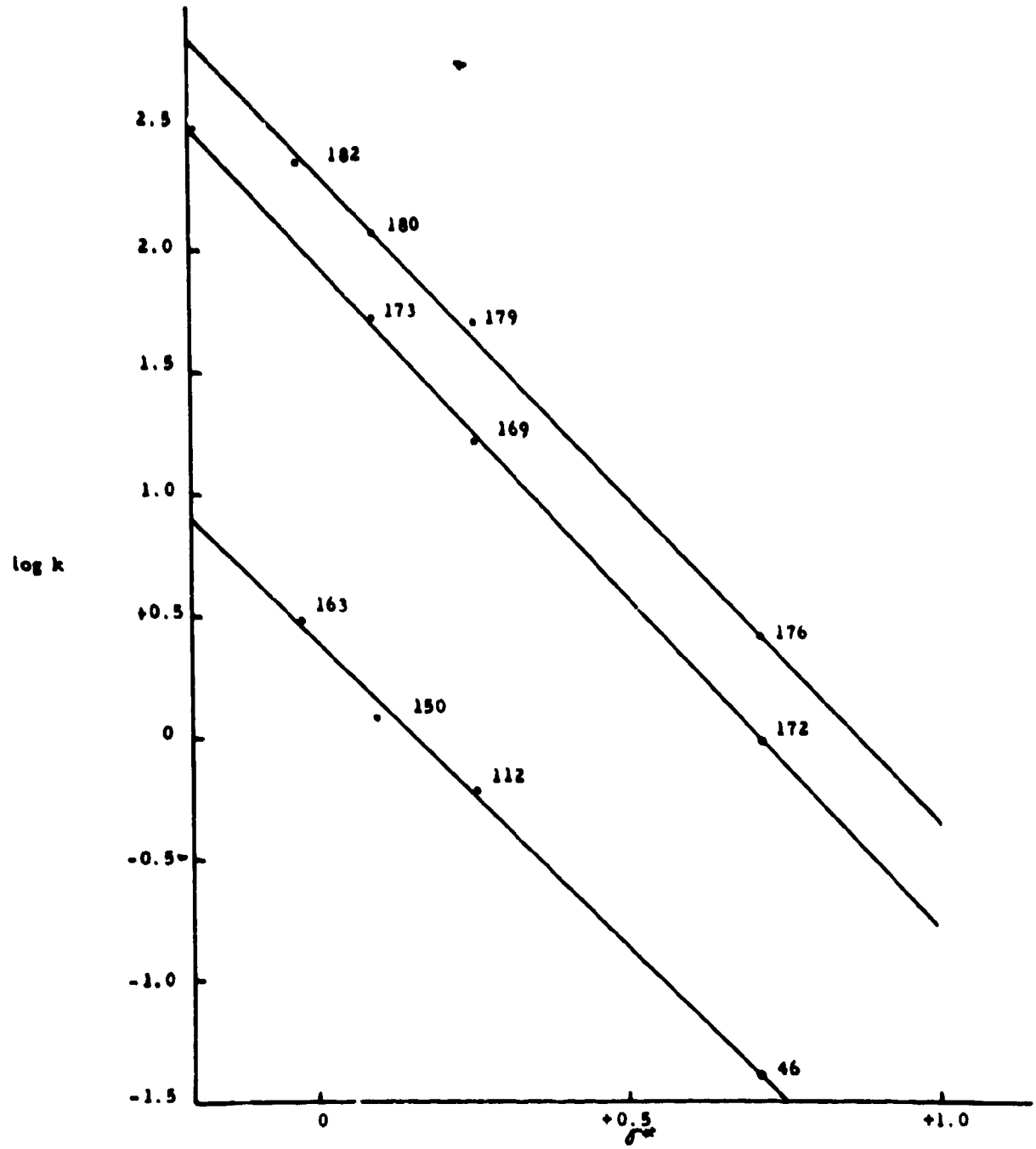

Fig. 4. Plot of log k Versus σ^* For Structurally Related Bifunctional Iodo-, Bromo- and Chloro-Sulfur Mustards.

MEASUREMENTS OF TRUE DARK CONDUCTIVITIES IN FERROCENE CRYSTALS

PFC EDWARD ZEHLER and CLAIRE LOSCOE BURKE
U. S. ARMY ELECTRONICS RESEARCH & DEVELOPMENT LABORATORIES
FORT MONMOUTH, NEW JERSEY

The existence of a true dark conductivity in organic materials has been widely questioned. Although recent investigations have clarified to some extent the mechanism of the photoconduction, up until now no proof has been offered that real conduction through the bulk occurs in the dark. In general, experimentally the conductivities of organics increase exponentially with 1/T which is typical behavior for intrinsic semiconductors, and has resulted in the name "organic semiconductors." However, activation energies calculated from these curves, together with the low conductivities, if ordinary band models are assumed, lead to unrealistically high mobilities which are not confirmed by photoconductivity measurements. Further more, the dark conductivity exhibits a "sluggish" behavior with voltage and temperature changes. Thus, the dark conductivity is usually ascribed to the effect of dielectric relaxation, blocking contacts, and impurity and surface effects.

In the present paper, we describe systematic dark conductivity measurements on a monomeric organic crystal. The material chosen was ferrocene which, because of its relatively low room temperature resistivity of the order of 10^{13} ohm cm and its simple structure, appears to be very suitable as a model substance for dark conductivity investigations. From the measurements performed, including voltage probing along the sample, long time observations, and measurement of resistivity with guard rings, it is established that the dark conductivity exists and cannot be explained as due to contact effects, dielectric relaxation or surface conduction. Dependences of the conductivity on impurity content and crystal direction are difficult to determine and are discussed. Thermoelectric power data show that the Seebeck effect is as large as 1.2 mV/degree and that holes are more mobile than electrons.

Slide 1 shows some of the properties of ferrocene.[1] Also

known as dicyclopentadienyliron, ferrocene is an organo-metallic compound consisting of two five-membered rings with an iron atom "sandwiched" between them. It melts at 173-174°C, and is stable in air and water. Ferrocene forms orange colored crystals in two shapes, needles and diamond-shaped plates whose faces are the (110) and (001) planes. The crystals are dichroic with the differences in absorption with directions of the plane of polarization of the radiation occuring when the incident radiation is perpendicular to the (110) face. When the crystal is observed in plane polarized white light its color changes from brownish-red to bright yellow as the plane of polarization is rotated.

All samples used in the measurements were single crystals of ferrocene grown in one of four ways: (1) by slow evaporation of a saturated benzene solution, (2) from the melt in an enclosed glass tube (Bridgman method), (3) from the vapor phase in the presence of a temperature gradient (sublimation) and, (4) from the melt within the enclosed zone refiner tube. The crystals were cut to the desired shape with a razor blade, polished by rubbing them on a benzene soaked paper, and finally rinsed in benzene to obtain clean shiny surfaces.

The nature of silver, finely powdered carbon, and copper iodide contacts to ferrocene was investigated by measuring the voltage drop between one end of the crystal and two different points along the sample. Slide 2 shows, in the upper left corner, a diagram of the sample arrangement. The end contacts were made by painting a suspension of the desired material on the ferrocene. Center probes were made in two ways, by melting fine wires into the crystal and by painting on contacts. Typical sample dimensions were 3 x 4 x 8 mm^3. A Cary vibrating-reed electrometer model 31 was used to measure the voltage between the end and the center contact. The graph shows the electrometer reading in volts at various times after 3 volts have been applied along the length of the crystal. It is seen that after a short time, i.e., five minutes, the electrometer reading is low, increases as the time increases, and finally after 90 minutes has reached equilibrium at a point on the ideal curve. Thus, if a sufficiently long time is allowed after initially applying the voltage, ferrocene shows a linear voltage drop along its length like an ordinary resistor. There is no evidence of the end contacts influencing the results, particularly there appear to be no blocking contacts. The long time needed for the electrometer reading to become constant is what would be expected for a circuit with a high resistance, i.e., there is a long time constant due to the high resistance of the ferrocene. These data were obtained using silver painted end contacts and center probes made by melting copper wires into the crystal. The same behavior was observed with end contacts of aquadag and copper iodide, with silver paint center probes, and also applied voltages of 1.5 V and 10 V.

Slide 3 shows the experimental arrangement for measuring the resistivity and the thermoelectric power of ferrocene as a function of temperature. Essentially the same apparatus was used for both measurements with minor changes indicated in the circled portion of the figure. Part (a) shows the arrangement for the resistivity measurements. The sample was placed in series with a battery and a known resistor of either 10^{10} or 10^{12} ohms, depending on the resistance of the sample. The voltage drop across the known resistor was measured with the Cary vibrating-reed electrometer. Thus, the current in the circuit and the resistance of the ferrocene sample are determined. It was observed that ten minutes between readings was a sufficient time to eliminate any dielectric relaxation effects. Resistivity measurements were also made using a guard ring attached to the top of the sample to minimize any surface conduction that may be present. It was found that the use of the guard ring in the circuit produced a negligible effect in the resistivity.

In order to obtain stable readings of the electrometer, it was necessary to shield the entire input circuit. The sample mount and electrometer head were enclosed in an aluminum box which was grounded to the electrometer case. The ambient temperature was controlled by a small dc electric heater placed outside the aluminum box, but arranged in such a way as to heat only a small portion of the shield which was insulated thermally, but not electrically from the main shield. The temperature was measured by means of a chromel-alumel thermocouple attached to the block on which the sample rested. Since all leads introduced into the shield box produced considerable static pickup in the electrometer, the wire leads for the thermocouples were disconnected at the box during the voltage measurements.

Part (b) shows the arrangement for the measurement of the thermoelectric power. Both the known resistor and the battery were removed and the guard ring was not used. A copper block with a thermocouple embedded in it was the top contact to the sample. The top of the copper block was painted black and was heated by means of a strong microscope light focused on the block through a hole in the shield. In this way the temperature difference necessary for obtaining the thermoelectric power was generated.

The resistivity is found, like that of an intrinsic semiconductor, to follow an exponential dependence on temperature. Slide 4 shows the logarithm of the resistivity as a function of 1000/T for five different ferrocene samples. For each sample the resulting graph is a straight line. From the slope of this line is calculated an "activation energy." It is noticed that whereas the room temperature resistivities of the samples vary from 10^{12} to 10^{14} ohm cm, the "activation energy" varies only slightly.

Similar curves were obtained for 27 samples which included crystals grown by each of the four methods previously outlined.

Slide 5 shows the distribution of these samples by resistivity in part (a), and by "activation energy" in part (b). It is seen that the spread in resistivity is large extending, at room temperature, over three orders of magnitude. Although more samples fall in the 6.4×10^{12} - 2.56×10^{13} block than in any other, there are enough samples in each block throughout the range to indicate that this is not a normal scattering due to some systematic error. The spread in resistivities cannot be correlated with impurities or crystal direction. It is possible, however, that crystal imperfections not detectable by the eye are responsible. On the other hand, the scattering in activation energy for the same samples appears to be small. The average ϵ for the 27 samples measured was 0.89 eV.

Resistivity measurements made both parallel and perpendicular to the (001) direction were also found to scatter through the same ranges as obtained for the undetermined directions. Thus, any anisotropy with crystal direction is probably slight. The role of impurities is more difficult to determine. Although material obtained from different positions along the zone refined tube gave a wide scattering in resistivities, encompassing the entire range of resistivities obtained, the nature of any impurities present, whether they are removed by the zone refining, and if they are present in crystals grown by the other three methods is not known.

The thermoelectric power was measured on crystals about 0.5 cm^2 and about 0.4 mm thick, grown by two methods, (1) from benzene solution and, (2) by sublimation. Contacts were silver or copper iodide. Measurements were made between room temperature and 80°C with temperature differences usually between 8 and 12°. Slide 6 shows the thermoelectric power (Seebeck coefficient) in millivolts per degree as a function of temperature for various samples. The effect is positive. Average values are about 1.2 mV/degree at room temperature and increase slightly with increasing temperature. There are no noticeable differences between the values for silver and copper iodide contacts. Likewise, there appear to be no differences between values for crystals grown from benzene solution and those grown by sublimation. The amount of scattering in the thermoelectric power for various samples is approximately $\pm$20 percent and is considerably smaller than the usual scattering in electrical properties of organic crystals. It is likely that some scattering may have been caused by tiny cracks in the samples.

As a result of experiments which included voltage probing along the crystal, long time observations, and resistivity measurements using guard rings, it is concluded that contact and surface effects and dielectric relaxation effects have a negligible effect on the conductivity of ferrocene crystals providing sufficient time is allowed for the measurements. A true dark conductivity exists in ferrocene which at room temperature varies from sample to sample over three orders of magnitude from 10^{-12} to 10^{-14} ohm^{-1} cm^{-1} with no apparent dependence on impurities or crystal direction, increases

exponentially with 1/T as the temperature increases, and yields with only small scattering of these data, and average "activation energy" of 0.89 eV. The thermoelectric power is about 1.2 mV/degree, and is positive indicating a higher mobility of positive rather than negative charges.

On the basis of its exponential dependence on reciprocal temperature, the conduction may be thought of as "intrinsic." The spread in conductivities, however, cannot be attributed to systematic error, impurities or anistropy due to crystal direction. Instead it is proposed that another mechanism, crystal imperfections, is responsible for the wide range of conductivities and to some extent influences the temperature dependence of the conductivity. Since imperfections occur in crystals as a result of cutting, polishing, and heat treatment, it is likely that such imperfections were introduced into our samples during their growth and preparation. It appears that future experiments to discover the kinds and numbers of imperfections present in molecular crystals, together with how they influence the conductivity will be necessary for the determination of the conduction mechanism in organics. It may be that the idea of "intrinsic conduction" will have to be redefined for molecular conductors.

LITERATURE:

1. J. D. Dunitz, and L. E. Orgel, Nature, 171, 121 (1953).

ACKNOWLEDGMENT:

The authors wish to express their appreciation to Mr. Herbert Mette, USAELRDL., for his helpful discussions and comments.

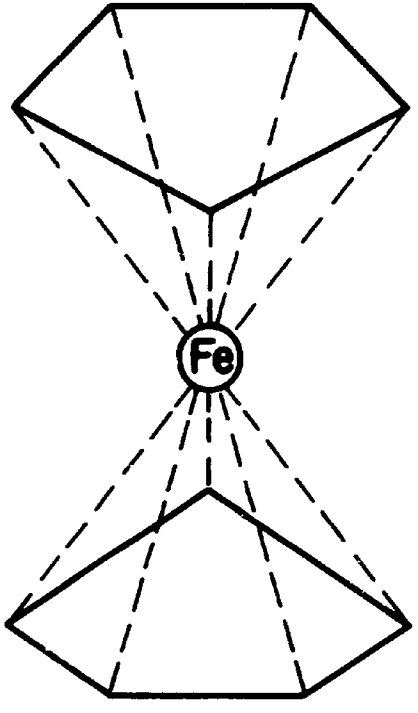

ORANGE CRYSTALS

MONOCLINIC WITH TWO MOLECULES PER UNIT CELL

DICHROIC

MELTS 173-174 °C

STABLE IN AIR AND WATER

FIG. I FERROCENE (DICYCLOPENTADIENYLIRON) DIAGRAM OF MOLECULE AND PROPERTIES

FIG. 2 ELECTROMETER READING BETWEEN ONE END AND TWO DIFFERENT POINTS ALONG CRYSTAL AT VARIOUS TIMES AFTER APPLICATION OF VOLTAGE (3 VOLTS).

SYMBOL	TIME
□	90 MIN
△	60
÷	30
▽	15
×	10
○	5

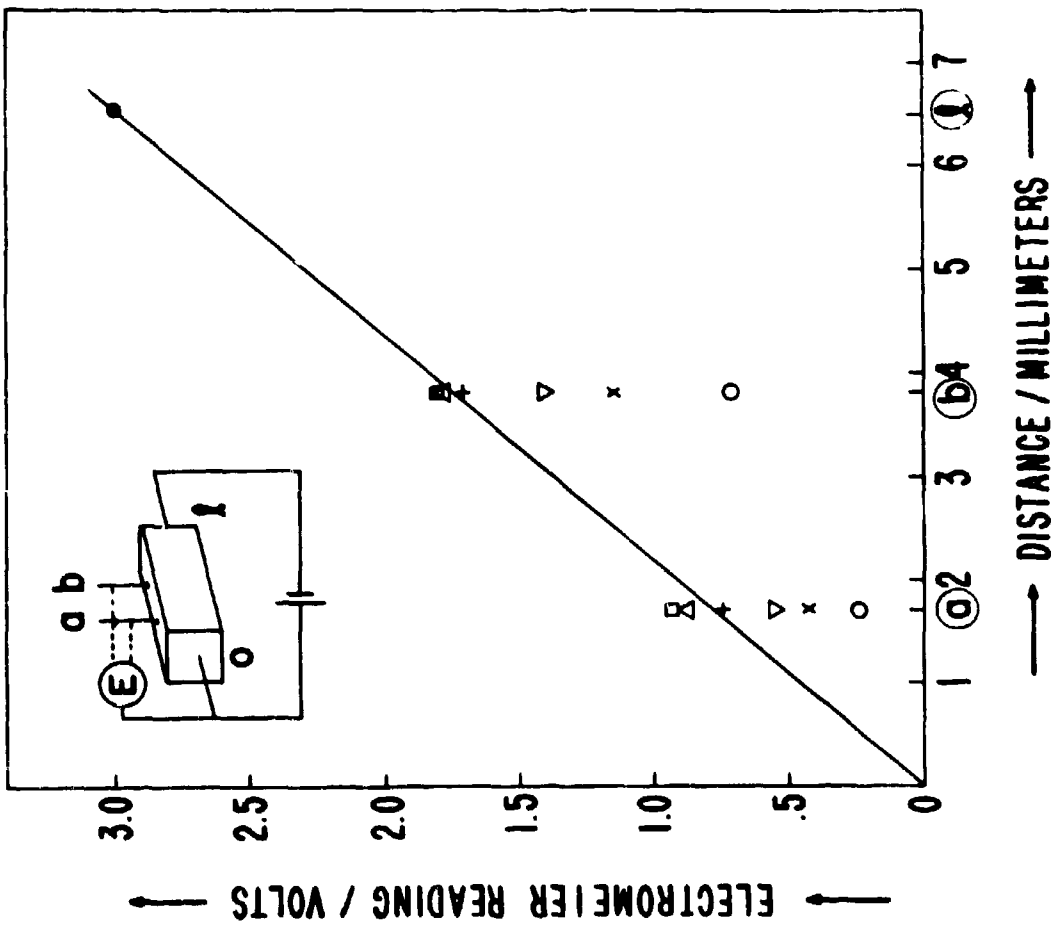

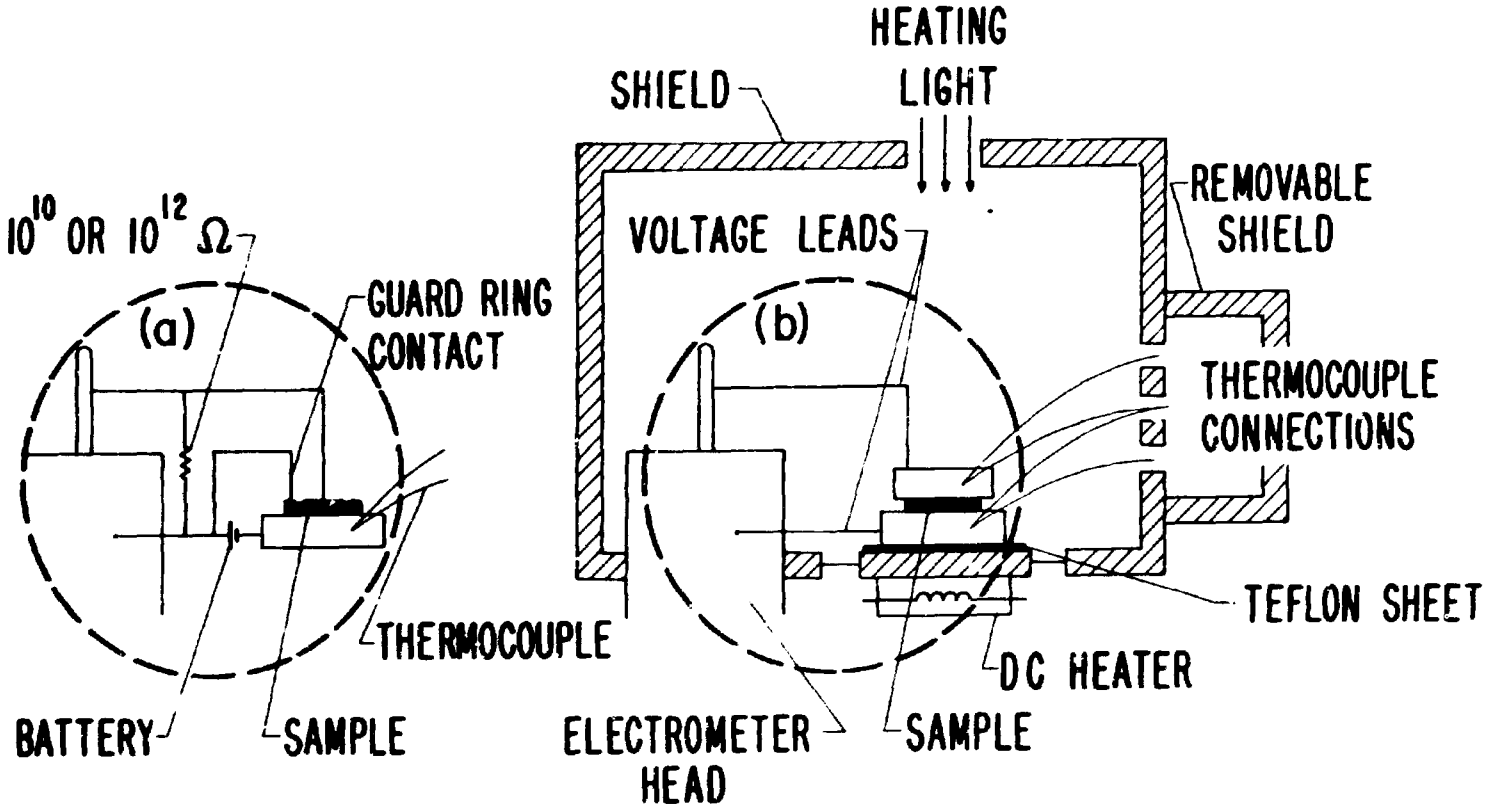

FIG. 3 EXPERIMENTAL ARRANGEMENT FOR MEASURING

(a) RESISTIVITY

(b) THERMOELECTRIC POWER OF FERROCENE CRYSTALS

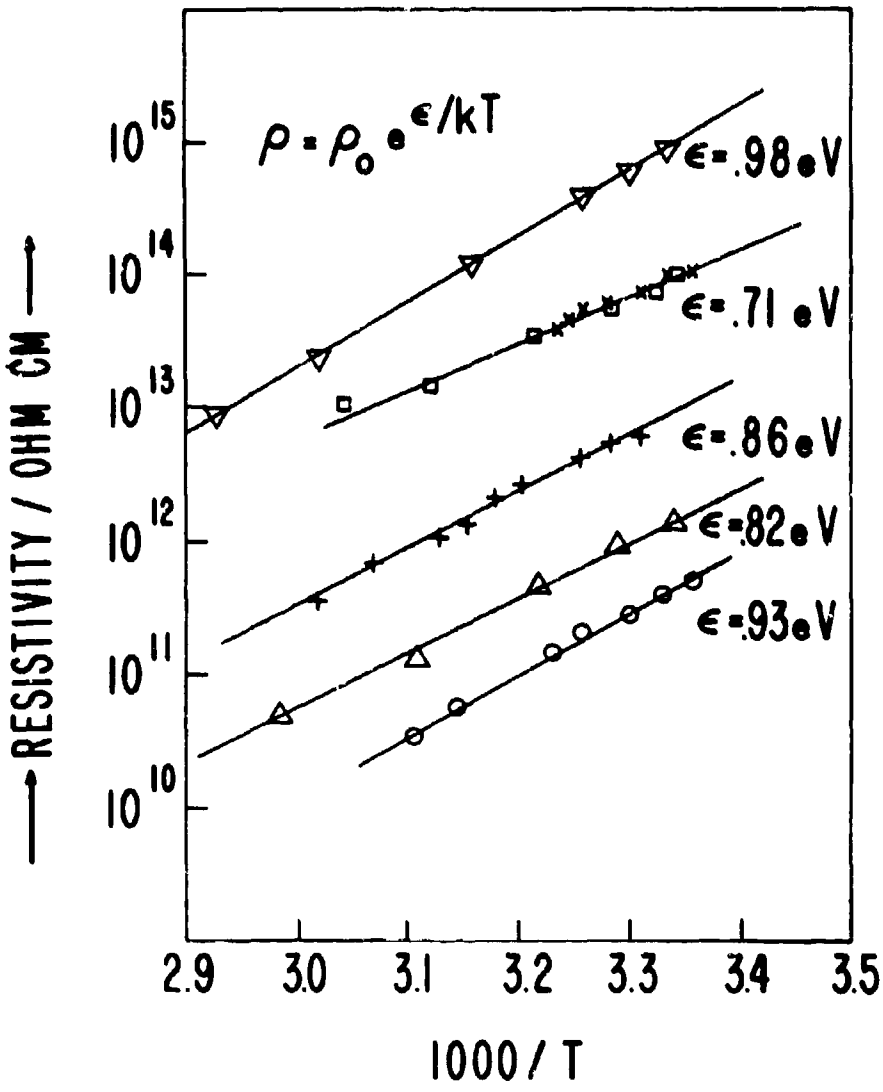

FIG. 4 RESISTIVITY OF VARIOUS FERROCENE SAMPLES AS A FUNCTION OF TEMPERATURE BETWEEN ROOM TEMPERATURE AND 70 °C.

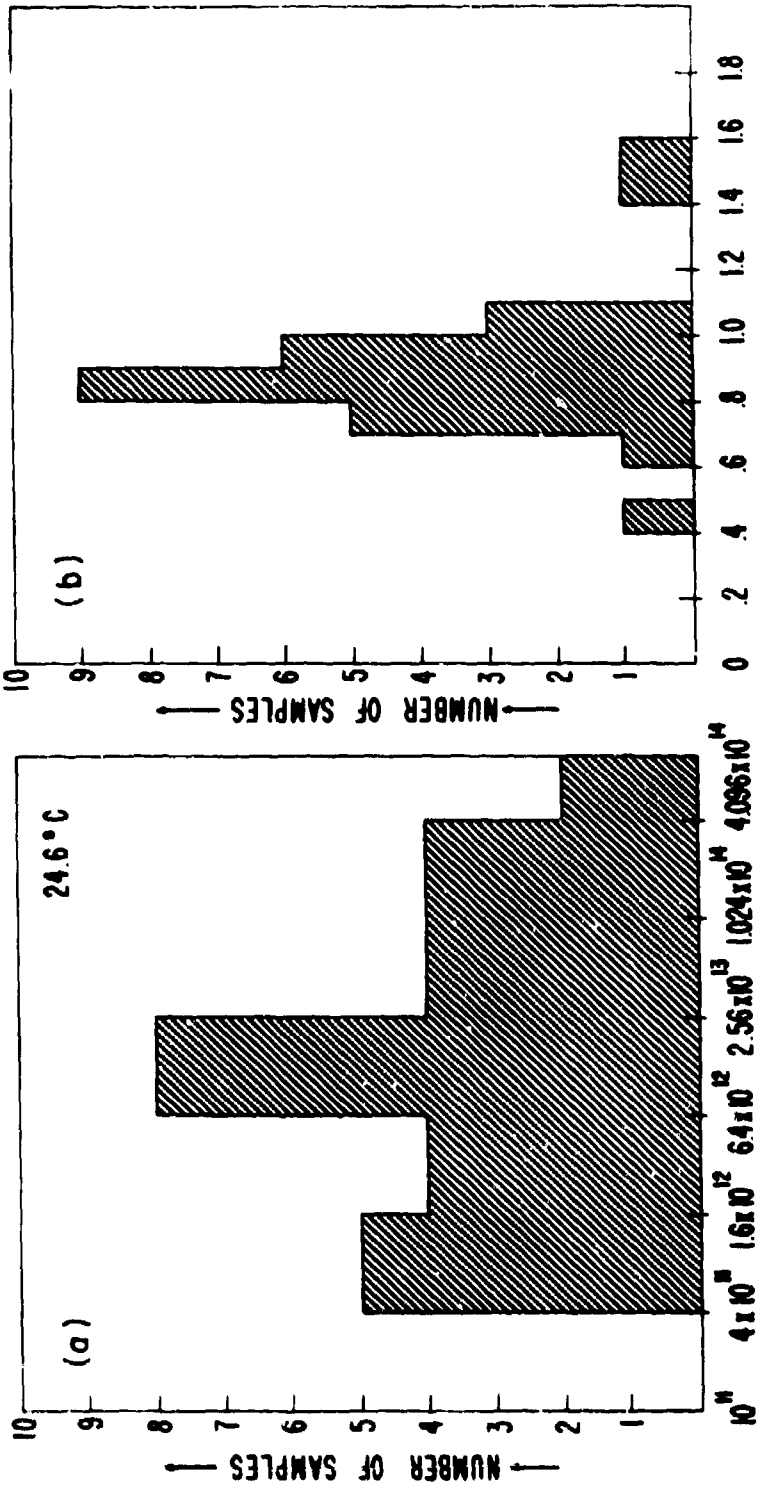

FIG. 5 DISTRIBUTION OF 27 SAMPLES BY

(a) RESISTIVITY (b) ACTIVATION ENERGY

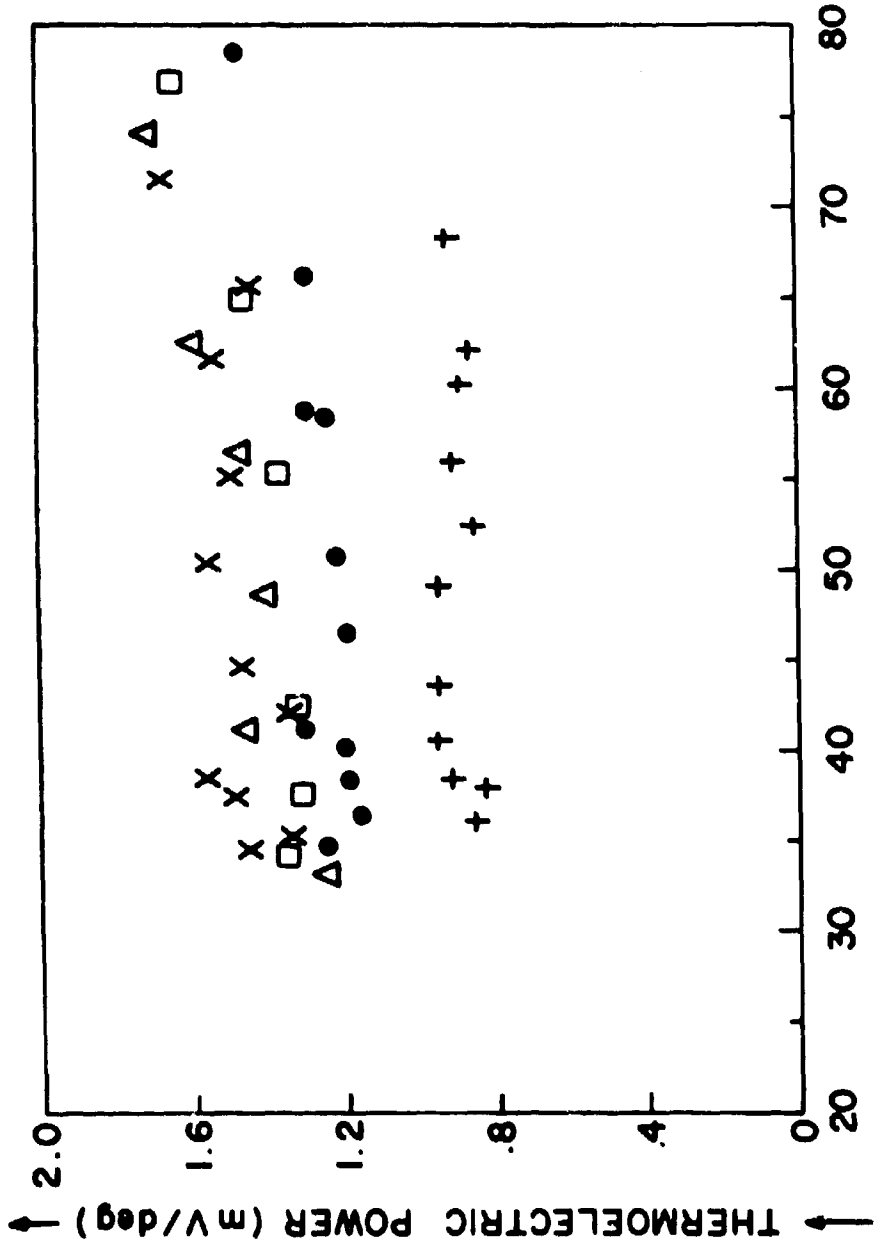

FIG. 6. THERMOELECTRIC POWER OF FERROCENE AS A FUNCTION OF TEMPERATURE BETWEEN 30° AND 80° C

DISTRIBUTION LIST

DEPARTMENT OF DEFFENSE

Director of Defense, Research & Engineering Washington 25, D. C.	1
Defense Documentation Center Building 5 Cameron Station Alexandria, Virginia 22314	250
Chief Defense Atomic Support Agency Washington 25, D. C.	1
Director Weapons Systems Evaluation Group Department of Defense Washington 25, D. C.	1
Director Armed Forces Institute of Pathology Washington 25, D. C.	1
Commandant Industrial College of the Armed Forces Fort Lesley J. McNair Washington 25, D. C. Attn: Library	1
Commandant National War College Fort Lesley J. McNair Washington 25, D. C. Attn: Library	1
Commandant Armed Forces Staff College Norfolk, Virginia Attn: Library	1

DEPARTMENT OF THE ARMY

Assistant Secretary of the Army (R&D) Department of the Army Washington 25, D. C.	1
Chief of Staff United States Army Washington 25, D. C.	1
Chief of Research and Development United States Army Washington 25, D. C. Attn: Scientific and Technical Information Division	10

DEPARTMENT OF THE ARMY (Continued)

Commanding Officer Army Research Office (Durham) Box CM, Duke Station Durham, North Carolina	1
Chief US Army R&D Liasion Group (9983) (Europe) APO 757 New York, New York	1
Commanding Officer US Army R&D Group (Far East) (9984) APO 343 San Francisco, California	1
Chief US Army Security Agency Arlington Hall Station Arlington 12, Virginia	1
Deputy Chief of Staff for Logistics United States Army Washington 25, D. C.	1
Deputy Chief of Staff for Military Operations United States Army Washington 25, D. C.	1
Deputy Chief of Staff for Personnel United States Army Washington 25, D. C.	1
Assistant Chief of Staff for Intelligence United States Army Washington 25, D. C.	1
Commanding Officer US Army Personnel Research Office Washington 25, D. C.	1

Army Materiel Command

Commanding General U. S. Army Materiel Command Washington, D. C.	1
Commanding General U. S. Army Materiel Command Attn: AMCSA-Chief Scientist Washington, D. C.	1
Commanding General U. S. Army Materiel Command Attn: AMCMS Washington, D. C.	1
Commanding General U. S. Army Materiel Command Attn: AMCMU Washington, D. C.	1
Commanding General U. S. Army Materiel Command Attn: AMCAD Washington, D. C.	1
Commanding General U. S. Army Materiel Command Attn: AMCIS Washington, D. C.	1
Commanding General U. S. Army Materiel Command Attn: AMCCP-C Washington, D. C.	1
Commanding General U. S. Army Materiel Command Attn: AMCRD-S Washington, D. C.	1
Commanding General U. S. Army Materiel Command Attn: AMCRD-I Washington, D. C.	1
Commanding General U. S. Army Materiel Command Attn: AMCRD-DE Washington, D. C.	1
Commanding General U. S. Army Materiel Command Attn: AMCDS Washington, D. C.	1
Commanding General U. S. Army Materiel Command Attn: AMCRD-DW Washington, D. C.	1
Commanding General U. S. Army Missile Command Redstone Arsenal, Alabama	10

Army Materiel Command (continued)

Commanding General U. S. Army Missile Command Attn: Director of Missile Intelligence Redstone Arsenal, Alabama	1
Commanding General White Sands Missile Range Las Cruces, New Mexico	1
Commanding General U. S. Electronics Proving Ground Fort Huachuca, Arizona	1
Commanding General U. S. Army Satellite Communications Agency Fort Monomouth, New Jersey	1
Commanding General U. S. Army Tank-Automotive Center Warren, Michigan	1
Commanding General U. S. Army Electronics Command Fort Monmouth, New Jersey	1
Commanding General U. S. Army Mobility Command Warren, Michigan	1
Commanding General U. S. Army Munitions Dover, New Jersey	2
Commanding General U. S. Army Supply & Maintenance Command Washington, D. C.	1
Commanding General U. S. Army Test & Evaluation Command Aberdeen Proving Ground, Maryland	1
Commanding General U. S. Army Weapons Command Rock Island Arsenal Rock Island, Illinois	1
Commanding General U. S. Army Weapons Command Attn: R&D Directorate Rock Island Arsenal Rock Island, Illinois	2
Commanding General Natick Laboratories Natick, Massachusetts	2
Commanding Officer U. S. Army Foreign Science & Technology Center Munitions Building Washington, D. C.	5
Commanding Officer U. S. Army Ballistic Laboratories Aberdeen Proving Ground, Maryland	1

Army Materiel Command (continued)

Commanding Officer U. S. Army Human Engineering Laboratories Aberdeen Proving Ground, Maryland	1
Commanding Officer U. S. Army Coating & Chemical Laboratory Aberdeen Proving Ground, Maryland	1
Commanding Officer U. S. Army Cold Regions Research and Engineering Laboratory Hanover, New Hampshire	2
Commanding Officer U. S. Army Materiels Research Agency Watertown Arsenal Watertown, Massachusetts	1
Commanding Officer Harry Diamond Laboratories Washington, D. C.	2
Commanding Officer U. S. Army Nuclear Defense Laboratory Edgewood Arsenal, Maryland	1
Commanding Officer Aberdeen Proving Ground Aberdeen Proving Ground, Maryland	1
Commanding Officer Dugway Proving Ground Salt Lake City, Utah	1
Commanding Officer Edgewood Arsenal Edgewood Arsenal, Maryland	1
Commanding Officer Frankford Arsenal Philadelphia, Pennsylvania	2
Commanding Officer Picatinny Arsenal Dover, New Jersey	2
Commanding Officer Rock Island Arsenal Rock Island, Illinois	2
Commanding Officer Springfield Armory Springfield, Massachusetts	2
Commanding Officer Watervliet Arsenal Watervliet, New York	2
Commanding Officer U. S. Army Biological Laboratories Fort Detrick, Maryland	1
Commanding Officer U. S. Army Chemical Research & Development Laboratories Edgewood Arsenal, Maryland	1

Army Materiel Command (continued)

Commanding Officer 1
U. S. Army Electronics Research & Development Laboratory
P. O. Box 205
Mountain View, California

Commanding Officer 1
U. S. Army Engineer Research & Development Laboratories
Fort Belvoir, Virginia

Commanding Officer 1
U. S. Army Transportation Research Command
Fort Eustis, Virginia

Office of the Project Manager, CCIS-70 1
Army Materiel Command
Fort Belvoir, Virginia

Office, Chief of Engineers

Chief of Engineers 4
Department of Army
Washington, D. C. 20315
Attn: Chief Scientific Advisor

Commanding General 1
U. S. Army Engineer Division
Ohio River Division Laboratories
Cincinnati 27, Ohio

Director 2
U. S. Army Waterways Experiment Station
P. O. Box 631
Vicksburg, Mississippi

Director 1
U. S. Army Engineer Geodesy Intelligence
and Mapping R&D Agency
Fort Belvoir, Virginia

Office of The Surgeon General

The Surgeon General 1
United States Army
Washington 25, D. C.

Commanding General 1
U. S. Army Medical R&D Command
Washington 25, D. C.

Commanding Officer 1
U. S. Army Research Institute of Environmental Medicine
Natick, Massachusetts

Office of The Surgeon General (continued)

Commanding Officer U. S. Army Medical Research Laboratory Fort Knox, Kentucky	1
Commanding Officer U. S. Army Medical Research & Nutrition Laboratory Fitzsimons Army Hospital Denver 30, Colorado	1
Commanding Officer U. S. Army Surgical Research Unit Brooke Army Medical Center Fort Sam Houston, Texas	1
Commanding Officer Medical Equipment Development Laboratory Fort Totten, New York	1
Director Walter Reed Army Institute of Research Walter Reed Army Medical Center Washington 12, D. C.	1

Other Army Agencies

Army War College, Library-B-205 Carlisle Barracks Carlisle, Pennsylvania	1
Command and General Staff College Fort Leavenworth, Kansas Attn: Library	1
Commanding General U. S. Continental Army Command Fort Monroe, Virginia	1
U. S. Continental Army Command U. S. Combat Development Experimentation Center Fort Ord, California	1
Office of Special Weapons Development Fort Bliss, Texas	1
Combat Operations Research Group Headquarters, Continental Army Command Fort Monroe, Virginia	1
President U. S. Army Air Defense Board Fort Bliss, Texas	1
Combat Developments Office U. S. Army Infantry School Fort Benning, Georgia	1
Superintendent United States Military Academy West Point, New York	1

DEPARTMENT OF THE NAVY

Chief of Naval Operations 1
Washington 25, D. C.

Chief of Naval Research 1
Office of Naval Research (Code 407)
Washington 25, D. C.

Director 1
U. S. Naval Research Laboratories
Washington 25, D. C.

Director 1
Weapons Systems Analysis Division
Bureau of Naval Weapons
Washington 25, D. C.

DEPARTMENT OF THE AIR FORCE

Headquarters U. S. Air Force (AFCOA) 1
Washington 25, D. C.

Commander 1
Air Force Systems Command
Andrews Air Force Base
Washington 25, D. C.

Commander 1
Office of Aero Space Research
Building T-D
Washington 25, D. C.

Director 1
Air University Library
Maxwell Air Force Base, Alabama
Attn: AUL-8641

Commanding Officer 1
Wright Patterson Air Force Base, Ohio

OTHER GOVERNMENT AGENCIES

Atomic Energy Commission 1
1901 Constitution Avenue, N. W.
Washington 25, D. C.

National Aeronautics and Space Agency 1
Washington 25, D. C.

National Bureau of Standards 1
Connecticut Avenue & Van Ness Streets, N. W.
Washington 25, D. C.

Human Performance Requirements 1
NASA, Ames Research Center
Moffett Field, California

Director 1
Science Information Exchange
Smithsonian Institution
Washington 25, D. C.

National Bureau of Standards 1
Boulder, Colorado

OTHER GOVERNMENT AGENCIES (continued)

National Institutes of Health Bethesda, Maryland Attn: Director	1
National Science Foundation Washington 25, D. C.	1
The Library of Congress Washington 25, D. C.	1

OTHER AGENCIES

British Joint Services Mission Thru: Foreign Liaison Office Assistant Chief of Staff, Intelligence Department of the Army Washington 25, D. C.	1
Canadian Joint Staff Thru: Foreign Liaison Office Assistant Chief of Staff, Intelligence Department of the Army Washington 25, D. C.	1
Human Resources Research Office The George Washington University 2013 G Street, N. W. Washington 7, D. C.	1
National Academy of Sciences 2101 Constitution Avenue, N. W. Washington, D. C.	1
Research Analysis Corporation 6935 Arlington Road Bethesda, Maryland	1
Special Operations Research Office American University 4501 Massachusetts Avenue, N. W. Washington 16, D. C.	1
Mathematics Research Center, U. S. Army University of Wisconsin Madison, Wisconsin	1

U. S. GOVERNMENT PRINTING OFFICE : 1965 O - 762 184